ΕΘΝΙΚΟ ΜΕΤΣΟΒΙΟ ΠΟΛΥΤΕΧΝΕΙΟ

ΣΧΟΛΗ ΠΟΛΙΤΙΚΩΝ ΜΗΧΑΝΙΚΩΝ

ΤΟΜΕΑΣ ΥΔΑΤΙΚΩΝ ΠΟΡΩΝ ΚΑΙ ΠΕΡΙΒΑΛΛΟΝΤΟΣ

ΕΡΓΑΣΤΗΡΙΟ ΛΙΜΕΝΙΚΩΝ ΕΡΓΩΝ

ΜΟΡΦΟΔΥΝΑΜΙΚΗ ΑΚΤΗΣ ΜΕ ΥΦΑΛΟΥΣ ΚΥΜΑΤΟΘΡΑΥΣΤΕΣ

MORPHODYNAMICS IN A BEACH WITH SUBMERGED BREAKWATERS

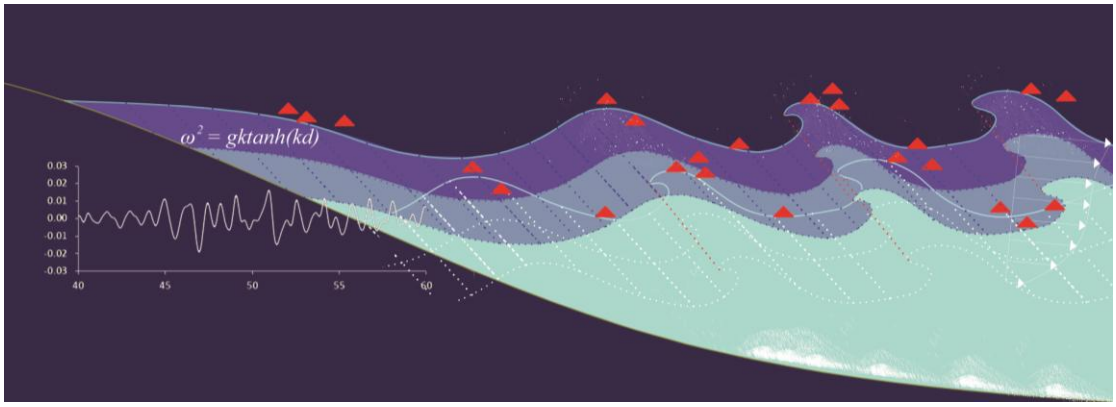

ΔΙΔΑΚΤΟΡΙΚΗ ΔΙΑΤΡΙΒΗ

ΓΕΩΡΓΙΟΣ Θ. ΚΛΩΝΑΡΗΣ

Διπλωματούχος Πολιτικός Μηχανικός Α.Π.Θ., ΜΔΕ Ε.Μ.Π.

Αθήνα, Νοέμβριος 2016

NATIONAL TECHNICAL UNIVERSITY OF ATHENS

SCHOOL OF CIVIL ENGINEERING

DEPARTMENT OF WATER RESOURCES AND ENVIRONMENTAL ENGINEERING

LABORATORY OF HARBOUR WORKS

MORPHODYNAMICS IN A BEACH WITH SUBMERGED BREAKWATERS

DISSERTATION

for the degree of Doctor of Philosophy

submitted to School of Civil Engineering of National Technical University of Athens

by

Georgios Th. Klonaris

Defended in public: 11 November 2016

in Athens, Greece

Members of the Examining Committee:

Prof. Emeritus Constantine D. Memos	School of Civil Eng., NTUA	*Supervisor*
Prof. Theophanis V. Karambas	Dep. of Civil Eng., AUTh	*Adv. Committee*
Dr. Rolf Deigaard	CED Dep., DHI	*Adv. Committee*
Prof. Athanassios A. Dimas	Dep. of Civil Eng., University of Patras	
Prof. Yannis N. Krestenitis	Dep. of Civil Eng., AUTh	
Associate Prof. Vicky K. Tsoukala	School of Civil Eng., NTUA	
Lecturer Samson A. Azorakos	School of Civil Eng., NTUA	

This doctoral thesis was financially supported by the “Onassis Foundation” and, partly, by the Danish Council for Strategic Research (DSF).

“All models are wrong. Some models are useful.”

George E. P. Box (1919-2013)

“The purpose of models is not to fit the data but to sharpen the questions.”

Samuel Karlin (1924-2007)

Preface

Our contact with the sea offers a strange feeling of mystery and charm at the same time. The picturesque and relaxing view of the calm water of a beautiful beach can be easily followed, in our mind, by the terrifying image of giant waves in deep oceans. They are two sides of the same coin. This power of the sea water to influence and visualize our feelings is very impressive and magical. It is this mystery that has been calling the sailors offshore to cross the oceans and investigate their secrets. And it is also the same charm that sometimes dresses with the simplicity of our carefree playing at the beach or the complexity of the physical processes that coastal scientists struggle with. Even from ancient times, the populations that have settled in coastal areas have recognized the importance of sea for their civilization and thus have dedicated divine figures and creatures for placating it.

One of the most attractive aspects of the sea environment is the impressive diversity of shore types and shapes. From the Scandinavian fjords to the indented coastlines of Greek islands, and from the mudflats of the Wadden Sea to the coral Pacific islands, a variety of coastal geomorphological processes are revealed. These processes, along with associated sediment transport mechanisms, hide the highest degree of uncertainty among the coastal phenomena. My personal curiosity to discover and understand these complex morphological processes in coastal zones was, by far, the major motivation for pursuing the present dissertation. Of course, my additional intention was to try to offer some original contribution to engineering solutions to the problem of coastal erosion and it would be flattering if this objective has been achieved. However, notwithstanding the extreme technocracy of present times, I have also tried to justify the philosophical point of view that a Ph.D. thesis, by definition, implies. This is something that I have tried to keep in mind throughout this four-year endeavour.

Upon the completion of this journey to uncharted for me seas, I would like to deeply thank my supervisor, Professor Emeritus Constantine Memos, for assigning this very interesting and challenging thesis, as well as for his invaluable support and guidance. I feel that I rarely meet people that can truly inspire me, and he is definitely one of the very few. I immensely enjoyed our collaboration and apart from being a great teacher, I also feel that I have made a good friend. I will be grateful for the rest of my life.

I would also like to sincerely thank Professor Theophanis Karambas for serving on my Advisory Committee. His contribution in choosing the topic of the dissertation is greatly appreciated. I have enjoyed our fruitful discussions during the course of my research and his comments and recommendations were invaluable.

I also profoundly thank Dr. Rolf Deigaard for serving on my Advisory Committee. Working with him was very helpful and instructive for me due to his experience and expertise in sediment transport processes. His guidance, support and comments were invaluable. I am doubly grateful to him for offering to me the opportunity to work for one year in DHI in Denmark. It was a great experience that I will always remember.

Special thanks are also due to Nils Drønen for his assistance and suggestions on modeling issues during my stay in DHI. I would also like to thank Ida Brøker, head of CED Department in DHI, for approving my stay there and for her interest for my progress. Many thanks also go to my close friends Maziar, Asger, Kevin, Michele and Rubén for their continuous support.

I would also like to thank Professor Athanassios Dimas for kindly providing the facilities of the Hydraulic Engineering Laboratory of the Civil Engineering Department at University of Patras and for his continuous assistance and guidance during the performance of the experiments. In addition, I thank him for serving on the defense committee of my dissertation. I am also grateful to Ph.D. candidate Nantia Galani for her invaluable help during this procedure and to Giannis Dimou for his technical support. Many thanks are also due to Dr. Fivos Sargentis and Associate Professor Dionissios Kalivas for their help in measuring the percentage of clay and organic matter of the soil material used in these experiments.

Special thanks are also due to Professor Yannis Krestenitis, Associate Professor Vicky Tsoukala and Lecturer Samson Azorakos for serving on the defense committee of my dissertation.

My sincere gratitude goes to my colleague and good friend Tasos for his comments, help and continuous support during our common course. The assistance and useful comments of the rest members of the research group, Michalis, Franka, and Maria-Eirini, are also acknowledged.

I would also like to thank K.A. Rakha and M.F. Gobbi for kindly providing the results of their models. In addition, many thanks go to S. Beji, M.B. Gravens, L. Hamm, J.T. Kirby, C. Makris and V. Roeber for kindly providing full experimental datasets. Useful comments and suggestions made by O.R. Sørensen and P.A. Madsen are also appreciated.

This work was accomplished through a scholarship provided by the "Onassis Foundation" which is gratefully acknowledged. In addition, financial support was also provided by the Danish Council for Strategic Research (DSF) under the project: Danish Coasts and Climate Adaptation - flooding risk and coastal protection (COADAPT), project no. 09-066869. This support is also acknowledged.

Most of all, I would like to thank my parents, Chrysa and Thodoros, and my sister, Vasiliki, for their continuous encouragement and support at all levels for accomplishing this work. It would not have been possible without them. Conducting a doctoral thesis is a lonely trip hiding many mind traps. I would have never made it without my very special Elena. I am grateful for

her support and patience. There were many instances in which I was close to quitting, but she was there to carry me. I feel that a part of this work was made by her.

The research effort began in October 2012 and its greatest part was conducted at the Laboratory of Harbour Works in National Technical University of Athens. From March 2013 to March 2014 a part of the work was carried out at DHI in Hørsholm in Denmark. Finally, the experiments were performed at the Hydraulic Engineering Laboratory of University of Patras from May to September 2015.

Athens, September 2016

Georgios Klonaris

Εκτενής Περίληψη
(Extended Abstract)

Μορφοδυναμική ακτής με ύφαλους κυματοθραύστες

του Γεώργιου Θ. Κλωνάρη

Εθνικό Μετσόβιο Πολυτεχνείο
Σχολή Πολιτικών Μηχανικών
Τομέας Υδατικών Πόρων και Περιβάλλοντος
Εργαστήριο Λιμενικών Έργων

1. Εισαγωγή

Η παράκτια ζώνη αποτελεί ελκυστικό περιβάλλον για τον άνθρωπο από τα αρχαία χρόνια. Τα παράκτια ύδατα προσέφεραν πάντοτε ποιοτική τροφή, δυνατότητες ανάπτυξης του εμπορίου και της ναυτιλίας, στρατιωτικό πλεονέκτημα και, πιο πρόσφατα, τη δυνατότητα βιομηχανικής ανάπτυξης και δραστηριοτήτων αναψυχής. Σήμερα, πάνω από το 40% του παγκόσμιου πληθυσμού κατοικεί σε παράκτιες περιοχές, όπου συγκεντρώνεται και η πλειοψηφία των μεγαλουπόλεων. Η υπερσυγκέντρωση πληθυσμών στις ευαίσθητες αυτές ζώνες συνεπάγεται υπερβολικές πιέσεις τόσο στη στεριά, όσο και στη θάλασσα. Οι πιο κρίσιμες ανάμεσά τους αφορούν στην υπερεκμετάλλευση της γης, όσο το δυνατόν εγγύτερα στη θάλασσα, για λόγους στέγασης και βιομηχανικής ή τουριστικής ανάπτυξης. Συνεπώς, οι πιέσεις αυτές μεταφράζονται, κατ' ουσίαν, στην ανάγκη για διατήρηση μιας σταθερής ακτογραμμής.

Αυτή η απαίτηση βρίσκεται συχνά σε σύγκρουση με τις φυσικές διεργασίες που λαμβάνουν χώρα στις παράκτιες περιοχές και μεταβάλλουν διαρκώς την ακτογραμμή. Το αποτέλεσμα αυτής της διαμάχης πολύ συχνά είναι η εκτεταμένη διάβρωση των ακτών. Το πρόβλημα εντείνεται από την κλιματική αλλαγή με τη σχετιζόμενη άνοδο της στάθμης της θάλασσας και τις συχνές καταστροφικές πλημμύρες. Μάλιστα, οι επιστημονικές προβλέψεις εμφανίζονται δυσοίωνες, καθώς το πρόβλημα αναμένεται να ενταθεί τα προσεχή χρόνια, αυξάνοντας την επικινδυνότητα στις παραθαλάσσιες περιοχές.

Μέχρι πρόσφατα, η απουσία βιώσιμου σχεδιασμού στις παράκτιες ζώνες επέφερε ραγδαία αύξηση της διάβρωσης των ακτών παγκοσμίως. Σήμερα, τα περισσότερα κράτη εφαρμόζουν νομοθεσία για την προστασία του περιβάλλοντος που επιβάλλει περιορισμούς στις

κατασκευές πλησίον της ακτογραμμής, καθώς και την εκπόνηση ακτομηχανικών μελετών και μελετών περιβαλλοντικών επιπτώσεων. Παρόλα αυτά, για πολλά χρόνια, τα παράκτια έργα βασίζονταν στη λογική της λεγόμενης «σκληρής» προστασίας η οποία περιλαμβάνει την κατασκευή ογκωδών έργων από σκυρόδεμα ή φυσικούς ογκόλιθους, παρόμοια με τους κυματοθραύστες των λιμένων. Επιπλέον, η επίδραση της κατασκευής τέτοιων έργων, σε ακτομηχανικό επίπεδο, αντιμετωπιζόταν ημι-εμπειρικά και αποσπασματικά. Έτσι, σε πολλές περιπτώσεις, ο σχεδιασμός οδηγούσε στο ακριβώς αντίθετο από το επιθυμητό αποτέλεσμα, ενώ οι περιβαλλοντικές επιπτώσεις αγνοούνταν, π.χ. δραστική διατάραξη των πληθυσμών χλωρίδας και πανίδας, μειωμένη ανανέωση των υδάτων και αισθητική υποβάθμιση της περιοχής.

Πλέον, έχει γίνει ευρέως κατανοητό ότι η ευαίσθητη παράκτια ζώνη απαιτεί ένα ολοκληρωμένο σχέδιο διαχείρισης και όχι αποσπασματικές λύσεις. Στο πλαίσιο αυτό, μία ηπιότερη προσέγγιση για την προστασία των ακτών έχει προταθεί και εφαρμοστεί, η οποία περιλαμβάνει έργα όπως η τεχνητή αναπλήρωση, η αποστράγγιση των παραλιών (beach drainage), η διαχείριση των αμμόλοφων (sand dune management), κ.α. Ανάμεσα στις ήπιες αυτές μεθόδους, τη «σκληρότερη» όλων αποτελεί η κατασκευή των ύφαλων κυματοθραυστών.

Κατά τη διάρκεια των τελευταίων ετών, οι ύφαλοι κυματοθραύστες έχουν κινήσει το επιστημονικό ενδιαφέρον ως μία εναλλακτική λύση έναντι των συμβατικών για την παράκτια προστασία. Αποτελούν ηπιότερη μέθοδο προστασίας και συνεπώς είναι γενικά λιγότερο αποτελεσματικά, από άποψη παράκτιας μηχανικής, σε σχέση με τις έξαλες κατασκευές. Ωστόσο, σε περιπτώσεις ήπιου υδροδυναμικού καθεστώτος τα ύφαλα έργα μπορεί να είναι πιο ελκυστικά από τα συμβατικά, καθότι είναι περισσότερο φιλικά προς το περιβάλλον, υπερτερούν αισθητικά και είναι συνήθως χαμηλότερου κόστους.

Η επιστημονική έρευνα γύρω από τους ύφαλους κυματοθραύστες ξεκίνησε σχετικά πρόσφατα και περιλαμβάνει τρεις μεθόδους για τη μελέτη της συμπεριφοράς τους: παρατηρήσεις πεδίου, εργαστηριακά πειράματα σε φυσικά μοντέλα και αριθμητική προσομοίωση. Ένας σημαντικός αριθμός εργαστηριακών πειραμάτων έχει εκτελεστεί από τη δεκαετία του ’70 με στόχο τη διερεύνηση, κυρίως, της υδροδυναμικής συμπεριφοράς των ύφαλων κυματοθραυστών. Το πιο ολοκληρωμένο σετ εργαστηριακών μετρήσεων περιλαμβάνεται στο ευρωπαϊκό ερευνητικό πρόγραμμα DELOS (Kramer *et al*., 2005). Αντιθέτως, ελάχιστες πειραματικές εργασίες εξετάζουν την εξέλιξη της μορφολογίας στα κατάντη ύφαλων κυματοθραυστών (Groenewoud *et al*., 1996; van der Biezen *et al*., 1997; Turner *et al*., 2001).

Επιπλέον, αρκετά αριθμητικά μοντέλα έχουν αναπτυχθεί για την περιγραφή της κυματικής διάδοσης και των κυματογενών ρευμάτων πάνω και γύρω από ύφαλους κυματοθραύστες. Τα περισσότερα εξ αυτών αντιμετωπίζουν τους τελευταίους ως αδιαπέρατες κατασκευές και

μόνο λίγα λαμβάνουν υπόψη τη διαπερατότητά τους (Cruz *et al*., 1997; Hsiao *et al*., 2002; Avgeris *et al*., 2004; Chen, 2006). Αντιθέτως, ελάχιστα αριθμητικά μοντέλα έχουν παρουσιαστεί για την περιγραφή της μορφολογίας στα κατάντη ύφαλων κυματοθραυστών (Zyserman *et al*., 1999; Lesser *et al*., 2003; Koutsouvela *et al*., 2007; Ranasinghe *et al*., 2010; Karambas and Samaras, 2014). Ωστόσο, ελάχιστα εξ αυτών έχουν επαληθευτεί με μετρήσεις που αναφέρονται σε δύο οριζόντιες διαστάσεις.

Η παρούσα Διδακτορική Διατριβή εντάσσεται στο πλαίσιο της έρευνας σχετικά με τη συμπεριφορά των ύφαλων κυματοθραυστών ως έργων προστασίας των ακτών. Οι βασικοί στόχοι της συγκεκριμένης ερευνητικής εργασίας είναι οι εξής:

- Να συνεισφέρει στην κατανόηση των σύνθετων υδροδυναμικών και μορφοδυναμικών διεργασιών που λαμβάνουν χώρα σε παράκτιες ζώνες οι οποίες προστατεύονται από απλούς ή συστήματα ύφαλων κυματοθραυστών.

- Να αναπτυχθεί ένα ολοκληρωμένο αριθμητικό μοντέλο για την προσομοίωση της κυματικής διάδοσης, του πεδίου των κυματογενών ρευμάτων, της παράκτιας στερεομεταφοράς, της διάβρωσης και απόθεσης και τελικά να περιγράφει την εξέλιξη του κάθετου στην ακτή προφίλ του πυθμένα, καθώς και της ακτογραμμής, στα κατάντη ενός συστήματος ύφαλων διαπερατών κυματοθραυστών.

- Να εκτελεστούν εργαστηριακά πειράματα σε δύο οριζόντιες διαστάσεις που αφορούν στην εξέλιξη της μορφολογίας αμμώδους πυθμένα στα κατάντη ύφαλου διαπερατού κυματοθραύστη. Ο στόχος των πειραμάτων ήταν διπλός. Πρώτον, να εξαχθούν κάποια συμπεράσματα για τη συμπεριφορά των έργων αυτών, απευθείας από τις παρατηρήσεις. Δεύτερον, να εξαχθεί ένα σετ μετρήσεων για την επαλήθευση του αριθμητικού μοντέλου.

- Να εκτελεστεί μία σειρά αριθμητικών πειραμάτων, ώστε να μελετηθεί η απόκριση της ακτογραμμής σε ένα σύστημα ύφαλων κυματοθραυστών. Σκοπός ήταν η εξαγωγή κάποιων γενικών κατευθυντήριων γραμμών σχετικά με το σχεδιασμό των έργων αυτών από ακτομηχανική άποψη.

2. Μεθοδολογία προσέγγισης

Όπως αναφέρθηκε παραπάνω, αντικείμενο της Διατριβής αποτελεί η μελέτη της εξέλιξης της μορφολογίας του πυθμένα κατάντη ύφαλων κυματοθραυστών. Οι μορφολογικές αυτές αλλαγές εξετάστηκαν τόσο αριθμητικά, όσο και πειραματικά σε δεξαμενή κυμάτων.

Συγκεκριμένα, αναπτύχθηκε ένα σύνθετο αριθμητικό μοντέλο που συνδυάζει τέσσερα υπο-μοντέλα σε μία ενιαία μορφή. Το σύνθετο αυτό εργαλείο περιλαμβάνει: κυματικό μοντέλο,

υδροδυναμικό μοντέλο για την προσομοίωση των κυματογενών ρευμάτων, μοντέλο παράκτιας στερεομεταφοράς και μοντέλο μορφοδυναμικής. Τα υπο-μοντέλα εφαρμόζονται διαδοχικά, το ένα μετά το άλλο, σε μία αυτοματοποιημένη και ενοποιημένη διαδικασία, με τελικό αποτέλεσμα την προσομοίωση βραχυπρόθεσμων μεταβολών της μορφολογίας του πυθμένα. Μάλιστα, το σύνθετο μοντέλο επεκτάθηκε σε πορώδεις πυθμένες, ώστε να εφαρμόζεται και για διαπερατούς ύφαλους κυματοθραύστες. Η ακρίβεια και αξιοπιστία καθενός από τα υπομοντέλα ελέγχθηκε μέσω εκτενούς επαλήθευσης με πειραματικά δεδομένα της διεθνούς βιβλιογραφίας.

Επιπλέον, εκτελέστηκαν εργαστηριακά πειράματα δύο οριζόντιων διαστάσεων, κατά τη διάρκεια των οποίων μετρήθηκε η εξέλιξη της τοπογραφίας αμμώδους πυθμένα κατάντη διαπερατού ύφαλου κυματοθραύστη. Οι μετρήσεις αυτές χρησίμευσαν και για την επαλήθευση του σύνθετου αριθμητικού μοντέλου.

Τέλος, εκτελέστηκε μια σειρά από αριθμητικά πειράματα σε διατάξεις που περιλάμβαναν συστήματα ύφαλων κυματοθραυστών. Συγκεκριμένα, εξετάστηκε η απόκριση της ακτογραμμής στις μεταβολές κάποιων βασικών παραμέτρων σχεδιασμού των ύφαλων κυματοθραυστών. Έτσι, εξήχθησαν κάποια συμπεράσματα και γενικές κατευθυντήριες γραμμές για το σχεδιασμό των έργων αυτών.

Η μεγάλη πλειοψηφία των μοντέλων στερεομεταφοράς και μορφολογίας που έχουν παρουσιαστεί λαμβάνουν ως δεδομένα εισόδου τα αποτελέσματα ολοκληρωμένων στην περίοδο κυματικών μοντέλων (phase-averaged models). Επιπλέον, τα επιμέρους υπο-μοντέλα εφαρμόζονται από το χρήστη ξεχωριστά το ένα από το άλλο, σε μία επαναληπτική διαδικασία που ολοκληρώνεται όταν παρατηρηθεί ότι η αλλαγή της μορφολογίας είναι πλέον ασήμαντη. Μάλιστα, επειδή η διαδικασία αυτή είναι επίπονη και χρονοβόρα, στην πράξη πολλές φορές εφαρμόζεται περιορισμένος αριθμός επαναλήψεων, με στόχο τον υπολογισμό μόνο των αρχικών ρυθμών διάβρωσης και απόθεσης.

Αντιθέτως, στην παρούσα διατριβή επιλέχθηκε ως βάση του σύνθετου μοντέλου ένα μη ολοκληρωμένο στην περίοδο κυματικό μοντέλο (phase-resolving model) και συγκεκριμένα ένα μοντέλο τύπου Boussinesq. Ο συνδυασμός ενός τέτοιου κυματικού μοντέλου με ένα μοντέλο στερεομεταφοράς αποτελεί αντικείμενο σύγχρονης έρευνας λόγω των πλεονεκτημάτων του. Συγκεκριμένα, τα μοντέλα τύπου Boussinesq μπορούν να υπολογίσουν τη μη γραμμικότητα και την ασυμμετρία των κυμάτων, καθώς και τις μη γραμμικές αλληλεπιδράσεις τους. Η συμπερίληψη των διεργασιών αυτών είναι πολύ σημαντική για τον ορθό υπολογισμό της στερεομεταφοράς καθώς, εκτός των άλλων, λαμβάνεται υπόψη η αλληλουχία των κυμάτων και τα φαινόμενα υστέρησης της απόκρισης του ιζήματος στις μεταβολές του υδροδυναμικού πεδίου. Επιπλέον, η αυτόματη σύζευξη των υπο-μοντέλων σε μία ενιαία διαδικασία διευκολύνει την προσομοίωση της αλλαγής της μορφολογίας για ένα προδιαγεγραμμένο χρονικό διάστημα ή μέχρι την εγκαθίδρυση μιας κατάστασης ισορροπίας.

Τέλος, η εφαρμογή της αποτελεσματικής μεθόδου που βασίζεται στον ‘morphological acceleration factor’ (Morfac), f_{MOR}, επιτρέπει την προσομοίωση μορφολογικών μεταβολών σε μεγαλύτερες παράκτιες περιοχές και χρονικές κλίμακες (Lesser *et al*., 2004; Roelvink, 2006). Οι μορφολογικές διεργασίες εξελίσσονται με αρκετά πιο αργό ρυθμό σε σχέση με τις μεταβολές του υδροδυναμικού πεδίου. Η προαναφερθείσα τεχνική επιτρέπει το συνδυασμό των δύο αυτών χρονικών κλιμάκων, ώστε να καθίσταται δυνατή η πρόβλεψη της εξέλιξης της μορφολογίας του πυθμένα σε πρακτικές εφαρμογές. Εν προκειμένω, λόγω του αυξημένου υπολογιστικού κόστους ενός phase-resolving μοντέλου, εξετάστηκαν μόνο βραχυχρόνιες μορφολογικές μεταβολές, της τάξης ωρών ή λίγων ημερών. Η υπολογιστική πορεία που ακολουθείται φαίνεται στο Σχ. 1.

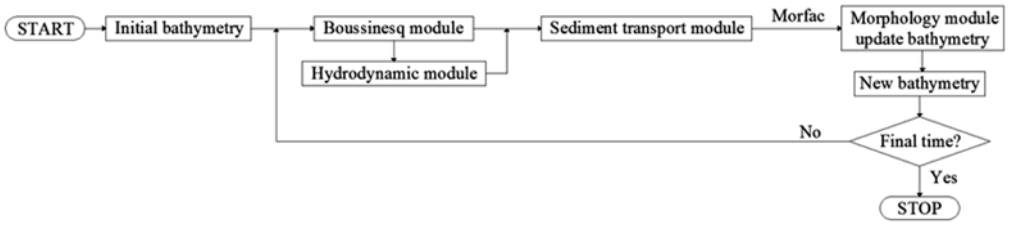

Σχ. 1. Διάγραμμα υπολογιστικής πορείας που συνδυάζει τα εξής μοντέλα: κυματικό, υδροδυναμικό, στερεομεταφοράς και γεωμορφολογίας.

Η ερευνητική εργασία διακρίνεται σε τέσσερα στάδια, τα οποία περιγράφονται στη συνέχεια. Το πρώτο βήμα αφορά στην επιλογή του κατάλληλου κυματικού μοντέλου που αποτελεί τη βάση της Διατριβής. Η επιλογή έγινε μέσα από μια διαδικασία μαθηματικής ανάλυσης και σύγκρισης διάφορων μοντέλων. Το δεύτερο στάδιο αφορά στην πλήρη ανάπτυξη και επέκταση του σύνθετου αριθμητικού μοντέλου. Το τρίτο βήμα περιλαμβάνει την εκτέλεση εργαστηριακών πειραμάτων και την επαλήθευση του μοντέλου με τις μετρήσεις αυτών. Το τελευταίο στάδιο αναφέρεται σε αριθμητικά πειράματα που εκτελέστηκαν, ώστε να μελετηθεί η απόκριση της ακτογραμμής σε ένα σύστημα ύφαλων κυματοθραυστών και να εξαχθούν κάποια πρακτικά συμπεράσματα για το σχεδιασμό τους.

3. Ανάλυση μη γραμμικών μοντέλων τύπου Boussinesq ανώτερης τάξης

Το κυματικά μοντέλα τύπου Boussinesq αποτελούν μία επέκταση των μη γραμμικών εξισώσεων μακρών κυματισμών (NSWE), ώστε να ληφθεί υπόψη και η διασπορά των κυμάτων. Για τη μελέτη των χαρακτηριστικών τους είναι χρήσιμο να οριστούν δύο αδιάστατες παράμετροι, $\varepsilon = H'/ d_o'$ και $\sigma^2 = (d_o'/ L')^2$, όπου d_o', L' και H' είναι, αντίστοιχα, ένα βάθος, μήκος και ύψος κύματος αναφοράς. Η πρώτη παράμετρος εκφράζει τα χαρακτηριστικά μη γραμμικότητας των εξισώσεων, ενώ η δεύτερη τα χαρακτηριστικά διασποράς. Στις μη γραμμικές εξισώσεις ρηχών νερών η διασπορά των κυμάτων θεωρείται

αμελητέα, $O(\sigma^2) << 1$. Ωστόσο, στην αρχική θεωρία του Boussinesq (1872) και στις μετέπειτα «κλασικές» εξισώσεις του Peregrine (1967), ο περιορισμός αυτός χαλαρώνει ώστε να επιτρέπεται ελαφρά μη γραμμικότητα και διασπορά των κυμάτων, ήτοι:

$$O(\varepsilon) = O(\sigma^2) < 1 \tag{1}$$

Στα επόμενα χρόνια, ο αρχικός αυτός περιορισμός άρθηκε σε μεγάλο βαθμό με αποτέλεσμα την επέκταση της ισχύος των μοντέλων τύπου Boussinesq σε ολόκληρο το εύρος βαθών, από τα ρηχά έως τα βαθιά νερά. Τα μοντέλα αυτά περιλαμβάνουν εξισώσεις ανώτερης τάξης ως προς τη μη γραμμικότητα και τη διασπορά, οι οποίες συνήθως εξάγονται μέσω αναπτυγμάτων σε σειρές των αρχικών εξισώσεων ορμής ως προς την παράμετρο ε.

Μέσα από μία εκτενή βιβλιογραφική ανασκόπηση των διάφορων μοντέλων τύπου Boussinesq που έχουν παρουσιαστεί, τελικώς επιλέχθηκαν δύο μοντέλα. Το πρώτο είναι το μοντέλο των Karambas and Koutitas (2002), το οποίο είναι βελτιωμένης διασποράς και μη γραμμικότητας, περιλαμβάνει όρους $O(1, \varepsilon, \sigma^2, \varepsilon\sigma^2)$ και στο εξής θα αναφέρεται ως KK02. Το δεύτερο είναι το μοντέλο των Karambas and Memos (2009), το οποίο είναι πλήρους γραμμικής διασποράς και ήπιας μη γραμμικότητας, περιλαμβάνει όρους $O(1, \varepsilon, \sigma^2)$ και στο εξής θα αναφέρεται ως KM09.

Στη συνέχεια, εξήχθη μία βελτιωμένη έκδοση του μοντέλου KK02 ως προς τη μη γραμμικότητα. Η μαθηματική διαδικασία που ακολουθήθηκε είναι παρόμοια με αυτή των Karambas and Koutitas (2002), όπου η ταχύτητα των μορίων του νερού θεωρείται ομοιόμορφη κατά βάθος. Η διαφορά είναι ότι στην προκειμένη περίπτωση διατηρήθηκαν οι επιπλέον όροι $O(\varepsilon^2\sigma^2)$ στην τελική εξίσωση ορμής, γεγονός που αναβαθμίζει τα μη γραμμικά χαρακτηριστικά των εξισώσεων τύπου Boussinesq. Οι μονοδιάστατες εξισώσεις του νέου αυτού μοντέλου, το οποίο στο εξής θα αναφέρεται ως KK02e, είναι σε αδιάστατη μορφή:

$$\frac{\partial \zeta}{\partial t} + \frac{\partial[(d+\varepsilon\zeta)U]}{\partial x} = 0 \tag{2}$$

$$\begin{aligned}
\frac{\partial U}{\partial t} + \varepsilon U\frac{\partial U}{\partial x} + \frac{\partial \zeta}{\partial x} = {} & \sigma^2\frac{d^2+2\varepsilon d\zeta}{3}\frac{\partial^3 U}{\partial x^2\partial t} + \sigma^2(d+\varepsilon\zeta)\frac{\partial d}{\partial x}\frac{\partial^2 U}{\partial x\partial t} + \varepsilon\sigma^2\frac{d^2}{3}\left(U\frac{\partial^3 U}{\partial x^3} - \frac{\partial U}{\partial x}\frac{\partial^2 U}{\partial x^2}\right) \\
& + \varepsilon\sigma^2\left(d\frac{\partial \zeta}{\partial x}\frac{\partial^2 U}{\partial x\partial t} + d\frac{\partial d}{\partial x}U\frac{\partial^2 U}{\partial x^2} + \frac{\partial d}{\partial x}\frac{\partial \zeta}{\partial x}\frac{\partial U}{\partial t}\right) \\
& + \varepsilon^2\sigma^2\left(\frac{\zeta^2}{3}\frac{\partial^3 U}{\partial x^2\partial t} + \zeta\frac{\partial \zeta}{\partial x}\frac{\partial^2 U}{\partial x\partial t}\right) + \varepsilon^2\sigma^2\frac{2d\zeta}{3}\left(U\frac{\partial^3 U}{\partial x^3} - \frac{\partial U}{\partial x}\frac{\partial^2 U}{\partial x^2}\right) \\
& + \varepsilon^2\sigma^2\left(Ud\frac{\partial^2 U}{\partial x^2}\frac{\partial \zeta}{\partial x} + \frac{\partial d}{\partial x}U\frac{\partial U}{\partial x}\frac{\partial \zeta}{\partial x} + \frac{\partial d}{\partial x}U\frac{\partial^2 U}{\partial x^2}\zeta\right) - \varepsilon^2\sigma^2 d\frac{\partial \zeta}{\partial x}\left(\frac{\partial U}{\partial x}\right)^2 \\
& + \sigma^2 \mathrm{B} d^2\left(\frac{\partial^3 U}{\partial x^2\partial t} + \frac{\partial^3 \zeta}{\partial x^3} + \varepsilon\frac{\partial^2\left(U\frac{\partial U}{\partial x}\right)}{\partial x^2}\right) + \sigma^2 2\mathrm{B}_2 d\frac{\partial d}{\partial x}\left(\frac{\partial^2 U}{\partial x\partial t} + \frac{\partial^2 \zeta}{\partial x^2} + \varepsilon\frac{\partial\left(U\frac{\partial U}{\partial x}\right)}{\partial x}\right)
\end{aligned} \tag{3}$$

όπου ζ είναι η ανύψωση της ελεύθερης επιφάνειας, U είναι η μέση κατά βάθος οριζόντια ταχύτητα των μορίων του νερού, d είναι το βάθος ηρεμίας, B και B_2 είναι ελεύθερες παράμετροι, x είναι η οριζόντια διάσταση και t ο χρόνος.

Μία επιπρόσθετη διαφορά με το μοντέλο KK02 είναι η ύπαρξη στην εξ. (3) της επιπλέον παραμέτρου B_2, πέραν της B. Η πρώτη εισήχθη για τη βελτίωση της περιγραφής της γραμμικής ρήχωσης, ενώ η δεύτερη ελέγχει τη γραμμική διασπορά.

Επιπλέον, εξήχθησαν δύο εκδόσεις ανώτερης τάξης μη γραμμικότητας του μοντέλου KM09. Στις περιπτώσεις αυτές, η πορεία που ακολουθήθηκε δεν ήταν η ίδια με αυτή στο πρωταρχικό μοντέλο, καθώς η εφαρμογή ενός μετασχηματισμού Fast Fourier σε όρους ανώτερης τάξης οδηγεί σε πολύ σύνθετους υπολογισμούς, οι οποίοι, πιθανότατα, δεν επιδέχονται αναλυτική λύση. Αντιθέτως, η σημειακή οριζόντια ταχύτητα εκφράστηκε ως συνάρτηση της μέσης κατά βάθος τιμής της και προέκυψε η αδιάστατη εξίσωση ορμής κατά x:

$$\frac{\partial U}{\partial t} + \varepsilon U \frac{\partial U}{\partial x} = -\frac{\partial \zeta}{\partial x} + \frac{1}{k^2}\left[\frac{\sigma kd}{\tanh(\sigma kd)} - 1\right]\frac{\partial^3 U}{\partial x^2 \partial t}$$

$$+\varepsilon\left[\frac{\sigma d}{\sinh(\sigma kd)}\right]^2\left(\frac{3}{4}\cosh(2\sigma kd) + \frac{1}{8}\frac{\sinh(2\sigma kd)}{\sigma kd} - 1\right)\frac{\partial U}{\partial x}\frac{\partial^2 U}{\partial x^2}$$

$$+\varepsilon\left[\frac{\sigma d}{\sinh(\sigma kd)}\right]^2\left(\frac{1}{4}\cosh(2\sigma kd) - \frac{1}{8}\frac{\sinh(2\sigma kd)}{\sigma kd}\right)U\frac{\partial^3 U}{\partial x^3} \qquad (4)$$

όπου k είναι ο κυματαριθμός.

Το μοντέλο που περιλαμβάνει τις εξισώσεις συνέχειας (2) και ορμής (4) αποτελεί μία αναβάθμιση του KM09 ως προς τη μη γραμμικότητα, καθώς εμπεριέχει τους επιπλέον όρους $O(\varepsilon\sigma^2)$ και στο εξής θα αναφέρεται ως KM09em. Αξίζει να σημειωθεί ότι η διαδικασία που περιγράφηκε παραπάνω οδηγεί αυστηρά σε μία ελαφρώς διαφορετική εκδοχή της εξ. (4), όπου ο συντελεστής του όρου μετάθεσης, $U\frac{\partial U}{\partial x}$, δεν είναι μονάδα, αλλά $\left[\frac{\sigma kd}{\sinh(\sigma kd)}\right]^2\left[1 + \frac{\sinh(2\sigma kd)}{2\sigma kd}\right]$. Το μοντέλο που περιλαμβάνει την εκδοχή αυτή της εξίσωσης ορμής και την εξίσωση συνέχειας (2) αναφέρεται ως KM09e και περιλαμβάνει επίσης όρους $O(1, \varepsilon, \sigma^2, \varepsilon\sigma^2)$. Το θεωρητικό υπόβαθρο του KM09e βασίζεται σε μία ακριβή λύση πρώτης τάξης της εξίσωσης συνέχειας. Η υπόθεση αυτή δεν είναι ιδιαίτερα ακριβής στα ρηχά νερά και έτσι το μοντέλο KM09e δεν τείνει στις μη γραμμικές εξισώσεις μακρών κυματισμών για $kd \to 0$. Η ασυνέπεια αυτή οδήγησε στη θεώρηση του τροποποιημένου μοντέλου KM09em.

Εν συνεχεία, έγινε μία μαθηματική διερεύνηση και σύγκριση των γραμμικών και μη γραμμικών χαρακτηριστικών των πέντε προαναφερθέντων μοντέλων, καθώς και αυτού των Madsen and Schäffer (1998), το οποίο περιλαμβάνει όρους έως $O(\varepsilon\sigma^4)$ και στο εξής θα αναφέρεται ως MS98. Καταρχάς, εφαρμόστηκε μία ανάλυση Fourier $1^{ης}$, $2^{ης}$ και $3^{ης}$ τάξης σε

οριζόντιο πυθμένα. Στην ανάλυση $1^{ης}$ τάξης, ως λύση αναφοράς θεωρήθηκε η γνωστή σχέση διασποράς του Airy. Τα μοντέλα KK02 και KK02e δίνουν την ίδια λύση πρώτης τάξης, καθώς συμπίπτουν αν διατηρηθούν μόνο οι γραμμικοί όροι $O(1, \sigma^2)$. Το ίδιο ισχύει και για τα μοντέλα KM09, KM09e και KM09em. Τα αποτελέσματα συνοψίζονται συγκριτικά στο Σχ. 2, όπου $\kappa = kd$ είναι το αδιάστατο βάθος.

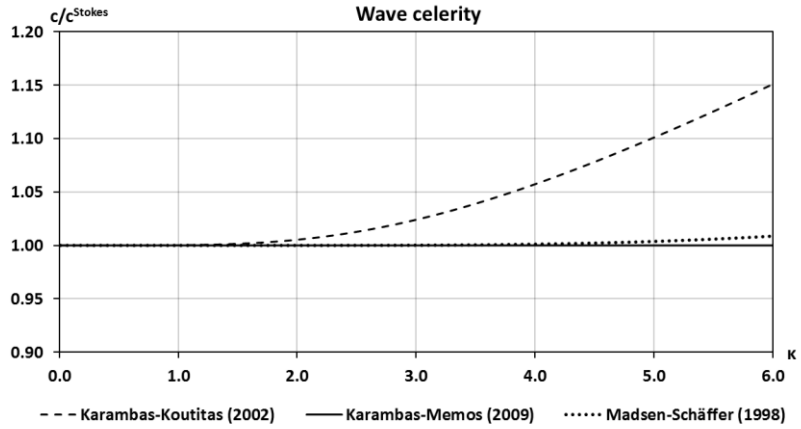

Σχ. 2. Αδιάστατη ταχύτητα φάσης, c/c^{Stokes}, για τα μοντέλα KK02, KM09 και MS98, όπου η ταχύτητα c^{Stokes} δίνεται από τη γραμμική θεωρία.

Από το παραπάνω σχήμα προκύπτει ότι τα μοντέλα KK02 και KK02e περιγράφουν με μεγάλη ακρίβεια τη γραμμική διασπορά έως το όριο των βαθειών νερών, $\kappa \approx 3$, ενώ το μοντέλο MS98 δίνει άριστα αποτελέσματα μέχρι $\kappa = 6$. Η ελαχιστοποίηση του σφάλματος για τα δύο πρώτα μοντέλα προκύπτει για την τιμή $\mathrm{B} = 1/15$. Τα μοντέλα KM09, KM09e και KM09em είναι πλήρους γραμμικής διασποράς, οπότε δεν έχουν κανέναν περιορισμό βάθους ως προς το χαρακτηριστικό αυτό.

Συνεχίζοντας την ανάλυση σε 2^{η} τάξη προκύπτουν οι λύσεις των Σχημάτων 3 και 4. Όπως παραπάνω, οι λύσεις για τα μοντέλα KK02 και KK02e ταυτίζονται και σε 2^{η} τάξη. Αποδεχόμενοι ένα σφάλμα έως 10%, η δεύτερη αρμονική υπολογίζεται με ακρίβεια μέχρι $\kappa \approx 1.19$. Το ίδιο όριο για το μοντέλο MS98 είναι $\kappa \approx 1.83$. Αντιθέτως, τα μοντέλα KM09, KM09e και KM09em υπερεκτιμάνε τη 2^{η} αρμονική στα ρηχά και ενδιάμεσου βάθους νερά. Τα KM09e και KM09em προσφέρουν μία βελτίωση στα βαθειά νερά σε σχέση με το KM09 λόγω της συμπερίληψης των επιπλέον όρων $O(\varepsilon\sigma^2)$. Ωστόσο, παρότι και τα τρία μοντέλα είναι πλήρους γραμμικής διασποράς, τα μη γραμμικά χαρακτηριστικά τους είναι σαφώς κατώτερα από αυτά των KK02 και KK02e.

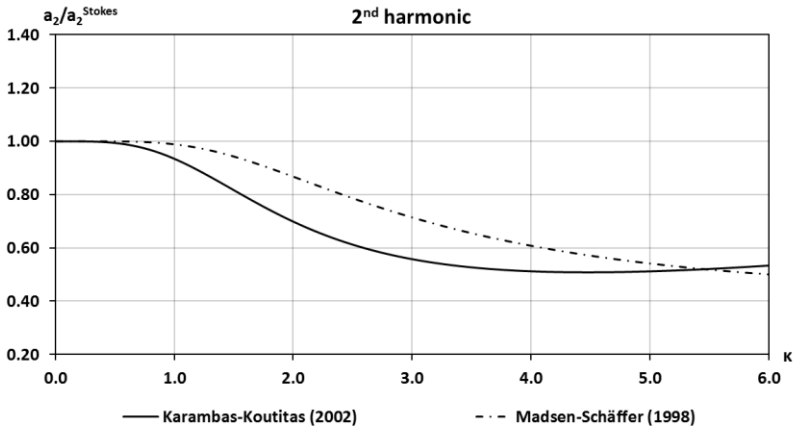

Σχ. 3. Αδιάστατο εύρος της $2^{ης}$ αρμονικής, a_2/a_2^{Stokes}, για τα μοντέλα KK02 και MS98, όπου το εύρος a_2^{Stokes} προκύπτει από τη λύση των Skjelbreia and Hendrickson (1960).

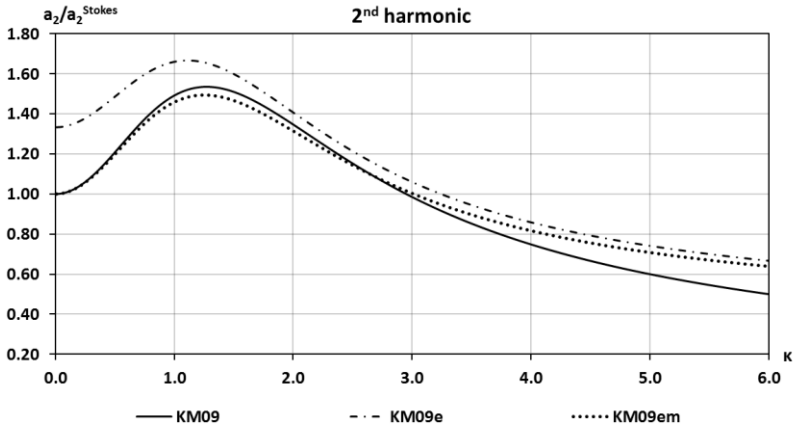

Σχ. 4. Αδιάστατο εύρος της $2^{ης}$ αρμονικής, a_2/a_2^{Stokes}, για τα μοντέλα KM09, KM09e και KM09em, όπου το εύρος a_2^{Stokes} προκύπτει από τη λύση των Skjelbreia and Hendrickson (1960).

Η ανάλυση συνεχίστηκε στην $3^{η}$ τάξη και στο Σχ. 5 φαίνεται ενδεικτικά η λύση για τη μη γραμμική διασπορά των μοντέλων KK02, KK0e και MS98. Παρατηρείται ότι το μοντέλο KK02e προσφέρει μία βελτίωση σε σχέση με τον προκάτοχό του, KK02.

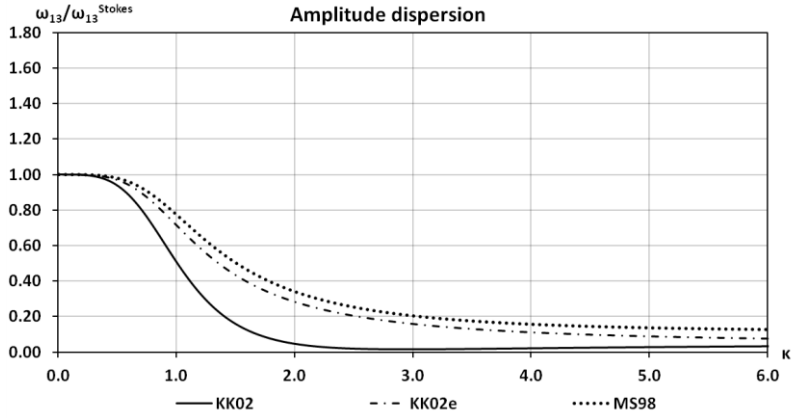

Σχ. 5. Αδιάστατη μη γραμμική διασπορά ύψους κύματος, $\omega_{13}/\omega_{13}^{\text{Stokes}}$, για τα μοντέλα KK02, KK02e και MS98, όπου ο όρος $\omega_{13}^{\text{Stokes}}$ προκύπτει από τη λύση των Skjelbreia and Hendrickson (1960).

Εκτός των παραπάνω, εφαρμόστηκε και γραμμική ανάλυση ρήχωσης. Λύση αναφοράς θεωρήθηκε αυτή των Madsen and Sørensen (1992) για το γραμμικό τελεστή ρήχωσης, γ_0^{Stokes}. Τα μοντέλα KM09, KM09e και KM09em έχουν θεωρητικά εξαχθεί για οριζόντιους πυθμένες (παρότι μπορούν να εφαρμοστούν και σε ήπιες κλίσεις) και για το λόγο αυτό η ανάλυση ρήχωσης δεν ήταν δυνατό να εφαρμοστεί. Οι λύσεις για το μοντέλα KK02 (όμοια για το KK02e) και MS98 φαίνονται στο Σχ. 6. Τα αποτελέσματα του μοντέλου MS98 είναι άριστα μέχρι το αδιάστατο βάθος $\kappa = 6$. Αντίθετα, το μοντέλο KK02 δίνει πολύ ακριβή αποτελέσματα έως $\kappa \approx 1.50$ και γενικά αποδεκτά έως $\kappa = 3$. Για την παράμετρο B_2 επιλέχθηκε η τιμή 0.0653 για την οποία ελαχιστοποιείται το σφάλμα στον υπολογισμό του συντελεστή ρήχωσης (Schäffer and Madsen, 1995).

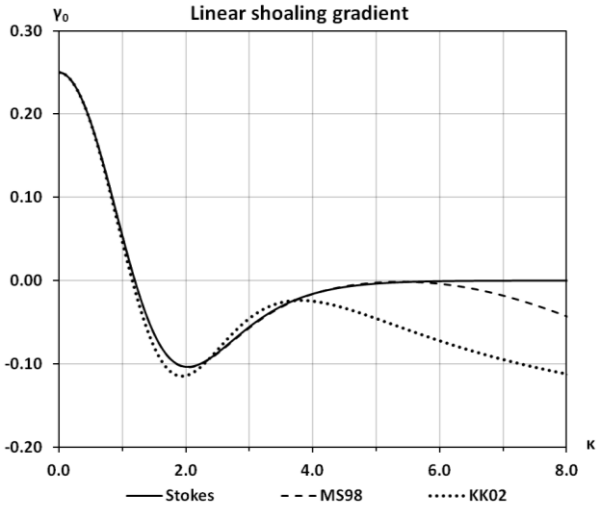

Σχ. 6. Γραμμικός τελεστής ρήχωσης γ_0 όπως υπολογίζεται από τη θεωρία Stokes και τα μοντέλα MS98 και KK02.

Επιπλέον, εξετάστηκαν οι συναρτήσεις μεταφοράς ενέργειας (transfer functions) $2^{\eta\varsigma}$ τάξης, όπως αυτές υπολογίζονται από τα διάφορα μοντέλα. Τα μοντέλα KK02 και KK02e (ταυτίζονται οι λύσεις τους σε 2^{η} τάξη) εκτιμούν τις συναρτήσεις αυτές μέχρι το βάθος $\kappa \approx 1.16$, με ένα σφάλμα έως 10%. Το ίδιο όριο για το μοντέλο MS98 είναι $\kappa \approx 1.80$. Αντιθέτως, όπως τονίστηκε παραπάνω, τα μη γραμμικά χαρακτηριστικά των μοντέλων KM09 και KM09em είναι φτωχά, καθώς το αντίστοιχο όριο είναι και για τα δύο μοντέλα $\kappa \approx 0.3$.

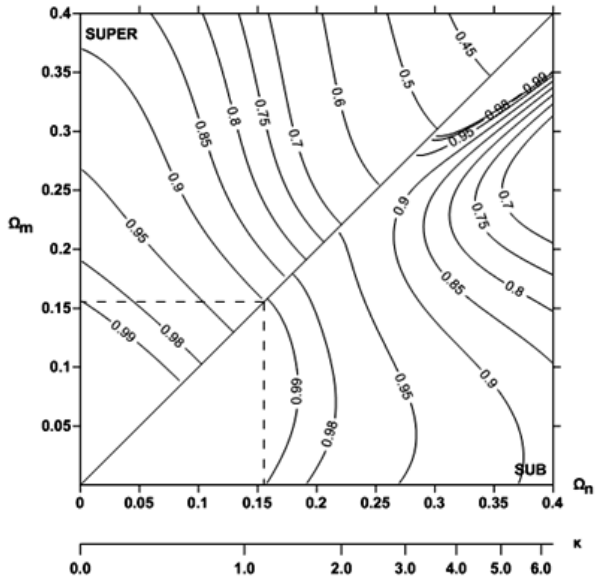

Σχ. 7. Αδιάστατες συναρτήσεις μεταφοράς ενέργειας (transfer functions) $2^{\eta\varsigma}$ τάξης, $G_\zeta / G_\zeta^{\text{Stokes}}$, για το μοντέλο KK02. Τα αποτελέσματα για τις υπερ-αρμονικές (super-harmonics) εμφανίζονται πάνω από τη διαγώνιο, ενώ για τις υπο-αρμονικές (sub-harmonics) κάτω από αυτή. Το τετράγωνο με τη διακεκομμένη γραμμή δηλώνει σφάλμα 10%. Η λύση αναφοράς, G_ζ^{Stokes}, προκύπτει από τους Sand and Mansard (1986) για τις υπερ-αρμονικές και τους Ottesen-Hansen (1978) για τις υπο-αρμονικές.

Από την ανάλυση και σύγκριση των έξι μοντέλων τύπου Boussinesq, επιλέχθηκε τελικά το KK02e να αποτελέσει τη βάση του σύνθετου μοντέλου. Τα μαθηματικά χαρακτηριστικά του μοντέλου MS98 είναι ανώτερα. Ωστόσο, το μοντέλο αυτό περιλαμβάνει μεγάλο αριθμό όρων με παραγώγους ανώτερης τάξης, γεγονός που δυσχεραίνει την αριθμητική επίλυση και αυξάνει τον κίνδυνο των αριθμητικών ασταθειών. Επειδή λοιπόν το βασικό αντικείμενο της Διατριβής είναι η μελέτη της στερεομεταφοράς και μορφολογίας, προτιμήθηκε το κυματικό μοντέλο KK02e που είναι απλούστερο του MS98 και ταυτόχρονα αρκετά ακριβές και βελτιωμένο σε σχέση με τον προκάτοχο του, KK02.

4. Περιγραφή του σύνθετου αριθμητικού μοντέλου

Μετά την επιλογή των βασικών εξισώσεων τύπου Boussinesq, ακολουθεί η πλήρης ανάπτυξη του σύνθετου αριθμητικού μοντέλου. Όπως αναφέρθηκε παραπάνω, το μοντέλο αυτό περιλαμβάνει τέσσερα υπο-μοντέλα, τα οποία περιγράφονται στη συνέχεια.

4.1 Ολοκληρωμένο κυματικό μοντέλο τύπου Boussinesq

Παραπάνω παρουσιάστηκαν οι βασικές εξισώσεις του επιλεγμένου μοντέλου τύπου Boussinesq, στη μονοδιάστατη εκδοχή τους. Στη συνέχεια, εξήχθησαν οι αντίστοιχες εξισώσεις για δύο οριζόντιες διαστάσεις. Επιπλέον, το μοντέλο επεκτάθηκε ώστε να

εφαρμόζεται στις ζώνες θραύσης και διαβροχής, ενώ ενσωματώθηκε και η περιγραφή της τριβής πυθμένα και των τυρβωδών διεργασιών ανάμιξης σε υποπλεγματική κλίμακα (subgrid turbulent mixing). Τέλος, το μοντέλο επεκτάθηκε και σε πορώδεις πυθμένες, ώστε να μπορεί να προσομοιωθεί η κυματική διάδοση πάνω από διαπερατούς ύφαλους κυματοθραύστες. Η επέκταση αυτή περιλαμβάνει την εισαγωγή μίας επιπλέον εξίσωσης Darcy-Forchheimer για την προσομοίωση της ροής εντός πορώδους μέσου, καθώς και επιπρόσθετων όρων στις εξισώσεις συνέχειας και ορμής. Η τελική μορφή των εξισώσεων στις οποίες βασίζεται το μοντέλο Boussinesq είναι η εξής:

$$\beta \frac{\partial \zeta}{\partial t} + \nabla \cdot \left(\Lambda \vec{U}\right) + \lambda \nabla \cdot \left(h_s \vec{U}_s\right) = 0 \tag{5}$$

$$\vec{U}_t + \left(\vec{U} \cdot \nabla\right)\vec{U} + \mathrm{g}\nabla\zeta = \vec{\psi}_I + \vec{\psi}_{II} + \vec{\psi}_{III} + \frac{\lambda}{2} d \nabla\left[\nabla \cdot \left(h_s \vec{U}_{st}\right)\right] + \vec{F}_{br} - \frac{\vec{\tau}_b}{d+\zeta} + \vec{F}_{\mathrm{eddy}} + \vec{F}_{\mathrm{sp}} \tag{6}$$

$$c_{\mathrm{r}}\left[\vec{U}_{st} + \left(\vec{U}_s \cdot \nabla\right)\vec{U}_s\right] + \mathrm{g}\nabla\zeta + \alpha_1 \vec{U}_s + \alpha_2 \left|\vec{U}_s\right| \vec{U}_s + \vec{\psi}_I^{(s)} = \vec{0} \tag{7}$$

όπου $\nabla = \left(\frac{\partial}{\partial x}, \frac{\partial}{\partial y}\right)$ είναι ο οριζόντιος τελεστής κλίσης, ζ η ανύψωση της ελεύθερης επιφάνειας, $\vec{U} = (U, V)$ η μέση κατά βάθος οριζόντια ταχύτητα των μοριών στη στήλη νερού, $\vec{U}_s$ η μέση κατά βάθος οριζόντια ταχύτητα των μοριών εντός του πορώδους μέσου πάχους h_s, λ το πορώδες, d το βάθος νερού, g η επιτάχυνση της βαρύτητας, $\vec{F}_{br}$ ο όρος θραύσης, $\vec{\tau}_b$ η τριβή πυθμένα, $\vec{F}_{\mathrm{eddy}}$ ο όρος της τυρβώδους ανάμιξης, $\vec{F}_{\mathrm{sp}}$ όρος απόσβεσης για τα απορροφητικά όρια του πεδίου, c_{r} ένας συντελεστής αδράνειας, α_1 και α_2 υποδηλώνουν τη συνεισφορά στη συνολική αντίσταση της στρωτής και τυρβώδους ροής, αντίστοιχα. Επιπλέον, $\vec{\psi}_I$, $\vec{\psi}_{II}$ και $\vec{\psi}_{III}$ συμβολίζουν τους όρους Boussinesq στην εξίσωση ορμής, οι οποίοι είναι $O(\sigma^2)$, $O(\varepsilon\sigma^2)$ και $O(\varepsilon^2\sigma^2)$, αντίστοιχα. Επίσης, ο όρος $\vec{\psi}_I^{(s)}$ στην εξίσωση Darcy-Forchheimer είναι $O(\sigma^2)$. Τέλος, οι μεταβλητές β και Λ προκύπτουν από την εφαρμογή της μεθόδου των «σχισμών» για την προσομοίωση της αναρρίχησης και καταρρίχησης των κυματισμών και περιγράφονται στη συνέχεια. Αν οι «σχισμές» αυτές απουσιάζουν, τίθεται $\beta = 1$ και $\Lambda = d + \zeta$.

Η επέκταση στη ζώνη θραύσης επιτυγχάνεται με την εφαρμογή του μοντέλου τυρβώδους συνεκτικότητας των Kennedy *et al*. (2000) και Chen *et al*. (2000). Η μέθοδος αυτή εισάγει επιπρόσθετους όρους θραύσης, $\vec{F}_{br} = (F_{br}, G_{br})$, στις εξισώσεις ορμής κατά x και y, αντίστοιχα:

$$F_{br} = \frac{1}{d+\zeta}\left\{\left\{v_{br}[(d+\zeta)U]_x\right\}_x + \frac{1}{2}\left\{v_{br}[(d+\zeta)U]_y + v_{br}[(d+\zeta)V]_x\right\}_y\right\} \tag{8}$$

$$G_{br} = \frac{1}{d+\zeta}\left\{\left\{v_{br}[(d+\zeta)V]_y\right\}_y + \frac{1}{2}\left\{v_{br}[(d+\zeta)V]_x + v_{br}[(d+\zeta)U]_y\right\}_x\right\} \tag{9}$$

όπου v_{br} είναι ο συντελεστής συνεκτικότητας, ο οποίος μεταβάλλεται στο χώρο και στο χρόνο σύμφωνα με τη σχέση

$$v_{br} = B_{br}\delta_b^2(d+\zeta)\zeta_t \tag{10}$$

όπου δ_b είναι ένα εμπειρικός συντελεστής που συνδέεται με το μήκος ανάμιξης και τίθεται ίσος με 1.2, ενώ B_{br} είναι μία ομαλά μεταβαλλόμενη συνάρτηση που παίρνει τιμές μεταξύ 0 και 1 και εξαρτάται από την τιμή της χρονικής παραγώγου της ανύψωσης της ελεύθερης επιφάνειας, ζ_t και μία κρίσιμη τιμή αυτής, ζ_t^*. Η τελευταία καθορίζει την έναρξη, συνέχιση και ολοκλήρωση της θραύσης ενός κυματισμού. Η κρίσιμη αυτή τιμή είναι μεταβαλλόμενη στο χρόνο και το φαινόμενο της θραύσης εκκινεί και συνεχίζεται όσο η ζ_t είναι μεγαλύτερη της στιγμιαίας τιμής του ζ_t^*. Η χρονική μεταβολή του ζ_t^* ακολουθεί ένα γραμμικό νόμο από μία αρχική τιμή, $\zeta_t^{(I)}$, σε μία τελική, $\zeta_t^{(F)}$, οι οποίες συνήθως τίθενται $(0.35\div0.65)\sqrt{gd}$ και $0.15\sqrt{gd}$, αντίστοιχα.

Η επέκταση στη ζώνη διαβροχής έγινε βάσει της διαδικασίας που πρότειναν οι Kennedy *et al*. (2000) και Chen *et al*. (2000), η οποία αποτελεί μία τροποποίηση της αρχικής μεθόδου των «σχισμών» της Tao (1983). Η κεντρική ιδέα είναι ότι το μοντέλο δεν «ακολουθεί» τη χρονικά μεταβαλλόμενη ακτογραμμή αλλά, αντιθέτως, ολόκληρο το υπολογιστικό πεδίο θεωρείται ενεργό, ενώ όπου υπάρχει ελάχιστο ή καθόλου νερό, η εξίσωση συνέχειας τροποποιείται. Η βασική υπόθεση είναι ότι ο πυθμένας δε θεωρείται αδιαπέρατος, αλλά περιλαμβάνει στενές «σχισμές» τις οποίες πρέπει να γεμίζει το νερό, με αποτέλεσμα να είναι δυνατό η ελεύθερη επιφάνεια να βρίσκεται κάτω από την επιφάνεια του πυθμένα. Έτσι, η ακτογραμμή προσδιορίζεται σε κάθε χρονική στιγμή από την τομή της ελεύθερης επιφάνειας του νερού με την επιφάνεια του πυθμένα. Η τροποποίηση των Kennedy *et al*. (2000) διασφαλίζει ότι δεν υπάρχει απώλεια νερού όταν η επιφάνεια του βρίσκεται πάνω από την κορυφή της «σχισμής», κάτι που δεν ισχύει στην αρχική μέθοδο (Madsen *et al*., 1997). Στο Σχ. 8 φαίνεται η εφαρμογή της μεθόδου.

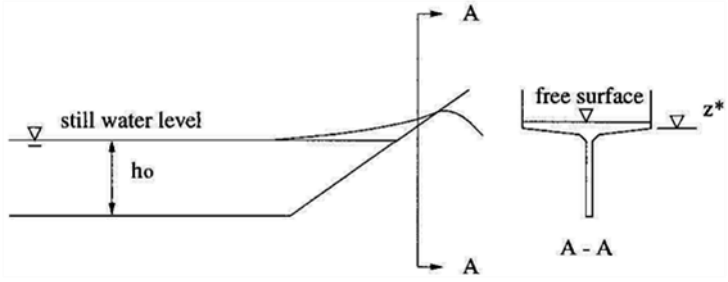

Σχ. 8. Σκαρίφημα διώρυγας όπου ο πυθμένας περιλαμβάνει στενές «σχισμές» (πηγή: Kennedy *et al*., 2000).

Το πλάτος του καναλιού δίνεται από τη σχέση:

$$b(\zeta) = \begin{cases} 1, & \zeta > z^* \\ \delta + (1-\delta)e^{\lambda'(\zeta - z^*)/\mathrm{h_o}}, & \zeta \le z^* \end{cases} \quad (11)$$

όπου λ' είναι παράμετρος η οποία τίθεται ίση με 80, $\mathrm{h_o}$ είναι το βάθος αναφοράς, δ είναι το σχετικό πλάτος της «σχισμής» ως προς το μοναδιαίο πλάτος παραλίας, το οποίο παίρνει τιμές στο διάστημα (0.001 ÷ 0.01). Η στάθμη του πυθμένα στην οποία είναι $b = 1$ ισούται με $z^* = -d/(1-\delta) + \mathrm{h_o}\left[\delta/(1\text{-}\delta) + 1/\lambda\right]$, ενώ η επιφάνεια μιας κάθετης διατομής δίνεται από τη σχέση:

$$A(\zeta) = \begin{cases} (\zeta - z^*) + \delta(z^* + \mathrm{h_o}) + \frac{(1-\delta)\mathrm{h_o}}{\lambda'}\left[1 - e^{-\lambda'(1+z^*/\mathrm{h_o})}\right], & \zeta > z^* \\ \delta(\zeta + \mathrm{h_o}) + \frac{(1-\delta)\mathrm{h_o}}{\lambda'}e^{\lambda'(\zeta - z^*)/\mathrm{h_o}}\left[1 - e^{-\lambda'(1+\zeta/\mathrm{h_o})}\right], & \zeta \le z^* \end{cases} \quad (12)$$

Στην Εξ. (5) είναι $\beta = b(\zeta)$ και $\Lambda = A(\zeta)$, ενώ στα τμήματα στα οποία ο πυθμένας θεωρείται αδιαπέρατος είναι $\beta = 1$ και $\Lambda = d + \zeta$.

Για την τριβή πυθμένα το μοντέλο προσφέρει δύο εναλλακτικές. Η πρώτη βασίζεται στο συνήθη τετραγωνικό νόμο για τις στιγμιαίες διατμητικές τάσεις:

$$\vec{\tau}_b = \left(\tau_{bx}, \tau_{by}\right) = \frac{1}{2} f_{cw} \vec{U}\left|\vec{U}\right| \quad (13)$$

όπου ο συντελεστής τριβής, f_{cw}, λαμβάνει υπόψη την αλληλεπίδραση ρεύματος και κυμάτων (Jonsson, 1966; Ribberink, 1998). Η δεύτερη εναλλακτική βασίζεται στην πιθανοτική ανάλυση των Kobayashi *et al*. (2007), η οποία προϋποθέτει την ισοδυναμία μεταξύ της μέσης χρονικά ταχύτητας και της μέσης τιμής της πιθανοτικής κατανομής αυτής. Επιπλέον, γίνεται η υπόθεση ότι το εύρος της ταχύτητας λόγω κύματος ακολουθεί κατανομή Gauss.

Μία μέθοδος ανάλογη αυτής των μεγάλων δινών (Large Eddy Simulation – LES) εφαρμόστηκε στο οριζόντιο επίπεδο για την παραμετροποίηση των μη υπολογιζόμενων κινήσεων μικρής κλίμακας. Συγκεκριμένα, η επίδραση των τυρβωδών διεργασιών ανάμιξης σε υποπλεγματική κλίμακα (subgrid turbulent mixing) ελήφθη υπόψη μέσω της εφαρμογής ενός μοντέλου τύπου Smagorinsky (Chen *et al*., 1999; Zhan *et al*., 2003).

Η επέκταση σε πορώδεις πυθμένες έγινε ακολουθώντας την εργασία των Cruz *et al*. (1997) και απαιτεί την επίλυση μίας επιπλέον εξίσωσης Darcy-Forchheimer, καθώς και την εισαγωγή επιπρόσθετων όρων πορώδους στις εξισώσεις συνέχειας (5) και ποσότητας κίνησης (6). Μία επιπλέον βελτίωση του παρόντος μοντέλου σε σχέση με προκατόχους του χαμηλότερης τάξης είναι η εισαγωγή των όρων $O(\sigma^2)$ στην Εξ. (7), $\vec{\psi}_I^{(s)}$, οι οποίοι είχαν αμεληθεί (Avgeris *et al*., 2004; Metallinos *et al*., 2014). Οι όροι αυτοί αποδεικνύονται σημαντικοί όταν προσομοιώνεται η διάδοση βραχέων κυματισμών ή ο πορώδης πυθμένας βρίσκεται σε βαθειά ή ενδιάμεσου βάθους νερά. Σύμφωνα με τους Sollitt και Cross (1972), οι συντελεστές αντίστασης δίνονται από τις σχέσεις

$$\alpha_1 = \frac{\nu\lambda}{K} \quad \text{και} \quad \alpha_2 = \frac{C_f\lambda^2}{\sqrt{K}} \tag{14}$$

όπου C_f είναι ένας τυρβώδης συντελεστής τριβής (van Gent, 1995) και K μία μεταβλητή διαπερατότητας που δίνεται από τη σχέση

$$K = \frac{{d_{50}}^2\lambda^3}{\xi(1-\lambda)^2} \tag{15}$$

όπου d_{50} η μέση διάμετρος του υλικού του πυθμένα και ξ μία εμπειρική παράμετρος με τυπική τιμή 1000.

Η διακριτοποίηση των εξισώσεων γίνεται με τη χρήση πεπερασμένων διαφορών σε κεντρικό κάναβο, κεντρικών ως προς το χώρο και εμπρόσθιων ως προς το χρόνο. Συγκεκριμένα, για τις πρώτες χωρικές παραγώγους χρησιμοποιούνται πεπερασμένες διαφορές $4^{ης}$ τάξης, ενώ για τις χωρικές παραγώγους ανώτερης τάξης χρησιμοποιούνται πεπερασμένες διαφορές $2^{ης}$ τάξης. Το αριθμητικό σχήμα επίλυσης είναι ένα γενικευμένο σχήμα πρόβλεψης-διόρθωσης πολλαπλών βημάτων (generalized multi-step predictor-corrector), το οποίο προτάθηκε από τους Zlatev *et al*. (1984). Το στάδιο πρόβλεψης είναι $3^{ης}$ τάξης, ενώ η διόρθωση $4^{ης}$ τάξης. Το συγκεκριμένο σχήμα αποτελεί μία γενίκευση του σχήματος Adams-Bashforth-Moulton (ABM) που εισήχθη από τους Wei and Kirby (1995) στα αριθμητικά μοντέλα τύπου Boussinesq και που έκτοτε χρησιμοποιείται ευρέως. Το χρησιμοποιούμενο εδώ σχήμα προσφέρει βελτιωμένη ακρίβεια και ευστάθεια σε σχέση με το σχήμα ABM.

Η γένεση των κυματισμών επιτυγχάνεται με την εφαρμογή της μεθόδου της συνάρτησης πηγής (Memos *et al*., 2005; Klonaris *et al*., 2016). Στα ανακλαστικά όρια του υπολογιστικού πεδίου εφαρμόζονται οι οριακές συνθήκες:

$$\vec{U}\cdot\vec{n} = 0 \ , \ \nabla\zeta\cdot\vec{n} = 0 \ , \ \frac{\partial\vec{U}_T}{\partial\vec{n}} = 0 \ , \ \forall\ \vec{x}\in\partial\Omega \tag{16}$$

όπου $\vec{n}$ το μοναδιαίο κάθετο διάνυσμα στο όριο $\partial\Omega$, Ω το υπολογιστικό πεδίο, $\vec{U}_T$ είναι η παράλληλη στο όριο συνιστώσα της ταχύτητας και $\vec{x}$ τυχαία θέση στο πεδίο.

Στα απορροφητικά όρια του πεδίου ενεργοποιείται ο όρος απόσβεσης $\vec{F}_{sp}$. Συγκεκριμένα:

$$\vec{F}_{sp} = -w_1(x,y)\vec{U} - w_2(x,y)\nabla^2\vec{U} \tag{17}$$

όπου $w_1(x,y)$ και $w_2(x,y)$ είναι συναρτήσεις απόσβεσης σύμφωνα με τους Wei and Kirby (1995).

Το κυματικό μοντέλο επαληθεύτηκε με μία σειρά πειραματικών μετρήσεων σε μία και δύο οριζόντιες διαστάσεις. Τα τεστ περιλάμβαναν τόσο απλούς, όσο και τυχαίους κυματισμούς που διαδίδονται σε παραλίες και πάνω από ύφαλα εμπόδια. Μερικά αυτά ήταν ιδιαίτερα απαιτητικά, καθώς συνδύαζαν έναν αριθμό φυσικών διεργασιών, όπως ρήχωση, διάθλαση, περίθλαση, θραύση, αναρρίχηση, υπερπήδηση εμποδίου και μη γραμμικές κυματικές αλληλεπιδράσεις.

Καταρχάς, προσομοιώθηκε η μονοδιάστατη διάδοση θραυόμενων μονοχρωματικών κυματισμών σε επίπεδο πυθμένα κλίσης 1:34.26, σύμφωνα με το πείραμα των Hansen and Svendsen (1979). Παρουσιάζεται, ενδεικτικά, η περίπτωση της θραύσης τύπου spilling κυματισμών με περίοδο T = 2.0 s και ύψος H_o = 0.036 m στην περιοχή σταθερού βάθους 0.36 m ανάντη του κεκλιμένου πυθμένα. Στα σχήματα 9 και 10 φαίνεται το ύψος κύματος και η ανύψωση της μέσης στάθμης κυματισμών (wave setup), αντίστοιχα. Τα αποτελέσματα του μοντέλου είναι ιδιαίτερα ακριβή, εκτός από μία μικρή υπερεκτίμηση των δύο μεγεθών στην εσωτερική ζώνη θραύσης.

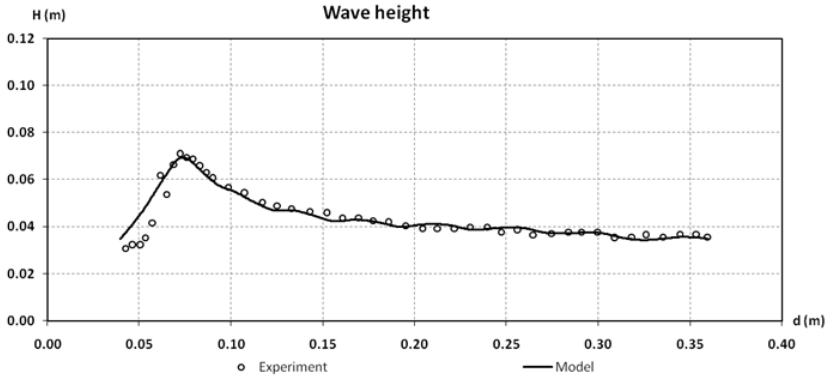

Σχ. 9. Σύγκριση μετρήσεων και αποτελεσμάτων μοντέλου για το ύψος κύματος στο σενάριο No. 051041 που περιλαμβάνει θραύση τύπου spilling.

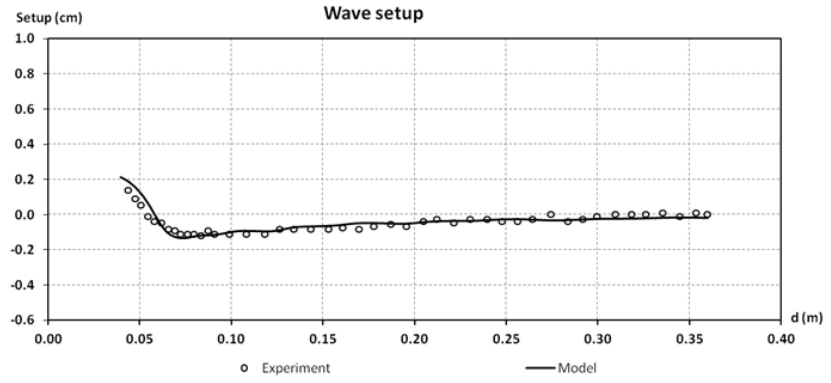

Σχ. 10. Σύγκριση μετρήσεων και αποτελεσμάτων μοντέλου για τη μέση στάθμη κυματισμών στο σενάριο No. 051041 που περιλαμβάνει θραύση τύπου spilling.

Επίσης, ελέγχθηκε η ικανότητα του μοντέλου να αναπαράγει την αναρρίχηση και καταρρίχηση των κυματισμών, μέσω σύγκρισης με τις μετρήσεις του Synolakis (1987). Το

συγκεκριμένο πείραμα αναφέρεται στη διάδοση και θραύση μοναχικού κύματος σε πυθμένα κλίσης 1:19.85. Ανάντη της κλίσης, σε περιοχή με σταθερό βάθος d = 0.2 m, το ύψος κύματος ήταν H = 0.056 m. Στο Σχ. 11 φαίνονται στιγμιότυπα της αδιάστατης ελεύθερης επιφάνειας, ζ/d, για διάφορες τιμές του αδιάστατου χρόνου $t' = t\sqrt{g/d}$. Τα αποτελέσματα είναι αρκετά ακριβή, εκτός από μία ελαφρώς λεπτότερη υπολογιζόμενη φλέβα νερού κατά την φάση της καταρρίχησης.

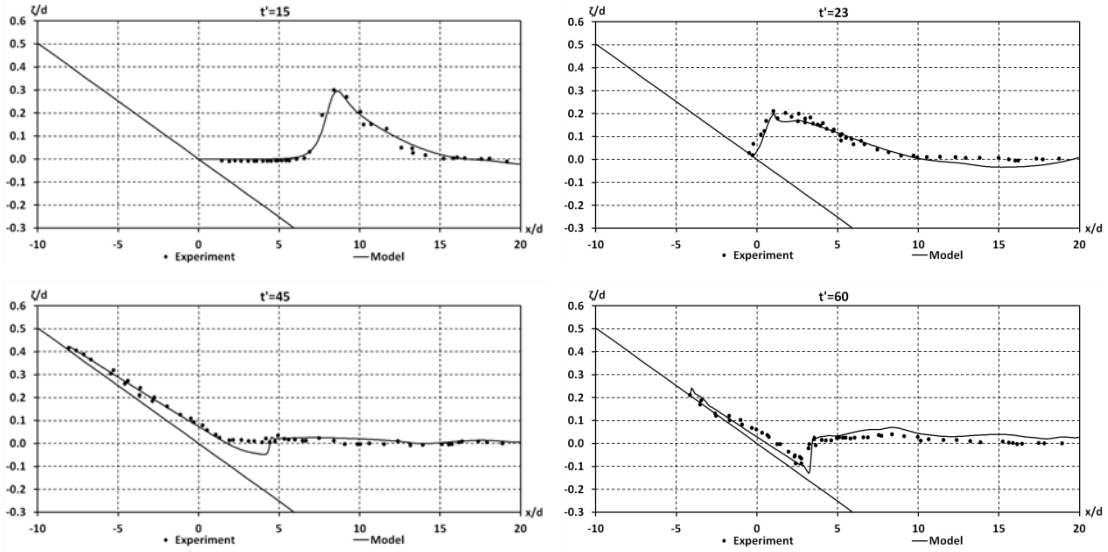

Σχ. 11. Στιγμιότυπων της ελεύθερης επιφάνειας με βάση τις μετρήσεις του Synolakis (1987) και τα αποτελέσματα του μοντέλου.

Επιπλέον, ελέγχθηκε η διάδοση και θραύση σύνθετων κυματισμών πάνω από μονοδιάστατο ύφαλο εμπόδιο τραπεζοειδούς διατομής, σύμφωνα με το πείραμα των Beji and Battjes (1994). Οι προσπίπτοντες κυματισμοί αντιστοιχούν σε φάσμα Jonswap με περίοδο αιχμής T_p = 2 s. Στο Σχ. 12 φαίνεται η πειραματική διάταξη και στο Σχ. 13 η σύγκριση των φασμάτων στους σταθμούς 4 και 6 με βάση τις μετρήσεις και τα αποτελέσματα του μοντέλου.

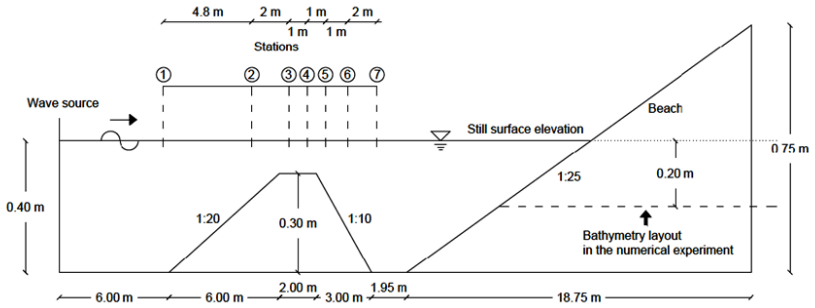

Σχ. 12. Πειραματική διάταξη των Beji and Battjes's (1994).

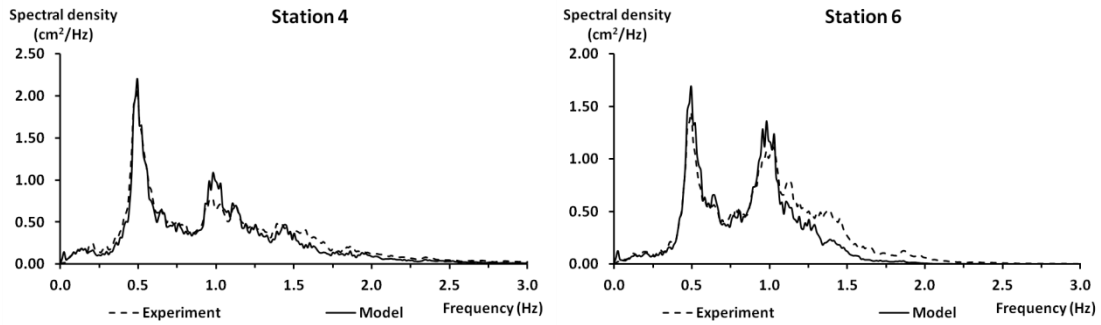

Σχ. 13. Ενεργειακά φάσματα όπως υπολογίζονται από τις μετρήσεις των Beji and Battjes (1994) και τα αποτελέσματα του μοντέλου.

Η ακρίβεια στον υπολογισμό των φασμάτων από το μοντέλο είναι αποδεκτή, όπως και της απώλειας ενέργειας λόγω θραύσης. Παρόλα αυτά εμφανίζεται μια υπερεκτίμηση της δευτερεύουσας κορυφής και μια υποεκτίμηση της μεταφοράς ενέργειας στις ανώτερες αρμονικές.

Στη συνέχεια, προσομοιώθηκαν πειράματα που αναφέρονται σε δύο οριζόντιες διαστάσεις. Ένα τέτοιο παράδειγμα είναι το πείραμα των Berkhoff *et al.* (1982), που αναφέρεται στην πλάγια πρόσπτωση μη θραυόμενων απλών κυματισμών σε επίπεδο πυθμένα κλίσης 1:50 με εμπόδιο ελλειπτικής διατομής. Οι κυματισμοί έχουν περίοδο T = 1.0 s και ύψος H_o = 0.0464 m στην περιοχή σταθερού βάθους d = 0.45 m. Στο Σχ. 14 φαίνεται η πειραματική διάταξη και ένα στιγμιότυπο της υπολογιζόμενης ελεύθερης επιφάνειας.

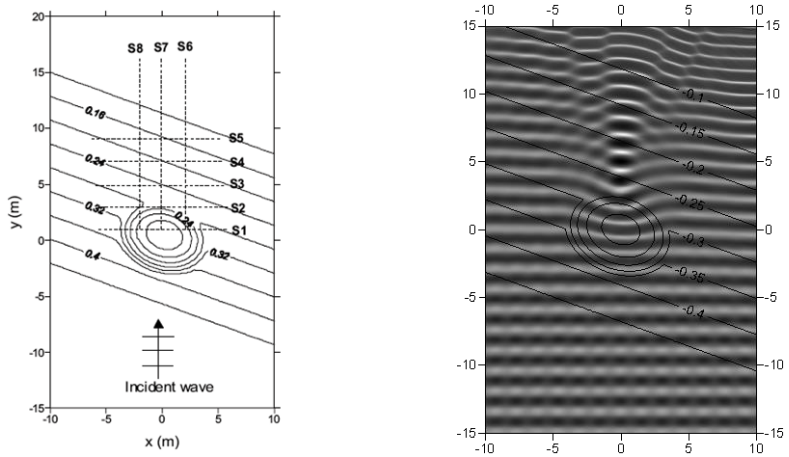

Σχ. 14. Αριστερά: Πειραματική διάταξη των Berkhoff *et al.*'s (1982) (ισοβαθείς σε m). Δεξιά: Στιγμιότυπο της ελεύθερης επιφάνειας σε κάτοψη.

Στο Σχ. 15 φαίνεται η σύγκριση των αποτελεσμάτων του μοντέλου και των μετρήσεων για το αδιάστατο ύψος κύματος H/H_o. Η ακρίβεια των αποτελεσμάτων είναι ικανοποιητική, καθώς ο συνδυασμός της διάθλασης και περίθλασης αναπαράγεται επαρκώς.

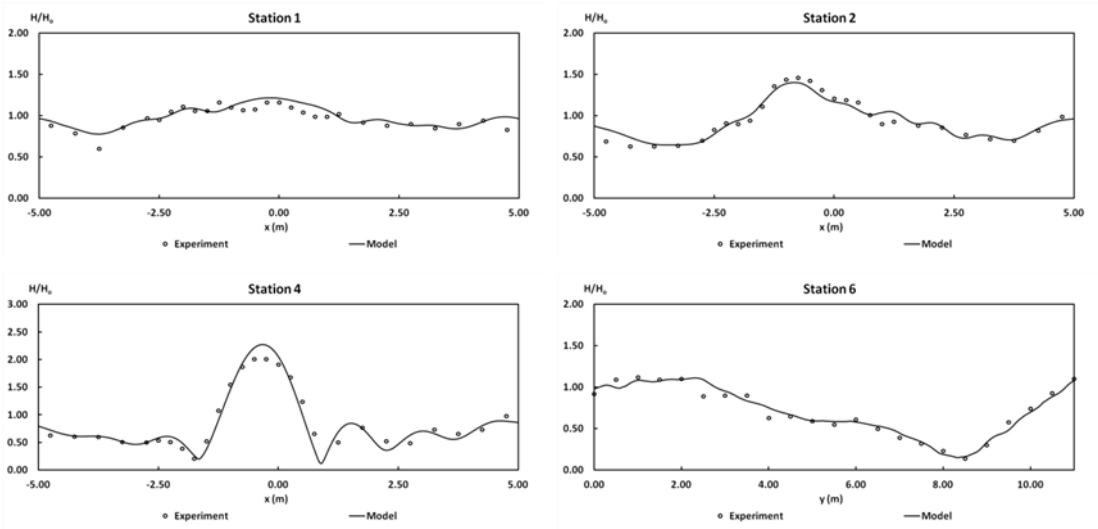

Σχ. 15. Σύγκριση μετρήσεων των Berkhoff *et al.*'s (1982) και αποτελεσμάτων μοντέλου για το αδιάστατο ύψος κύματος, H/H_0.

4.2 Υδροδυναμικό μοντέλο για τα κυματογενή ρεύματα

Η παραδοσιακή αντιμετώπιση των υδροδυναμικών διεργασιών στην παράκτια ζώνη απαιτεί το διαχωρισμό του πεδίου ροής σε δύο επιμέρους τμήματα, ένα λόγω ρεύματος και ένα λόγω κυμάτων. Η μέθοδος των τάσεων ακτινοβολίας των Longuet-Higgins and Stewart (1961) είναι αυτή που συνήθως εφαρμόζεται για τον υπολογισμό της παράκτιας κυκλοφορίας. Συγκεκριμένα, εφαρμόζεται, συνήθως, αρχικά ένα ολοκληρωμένο στην περίοδο κυματικό μοντέλο (phase-averaged) και από τα αποτελέσματά του προκύπτουν οι τάσεις ακτινοβολίας. Στη συνέχεια, οι παράγωγοι αυτών εισάγονται σε ένα μοντέλο που περιλαμβάνει τις μη γραμμικές εξισώσεις ρηχών νερών και τελικά προκύπτει η κυματογενής κυκλοφορία. Η μέθοδος αυτή αποδεικνύεται ιδιαίτερα αξιόπιστη, αλλά αμελεί φαινόμενα όπως η αλληλεπίδραση ρευμάτων-κυμάτων, οι μη γραμμικές κυματικές αλληλεπιδράσεις και η κυματική αναρρίχηση.

Αντιθέτως, μια τέτοια τμηματική αντιμετώπιση δεν απαιτείται για ένα μη γραμμικό μοντέλο τύπου Boussinesq που έχει επεκταθεί στις ζώνες θραύσης και διαβροχής (Basco, 1983). Τα μοντέλα αυτού του τύπου συμπεριλαμβάνουν τις προαναφερθείσες αλληλεπιδράσεις αυτόματα, χωρίς την ανάγκη για ένα ρητό υπολογισμό των τάσεων ακτινοβολίας. Συγκεκριμένα, η στιγμιαία οριζόντια ταχύτητα, $\vec{u}$, εκφράζεται ως το άθροισμα μίας ομοιόμορφης στο βάθος μέσης χρονικά συνιστώσας, $\vec{\overline{U}} = (\overline{U}, \overline{V})$ και μιας συνιστώσας λόγω κύματος, $\vec{u}_w$. Εν συνεχεία, η $\vec{\overline{U}}$ ορίζεται με τρόπο ώστε πολλαπλασιαζόμενη με το μέσο βάθος να δίνει τη μέση χρονικά ροή μάζας. Δηλαδή, αν το σύμβολο $\overline{(\,)}$ δηλώνει μέση χρονικά τιμή, τότε:

$$\vec{\bar{U}} = \frac{1}{d+\bar{\zeta}} \overline{\int_{-d}^{\zeta} \vec{u}\, \mathrm{d}z} \tag{18}$$

Έτσι, προκύπτει ότι $\overline{\int_{-d}^{\zeta} \vec{u}_w\, \mathrm{d}z} = 0$ και συνεπώς η $\vec{\bar{U}}$ περιλαμβάνει τόσο την ταχύτητα του κυματογενούς ρεύματος, όσο και τη μεταφορά μάζας λόγω του κύματος. Οι μέσες χρονικά ταχύτητες υπολογίζονται με τη μέθοδο των Rakha *et al.* (1997).

Μέσα στη ζώνη θραύσης εμφανίζεται μία ροή προς την ακτή λόγω δύο μηχανισμών, του wave drift και των επιφανειακών «κυλίνδρων» που σχηματίζονται λόγω θραύσης (breaking surface rollers) και μεταφέρουν νερό. Για να διατηρείται το ισοζύγιο μάζας σε μία διατομή νερού, οι δύο αυτοί μηχανισμοί εξισορροπούνται από το σχηματισμό ενός ρεύματος (undertow) με φορά προς τα ανοιχτά (Fredsøe and Deigaard, 1992).

Το παρόν μοντέλο λαμβάνει υπόψη προσεγγιστικά το μηχανισμό του undertow. Συγκεκριμένα, εφαρμόζεται ένας συνδυασμός των μοντέλων θραύσης της τυρβώδους συνεκτικότητας (eddy viscosity) και του επιφανειακού κυλίνδρου (surface roller) και υιοθετώντας το προφίλ της ταχύτητας των Schäffer *et al.* (1992) και Madsen *et al.* (1997), το οποίο απεικονίζεται στο Σχ. 16, προκύπτει μία προσέγγιση του μέσου κατά βάθος undertow, $\vec{\bar{U}}_o$, όπου:

$$\vec{U}_o = (U_o, V_o) = \frac{(d+\zeta)\vec{\bar{U}} - \vec{c}\delta_{roller}}{d+\zeta-\delta_{roller}} \tag{19}$$

όπου δ_{roller} το πάχος του επιφανειακού κυλίνδρου και $\vec{c} = \left(c^{(x)}, c^{(y)}\right)$ η ταχύτητά του σύμφωνα με τους Sørensen *et al.* (2004).

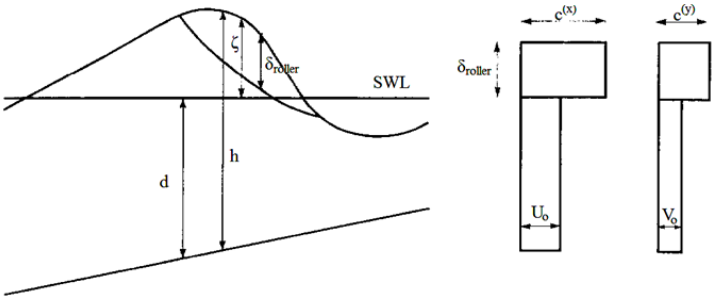

Σχ. 16. Διατομή ενός θραυόμενου κυματισμού και κατακόρυφο προφίλ της οριζόντιας ταχύτητας των μορίων του νερού (πηγή: Madsen *et al.*, 1997, τροποποιημένο).

Τέλος, η τιμή του undertow κοντά στον πυθμένα υπολογίζεται από το μοντέλο σύμφωνα με τη μέθοδο των Putrevu and Svendsen (1993).

Το πείραμα του Hamm (1992) που περιλαμβάνει ένα κανάλι στο οποίο σχηματίζεται ρεύμα επαναφοράς (rip current) είναι ένα απαιτητικό τεστ για την επαλήθευση τόσο του κυματικού, όσο και του υδροδυναμικού μοντέλου. Μία κάτοψη της βυθομετρίας της πειραματικής

διάταξης φαίνεται στο Σχ. 17. Απλοί κυματισμοί περιόδου 1.25 s και ύψους 0.07 m προσπίπτουν κάθετα από αριστερά προς τα δεξιά.

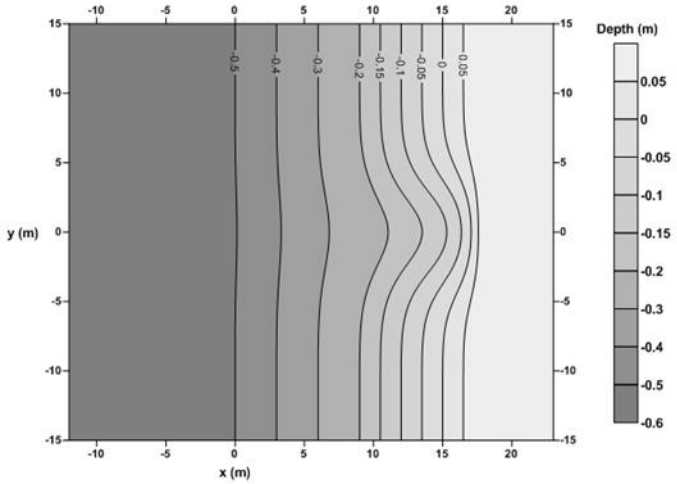

Σχ. 17. Βυθομετρία στο πείραμα του Hamm (1992).

Στο Σχ. 18 απεικονίζεται το πεδίο των κυματογενών ρευμάτων όπως υπολογίζεται από το μοντέλο στο μισό, λόγω συμμετρίας, υπολογιστικό πεδίο. Διακρίνεται ο σχηματισμός του κ.μ.α. ρεύματος, του ρεύματος επαναφοράς κοντά στον άξονα συμμετρίας, καθώς και στροβίλων μέσα στη ζώνη θραύσης.

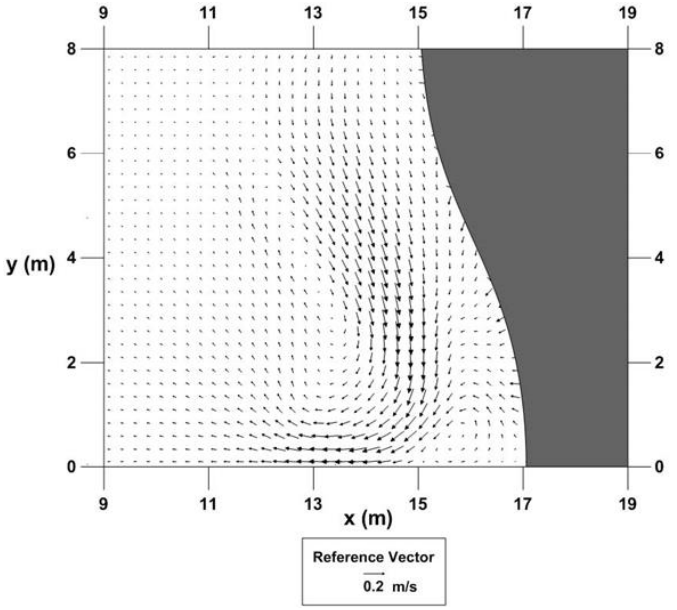

Σχ. 18. Το πεδίο των κυματογενών ρευμάτων, όπως υπολογίζεται από το μοντέλο.

4.3 Μοντέλο παράκτιας στερεομεταφοράς

Τα αποτελέσματα του κυματικού και υδροδυναμικού μοντέλου εισάγονται στη συνέχεια στο μοντέλο παράκτιας στερεομεταφοράς. Στα ανοιχτά και στη ζώνη θραύσης, η κίνηση του

ιζήματος, συνήθως, χωρίζεται στο φορτίο πυθμένα και στο φορτίο σε αιώρηση. Η αύξηση της ταχύτητας των μορίων του νερού λόγω κύματος, καθώς αυτό διαδίδεται προς τα ρηχά, θέτει σε κίνηση το υλικό του πυθμένα σε μία ζώνη με βάθος μικρότερο μιας κρίσιμης τιμής. Ένα μέρος του υλικού αυτού τίθεται σε αιώρηση καθώς αποσπάται από την άκρη των αμμοκυμάτιων του πυθμένα. Καθώς οι κυματισμοί προσεγγίζουν τη γραμμή θραύσης, ευνοείται η κίνηση των φερτών σε ένα λεπτό στρώμα κοντά στον πυθμένα (sheet flow). Αντιθέτως, εντός της ζώνης θραύσης, λόγω της έντονης ανάδευσης προκαλείται αυξημένη αιώρηση του ιζήματος, το οποίο μεταφέρεται κυρίως από τα κυματογενή ρεύματα. Στη ζώνη διαβροχής, η μεταφορά των φερτών γίνεται και πάλι σε ένα λεπτό «φιλμ» κοντά στον πυθμένα, κατά την αναρρίχηση και καταρρίχηση. Οι μηχανισμοί αυτοί έχουν ενσωματωθεί στο μοντέλο στερεομεταφοράς.

Στα ανοιχτά και στη ζώνη θραύσης

(i) <u>Φορτίο πυθμένα</u>

Για τον υπολογισμό του φορτίου πυθμένα ανά μονάδα πλάτους, $\vec{q}_{sb}$, εφαρμόζονται οι ημι-εμπειρικές σχέσεις των Camenen and Larson (2005, 2006, 2007) που ισχύουν για συνδυασμό κυμάτων και ρεύματος. Συγκεκριμένα:

$$\frac{q_{sb,w}}{\sqrt{(s-1)\mathrm{g}{d_{50}}^3}} = \alpha_{\mathrm{w}} \frac{\theta_{\mathrm{cw,net}}}{\sqrt{|\theta_{\mathrm{cw,net}}|}} \theta_{\mathrm{cw,m}} \exp\left(-\mathrm{b}\frac{\theta_{\mathrm{cr}}}{\theta_{\mathrm{cw}}}\right) \tag{20α}$$

$$\frac{q_{sb,n}}{\sqrt{(s-1)\mathrm{g}{d_{50}}^3}} = \alpha_{\mathrm{n}} \frac{\theta_{\mathrm{cn}}}{\sqrt{|\theta_{\mathrm{cn}}|}} \theta_{\mathrm{cw,m}} \exp\left(-\mathrm{b}\frac{\theta_{\mathrm{cr}}}{\theta_{\mathrm{cw}}}\right) \tag{20β}$$

όπου οι δείκτες w και n αναφέρονται, αντίστοιχα, στη διεύθυνση του κύματος και στην κάθετη σε αυτή διεύθυνση, α_w, α_n και b είναι εμπειρικοί συντελεστές και s είναι ο λόγος της πυκνότητας του ιζήματος, ρ_s, προς την πυκνότητα του νερού, ρ. Στη γενική περίπτωση, η διεύθυνση διάδοσης των κυματισμών σχηματίζει μία τυχαία γωνία, φ, με τη διεύθυνση του ρεύματος (βλ. Σχ. 19). Έτσι, οι στιγμιαίες παράμετροι Shields λόγω κύματος και ρεύματος, αντίστοιχα, δίνονται από τις σχέσεις:

$$\vec{\theta}_{\mathrm{w}}(\mathrm{t}) = \frac{\frac{1}{2}\mathrm{f_w}|\vec{\mathrm{U}}_{\mathrm{w}}(\mathrm{t})|\vec{\mathrm{U}}_{\mathrm{w}}(\mathrm{t})}{(\mathrm{s}-1)\mathrm{g}\mathrm{d}_{50}} \quad \text{και} \quad \vec{\theta}_{\mathrm{c}} = \frac{\frac{1}{2}\mathrm{f_c}|\vec{\mathrm{U}}_{\mathrm{c}}|\vec{\mathrm{U}}_{\mathrm{c}}}{(\mathrm{s}-1)\mathrm{g}\mathrm{d}_{50}} \tag{21}$$

όπου $\vec{U}_{\mathrm{w}}(t)$ και $\vec{U}_{\mathrm{c}}$ είναι οι στιγμιαίες ταχύτητες κοντά στον πυθμένα λόγω κύματος και ρεύματος, αντίστοιχα, ενώ f_{w} και f_{c} είναι οι συντελεστές τριβής πυθμένα λόγω κύματος και ρεύματος, αντίστοιχα.

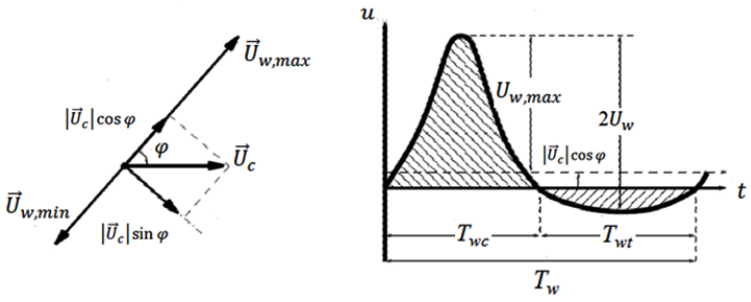

Σχ. 19. Αριστερά: Αλληλεπίδραση κύματος και ρεύματος. Δεξιά: Τυπική μεταβολή της ταχύτητας σε μία περίοδο στη διεύθυνση διάδοσης του κυματισμού, περιλαμβάνοντας την επίδραση του κύματος (πηγή: Camenen and Larson, 2007, τροποποιημένο).

Στις Εξ. (20α,β) $\theta_{\mathrm{cw,m}}$ και θ_{cw} είναι, αντίστοιχα, η μέση χρονικά κατά απόλυτη τιμή και η μέγιστη παράμετρος Shields για το συνδυασμό ρεύματος και κύματος. Η παράμετρος Shields στην κάθετη στον κυματισμό διεύθυνση, θ_{cn}, οφείλεται μόνο στο ρεύμα. Ο τελευταίος εκθετικός όρος στις εξισώσεις αυτές έχει εισαχθεί ώστε να επιτρέπεται μικρή μεταφορά ιζημάτων ακόμη κι αν η στιγμιαία παράμετρος Shields είναι μικρότερη από την κρίσιμη τιμή. θ_{cr}. Μία τέτοια συμπεριφορά έχει παρατηρηθεί και πειραματικά.

Οι χρησιμοποιούμενες εξισώσεις έχουν το πλεονέκτημα ότι λαμβάνουν υπόψη τα μη μόνιμα φαινόμενα υστέρησης κατά την κίνηση του ιζήματος. Στη φύση, η μεταβολή της συγκέντρωσης των φερτών δεν ανταποκρίνεται ακαριαία στη μεταβολή του πεδίου των ταχυτήτων του νερού. Έτσι, αν χωριστεί η περίοδος του κύματος σε δύο φάσεις, μία με θετική και μία με αρνητική ταχύτητα των μορίων, ένα τμήμα του αιωρούμενου ιζήματος δεν προλαβαίνει να επικαθίσει μέχρι την ολοκλήρωση της πρώτης φάσης και αντιθέτως, παραμένει σε αιώρηση κατά τη μετάβαση στην επόμενη φάση που περιλαμβάνει αντίθετης φοράς ταχύτητα. Το φαινόμενο αυτό επιδρά στον υπολογισμό του καθαρού ρυθμού στερεομεταφοράς κατά τη διάρκεια μίας κυματικής περιόδου. Το παρόν μοντέλο λαμβάνει υπόψη αυτή την επίδραση μέσω της θεώρησης της «καθαρής» (net) παραμέτρου Shields:

$$\theta_{\mathrm{cw,net}} = \left(1 - \alpha_{\mathrm{pl,b}}\right)\theta_{\mathrm{cw,onshore}} + \left(1 + \alpha_{\mathrm{pl,b}}\right)\theta_{\mathrm{cw,offshore}} \tag{22}$$

όπου $\theta_{\mathrm{cw,onshore}}$ και $\theta_{\mathrm{cw,offshore}}$ είναι οι μέσες χρονικά παράμετροι Shields κατά τη διάρκεια των τμημάτων της περιόδου στα οποία η κίνηση των μορίων του νερού είναι προς την ακτή και προς τα ανοιχτά, αντίστοιχα, ενώ $\alpha_{\mathrm{pl,b}}$ είναι ένας συντελεστής που λαμβάνει υπόψη τα φαινόμενα υστέρησης (phase-lag effects).

(ii) Φορτίο σε αιώρηση

Για τον υπολογισμό του φορτίου σε αιώρηση το μοντέλο προσφέρει δύο εναλλακτικές. Η πρώτη βασίζεται στην επίλυση της ολοκληρωμένης στο βάθος εξίσωσης μετάθεσης-διάχυσης για τη μέση κατά βάθος συγκέντρωση φερτών στη στήλη νερού, C_{ave}:

$$\frac{\partial(C_{ave}h)}{\partial t}+\frac{\partial(C_{ave}hU)}{\partial x}+\frac{\partial(C_{ave}hV)}{\partial y}=\frac{\partial}{\partial x}\left(K_x h\frac{\partial C_{ave}}{\partial x}\right)+\frac{\partial}{\partial y}\left(K_y h\frac{\partial C_{ave}}{\partial y}\right)+P_r-D_r \qquad (23)$$

όπου $h=d+\zeta$ είναι το στιγμιαίο βάθος νερού, $K_x=K_y=5.93u_{*,c}h$ είναι οι συντελεστές διασποράς του ιζήματος, $u_{*,c}$ είναι η ταχύτητα τριβής λόγω ρεύματος, P_r και D_r είναι ο ρυθμός αιώρησης και εναπόθεσης του ιζήματος, αντίστοιχα, που ισούνται με:

$$P_r=c_R W_s \quad \text{και} \quad D_r=\frac{C_{ave}}{\beta_d}W_s \qquad (24)$$

όπου W_s είναι η ταχύτητα καθίζησης του ιζήματος, β_d ένας συντελεστής (Camenen and Larson, 2008) και c_R η συγκέντρωση αναφοράς του ιζήματος κοντά στον πυθμένα, η οποία δίνεται από τη σχέση:

$$c_R=A_{cr}\theta_{cw,m}\exp\left(-b\frac{\theta_{cr}}{\theta_{cw}}\right) \qquad (25)$$

όπου A_{cr} είναι συντελεστής που λαμβάνει υπόψη το μέγεθος των κόκκων του ιζήματος (Camenen and Larson, 2007).

Ο ρυθμός στερεομεταφοράς είναι συνήθως ιδιαίτερα υψηλός κοντά στην ακτογραμμή λόγω των δυναμικών διεργασιών στη ζώνη διαβροχής. Τα περισσότερα μοντέλα τείνουν να προβλέπουν μία απότομη και μη ρεαλιστική μεταβολή του ρυθμού στερεομεταφοράς από τη ζώνη διαβροχής προς τα ανοιχτά. Αντιθέτως, ένα επιπλέον πλεονέκτημα του παρόντος μοντέλου είναι ότι ενσωματώνει την τροποποίηση των Nam *et al*. (2009) για τον υπολογισμό των ρυθμών αιώρησης και εναπόθεσης του ιζήματος. Έτσι, χρησιμοποιώντας το ρυθμό στερεομεταφοράς που προκύπτει από τους υπολογισμούς για τη ζώνη διαβροχής ως οριακή συνθήκη για την επίλυση της Εξ. (23), προκύπτει μία ρεαλιστική αλληλεπίδραση μεταξύ της ζώνης αυτής και της εσωτερικής ζώνης θραύσης.

Τελικά, από την επίλυση της Εξ. (23) προκύπτει το μέσο χρονικά φορτίο σε αιώρηση ανά μονάδα πλάτους:

$$\vec{q}_{ss}=\left(\overline{C_{ave}h-K_x h\frac{\partial C_{ave}}{\partial x}},\overline{C_{ave}h-K_y h\frac{\partial C_{ave}}{\partial y}}\right) \qquad (26)$$

Η δεύτερη εναλλακτική που προσφέρει το μοντέλο για τον υπολογισμό του φορτίου σε αιώρηση βασίζεται στο εκθετικό προφίλ της συγκέντρωσης του ιζήματος των Camenen and Larson (2008):

$$q_{ss,w} = \left(U_{\text{cw,onshore}} - U_{\text{cw,offshore}}\right) c_R \frac{\varepsilon}{W_s}\left[1 - \exp\left(-\frac{W_s h}{\varepsilon}\right)\right] \quad (27\alpha)$$

$$q_{ss,n} = \left|\vec{U}_c\right| \sin\varphi \; c_R \frac{\varepsilon}{W_s}\left[1 - \exp\left(-\frac{W_s h}{\varepsilon}\right)\right] \quad (27\beta)$$

όπου $U_{\text{cw,onshore}}$ και $U_{\text{cw,offshore}}$ είναι οι rms τιμές της ταχύτητας λόγω συνδυασμού ρεύματος και κυμάτων κατά τη διάρκεια των τμημάτων της περιόδου στα οποία η κίνηση των μορίων του νερού είναι προς την ακτή και προς τα ανοιχτά, αντίστοιχα. Ο συντελεστής διάχυσης του ιζήματος, ε, θεωρείται ομοιόμορφος στο βάθος και λαμβάνεται ως:

$$\varepsilon = \left(\frac{k_{\text{b}}^3 D + k_{\text{c}}^3 D_{\text{c}} + k_{\text{w}}^3 D_{\text{w}}}{\rho}\right)^{1/3} h \quad (28)$$

όπου D, D_{c} και D_{w} η απώλειας ενέργειας ανά μονάδα επιφάνειας εξαιτίας της θραύσης, της τριβής πυθμένα λόγω ρεύματος και λόγω κύματος, αντίστοιχα, ενώ k_{b}, k_{c} και k_{w} είναι συντελεστές.

Στη ζώνη διαβροχής

Ο υπολογισμός της στερεομεταφοράς στη ζώνη διαβροχής βασίζεται στους τύπους των Larson and Wamsley (2007) για τη διεύθυνση κάθετα στην ακτή και παράλληλα σε αυτή:

$$q_{bc,\text{net}} = K_c \frac{\tan\varphi_m}{\tan^2\varphi_m - \left(\frac{dd}{dx}\right)^2} \frac{u_o^3}{\text{g}} \left(\frac{dd}{dx} - \tan\beta_e\right) \frac{t_o}{T} \quad (29)$$

$$q_{bl,\text{net}} = K_l \frac{\tan\varphi_m}{\tan^2\varphi_m - \left(\frac{dd}{dx}\right)^2} \frac{u_o^2 v_0}{\text{g}} \frac{t_o}{T} \quad (30)$$

όπου φ_m είναι η γωνία εσωτερικής τριβής (≈ 30º), u_0, v_0 και t_o είναι ταχύτητες και χρόνος αναφοράς, αντίστοιχα, $\tan\beta_e$ είναι η κλίση ισορροπίας της ακτής, T είναι η διάρκεια του κύκλου αναρρίχησης-καταρρίχησης (προϋποτίθεται ίση με την περίοδο του κύματος) και K_c και K_l είναι εμπειρικοί συντελεστές, για τους οποίους οι Nam *et al*. (2009) πρότειναν την τιμή 0.0008. Η τοπική κλίση ισορροπίας υπολογίζεται σύμφωνα με τους Larson *et al*. (1999):

$$\tan\beta_e = \frac{I_U - I_B}{I_U + I_B} \tan\varphi_m \quad (31)$$

όπου

$$I_U = \frac{1}{T}\int_{t_s}^{t_m}\left[\frac{|\vec{\tau}_b(t)|}{(s-1)\rho g d_{50}}\right]^{3/2} dt \quad (32\alpha)$$

$$I_B = \frac{1}{T}\int_{t_m}^{t_e}\left[\frac{|\vec{\tau}_b(t)|}{(s-1)\rho g d_{50}}\right]^{3/2} dt \quad (32\beta)$$

με $\vec{\tau}_b(t)$ τη διατμητική τάση πυθμένα λόγω τριβής, t_s και t_e τις χρονικές στιγμές της έναρξης και λήξης του κύκλου αναρρίχησης-καταρρίχησης του κύματος, αντίστοιχα και t_m τη χρονική στιγμή στην οποία το μέτωπο του αναρριχώμενου κυματισμού αλλάζει φορά και πλέον κινείται προς τα ανοιχτά.

Συνοπτικά, ο συνολικός «καθαρός» (net) ρυθμός στερεομεταφοράς ανά μονάδα πλάτους, $\vec{q}_{tot} = \left(q_{x,tot}, q_{y,tot}\right)$, ισούται με το άθροισμα των φορτίων πυθμένα και σε αιώρηση, $\vec{q}_{sb} + \vec{q}_{ss}$, στη ζώνη θραύσης και στα ανοιχτά. Στη ζώνη διαβροχής ισούται με το φορτίο $\vec{q}_{sz}$, το οποίο έχει συνιστώσες κάθετα στην ακτή και παράλληλα σε αυτή που δίνονται από τις Εξ. (29) και (30), αντίστοιχα.

4.4 Μοντέλο γεωμορφολογίας

Το μοντέλο γεωμορφολογίας προσομοιώνει την εξέλιξη της τοπογραφίας του πυθμένα μέσω της επίλυσης της εξίσωσης ισοζυγίου των φερτών:

$$\frac{\partial d}{\partial t} = \frac{1}{1-n_p}\nabla \cdot \vec{q}'_{tot} \quad (33)$$

όπου n_p είναι το πορώδες του ιζήματος ($\approx$ 0.4). Σύμφωνα με τον Watanabe (1988), η επίδραση της κλίσης του πυθμένα λαμβάνεται υπόψη για τον υπολογισμό του ισοδύναμου συνολικού ρυθμού στερεομεταφοράς στις διευθύνσεις *x* και *y*:

$$q'_{x,tot} = q_{x,tot} + \varepsilon_{xx}\left|q_{x,tot}\right|\frac{\partial d}{\partial x} + \varepsilon_{xy}\left|q_{x,tot}\right|\frac{\partial d}{\partial y} \quad (34\alpha)$$

$$q'_{y,tot} = q_{y,tot} + \varepsilon_{yx}\left|q_{y,tot}\right|\frac{\partial d}{\partial x} + \varepsilon_{yy}\left|q_{y,tot}\right|\frac{\partial d}{\partial y} \quad (34\beta)$$

όπου ε_{xx}, $\varepsilon_{xy} = \varepsilon_{yx}$ και ε_{yy} είναι εμπειρικοί συντελεστές, ο οποίοι συνεισφέρουν και στην ευστάθεια του αριθμητικού σχήματος επίλυσης της Εξ. (33). Το μοντέλο προσφέρει δύο επιλογές για την επίλυση αυτή. Η πρώτη βασίζεται σε ένα σχήμα upwind $2^{ης}$ τάξης και η δεύτερη σε ένα τροποποιημένο σχήμα Lax-Wendroff $2^{ης}$ τάξης.

Όπως αναφέρθηκε, η εφαρμογή της μεθόδου που βασίζεται στο ‘morphological acceleration factor’ επιτρέπει την προσομοίωση μορφολογικών μεταβολών για χρονικά διαστήματα που απαιτούνται σε πρακτικές εφαρμογές μηχανικών. Συγκεκριμένα, το μορφολογικό χρονικό βήμα επίλυσης της Εξ. (33), Δt_{mor}, είναι διαφορετικό από το βήμα επίλυσης του κυματικού μοντέλου, Δt και συνδέονται με τη σχέση:

$$\Delta t_{\text{mor}} = f_{\text{MOR}} \cdot \Delta t \tag{35}$$

Ωστόσο, πρέπει να δίνεται ιδιαίτερη προσοχή στην επιλογή της τιμής του παράγοντα f_{MOR}, καθώς μία ιδιαίτερα υψηλή τιμή του οδηγεί σε μη ρεαλιστική αλληλεπίδραση του κυματικού, υδροδυναμικού και γεωμορφολογικού μοντέλου. Στην παρούσα Διατριβή ο παράγοντας αυτός έπαιρνε τιμές μεταξύ 1-20 χωρίς να έχει μη ρεαλιστική επίδραση στα αποτελέσματα του κυματικού μοντέλου. Έτσι, προσομοιώθηκαν βραχυχρόνιες μορφολογικές μεταβολές, της τάξης κάποιων ωρών ή λίγων ημερών.

Το σύνθετο μοντέλο επαληθεύτηκε με μία σειρά πειραμάτων που περιλαμβάνουν αλλαγή της τοπογραφίας του πυθμένα σε μία ή δύο οριζόντιες διαστάσεις. Για παράδειγμα, προσομοιώθηκε το πείραμα LIP 11D Delta Flume ’93 και συγκεκριμένα το σενάριο που αναφέρεται σε τυχαίους κυματισμούς περιόδου T_p = 8 s και ύψους κύματος H_{m_o}= 0.60 m (Roelvink and Reniers, 1995). Η μέση διάμετρος των κόκκων άμμου ήταν d_{50}= 0.20 mm και η διάρκεια του τεστ 13 hrs. Στο Σχ. 20 φαίνεται η σύγκριση μεταξύ των μετρήσεων και των αποτελεσμάτων του παρόντος μοντέλου και αυτού των Rakha *et al.* (1997). Το μονοδιάστατο αυτό μοντέλο βασίζεται επίσης στο συνδυασμό ενός μοντέλου τύπου Boussinesq και ενός μοντέλου στερεομεταφοράς και μορφολογίας.

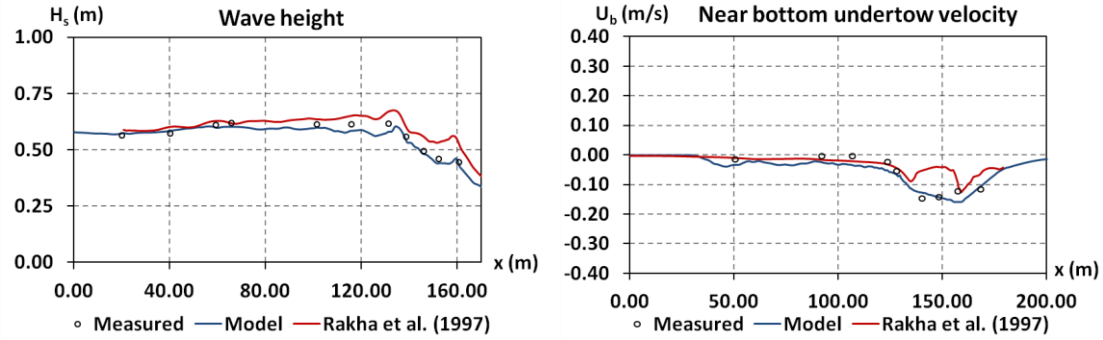

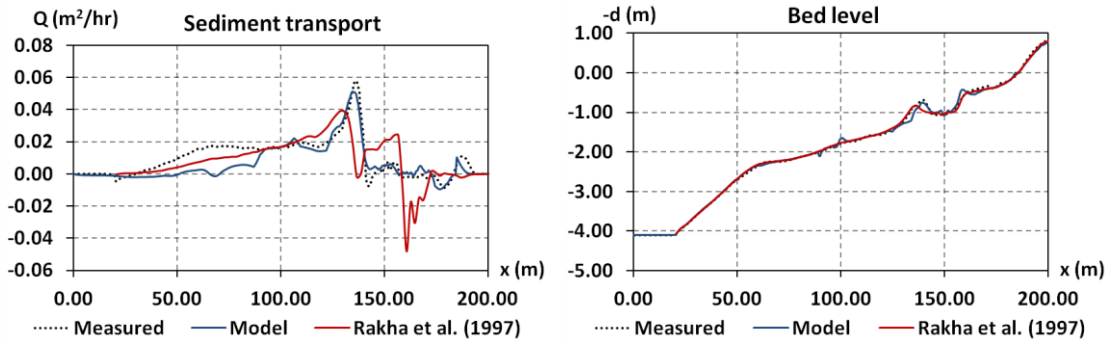

Σχ. 20. Σύγκριση μετρήσεων και αποτελεσμάτων παρόντος μοντέλου και μοντέλου των Rakha *et al.* (1997) για το πείραμα LIP 11D. Η σύγκριση αναφέρεται στο ύψος κύματος, την ταχύτητα του undertow κοντά στον πυθμένα, το ρυθμό στερεομεταφοράς και στην τελική μορφολογία του πυθμένα.

Τα αποτελέσματα του μοντέλου είναι ικανοποιητικά και σε γενικές γραμμές ελαφρώς καλύτερα από αυτά των Rakha *et al.* (1997). Αυτό οφείλεται στη χαμηλότερη τάξη του μοντέλου τύπου Boussinesq που χρησιμοποιούν, $O(\varepsilon\sigma^2)$, καθώς και στις διαφορετικές σχέσεις για τον υπολογισμό της στερεομεταφοράς (Engelund and Fredsøe, 1976).

Με βάση το συγκεκριμένο πείραμα, έγινε και μια σύγκριση διαφόρων σχέσεων για τον υπολογισμό της στερεοεμεταφοράς, όπως φαίνεται στο Σχ. 21. Από τη σύγκριση προκύπτει ότι οι σχέσεις που χρησιμοποιούνται στο μοντέλο δίνουν τα καλύτερα αποτελέσματα, ενώ αρκετά ακριβής είναι και η εξίσωση των Dibajnia *et al.* (2001). Οι δύο αυτές σχέσεις είναι οι μόνες, από αυτές που εξετάστηκαν, που λαμβάνουν υπόψη τα μη μόνιμα φαινόμενα υστέρησης.

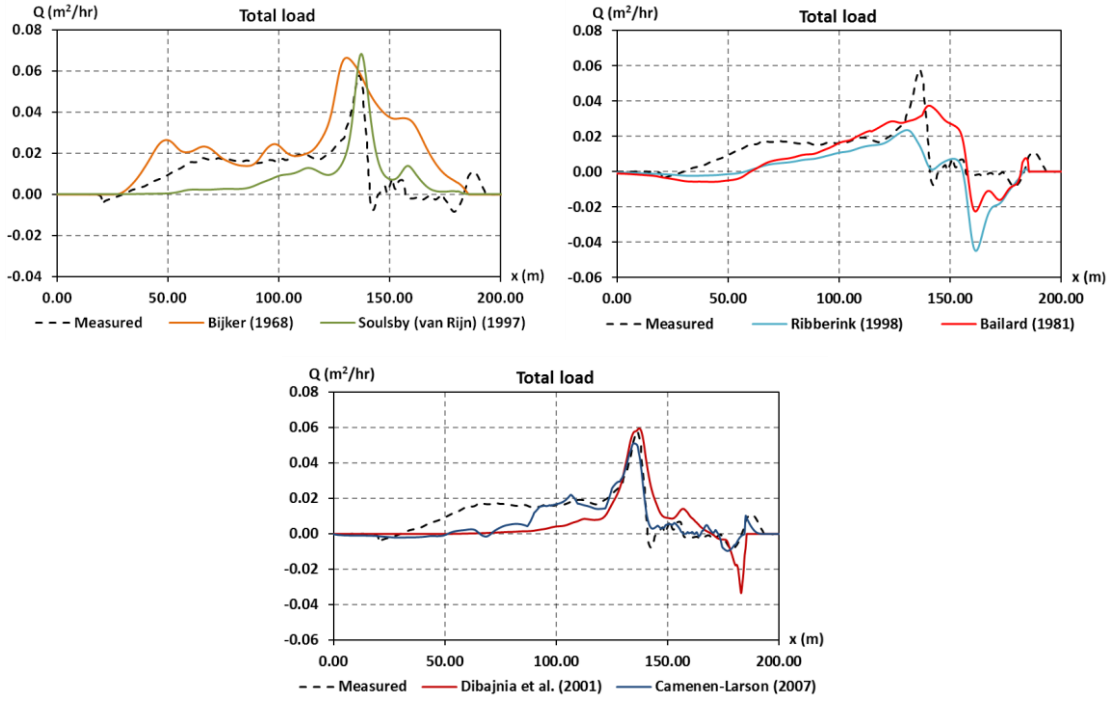

Σχ. 21. Σύγκριση διάφορων σχέσεων για τον υπολογισμό του ολικού φορτίου στερεομεταφοράς για το πείραμα LIP 11D.

Επίσης, το μοντέλο ελέγχθηκε και με πειραματικές μετρήσεις σε δύο οριζόντιες διαστάσεις. Ένα από τα πειράματα που χρησιμοποιήθηκαν είναι αυτό των Gravens and Wang (2007) που αναφέρεται σε πλάγια πρόσπτωση σύνθετων κυματισμών φάσματος TMA. Οι κυματισμοί έχουν περίοδο αιχμής T_p = 1.468 s και σημαντικό ύψος κύματος H_{m_o} = 0.225 m, ενώ προσπίπτουν υπό γωνία 10°. Με ένα σύστημα αντλιών στο κατάντη πλευρικό άκρο της δεξαμενής επιτυγχάνεται η επανακυκλοφορία του κ.μ.α. κυματογενούς ρεύματος και έτσι εγκαθίστανται μόνιμες συνθήκες. Η διάρκεια του τεστ ήταν 165 min και στο Σχ. 22 φαίνεται η πειραματική διάταξη.

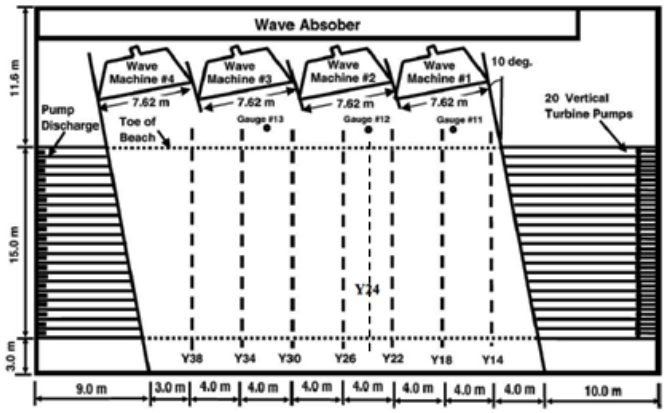

Σχ. 22. Πειραματική διάταξη των Gravens and Wang (2007) (πηγή: Nam *et al.*, 2009, τροποποιημένο).

Στο Σχ. 23 φαίνεται η σύγκριση των μετρήσεων και των αποτελεσμάτων του μοντέλου κατά μήκος της διατομής Y24 (βλ. Σχ. 22). Η σύγκριση αφορά στο σημαντικό ύψος κύματος, στο wave setup, στο κατά μήκος της ακτής κυματογενές ρεύμα και στη στερεομεταφορά κατά μήκος της ακτής. Η ακρίβεια του μοντέλου είναι αρκετά καλή, εκτός από μία υπο-εκτίμηση του ελάχιστου set-down και του παράκτιου ρεύματος στην εσωτερική ζώνη θραύσης.

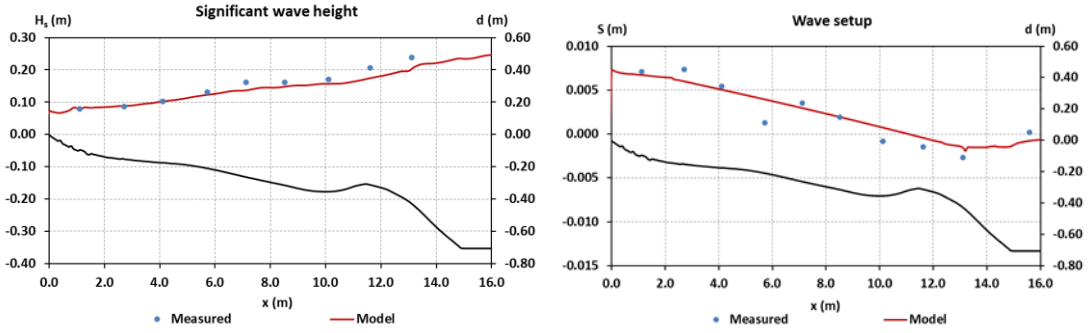

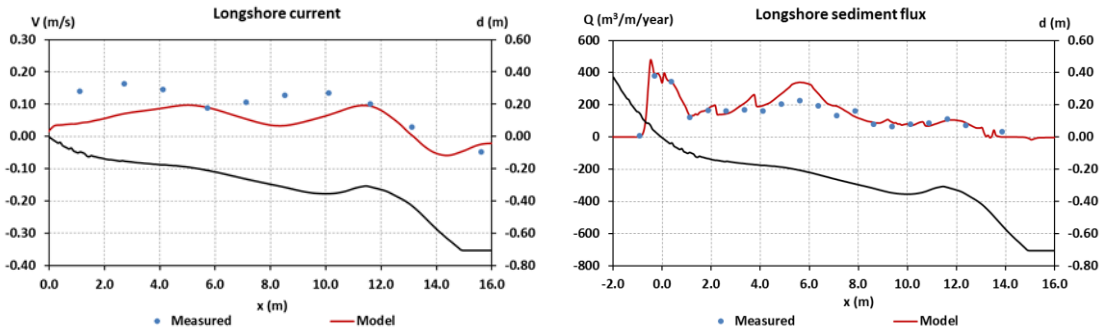

Σχ. 23. Σύγκριση μετρήσεων των Gravens and Wang (2007) και αποτελεσμάτων του μοντέλου για το σημαντικό ύψος κύματος, το wave setup, το κ.μ.α. κυματογενές ρεύμα και την κ.μ.α. στερεομεταφορά.

Στο Σχ. 24 φαίνεται η τελική μορφολογία του πυθμένα, όπως μετρήθηκε στο εργαστήριο και όπως υπολογίζεται από το μοντέλο.

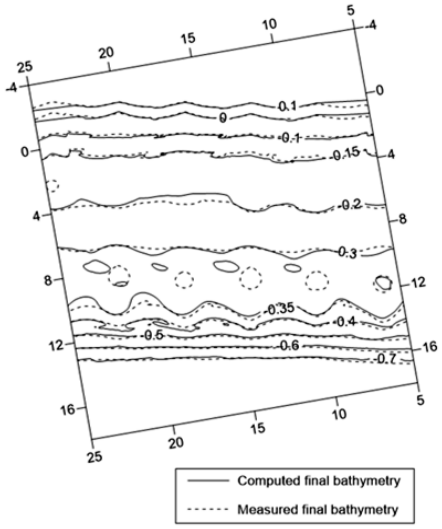

Σχ. 24. Σύγκριση τελικής βυθομετρίας, όπως μετρήθηκε από τους Gravens and Wang (2007) και όπως υπολογίζεται από το μοντέλο (ισοβαθείς σε m).

Η συμφωνία είναι γενικά ικανοποιητική, εκτός από κάποιες ανακρίβειες στην εξωτερική ζώνη θραύσης με $x \approx 10$ m.

5. Εργαστηριακά πειράματα με ύφαλους κυματοθραύστες

Στα πλαίσια της Διατριβής πραγματοποιήθηκαν και εργαστηριακά πειράματα με σκοπό τη μελέτη της εξέλιξης της μορφολογίας αμμώδους πυθμένα στα κατάντη διαπερατού ύφαλου κυματοθραύστη. Τα πειράματα εκτελέστηκαν στο Εργαστήριο Υδραυλικής Μηχανικής του Τμήματος Πολιτικών Μηχανικών του Πανεπιστημίου Πατρών, σε δεξαμενή κυμάτων ορθογωνικής διατομής με οριζόντιες διαστάσεις 12 m x 7 m και μέγιστο βάθος 1.05 m. Τα τοιχώματα και ο πυθμένας της δεξαμενής ήταν κατασκευασμένα από σκυρόδεμα με σχετικά λεία επιφάνεια.

Στο ένα άκρο της δεξαμενής, παράλληλα με τη μικρή πλευρά της μήκους 7 m, ήταν τοποθετημένη μία κυματογεννήτρια τύπου αναδευτήρα με άρθρωση (paddle) που περιλάμβανε σύστημα ελέγχου ενεργητικής απόσβεσης της ανάκλασης κυμάτων. Η κυματογεννήτρια μπορούσε να δημιουργήσει μόνο κάθετα προσπίπτοντες κυματισμούς, τόσο μονοχρωματικούς, όσο και σύνθετους.

Προκειμένου να προσομοιωθεί η ρήχωση κυματισμών, κατασκευάστηκε μία ράμπα από λεία πάνελ αλουμινίου, συνολικού πλάτους 4 m και μήκους 9 m. Η ράμπα τοποθετήθηκε υπό ήπια κλίση, περίπου 1:14.97, συμμετρικά ως προς τον άξονα συμμετρίας της δεξαμενής που είναι παράλληλος στη μεγάλη πλευρά της. Στη θέση της πηγής το βάθος ήταν σταθερό 1.05 m, ενώ στην ανάντη ακμή της ράμπας, σε απόσταση 1.73 m από την κυματογεννήτρια, 0.45 m. Μπροστά από την κύρια ράμπα τοποθετήθηκε επιπλέον φύλλο λαμαρίνας κλίσης 1:2. Εκατέρωθεν της κεκλιμένης ακτής τοποθετήθηκαν κατακόρυφα φύλλα αλουμινίου, ώστε να λειτουργούν ως πλευρικοί τοίχοι-οδηγοί για τη διάδοση των κυματισμών. Στο κατάντη άκρο της δεξαμενής, εκατέρωθεν της κεκλιμένης ακτής, τοποθετήθηκαν κεκλιμένα απορροφητικά όρια από λιθορριπή. Η γενική διάταξη της εγκατάστασης φαίνεται στο Σχ. 25.

Στη συνέχεια κατασκευάστηκε διαπερατός ύφαλος κυματοθραύστης από λιθορριπή μέσης διαμέτρου d_{50} = 0.05 m. Το μήκος του κυματοθραύστη ήταν 3 m, δημιουργώντας δύο κενά πλάτους 0.50 m το καθένα εκατέρωθεν αυτού. Το ελεύθερο ύψος (free board) του ύφαλου ήταν 0.05 m και το πορώδες του μετρήθηκε $\lambda = 0.52$.

Στα κατάντη του ύφαλου διαστρώθηκε σχετικά λεπτόκοκκη άμμος μέσης διαμέτρου d_{50} = 0.21 mm, διαμορφώνοντας ένα στρώμα μέσου πάχους 4 cm. Πριν από κάθε σενάριο γινόταν προσεκτική διάστρωση της άμμου, ώστε ο πυθμένας να είναι επίπεδος με κλίση περίπου 1:15. Στο Σχ. 26 φαίνεται σε σκαρίφημα η διάταξη των έργων και στο Σχ. 27 μία όψη αυτών κατά τη φάση της κατασκευής του φυσικού μοντέλου.

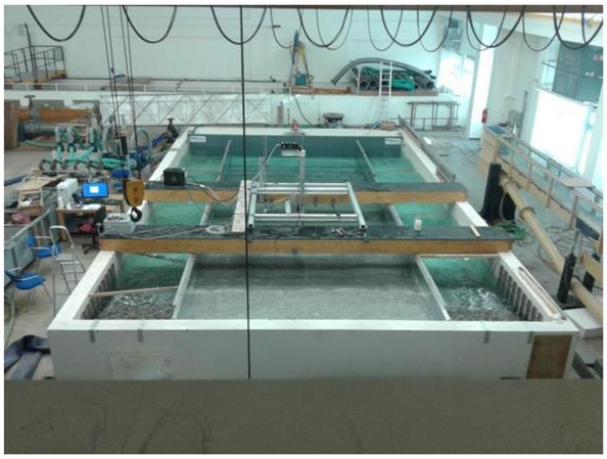

Σχ. 25. Γενική όψη της πειραματικής διάταξης πριν την κατασκευή του κυματοθραύστη και την τοποθέτηση της άμμου.

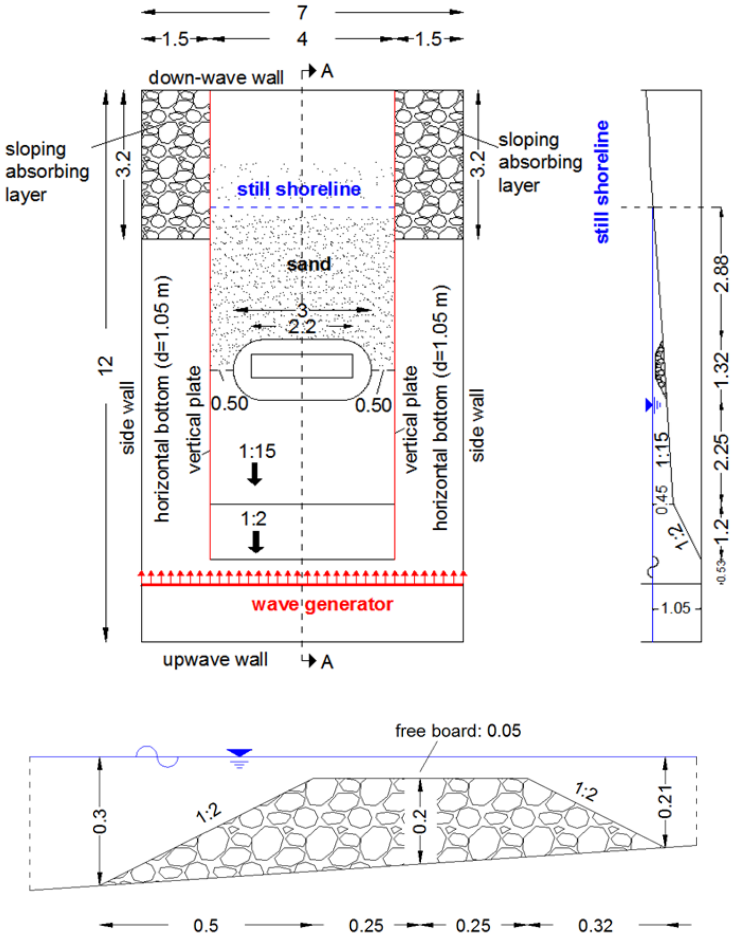

Σχ. 26. Γενική όψη της πειραματικής διάταξης πριν την κατασκευή του κυματοθραύστη και την τοποθέτηση της άμμου.

Σχ. 27. Όψη του κυματοθραύστη και της αμμώδους ακτής κατά τη φάση κατασκευής.

Εξετάστηκαν 8 σενάρια, τα οποία περιλάμβαναν θραυόμενους και μη-θραυόμενους, απλούς μονοχρωματικούς και σύνθετους κυματισμούς. Τα χαρακτηριστικά των διαφορετικών σεναρίων συνοψίζονται στον πίνακα 1. Σε κάθε σενάριο μετρήθηκε η αρχική και τελική βυθομετρία. Επίσης, καταγράφηκαν χρονοσειρές της ανύψωσης της ελεύθερης επιφάνειας με τη χρήση 7 κυματομετρητών, η θέση των οποίων αποτυπώνεται στο Σχ. 28. Κάθε σενάριο

ολοκληρωνόταν όταν πλέον δεν παρατηρούταν σημαντική αλλαγή της τοπογραφίας του πυθμένα.

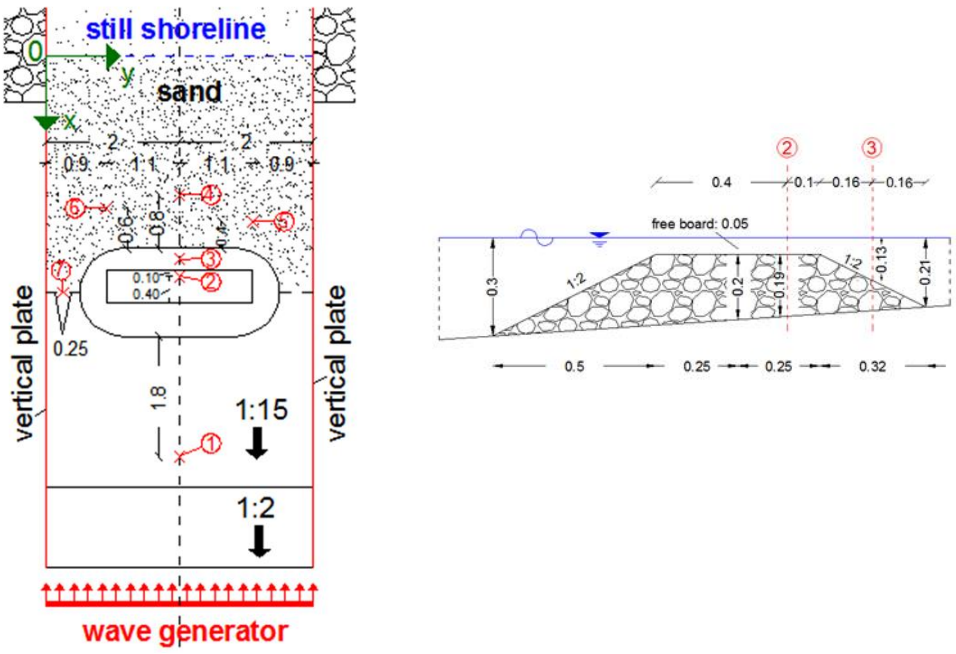

Σχ. 28. Θέση των 7 κυματομετρητών.

Στο Σχ. 29 φαίνεται η αρχική και τελική ακτογραμμή για το σενάριο No. 3. Πίσω από τον κυματοθραύστη σχηματίστηκε ένα salient. Αντίθετα, η απόθεση εξασθενεί προς τους πλευρικούς τοίχους, με αποτέλεσμα να εμφανίζεται ήπια διάβρωση πίσω από τα ανοίγματα, εκατέρωθεν του ύφαλου.

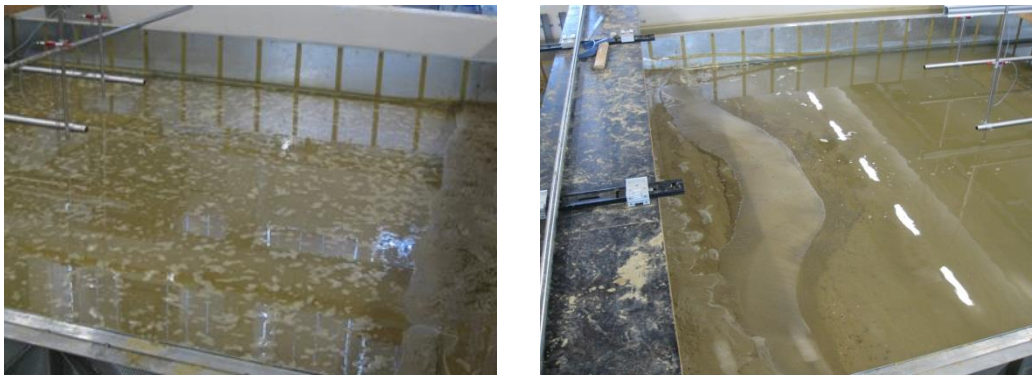

Σχ. 29. Όψη της αρχικής (στα αριστερά) και τελικής (μετά από 5 ώρες κυματικής δράσης, στα δεξιά) ακτογραμμής στο σενάριο No. 3.

6. Επαλήθευση του σύνθετου μοντέλου

Τα εργαστηριακά πειράματα προσέφεραν τη δυνατότητα απευθείας εξαγωγής κάποιων συμπερασμάτων σχετικά με τις μορφοδυναμικές διεργασίες πίσω από ύφαλους κυματοθραύστες. Παράλληλα, όμως, παρείχαν και ένα σύνολο δεδομένων για την επαλήθευση του σύνθετου αριθμητικού μοντέλου.

Η απόκριση του μοντέλου διερευνήθηκε και για τα 8 σενάρια των πειραμάτων. Στο Σχ. 30 φαίνεται η σύγκριση των μετρήσεων και του μοντέλου για τις χρονοσειρές της ανύψωσης της ελεύθερης επιφάνειας του σεναρίου No. 4. Το συγκεκριμένο σενάριο αναφέρεται σε απλούς μονοχρωματικούς κυματισμούς με περίοδο T = 2.0 s και H_o = 0.08 m στη θέση της πηγής. Στον πόδα της κεκλιμένης ακτής, όπου το βάθος είναι 0.45 m, είναι $d/L \approx 0.12$ και $\varepsilon = H/d \sim 0.18$. Κατά τη διέλευση των κυματισμών πάνω από τον ύφαλο εμφανίζεται θραύση τύπου spilling. Τα χωρικά βήματα διακριτοποίησης επιλέχθηκαν $\Delta x = \Delta y$ = 0.04 m και το χρονικό Δt = 0.008 s. Προσομοιώθηκε η εξέλιξη της μορφολογίας για 4.3 hrs, όπως και στο πείραμα.

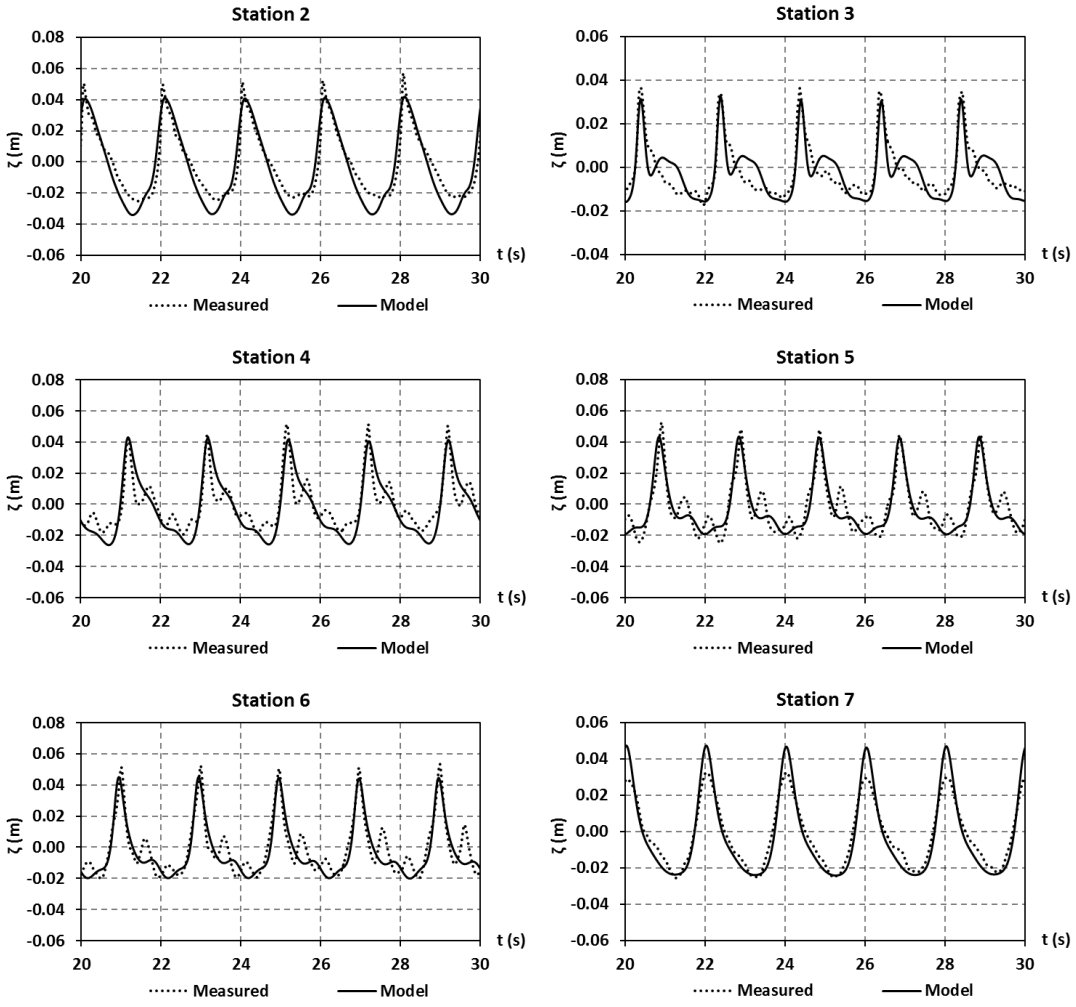

Σχ. 30. Χρονοσειρές της ανύψωσης της ελεύθερης επιφάνειας, όπως προκύπτουν από τις μετρήσεις και τα αποτελέσματα του μοντέλου για το σενάριο No. 4.

Η ακρίβεια είναι, σε γενικές γραμμές, αποδεκτή εκτός από κάποια υπερεκτίμηση της δευτερεύουσας κορυφής στο σταθμό 3 και του ύψους κύματος στο σταθμό 7, ο οποίος βρίσκεται και στο κενό μεταξύ ακρομωλίου και πλευρικού τοίχου. Στο Σχ. 31 φαίνεται η σύγκριση αρχικής και τελικής βυθομετρίας όπως μετρήθηκε και υπολογίζεται από το μοντέλο.

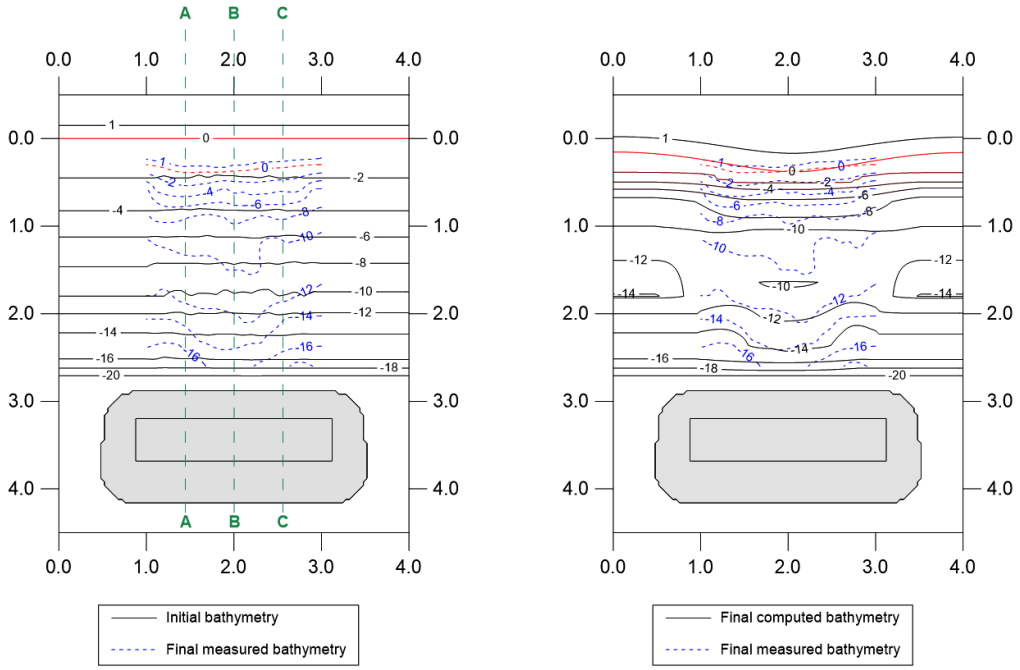

Σχ. 31. Αρχική και τελική μετρημένη βυθομετρία (αριστερά) και σύγκριση μεταξύ μετρήσεων και αποτελεσμάτων μοντέλου για την τελική βυθομετρία (δεξιά) για το σενάριο No. 4 (ισοβαθείς σε cm).

Η απόκριση του μοντέλου είναι γενικά αποδεκτή. Το πλάτος του σχηματιζόμενου salient προβλέπεται με ικανοποιητική ακρίβεια, ενώ η απόθεση κοντά στην ακτογραμμή μειώνεται προς τους πλευρικούς τοίχους. Βέβαια, η απόθεση στο κέντρο, κατά την έννοια του πλάτους, γύρω από την ισοβαθή των 10 cm υποεκτιμάται από το μοντέλο, ενώ αντιθέτως προβλέπεται μία ήπια διάβρωση. Επίσης, το μοντέλο περιγράφει το σχηματισμό του ύφαλου (bar) λόγω θραύσης στο κέντρο, πίσω από τον κυματοθραύστη.

Το σενάριο No. 5 αναφέρεται στη διάδοση σύνθετων κυματισμών φάσματος Jonswap με περίοδο αιχμής T_p = 1.25 s και σημαντικό ύψος κύματος H_{so} = 0.045 m στη θέση της πηγής. Πρόκειται για σχετικά βραχείς κυματισμούς με μικρό ποσοστό θραυόμενων πάνω από το ύφαλο. Στο Σχ. 32 φαίνεται η σύγκριση των φασμάτων όπως προκύπτουν από τις μετρημένες και τις υπολογισμένες από το μοντέλο χρονοσειρές της ανύψωσης της ελεύθερης επιφάνειας.

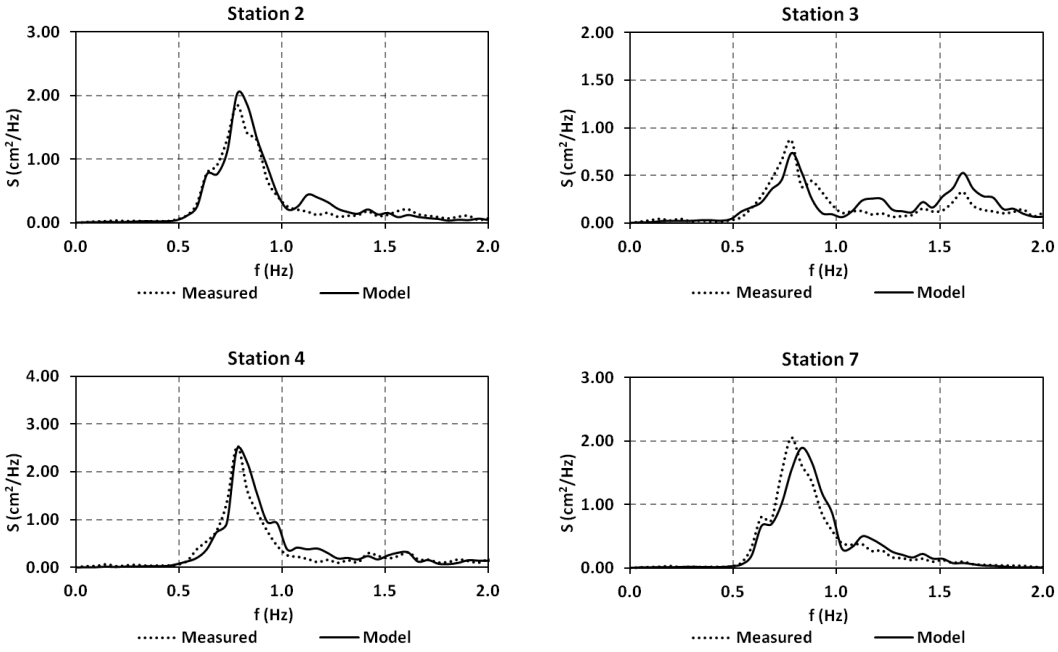

Σχ. 32. Σύγκριση φασμάτων, όπως υπολογίζονται από τις μετρημένες και τις υπολογισμένες από το μοντέλο χρονοσειρές της ανύψωσης της ελεύθερης επιφάνειας για το σενάριο No. 5.

Το σχήμα των φασμάτων περιγράφεται ικανοποιητικά, όπως και οι μέγιστες τιμές της πυκνότητας ενέργειας στους διάφορους σταθμούς. Επίσης, το μοντέλο υπολογίζει τη μεταφορά ενέργειας στις ανώτερες αρμονικές στα κατάντη του ύφαλου, αλλά με μία υπερεκτίμηση στο σταθμό 3 γύρω στο $kd \sim 1.50$. Από τη μη γραμμική ανάλυση που προηγήθηκε θα αναμενόταν μία υποεκτίμηση των transfer functions στους αδιάστατους αυτούς αριθμούς. Παρόλα αυτά, η ανάλυση αυτή αναφερόταν σε αδιαπέρατους πυθμένες, ενώ το πορώδες μπορεί να έχει σημαντική επίδραση στις κυματικές ιδιότητες. Επίσης, επίδραση ασκούν και τα φαινόμενα της διάθλασης και περίθλασης.

Στο Σχ. 33 φαίνεται η σύγκριση αρχικής και τελικής βυθομετρίας όπως μετρήθηκε και υπολογίζεται από το μοντέλο.

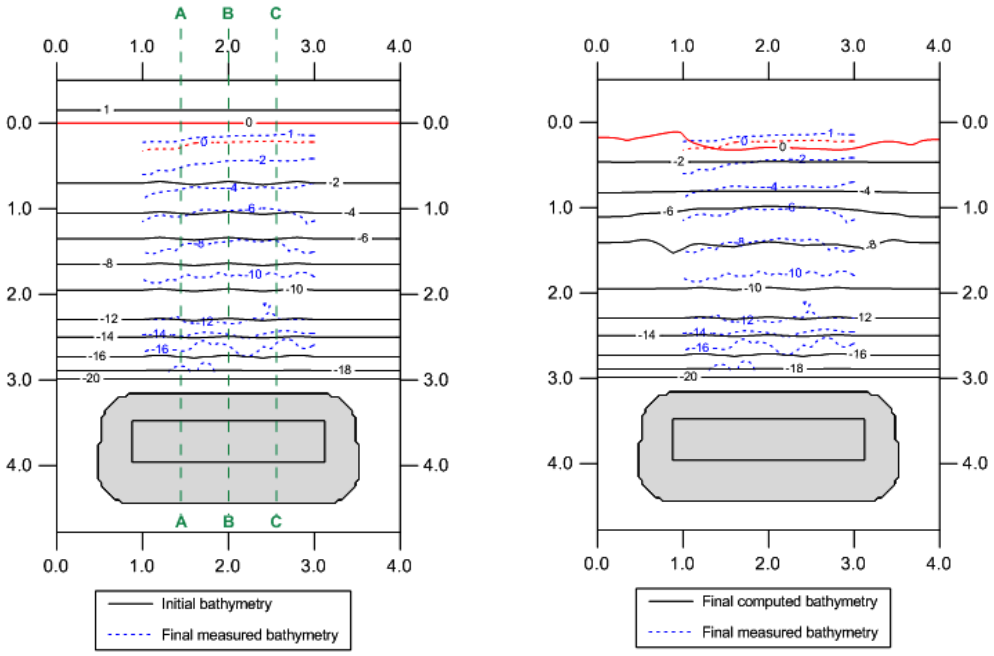

Σχ. 33. Αρχική και τελική μετρημένη βυθομετρία (αριστερά) και σύγκριση μεταξύ μετρήσεων και αποτελεσμάτων μοντέλου για την τελική βυθομετρία (δεξιά) για το σενάριο No. 5 (ισοβαθείς σε cm).

Η εξέλιξη της ακτογραμμής υπολογίζεται και στην περίπτωση αυτή με λογική ακρίβεια. Εδώ το σχηματιζόμενο salient είναι περισσότερο πεπλατυσμένο και η εξέλιξη των ισοβαθών ακολουθεί περισσότερο μία παράλληλη μετατόπιση προς την ακτή και τα ανοιχτά, αντίστοιχα. Σε γενικές γραμμές, η απόκριση του μοντέλου ως προς τη μορφολογική εξέλιξη κρίνεται επαρκής.

7. Αριθμητική διερεύνηση της απόκριση της ακτογραμμής σε σύστημα ύφαλων κυματοθραυστών

Η απόκριση της ακτογραμμής στην κατασκευή παράκτιων τεχνικών έργων είναι μείζον ζήτημα για τους μηχανικούς. Συγκεκριμένα, στην περίπτωση των έξαλων κυματοθραυστών έχουν προταθεί κάποιες εμπειρικές σχέσεις και κριτήρια που προβλέπουν το σχηματισμό salient ή tombolo βάσει των γεωμετρικών χαρακτηριστικών των έργων και των υδροδυναμικών συνθηκών (Dally and Pope, 1986).

Παρόμοιες εμπειρικές παρατηρήσεις έχουν παρουσιαστεί, κυρίως για φυσικούς ύφαλους (Black and Andrews, 2001). Ωστόσο, η επαλήθευσή τους κρίνεται ανεπαρκής, ενώ και η αξιοπιστία τους τίθεται υπό αμφισβήτηση (Ranasinghe *et al.*, 2001). Ο Pilarczyk (2003) ενσωμάτωσε την επίδραση του συντελεστή διάδοσης στα εμπειρικά κριτήρια των συμβατικών κυματοθραυστών ώστε να εφαρμόζονται και για ύφαλους. Παρόλα αυτά και στην περίπτωση αυτή δεν έχει παρουσιαστεί επαρκής επαλήθευση των σχέσεων. Επιπλέον,

κάποια αποτελέσματά του, π.χ. η δυνατότητα σχηματισμού tombolo πίσω από διαπερατούς ύφαλους κυματοθραύστες, έχουν αμφισβητηθεί (Karambas *et al.*, 2016).

Επομένως, υπάρχει ένα κενό στη διεθνή βιβλιογραφία σχετικά με την πρόβλεψη της απόκρισης της ακτογραμμής στην κατασκεύη ύφαλων κυματοθραυστών. Η υδροδυναμική συμπεριφορά των έργων αυτών είναι πιο σύνθετη από αυτή των συμβατικών κυματοθραυστών. Συνεπώς, η ακτομηχανική συμπεριφορά τους είναι φαινόμενο που εξαρτάται από πλήθος παραμέτρων και είναι δύσκολο να συστηματοποιηθεί. Άρα, είναι πιθανό να μη δύναται να εξαχθούν εμπειρικές σχέσεις και κριτήρια με γενική ισχύ για την περίπτωση των ύφαλων.

Στην κατεύθυνση αυτή, στην παρούσα Διατριβή, διερευνήθηκε αριθμητικά η απόκριση της ακτογραμμής σε ένα σύστημα ύφαλων κυματοθραυστών, ώστε να εξαχθούν κάποια συμπεράσματα σχετικά με την εξάρτησή της από κάποιες βασικές παραμέτρους σχεδιασμού των έργων. Συγκεκριμένα, εκτελέστηκε ένα σετ αριθμητικών πειραμάτων που αναφέρονταν σε ένα σύστημα πέντε ύφαλων κυματοθραυστών σε ευθεία και παράλληλα στην ακτογραμμή. Διερευνήθηκε η επίδραση του μήκους των κυματοθραυστών, B, της απόστασής τους από την αρχική ακτογραμμή, S, του κενού ανάμεσά τους, G, του πορώδους τους, λ, της περιόδου του κύματος, T και της γωνίας πρόσπτωσης των κυματισμών, θ. Ως σενάριο αναφοράς επιλέχθηκε το No. 4 των εργαστηριακών πειραμάτων που αναφερόταν σε απλούς κυματισμούς με T = 2.0 s και H_o = 0.08 m. Η αρχική βυθομετρία ήταν αυτή του πειράματος, επαναλαμβανόμενη συμμετρικά για τους πέντε κυματοθραύστες.

Αρχικά, εξετάστηκαν 10 διαφορετικές τιμές του λόγου B/S από 0.3 έως 3.0. Ενδεικτικά στο Σχ. 34 φαίνεται η τελική ακτογραμμή για τέσσερις διαφορετικές γωνίες πρόσπτωσης στην περίπτωση με $B/S = 0.90$. Από τις περιπτώσεις που εξετάστηκαν προέκυψε το Σχ. 35, όπου X είναι το πλάτος του πλατύτερου από τα salient που σχηματίστηκαν.

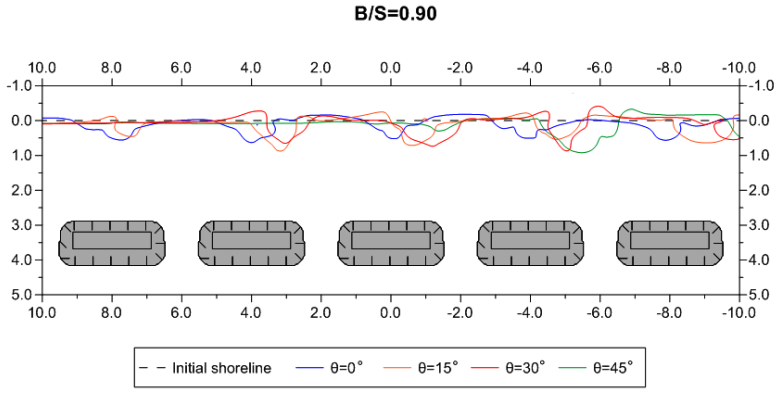

Σχ. 34. Τελική υπολογιζόμενη ακτογραμμή για μήκος κυματοθραυστών $B = 3.11$ m και λόγο $B/S = 0.90$.

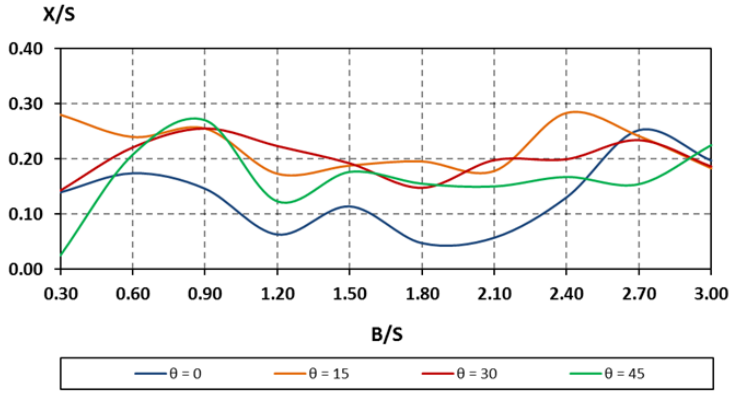

Σχ. 35. Το αδιάστατο πλάτος του salient X/S συναρτήσει του λόγου B/S, μεταβάλλοντας το μήκος B.

Καταρχάς, σε καμία των περιπτώσεων δε σχηματίστηκε tombolo. Επίσης, φαίνεται ότι η συμπεριφορά των καμπυλών δεν είναι μονότονη. Το πλάτος των salient αυξάνει με το μήκος των κυματοθραυστών μέχρι $B/S \approx 0.90$. Στη συνέχεια παρατηρείται μία μείωση, μέχρι περίπου το λόγο $B/S \approx 2.0$. Για μεγαλύτερους λόγους B/S ξαναπαρατηρείται αύξηση του X/S. Ωστόσο, αυτή η ταλαντευόμενη συμπεριφορά φαίνεται να συνεχίζεται περεταίρω. Μία πιθανή εξήγηση για τη μη μονότονη αύξηση του X/S είναι ότι καθώς το μήκος των κυματοθραυστών αυξάνει πέραν ενός ορίου, η αλληλεπίδραση των δύο σχηματιζόμενων στροβίλων στα κατάντη τους μειώνεται και τελικώς δημιουργείται μία ουδέτερη ζώνη με αμελητέα κυκλοφορία. Πάντως, σε όλες τις περιπτώσεις ο λόγος X/S κυμαίνεται στο εύρος $0.05 \div 0.30$, που είναι τιμές αρκετά μικρότερες από τις αναμενόμενες για ένα αντίστοιχο σύστημα έξαλων κυματοθραυστών.

Αντίστοιχα, το διάγραμμα του Σχ. 36 προέκυψε για τη μεταβολή της απόστασης των κυματοθραυστών από την ακτογραμμή. Παρόμοια με παραπάνω, παρατηρείται μία μη μονότονη συμπεριφορά, καθώς για ένα εύρος τιμών του λόγου B/S, το πλησίασμα των κυματοθραυστών στην ακτογραμμή δεν οδηγεί απαραίτητα σε μεγαλύτερα salient. Αυτό οφείλεται στο γεγονός ότι οι δύο σχηματιζόμενοι στρόβιλοι συμπιέζονται και τελικώς συγχωνεύονται με τα ρεύματα επαναφοράς, με αποτέλεσμα να παρατηρείται ακόμη και ήπια διάβρωση πίσω από κάποιους κυματοθραύστες. Αυτή είναι μία βασική διαφορά με τους συμβατικούς κυματοθραύστες, πίσω από τους οποίους δεν παρατηρείται ποτέ διάβρωση.

Αντίστοιχα διαγράμματα παρήχθησαν και για τις υπόλοιπες παραμέτρους που εξετάστηκαν. Όσον αφορά στη διάβρωση, αυτή συνήθως παρατηρήθηκε πίσω από τα κενά μεταξύ των κυματοθραυστών και το εύρος της κυμαινόταν μεταξύ του 20% και 60% του πλάτους του salient. Παρόλα αυτά, σε πολλές περιπτώσεις το πλάτος των ζωνών διάβρωσης ήταν μεγαλύτερο από το πλάτος των ζωνών απόθεσης.

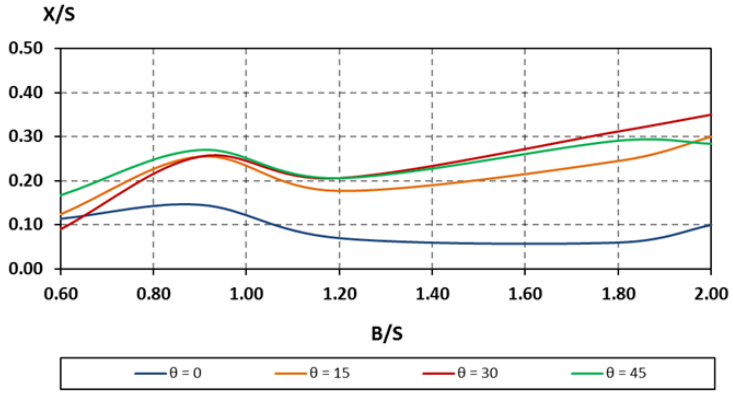

Σχ. 36. Το αδιάστατο πλάτος του salient X/S συναρτήσει του λόγου B/S, μεταβάλλοντας το μήκος S.

8. Συμπεράσματα

Η διάβρωση των ακτών είναι ένα παγκόσμιο πρόβλημα που προκαλείται από διάφορες φυσικές διεργασίες, αλλά και ανθρώπινες δραστηριότητες. Σε πολλές περιπτώσεις, η ανθρώπινη παρέμβαση εντείνει και επιταχύνει ραγδαία το πρόβλημα. Τις τελευταίες δεκαετίες, η λεγόμενη «ήπια» προσέγγιση για την προστασία των ακτών κερδίζει διαρκώς έδαφος. Η κατασκευή των ύφαλων κυματοθραυστών θα μπορούσε να ενταχθεί σε αυτό το πλαίσιο. Από τη βιβλιογραφική ανασκόπηση που διενεργήθηκε στα πλαίσια της Διατριβής προέκυψαν κάποια συμπεράσματα για τα έργα αυτά.

Καταρχάς, από τεχνική άποψη, οι ύφαλοι κυματοθραύστες είναι λιγότερο αποτελεσματικοί από τους έξαλους, ιδιαίτερα σε περιβάλλον σημαντικής παλίρροιας. Ωστόσο, υπερτερούν περιβαλλοντικά καθώς επιτρέπουν αυξημένη ανανέωση των υδάτων, ενώ ασκούν μικρότερη επίδραση στους βιοτικούς και αβιοτικούς παράγοντες της περιοχής. Επιπλέον, υπερτερούν αισθητικά και σε γενικές γραμμές είναι χαμηλότερου κόστους. Παρότι έχει κατασκευαστεί ένας αριθμός ύφαλων κυματοθραυστών παγκοσμίως, η αποτελεσματικότητά τους, από ακτομηχανική άποψη, ποικίλει σημαντικά. Για παράδειγμα, σε κάποιες περιπτώσεις εμφανίστηκε διάβρωση εκεί που αναμενόταν απόθεση, με αποτέλεσμα ο σχεδιασμός των συγκεκριμένων έργων να κρίνεται αποτυχημένος. Συμπεραίνεται, λοιπόν, ότι η συμπεριφορά των έργων αυτών και η επίδρασή τους στη μορφολογία της περιοχής δεν έχουν γίνει πλήρως κατανοητές.

Όσον αφορά στους βασικούς στόχους της Διατριβής, εξήχθησαν τα παρακάτω συμπεράσματα:

- Αναπτύχθηκε ένα ολοκληρωμένο διδιάστατο αριθμητικό μοντέλο για την πρόβλεψη της εξέλιξης της βυθομετρίας στα κατάντη ενός συστήματος ύφαλων κυματοθραυστών. Η επαλήθευσή του με τις πειραματικές μετρήσεις έδειξε ικανοποιητική ακρίβεια. Επειδή τα τεστ αυτά αναφέρονταν σε ένα πλήθος διαφορετικών κυματικών συνθηκών, μπορεί να

στηριχθεί το συμπέρασμα ότι το εν λόγω μοντέλο είναι ένα αξιόπιστο εργαλείο για τη μελέτη σύνθετων υδροδυναμικών και μορφοδυναμικών διεργασιών.

- Το μοντέλο είναι σύνθετο και αποτελείται από τέσσερα υπομοντέλα, το κυματικό, το υδροδυναμικό, στερεομεταφοράς και το γεωμορφολογικό. Καθένα από αυτά τα επιμέρους μοντέλα επαληθεύτηκε επαρκώς και συνεπώς μπορούν να χρησιμοποιηθούν για την προσομοίωση υδροδυναμικών και μορφολογικών διεργασιών στην παράκτια ζώνη, ανεξαρτήτως από την παρουσία των ύφαλων κατασκευών.

- Η εφαρμογή της τεχνικής που βασίζεται στον 'morphological acceleration factor', σε συνδυασμό με την αυξανόμενη ισχύ των υπολογιστών επιτρέπουν την εφαρμογή γεωμορφολογικών μοντέλων που βασίζονται σε κυματικά μοντέλα του χώρου των φάσεων (phase-resolving models). Πρακτικά, το παρόν μοντέλο μπορεί να εφαρμοστεί για την προσομοίωση της βραχυχρόνιας εξέλιξης της μορφολογίας, της τάξης ωρών ή μερικών ημερών.

- Διενεργήθηκαν τριδιάστατα εργαστηριακά πειράματα σε δεξαμενή κυμάτων, τα οποία περιελάμβαναν αμμώδη πυθμένα στα κατάντη ενός διαπερατού ύφαλου κυματοθραύστη. Η εξέλιξη της βυθομετρίας και της ακτογραμμής δεν απείχε πολύ από αυτή που αναμενόταν θεωρητικά, παρότι το πλάτος των σχηματιζόμενων salient ήταν, σε γενικές γραμμές, μικρότερο του προβλεπόμενου (Ahrens and Cox, 1990; Black and Andrews, 2001). Επομένως, συμπεραίνεται ότι οι σχετιζόμενες με τους ύφαλους μορφολογικές διεργασίες μπορούν να εξεταστούν σε φυσικά ομοιώματα με κινητό πυθμένα, εφόσον επιλεχθούν με προσοχή οι χωροχρονικές κλίμακες.

- Τόσο τα εργαστηριακά πειράματα, όσο και η εφαρμογή του αριθμητικού μοντέλου οδήγησε σε όλες τις περιπτώσεις στο σχηματισμό salient στα κατάντη του διαπερατού ύφαλου κυματοθραύστη. Το μήκος και το πλάτος του salient εξαρτάται από τα κυματικά χαρακτηριστικά. Για παράδειγμα, οι πιο βραχείς κυματισμοί με μεγαλύτερο ύψος οδηγούν σε πιο «αιχμηρά» salient από ότι οι μακρύτεροι κυματισμοί. Επίσης, οι απλοί μονοχρωματικοί κυματισμοί συνδέονται με το σχηματισμό μεγαλύτερων salient από ότι οι αντίστοιχοι σύνθετοι κυματισμοί με ίδιο σημαντικό ύψος κύματος και περίοδο αιχμής. Τέλος, σε αντίθεση με τις προβλέψεις του Pilarczyk (2003), σε καμία από τις περιπτώσεις που εξετάστηκαν δεν παρατηρήθηκε ο σχηματισμός tombolo.

- Από τα αριθμητικά πειράματα που διενεργήθηκαν συμπεραίνεται ότι η απόκριση της ακτογραμμής σε ένα σύστημα ύφαλων κυματοθραυστών εξαρτάται από κάποιες βασικές γεωμετρικές παραμέτρους σχεδιασμού: το μήκος των κυματοθραυστών, την απόστασή τους από την αρχική ακτογραμμή, το κενό ανάμεσά τους και το πορώδες τους. Επιπλέον,

η εξέλιξη της ακτογραμμής εξαρτάται και από τα κυματικά χαρακτηριστικά: την περίοδο, το ύψος και τη γωνία πρόσπτωσης των κυμάτων. Επίσης, μια κρίσιμη παράμετρος είναι ο συντελεστής διάδοσης πάνω από τον ύφαλο. Ωστόσο, σε αντίθεση με τους συμβατικούς κυματοθραύστες, αυτή η εξάρτηση δεν είναι μονότονη. Για παράδειγμα, η τοποθέτηση ύφαλων κυματοθραυστών όλο και πιο κοντά στην ακτογραμμή δεν οδηγεί σε μονότονη αύξηση του πλάτους του σχηματιζόμενου salient. Αντίθετα, μπορεί να παρατηρηθεί ακόμη και διάβρωση αντί απόθεσης. Επομένως, οι διεργασίες που σχετίζονται με την εξέλιξη της ακτογραμμής είναι διαφοροποιημένες στην περίπτωση των ύφαλων σε σχέση με αυτές στους έξαλους κυματοθραύστες. Μάλιστα, λόγω της αυξημένης πολυπλοκότητας των διεργασιών αυτών, είναι δύσκολο να εξαχθούν γενικοί κανόνες σχεδιασμού των ύφαλων έργων ή εμπειρικών κριτηρίων, παρόμοιων με αυτών των συμβατικών κυματοθραυστών. Από την αριθμητική διερεύνηση που διενεργήθηκε παρήχθησαν διαγράμματα που παρέχουν κάποια ποσοτικά αποτελέσματα για την εξάρτηση της εξέλιξης της ακτογραμμής από βασικές παραμέτρους σχεδιασμού. Ωστόσο, θα πρέπει να λογίζονται ως προσεγγιστικά, καθώς απαιτείται περεταίρω επαλήθευσή τους με μετρήσεις, κυρίως στο πεδίο.

Παραπάνω συνοψίστηκαν τα κεντρικά συμπεράσματα της Διατριβής. Κατά την εξέλιξή της εξήχθησαν αρκετά επιπλέον συμπεράσματα που αναφέρονται στα επιμέρους τμήματα της έρευνας.

Βιβλιογραφικές αναφορές

Ahrens, J. P., and Cox, J. (1990). “Design and performance of reef breakwaters.” *J. Coast. Res.*, 6 (1), 61-75.

Avgeris, I., Karambas, Th. V., and Prinos, P. (2004). “Boussinesq modeling of wave interaction with porous submerged breakwaters.” *Proc. 29th Int. Conf. on Coastal Eng.*, J. M. Smith, ed., Lisbon, Portugal, 604-616.

Bailard, J. (1981). “An energetics total load sediment transport model for a plane sloping beach.” *J. Geophys. Res.*, 86 (C11), 10938–10954.

Basco, D. R. (1983). "Surfzone currents." *Coast. Eng*., 7 (4), 331-355.

Beji, S., and Battjes, J. A. (1994). "Numerical simulation of nonlinear wave propagation over a bar." *Coast. Eng*., 23 (1-2), 1-16.

Berkhoff, J. C. W., Booij, N., and Radder, A. C. (1982). "Verification of numerical wave propagation models for simple harmonic linear water waves." *Coast. Eng*., 6 (3), 255–279.

Bijker, E. W. (1968). “Littoral drift as function of waves and current.” *Proc. 11th Int. Conf. on Coastal Engineering*, ASCE, London, United Kingdom, vol. I, chapter 26, pp. 415-435.

Black, K., and Andrews, C. (2001). “Sandy shoreline response to offshore obstacles: Part 1. Salient and tombolo geometry and shape.” *J. Coast. Res.*, Special Issue 29 Natural and Artificial Reefs for Surfing and Coastal Protection, pp. 82– 93.

Boussinesq, M. J. (1872). “Théorie des ondes et des remous qui se propagent le long d' un canal rectangulaire horizontal, en communiquant au liquide contenu dans ce canal des vitesses sensiblement pareilles de la surface au fond.” *J. Math. Pures Appl.*, Deuxième Série, 17: 55-108.

Camenen, B., and Larson, M. (2005). “A general formula for non-cohesive bed load sediment transport.” *Estuar. Coast. Shelf Sci.*, 63 (1-2), 249–260.

Camenen, B., and Larson, M. (2006). “Phase-lag effects in sheet flow transport.” *Coast. Eng.*, 53 (5-6), 531–542.

Camenen, B., and Larson, M. (2007). “A unified sediment transport formulation for coastal inlet application.” *Tech. rep. ERDC/CHL CR-07-1*, U.S. Army Engineer Research and Development Center, Vicksburg, MS, U.S.A., 231 pp.

Camenen, B., and Larson, M. (2008). “A general formula for noncohesive suspended sediment transport.” *J. Coastal Res.*, 24 (3), 615–627.

Chen, Q. (2006). "Fully nonlinear Boussinesq-type equations for waves and currents over porous beds." *J. Eng. Mech.*, 132 (2), 220-230.

Chen, Q., Dalrymple, R. A., Kirby, J. T., Kennedy, A. B., and Haller, M. C. (1999). "Boussinesq modeling of a rip current system." *J. Geophys. Res*., 104 (C9), 20617-20637.

Chen, Q., Kirby, J. T., Dalrymple, R. A., Kennedy, A. B., and Chawla, A. (2000). "Boussinesq modeling of wave transformation, breaking and runup. II: 2D." *J. Waterw. Port Coast. Ocean Eng*., 126 (1), 48-56.

Cruz, E. C., Isobe, M., and Watanabe, A. (1997). “Boussinesq equations for wave transformation on porous beds.” *Coast. Eng.*, 30 (1-2), 125-156.

Dally, W. R., and Pope, J. (1986). “Detached breakwaters for shore protection.” *Tech. Rep.*, CERC-86-1, U.S. Army Engineer Waterways Experiment Station, Vicksburg, MS, U.S.A.

Dibajnia, M., Moriya, T., and Watanabe, A. (2001). “A representative wave model for estimation of nearshore local transport rate.” *Coast. Eng. J.*, 43 (1), 1-38.

Engelund, F., and Fredsøe, J. (1976). “A sediment transport model for straight alluvial channels.” *Nord. Hydrol.*, 7, 293-306.

Fredsøe, J., and Deigaard, R. (1992). "Mechanics of coastal sediment transport." *Advanced Series on Ocean Engineering*, World Scientific Publishing, Singapore, vol. 3, 369 pp.

Gravens, M. B., and Wang, P. (2007). "Data report: laboratory testing of longshore sand transport by waves and currents; morphology change behind headland structures." *Tech. Rep.*, ERDC/CHL TR-07-8, Coastal and Hydraulics Laboratory, U.S. Army Engineer Research and Development Center, Vicksburg, MS, U.S.A.

Groenewoud, M., Van der Graaff, J., Claessen, E., and Van der Beizen, S. (1996). "Effect of submerged breakwater on profile development." *Proc. 25th Int. Conf. on Coastal Eng.*, B. L. Edge, ed., Orlando, Florida, U.S.A., pp. 2428–2441.

Hamm, L. (1992b). "Random wave propagation in the nearshore zone: experiments in a directional wave basin." *Internal report*, MAST-G6M, SOGREAH.

Hansen, J. B., and Svendsen, I. A. (1979). "Regular waves in shoaling water, experimental data." Inst. Hydrodyn. Hydr. Eng., *Series Paper*, 21.

Hsiao, S., Liu, P. L.-F., and Chen, Y., (2002). "Nonlinear water waves propagating over a permeable bed." *Proc. R. Soc. London*, Ser. A, 458, 1291–1322.

Jonsson, I.G. (1966). "Wave boundary layers and friction factors." *Proc. 10th Int. Conf. on Coastal Engineering*, J. W. Johnson, ed., ASCE, Tokyo, Japan, pp. 127-148.

Karambas, Th. V., and Koutitas, C. (2002). "Surf and swash zone morphology evolution induced by nonlinear waves." *J. Waterway, Port, Coastal, Ocean Eng.*, 10.1061/(ASCE)0733-950X(2002)128:3(102), 102-113.

Karambas, Th., Krestenitis, I., and Koutitas, Ch. (2016). *Coastal Engineering – Shore Protection Structures*. Hellenic Academic Libraries, 156 pp. (in greek).

Karambas, Th. V., and Memos, C. D. (2009). "Boussinesq model for weakly nonlinear fully dispersive water waves." *J. Waterway, Port, Coastal, Ocean Eng.*, 10.1061/(ASCE)0733-950X(2009)135:5(187), 187-199.

Karambas, Th. V., and Samaras, A. G. (2014). "Soft shore protection methods: The use of advanced numerical models in the evaluation of beach nourishment." *Ocean Eng.*, 92, 129-136.

Kennedy, A. B., Chen, Q., Kirby, J. T., and Dalrymple, R. A. (2000). "Boussinesq modeling of wave transformation, breaking and runup. I: 1D." *J. Waterw. Port Coast. Ocean Eng*., 126 (1), 39-47.

Klonaris, G. Th., Memos, C. D., and Drønen, N. K. (2016). "High-order Boussinesq-type model for integrated nearshore dynamics." *J. Waterw. Port Coast. Ocean Eng*., 142 (6), 04016010.

Kobayashi, N., Agarwal, A., and Bradley, D. J. (2007). "Longshore current and sediment transport on beaches." *J. Waterw. Port Coast. Ocean Eng*., 133 (4), 296-304.

Koutsouvela, D., Karambas, Th. V., Avgeris, I., and Karathanassi, E. (2007). "Functional design of submerged breakwaters for coastal protection using two wave/morphological models." *Proc. Coastal Structures '07*, Venice, Italy, pp. 1205-1216.

Kramer, M., Zanuttigh, B., Baoxing, W., Van der Meer, J., Vidal, C., Gironella, F. (2005). "Laboratory experiments on low-crested breakwaters." *Coast. Eng*., 52 (10-11), 867-885.

Larson, M., Kraus, N. C., and Wise, R. A. (1999). "Equilibrium beach profiles under breaking and non-breaking waves." *Coast. Eng.*, 36 (1), 59–85.

Larson, M., and Wamsley, T. V. (2007). "A formula for longshore sediment transport in the swash." *Proceedings Coastal Sediments '07*, ASCE, New Orleans, U.S.A., pp. 1924–1937.

Lesser, G. R., Roelvink, J. A., van Kester, J. A. T. M., and Stelling, G. S. (2004). "Development and validation of a three-dimensional morphological model." *Coast. Eng.*, 51 (8–9), 883– 915 (October).

Lesser, G. R., Vroeg, J. H., Roelvink, J. A., de Gerloni, M., and Ardone, V. (2003). "Modelling the morphological impact of submerged offshore breakwaters." *Proc. Coastal Sediments '03*, World Scientific Publishing Co, Clearwater Beach, Florida, USA, May 18-23, on CD-ROM.

Longuet-Higgins, M. S., and Stewart, R. W. (1961). "The changes in amplitude of short gravity waves on steady non-uniform currents." *J. Fluid Mech*., 10 (4), 529–549.

Madsen, P. A., and Schäffer, H. A. (1998). "Higher-order Boussinesq-type equations for surface gravity waves: derivation and analysis." *Phil. Trans. R. Soc. Lond. A*, 356(1749), 3123-3184.

Madsen, P. A., and Sørensen, O. R. (1992). "A new form of the Boussinesq equations with improved linear dispersion characteristics. Part 2. A slowly-varying bathymetry." *Coast. Eng.*, 18(3-4), 183-204.

Madsen, P. A., Sørensen, O. R., and Schäffer, H. A. (1997). "Surf zone dynamics simulated by a Boussinesq type model. Part I. Model description and cross-shore motion of regular waves." *Coast. Eng*., 32 (4), 255-287.

Memos, C. D., Karambas, Th. V., and Avgeris, I. (2005). "Irregular wave transformation in the nearshore zone: experimental investigations and comparison with a higher order Boussinesq model." *Ocean Eng*., 32 (11-12), 1465-1485.

Metallinos, A. S., Emmanouilidou, M.-E. A., and Memos, C. D. (2014). "Wave-induced pore pressures in submerged rubble mound breakwaters simulated by a compound Boussinesq model." *J. Hydraul. Res*., 52 (1), 24–35.

Nam, P. T., Larson, M., Hanson, H., and Hoan, L. H. (2009). "A numerical model of nearshore waves, currents, and sediment transport." *Coast. Eng*., 56 (11-12), 1084-1096.

Ottesen-Hansen, N. E. (1978). “Long period waves in natural wave trains.” *Progress report*, No. 46, Institute of Hydrodynamics and Hydraulic Engineering, Technical University of Denmark, pp. 13-24.

Peregrine, D. H. (1967). “Long waves on a beach.” *J. Fluid Mech.*, 27 (4), 815-827.

Pilarczyk, K. W. (2003). “Design of low-crested (submerged) structures – an overview –.” *6th International Conference on Coastal and Port Engineering in Developing Countries*, Colombo, Sri Lanka.

Putrevu, U., and Svendsen, I. A. (1993). “Vertical structure of the undertow outside the surf zone.” *J. Geophys. Res.*, 98 (C12), 22707–22716.

Rakha, K. A., Deigaard, R., and Brøker, I. (1997). “A phase-resolving cross-shore transport model for beach evolution.” *Coast. Eng*., 31 (1-4), 231-261.

Ranasinghe, R., Larson, M., and Savioli, J. (2010). “Shoreline response to a single shore-parallel submerged breakwater.” *Coast. Eng.*, 57 (11-12), 1006–1017.

Ribberink, J. S. (1998). “Bed-load transport for steady flows and unsteady oscillatory flows.” *Coast. Eng*., 34 (1-2), 59–82.

Roelvink, J. A. (2006). “Coastal morphodynamic evolution techniques.” *Coast. Eng.*, 53 (2-3), 277-287.

Roelvink, J. A., and Reniers, A. J. H. M. (1995). “LIP 11D delta flume experiments.” *Delta data Rep. H 2130*, Delft Hydraulics , Delft, The Netherlands.

Sand, S. E., and Mansard, E. P. D. (1986). “Reproduction of higher harmonics in irregular waves.” *Ocean Eng.*, 13(1), 57-83.

Schäffer, H. A., Deigaard, R., and Madsen, P. A. (1992). “A two-dimensional surf zone model based on the Boussinesq equations.” *Proc. 23rd Int. Conf. on Coastal Engineering*, B. L. Edge, ed., ASCE, Venice, Italy, pp. 576-590.

Schäffer, H. A., and Madsen, P. A. (1995). “Further enhancements of Boussinesq-type equations.” *Coast. Eng.*, 26(1-2), 1-14.

Skjelbreia, L., and Hendrickson, J. (1960). “Fifth order gravity wave theory.” *Proc. 7th Int. Conf. on Coastal Engineering*, J. W. Johnson, ed., Vol. 1, The Hague, Netherlands, 184-196.

Sollitt, C. K., and Cross, R. H. (1972). “Wave transmission through permeable breakwaters.” *Proc. 13th Int. Conf. on Coastal Engineering*, ASCE, Vancouver, Canada, pp. 1827-1846.

Sørensen, O. R., Schäffer, H. A., and Sørensen, L. S. (2004). “Boussinesq-type modelling using an unstructured finite element technique.” *Coast. Eng*., 50 (4), 181-198.

Soulsby, R. (1997). *Dynamics of marine sands, a manual for practical applications*. Thomas Telford, H.R. Wallingford, England, 249 pp.

Synolakis, C. E. (1987). "The runup of solitary waves." *J. Fluid Mech*., 185, 523–545.

Tao, J. (1983). "Computation of wave run-up and wave breaking." *Internal Report*, Danish Hydraulic Institute, 40 pp.

Turner, I. L., Leyden, V. M., Cox, R. J., Jackson, L. A., and McGrath, J. (2001). "Physical model study of the gold coast artificial reef." *J. Coast. Res.*, Special Issue 29, 131–146.

Van der Biezen, S. C., Van der Graaff, J., Schaap., J., Torrini, L. (1997). "Small scale tests and numerical modeling of the hydrodynamic and morphological effects of submerged breakwaters." *Proc. Combined Australian Coastal Engineering and Ports Conf.*, 219-224.

Van Gent, M. R. A. (1995). "Wave interaction with permeable coastal structures." Ph.D. thesis, Delft University of Technology, The Netherlands.

Watanabe, A. (1988) "Modeling of sediment transport and beach evolution." In: *Nearshore Dynamics and Coastal Processes*, K. Horikawa, ed., University of Tokyo Press, Tokyo, Japan, pp. 292– 302.

Wei, G., and Kirby, J. T. (1995). "Time-dependent numerical code for extended Boussinesq equations." *J. Waterw. Port Coast. Ocean Eng.*, 121 (5), 251-261.

Zhan, J. M., Li, Y. S., and Wai, O. W. H. (2003). "Numerical modeling of multi-directional irregular waves incorporating 2-D numerical wave absorber and subgrid turbulence." *Ocean Eng*., 30 (1), 23-46.

Zlatev, Z., Berkowicz, R., Prahm L. P. (1984). "lmplementation of a variable stepsize variable formula method in the time-integration part of a code for treatment of long-range transport of air pollutants." *J. Comput. Phys*., 55 (2), 278-301.

Zyserman, J. A., Jorgensen, K., and Christensen, E. D. (1999). "Sediment transport and morphology in the vicinity of shore parallel breakwaters." *Proc. Coastal Structures '99*, ASCE, Santander, Spain, pp. 857-863.

Abstract

Morphodynamics in a beach with submerged breakwaters

by Georgios Th. Klonaris

National Technical University of Athens
School of Civil Engineering
Department of Water Resources and Environmental Engineering
Laboratory of Harbour Works

Coastal zone has been an attractive environment for man since ancient times. However, the extreme accumulation of human activities has resulted to undue pressure to these vulnerable areas with adverse social, environmental and economic effects. A significant problem that the humanity faces is the accelerating number of conflicts between development on the coast and coastal erosion. In addition, the so-called greenhouse effect and other, not of human origin, long-scale climate variations are predicted to intensify the global erosion problem.

Nowadays, most countries have legislations for nature protection, which enforces restrictions on construction activities near the coastline and force the performance of impact assessment studies. Nevertheless, until recently, the great majority of coastal interventions relied on the "hard" protection concept which includes the construction of large structures made of concrete or stones, similar to harbour works. However, conventional hard protection projects can cause severe transformation of the coastal processes that may occasionally lead to a total inverse of the desired result. In the light of this discussion, 'soft' protection projects become more and more popular among coastal engineers.

During the last years submerged breakwaters have stimulated the scientific interest as an alternative solution to conventional ones for coastal defense. They form a somehow soft protection project and consequently they are generally less effective, in coastal engineering terms, than emerging structures. However, in cases of weak wave and tidal regimes submerged structures can be more attractive than conventional ones since they are friendlier to the environment, aesthetically superior and usually of lower cost. The present research effort intends to contribute to this direction as it tackles coastal numerical modelling in combination to the existence of submerged breakwaters.

In particular, two were the main objectives of the present Ph.D. thesis. At first, to contribute in the understanding of the complex hydrodynamic and morphodynamic processes that take

place in coastal zones protected by a single or arrays of submerged breakwaters. Secondly, to develop an integrated numerical model that simulates the wave propagation, the wave-induced currents, the coastal sediment transport, the bed erosion and accretion, and finally describe the cross-shore profile and the coastline evolution in the lee of a system of permeable submerged breakwaters.

The first step was to choose the wave model that forms the basis of the integrated numerical model. In most of the existing sediment transport models, the required wave input is taken from the results of phase-averaged wave models. However, in the present dissertation a more sophisticated sediment transport modelling was required. Thus, a phase-resolving wave model was developed. Wave resolving models have the advantage that they can inherently predict the wave skewness and asymmetry which are very important for an accurate estimation of the intra-wave sediment transport rates. In addition, Boussinesq-type models take into account the effect of wave irregularity, bound and free long waves, wave groups, and the nonlinear wave-wave interactions. These features are also very important for the accurate calculation of sediment loads. For these reasons, the wave model was decided to be of Boussinesq-type. Hence, enhanced nonlinear versions of two existing Boussinesq-type models were derived. Then, through a mathematical analysis and comparison of the characteristics of dispersion and nonlinearity of the aforementioned models, the most suitable for the scope of the present thesis was chosen. The specific model can simulate wave propagation from deep to shallow water and it is of enhanced nonlinearity compared to its predecessor. In addition, both 1DH and 2DH model versions were derived.

The second step was to extend the basic Boussinesq solver to account for the entire nearshore zone. In particular, it was extended to the surf and swash zones in order to simulate wave breaking and wave runup and run-down. Bottom friction and subgrid turbulent mixing were also incorporated. Due to its nonlinear character the model can also offer an estimation of the wave-induced current field, including the depth-averaged and the near-bed undertow. Furthermore, an improved numerical scheme was presented compared to Adams-Bashforth-Moulton scheme, which was widely used by other model predecessors. An investigation of the numerical properties of the model is also presented. Finally, an extensive validation of the wave model was performed including a number of physical processes, such as shoaling, depth refraction, diffraction, breaking, wave run-up, overtopping, nonlinear energy transfer, and interactions with the wave-induced current field.

After testing the wave and hydrodynamic modules, the non-cohesive sediment transport module was developed. The bed load in the surf zone is computed from a sophisticated semi-empirical formula, while the suspended load can be calculated through the solution of the advection-diffusion equation for the sediment or alternatively from a simplified formula. The estimation of the sediment transport in the swash zone is based on the ballistic theory. The

unified sediment transport module is valid under combined waves and currents including the wave asymmetry and phase-lag effects. Then, the geomorphological module was developed. In particular, the bathymetry is updated through the sediment conservation equation and the morphological accelerator factor technique accounts for extended simulation periods allowing practical applications of the model. The compound model was validated against a number of short-term tests both in one and two horizontal dimensions and its response was generally good, with most of the morphological features being reproduced both in the cross-shore and longshore directions. A sensitivity analysis was also performed illustrating the significance of the accurate estimation of some parameters and the need for inclusion of the unsteady effects.

The following step was the execution of a set of laboratory experiments in a wave tank with horizontal dimensions 12 m x 7 m and maximum water depth 1.05 m. The layout included a permeable submerged breakwater with a length of 3 m, placed on a sloping ramp made of aluminum which had a width of 4 m. Down-wave of the submerged breakwater fine sand was placed representing a sandy beach. Eight test cases were studied referring to normal incidence of both regular and irregular waves. Before the initiation of each test the sandy bed was carefully reshaped to a plane beach. After some hours of wave incidence, a steady state was established and the final bed elevation was measured. Throughout the international literature there is a lack of measurements referring to morphology evolution in the lee of submerged breakwaters. From this point of view, the specific experiments themselves may offer some original contribution, both by providing a dataset for model validation, but also by helping in drawing some conclusions for the behaviour of submerged breakwaters straight from laboratory observations.

The compound model was then extended to account for porous beds. This task required the modification of the basic solver in order to include an additional flow equation for the porous medium. The mathematical properties of the extended equations were also investigated and improved compared to some previously presented models. Finally, the aforementioned eight experimental scenarios were simulated by the model in order to check its efficiency to reproduce the complex hydrodynamic and morphological processes associated with the presence of submerged breakwaters.

The last step included the performance of a number of numerical experiments in order to investigate the shoreline response to an array of permeable submerged breakwaters. In particular, the effect of a number of design parameters on the shoreline evolution was studied, i.e. breakwaters' length, distance from the initial shoreline, gap length between adjacent breakwaters, porosity, wave period. A number of empirical design rules and criteria have been proposed in the past for emergent breakwaters based on these design parameters. However, this is not the case for submerged breakwaters. There is a gap in the international literature about reliable guidelines for the design of submerged breakwaters. From the present

investigation, a number of figures connecting the shoreline response to various design parameters were produced. Although, these figures may contribute to the understanding of this very complex behaviour, a further investigation is needed before concluding whether general design rules for submerged breakwaters are feasible. Nevertheless, judging from the results of the present research and other similar works, the processes governing the shoreline response to submerged and emergent structures seem to be quite different.

In brief, the main objective of the dissertation to develop an integrated numerical tool for studying the morphodynamics associated with permeable submerged breakwaters was adequately reached. On the way to fulfill this objective the development and validation of the various modules offered some individual conclusions for the wave propagation, wave-induced currents, sediment transport processes, and coastal geomorphology. Also, the laboratory experiments offered useful information and datasets for model validation. Finally, some practical conclusions were drawn for the shoreline evolution in the lee of systems of submerged breakwaters. However, a number of issues require further investigation and suggestions for future research have been also included.

Contents

List of Figures

Chapter 1. Introduction

Chapter 2. Nonlinear analysis of higher order Boussinesq-type wave models

Chapter 3. Integrating nearshore dynamics with the Boussinesq-type wave model

Chapter 4. Sediment transport model

Chapter 5. Laboratory experiments with submerged breakwaters

Chapter 6. Model extension to porous beds

Chapter 7. Shoreline response to an array of submerged breakwaters

Chapter 8. Conclusions and future research

List of Tables

List of Symbols

The symbols used are listed below. Due to the large number of parameters, it has been decided to use some double symbols. In most cases their use is restricted to a single chapter or subsection, as stated in the following list. In any case, it should be easy to distinguish between these parameters from the context they are used in.

A (chapter 2)	wave amplitude
A (subsection 3.2.2)	cross-sectional area in the slot technique
A (subsection 3.3.3)	Amplification matrix
A (chapter 4)	parameter associated with Einstein's (1950) integrals
A	parameter in Dean's (1991) equilibrium profile
A_b	water particle amplitude of the near-bottom horizontal oscillation
A_{sb}, A_{ss}	auxiliary variables in Soulsby's (1997) formula
a_1, a_2, a_3	wave amplitude of first-, second- and third-order Stokes waves
B	breakwater length
B, B_1, B_2	free parameters
B′	constant
B_{br}, δ_b, ζ_t^* $\zeta_t^{(F)}$, $\zeta_t^{(I)}$, t_0, T^*	parameters related to wave breaking
b	width of the equivalent wave flume in the slot technique
b_d, b	parameters in Bailard's (1981) formula
$C(z)$	sediment concentration vertical profile
c	phase celerity
c	sediment's volume concentration in Soulsby's (1997) formula
C_a, c_R	sediment reference concentration at the height z_a
C_{ave}	depth-averaged sediment concentration
C_b, μ_c, ξ_B	parameters in Bijker's (1968) formulae
C_c	Chezy friction coefficient
C_c	coefficient of curvature
C_D	drag coefficient
C_f	turbulent friction coefficient
c_m	added mass coefficient
CPU	computational time
C_r	Courant number
c_r	inertial coefficient
c_s	mixing coefficient
C_u	coefficient of uniformity
$c^{(x)}$, $c^{(y)}$	wave celerity in the *x* and *y* directions, respectively
c_0	parameter in the original Boussinesq equations

D	wave energy dissipation per unit area due to breaking
$D(x), \Psi(x), \varphi(x)$	functions
d, h_0	still water depth
D_{b}	dissipation of turbulent kinetic energy
d_{b}	still water depth at the breaking line
D_{c}	energy dissipation per unit area from the bed friction due to current
$d_o^{'}$	reference still water depth
D_r	sediment deposition rate
$\widetilde{D}_r$	modified sediment deposition rate
D_s	magnitude of the source function
d_s	average depth at the breakwater
D_{w}	energy dissipation per unit area from the bed friction due to waves
d_{10}, d_{30}, d_{60}, d_{84}	Characteristic diameters of sediments
d_{50}	median grain diameter
d_*	dimensionless grain size
E, E'	
F, F', F_1, F_2	auxiliary functions
G, G', G_1, G_2	
Er	relative error of water volume
f	wave frequency
F'	dimensional velocity potential
F_{br}, G_{br}	wave breaking terms in the *x* and *y* directions, respectively
$F_{\mathrm{eddy}}, G_{\mathrm{eddy}}$	Smagorinsky-type terms in the *x* and *y* directions, respectively
Fr	Froude number
F_{sp}, G_{sp}	Sponge layer terms in the *x* and *y* directions, respectively
F_U, F_α, F_V, f	functions
f_c (chapter 2)	cutoff frequency
f_c (chapter 3)	bed friction coefficient due to current
f_{ct}	total friction coefficient
f_{cw}, $\mathrm{c_f}$	bed friction coefficient for combined wave and current
f'_{cw}	wave-current skin friction factor
f_{MOR}, MF	morphological accelerator factor
F_o	Dean's (1973) parameter
f_p	Peak frequency
f^r, f, f^*	auxiliary variables
F_s	auxiliary function related to the wave source
f_s	source function term
f_w	bed friction coefficient due to waves
f_{wt}	total friction coefficient due to waves
F_*	densimetric Froude number
$f_{2.5}$	wave friction factor based on an equivalent roughness $K_N^{'} = 2.5d_{50}$

G	gap length between two adjacent breakwaters
G_{bx}, G_{by}	improper integrals
$G_{\zeta}^{\pm}$, $G_{U}^{\pm}$	second-order transfer functions
g	gravitational accelerate
H'	reference wave height
H_{b}	wave height at the breaking line
h_b (chapter 6)	vertical distance from the SWL to the impermeable bottom
h_b (chapter 7)	total depth at the center of the breakwater
h_{c}	water depth at crest of the structure
H_{deep}	wave height in deep water
H_i	incident wave height at submerged breakwater
$H_{\mathrm{m_o}}$	significant wave height as computed by the spectrum
H_{rms}	root-mean-square wave height
H_s	significant wave height
h_s	porous layer thickness
H_t	transmitted wave height over submerged breakwater
H_{w}	wave height in Bijker's (1968) formula
h	instantaneous total water depth
I	auxiliary variable related to the source function
I_s	beach response index according to Ahrens and Cox (1990)
I_U, I_B	auxiliary variables related to the foreshore equilibrium slope
I_1, I_2	Einstein integrals
K	intrinsic permeability
KC	Keulegan-Carpenter number
K_c, K_l u_0, v_0, t_o, z_o t_s, t_e, t_m	parameters related to Larson and Wamsley's (2007) formula
K_d	wave diffraction coefficient
$K_{d,t}$	global transmission coefficient combining K_d and K_t
K_N	bed roughness
$K_N{}'$	equivalent bed roughness equal to $2.5d_{50}$
k (chapter 2)	wavenumber
k (chapter 4)	turbulent kinetic energy
$\bar{k}$	depth- and time-averaged turbulent kinetic energy
k_r, k_i	real and imaginary parts of the wavenumber
$k_o{}'$	reference wavenumber
k_{sct}, k_{swt}	total bed roughness due to current and waves, respectively
K_t	transmission coefficient
K_x, K_y	diffusion coefficients in the AD-equation for suspended sediment
L'	reference wavelength
L_{B_1}, L_{B_2}, L_γ	linear operators

L_{deep}	Wavelength in deep water
$L_{loc}{}'$	wavelength of a regular wave
l_s	non-dimensional length in physical model
L_x, L_y	wavelength in the *x* and *y* directions, respectively
M	solid fraction of the gross sediment volume
$m_{11}^{(1)}$, $m_{12}^{(1)}$ $m_{21}^{(1)}$, $m_{22}^{(1)}$	auxiliary variables related to first-order solution in Fourier analysis
$m_{11}^{(2)}$, $m_{12}^{(2)}$, F_1 $m_{21}^{(2)}$, $m_{22}^{(2)}$, F_2	auxiliary variables related to second-order solution in Fourier analysis
$m_{11}^{(3)}$, $m_{12}^{(3)}$, F_1 $m_{21}^{(3)}$, $m_{22}^{(3)}$, F_2	auxiliary variables related to third-order solution in Fourier analysis
N_L	geometrical scale factor
N_{q}	sediment transport scale
n_p	sediment porosity
N_T	time scale factor
$N_{t,mor}$	morphological time scale factor
N_v	kinematic viscosity scale factor
N_z	vertical length scale
N_ω	settling velocity scale
$N_{(1-\text{p})}$	material porosity scale
p	water pressure
p	fraction of sediment particles transported near the bed in Engelund and Fredsøe's (1976) formula
P_r	sediment pick-up rate
$\tilde{P}_r$	modified sediment pick-up rate
p_{s}	pore pressure
$q_{bc,\text{net}}$	net cross-shore sediment transport rate in the swash zone
$q_{bl,\text{net}}$	net longshore sediment transport rate in the swash zone
Q_{meas}	integral volume of sediment transport computed from measured bed elevation
q_{sb}	dimensional volumetric bed load rate per unit width
$q_{sb,w}$	dimensional bed load rate per unit width in the wave direction
$q_{sb,n}$	dimensional bed load rate per unit width in the direction normal to waves
q_{ss}	dimensional suspended load rate per unit width
$q_{ss,w}$	dimensional suspended load rate per unit width in the wave direction
$q_{ss,n}$	dimensional suspended load rate per unit width in the direction normal to waves
q_{tot}	total sediment transport load per unit width

$q_{x,tot}$, $q_{y,tot}$	total sediment transport rate per unit width in the *x* and *y* directions, respectively
$q'_{x,tot}$, $q'_{y,tot}$	modified total sediment transport rate per unit width in the *x* and *y* directions, respectively
R (chapter 4)	wave run-up height
R (chapter 6)	Non-dimensional permeability
R^*	response function
R_*	grain size Reynolds number
R'_*, m_b, l'_s, V'_ω	dimensionless numbers associated with suspension-dominated movable-bed physical models
r_{w}	wave asymmetry coefficient
S	distance from breakwater to the initial shoreline
s (chapter 2)	auxiliary variable
s, S_s (chapters 3, 5)	relative density of sediments
s_b	free board
T, T_w	regular wave period
t	time
$T_{\max}$, $T_{\min}$	cut-off periods in irregular wave generation
$\tan\beta$	bed slope
$\tan\beta_e$	foreshore equilibrium slope
T_{p}	peak wave period
T_{wc}, T_{wt}	duration of the onshore and offshore portions of the wave period in Camenen and Larson's (2006, 2007) formula
U	depth-averaged horizontal fluid velocity in the *x* direction
$\widehat{U}$	maximum velocity in the porous medium
U_b	near bottom undertow velocity
U_c	current velocity
$\overline{U}_{\mathrm{cr}}$	threshold current velocity
$U_{\mathrm{cw,onshore}}$ $U_{\mathrm{cw,offshore}}$	root-mean-square value of the near bed velocity over the onshore and offshore portions of the wave period, respectively
U'_f	bed shear velocity related to skin friction
U_o, V_o	uniform velocities below the surface roller in the *x* and *y* directions, respectively
Ur	Ursell number
U_{rms}	root-mean-square wave orbital velocity
U_T	depth-averaged oscillatory horizontal velocity with zero mean in the wave propagation direction
U_1, U_2, U_3	velocity amplitude of first-, second- and third-order Stokes waves
U_{13}	third-order correction to the first-order velocity amplitude solution

u	horizontal water particle velocity in the *x* direction
u_o, v_o	near-bottom velocities in the *x* and *y* directions, respectively
u_{ow}	oscillatory component of near-bottom velocity
u_{ow-max}	amplitude of the oscillatory component of the near-bottom velocity
u_s (chapter 4)	speed of the wave front at the start of the uprush
u_s, v_s (chapter 6)	seepage horizontal velocity in the porous layer in the *x* and *y* directions, respectively
U_{s1}	velocity amplitude of first-order Stokes waves inside the porous layer
U_{w}	peak value of the wave orbital velocity at the bottom in Bijker's (1968) formula
$U_{\mathrm{w}}(t)$	instantaneous near bed velocity in the wave direction
$U_{\mathrm{w,crsf}}$	critical velocity for the inception of sheet flow
$U_{\mathrm{w,max}}$	maximum value of the instantaneous near bed wave velocity
u_*, v_*	bed friction velocity
$u_{*,\mathrm{c}}$	bed friction velocity due to current only
$u_{*,\mathrm{w}}$	bed friction velocity due to waves only
$u_{*,\mathrm{cr}}$	critical bed friction velocity
V	depth-averaged horizontal fluid velocity in the *y* direction
V (subsection 3.3.3)	water volume in the wave tank in the ring test
v (chapter 2)	horizontal water particle velocity in the *y* direction
v (chapter 3)	kinematic viscosity
v_{br}	eddy viscosity coefficient
v_e	eddy viscosity coefficient due to the subgrid turbulence
V_{long}	average longshore current across the surf zone
v_{T}	vertical eddy viscosity
v_{tg}	eddy viscosity coefficient inside the bottom boundary layer
v_{tz}	eddy viscosity coefficient outside the bottom boundary layer
V_ω	relative fall speed
W	crest width of submerged breakwaters
w	vertical water particle velocity
W_s, ω	settling velocity
w_s	seepage vertical velocity in the porous layer
w_1, w_2, f	functions related to the sponge layers
X	maximum length of salient
x, y	horizontal co-ordinates
X_b	width of the surf zone
X_g	maximum erosion behind the gap between adjacent breakwaters
Y	distance from the salient apex to breakwater
z	vertical co-ordinate

z_a	reference level for bed reference sediment concentration
z^*	reference elevation in the slot technique
α, α^* p_1, p_2, p_3 c_1, c_2, c_3, c_4	parameters related to the numerical scheme
α_{cw}	coefficient in van Rijn's (1989) formula
α_{dw}	coefficient in Dibajnia *et al*.'s (2001) formula
$\alpha_{pl,b}$, α_{on}, α_{off}	phase-lag parameters in Camenen and Larson's (2006, 2007) bed load formulation
α_s	angle between the direction of the wave front at the start of the uprush and the still shoreline
α_w, α_n, b	parameters related to Camenen and Larson's (2006, 2007) bed load formula
α_1, α_2, β_1, β_2 (chapter 2)	free parameters
α_1, β_1 (chapter 3)	parameters related to the undertow velocity
α_1, α_2, α (chapter 6)	coefficients related to drag resistance in the porous layer
α_1, α_2, v_{sp}	Parameters related to the sponge layers
β, Λ	auxiliary parameters in the slot technique
β_D	function of the angle of inclination of the roller
β_d, k_b, k_w, k_c A_{cr}, $\tilde{\theta}$, $\tilde{\mu}$	parameters related to suspended sediment transport
β_s	Shape coefficient related to the source function
γ	parameter in KdV equation
γ (chapter 3)	enhancement factor in Jonswap spectrum
γ (chapter 6)	free parameter
γ_i	submerged sediment specific weight
γ_0	Shoaling gradient
γ_1, γ_2, γ_3, γ_4, γ_5	auxiliary variables
δ_{roller}	surface roller thickness
δ_s	parameter related to the source function
δ_w	wave boundary layer thickness
Δf	Relative error
Δt	time step
Δt_{mor}	morphological time step
$\Delta t'$	time difference between measurement intervals
Δx, dx	spatial grid step in the *x* direction
Δy, dy	spatial grid step in the *y* direction
Δz_b	difference in bed elevation between measurement intervals
δ	slot width

δ	parameter
δ_c	dimensionless thickness of the bed load layer
ε	nonlinearity parameter
ε (subsection 3.3.2)	random phase
ε (subsection 4.11)	instantaneous eddy diffusivity of sediments
ε_B, ε_s	parameters in Bailard's (1981) formula
ε_h	horizontal eddy diffusivity of sediments
ε_{scw}	sediment mixing coefficient for combined waves-current
ε_v	vertical eddy diffusivity of sediments
ε_{xx}, ε_{xy}, ε_{yx}, ε_{yy}	empirical coefficients associated with the morphological module
ζ	free surface elevation
η_r	bed ripple height
η_o	initial free surface elevation of a Gaussian hump
θ (chapter 2)	wave phase
θ (chapter 3)	wave incidence angle
θ (chapter 4)	Shields parameter
θ_{cn}	Shields parameter in the direction normal to the wave direction
θ_{cr}, θ_c	critical Shields parameter
θ_{cw}	maximum Shields parameter for combined waves-current
$\theta_{cw,m}$	mean absolute Shields parameter for combined waves-current
$\theta_{cw,net}$	net Shields parameter for combined waves-current
$\theta_{cw,onshore}$	mean Shields parameter of the onshore movement of sediment
$\theta_{cw,offshore}$	mean Shields parameter of the offshore movement of sediment
$\theta_{2.5}$	Shields parameter based on an equivalent roughness $K_N{}' = 2.5d_{50}$
θ'	Shields parameter due to skin friction only
κ	Von Karman constant
λ (chapter 3)	shape parameter in the slot technique
λ (chapter 6)	porosity of the permeable bottom
λ_i	eigenvalues
λ_r	bed ripple length
μ, σ	dispersion parameter
μ, ξ, q	empirical coefficients
μ_d, λ	parameter in Engelund and Fredsøe's (1976) formula
ξ, Λ', κ, σ_*, r, U' Z, Z_i^*, γ, w, y, κ_s φ, κ_r, κ_i	auxiliary variables
ρ	water density
ρ_s	sediment density
σ	Schmidt number
σ_U, σ_V, σ_T, σ_ζ	standard deviations of U, V, U_T, ζ, respectively

τ_b	bed shear stress due to a uniform steady current in Meyer-Peter and Müller's (1948) formula
$\tau_{\mathrm{b,cr}}$, τ_{cr}	threshold bed-shear stress
τ_{bx}, τ_{by}	bed shear stresses in the *x* and *y* directions, respectively
T_c, T_t	duration of the positive and negative portions of the total velocity profile in Dibajnia *et al.*'s (2001) formula
τ_{c}	bed shear stress due to current only
τ_{cw}	bed shear stress for combined waves and current
τ_{sb}	steady bottom streaming term
φ (chapter 3)	Angle between the wave propagation direction and the *x* axis
φ (subsection 4.3)	phi-parameter related to sediment grain size
φ (subsection 4.8.1)	angle between waves and current in the sediment transport module
Φ_b	non-dimensional bed load transport rate
φ_d	dynamic friction angle for the bed load sediment
φ_m	angle of repose or angle of internal friction
ψ	mobility number
$\psi_I^{(x)}$, $\psi_{II}^{(x)}$, $\psi_{III}^{(x)}$ $\psi_I^{(y)}$, $\psi_{II}^{(y)}$, $\psi_{III}^{(y)}$	dimensional higher order Boussinesq terms
Ω	Non-dimensional angular frequency
Ω	Fluid computational domain
ω	angular frequency
Ω_c, $\Omega_c^{'}$, Ω_t, $\Omega_t^{'}$ t_0, ω, ω_{cr}, γ Ψ_{sheet}, Ψ_{cr}, Ψ β^*, β', β'', Λ	parameters in Dibajnia *et al.*'s (2001) formula
ω_1	angular frequency of a first-order Stokes wave
ω_{13}	third-order correction to the first-order angular frequency solution
$\vec{c}$	wave celerity
$\vec{F}_{br}$	wave breaking term
$\vec{F}_{\mathrm{eddy}}$	Smagorinsky-type term
$\vec{F}_i$	inertial resistance term
$\vec{F}_r$	drag resistance term
$\vec{F}_{\mathrm{sp}}$	sponge layer term
$\vec{K}_1$, $\vec{K}_2$	vector functions representing non-dimensional higher order Boussinesq terms
$\vec{n}$	outward unit normal vector
$\vec{Q}$	horizontal volume flux
$\vec{q}_s$	volumetric sediment transport rate from Dibajnia *et al.*'s (2001) formula
$\vec{q}_{sb}$	time-averaged bed sediment transport load

$\vec{q}_{ss}$	time-averaged depth-integrated suspended sediment transport load
$\vec{q}_{sz}$	net sediment transport rate per unit width in the swash zone
$\vec{q}_{tot}$	total sediment transport rate per unit width
$\vec{q}'_{tot}$	modified total sediment transport rate per unit width
$\vec{U}$	depth-averaged horizontal fluid velocity
$\vec{u}$	horizontal water particle velocity
$\vec{U}_s$	depth-averaged horizontal fluid velocity inside the porous layer
$\vec{U}_{\mathrm{w}}(t)$	near bed instantaneous oscillatory velocity
$\vec{u}_b(t)$	instantaneous near-bottom total velocity for combined waves-current
$\vec{U}_{\mathrm{c}}$	near bed current velocity
$\vec{u}_c$, $\vec{u}_t$	representative velocity amplitudes for the positive and negative portions of the total velocity profile in Dibajnia *et al.*'s (2001) formula
$\vec{U}_o$	uniform velocity below the surface roller
$\vec{u}_o$	near-bottom velocity
$\vec{u}_{ow}$	oscillatory component of near-bottom velocity
$\vec{u}_s$	horizontal seepage velocity inside the porous medium
$\vec{u}_{s,3}$	seepage velocity inside the porous medium
$\vec{U}_T$	velocity component tangent to a reflective boundary
$\vec{u}_w$	oscillatory component of water particle velocity
$\vec{u}_3$	water particle velocity in the free water body
$\vec{x}$	horizontal co-ordinates
$\vec{\theta}_{\mathrm{c}}$	Shields parameter due to current
$\vec{\theta}_{\mathrm{w}}$	maximum absolute wave Shields parameter
$\vec{\theta}_{\mathrm{w}}(\mathrm{t})$	instantaneous Shields parameter due to waves
$\vec{\theta}_{\mathrm{w,m}}$	mean wave Shields parameter
$\vec{\theta}'(t)$	instantaneous skin Shields parameter in Ribberink's (1998) formula
$\vec{\tau}_b$	bed shear stress
$\vec{\tau}'_b(t)$	instantaneous bed skin shear stress in Ribberink's (1998) formula
$\vec{\Omega}$	vorticity vector
∇	horizontal gradient operator
∇_3	three-dimensional gradient operator
′	denotes dimensional variables
$\overline{(\ldots)}$, $\langle(\ldots)\rangle$	denote time-averaging

Chapter 1

Introduction

1.1 Background and research objectives

Man has been attracted to the coast since ancient times. Coastal waters offered quality food, potential for commerce development and seafaring, advantage in military naval power, and, more recently, opportunities for industrial and pleasure activities. Nowadays, over 40 percent of the global population lives in coastal areas. In addition, most of the largest cities in the world are located by the coast. With more people crowding in these vulnerable zones undue pressures are imposed by human activities over both land and sea. The most critical of them are associated with land acquisition as close as possible to the sea, housing, development of industries or touristic installations. These pressures are in essence translated into requirement for a stable shoreline.

However, this requirement is not always in line with the natural processes present in the coastal zone. Thus, a conflict emerges: man requires a stable coastline whereas nature transposes the latter, invariably with time, landwards or seawards. The net result of this conflict is often increased erosion and loss of beaches. The problem is intensified by climate change that can trigger environmental disruptions, such as sea level rise, catastrophic floods, disappearance of species, etc. Recent studies have shown that more than 20% of the European coastline erodes irreversibly (Eurosion Reports, European Commission, 2004). The situation is expected to be intensified in the foreseeable future and consequently coastal risks of any kind be increased. Particularly, in Greece, 1/3 of the population lives in coastal communities within a 10 km wide band. Thus, coastal erosion is a great problem threatening tourism, commerce and industrial activity.

Hence a problem that humans face is the accelerating number of conflicts between coastal development and erosion. Lack of sustainable planning has, in many cases, permitted urbanization and infrastructures too close to eroding coastlines, aggravating the consequences of ongoing erosion (Mangor, 2004). In addition, the so-called greenhouse effect and other, not

of human origin, long-scale climate variations will predictably intensify the global erosion problem. Fig. 1.1 shows the extend of the problem at European level. This particular map was produced in the context of Eurosion, a research project by European Commission (2004). It shows that a great part of the European coasts, also in Greece, faces a grave problem of coastal erosion.

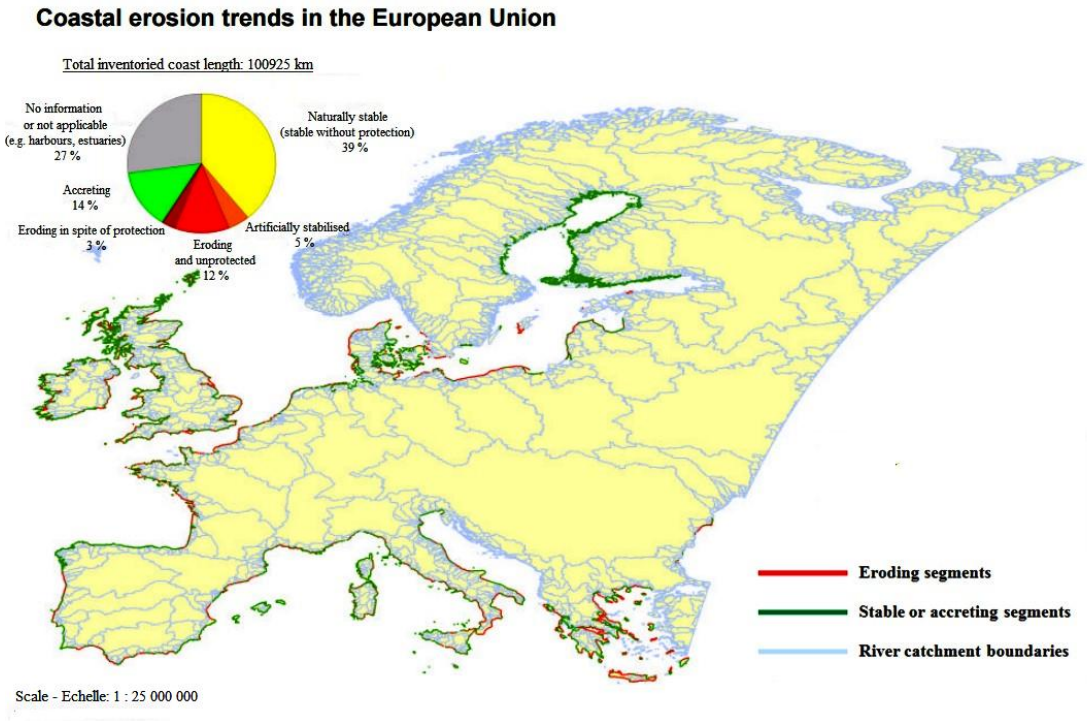

Fig. 1.1. Map of European coasts facing erosion problems (from Eurosion, European Commission, 2004, modified).

Nowadays, most countries have legislations for nature protection, that enforces restrictions on construction activities near the coastline and force the execution of impact assessment studies. However, for many years now no serious environmental protection measures were taken during human interventions since the coastal zone was, generally, considered as an environment which is, more or less, stable. Until recently, the great majority of coastal interventions to enhance coastline stability relied on the "hard" protection concept which includes the construction of large structures made of concrete or natural stones, similar to harbour breakwaters. In particular such coastal defense projects refer to conventional groynes and detached breakwaters, seawalls, revetments, etc. However, in the past decades, the impact of these conventional structures upon the coastal environment was generally treated semi-empirically and fragmentarily. In many cases, their negative effect on the sea environment was ignored, such as drastic impact on flora and fauna populations, creation of closed basins with reduced water renewal, aesthetic degradation. In addition, the fragmentary knowledge

about their behaviour has often caused severe modification of the coastal processes that may occasionally lead to a total inverse of the desired result.

An example of erosion induced by the construction of a coastal defense system in Adelaide is shown in Fig. 1.2. Fig. 1.3 shows a map of the European coasts that continue to erode despite the construction of coastal protection works. In general, the absence of a long-term sustainable design and an effective legislation, in addition to the lack of an in-depth understanding of coastal processes, have resulted to a negative until recently situation.

Fig. 1.2. Erosion downdrift of a coastal defense system in a beach with undue human pressure in Glenelg, Adelaide, Australia (photo: Web-Based Geohazards Project, University of Adelaide, www.coastalerosionsa.wordpress.com).

Nowadays, it is being widely understood that the vulnerable coastal zones require an integrated management, rather than fragmentary solutions. In this context, shoreline management guidelines are being proposed so that coastal engineers, planners, administrators, private landowners and politicians have a common basis to plan sustainable activities along the shores. This is a hard task due to the multiple aspects, i.e. social, environmental, economic and geomorphological, that should be considered and combined. In the light of such an integrated approach, 'soft' protection projects become more and more popular among coastal engineers. Soft or mild interventions include beach nourishment, beach drainage, sand dune management and to a lesser degree submerged coastal structures, or combination of the above, e.g. beach replenishment combined with submerged breakwaters, etc. Due to the superiority of soft interventions with regard to beach amenity and aesthetics, there is an increased community pressure on coastal management authorities and government agencies to consider them for beach protection.

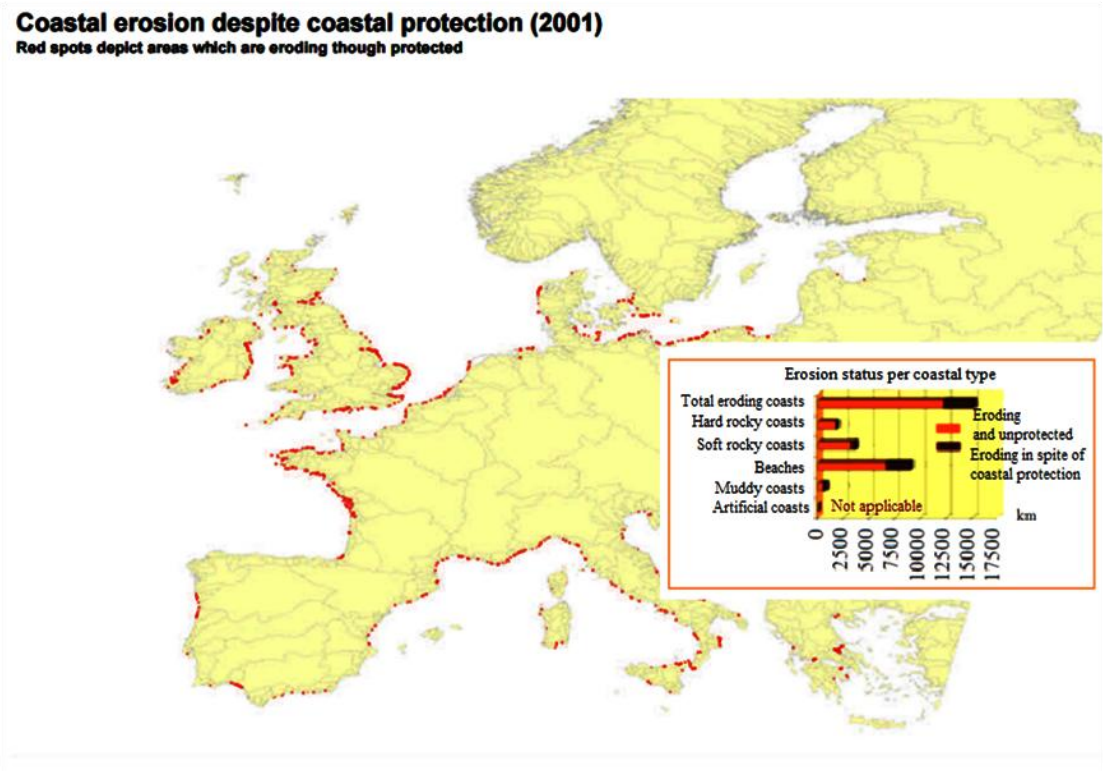

Fig. 1.3. Map of European coasts facing erosion despite being protected (from Eurosion, European Commission, 2004).

In particular, submerged breakwaters have stimulated the scientific interest as an alternative solution to conventional emergent ones for coastal defense. They form a somehow less aggressive quasi-hard project and consequently they are generally less effective, in engineering terms, than emerging structures. However, in cases of weak hydrodynamic regimes submerged structures can be more attractive than conventional ones since they are friendlier to the environment, aesthetically superior and usually of lower cost. An example of a submerged breakwater in Niigata Beach in Japan is depicted in Fig. 1.4.

Scientific research concerning submerged breakwaters is relatively new. In order to study the associated physical processes, three methods are mainly used: field observations, laboratory experiments using physical models and numerical modelling. Each of them has advantages and disadvantages and in many cases a combination of them is applied. A large number of laboratory experiments have been performed since the ‘70s in order to mainly investigate hydrodynamic parameters related to submerged breakwaters, e.g. wave transmission coefficient, wave setup, wave-induced currents, etc. A detailed literature review of these works is presented in chapter 5. Among them, the most complete database is the one included in DELOS project (Kramer *et al.*, 2005). The project was oriented to the hydrodynamic behaviour of submerged breakwaters and led to the derivation of some empirical formulae and general guidelines. On the other hand, very few laboratory

experiments concerning the morphological response of submerged breakwaters have been reported in the international literature (Groenewoud *et al*., 1996; van der Biezen *et al*., 1997). Turner *et al*. (2001) and Ranasinghe *et al*. (2006) studied in a physical model the morphological bed evolution in the lee of the V-shaped artificial reef at the Gold Coast in Australia.

Fig. 1.4. Aerial view of a submerged breakwater (in yellow ellipse) in Niigata beach, Japan (from Google, 2016).

Numerical models are the most popular tool for studying the hydrodynamic and morphological response of submerged breakwaters. This is true due to their, in general, lower cost and also because they offer the possibility to study an increased number of scenarios compared to physical models. However, in order to be efficient, they should be at first accurately calibrated. Hence, due to the restricted number of available measured datasets that refer to submerged breakwaters, the models' validation is usually incomplete. Thus, their results include in many cases an increased level of uncertainty.

A number of numerical models have been developed to simulate the wave propagation and the wave-induced current field around submerged breakwaters (Beji and Battjes, 1994; van Gent, 1994; Losada *et al*., 1996; Chen, 1999; Garcia *et al*., 2004; Johnson *et al*., 2005; Cáceres *et al*., 2005; Kobayashi *et al*., 2007). The equations that these models involve are of various types, i.e. Reynolds-averaged Navier-Stokes equations (RANS), mild-slope equations, Nonlinear Shallow Water equations (NSWE), Boussinesq-type equations or 3D Navier-Stokes. Most of them treat the involved submerged breakwaters as impermeable structures and only a few take into account their permeability (Cruz *et al*., 1997; Hsiao *et al*., 2002;

Avgeris *et al*., 2004; Chen, 2006). On the other hand, only a small number of numerical models have been presented to simulate morphodynamics related to submerged structures (Hanson and Kraus, 1990; Zyserman *et al*., 1999; van der Biezen *et al*., 1998; Lesser *et al*., 2003; Koutsouvela *et al*., 2007; Ranasinghe *et al*., 2010; Karambas and Samaras, 2014). Among them, very few have been validated against 2DH measurements of bed elevation. A comprehensive literature review of these research works is presented in chapter 6.

In the context of behaviour of submerged breakwaters, the main objectives of the present Ph.D. thesis are the following:

- To contribute to the understanding of the complex hydrodynamic and morphodynamic processes that take place in coastal zones protected by single or multiple submerged breakwaters.

- To develop an integrated numerical model that simulates the wave propagation, the wave-induced currents, the coastal sediment transport, the bed erosion and accretion, and finally describe the cross-shore profile and the coastline evolution in the lee of a system of permeable submerged breakwaters. The behaviour of such a system has not been described so far in a general and quantitatively consistent manner and so the thesis could offer original contribution in this subject.

- To perform 2DH laboratory experiments in order to also study experimentally the hydrodynamic and morphological response of permeable submerged breakwaters. In the context of the conducted experiments, the evolution of the bed elevation and the shoreline response were measured and analysed.

- To provide to the scientific community a set of experimental data referring to the 2DH morphological change down-wave of permeable submerged breakwaters. This dataset will contribute to covering a gap that exists in the international literature on this issue.

- To validate the aforementioned compound numerical model with the aforementioned measurements.

- To perform numerical experiments in order to investigate the shoreline response to an array of submerged breakwaters. The effect of some significant geometric and wave parameters was studied in order to draw some guidelines for the optimal design of these structures with respect to their positioning and geometric layout.

The basic tool for this research is the compound numerical model that was developed and is presented herein. The integrated model consists of four parts: the wave, the hydrodynamic,

the sediment transport and the geomorphological modules. The development of these four modules defined some additional objectives for the dissertation.

The basis of the numerical model is a 2DH Boussinesq-type wave solver of enhanced nonlinearity and dispersion, while a 1DH version has been also developed. Boussinesq-type models form an extension of the NSWE to account for dispersive waves. Their characteristics are expressed through two non-dimensional parameters, $\varepsilon = H'/ d_o'$ and $\sigma^2 = (d_o'/ L')^2$, where d_o', L' and H' are a reference water depth, the wavelength and wave height, respectively. The former parameter controls the nonlinear characteristics and the latter the dispersive characteristics of the equations. The original assumption behind this type of equations is that these two parameters are of the same order of magnitude. Peregrine (1967) derived the 'classical' form of Boussinesq equations for water waves assuming weak dispersion and weak nonlinearity and he practically extended their range of applicability to $kd < 0.75$, where k is the wave number and d the still water depth. Since then, the main scope of the research concerning Boussinesq-type models has been the enhancement of their dispersive and nonlinear character in order to be applicable to more and more deep water and finally face no limitation with respect to depth. A significant step in this direction was made by Witting (1984) who introduced Padé approximations for studying the linear characteristics of the various Boussinesq equations. Based on this method, Madsen *et al*. (1991) and Madsen and Sørensen (1992) extended the classical Boussinesq equations, expressed in terms of the volume flux, to deeper water. In particular, by introducing extra terms and an adjustable coefficient, they optimized the linear characteristics of the model up to the deep water limit.

In parallel, Nwogu (1993) achieved the same dispersion equation by using the velocity at an arbitrary level z_α as dependent variable in the derived equations and got a new form of Boussinesq-type equations. Nwogu's (1993) equations embedded weak nonlinearity since only terms of $O(1, \varepsilon, \mu^2)$ where retained, with $\mu^2 = (k_o' d_o')^2$ and k_o' a reference wavenumber. Wei *et al*. (1995) enhanced the nonlinearity of the previous model by retaining additional terms of $O(\varepsilon\mu^2)$. Gobbi *et al*. (2000) further enhanced the nonlinearity of the aforementioned models by deriving a formulation of $O(\varepsilon\mu^2, \mu^4)$ based on a linear combination of the velocities at two arbitrary z-levels. The velocity profile obtained from their method is applicable up to $kd = 4$, while their dispersion relation is applicable up to $kd = 6$.

Madsen and Schäffer (1998) by taking more terms in the Taylor series obtained a number of models with dispersion characteristics of up to $O(\mu^4)$. Their accuracy appears to be very good for $kd < 6$. In addition, Karambas and Koutitas (2002) derived a model of enhanced nonlinearity by retaining terms of $O(\varepsilon\sigma^2)$ and, by following the method by Madsen *et al*. (1991), they extended the linear dispersion characteristics up to the limit of deep waters.

Madsen *et al*. (2002, 2003) derived a formulation with very accurate linear dispersion and nonlinear characteristics up to $kd = 40$. Their idea was to replace the infinite series operators of the exact Laplace equation solution by finite series approximations. Lynett and Liu (2004) proposed a multi-layer formulation which significantly improves the linear dispersion characteristics up to very deep water. Karambas and Memos (2009) derived a fully linear dispersive and weakly nonlinear Boussinesq-type model. Their formulation offers significant advantages due to the small number of terms involved in both the mass and the momentum equations. A detailed literature review about Boussinesq-type models is presented in chapter 2.

In most of the sediment transport models, the required wave input is taken from the results of phase-averaged wave models. However, in the present dissertation a more sophisticated sediment transport modelling was sought after. Thus, a phase-resolving wave model was developed to form the basis of the compound numerical model. Wave resolving models have the advantage that they can inherently predict the wave skewness and asymmetry which are very important for an accurate estimation of the intra-wave sediment transport rates. A correct description of these two parameters also allows the inclusion of phase-lag effects in the computation of sediment transport if suitable formulae are employed. In addition, Boussinesq-type models take into account the effect of wave irregularity, bound and free long waves, wave groups, and the nonlinear wave-wave interactions. These features are also very important for the accurate calculation of sediment loads. For these reasons, a Boussinesq-type wave model was chosen, that in contrast to NSWE, embeds the wave dispersivity and thus accounts for deeper water, too. On the other hand, a wave model solving the full 3D Navier-Stokes equations would not justify the very high computational cost required. In the light of this discussion, the development of the Boussinesq-type model defined some additional objectives for the present Ph.D. thesis:

- To derive enhanced nonlinear versions of two existing Boussinesq-type models, i.e. the ones by Karambas and Memos (2009) and Karambas and Koutitas (2002).
- To study and compare the linear and nonlinear characteristics of the aforementioned models in order to choose the one that will be the wave module of the compound model.
- To extend the wave module in order to account for porous beds. This objective should be fulfilled so that the model be able to simulate the wave propagation over permeable submerged breakwaters.
- To extend the wave model to the surf and swash zones.

- To develop a hydrodynamic module in order to compute the wave-induced currents which are required for the calculation of the sediment transport.

- To thoroughly validate the Boussinesq-type model against a number of experimental data which are available in the international literature. These measurements should refer to the most important physical processes present in the coastal zone in order to check the wave and hydrodynamic modules' reliability.

Only a few examples of coupling a Boussinesq-type model with a sediment transport and a morphological model have been reported (Rakha *et al*., 1997; Rakha, 1998; Long and Kirby, 2003; Karambas and Karathanassi, 2004; Wenneker *et al*., 2011; Rahman *et al*., 2013; Karambas and Samaras, 2014). Most of these models refer to 1DH applications while 2DH validation tests including morphological evolution have been rarely documented.

To accurately estimate coastal sediment transport is a very hard task due to the complexity of the environmental processes at play and their dependence on a large number of factors, which are difficult to be predicted. In the early years, the application of some sediment transport formulae that were developed for inland waters was extended to coastal zones (Meyer-Peter and Müller, 1948; Frijlink, 1952). However, the sediment's motion in the sea environment is much different due to the major role of water acceleration there, the multi-directionality and the combined action of waves and currents. Thus, a number of new formulae have been proposed for the estimation of the coastal sediment transport rates in terms of bed, suspended or total loads.

The pioneer work by Bagnold (1963, 1966) introduced the energetics model which relies on considerations of energy balance and mechanical equilibrium. Some years later, Bailard (1981) derived a formula for the total load directly from Bagnold's approach. Roelvink and Stive (1989) modified this latter formula to take into account the additional stirring of sediment by the surface breaking-induced turbulence.

A commonly used formulation in engineering applications was proposed by Bijker (1968) for wave-current interaction. Engelund and Fredsøe (1976) derived a semi-empirical law for the total load assuming that only a certain fraction of the particles in a single bed layer is transported. Van Rijn (1989) and Soulsby (1997) also proposed wave-current formulations for the total sediment load. Ribberink (1998) proposed a quasi-steady model for bed load transport under the combined wave-current action. Dibajnia and Watanabe (1992) and Dibajnia *et al*. (2001) derived a formulation for sheet flow conditions and bed ripples that takes into account unsteady effects. These effects are also taken into account by Camenen and Larson's (2007) unified sediment transport model for combined waves and currents.

Prediction of the coastal morphological evolution is the final and probably the most important issue in coastal engineering problems. Predicting detailed morphological changes in coastal areas of complex topography requires the application of advanced process-based morphodynamic models. However, as already mentioned, it is mainly cross-shore cases that have been studied where phase-resolving wave models were employed. In this context, some additional objectives for the present dissertation were set:

- To develop a sediment transport model based on advanced formulae that are valid offshore but also inside the surf and swash zones.
- To develop a geomorphological module that computes the evolution of the bed level using the results of the sediment transport module as input.
- To develop the final compound model by coupling all four modules together, i.e. wave, hydrodynamic, sediment transport and geomorphological modules. An acceleration technique was also applied in order to achieve longer simulation periods with regard to morphology evolution.
- To thoroughly validate the compound model against a number of experimental data which are available in the international literature.
- To investigate the effect of various parameters in order to contribute in the understanding of the complex sediment transport processes.

The above discussion described the background and the objectives of the present Ph.D. thesis. It also set the frame of the associated research so that the effort stayed within its limits. The scientific methods applied included the observation in laboratory scale, mathematical computations referring to numerical modelling and simulation, and finally validation and verification. One next step could be the performance of field measurements and the further model validation with these data referring to natural scale.

1.2 Innovative points and highlights

In the previous subsection the framework of the basic research of the present dissertation was defined. Beach erosion and accretion are technically the most interesting processes for the coastal engineer. In addition, submerged structures are a modern solution for coastal defense. The combination of these two aspects forms an attractive research field to which this thesis offers both theoretical and practical results. The main motivation of the specific work was that the hydrodynamic and morphodynamic behavior of arrays of submerged breakwaters

has not been described so far in a thorough and quantitatively consistent manner. Thus, the thesis could offer contribution to this scope. During this effort, some original results that deserve mentioning have been achieved:

- Modification and upgrade of two existing Boussinesq-type wave models, i.e. the ones by Karambas and Koutitas (2002) and Karambas and Memos (2009), which resulted to the derivation of two new enhanced models.

- A thorough analysis of the linear and nonlinear characteristics of the aforementioned models, in addition to two more models. This analysis revealed the properties of the various Boussinesq-type models, so that one can select the most appropriate for the purpose of his work. It also led to the choice of the wave model used in the present research.

- Extension of this basic Boussinesq solver into the surf and swash zones. Thus, a 1DH and 2DH robust tool was developed for studying integrated nearshore dynamics. Only a restricted number of such integrated phase-resolving models have been presented, and most of them either embed lower-order wave characteristics or/and lack a thorough 2DH validation. In addition, the present model offers an inherent estimation of the wave-induced current field without the need to de-couple the wave and the current motions. This aspect has been investigated only in a small number of Boussinesq models of the international literature.

- Compared to its weakly nonlinear counterparts (Karambas and Koutitas, 2002; Karambas and Karathanassi, 2004; Memos *et al*., 2005) an improved numerical scheme was employed which offers better stability properties.

- Sediment transport and geomorphological models were developed and coupled with the wave and hydrodynamic modules in order to form a compound model for studying coastal morphodynamics. In this process, advanced sediment transport formulae were used which take into account the associated unsteady effects. Both 1DH and 2DH model validation has been performed. Very few sediment transport models coupled with Boussinesq-type wave models have been presented in the international literature. Almost all of them either refer to only 1DH applications (Rakha *et al*., 1997; Karambas and Koutitas, 2002; Long and Kirby, 2003; van Dongeren *et al*., 2006) or a validation of the morphological evolution in 2DH tests is not presented (Rakha, 1998; Karambas and Karathanassi, 2004; Wenneker *et al*., 2011). The exceptions of works including 2DH tests either rely on less sophisticated sediment transport formulae (Drønen and Deigaard,

2011; Rahman *et al*., 2013) or lower-order nonlinear Boussinesq equations (Karambas and Samaras, 2014).

- The compound model was extended to account for porous beds by including the solution of the additional Darcy-Forchheimer equation for the flow inside the porous medium. In previous similar efforts based on Karambas and Koutitas's (2002) Boussinesq-type equations terms of $O(1, \varepsilon)$ were only retained in the Darcy-Forchheimer equation (Avgeris *et al*., 2004; Metallinos *et al*., 2014). In contrary, in the presented model additional terms of $O(\sigma^2)$ were also retained in this latter equation. From the validation tests performed, these terms proved to be significant when short wave propagation over permeable submerged breakwaters is simulated. In particular, their inclusion improved the model results when these structures were located in intermediate water depth.

- The development of a 2DH numerical model that simulates the morphological evolution in the lee of an array of permeable submerged breakwaters is another point of originality of the present thesis. There have been some other works simulating 2DH morphodynamics related to submerged breakwaters. However, either they employed phase-averaged wave models (Ranasinghe *et al*., 2006, 2010) or NSWE (van der Biezen *et al*., 1998; Lesser *et al*., 2003). Koutsouvela (2010) also studied the morphological evolution behind submerged breakwaters using a Boussinesq-type model but no comparison with measurements was provided. In addition, only normal incidence of regular waves was considered in this latter work. Finally, in all the previous works, the submerged structures were considered to be impermeable, in contrary to the present dissertation where the permeability of the breakwaters is also taken into account.

- The performance of 3D laboratory experiments referring to the morphological evolution of a sandy beach in the lee of permeable submerged breakwaters is another point of innovation of this research. The tests included both regular and irregular waves. To the best of the author's knowledge, only Groenewoud *et al*. (1996) have performed similar experiments involving a movable bed behind submerged breakwaters. However, only regular wave cases were considered and also, according to the researchers, an equilibrium state was not reached during their experiments. Thus, their measurements are of limited practical value. Consequently, the present measurements can contribute to covering a gap that exists in the international literature in terms of beach evolution behind submerged breakwaters. The experiments can both offer some direct conclusions for the behavior of submerged breakwater and also provide a dataset for the validation of numerical models.

- The shoreline response to an array of permeable submerged breakwaters was studied numerically. The effect of various important design parameters was investigated and some figures were produced showing relevant tendencies. In contrary to emergent breakwaters, only fragmentary and, in many cases, inconsistent with each other results have been reported in the international literature on this issue. It cannot be claimed that functional design rules were derived but some practical conclusions and guidelines, both qualitative and quantitative, were drawn in this direction.

1.3 Organization of the dissertation

Further to this introductive chapter 1, the dissertation is organized as follows. Chapter 2 starts with the basics of the original Boussinesq wave theory and the extension that it offered to the NSWE. In addition, a detailed literature review of the various Boussinesq-type models is offered. In the next section, the derivation of enhanced nonlinear versions of two existing Boussinesq-type models is presented. In the following, a mathematical analysis and comparison of the characteristics of dispersion and nonlinearity of a number of models is performed in order to choose the most suitable for the scope of the present thesis. The chapter ends with a discussion on relevant issues.

Chapter 3 presents an extension of the basic 2DH Boussinesq solver to account for the entire nearshore zone. At first the model is extended to the surf and swash zones, as the mathematical background of the wave breaking and run-up techniques that were adopted is presented. The hydrodynamic module is then described since the model can estimate the wave-induced currents, including the depth-averaged undertow. Furthermore, numerical aspects referring to the numerical scheme and the boundary conditions are discussed. The chapter also includes an extensive validation involving both 1DH and 2DH tests. Chapter 3 closes with a discussion on the integrated Boussinesq model.

Chapter 4 concerns sediment transport. It begins with a detailed literature review of the various formulae and numerical models for coastal sediment transport and geomorphology. In the following sections, physical properties of coastal sediments and related processes are described. Some selected widely used formulae are also presented. In addition, the sediment transport and the morphology modules of the compound model are described in detail. Both 1DH and 2DH validation tests are also included, followed by a sensitivity analysis section for studying the effect of various parameters and the efficiency of different sediment transport formulae. The chapter ends with a discussion on the sediment transport model.

Chapter 5 is dedicated to the laboratory experiments performed in the context of the Ph.D. thesis. At first, an introduction mentions other experimental works including submerged

breakwaters. Then, some general features of these structures and relevant coastal processes are described. In the next sections a detailed description of the laboratory facilities, the experimental layout and the scenarios studied is presented. Furthermore, a section about scale effects is also included. The chapter ends with a general discussion on the experiments performed.

Chapter 6 begins with a literature review about numerical models simulating wave propagation over submerged breakwaters. The mathematical extension of the compound model to porous beds follows. In the next section the model is validated against the measurements from the laboratory experiments described in the previous chapter. Chapter 6 ends with a discussion about the model extension to porous beds and the wave propagation over permeable submerged breakwaters.

Chapter 7 refers to a numerical investigation of the shoreline response to an array of submerged breakwaters. The chapter begins with some results and design rules from the international literature concerning, mainly, emergent breakwaters, although some discussion about submerged breakwaters is also included. In the next section, a number of numerical experiments are presented in order to study the effect of various design parameters on the shoreline response. Chapter 7 closes with a discussion and some conclusions of practical interest for this issue.

In chapter 8, the conclusions drawn from this work are summarized. Some important results are highlighted, while issues requiring further investigation and fields for future research are mentioned.

References

Avgeris, I., Karambas, Th. V., and Prinos, P. (2004). "Boussinesq modeling of wave interaction with porous submerged breakwaters." *Proc. 29th Int. Conf. on Coastal Eng.*, J. M. Smith, ed., Lisbon, Portugal, 604-616.

Bagnold, R. (1963). "An approach of marine sedimentation." In: *The Sea: Ideas and Observations on Progress in the Study of the Seas*, M. N. Hill, ed., Interscience, New York, vol. 3, pp. 507-528.

Bagnold, R. (1966). "An approach of sediment transport model from general physics." *Prof. Paper 422-I*, U. S. Geol. Surv., 37 pp.

Bailard, J. (1981). "An energetics total load sediment transport model for a plane sloping beach." *J. Geophys. Res.*, 86 (C11), 10938–10954.

Beji, S., and Battjes, J. A. (1994). "Numerical simulation of nonlinear wave propagation over a bar." *Coast. Eng.*, 23(1-2), 1-16.

Bijker, E. W. (1968). "Littoral drift as function of waves and current." *Proc. 11th Int. Conf. on Coastal Engineering*, ASCE, London, United Kingdom, vol. I, chapter 26, pp. 415-435.

Cáceres, I., Sánchez-Arcilla, A., Alsina, J.-M., González-Marco, D., and Sierra, J. P. (2005). "Coastal dynamics around a submerged barrier." *Proc. Coastal Dyn. '05*, A. Sanchez-Arcilla, ed., ASCE, Barcelona, Spain, pp. 1-14.

Camenen, B., and Larson, M. (2007). "A unified sediment transport formulation for coastal inlet application." Tech. rep. ERDC/CHL CR-07-1, U.S. Army Engineer Research and Development Center, Vicksburg, MS, U.S.A., 231 pp.

Chen, Q. (2006). "Fully nonlinear Boussinesq-type equations for waves and currents over porous beds." *J. Eng. Mech.*, 132 (2), 220-230.

Chen, Q., Dalrymple, R. A., Kirby, J. T., Kennedy, A. B., and Haller, M. C. (1999). "Boussinesq modeling of a rip current system." *J. Geophys. Res*., 104 (C9), 20617-20637.

Cruz, E. C., Isobe, M., and Watanabe, A. (1997). "Boussinesq equations for wave transformation on porous beds." *Coast. Eng.*, 30 (1-2), 125-156.

Dibajnia, M., Moriya, T., and Watanabe, A. (2001). "A representative wave model for estimation of nearshore local transport rate." *Coast. Eng. J.*, 43 (1), 1-38.

Dibajnia, M., and Watanabe, A. (1992). "Sheet flow under nonlinear waves and currents." *Proc. 23rd Int. Conf. on Coastal Engineering*, B. L. Edge, ed., Venice, Italy, part V, chapter 155, pp. 2015-2028.

Drønen, N., and Deigaard, R. (2011). "A model for wave induced erosion of sandy barriers." *Proc. 7th IAHR Symp. River, Coastal and Estuarine Morphodynamics (RCEM)*, Beijing, China.

Engelund, F., and Fredsøe, J. (1976). "A sediment transport model for straight alluvial channels." *Nord. Hydrol.*, 7, 293-306.

European Commission (2004). "Living with coastal erosion in Europe: sediment and space for sustainability. Part II - Maps and statistics." *Eurosion*, Directorate General Environment, 25 pp.

Frijlink, H. C. (1952). "Discussion des formulas de debit solide de Kalinske, Einstein et Meyer-Peter et Müller compte tenue des measures récentes de transport dans les rivières néerlandaises." *2ième Journal Hydr.*, Soc. Hydrotechn. de France, Grenoble, France, 98–103 (in french).

Garcia, N., Lara, J. L., and Losada, I. J. (2004). "2-D numerical analysis of near-field flow at low-crested permeable breakwaters." *Coast. Eng.*, 51 (10), 991–1020.

Gobbi, M. F., Kirby, J. T., and Wei, G. (2000). "A fully nonlinear Boussinesq model for surface waves. Part 2. Extension to $O(kh)^4$." *J. Fluid Mech.*, 405, 181-210.

Groenewoud, M., Van der Graaff, J., Claessen, E., and Van der Beizen, S. (1996). "Effect of submerged breakwater on profile development." *Proc. 25th Int. Conf. on Coastal Eng.*, B. L. Edge, ed., Orlando, Florida, U.S.A., pp. 2428–2441.

Hsiao, S., Liu, P. L.-F., and Chen, Y., (2002). "Nonlinear water waves propagating over a permeable bed." *Proc. R. Soc. London*, Ser. A, 458, 1291–1322.

Johnson, H. K., Karambas, Th. V., Avgeris, I., Zanuttigh, B., Gonzalez-Marco, D., and Caceres, I. (2005). "Modelling of waves and currents around submerged breakwaters." *Coast. Eng.*, 52 (10-11), 949–969.

Hanson, H., and Kraus, N. C. (1990). "Shoreline response to a single transmissive breakwater." Proc. *22nd Int. Conf. on Coastal Engineering*, B. L. Edge, ed., Delft, The Netherlands, part V, chapter 154, pp. 2034-2046.

Karambas, Th. V., and Karathanassi, E. K. (2004). "Longshore sediment transport by nonlinear waves and currents." *J. Waterw. Port Coast. Ocean Eng.*, 130 (6), 277-286.

Karambas, Th. V., and Koutitas, C. (2002). "Surf and swash zone morphology evolution induced by nonlinear waves." *J. Waterway, Port, Coastal, Ocean Eng.*, 10.1061/(ASCE)0733-950X(2002)128:3(102), 102-113.

Karambas, Th. V., and Memos, C. D. (2009). "Boussinesq model for weakly nonlinear fully dispersive water waves." *J. Waterway, Port, Coastal, Ocean Eng.*, 10.1061/(ASCE)0733-950X(2009)135:5(187), 187-199.

Karambas, Th. V., and Samaras, A. G. (2014). "Soft shore protection methods: The use of advanced numerical models in the evaluation of beach nourishment." *Ocean Eng.*, 92, 129-136.

Kobayashi, N., Meigs, L., Ota, T., and Melby, J. (2007). "Irregular breaking wave transmission over submerged porous breakwater." *J. Waterw. Port Coast. Ocean Eng.*, 133 (2), 104-116.

Koutsouvela, D., Karambas, Th. V., Avgeris, I., and Karathanassi, E. (2007). "Functional design of submerged breakwaters for coastal protection using two wave/morphological models." *Proc. Coastal Structures '07*, Venice, Italy, pp. 1205-1216.

Kramer, M., Zanuttigh, B., Baoxing, W., Van der Meer, J., Vidal, C., Gironella, F. (2005). "Laboratory experiments on low-crested breakwaters." *Coast. Eng.*, 52 (10-11), 867-885.

Lesser, G. R., Vroeg, J. H., Roelvink, J. A., de Gerloni, M., and Ardone, V. (2003). "Modelling the morphological impact of submerged offshore breakwaters." *Proc. Coastal Sediments '03*, World Scientific Publishing Co, Clearwater Beach, Florida, USA, May 18-23, on CD-ROM.

Long, W., and Kirby, J. T. (2003). "Cross-shore sediment transport model based on the Boussinesq equations and an improved Bagnold formula." *Proc. Coastal Sediments '03*, Clearwater Beach, Florida, U.S.A., May 18-23.

Losada, I. J., Silva, R., and Losada, M. A. (1996). "3-D non-breaking regular wave interaction with submerged breakwaters." Coast. Eng., 28 (1-4), 229–248.

Lynett, P., and Liu, P. L.-F. (2004a). "A two-layer approach to wave modelling." *Proc. R. Soc. Lond. A*, 460(2049), 2637-2669.

Madsen, P. A., Bingham, H. B., and Liu, H. (2002). "A new Boussinesq method for fully nonlinear waves from shallow to deep water." *J. Fluid Mech.*, 462, 1-30.

Madsen, P. A., Bingham, H. B., and Schäffer, H. A. (2003). "Boussinesq-type formulations for fully nonlinear and extremely dispersive water waves: derivation and analysis." *Proc. R. Soc. Lond. A*, 459(2033), 1075– 1104.

Madsen, P. A., Murray, R., and Sørensen, O. R. (1991). "A new form of the Boussinesq equations with improved linear dispersion characteristics." *Coast. Eng.*, 15(4), 371-388.

Madsen, P. A., and Schäffer, H. A. (1998). "Higher-order Boussinesq-type equations for surface gravity waves: derivation and analysis." *Phil. Trans. R. Soc. Lond. A*, 356(1749), 3123-3184.

Madsen, P. A., and Sørensen, O. R. (1992). "A new form of the Boussinesq equations with improved linear dispersion characteristics. Part 2. A slowly-varying bathymetry." *Coast. Eng.*, 18(3-4), 183-204.

Mangor, K. (2004). *Shoreline management guidelines*. DHI Water & Environment, 294 pp.

Memos, C. D., Karambas, Th. V., and Avgeris, I. (2005). "Irregular wave transformation in the nearshore zone: experimental investigations and comparison with a higher order Boussinesq model." *Ocean Eng*., 32 (11-12), 1465-1485.

Metallinos, A. S., Emmanouilidou, M.-E. A., and Memos, C. D. (2014). "Wave-induced pore pressures in submerged rubble mound breakwaters simulated by a compound Boussinesq model." J. Hydraul. Res., 52 (1), 24–35.

Meyer-Peter, E., and Müller, R. (1948). "Formulas for bed-load transport." *Rep. 2nd Meet. Int. Assoc. Hydraul. Struc. Res.*, Stockholm, Sweden, pp. 39–64.

Nwogu, O. (1993). "Alternative form of Boussinesq equations for nearshore wave propagation." *J. Waterway, Port, Coastal, Ocean Eng.*, 10.1061/(ASCE)0733-950X(1993)119:6(618), 618-638.

Peregrine, D. H. (1967). "Long waves on a beach." *J. Fluid Mech.*, 27 (4), 815-827.

Rahman, S., Mano, A., and Udo, K. (2013). "Quasi-2D sediment transport model combined with Bagnold-type bed load transport." *Proc. 12th International Coastal Symposium*, Plymouth, United Kingdom, vol. 1, pp. 368-373.

Rakha, K. A. (1998). "A Quasi-3D phase-resolving hydrodynamic and sediment transport model." *Coast. Eng*., 34 (3-4), 277–311.

Rakha, K. A., Deigaard, R., and Brøker, I. (1997). "A phase-resolving cross-shore transport model for beach evolution." Coast. Eng., 31 (1-4), 231-261.

Ranasinghe, R., Larson, M., and Savioli, J. (2010). "Shoreline response to a single shore-parallel submerged breakwater." *Coast. Eng.*, 57 (11-12), 1006–1017.

Ranasinghe, R., Turner, I. L., and Symonds, G. (2006). "Shoreline response to multi-functional artificial surfing reefs: A numerical and physical modelling study." *Coast. Eng.*, 53 (7), 589–611.

Ribberink, J. S. (1998). "Bed-load transport for steady flows and unsteady oscillatory flows." *Coast. Eng*., 34 (1-2), 59–82.

Roelvink, J. A., and Stive, M. J. F. (1989). "Bar-generating cross-shore flow mechanics on a beach." *J. Geophys. Res.*, 94 (C4), 4785–4800.

Soulsby, R. (1997). *Dynamics of marine sands, a manual for practical applications*. Thomas Telford, H.R. Wallingford, England, 249 pp.

Turner, I. L., Leyden, V. M., Cox, R. J., Jackson, L. A., and McGrath, J. (2001). "Physical model study of the gold coast artificial reef." *J. Coast. Res.*, Special Issue 29, 131–146.

Van der Biezen, S. C, Roelvink, J. A., van de Graaff, J., Schaap, J., and Torrini, L. (1998). "2DH morphological modelling of submerged breakwaters." *Proc. 26th Int. Conf. on Coastal Eng.*, B. L. Edge, ed., Copenhagen, Denmark, vol. 2, pp. 2028–2041.

Van der Biezen, S. C., Van der Graaff, J., Schaap., J., Torrini, L. (1997). "Small scale tests and numerical modeling of the hydrodynamic and morphological effects of submerged breakwaters." *Proc. Combined Australian Coastal Engineering and Ports Conf.*, 219-224.

Van Dongeren, A. R., Wenneker, I., Roelvink, D., and Rusdin, A. (2006). "A Boussinesq-type wave driver for a morphodynamical model." *Proc. 30th Int. Conf. on Coastal Engineering*, J. M. Smith, ed., San Diego, U.S.A., vol. 3, pp. 3207-3219.

Van Gent, M. R. A. (1994). "The modelling of wave action on and in coastal structures." *Coast. Eng.*, 22 (3-4), 311–339.

Van Rijn, L. (1989). "Handbook Sediment Transport by Currents and Waves." *Rep. No. H 461*, Delft Hydraulics, Delft, The Netherlands.

Wei, G., Kirby, J. T., Grilli, S. T., and Subramanya, R. (1995). “A fully nonlinear Boussinesq model for surface waves. Part 1. Highly nonlinear unsteady waves.” *J. Fluid Mech.*, 294, 71-92.

Wenneker, I., van Dongeren, A., Lescinski, J., Roelvink, D., and Borsboom, M. (2011). “A Boussinesq-type wave driver for a morphodynamical model to predict short-term morphology.” *Coast. Eng.*, 58 (1), 66‑84.

Witting, J. M. (1984). “A unified model for the evolution of nonlinear water waves.” *J. Comput. Phys.*, 56(2), 203-236.

Zyserman, J. A., Jorgensen, K., and Christensen, E. D. (1999). "Sediment transport and morphology in the vicinity of shore parallel breakwaters." *Proc. Coastal Structures ’99*, ASCE, Santander, Spain, pp. 857-863.

Chapter 2

Nonlinear analysis of higher order Boussinesq-type wave models

2.1 Introduction

In order to describe more accurately the propagation of water waves it is necessary to use three-dimensional numerical models. These models are based on the solution of the fully three-dimensional Navier-Stokes equations including the turbulent effects through application of various methods, such as RANS (Reynolds Averaged Navier-Stokes), LES (Large Eddy Simulation), SPH (Smoothed Particle Hydrodynamics) etc. However, 3D models are generally quite complex and require very powerful computers in order to obtain numerical results. Thus, despite the more and more increasing efficiency of computers during the last decades, these approaches still remain a non-attractive choice for most coastal engineering applications.

On the other hand, two-horizontal dimensional (2DH) models offer reasonably good approximations to 3D models by eliminating the vertical dependency with a much lower computational cost. Therefore, great effort has been spent by coastal engineers and scientists on developing 2DH numerical models. The existing models include, among others, the ray tracing model, the mild-slope model (Berkhoff, 1972), the nonlinear shallow water model (Airy, 1845; Lamb, 1932), the Boussinesq models, the Serre models, the Hamiltonian formulation models, and the Green-Naghdi models. The first two types of models are based on the linear wave approximation, while the rest, at least originally, rely on the long wave approximation.

The study of shallow water regions has gained scientific interest due to their importance in the design of coastal structures and in studying estuaries and lagoons. Hence, long wave models have been a very popular solution for various coastal engineering problems in the nearshore zone. In order to study the mathematical properties of different nonlinear long wave models, it is convenient to define three length scales, which involve a reference water depth

d_o', a reference wavelength L', and a reference wave height H'. On the basis of these three scales two independent dimensionless parameters are defined. The first one is the nonlinearity parameter $\varepsilon = H'/ d_o'$, while the other is the dispersion parameter $\sigma^2 = (d_o'/ L')^2$. The former determines the magnitude of nonlinearity, which is a property related to any effects of real wave motion that cannot be reproduced by linear analysis, i.e. by neglecting products of the disturbances. On the other hand, the dispersion parameter determines the dispersive effect and can be also met as $\mu^2 = (k_o' d_o')^2$ in the international literature, where k_o' is a reference wavenumber. Depending on the relative magnitude of these two parameters different mathematical models can be derived.

Airy's (1845) theory was the basis of the nonlinear shallow water (NSW) equations. He basically assumed the dispersion effect to be negligible, i.e. $O(\mu^2) << 1$, but imposed no restriction for the nonlinearity, i.e. $O(\varepsilon) = 1$. Moreover, the horizontal velocity was assumed uniform over depth and the pressure of the fluid was hydrostatic. However, the shallow water approximation works quite well if the ratio of water depth to wavelength is small, i.e. $kd << 1$, k wavenumber and d still water depth, or equivalently for simulating tidal waves, tsunami, and infra-gravity waves whose wavelengths are quite large. Due to the assumed non-dispersion, the resulting linear phase speed is only a function of the water depth and is independent of the wave frequency which is a rather poor approximation of the exact linear dispersion relation if the water depth is not extremely small. Consequently, since there are no dispersion terms to balance the nonlinear terms, the front face of a propagating wave will steepen continuously even when the propagation is over a horizontal bed. Therefore, in intermediate water depths, the NSW equations offer no permanent wave solution and Boussinesq or other wave models have to be applied instead.

2.2 Review of Boussinesq-type wave models

In practice the threshold above which the waves are regarded as long waves in shallow waters is taken $L/d = 20$, where L wavelength. In such depths the waves tend to lose their frequency dispersion characteristics. If the above constraint be relaxed, i.e. for ratios L/d in the range between 10, say, and 20, the waves become weakly dispersive and the long waves approximation should be modified. For such "fairly long" waves of weak nonlinearity a theory by Boussinesq (1871, 1872) was developed.

In the original Boussinesq theory both nonlinearity and dispersion were considered small, but not negligible. This assumption was expressed formally by

$$O(\varepsilon) = O(\mu^2) < 1 \tag{2.1}$$

and the original equations attributed to Boussinesq read (Whitham, 1974)

$$h_t + (Uh)_x = 0 \tag{2.2}$$

$$U_t + UU_x + gh_x + \frac{1}{3}h_0 h_{xtt} = 0 \tag{2.3}$$

where $h = h_0 + \zeta$ is the total water depth, h_0 is the still water depth, ζ is the free surface elevation, U is the depth-averaged fluid velocity, g is the gravitational acceleration and the subscripts x and t denote differentiation with respect to space and time respectively. By combining (2.2) and (2.3) and linearising one gets

$$\zeta_{tt} - {c_0}^2\zeta_{xx} - \frac{1}{3}{h_0}^2\zeta_{xxtt} = 0 \tag{2.4}$$

where $c_0 = \sqrt{gh_0}$.

The associated dispersion relation reads

$$\omega^2 = \frac{{c_0}^2 k^2}{(1+\frac{1}{3}k^2{h_0}^2)} \tag{2.5}$$

where ω is the angular frequency.

The Boussinesq equations were restricted to horizontal bottom and one horizontal dimension (1DH), the vertical velocity was simply assumed to vary linearly from zero at the bottom to a maximum at the free surface, and the non-hydrostatic pressure was a consequence of the local acceleration of this velocity. The horizontal velocity had a quadratic variation with depth instead of being uniform.

At the end of the 19th century Korteweg and de Vries (1895) developed a similar wave theory for the same as previously range of applicability but for waves moving to only one direction, rather than two as in Boussinesq theory. The surface elevation is the only dependent variable in the KdV equation:

$$\zeta_t + c_0\left(1 + \frac{3}{2}\frac{\zeta}{h_0}\right)\zeta_x + \gamma\zeta_{xxx} = 0 \tag{2.6}$$

with $\gamma = \frac{1}{6}c_0{h_0}^2$.

The significance of the balance between the nonlinearity and dispersion effects depends on the parameter HL^2/d^3, H the wave height, as was firstly clarified by Ursell (1953), who stated that this parameter plays a central role in deciding the approximations to be applied and the associated physics in each particular case of wave propagation considered. Lighthill (1978) showed that when the value of this parameter is less than about 16, ε and μ^2 are of the same order, along with the assumption for moderately long waves, i.e. $kd < 0.6$. For this range

of kd a balance between waveform steepening and dispersion turns out to be possible and, therefore, periodic waves of unchanging form can propagate over a horizontal bottom. In particular, the KdV equation admits permanent wave solutions such as solitary waves and cnoidal waves.

Based on perturbation theory, Mei and Le Méhauté (1966) and Peregrine (1967) derived Boussinesq equations that are valid for variable water depth and two horizontal dimensions. Peregrine's (1967) equations used the depth-averaged velocity as the dependent variable and are considered to be the "classical" Boussinesq equations for water waves incorporating weak dispersion and weak nonlinearity. In practice he extended their range of applicability up to $kd < 0.75$. Soon this range was expanded in practice up to $kd = 1$ with equally stable results (Infeld and Rowlands, 1990). The early Boussinesq models have proven to be quite accurate, especially when applied to relatively shallow waters. Therefore, recent developments in computing technology were tempting researchers to expand further the applicability range of the theory that, under its original constraint $O(\varepsilon) = O(\mu^2)$, safeguarded the balance between dispersion and nonlinearity and produced stable solutions to the equation of motion. In practice it was desirable to derive a general wave model for the entire coastal zone from shallow ($kd = 0.31$) to deep water ($kd = 3.14$). In the critical range between $kd = 1$ and $kd = 3.14$ it is obvious that μ^2 is no longer less than 1 and more over dispersion cannot be balanced by nonlinearity since ε cannot get values higher than roughly 0.8 anywhere and much less for $\mu^2 > 1$. Furthermore, for values $kd > 1$ instabilities can inherently be present, as it is the case at $kd = 1.363$, where the lowest-order class I instability may be at play (Benjamin-Feir, 1967; McLean *et al*., 1981).

Extension of the Boussinesq theory to higher order is normally obtained through power series expansions of the governing equations based on ε rather than on μ^2, since the former is always less than one and the series can eventually converge. Conversely, when μ^2 is allowed to take values larger than one in order to simulate fully dispersive conditions, mathematical manipulations should be employed to overcome this difficulty of not meeting conditions (2.1). Since these conditions of the original Boussinesq model are violated by such enhanced models, the latter are usually called Boussinesq-type wave models.

Dingemans (1973) was the first to derive higher-order Boussinesq-type equations of $O(\mu^4)$ by retaining more terms in the polynomial velocity expansion. However, his equations were shown by Madsen and Schäffer (1998) to include singularities both in linear and nonlinear properties. Benjamin *et al*. (1972) pointed out how leading order terms could be used to manipulate higher order dispersive terms and improve the linear dispersive characteristics of KdV equations. Following this idea Mei (1989) proposed various forms of the dispersive KdV equations.

In applied mathematics, a Padé approximant is a better representation of an analytical function than a Taylor series expansion of the same order. Witting (1984) was the first to introduce rational functions in studying the characteristics of Boussinesq equations with respect to the linear dispersion equation. His results suggested that modified Boussinesq-type equations could embed improved linear characteristics compared to the standard equations.

Madsen *et al*. (1991) and Madsen and Sørensen (1992) introduced additional third-order terms with adjustable coefficients into the momentum equation of Abbott *et al*.'s (1984) model. This model relies on the classical Boussinesq equations expressed in terms of the volume flux instead of the depth-averaged velocity. The additional terms come from the long wave equations and reduce to zero in shallow water. However, the adjustable coefficients offered an optimization of the linear characteristics of the model up to the deep water limit.

The same dispersion relation of the previous formulation was achieved by Nwogu (1993) by using the velocity at an arbitrary level z_α as dependent variable in the derived equations and got a new form of Boussinesq-type equations. The dispersion property of the latter can be optimized by choosing the velocity variable at a specific level. An alternative form of Nwogu's (1993) equations was derived by Chen and Liu (1995). However, they used the velocity potential, instead of the horizontal velocity, at a certain depth and produced a parabolic model for water wave propagation. Schröter *et al*. (1994) used the definition of velocity as introduced by Witting (1984) combined with the approach by Madsen *et al*. (1991), and achieved an error smaller than 1% in the celerity for $kd < 6$, with terms of only third order derivatives; the shoaling gradient was also optimized.

Schäffer and Madsen (1995) added third order terms to the momentum and continuity equations and the linear frequency dispersion and shoaling of equations were very accurately reproduced by choosing appropriate values for the free parameters that appear in the derivation process.

Madsen and Sørensen (1993) analyzed the nonlinear properties of Madsen *et al*.'s (1991) equations. They found that for increasing wavenumbers the bound second harmonics tend to be underestimated as compared to Stokes second order theory. Improvement of the nonlinear characteristics and the description of the wave interactions can be obtained by the inclusion of higher-order terms that combine the effects of nonlinearity and dispersion. Wei *et al*. (1995) developed a fully nonlinear Boussinesq model accurate to $O(\mu^2)$ based on Nwogu's (1993) formulation. Since no assumption of small nonlinearity was made, the equations were fully nonlinear and could provide significantly improved predictions of wave heights and internal kinematics for the wave motion prior to wave breaking.

Beji and Nadaoka (1996) gave a set of Boussinesq equations similar to the one by Madsen and Sørensen (1992) by adding and subtracting a dispersive term in the momentum equation.

Their formulation ensured the exact energy conservation. Madsen and Schäffer (1998) by taking more terms in the Taylor series obtained a number of models with dispersion characteristics of up to $O(\mu^4)$. Their accuracy appears to be very good for $kd < 6$. Zou (1999, 2000) also extended the limit of applicable water depths up to $kd \approx 3$. Through the insertion of an extra free parameter he also improved the nonlinear properties of his higher order equations of $O(\varepsilon\mu^2)$.

Moreover, Gobbi *et al*. (2000a) and Chen *et al*. (2003) extended Wei *et al*.'s (1995) equations to account for rotational flows and ensured that the vertical vorticity was consistent with the order of approximation for the wave motion. On the other hand, Boussinesq-type equations including the horizontal vorticity were reported by Rego and Neves (1997) and Veeramony and Svendsen (2000) in the vertical plane, and by Shen (2001) for the general three-dimensional case.

More recent efforts offered a wider range for Boussinesq models providing accurate linear dispersion and shoaling characteristics from shallow water to deep water of $kd > 3$. However, regarding nonlinearity most of these models incorporate weak far better than strong nonlinear characteristics.

Karambas (1999) offered an extension of the classical Boussinesq equations in deeper water for nonlinear monochromatic waves. By using hyperbolic functions he derived new equations that are exact at any depth with respect to linear dispersion if infinite terms are retained in the Taylor series that appear in his formulation. Agnon *et al*. (1999) presented a new procedure by which it is possible to achieve the same accuracy in nonlinear properties as in the linear ones. Their procedure is based on an exact formulation of the boundary conditions at the free surface and at the sea bottom combined with an approximate solution to the Laplace equation given in terms of truncated series expansions. Gobbi and Kirby (1999) and Gobbi *et al*. (2000b) applied a generalization of Nwogu's (1993) method and derived a formulation of $O(\mu^4)$ based on a linear combination of the velocities at two arbitrary z-levels. The velocity profile obtained from their method is applicable up to $kd = 4$, while their dispersion relation is applicable up to $kd = 6$. Another generalization of Wei et *al*.'s (1995) equations was presented by Kennedy *et al*. (2001) who considered the reference level z_α to be time-varying and offered an improvement of the nonlinear properties of the original model.

Karambas and Koutitas (2002) enhanced their model with extra nonlinearity by including terms $O(\varepsilon\sigma^2)$ and, by following the method by Madsen *et al*. (1991), they extended the linear dispersion characteristics up to the limit of deep waters.

Madsen *et al*. (2002, 2003) presented a model having as a starting point the exact solution to the Laplace equation and replaced the infinite series operators by finite series approximations involving up to fifth-order derivative operators. By manipulating the finite series to

incorporate Padé approximants the linear dispersion and nonlinear characteristics became very accurate up to $kd = 40$. This model was initially valid for mildly sloping beds but later it was also extended for rapidly varying bathymetries by Madsen *et al*. (2006). Linear shoaling could also be accurately optimized up to $kd = 30$. In parallel, Wu (1999, 2001) also derived fully dispersive and nonlinear formulations by using the exact surface conditions.

Lynett and Liu (2004a, b) divided the domain in multiple horizontal layers. Instead of employing a high-order polynomial for the vertical distribution of the flow field, they used a quadratic polynomial in each layer, and matched them at the interfaces. This gives an extra equation for each added layer, but the order of the derivatives is limited to three. For a four layer model, errors in the celerity are limited to 1% for $kd < 30$.

Bingham and Agnon (2005) derived also a Boussinesq-type model valid for fully dispersive waves, in the sense that the error of approximation is acceptably small for all $kd < \infty$. This was made possible by introducing the generalized two-dimensional Hilbert transform, evaluated by fast Fourier transform. Using a higher order approximation, very good dispersion characteristics could be achieved over the entire range of *kd*. Their model was also valid for a mildly sloping bottom. Li (2008) used a hyperbolic cosine function of the Stokes first-order solution instead of the bottom velocity potential function, as a first approximation, deriving thus a fully linear dispersive model. Karambas and Memos (2009) based on the works of Chester (1968) and Tsutsui *et al*. (1998) derived a model that offers significant advantages due to small number of terms involved in both the mass and the momentum equations and works for propagation of fully linear dispersive and weakly nonlinear water waves. In this model the Boussinesq-type dispersive terms are expressed through convolution integrals, which are estimated using appropriate impulse functions. Karambas and Memos' (2009) model was formally derived for horizontal bottoms. Schäffer (2004a) proposed a similar one-dimensional nonlinear post-Boussinesq model which is also exact with respect to the linear dispersion equation but has been extended to mild sloping beds. His model is expressed in terms of the surface elevation and the horizontal particle velocity at still water level, while the internal kinematics were treated as convolutions in space. A similar procedure was also used by Schäffer (2004b) for computing the velocity field from the kinematics at the still water level as provided by a numerical model. This convolution method was then extended to two horizontal dimensions (Schäffer, 2006), modified by Schäffer (2009) and further extended to complex-shaped domains (Schäffer, 2012).

Zou and Fang (2008) derived an alternative form of Boussinesq-type equations that are fully nonlinear up to $O(\mu^4)$ by applying an σ-transformation and imposing no limitation for the bottom slope. Their model was extended by Zou *et al*. (2009) for rapidly varying topographies with multiple sand bars by improving the prediction of the Bragg reflection.

Fang and Zou (2010) extended Zou's (2000) model to be fully nonlinear up to $O(\mu^2)$ and, by introducing two extra nonlinear terms, they offered and improvement of the amplitude dispersion and second- and third-order transfer functions. Another improvement of the nonlinear properties of Madsen and Schäffer's (1998) equations of $O(\mu^2)$ was also presented by Fang *et al*. (2013).

Chen (2006) derived a new set of Boussinesq-type equations for permeable and impermeable beds which retain the conservation of vertical potential vorticity to higher order than the previous correction of Wei *et al*.'s (1995) equations by Chen *et al*. (2003). Shi *et al*. (2001) expressed Wei *et al*.'s (1995) equations in generalized curvilinear co-ordinates in order to adapt computations to irregularly shaped fields and make them more efficient in large nearshore regions. A similar co-ordinate system was also adopted by Shi *et al*. (2012) for solving Chen's (2006) equations, extended to incorporate a moving reference level as in Kennedy *et al*. (2001). The numerical scheme of this model was also adopted by Kirby *et al*. (2013) who derived a nonlinear dispersive Boussinesq-type model which is expressed in spherical co-ordinates and includes the Coriolis effects in order to simulate tsunami propagation. Tsunami generation and propagation by a Boussinesq-type model was also studied by Fuhrman and Madsen (2009) by adding an extra term in the kinematic bottom condition of Madsen *et al*.'s (2006) model.

Galan *et al*. (2012) presented an optimization approach to improve the performance of Boussinesq-type equations. They included terms of $O(\varepsilon\mu^4)$ and by using an explicit fourth-order numerical scheme they obtained acceptable errors (~2%) for $kd < 10$. Chondros and Memos (2014) proposed a modified version of Madsen and Schäffer's (1998) equations of $O(\varepsilon\mu^4)$. They defined new coefficients in order to improve the linear and nonlinear characteristics of the equations. These coefficients, that govern the linear and nonlinear dispersion and shoaling, were allowed to be time and space dependent in contrast with previous studies, where they were assumed constants. This approach led to an improvement of linear dispersion, linear shoaling and nonlinearity at second order analysis at any depth. The possibility to use variable coefficients depending on water depth has also been exploited by Simarro *et al*. (2013). Liu and Fang (2015) derived also a two-layer model that describes very accurately the linear and second-order nonlinear wave characteristics up to $kd \approx 6$.

Besides the more or less standard procedure of series expansion applied in most of the models described above, there have been also proposed other groups of models with similar properties to Boussinesq-type wave models over the last decades. Serre (1953) derived a set of equations for long waves travelling over a constant depth by assuming the horizontal velocity to be uniform over depth and the vertical velocity to vary linearly. However, the flow was not assumed irrotational despite the assumption of an inviscid and incompressible fluid.

An interesting fact is that Serre's (1953) equations are equivalent to Mei's (1989) fully nonlinear standard Boussinesq equations (based on depth-averaged velocity) despite the different assumptions made during the derivation process. Seabra-Santos *et al*. (1987) extended the Serre equations to two horizontal dimensions and variable depth.

A similar, but much more general, family of models was derived by Green *et al*. (1974) and Green and Naghdi (1976). The only assumption behind the derivation was that the vertical and horizontal velocities were polynomials of order N and (N-1), respectively. The Green-Naghdi equations reduce to Serre's equations if N = 1. The original GN equations have been extended by using a combination of certain basis functions, rather than the original polynomial formulations. Boussinesq-type equations have been also derived using a Hamiltonian formulation (Broer, 1974; Broer, 1975; Broer *et al*., 1976). Although the linear characteristics of the original Hamiltonian-based models have been improved, they still remain weakly nonlinear due to their computational complexity. Comparative results of different models based on the various aforementioned formulations can be found in Dingemans (1994a,b).

A number of quite comprehensive reviews of Boussinesq-type models have been presented during the last twenty years (Kirby, 1997; Madsen and Schäffer, 1999; Kirby, 2003; Madsen and Fuhrman, 2010; Brocchini, 2013; Kirby, 2016). Recently, research concerning Boussinesq-type modelling has been trying to extend its traditional area of interest to different aspects such as rotationality, the turbulent structure of the flow field (Kim *et al*., 2009; Kim and Lynett, 2011; Zhang *et al*., 2014) or a more detailed description of the vertical dependency of the flow. Thus, a number of modern post-Boussinesq and non-hydrostatic models, which rather step towards the three-dimensional Navier-Stokes equations, have been developed, e.g. Ma *et al*. (2012); Antuono and Brocchini (2013) etc.

In this chapter, two existing Boussinesq models were enhanced in terms mainly of nonlinearity and tested against experimental data in order to select the one that fitted best the needs of the specific research in the framework of the present Ph.D. thesis. A key element in this selection was to distinguish how dominant is the role of extra terms of higher order in linear and nonlinear characteristics, considering always the computational time and the complexity of the numerical computations.

2.3 Derivation of model equations

2.3.1 Nonlinear enhancement of Karambas and Koutitas's (2002) model

Karambas and Koutitas (2002) –KK02 in the following– included in their 1DH model equations terms of $O(1, \varepsilon, \sigma^2, \varepsilon\sigma^2)$. In order to enhance the nonlinearity of the above model a similar procedure is followed as the one used by Veeramony and Svendsen (2000) whereby terms of order $O(1, \varepsilon, \sigma^2, \varepsilon\sigma^2, \varepsilon^2\sigma^2)$ are included. The 2DH derivation is presented in the following. The independent variables are scaled as (Madsen and Schäffer, 1998)

$$x = \frac{x'}{L'}\ , y = \frac{y'}{L'}\ , z = \frac{z'}{d_o'}\ , t = \frac{\sqrt{\mathrm{g}d_o'}}{L'}t' \tag{2.7}$$

where $\vec{x} = (x, y)$ denotes the horizontal dimensions, z the upward co-ordinate with zero on the still water surface, and t the time. The prime denotes dimensional variables whereas the non-dimensional ones stand without primes. The non-dimensional water depth (d), surface elevation (ζ), horizontal velocity ($\vec{u} = (u, v)$), vertical velocity (w) and pressure (p) are scaled as

$$d = \frac{d'}{d_o'}\ , \zeta = \frac{\zeta'}{H'}\ , \vec{u}' = \vec{u}\varepsilon\sqrt{\mathrm{g}d_o'}\ , w' = w\varepsilon\sigma\sqrt{\mathrm{g}d_o'}\ , p' = \varepsilon\rho\mathrm{g}d_o' p \tag{2.8}$$

where ρ is the water density.

Following this non-dimensionalization, the continuity equation, the momentum equations and the kinematic free-surface boundary and varying bottom conditions are written

$$\nabla\cdot\vec{u} + \frac{\partial w}{\partial z} = 0 \tag{2.9a}$$

$$\frac{\partial\vec{u}}{\partial t} + \varepsilon(\vec{u}\cdot\nabla)\vec{u} + \varepsilon w\frac{\partial\vec{u}}{\partial z} = -\nabla p \tag{2.9b}$$

$$\sigma^2\left[\frac{\partial w}{\partial t} + \varepsilon(\vec{u}\cdot\nabla)w + \varepsilon w\frac{\partial w}{\partial z}\right] = -\frac{\partial p}{\partial z} - \frac{1}{\varepsilon} \tag{2.9c}$$

$$w = \frac{\partial\zeta}{\partial t} + \varepsilon\vec{u}\cdot\nabla\zeta \qquad \text{at } z = \varepsilon\zeta \tag{2.9d}$$

$$w = -\vec{u}\cdot\nabla d \qquad \text{at } z = -d \tag{2.9e}$$

where $\nabla = \left(\frac{\partial}{\partial x}, \frac{\partial}{\partial y}\right)$ is the horizontal gradient operator and the symbol $\cdot$ denotes the dot product of two vectors.

By integrating the continuity Eq. (2.9a) over depth and using the free surface and bottom boundary conditions Eqs (2.9d) and (2.9e), the well-known depth-integrated version of continuity equation is obtained, after using the Leibnitz integration rule

$$\frac{\partial \zeta}{\partial t} + \nabla \cdot \vec{Q} = 0 \tag{2.10}$$

where $\vec{Q}$ is the volume flux $\vec{Q} = \vec{U}(d + \varepsilon\zeta)$ and $\vec{U} = (U, V)$ is the non-dimensional depth-averaged velocity defined by $\vec{U} = \frac{1}{d+\varepsilon\zeta}\int_{-d}^{\varepsilon\zeta} \vec{u}\, \mathrm{d}z$.

The depth-integrated horizontal and vertical momentum equations are written

$$\frac{\partial [U(d+\varepsilon\zeta)]}{\partial t} + \varepsilon\left[\frac{\partial}{\partial x}\left(\int_{-d}^{\varepsilon\zeta} u^2\, \mathrm{d}z\right) + \frac{\partial}{\partial y}\left(\int_{-d}^{\varepsilon\zeta} uv\, \mathrm{d}z\right)\right] = p|_{z=-d}\frac{\partial d}{\partial x} - \frac{\partial}{\partial x}\left(\int_{-d}^{\varepsilon\zeta} p\, \mathrm{d}z\right) \tag{2.11a}$$

$$\frac{\partial [V(d+\varepsilon\zeta)]}{\partial t} + \varepsilon\left[\frac{\partial}{\partial x}\left(\int_{-d}^{\varepsilon\zeta} uv\, \mathrm{d}z\right) + \frac{\partial}{\partial y}\left(\int_{-d}^{\varepsilon\zeta} v^2\, \mathrm{d}z\right)\right] = p|_{z=-d}\frac{\partial d}{\partial y} - \frac{\partial}{\partial y}\left(\int_{-d}^{\varepsilon\zeta} p\, \mathrm{d}z\right) \tag{2.11b}$$

$$p(z) = \left(\zeta - \frac{z}{\varepsilon}\right) + \sigma^2 \frac{\partial}{\partial t}\left(\int_z^{\varepsilon\zeta} w\, \mathrm{d}z\right) - \varepsilon\sigma^2 w^2 + \varepsilon\sigma^2 \nabla \cdot \left(\int_z^{\varepsilon\zeta} w\vec{u}\, \mathrm{d}z\right) \tag{2.12}$$

Integration of the local continuity equation (2.9a), with respect to z, yields

$$w = -\nabla \cdot \left(\int_{-d}^{z} \vec{u}\, \mathrm{d}z\right) \tag{2.13}$$

The pressure *p* from Eq. (2.12) and the vertical velocity *w* from Eq. (2.13) are substituted into Eqs (2.11a,b). By extending to two horizontal dimensions the assumption by Karambas and Koutitas (2002) for non-breaking waves, a uniform velocity profile over depth is adopted, i.e. $\vec{u} = \vec{U}$ for $-d \le z \le \varepsilon\zeta$. This assumption was also made by Serre (1953) and Schäffer *et al*. (1993). Applying this profile and neglecting terms that include spatial derivatives of water depth of order higher than first, the depth-averaged horizontal momentum equation is obtained

$$\vec{U}_t + \varepsilon\left(\vec{U} \cdot \nabla\right)\vec{U} + \nabla\zeta = \sigma^2\left\{\frac{1}{2}d\nabla\left[\nabla \cdot \left(d\vec{U}_t\right)\right] - \frac{1}{6}d^2\nabla\left(\nabla \cdot \vec{U}_t\right)\right\} + \varepsilon\sigma^2\vec{K}_1(\zeta, U, V, d)$$
$$+\varepsilon^2\sigma^2\vec{K}_2(\zeta, U, V, d) + O(\varepsilon^3\sigma^2) \tag{2.14}$$

where $\vec{K}_1$, $\vec{K}_2$ are vector functions of $\{\zeta, U, V, d\}$ and of their spatial and temporal derivatives. Their lengthy expressions coincide with $(\psi_{II}^{(x)}, \psi_{II}^{(y)})$ and $(\psi_{III}^{(x)}, \psi_{III}^{(y)})$ in Eqs (2.20), (2.23) and (2.21), (2.24), respectively, if the parameters B and B_2, which are described in the following, are set equal to 0.

The dispersion and shoaling characteristics of the model based on Eqs (2.10) and (2.14) are very poor for intermediate and deep-water waves because of the uniform profile assumption. Thus, following Madsen and Schäffer (1998) who adopted an enhancement technique for these characteristics, the following linear operators were applied

$$L_{B_1} = 1 + \mathrm{B}_1\sigma^2 d^2\nabla(\nabla\cdot) \quad \text{and} \quad L_{B_2} = 1 + \mathrm{B}_2\sigma^2 d\nabla[\nabla\cdot(d\,\cdot)] \tag{2.15}$$

where B_1 and B_2 are parameters to be defined.

By setting $\mathrm{B} = \mathrm{B}_1+\mathrm{B}_2$, reverting to dimensional variables and omitting primes, the continuity and momentum equations of the model are written:

$$\frac{\partial\zeta}{\partial t} + \frac{\partial[U(\mathrm{d}+\zeta)]}{\partial \mathrm{x}} + \frac{\partial[V(\mathrm{d}+\zeta)]}{\partial \mathrm{y}} = 0 \tag{2.16}$$

$$\frac{\partial U}{\partial t} + U\frac{\partial U}{\partial x} + V\frac{\partial U}{\partial y} + \mathrm{g}\frac{\partial\zeta}{\partial x} = \psi_I^{(x)} + \psi_{II}^{(x)} + \psi_{III}^{(x)} \tag{2.17}$$

$$\frac{\partial V}{\partial t} + U\frac{\partial V}{\partial x} + V\frac{\partial V}{\partial y} + \mathrm{g}\frac{\partial\zeta}{\partial y} = \psi_I^{(y)} + \psi_{II}^{(y)} + \psi_{III}^{(y)} \tag{2.18}$$

where $\psi_I^{(x)}, \psi_{II}^{(x)}, \psi_{III}^{(x)}, \psi_I^{(y)}, \psi_{II}^{(y)}, \psi_{III}^{(y)}$ are the Boussinesq terms given by

$$\psi_I^{(x)} = \left(\mathrm{B}+\frac{1}{3}\right)d^2\left(U_{xxt}+V_{xyt}\right) + (2\mathrm{B}_2+1)dd_xU_{xt} + \left(\mathrm{B}_2+\frac{1}{2}\right)dd_xV_{yt} + \left(\mathrm{B}_2+\frac{1}{2}\right)dd_yV_{xt} + \mathrm{B}\mathrm{g}d^2\left(\zeta_{xxx}+\zeta_{xyy}\right) + \mathrm{B}_2\mathrm{g}\left(2dd_x\zeta_{xx} + dd_y\zeta_{xy} + dd_x\zeta_{yy}\right) \tag{2.19}$$

$$\psi_{II}^{(x)} = \frac{2d\zeta}{3}\left(U_{xxt}+V_{xyt}\right) + (d\zeta_x+\zeta d_x)U_{xt} + \frac{1}{2}(d\zeta_x+\zeta d_x)V_{yt} + \frac{1}{2}\zeta d_yV_{xt} + \left(\mathrm{B}+\frac{1}{3}\right)d^2\left(UU_{xxx}+UV_{xxy}+VU_{xxy}+VV_{xyy}+V_xV_{yy}\right) + \left(3\mathrm{B}-\frac{1}{3}\right)d^2U_xU_{xx} + \left(3\mathrm{B}+\frac{1}{3}\right)d^2V_xU_{xy} + \left(2\mathrm{B}-\frac{2}{3}\right)d^2V_yV_{xy} + \left(\mathrm{B}-\frac{1}{3}\right)d^2U_xV_{xy} + 2\mathrm{B}d^2U_yV_{xx} - \frac{2d^2}{3}V_yU_{xx} + \left(\mathrm{B}_2+\frac{1}{2}\right)dd_x\left(VV_{yy}+UV_{xy}+2UU_{xx}+2VU_{xy}\right) + \left(3\mathrm{B}_2+\frac{1}{2}\right)dd_xU_yV_x + \left(\mathrm{B}_2-\frac{1}{2}\right)dd_xV_y{}^2 - dd_xV_yU_x + 2\mathrm{B}_2d_xU_x{}^2 + \left(\mathrm{B}_2+\frac{1}{2}\right)dd_y\left(V_xV_y+U_xV_x+UV_{xx}+VV_{xy}\right) + \zeta_x\left(d_xU_t+d_yV_t\right) \tag{2.20}$$

$$\psi_{III}^{(x)} = \frac{\zeta^2}{3}\left(U_{xxt}+V_{xyt}\right) + \zeta\zeta_x\left(U_{xt}+V_{yt}\right) + d\zeta_x\left(-U_x{}^2 - 2V_yU_x + VV_{yy} + VU_{xy} + UV_{xy} + UU_{xx} - V_y{}^2\right) + \frac{2d\zeta}{3}\left(UU_{xxx}+UV_{xxy}+VU_{xxy}+VV_{xyy}+V_xV_{yy}+V_xU_{xy}-U_xU_{xx}-\right.$$

$$2V_yU_{xx} - U_xV_{xy} - 2V_yV_{xy}\big) + \zeta d_x\left(VU_{xy} + UU_{xx} + \frac{1}{2}UV_{xy} + \frac{1}{2}U_yV_x + \frac{1}{2}VV_{yy} - \frac{1}{2}{V_y}^2 - V_yU_x\right) + \frac{1}{2}\zeta d_y\big(V_xV_y + U_xV_x + UV_{xx} + VV_{xy}\big) + \zeta_x d_x\big(VU_y + UU_x\big) + \zeta_x d_y\big(VV_y + UV_x\big) \quad (2.21)$$

$$\psi_I^{(y)} = \left(\mathrm{B} + \frac{1}{3}\right) d^2\big(V_{yyt} + U_{xyt}\big) + (2\mathrm{B}_2 + 1)dd_yV_{yt} + \left(\mathrm{B}_2 + \frac{1}{2}\right) dd_yU_{xt} + \left(\mathrm{B}_2 + \frac{1}{2}\right) dd_xU_{yt} + \mathrm{B}gd^2\big(\zeta_{yyy} + \zeta_{xxy}\big) + \mathrm{B}_2g\big(2dd_y\zeta_{yy} + dd_x\zeta_{xy} + dd_y\zeta_{xx}\big) \quad (2.22)$$

$$\psi_{II}^{(y)} = \frac{2d\zeta}{3}\big(V_{yyt} + U_{xyt}\big) + \big(d\zeta_y + \zeta d_y\big)V_{yt} + \frac{1}{2}\big(d\zeta_y + \zeta d_y\big)U_{xt} + \frac{1}{2}\zeta d_xU_{yt} + \left(\mathrm{B} + \frac{1}{3}\right) d^2\big(VV_{yyy} + UV_{xyy} + VU_{xyy} + UU_{xxy} + U_yU_{xx}\big) + \left(3\mathrm{B} - \frac{1}{3}\right) d^2V_yV_{yy} + \left(3\mathrm{B} + \frac{1}{3}\right) d^2U_yV_{xy} + \left(2\mathrm{B} - \frac{2}{3}\right) d^2U_xU_{xy} + \left(\mathrm{B} - \frac{1}{3}\right) d^2V_yU_{xy} + 2\mathrm{B}d^2V_xU_{yy} - \frac{2d^2}{3}U_xV_{yy} + \left(\mathrm{B}_2 + \frac{1}{2}\right) dd_y\big(UU_{xx} + VU_{xy} + 2VV_{yy} + 2UV_{xy}\big) + \left(3\mathrm{B}_2 + \frac{1}{2}\right) dd_yU_yV_x + \left(\mathrm{B}_2 - \frac{1}{2}\right) dd_y{U_x}^2 - dd_yV_yU_x + 2\mathrm{B}_2d_y{V_y}^2 + \left(\mathrm{B}_2 + \frac{1}{2}\right) dd_x\big(U_xU_y + U_yV_y + UU_{xy} + VU_{yy}\big) + \zeta_y\big(d_xU_t + d_yV_t\big) \quad (2.23)$$

$$\psi_{III}^{(y)} = \frac{\zeta^2}{3}\big(V_{yyt} + U_{xyt}\big) + \zeta\zeta_y\big(V_{yt} + U_{xt}\big) + d\zeta_y\big(-{V_y}^2 - 2U_xV_y + UU_{xx} + UV_{xy} + VU_{xy} + VV_{yy} - {U_x}^2\big) + \frac{2d\zeta}{3}\big(VV_{yyy} + VU_{xyy} + UV_{xyy} + UU_{xxy} + U_yU_{xx} + U_yV_{xy} - V_yV_{yy} - 2U_xV_{yy} - V_yU_{xy} - 2U_xU_{xy}\big) + \zeta d_y\left(UV_{xy} + VV_{yy} + \frac{1}{2}VU_{xy} + \frac{1}{2}V_xU_y + \frac{1}{2}UU_{xx} - \frac{1}{2}{U_x}^2 - U_xV_y\right) + \frac{1}{2}\zeta d_x\big(U_xU_y + V_yU_y + VU_{yy} + UU_{xy}\big) + \zeta_y d_y\big(UV_x + VV_y\big) + \zeta_y d_x\big(UU_x + VU_y\big) \quad (2.24)$$

The terms $\psi_I^{(x)}, \psi_I^{(y)}$ are of $O(\sigma^2)$, $\psi_{II}^{(x)}, \psi_{II}^{(y)}$ are of $O(\varepsilon\sigma^2)$ and $\psi_{III}^{(x)}, \psi_{III}^{(y)}$ are of $O(\varepsilon^2\sigma^2)$. It should be mentioned that the dispersion characteristics of the model are controlled by the free parameter B, which is the sum of B_1 and B_2, while the linear shoaling characteristics are controlled by the free parameter B_2.

The 1DH model version includes in non-dimensional form the equations

$$\frac{\partial\zeta}{\partial t} + \frac{\partial[(d+\varepsilon\zeta)U]}{\partial x} = 0 \quad (2.25)$$

$$\frac{\partial U}{\partial t} + \varepsilon U\frac{\partial U}{\partial x} + \frac{\partial\zeta}{\partial x} = \sigma^2\frac{d^2+2\varepsilon d\zeta}{3}\frac{\partial^3U}{\partial x^2\partial t} + \sigma^2(d+\varepsilon\zeta)\frac{\partial d}{\partial x}\frac{\partial^2U}{\partial x\partial t} + \varepsilon\sigma^2\frac{d^2}{3}\left(U\frac{\partial^3U}{\partial x^3} - \frac{\partial U}{\partial x}\frac{\partial^2U}{\partial x^2}\right) + \varepsilon\sigma^2\left(d\frac{\partial\zeta}{\partial x}\frac{\partial^2U}{\partial x\partial t} + d\frac{\partial d}{\partial x}U\frac{\partial^2U}{\partial x^2} + \frac{\partial d}{\partial x}\frac{\partial\zeta}{\partial x}\frac{\partial U}{\partial t}\right) + \varepsilon^2\sigma^2\left(\frac{\zeta^2}{3}\frac{\partial^3U}{\partial x^2\partial t} + \zeta\frac{\partial\zeta}{\partial x}\frac{\partial^2U}{\partial x\partial t}\right) + \varepsilon^2\sigma^2\frac{2d\zeta}{3}\left(U\frac{\partial^3U}{\partial x^3} - \frac{\partial U}{\partial x}\frac{\partial^2U}{\partial x^2}\right)$$

$$+\varepsilon^2\sigma^2\left(Ud\frac{\partial^2 U}{\partial x^2}\frac{\partial \zeta}{\partial x}+\frac{\partial d}{\partial x}U\frac{\partial U}{\partial x}\frac{\partial \zeta}{\partial x}+\frac{\partial d}{\partial x}U\frac{\partial^2 U}{\partial x^2}\zeta\right)-\varepsilon^2\sigma^2 d\frac{\partial \zeta}{\partial x}\left(\frac{\partial U}{\partial x}\right)^2$$

$$+\sigma^2 \mathrm{B}d^2\left(\frac{\partial^3 U}{\partial x^2\partial t}+\frac{\partial^3 \zeta}{\partial x^3}+\varepsilon\frac{\partial^2\left(U\frac{\partial U}{\partial x}\right)}{\partial x^2}\right)+\sigma^2 2\mathrm{B}_2 d\frac{\partial d}{\partial x}\left(\frac{\partial^2 U}{\partial x\partial t}+\frac{\partial^2 \zeta}{\partial x^2}+\varepsilon\frac{\partial\left(U\frac{\partial U}{\partial x}\right)}{\partial x}\right) \quad (2.26)$$

By reverting to dimensional variables and omitting primes, Eqs (2.25) and (2.26) are written

$$\frac{\partial \zeta}{\partial t}+\frac{\partial[(d+\zeta)U]}{\partial x}=0 \quad (2.27)$$

and

$$\frac{\partial U}{\partial t}+U\frac{\partial U}{\partial x}+\mathrm{g}\frac{\partial \zeta}{\partial x}=\frac{d^2+2d\zeta}{3}\frac{\partial^3 U}{\partial x^2\partial t}+(d+\zeta)\frac{\partial d}{\partial x}\frac{\partial^2 U}{\partial x\partial t}+\frac{d^2}{3}\left(U\frac{\partial^3 U}{\partial x^3}-\frac{\partial U}{\partial x}\frac{\partial^2 U}{\partial x^2}\right)$$

$$+\left(d\frac{\partial \zeta}{\partial x}\frac{\partial^2 U}{\partial x\partial t}+d\frac{\partial d}{\partial x}U\frac{\partial^2 U}{\partial x^2}+\frac{\partial d}{\partial x}\frac{\partial \zeta}{\partial x}\frac{\partial U}{\partial t}\right)+\mathrm{B}d^2\left(\frac{\partial^3 U}{\partial x^2\partial t}+\mathrm{g}\frac{\partial^3 \zeta}{\partial x^3}+\frac{\partial^2\left(U\frac{\partial U}{\partial x}\right)}{\partial x^2}\right)$$

$$+2\mathrm{B}_2 d\frac{\partial d}{\partial x}\left(\frac{\partial^2 U}{\partial x\partial t}+\mathrm{g}\frac{\partial^2 \zeta}{\partial x^2}+\frac{\partial\left(U\frac{\partial U}{\partial x}\right)}{\partial x}\right)+\left(\frac{\zeta^2}{3}\frac{\partial^3 U}{\partial x^2\partial t}+\zeta\frac{\partial \zeta}{\partial x}\frac{\partial^2 U}{\partial x\partial t}\right)$$

$$+\frac{2d\zeta}{3}\left(U\frac{\partial^3 U}{\partial x^3}-\frac{\partial U}{\partial x}\frac{\partial^2 U}{\partial x^2}\right)+\left(dU\frac{\partial^2 U}{\partial x^2}\frac{\partial \zeta}{\partial x}+\frac{\partial d}{\partial x}U\frac{\partial U}{\partial x}\frac{\partial \zeta}{\partial x}+\frac{\partial d}{\partial x}U\frac{\partial^2 U}{\partial x^2}\zeta\right)-d\frac{\partial \zeta}{\partial x}\left(\frac{\partial U}{\partial x}\right)^2 \quad (2.28)$$

By retaining terms of order $O(1, \varepsilon, \sigma^2, \varepsilon\sigma^2)$ in the one-dimensional version, Eq. (2.26) is reduced to the one of Karambas and Koutitas's (2002) model with the only difference being the free parameter B_2. In KK02 model one single free parameter was included to control linear dispersion and shoaling at the same time, while herein two parameters were introduced in order to optimize these two linear characteristics separately. Thus the model based on Eqs (2.27) and (2.28) is called in the following extended KK02 model (KK02e) and displays stronger nonlinear characteristics of $O(\varepsilon^2\sigma^2)$ than its original counterpart (KK02) of weaker nonlinearity of $O(\varepsilon\sigma^2)$. In addition, in the 2DH case, keeping terms of order $O(1, \varepsilon, \sigma^2, \varepsilon\sigma^2)$ leads to models almost identical to Memos *et al*. (2005); Zou (1999); Karambas and Karathanassi (2004). Hence, Eqs (2.17) and (2.18) offer an extension of these models up to $O(\varepsilon^2\sigma^2)$.

2.3.2 Nonlinear enhancement of Karambas and Memos's (2009) model

Karambas and Memos (2009) derived a fully linear dispersive Boussinesq-type model. Their model is weakly nonlinear since the momentum equation includes terms of order $O(1, \varepsilon, \sigma^2)$. Here the nonlinear characteristics of these fully dispersive equations shall be enhanced by including terms of order $O(\varepsilon\sigma^2)$.

Inviscid, incompressible fluid and irrotational flow are considered. The independent variables are scaled as given in Eq. (2.7). Irrotational flow implies the existence of a velocity

potential $F'(x', z', t')$ that describes the flow field. By definition the fluid velocities can be expressed by $u' = \partial F'/\partial x'$, $w' = \partial F'/\partial z'$.

The non-dimensional water depth (d), surface elevation (ζ), and horizontal velocity (u) are scaled as given in Eq. (2.8). The non-dimensional vertical velocity (w) and pressure (p) are scaled as follows:

$$w' = w\frac{\varepsilon}{\sigma}\sqrt{\mathrm{g}d_o'}\,,\; p' = \rho \mathrm{g} d_o' p \tag{2.29}$$

A reference wave number $k_o'=1/L'$ is defined in addition to the local dimensional wave number $k'=2\pi/L_{loc}'$, where L_{loc}' is the wavelength at depth d' for a regular wave. Hence we can define the non-dimensional wavenumber as

$$k = \frac{k'}{k_0'} \tag{2.30}$$

Following this non-dimensionalization, the continuity equation, the momentum equations and the kinematic free-surface boundary, and the varying bottom conditions are written

$$\sigma^2\frac{\partial u}{\partial x} + \frac{\partial w}{\partial z} = 0 \tag{2.31}$$

$$\frac{\partial u}{\partial t} + \varepsilon u\frac{\partial u}{\partial x} + \frac{\varepsilon}{\sigma^2}w\frac{\partial u}{\partial z} = -\frac{1}{\varepsilon}\frac{\partial p}{\partial x} \tag{2.32}$$

$$\frac{\partial w}{\partial t} + \varepsilon u\frac{\partial w}{\partial x} + \frac{\varepsilon}{\sigma^2}w\frac{\partial w}{\partial z} = -\frac{1}{\varepsilon}\frac{\partial p}{\partial z} - \frac{1}{\varepsilon} \tag{2.33}$$

$$w = \sigma^2\left(\frac{\partial \zeta}{\partial t} + \varepsilon u\frac{\partial \zeta}{\partial x}\right) \qquad \text{at } z = \varepsilon\zeta \tag{2.34}$$

$$w = -\sigma^2 u\frac{\partial d}{\partial x} \qquad \text{at } z = -d \tag{2.35}$$

By integrating the continuity Eq. (2.31) over depth and using the free-surface and bottom boundary conditions along with the Leibnitz integration rule, the depth integrated continuity equation is obtained as given in Eq. (2.25). The depth-integrated horizontal and vertical momentum equations are written

$$\frac{\partial}{\partial t}[U(d+\varepsilon\zeta)] + \varepsilon\frac{\partial}{\partial x}\int_{-d}^{\varepsilon\zeta} u^2\,\mathrm{d}z = -\frac{\partial}{\partial x}\int_{-d}^{\varepsilon\zeta}\left(\frac{p}{\varepsilon}\right)\mathrm{d}z + \frac{p}{\varepsilon}\Big|_{z=-d}\frac{\partial d}{\partial x} \tag{2.36}$$

and

$$p(x,z,t) = (\varepsilon\zeta - z) + \varepsilon\frac{\partial}{\partial t}\int_z^{\varepsilon\zeta} w\,\mathrm{d}z - \frac{\varepsilon^2}{\sigma^2}w^2 + \varepsilon^2\frac{\partial}{\partial x}\int_z^{\varepsilon\zeta} uw\,\mathrm{d}z \tag{2.37}$$

Integration of the local continuity equation (2.31) with respect to *z*, yields

$$w = -\sigma^2 \frac{\partial}{\partial x}\int_{-d}^{z} u\,\mathrm{d}z \tag{2.38}$$

Substitution of the pressure *p* from Eq. (2.37) and the vertical velocity *w* from Eq. (2.38) into Eq. (2.36), gives

$$\frac{\partial}{\partial t}[U(d+\varepsilon\zeta)] + \varepsilon\frac{\partial}{\partial x}\left(\int_{-d}^{\varepsilon\zeta} u^2\,\mathrm{d}z\right) = -(d+\varepsilon\zeta)\frac{\partial\zeta}{\partial x} + \sigma^2\int_{-d}^{\varepsilon\zeta}\frac{\partial^2}{\partial x\partial t}\int_{z}^{\varepsilon\zeta}\frac{\partial}{\partial x}\int_{-d}^{z} u\,\mathrm{d}z\mathrm{d}z\mathrm{d}z$$

$$+\varepsilon\sigma^2\int_{-d}^{\varepsilon\zeta}\frac{\partial}{\partial x}\left(\frac{\partial}{\partial x}\int_{-d}^{z} u\,\mathrm{d}z\right)^2\mathrm{d}z + \varepsilon\sigma^2\int_{-d}^{\varepsilon\zeta}\frac{\partial^2}{\partial x^2}\int_{z}^{\varepsilon\zeta} u\frac{\partial}{\partial x}\int_{-d}^{z} u\,\mathrm{d}z\mathrm{d}z\mathrm{d}z \tag{2.39}$$

Karambas and Memos (2009) retained only terms of order $O(1, \varepsilon, \sigma^2)$. Hence, for this level of approximation the upper limit of the first integral term of the right-hand side of Eq. (2.39) is approximated by $\varepsilon\zeta \approx 0$. Thus they derived the equation:

$$\frac{\partial U}{\partial t} + \varepsilon U\frac{\partial U}{\partial x} = -\frac{\partial\zeta}{\partial x} + \sigma^2\frac{1}{d}\int_{-d}^{0}\left(\frac{\partial^2}{\partial x\partial t}\int_{z}^{0}\frac{\partial}{\partial x}\int_{-d}^{z} u\mathrm{d}z\mathrm{d}z\right)\mathrm{d}z + O(\varepsilon\sigma^2, \varepsilon^2, \ldots) \tag{2.40}$$

The left hand side of Eq. (2.39) is written, by using the continuity equation (2.25)

$$\frac{\partial}{\partial t}[U(d+\varepsilon\zeta)] + \varepsilon\frac{\partial}{\partial x}\int_{-d}^{\varepsilon\zeta} u^2\,\mathrm{d}z = (d+\varepsilon\zeta)\left[\frac{\partial U}{\partial t} + \varepsilon U\frac{\partial U}{\partial x} + \frac{\varepsilon}{d+\varepsilon\zeta}\frac{\partial}{\partial x}\int_{-d}^{\varepsilon\zeta}(u^2 - U^2)\mathrm{d}z\right]$$

$$= (d+\varepsilon\zeta)\left[\frac{\partial U}{\partial t} + \varepsilon U\frac{\partial U}{\partial x} + \frac{\varepsilon}{d+\varepsilon\zeta}\frac{\partial}{\partial x}\int_{-d}^{\varepsilon\zeta}(u-U)^2\mathrm{d}z\right] \tag{2.41}$$

Tsutsui *et al*. (1998) followed a similar derivation. They mention that for waves in which the horizontal component of water particle velocity has properties that satisfy $|u-U| < O\left(\varepsilon^{1/2}\right)$ and/or is of $O(\sigma)$, the third term of the right-hand side of Eq. (2.41) is of $O(\varepsilon^2)$ and/or $O(\varepsilon\sigma^2)$, respectively, and thus can be neglected compared to the terms of $O(1, \varepsilon, \sigma^2)$. Adopting these assumptions, Eq. (2.40) is obtained for this level of approximation of $O(1, \varepsilon, \sigma^2)$.

Following a Fourier-type analysis, Karambas and Memos (2009) expressed the integral term on the right-hand side of Eq. (2.40) through a convolution integral and derived the following momentum equation:

$$\frac{\partial U}{\partial t} + \varepsilon U\frac{\partial U}{\partial x} = -\frac{\partial\zeta}{\partial x} + \frac{1}{\sigma\pi d}\int_{-\infty}^{+\infty}\frac{\partial}{\partial x}[\zeta(x-\xi,t) - \zeta(x,t)]\ln\left[\tanh\left(\frac{\pi|\xi|}{4\sigma d}\right)\right]\mathrm{d}\xi \tag{2.42}$$

and in dimensional variables (omitting primes):

$$\frac{\partial U}{\partial t} + U\frac{\partial U}{\partial x} + \mathrm{g}\frac{\partial\zeta}{\partial x} = \frac{\mathrm{g}}{\pi d}\int_{-\infty}^{+\infty}\frac{\partial}{\partial x}[\zeta(x-\xi,t) - \zeta(x,t)]\ln\left[\tanh\left(\frac{\pi|\xi|}{4d}\right)\right]\mathrm{d}\xi \tag{2.43}$$

The model KM09 is, therefore, based on Eqs (2.27) and (2.43). It has the advantage of satisfying exactly the linear dispersion equation, as will be shown in the next section.

However, since only terms up to the first-order of the nonlinearity parameter are retained, the model should be treated as weakly nonlinear. Subsequently, the nonlinear characteristics of the model would not be quite representative in deeper water conditions, where $\varepsilon\sigma^2 \sim \varepsilon$. For the derivation of their model, KM09 assumed a constant water depth. However, they extended the model's application to mildly sloping bottom since the structure of the kernel of the convolution integral in Eq. (2.43) is such that it dies off with x quicker than any mild variation of $d(x)$. Formally their model is applicable wherever $d(x)$ can be assumed constant inside the influence domain of the associated kernel. This domain is relatively small, i.e. up to four water depths as shown in Fig. 2.1 (see also Tsutsui *et al*., 1998; Schäffer, 2004a).

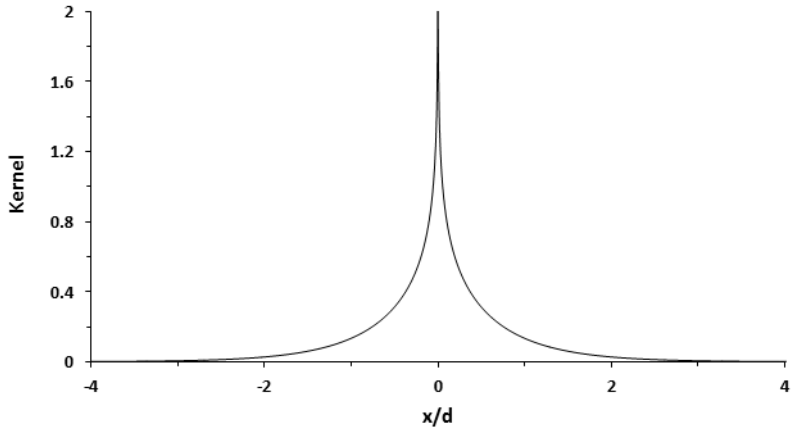

Fig 2.1. The 1DH kernel of Eq. (2.43) as function of x/d with $x = 0$ at an arbitrary reference point of the wave field.

These dimensions are less than usual codes suggest for their computational grids. Thus KM09 model can be applied also to mildly sloping bathymetries, especially in shallow waters, where its nonlinear characteristics are improved considerably. This extension of weakly nonlinear model's applicability to mildly sloping bed was followed also by Tsutsui *et al*. (1998) and Radder (1992). By making this assumption, the value of d in Eq. (2.43) can be considered as a mean value of the slowly varying depth within the domain x-ξ, between the points x and ξ. Quantitatively and to the lowest order of $\partial d/\partial x$, the modification of Eq. (2.43) due to a mildly sloping bottom can be approximated by taking as a starting point the said momentum equation. Such an exercise yields an additional term to the r.h.s. of Eq. (2.43) reading $-\mathrm{g}\frac{\zeta}{d}\frac{\partial d}{\partial x}\frac{1}{\cosh(kd)}\left[\frac{1}{\cosh(kd)}-1\right]$.

In the following, a fully linear dispersive model of higher order of nonlinearity than the one by KM09 shall be derived since terms of order $O(1, \varepsilon, \sigma^2, \varepsilon\sigma^2)$ will be retained. Applying the same as previously Fourier-transform approach on the $O(\varepsilon\sigma^2)$ terms, similar to those of Eq. (2.39), proved quite tedious and ineffective. Hence, a different simpler approach was

followed. By replacing the expressions of the fluid velocities $u' = \partial F'/\partial x'$, $w' = \partial F'/\partial z'$ into the continuity equation the dimensional Laplace equation is obtained:

$$\frac{\partial^2 F'}{\partial x'^2} + \frac{\partial^2 F'}{\partial z'^2} = 0 \tag{2.44}$$

Applying the separation of variables, we look for periodic in space and time solutions of Eq. (2.44). In order to get an analytical solution a constant depth has to be assumed as done by KM09 for their weakly nonlinear model as well. Hence the application of the bottom boundary condition leads to the solution

$$F'(x', z', t') = \mathrm{B}'\cosh[k'(d' + z')]\sin(k'x' - \omega' t') \tag{2.45}$$

$$u' = \frac{\partial F'}{\partial x'} = k'\mathrm{B}'\cosh[k'(d' + z')]\cos(k'x' - \omega' t') \tag{2.46}$$

where B′ a constant and ω' is the angular frequency $\omega' = 2\pi/T'$ with T' the regular wave period. By reverting to non-dimensional variables

$$u = k\mathrm{B}'\cosh[\sigma k(d + z)]\cos(kx - \omega t) \tag{2.47}$$

where ω is the non-dimensional angular frequency, $\omega = 2\pi/T$ with T the non-dimensional regular wave period, following the same scaling as in Eq. (2.7).
Hence the depth-averaged horizontal velocity is written:

$$U = \frac{1}{d+\varepsilon\zeta}\int_{-d}^{\varepsilon\zeta} u\mathrm{d}z = \frac{B'}{\sigma(d+\varepsilon\zeta)}\sinh[\sigma k(d + \varepsilon\zeta)]\cos(kx - \omega t) \tag{2.48}$$

and therefore

$$u(x, z, t) = \frac{\sigma k(d+\varepsilon\zeta)}{\sinh[\sigma k(d+\varepsilon\zeta)]}U(x, t)\cosh[\sigma k(d + z)] \tag{2.49}$$

By assuming $\varepsilon\zeta \approx 0$ for consistency with the KM09 weakly nonlinear model and setting $\mathrm{A}' = \frac{\sigma kd}{\sinh(\sigma kd)}$, one gets

$$u = \mathrm{A}'U\cosh[\sigma k(d + z)] \tag{2.50}$$

where A′ is invariant with respect to both x and t. Substitution of the horizontal velocity u from Eq. (2.50) into Eq. (2.39), equivalent to Eq. (2.40), gives

$$\frac{\partial U}{\partial t} + \varepsilon\left[\frac{\sigma kd}{\sinh(\sigma kd)}\right]^2\left[1 + \frac{\sinh(2\sigma kd)}{2\sigma kd}\right]U\frac{\partial U}{\partial x} = -\frac{\partial \zeta}{\partial x} + \frac{1}{k^2}\left[\frac{\sigma kd}{\tanh(\sigma kd)} - 1\right]\frac{\partial^3 U}{\partial x^2 \partial t}$$

$$+\varepsilon\left[\frac{\sigma d}{\sinh(\sigma kd)}\right]^2\left(\frac{3}{4}\cosh(2\sigma kd) + \frac{1}{8}\frac{\sinh(2\sigma kd)}{\sigma kd} - 1\right)\frac{\partial U}{\partial x}\frac{\partial^2 U}{\partial x^2}$$

$$+\varepsilon\left[\frac{\sigma d}{\sinh(\sigma kd)}\right]^2\left(\frac{1}{4}\cosh(2\sigma kd)-\frac{1}{8}\frac{\sinh(2\sigma kd)}{\sigma kd}\right)U\frac{\partial^3 U}{\partial x^3} \tag{2.51}$$

Reverting to dimensional variables and dropping primes

$$\frac{\partial U}{\partial t}+\left[\frac{kd}{\sinh(kd)}\right]^2\left[1+\frac{\sinh(2kd)}{2kd}\right]U\frac{\partial U}{\partial x}=-\mathrm{g}\frac{\partial \zeta}{\partial x}+\frac{1}{k^2}\left[\frac{kd}{\tanh(kd)}-1\right]\frac{\partial^3 U}{\partial x^2\partial t}+$$

$$+\frac{d^2}{\sinh^2(kd)}\left(\frac{3}{4}\cosh(2kd)+\frac{1}{8}\frac{\sinh(2kd)}{kd}-1\right)\frac{\partial U}{\partial x}\frac{\partial^2 U}{\partial x^2}+$$

$$+\frac{d^2}{\sinh^2(kd)}\left(\frac{1}{4}\cosh(2kd)-\frac{1}{8}\frac{\sinh(2kd)}{kd}\right)U\frac{\partial^3 U}{\partial x^3} \tag{2.52}$$

By comparing Eqs (2.51) and (2.42) three remarks can be made. First of all the two last terms on the right-hand side of Eq. (2.51) refer to the last two integral terms of $O(\varepsilon\sigma^2)$ on the right-hand side of Eq. (2.39). These terms have been neglected in KM09 derivation. Hence Eq. (2.51) yields an enhancement of nonlinearity of their weakly nonlinear model of $O(1, \varepsilon, \sigma^2)$. Secondly, the convolution integral in Eq. (2.42) that stands for the $O(\sigma^2)$ term of Eq. (2.39) is now replaced by a third order derivative of depth-averaged velocity. The latter affords a somehow more efficient numerical treatment. Thirdly, a difference between the coefficients of the term of $O(\varepsilon)$ on the left-hand side of Eqs (2.42) and (2.51) is observed. This relies on the approximation made by Tsutsui *et al.* (1998) and followed by KM09. In the present level of approximation where terms of $O(\varepsilon\sigma^2)$ are retained, the last integral terms on the right-hand side of Eq. (2.41) cannot be neglected. This leads to a coefficient of that term that is not unity as in Eq. (2.42) but includes a hyperbolic function of water depth.

This extended model, to be denoted by KM09e, incorporates thus Eqs (2.27) and (2.52). It includes terms of $O(1, \varepsilon, \sigma^2, \varepsilon\sigma^2)$, hence it is of higher nonlinearity than the weakly nonlinear one KM09, and it is fully linear dispersive too. However, the Eqs (2.25) and (2.51) do not reduce to the nonlinear shallow water equations in shallow water ($kd \to 0$) as they are expected to. This result can be explained by the fact that the derivation relies on an exact first-order solution of the local continuity equation which is not a very accurate assumption in shallow water. A similar assumption is also made in KM09 model. However, due to its weakly nonlinear character the aforementioned approximation by Tsutsui et al. (1998) is applicable in this case and thus Eqs (2.25) and (2.42) reduce to the NSW equations in shallow water. Because of this somehow invalid assumption, no thorough analysis of the KM09e model will be applied in the following. Only a Fourier analysis up to second order will be presented to further pronounce the described inaccuracy.

Additionally, since in shallow water, the main application area of Boussinesq models, the horizontal velocity distribution tends to be uniform, it is appealing to also follow the previously said approximation. Thus the dimensional momentum equation can be written:

$$\frac{\partial U}{\partial t}+U\frac{\partial U}{\partial x}=-\mathrm{g}\frac{\partial \zeta}{\partial x}+\frac{1}{k^2}\left[\frac{kd}{\tanh(kd)}-1\right]\frac{\partial^3 U}{\partial x^2\partial t}+$$

$$+\frac{d^2}{\sinh^2(kd)}\left(\frac{3}{4}\cosh(2kd)+\frac{1}{8}\frac{\sinh(2kd)}{kd}-1\right)\frac{\partial U}{\partial x}\frac{\partial^2 U}{\partial x^2}+$$

$$+\frac{d^2}{\sinh^2(kd)}\left(\frac{1}{4}\cosh(2kd)-\frac{1}{8}\frac{\sinh(2kd)}{kd}\right)U\frac{\partial^3 U}{\partial x^3} \tag{2.53}$$

More formally this modified equation can be obtained by applying the approximation used by Tsutsui *et al*. (1998) that neglects the third term in the r.h.s. of Eq. (2.41). The model based on Eqs (2.27) and (2.53) is, therefore, a modified version of KM09e and is denoted by KM09em. The specific model embeds the wavenumber k as a free parameter in the momentum equation, similarly to Li's (2008) model. In the case of regular waves k can be obtained from linear dispersion equation since the model is fully linear dispersive. However, sometimes even in the case of regular waves higher free harmonics are present, e.g. during propagation over and behind a submerged bar. Also in this case, the corresponding wave number to the main frequency of the regular wave through the linear dispersion equation is used. On the other hand, for irregular waves a representative value for the wavenumber should be adopted. In particular, in the validation tests for irregular waves presented in section 2.5, k was considered to be the wavenumber corresponding through the linear dispersion equation to the peak frequency. In any case, a numerical investigation of the models' behaviour showed a very weak sensitivity on this parameter.

In the present section two new Boussinesq-type models were derived that enhance the nonlinear characteristics of an existing model. The achieved enhancement of nonlinearity goes from $O(\varepsilon, \sigma^2)$ in KM09 to $O(\varepsilon\sigma^2)$ in KM09e or KM09em. It should be noted that all KK02 and KM09e or KM09em models include terms of $O(1, \varepsilon, \sigma^2, \varepsilon\sigma^2)$. However, they are regarded as weakly and strongly nonlinear, respectively, due to their counterparts KK02e strongly nonlinear and KM09 weakly nonlinear models.

2.4 Nonlinearity and dispersion characteristics of models

In this section an analysis and comparison of the embedded characteristics of nonlinearity and dispersion of the aforementioned models shall be presented. The aim of this analysis would be to examine the enhancement of these properties in the derived extended nonlinear versions of the models.

In addition to the models presented in section 2.3, that by Madsen and Schäffer (1998) – MS98 in the following– will be also included in this analysis. Among the different versions of this latter model, the one expressed in terms of the depth-averaged velocity U will be

examined. This is a Boussinesq-type model of higher order of nonlinearity and dispersion that contains terms of order $O(1, \varepsilon, \sigma^2, \varepsilon\sigma^2, \varepsilon^2\sigma^2, \varepsilon^3\sigma^2, \sigma^4, \varepsilon\sigma^4)$. Its nonlinear characteristics were enhanced through the application of a combination of linear operators similar to the one applied subsequently in KK02.

2.4.1 Fourier analysis of equations on a horizontal bottom

In this subsection the aforementioned models shall be analyzed to quantify the embedded characteristics with respect to dispersion and nonlinearity. Adopting the assumption of $O(\varepsilon)<1$ (i.e. weakly nonlinear solutions) and arbitrary σ, a Stokes-type Fourier analysis for a horizontal bottom will be followed in order to examine the capability of various models to approximate the linear dispersion and the higher order harmonics. Following MS98 we shall look for first-, second- and third-order solutions of the form,

$$\zeta = \mathrm{a}_1 cos\theta + \varepsilon \mathrm{a}_2 cos2\theta + \varepsilon^2 \mathrm{a}_3 cos3\theta \tag{2.54a}$$

and

$$U = U_1 cos\theta + \varepsilon U_2 cos2\theta + \varepsilon^2 U_3 cos3\theta \tag{2.54b}$$

where $\theta = \omega t - kx$. In the following analysis, which is performed directly in non-dimensional variables, it is convenient to introduce the definition

$$\kappa = \sigma k d \tag{2.55}$$

and κ is actually identical to $k'd'$, which is the product of the dimensional wave number and water depth, as defined in section 2.3.

Equation (2.26) is written for a horizontal bottom

$$\frac{\partial U}{\partial t} + \varepsilon U \frac{\partial U}{\partial x} + \frac{\partial \zeta}{\partial x} = \sigma^2 \frac{d^2 + 2\varepsilon d\zeta}{3} \frac{\partial^3 U}{\partial x^2 \partial t} + \varepsilon\sigma^2 \frac{d^2}{3}\left(U \frac{\partial^3 U}{\partial x^3} - \frac{\partial U}{\partial x}\frac{\partial^2 U}{\partial x^2}\right) + \varepsilon\sigma^2 d \frac{\partial \zeta}{\partial x}\frac{\partial^2 U}{\partial x \partial t} +$$
$$\varepsilon^2\sigma^2\left(\frac{\zeta^2}{3}\frac{\partial^3 U}{\partial x^2 \partial t} + \zeta \frac{\partial \zeta}{\partial x}\frac{\partial^2 U}{\partial x \partial t}\right) + \varepsilon^2\sigma^2 \frac{2d\zeta}{3}\left(U \frac{\partial^3 U}{\partial x^3} - \frac{\partial U}{\partial x}\frac{\partial^2 U}{\partial x^2}\right) + \varepsilon^2\sigma^2 dU \frac{\partial \zeta}{\partial x}\frac{\partial^2 U}{\partial x^2} -$$
$$\varepsilon^2\sigma^2 d \frac{\partial \zeta}{\partial x}\left(\frac{\partial U}{\partial x}\right)^2 + \sigma^2 \mathrm{B} d^2 \left(\frac{\partial^3 U}{\partial x^2 \partial t} + \frac{\partial^3 \zeta}{\partial x^3} + \varepsilon \frac{\partial^2\left(U\frac{\partial U}{\partial x}\right)}{\partial x^2}\right) \tag{2.56}$$

where B a parameter to be determined.

Neglecting terms of $O(\varepsilon^2\sigma^2)$ in Eq. (2.56) leads to the momentum equation of KK02 weakly nonlinear model for a horizontal bottom

$$\frac{\partial U}{\partial t}+\varepsilon U\frac{\partial U}{\partial x}+\frac{\partial \zeta}{\partial x}=\sigma^2\frac{d^2+2\varepsilon d\zeta}{3}\frac{\partial^3 U}{\partial x^2\partial t}+\varepsilon\sigma^2\frac{d^2}{3}\left(U\frac{\partial^3 U}{\partial x^3}-\frac{\partial U}{\partial x}\frac{\partial^2 U}{\partial x^2}\right)+\varepsilon\sigma^2 d\frac{\partial \zeta}{\partial x}\frac{\partial^2 U}{\partial x\partial t}+$$
$$\sigma^2 \mathrm{B}d^2\left(\frac{\partial^3 U}{\partial x^2\partial t}+\frac{\partial^3 \zeta}{\partial x^3}+\varepsilon\frac{\partial^2\left(U\frac{\partial U}{\partial x}\right)}{\partial x^2}\right) \tag{2.57}$$

(i) First-order solution

Following the notation by Madsen and Schäffer (1998), Eqs (2.54a,b) are substituted into Eqs (2.25) and (2.57). The following linear algebraic system is obtained at the $O(\varepsilon^0)$:

$$\begin{pmatrix} m_{11}^{(1)} & m_{12}^{(1)} \\ m_{21}^{(1)} & m_{22}^{(1)} \end{pmatrix}\begin{pmatrix} a_1 \\ U_1 \end{pmatrix}=\begin{pmatrix} 0 \\ 0 \end{pmatrix} \tag{2.58}$$

where

$$\left.\begin{array}{c} m_{11}^{(1)}=\omega,\ m_{12}^{(1)}=-kd, \\ m_{21}^{(1)}=-k(1+\mathrm{B}\kappa^2),\ m_{22}^{(1)}=\omega\left[1+\left(\mathrm{B}+\frac{1}{3}\right)\kappa^2\right] \end{array}\right\} \tag{2.59}$$

Hence, at first order one gets

$$U_1=\frac{\omega a_1}{kd} \tag{2.60}$$

and the dispersion relation

$$\frac{\omega^2}{k^2 d}=\frac{1+\mathrm{B}\kappa^2}{1+\left(\mathrm{B}+\frac{1}{3}\right)\kappa^2} \tag{2.61}$$

In this context the reference solution is the linear dispersion equation by Stokes

$$\left(\frac{\omega^2}{k^2 d}\right)^{\text{Stokes}}=\frac{tanh(\kappa)}{\kappa} \tag{2.62}$$

Equation (2.61) has the form of a Padé [2,2] expansion in κ of Eq. (2.62). The exact expansion is obtained by assuming $\mathrm{B}=\frac{1}{15}$. This value gives the closest approximation to linear dispersion and was also adopted by Madsen *et al*. (1991) and Schäffer and Madsen (1995).

Exactly the same dispersion relation is obtained at the $O(\varepsilon^0)$ for strongly nonlinear model KK02e based on Eqs (2.25) and (2.56). This was expected since the difference between Eqs (2.56) and (2.57) are only terms of $O(\varepsilon^2\sigma^2)$.

The same analysis was also applied for Madsen and Schäffer's (1998) higher order model. Since this Stokes-type Fourier analysis goes up to third order, terms including powers of ε

higher than two do not appear in the following momentum equation, Eq. (2.63), valid on a horizontal bottom.

$$\frac{\partial U}{\partial t}+\frac{\partial \zeta}{\partial x}-\sigma^2\left[\left(\alpha_1+\frac{1}{3}\right)d^2\frac{\partial^3 U}{\partial x^2\partial t}+\alpha_1 d^2\frac{\partial^3 \zeta}{\partial x^3}\right]+\sigma^4\left[\left(\beta_1+\frac{1}{3}\alpha_1-\frac{1}{45}\right)d^4\frac{\partial^5 U}{\partial x^4\partial t}+\beta_1 d^4\frac{\partial^5 \zeta}{\partial x^5}\right]+$$
$$\varepsilon U\frac{\partial U}{\partial x}+\varepsilon\sigma^2\left[-\frac{2}{3}d\zeta\frac{\partial^3 U}{\partial x^2\partial t}-d\frac{\partial \zeta}{\partial x}\frac{\partial^2 U}{\partial x\partial t}+\frac{1}{3}d^2\frac{\partial U}{\partial x}\frac{\partial^2 U}{\partial x^2}-\frac{1}{3}d^2U\frac{\partial^3 U}{\partial x^3}-\alpha_1 d^2\frac{\partial^2\left(U\frac{\partial U}{\partial x}\right)}{\partial x^2}\right]+$$
$$\varepsilon\sigma^4\left[\frac{1}{45}d^3\zeta\frac{\partial^5 U}{\partial x^4\partial t}+\alpha_1 d^3\frac{\partial^2\left(\frac{\partial \zeta}{\partial x}\frac{\partial^2 U}{\partial x\partial t}\right)}{\partial x^2}+\left(\frac{2}{3}\alpha_1-\frac{1}{9}\right)d^3\frac{\partial^2\left(\zeta\frac{\partial^3 U}{\partial x^2\partial t}\right)}{\partial x^2}+\left(\frac{1}{9}-\frac{2}{3}\alpha_1\right)d^4\frac{\partial^2\left(\frac{\partial U}{\partial x}\frac{\partial^2 U}{\partial x^2}\right)}{\partial x^2}-\right.$$
$$\left.\frac{1}{45}d^4\frac{\partial U}{\partial x}\frac{\partial^4 U}{\partial x^4}+\frac{1}{9}d^4\frac{\partial^2 U}{\partial x^2}\frac{\partial^3 U}{\partial x^3}-\frac{1}{45}d^4\frac{\partial\left(U\frac{\partial^4 U}{\partial x^4}\right)}{\partial x}+\frac{1}{3}\alpha_1 d^4\frac{\partial^3\left(U\frac{\partial^2 U}{\partial x^2}\right)}{\partial x^3}+\beta_1 d^4\frac{\partial^4\left(U\frac{\partial U}{\partial x}\right)}{\partial x^4}\right]+$$
$$\varepsilon^2\sigma^2\left[\frac{1}{6}\zeta^2\frac{\partial^3 U}{\partial x^2\partial t}-\frac{1}{3}\zeta d\frac{\partial U}{\partial x}\frac{\partial^2 U}{\partial x^2}-\frac{1}{3}d\frac{\partial^2 U}{\partial x^2}\frac{\partial(\zeta U)}{\partial x}+d\frac{\partial\left[\zeta\left(\frac{\partial U}{\partial x}\right)^2\right]}{\partial x}-\frac{1}{2}\frac{\partial\left(\zeta^2\frac{\partial^2 U}{\partial x\partial t}\right)}{\partial x}-\frac{2}{3}d\frac{\partial\left(\zeta U\frac{\partial^2 U}{\partial x^2}\right)}{\partial x}\right]=$$
$$O(\varepsilon^3\sigma^2,\varepsilon^2\sigma^4,\sigma^6) \qquad (2.63)$$

where α_1, β_1 parameters to be determined. The resulting dispersion relation is

$$\frac{\omega^2}{k^2 d}=\frac{1+\alpha_1\kappa^2+\beta_1\kappa^4}{1+\left(\alpha_1+\frac{1}{3}\right)\kappa^2+\left(\beta_1+\frac{1}{3}\alpha_1-\frac{1}{45}\right)\kappa^4} \qquad (2.64)$$

Equation (2.64) has the form of a Padé [4,4] expansion in κ of Eq. (2.62), which is matched identically by choosing parameters $\alpha_1=\frac{1}{9}$ and $\beta_1=\frac{1}{945}$. The application of the enhancement technique by Madsen and Schäffer (1998), apart from improving the accuracy of their equations with respect to linear dispersion equation, it also removed a singularity occurring at $\kappa\approx 4.2$ that limited any practical use of them. It should be also mentioned that setting $\alpha_1=\frac{1}{15}$ and $\beta_1=0$ leads to the Padé [2,2] expansion given by Eq. (2.61) with B $=\frac{1}{15}$.

Fourier analysis was also applied for KM09 weakly, extended and modified nonlinear models. At $O(\varepsilon^0)$, all three of them give exactly the same dispersion relation since their differences refer to higher order terms. In this case the linear system of equations includes the coefficients

$$\left.\begin{array}{c} m_{11}^{(1)}=\omega,\ m_{12}^{(1)}=-kd, \\ m_{21}^{(1)}=-k,\ m_{22}^{(1)}=\omega\kappa\coth(\kappa) \end{array}\right\} \qquad (2.65)$$

Solving the system of Eqs (2.58) one gets Eq. (2.60) and the dispersion equation

$$\frac{\omega^2}{k^2 d}=\frac{tanh(\kappa)}{\kappa} \qquad (2.66)$$

which is identical to the linear dispersion relation of Stokes waves. Hence, all three versions of KM09 model are fully linear dispersive at any water depth. Therefore, they face no practical limitation of their application field as far as linear dispersive characteristics are concerned.

Figure 2.2 shows the ratio of phase celerities c/c^{Stokes} as a function of κ, where c is determined from Eqs (2.61), (2.64) and (2.66) respectively, and c^{Stokes} from Eq. (2.62). Both versions of KK02 model give the same results at first order. The same is true for all three versions of KM09 model. Hence, they are referred in Fig. 2.2 as 'Karambas-Koutitas (2002)' and 'Karambas-Memos (2009)', respectively.

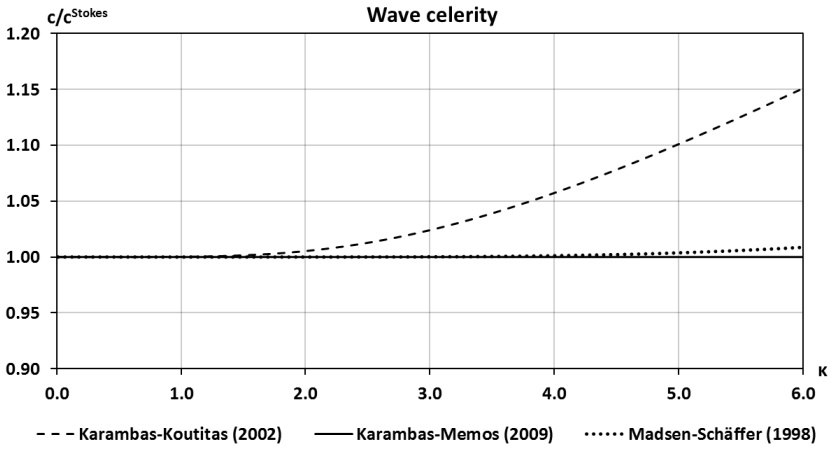

Fig. 2.2. Ratio of phase celerity, c/c^{Stokes}, where c is determined from Eqs (2.61), (2.64), and (2.66) for KK02, MS98 and KM09 models respectively, and c^{Stokes} from Eq. (2.62).

It is observed that KK02 model gives very good results up to the traditional deep-water limit $\kappa \approx 3$ where the error is about 2%. However, in deeper water this error increases significantly. MS98 model is seen to be excellent even for κ as large as 6. Finally, KM09 model reproduces exactly the Stokes wave celerity to the first order over the entire depth range, proving thus its advantage of being fully linear dispersive.

(ii) Second-order solution

Continuing the present analysis to second order firstly for KK02 weakly nonlinear model, Eqs (2.54a,b) are substituted into Eqs (2.25) and (2.57) and terms of $O(\varepsilon)$ are collected. The only difference between Eqs (2.56) and (2.57) is the presence of extra terms of $O(\varepsilon^2\sigma^2)$ in Eq. (2.56). Therefore, the results of the two nonlinear versions of the model are identical at second order. Hence, they will both be referred to as KK02 model in this analysis of $O(\varepsilon)$. The following linear algebraic system is obtained:

$$\begin{pmatrix} m_{11}^{(2)} & m_{12}^{(2)} \\ m_{21}^{(2)} & m_{22}^{(2)} \end{pmatrix} \begin{pmatrix} \mathrm{a}_2 \\ U_2 \end{pmatrix} = \frac{\mathrm{a}_1^2}{d} \begin{pmatrix} F_1 \\ F_2 \end{pmatrix} \tag{2.67}$$

where

$$\left.\begin{array}{c} m_{11}^{(2)} = 2\omega,\ m_{12}^{(2)} = -2kd, \\ m_{21}^{(2)} = -2k(1+4\mathrm{B}\kappa^2),\ \ m_{22}^{(2)} = 2\omega\left[1+4\left(\mathrm{B}+\frac{1}{3}\right)\kappa^2\right] \end{array}\right\} \tag{2.68a}$$

$$F_1 = \omega,\ F_2 = \frac{\omega^2}{2kd}\left[1+\left(4\mathrm{B}-\frac{5}{3}\right)\kappa^2\right] \tag{2.68b}$$

Hence at second order one gets the solution for a_2:

$$\mathrm{a}_2 = \frac{3}{4}\frac{\mathrm{a}_1^2}{d}\frac{1}{\kappa^2}\left(1+\frac{2}{3}\kappa^2+\frac{1}{25}\kappa^4\right) \tag{2.69}$$

The reference in this context is the Stokes second-order solution by Skjelbreia and Hendrickson (1960) as proposed by Madsen and Schäffer (1998):

$$\mathrm{a}_2^{\mathrm{Stokes}} = \frac{1}{4}\frac{\mathrm{a}_1^2}{d}\kappa\coth(\kappa)[3\coth^2(\kappa)-1] \tag{2.70}$$

of which an expansion around $\kappa = 0$ yields

$$a_2^{\mathrm{Stokes}} = \frac{3}{4}\frac{a_1^2}{d}\frac{1}{\kappa^2}\left(1+\frac{2}{3}\kappa^2+\frac{7}{45}\kappa^4+\frac{2}{315}\kappa^6+O(\kappa^8)\right) \tag{2.71}$$

Application of second-order analysis for MS98 higher order model leads to the solution

$$a_2 = \frac{3}{4}\frac{a_1^2}{d}\frac{1}{\kappa^2}\left(1+\frac{2}{3}\kappa^2+\frac{7}{45}\kappa^4+O(\kappa^6)\right) \tag{2.72}$$

where the values $(\alpha_1, \beta_1) = \left(\frac{1}{9}, \frac{1}{945}\right)$ determined above have been used. As mentioned by Madsen and Schäffer (1998), if terms of $O(\sigma^4, \varepsilon\sigma^2)$ are only retained, the coefficients of κ^2 and κ^4 in Eq. (2.72) take the values $\frac{2}{3}$ and $\frac{88}{945}$ respectively. By neglecting all σ^4 terms and retaining only terms of $O(\sigma^2, \varepsilon\sigma^2)$ with $\alpha_1 = \frac{1}{15}$, the solution applicable to MS98 reduces to the one given by Eq. (2.69) for KK02 model.

Figure 2.3 shows the deviation of second harmonic from the target value, $\mathrm{a}_2/\mathrm{a}_2^{\mathrm{Stokes}}$, for KK02 models (weakly and strongly nonlinear) and MS98 model. Observing Eqs (2.69) and (2.71) we notice that the constant term and the κ^2-term are matched while there is a difference in the coefficient of κ^4-term. On the other hand Eq. (2.72) matches Eq. (2.71) even at fourth order.

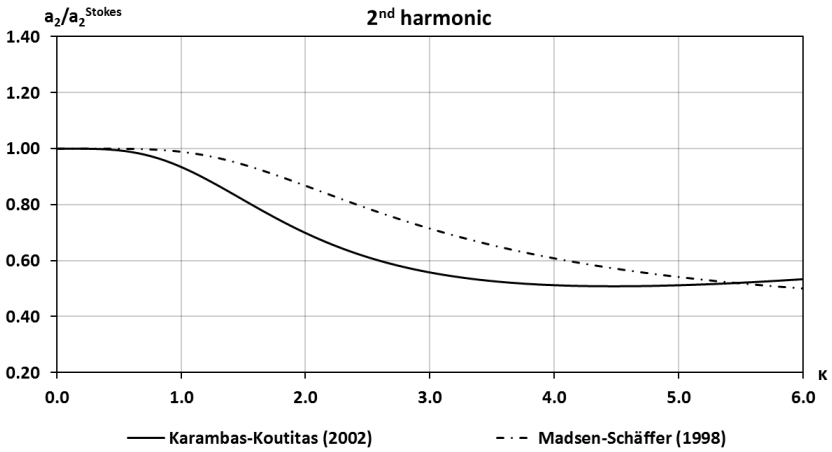

Fig. 2.3. Ratio of second harmonic, a_2/a_2^{Stokes}, where a_2 is determined from Eqs (2.69) and (2.72) for KK02 and MS98 respectively, and a_2^{Stokes} from Eq. (2.70).

Madsen and Schäffer (1998) explained that the linear enhancement technique allows to waive the requirement of including higher order terms for a desired accuracy. For example, matching the coefficient of κ^4-term in Eq. (2.71) would normally require $O(\sigma^6,\ \varepsilon\sigma^4)$ formulations of Boussinesq equations. However, the insertion of (α_1, β_1) reduces this requirement to $O(\sigma^4, \varepsilon\sigma^4)$ as presented above. In addition, the enhancement method removes a singularity occurring for $\kappa = \sqrt{3}$. In the same manner, KK02 model succeeds in matching the κ^2-term coefficient through the insertion of B coefficient even though terms of order $O(\sigma^4, \varepsilon\sigma^2)$ would be normally required. However, Madsen and Schäffer (1998) add that the potential of the linear improvement is fully utilized with regard to the second-order transfer only if a sufficient order of dispersion is retained also in the nonlinear terms.

It can be noticed from Fig. 2.3 that MS98 model is superior to KK02 model for the practical range of depths $\kappa < 5.5$, as expected due to its higher order formulation. In deeper water the higher order terms of Eq. (2.71) become significant, hence the mismatch of the relevant coefficients in both models leads to significant errors. Therefore, the apparent superiority of KK02 model in this range of depths has no physical meaning. In shallower water MS98 model is almost perfect for $\kappa < 1$, while the second harmonic is gradually underestimated for larger values of κ reaching a 50% of the Stokes target value for $\kappa = 6$. On the other hand, the error for KK02 model increases more abruptly, reaching 7% for $\kappa = 1$ and approximately 50% for $\kappa = 4.5$.

Second-order analysis was also applied to the three versions of KM09 model. Here the results are different in each version due to $O(\varepsilon\sigma^2)$ terms. For KM09 weakly nonlinear model the linear system to be solved contains the coefficients

$$\left.\begin{array}{c} m_{11}^{(2)} = 2\omega,\ m_{12}^{(2)} = -2kd, \\ m_{21}^{(2)} = -k\frac{\tanh(2\kappa)}{\kappa},\ m_{22}^{(2)} = 2\omega \end{array}\right\} \tag{2.73a}$$

$$F_1 = \omega,\ F_2 = \frac{\omega^2}{2kd} \tag{2.73b}$$

Hence at second order one gets the solution for a_2:

$$\mathrm{a}_2 = \frac{3}{2}\frac{\mathrm{a}_1^2}{d}\frac{\tanh(\kappa)}{[2\tanh(\kappa)-\tanh(2\kappa)]} \tag{2.74}$$

of which an expansion at $\kappa = 0$ yields

$$\mathrm{a}_2 = \frac{3}{4}\frac{\mathrm{a}_1^2}{d}\frac{1}{\kappa^2}\left(1+\frac{5}{3}\kappa^2+\frac{1}{15}\kappa^4+O(\kappa^6)\right) \tag{2.75}$$

KM09 extended nonlinear model leads to the linear system containing the coefficients

$$\left.\begin{array}{c} m_{11}^{(2)} = 2\omega,\ m_{12}^{(2)} = -2kd, \\ m_{21}^{(2)} = -2k,\ \ m_{22}^{(2)} = -2\omega[3-4\kappa\coth(\kappa)] \end{array}\right\} \tag{2.76a}$$

$$F_1 = \omega,\ F_2 = \frac{\omega^2}{2kd}[\kappa\coth(\kappa)+\kappa^2\cosh(2\kappa)\mathrm{csch}^2(\kappa)] \tag{2.76b}$$

Hence at second order one gets the solution for a_2:

$$\mathrm{a}_2 = \frac{\mathrm{a}_1^2}{d}\frac{\{\kappa[9+2\kappa\coth(2\kappa)]-6\tanh(\kappa)\}}{12[\kappa-\tanh(\kappa)]} \tag{2.77}$$

of which an expansion at $\kappa = 0$ gives

$$\mathrm{a}_2 = \frac{3}{4}\frac{\mathrm{a}_1^2}{\mathrm{d}}\frac{1}{\kappa^2}\left(\frac{4}{3}+\frac{74}{45}\kappa^2+\frac{268}{4725}\kappa^4+\mathrm{O}\left(\kappa^6\right)\right) \tag{2.78}$$

The leading term of the series in Eq. (2.78) is not unity contrary to the aforementioned models. In particular the limit of $\mathrm{a}_2/\mathrm{a}_2^{\mathrm{Stokes}}$ as $\kappa \to 0$ is $\frac{4}{3}$ rather than unity. Hence, the model does not converge to Stokes solution at second-order. This was the reason for considering a modified momentum equation (Eq. (2.53)), slightly different from the one of KM09e. This approximation, used also by Tsutsui *et al*. (1998), yields KM09em model that includes terms of order $O(1, \varepsilon, \sigma^2, \varepsilon\sigma^2)$ similarly to KM09e model. The second-order analysis of KM09em leads to the linear system with coefficients

$$\left.\begin{array}{c} m_{11}^{(2)} = 2\omega,\ m_{12}^{(2)} = -2kd, \\ m_{21}^{(2)} = -2k,\ \ m_{22}^{(2)} = -2\omega[3-4\kappa\coth(\kappa)] \end{array}\right\} \tag{2.79a}$$

$$F_1 = \omega,\ F_2 = \frac{\omega^2}{2kd}\left[1-\kappa^2\mathrm{csch}^2(\kappa)+\kappa^2\cosh(2\kappa)\mathrm{csch}^2(\kappa)\right] \tag{2.79b}$$

and finally to the solution

$$a_2 = \frac{a_1^2}{d}\frac{\left[8\kappa+\left(2\kappa^2-5\right)\tanh(\kappa)\right]}{12[\kappa-\tanh(\kappa)]} \tag{2.80}$$

of which an expansion at $\kappa = 0$ gives

$$a_2 = \frac{3}{4}\frac{a_1^2}{d}\frac{1}{\kappa^2}\left(1+\frac{73}{45}\kappa^2+\frac{67}{1575}\kappa^4+O(\kappa^6)\right) \tag{2.81}$$

It can be observed that this solution converges to the one given by Stokes theory as $\kappa \to 0$, similarly to KM09 weakly nonlinear model. Fig. 2.4 shows the ratio of second harmonic, a_2/a_2^{Stokes} for the three versions of KM09 model.

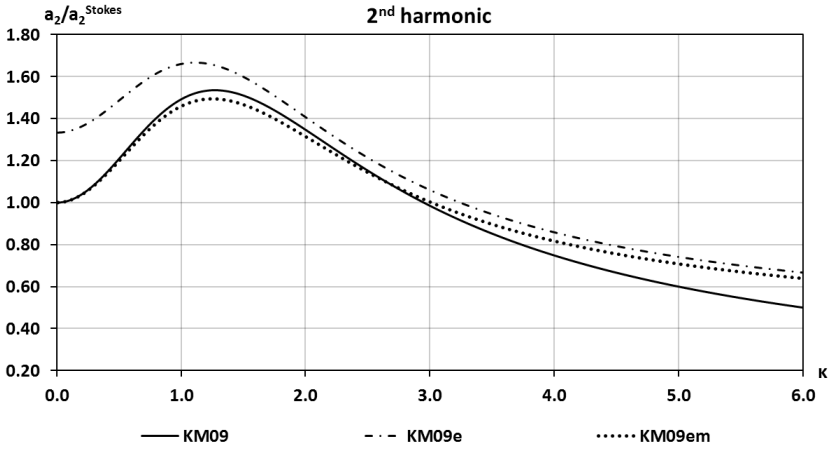

Fig. 2.4. Ratio of second harmonic, a_2/a_2^{Stokes}, where a_2 is determined from Eqs (2.74), (2.77) and (2.80) for KM09, KM09e and KM09em models respectively, and a_2^{Stokes} from Eq. (2.70).

Figure 2.4 shows that the results for the second harmonic are poorer than those of KK02 models. All three versions overestimate the second harmonic in shallow and intermediate water. This result was expected since their derivation relies on an exact first-order solution of the local continuity equation. The omission of higher order terms of the vertical profile of the horizontal particle velocity leads to discrepancies when compared to higher order Stokes solutions. In deep water, where $\kappa > 3$, an improvement of KM09e and KM09em is observed as compared to the weakly nonlinear model since the extra terms of order $O(\varepsilon\sigma^2)$ become significant. Nevertheless, despite the fact that the three versions of KM09 model have the advantage of being fully linear dispersive, their nonlinear characteristics are poorer in shallow and intermediate water than the ones given by models derived following the usual Taylor expansion (e.g. Karambas and Koutitas, 2002; Madsen and Schäffer, 1998).

(iii) Third-order solution

The Stokes-type Fourier analysis is extended to third order for the aforementioned models. The terms proportional to $\sin(3\theta)$ lead directly to a matrix problem of the form

$$\begin{pmatrix} m_{11}^{(3)} & m_{12}^{(3)} \\ m_{21}^{(3)} & m_{22}^{(3)} \end{pmatrix} \begin{pmatrix} a_3 \\ U_3 \end{pmatrix} = \frac{a_1^3}{d^2} \begin{pmatrix} F_1 \\ F_2 \end{pmatrix} \tag{2.82}$$

which results in third-order solutions for a_3 and U_3. Following Madsen and Schäffer (1998), it should be mentioned that terms proportional to $\sin(\theta)$ need to be removed to avoid secular unbounded solutions. In order to solve this problem ω and U_1 are expanded as

$$\omega = \omega_1(1 + \varepsilon^2 \omega_{13}) \quad \text{and} \quad U_1 = \left(\frac{\omega a_1}{kd}\right)(1 + \varepsilon^2 U_{13}) \tag{2.83}$$

where ω_1 refers to the first-order solution, ω_{13} represents the amplitude dispersion and U_{13} the third-order correction to the first-order velocity amplitude. The reference in this context is the Stokes third-order solution by Skjelbreia and Hendrickson (1960)

$$a_3^{\text{Stokes}} = \frac{3}{64}\frac{a_1^3}{d^2}\kappa^2 \frac{1+8\cosh^6(\kappa)}{\sinh^6(\kappa)} \quad \text{and} \quad \omega_{13}^{\text{Stokes}} = \frac{1}{16}\frac{a_1^2}{d^2}\kappa^2 \frac{9\tanh^4(\kappa)-10\tanh^2(\kappa)+9}{\tanh^4(\kappa)} \tag{2.84}$$

of which an expansion at $\kappa = 0$ gives

$$\left.\begin{aligned} a_3^{\text{Stokes}} &= \frac{27}{64}\frac{a_1^3}{d^2}\frac{1}{\kappa^4}\left(1+\frac{5}{3}\kappa^2+\frac{64}{45}\kappa^4+\frac{85}{189}\kappa^6+O(\kappa^8)\right) \\ \omega_{13}^{\text{Stokes}} &= \frac{9}{16}\frac{a_1^2}{d^2}\frac{1}{\kappa^2}\left(1+\frac{2}{9}\kappa^2+\frac{113}{135}\kappa^4-\frac{2}{315}\kappa^6+O(\kappa^8)\right) \end{aligned}\right\} \tag{2.85}$$

As noted elsewhere in this paper, accepting as targets the Stokes wave solutions may be questionable since each order of the Stokes wave is associated with a particular area of applicability. However, it appears that there exist no better options given the general nature of the comparisons at hand, where the wave conditions are not specified. Additionally, the Stokes wave of any order of nonlinearity covers a comparatively wide area of conditions in terms of wave height and water depth.

Third-order analysis for KK02, KK02e and MS98 models leads to the solutions shown in Figs 2.5 and 2.6. It turns out that MS98 model is accurate in shallow water with respect to Stokes theory but in deep and intermediate water the third harmonic and the amplitude dispersion are significantly underestimated. Application of the enhancement technique with coefficients $(\alpha_1, \beta_1) = \left(\frac{1}{9}, \frac{1}{945}\right)$, as proposed by Madsen and Schäffer (1998), eliminates the singularities occurring at $\kappa = \sqrt{3}$ and $\kappa = \sqrt{\frac{3}{2}}$ for a_3 and ω_{13} respectively; the lengthy expressions of these variables are not given here.

The extra nonlinear terms of order $O(\varepsilon^2\sigma^2)$ in KK02e model improve obviously the amplitude dispersion characteristics when compared to KK02 weakly nonlinear model. However, they remain quite poor, especially in deep water. On the other hand, both models' solutions for the third harmonic match the κ^2-term coefficient of the series in the parenthesis of Eq. (2.85) but not the coefficients of higher order. The deviation of the coefficients of higher order terms is less for the weakly nonlinear model KK02 than the extended nonlinear one KK02e and this leads a slightly better result with respect to the third harmonic. The extra nonlinear terms of MS98 model are of order $O(\sigma^4, \varepsilon\sigma^4)$, i.e. of higher order with respect to σ. Hence, its third-order solution is more accurate than that of KK02 models.

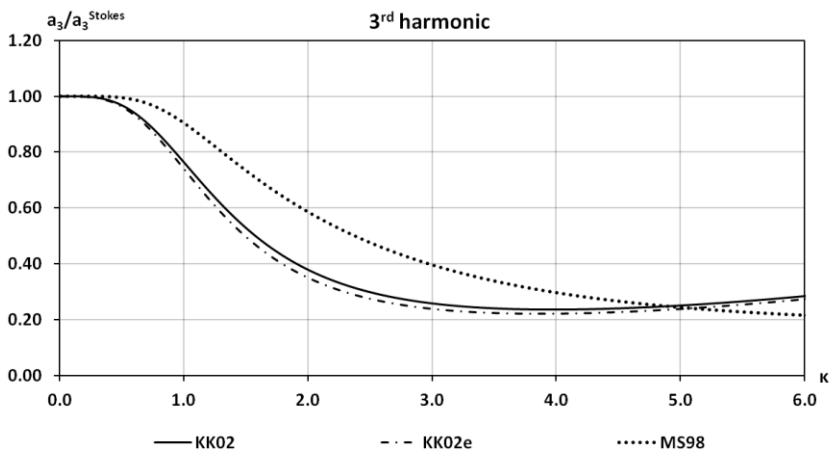

Fig. 2.5. Ratio of third harmonic, a_3/a_3^{Stokes} for KK02, KK02e and MS98, a_3^{Stokes} from Eq. (2.84).

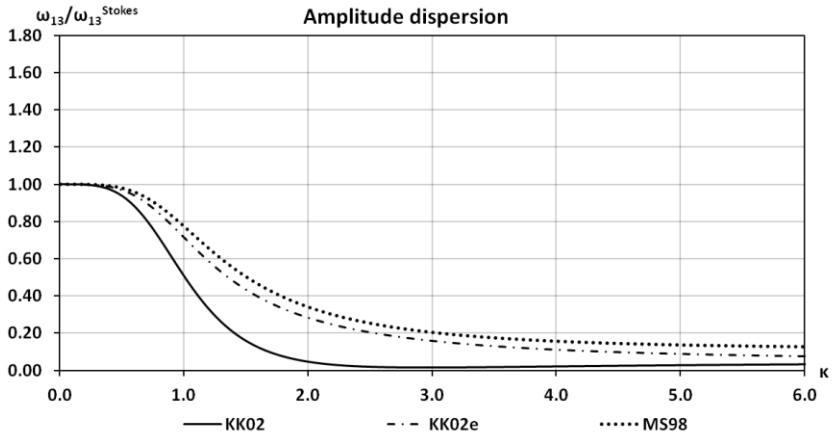

Fig. 2.6. Ratio of amplitude dispersion, $\omega_{13}/\omega_{13}^{\text{Stokes}}$ for KK02, KK02e and MS98 models, $\omega_{13}^{\text{Stokes}}$ from Eq. (2.84).

Third-order solutions for KM09 weakly nonlinear and extended modified models are shown in Figs 2.7 and 2.8. KM09em model converges to Stokes solutions in shallow water, while KM09 significantly underestimates them.

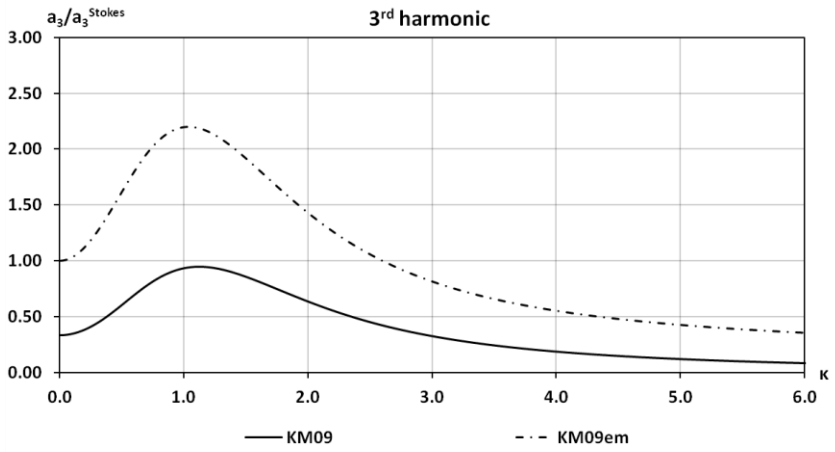

Fig. 2.7. Ratio of third harmonic, a_3/a_3^{Stokes} for KM09 and KM09em models, a_3^{Stokes} from Eq. (2.84).

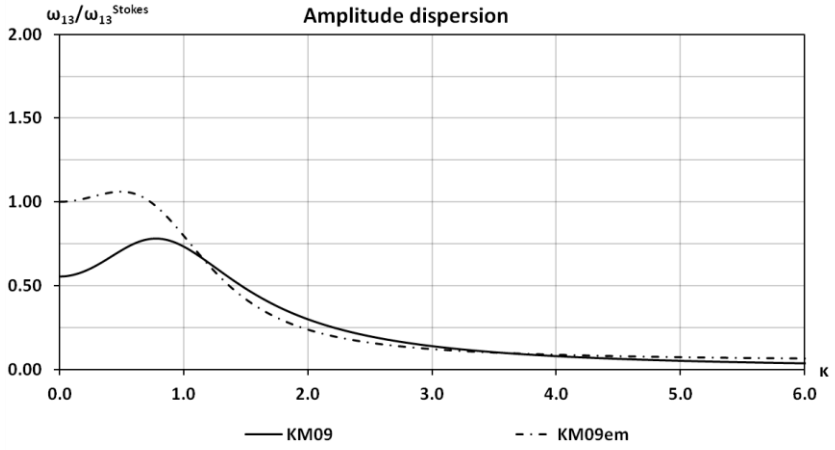

Fig. 2.8. Ratio of amplitude dispersion, $\omega_{13}/\omega_{13}^{\text{Stokes}}$ for KM09 and KM09em models, $\omega_{13}^{\text{Stokes}}$ from Eq. (2.84).

The modified model shows quite improved behaviour in deeper water with regard to the 3rd harmonic amplitude, when compared to the weakly nonlinear one due to the extra terms of $O(\varepsilon\sigma^2)$. Despite being fully linear dispersive, both versions of KM09 model show quite poor characteristics of nonlinear amplitude dispersion in intermediate and deep water.

2.4.2 Linear shoaling analysis

Madsen and Sørensen (1992) introduced the linear shoaling gradient γ_0 in order to check the applicability of their Boussinesq equations under shoaling water conditions. This quantity was defined by

$$\frac{A_x}{A} = -\frac{d_x}{d}\gamma_0 \tag{2.86}$$

where A is the local wave amplitude and index x denotes partial derivative with respect to x. The shoaling gradient γ_0 is a function of the local variable κ. Madsen and Sørensen (1992) combined Stokes's linear theory with conservation of energy flux and derived the reference gradient

$$\gamma_0^{Stokes} = \frac{2\kappa \sinh(2\kappa)+2\kappa^2[1-\cosh(2\kappa)]}{[2\kappa+\sinh(2\kappa)]^2} \tag{2.87}$$

of which a Taylor expansion at $\kappa = 0$ yields

$$\gamma_0^{\text{Stokes}} = \frac{1}{4} - \frac{1}{4}\kappa^2 + \frac{1}{18}\kappa^4 + \frac{1}{540}\kappa^6 - \frac{11}{3150}\kappa^8 + O(\kappa^{10}) \tag{2.88}$$

The analysis by Madsen and Schäffer (1998) will be followed. Hence, their argument about the applicability of the linear shoaling gradient will be adopted. Chen and Liu (1995) rejected this gradient as being a reliable measure of the linear shoaling effect, since they claimed that a deviation from the target gradient produces a reduced effect as the relative depth increases and errors occurring in intermediate and deep water exaggerate the actual difference of the resulting shoaling amplitude. However, the shoaling gradient is the most obvious analytical measure of the linear shoaling characteristics of Boussinesq equations. In addition, the insertion of just two tuning parameters (α_2, β_2) was enough for MS98 model to achieve easily a high accuracy in this respect. Hence, the linear shoaling gradient analysis will be followed as proposed by Madsen and Schäffer (1998).

KM09 weakly nonlinear and modified models were derived on the assumption of a horizontal bottom. However, their applicability can be extended to mildly varying depth as discussed in subsection 2.3.2. Nevertheless, the momentum equation of these models does not include terms of the spatial derivative of depth. Additionally, the approximation mentioned in subsection 2.3.2 that quantifies the depth variation effect by adding an extra term in the momentum equation does not contribute to the $O(\sigma^2)$ at which the linear shoaling analysis is performed. Therefore, the following analysis is not applicable to these models.

The aforementioned gradient refers to linear shoaling. Hence, all nonlinear terms have to be neglected. Consequently, all terms of order $O(\varepsilon, \varepsilon\sigma^2, \varepsilon^2\sigma^2)$ will be removed from KK02 weakly and strongly nonlinear models. In this way the two models coincide and thus they will be both referred to as KK02 model in this section. The non-dimensional continuity equation for KK02 and MS98 models is reduced to

$$\zeta_t + dU_x + d_x U = O(\varepsilon) \tag{2.89}$$

while the momentum equation of KK02 model is reduced to

$$U_t + \zeta_x - \sigma^2 \frac{d^2}{3} U_{xxt} - \sigma^2 d d_x U_{xt} - \sigma^2 \mathrm{B} d^2 (U_{xxt} + \zeta_{xxx}) - \sigma^2 2\mathrm{B}_2 d d_x (U_{xt} + \zeta_{xx}) = O(\varepsilon) \tag{2.90}$$

At this point, it should be mentioned once again, that the original Karambas and Koutitas's (2002) model includes one single free parameter for controlling both the linear dispersion and linear shoaling characteristics and thus the coefficient of the last term on the l.h.s of Eq. (2.90) is B instead of $2B_2$. A similar linear shoaling analysis for the original Karambas and Koutitas's (2002) model can be found in Memos *et al*. (2016).

Following Schäffer and Madsen (1995), we look for solutions of the form

$$\zeta(x,t) = A(x) e^{i[\omega t - \Psi(x)]} \tag{2.91a}$$

$$U(x,t) = D(x)[1 + i\varphi(x) d_x] e^{i[\omega t - \Psi(x)]} \tag{2.91b}$$

where

$$\frac{\partial \Psi}{\partial x} = k(x) \tag{2.92}$$

and A, D and φ are real slowly varying functions of x. Introduction of the φ term permits a small phase shift for a mildly sloping bed, while in constant depth U is in phase with ζ. First derivatives of A, D, φ, k and d are assumed to be small, and thus products of derivatives as well as higher derivatives of these quantities are neglected in the analysis.

Applying the procedure by Madsen and Schäffer (1998), Eqs (2.91a) and (2.91b) are substituted into the continuity equation (2.89) and real and imaginary terms are collected. Thus two equations are derived:

$$D = \frac{\omega A}{kd} \tag{2.93}$$

$$\frac{D_x}{D} + (1 + \varphi k d) \frac{d_x}{d} = 0 \tag{2.94}$$

Differentiating Eq. (2.93) with respect to x leads to

$$\frac{D_x}{D} = \frac{A_x}{A} - \frac{k_x}{k} - \frac{d_x}{d} \tag{2.95}$$

which in combination with Eq. (2.94) yields

$$\varphi k d \frac{d_x}{d} = \frac{k_x}{k} - \frac{A_x}{A} \tag{2.96}$$

Equations (2.91a) and (2.91b) are then substituted into the momentum equation (2.90). Combining the imaginary part with Eq. (2.93), the dispersion relation (2.61) is obtained. The real part, after using Eqs (2.93), (2.95) and (2.96), can be expressed as

$$\gamma_1 \frac{A_x}{A} + \gamma_2 \frac{k_x}{k} + \gamma_3 \frac{d_x}{d} = 0 \tag{2.97}$$

where

$$\gamma_1 = 1 + s^2 + \kappa^2 \left[3\mathrm{B} - \left(\mathrm{B} + \frac{1}{3}\right) s^2\right] \tag{2.98a}$$

$$\gamma_2 = -s^2 + 3\mathrm{B}\kappa^2 \tag{2.98b}$$

$$\gamma_3 = \kappa^2 \left[2\mathrm{B}_2 + s^2 \left(2\mathrm{B} - 2\mathrm{B}_2 - \frac{1}{3}\right)\right] \tag{2.98c}$$

and where s is defined by

$$s = \frac{\omega}{k\sqrt{d}} = \frac{c'}{\sqrt{gd'}} \tag{2.99}$$

where c' and d' the dimensional wave celerity and still water depth, respectively.

The first spatial derivative of the wavenumber k can be expressed in terms of the first spatial derivative of d by differentiating the dispersion relation (2.61) with respect to x, and this leads to

$$\gamma_4 \frac{k_x}{k} + \gamma_5 \frac{d_x}{d} = 0 \tag{2.100}$$

where

$$\gamma_4 = 2\left\{1 + \kappa^2 \left[2\mathrm{B} - s^2 \left(\mathrm{B} + \frac{1}{3}\right)\right]\right\} \tag{2.101a}$$

$$\gamma_5 = 1 + \kappa^2 \left[3\mathrm{B} - 2s^2 \left(\mathrm{B} + \frac{1}{3}\right)\right] \tag{2.101b}$$

The linear shoaling gradient γ_0 is obtained by substituting Eq. (2.100) into Eq. (2.97). It is found

$$\gamma_0 = \frac{\gamma_3\gamma_4 - \gamma_2\gamma_5}{\gamma_1\gamma_4} \tag{2.102}$$

Adopting the value $\mathrm{B} = \frac{1}{15}$ which optimizes the linear dispersion characteristics as discussed above, the expansion of Eq. (2.102) at $\kappa = 0$ gives

$$\gamma_0 = \frac{1}{4} - \frac{1}{4}\kappa^2 + \left(\frac{1}{45} + \frac{1}{3}\mathrm{B}_2\right)\kappa^4 + \left(\frac{13}{1350} - \frac{2}{45}\mathrm{B}_2\right)\kappa^6 + \left(-\frac{11}{3375} - \frac{2}{675}\mathrm{B}_2\right)\kappa^8 + O(\kappa^{10}) \tag{2.103}$$

By setting $\mathrm{B}_2 = \mathrm{B}_1 = \frac{1}{30}$, the corresponding solution for the original Karambas and Koutitas (2002) model appears, which after expansion gives

$$\gamma_0 = \frac{1}{4} - \frac{1}{4}\kappa^2 + \frac{1}{30}\kappa^4 + \frac{11}{1350}\kappa^6 - \frac{34}{10125}\kappa^8 + O(\kappa^{10}) \tag{2.104}$$

Matching up to κ^4-terms between Eqs (2.103) and (2.88) yields $\mathrm{B}_2 = \frac{1}{10}$. This value gives the best fit for the shoaling gradient for $kd < 1.2$, but since much higher-order terms in γ_0 are inevitable, a good fit for a larger range of kd-values is required. A minimization of the error compared to Stokes's target solution up to the traditional limit of deep water, $kd = 3$, yields $\mathrm{B}_2 = 0.0653$, which is only marginally different from Madsen and Sørensen's (1992) result corresponding to $\mathrm{B}_2 = \frac{1}{15} \approx 0.0667$ (see also Schäffer and Madsen, 1995).

Madsen and Schäffer (1998) applied the aforementioned linear shoaling analysis to their model too. Their momentum equation is thus reduced to

$$U_t + \zeta_x - \sigma^2\left[\left(\alpha_1 + \frac{1}{3}\right)d^2U_{xxt} + \alpha_1 d^2\zeta_{xxx}\right] - \sigma^2 d_x[(1+2\alpha_2)dU_{xt} + 2\alpha_2 d\zeta_{xx}] + \sigma^4\left[\left(\beta_1 + \frac{1}{3}\alpha_1 - \frac{1}{45}\right)d^4U_{xxxxt} + \beta_1 d^4\zeta_{xxxxx}\right] + \sigma^4 d_x\left[\left(\beta_2 + \frac{7}{3}\alpha_1 + \frac{2}{3}\alpha_2 - \frac{2}{9}\right)d^3U_{xxxt} + \beta_2 d^3\zeta_{xxxx}\right] = O(\varepsilon) \tag{2.105}$$

Equations (2.91a) and (2.91b) are substituted into Eqs (2.89) and (2.105) and after applying the values $(\alpha_1, \beta_1) = \left(\frac{1}{9}, \frac{1}{945}\right)$ as above, the linear shoaling gradient is obtained for MS98 (for more details see Madsen and Schäffer, 1998). By expanding their solution at $\kappa = 0$ one gets

$$\gamma_0 = \frac{1}{4} - \frac{1}{4}\kappa^2 + \frac{1}{18}\kappa^4 + \frac{1}{540}\left(\frac{43}{21} - 12\alpha_2 + 90\beta_2\right)\kappa^6 + \frac{1}{3150}\left(-\frac{1006}{81} + \frac{130}{9}\alpha_2 - \frac{280}{3}\beta_2\right)\kappa^8 + O(\kappa^{10}) \tag{2.106}$$

As stated in MS98, the most attractive technique for the determination of (α_2, β_2) is the one proposed by Schäffer and Madsen (1995). This relies on the minimization of the integral error $\frac{1}{\kappa_0}\int_0^{\kappa_0}\left(\gamma_0^{\text{Stokes}} - \gamma_0\right)^2 d\kappa$. Setting $\kappa_0 = 6$, Eqs (2.88) and (2.106) give $(\alpha_2, \beta_2) = (0.146488, 0.00798359)$. Fig. 2.9 shows the linear shoaling gradient as computed by Stokes theory, KK02, and MS98 models. Madsen and Schäffer's (1998) model behaviour is excellent

up to $\kappa = 6$ which is twice the traditional deep water limit. This was expected since this model embeds two free parameters to be optimized over linear shoaling. It can be noticed on this that Eq. (2.106) matches Eq. (2.88) up to fourth order terms. By setting $(\alpha_2, \beta_2) = \left(\frac{1}{6}, \frac{2}{189}\right)$ leads to a matching up to κ^8 terms but the aforementioned integral error technique gives some deviation in deep water ($\kappa > 6$) where higher order terms become significant too. KK02 gives very good results up to approximately $\kappa = 1.5$, and in general acceptable results up to $\kappa = 3$, since the value $B_2 = 0.0653$ has been used to minimize the total error over this depth range, as already discussed above.

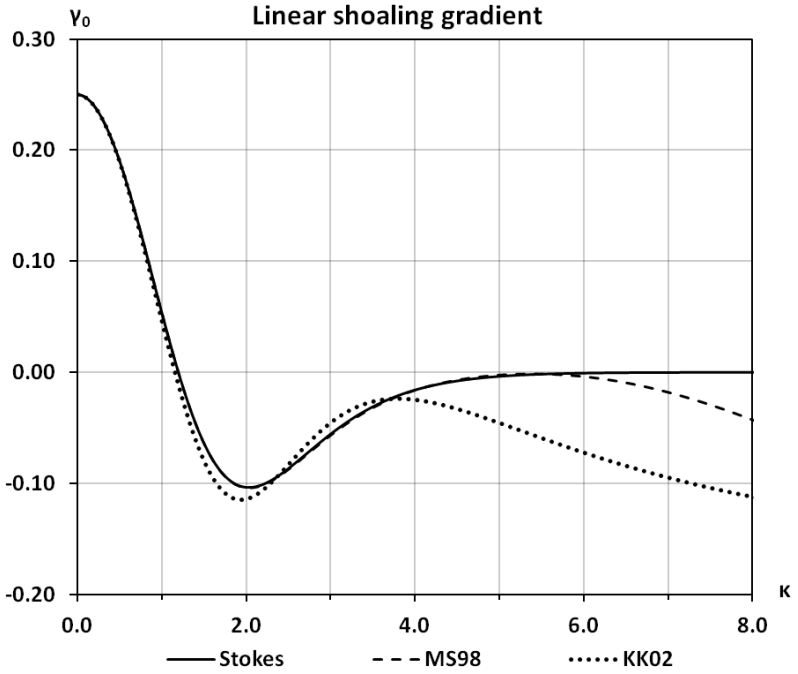

Fig. 2.9. Linear shoaling gradient γ_0 computed by Stokes theory, MS98, and KK02 models.

2.4.3 Transfer functions for sub- and super-harmonics

In this subsection the transfer functions for second-order bound sub- and super-harmonics are derived for the aforementioned Boussinesq-type models. It should be mentioned that the accuracy of second-order energy transfer is by far more important in shallow water where this transfer is high.

The procedure presented by Madsen and Schäffer (1998) shall be applied. A first-order wave group made up of just two frequencies ω_n and ω_m can be described as follows

$$\zeta(x,t) = \zeta_n + \zeta_m \tag{2.107a}$$

$$\zeta_n = a_n \cos(\omega_n t - k_n x) + b_n \sin(\omega_n t - k_n x) \tag{2.107b}$$

$$\zeta_m = a_m \cos(\omega_m t - k_m x) + b_m \sin(\omega_m t - k_m x) \tag{2.107c}$$

Each of the two wave components is considered to be solution to the relevant linearized Boussinesq equations. Thus both sets (ω_n, k_n) and (ω_m, k_m) should satisfy the corresponding linear dispersion relation.

Through the nonlinear terms of $O(\varepsilon)$, a first-order bichromatic wave train forces a second-order wave train consisting of four contributors, one sub-harmonic, $\omega_p = \omega_n - \omega_m$ and three super-harmonics, $\omega_p = \omega_n + \omega_m$, $\omega_p = 2\omega_n$ and $\omega_p = 2\omega_m$ with corresponding wave numbers determined by $k_p = k_n - k_m$, $k_p = k_n + k_m$, $k_p = 2k_n$ and $k_p = 2k_m$ respectively. These waves are bound or phase-locked to the first-order wave train and pair (ω_p, k_p) does not satisfy the linear dispersion equation. Super-harmonics contribute in wave profile vertical asymmetry, i.e. wave crests get higher and sharper, wave troughs get flattened, while sub-harmonics may induce long waves over the coast that may resonate when they penetrate into harbours and cause the large motion of moored ships (Zou, 1999). The second-order wave train is expressed by

$$\zeta^{(2)}(x,t) = \zeta_{nm}^{-} + \zeta_{nm}^{+} + \zeta_{nn}^{+} + \zeta_{mm}^{+} \tag{2.108}$$

where

$$\zeta_{nm}^{\pm} = \varepsilon\delta G_{\zeta}^{\pm}\left[a_p \cos(\omega_p t - k_p x) + b_p \sin(\omega_p t - k_p x)\right] \tag{2.109a}$$

and

$$a_p = \frac{1}{d}(a_n a_m \mp b_n b_m) \quad \text{and} \quad b_p = \frac{1}{d}(a_m b_n \pm a_n b_m) \tag{2.109b}$$

$$\omega_p = \omega_n \pm \omega_m \quad \text{and} \quad k_p = k_n \pm k_m \tag{2.109c}$$

$$\delta = \begin{cases} \frac{1}{2} & \text{for n=m} \\ 1 & \text{for n}\neq\text{m} \end{cases} \tag{2.109d}$$

The sub/super-harmonic contributors of Eq. (2.108) are determined by using the lower/upper signs in Eqs (2.109a) to (2.109c). Functions G_{ζ}^{-} and G_{ζ}^{+} are the second-order surface elevation transfer functions to be determined. Expressions for the second-order velocity can be obtained in a similar manner by using $G_{U}^{\pm}$ instead of $G_{\zeta}^{\pm}$ in Eq. (2.109a).

Following Madsen and Schäffer (1998), the reference solutions here are the one given by Ottesen-Hansen (1978) for the sub-harmonics and the one by Sand and Mansard (1986) for the super-harmonics. Their solutions are determined directly from the nonlinear boundary value problem for the Laplace equation.

Figure 2.10 shows the target second order transfer $G_\zeta^{\pm}$ as a function of Ω_n and Ω_m defined by

$$\Omega_n = \frac{\omega_n'}{2\pi}\sqrt{\frac{d'}{g}} \quad \text{and} \quad \Omega_m = \frac{\omega_m'}{2\pi}\sqrt{\frac{d'}{g}} \tag{2.110}$$

where primes denote dimensional quantities as before.

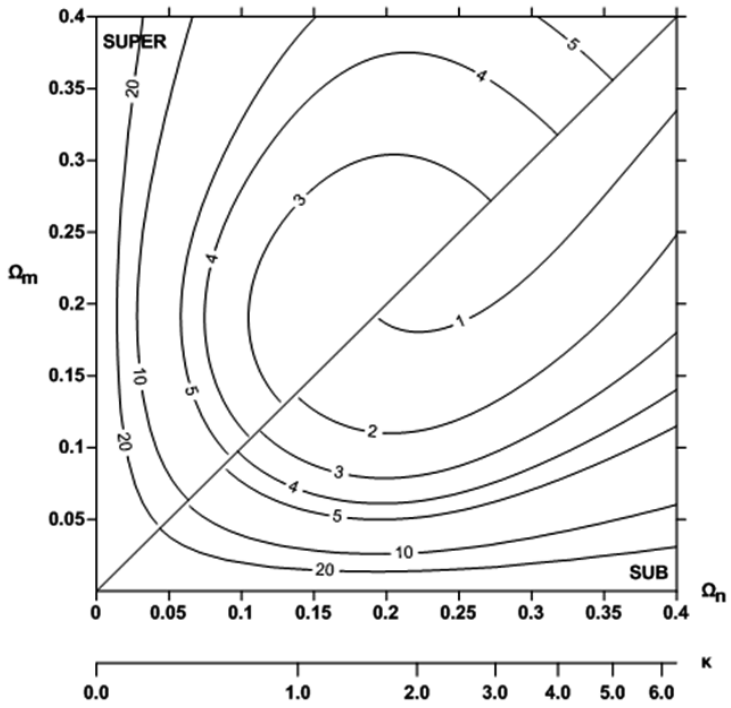

Fig. 2.10. Second-order transfer function G_ζ^{Stokes} for Stokes theory. Results for super-harmonics, G_ζ^+, are shown above the diagonal; results for sub-harmonics, $-G_\zeta^-$, are shown below it.

A corresponding axis in terms of κ is also shown, where the wavelength is computed from the linear wave theory. The upper triangular represents the super-harmonic transfer from ω_n and ω_m to $\omega_p = \omega_n + \omega_m$, while the lower triangle represents the sub-harmonic transfer from ω_n and ω_m to $\omega_p = \omega_n - \omega_m$. The diagonal line on which ω_n equals ω_m represents the second-harmonic transfer discussed in subsection 2.4.1.

As mentioned by Madsen and Schäffer (1998), the super-harmonic transfer function has a local minimum in intermediate water depth, while the sub-harmonic is gradually reduced from shallow to deep water. Both functions tend to infinity in the shallow water limit, where the difference between bound and free wavenumbers vanishes. As presented in detail by

Madsen and Sørensen (1993), when approaching this limit the generated bound waves are no longer small compared to the primary waves and near-resonant energy exchange takes place.

In the following the second-order transfer functions $G_{\zeta}^{\pm}$ will be derived for the aforementioned Boussinesq-type models. The analysis will be performed over a horizontal bottom, thus the Boussinesq equations for the various models are the reduced ones used in subsection 2.4.1.

Since Eqs (2.107) provide a solution to the linearized equations, (ω_n, k_n) and (ω_m, k_m) will satisfy the relevant to each model linear dispersion equation. Hence, the first-order velocity can be expressed as

$$U^{(1)}(x,t) = \frac{\omega_n}{k_n d}\zeta_n + \frac{\omega_m}{k_m d}\zeta_m \tag{2.111}$$

while the second-order velocity $U^{(2)}$ can be obtained by Eq. (2.109a) by using $G_U^{\pm}$ instead of $G_{\zeta}^{\pm}$.

Eqs (2.107), (2.108), (2.109) and (2.111) are substituted into momentum and continuity equations of the various Boussinesq models and collecting terms of $O(\varepsilon)$, we obtain algebraic systems of the form

$$\begin{pmatrix} m_{11}^{(2)} & m_{12}^{(2)} \\ m_{21}^{(2)} & m_{22}^{(2)} \end{pmatrix} \begin{pmatrix} G_{\zeta}^{\pm} \\ G_U^{\pm} \end{pmatrix} = \begin{pmatrix} F_1^{\pm} \\ F_2^{\pm} \end{pmatrix} \tag{2.112}$$

leading to solutions reading

$$G_{\zeta}^{\pm} = \frac{F_1^{\pm} m_{22}^{(2)} - F_2^{\pm} m_{12}^{(2)}}{m_{11}^{(2)} m_{22}^{(2)} - m_{21}^{(2)} m_{12}^{(2)}} \tag{2.113}$$

In this subsection a second-order analysis is presented. Consequently, KK02 weakly and strongly nonlinear models give the same results at the $O(\varepsilon)$ since they differ only with respect to terms of $O(\varepsilon^2\sigma^2)$. Thus the analysis is common for both models and will be both referred to as KK02 model in the present subsection.

For KK02 model the coefficients of the linear system for the case of super-harmonic $\omega_p = \omega_n + \omega_m$ are

$$\left.\begin{array}{c} m_{11}^{(2)} = \omega_p,\ m_{12}^{(2)} = -k_p d, \\ m_{21}^{(2)} = -k_p\left(1 + \mathrm{B}\kappa_p^2\right),\ \ m_{22}^{(2)} = \omega_p\left[1 + \left(\frac{1}{3} + \mathrm{B}\right)\kappa_p^2\right] \end{array}\right\} \tag{2.114a}$$

$$F_1^{+} = \frac{1}{2} k_p \left(\frac{\omega_n}{k_n} + \frac{\omega_m}{k_m}\right) \tag{2.114b}$$

$$F_2^+ = \frac{1}{2}k_p\frac{\omega_n\omega_m}{dk_nk_m}\left\{1+\frac{1}{3}\left[(\kappa_n-\kappa_m)^2+3\mathrm{B}(\kappa_n+\kappa_m)^2-\kappa_n^2\frac{s_n}{s_m}\left(\frac{2\kappa_n+3\kappa_m}{\kappa_n+\kappa_m}\right)-\kappa_m^2\frac{s_m}{s_n}\left(\frac{2\kappa_m+3\kappa_n}{\kappa_n+\kappa_m}\right)\right]\right\} \quad (2.114c)$$

where s is defined by Eq. (2.99), κ is defined by Eq. (2.55), $k_p = k_n + k_m$ and $\kappa_p = \kappa_n + \kappa_m$. The sub-harmonic transfer function is obtained simply by changing the sign of the quantities $(\omega_m, k_m, \kappa_m)$ in Eqs (2.114a), (2.114b) and (2.114c). For the case of $\omega_n = \omega_m$, the problem is reduced to the second-harmonic transfer presented in subsection 2.4.1.

Figure 2.11 shows the ratio between the transfer function given by Eqs (2.113), (2.114) for KK02 model and the target transfer function shown in Fig. 2.10. The graph includes also a 10% error square. This square has its lower left vertex at $(\Omega_n, \Omega_m) = (0,0)$ and the maximum side length for which the error is less than 10% for anyone set (Ω_n, Ω_m). This option was favoured against the one adopted by Madsen and Schäffer (1998) who defined an error circle instead. Although their argument about superiority of a circle instead of a square with $\Omega_R = \max(\Omega_n, \Omega_m)$ is appreciated, their method leads to an overestimation of the accepted κ-values range. On the other hand, by using the error square defined herein it is ensured that the associated range of κ leads always to accepted errors for every pair (Ω_n, Ω_m). The side length of the error square for KK02 model is $\Omega_S = 0.155$ which corresponds to $\kappa \approx 1.16$.

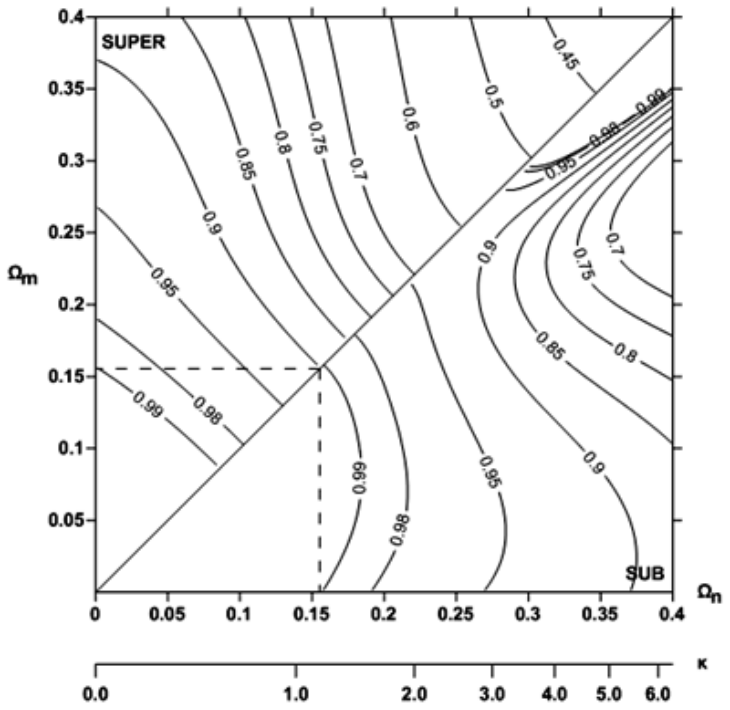

Fig. 2.11. Ratio of second-order transfer functions, $G_\zeta / G_\zeta^{\mathrm{Stokes}}$, where G_ζ is given by Eq. (2.113) for KK02 model. Results for super-harmonics are shown above the diagonal; results for sub-harmonics are shown below it. The dashed square indicates a 10% error.

The same analysis was applied for the MS98 model too. The coefficients of the linear system (2.112) for the case of super-harmonic are written

$$m_{11}^{(2)} = \omega_p,\ m_{12}^{(2)} = -k_p d,$$
$$m_{21}^{(2)} = -k_p\left(1 + \alpha_1\kappa_p^2 + \beta_1\kappa_p^4\right),$$
$$m_{22}^{(2)} = \omega_p\left[1 + \left(\tfrac{1}{3} + \alpha_1\right)\kappa_p^2 + \left(\beta_1 + \tfrac{1}{3}\alpha_1 - \tfrac{1}{45}\right)\kappa_p^4\right] \tag{2.115a}$$

$$F_1^+ = \tfrac{1}{2}k_p\left(\tfrac{\omega_n}{k_n} + \tfrac{\omega_m}{k_m}\right) \tag{2.115b}$$

$$F_2^+ = \tfrac{1}{2}k_p\,\tfrac{\omega_n\omega_m}{dk_nk_m}\Big\{1 + \tfrac{1}{3}\Big[(\kappa_n-\kappa_m)^2 + 3a_1(\kappa_n+\kappa_m)^2 - \kappa_n^2\tfrac{s_n}{s_m}\left(\tfrac{2\kappa_n+3\kappa_m}{\kappa_n+\kappa_m}\right) - \kappa_m^2\tfrac{s_m}{s_n}\left(\tfrac{2\kappa_m+3\kappa_n}{\kappa_n+\kappa_m}\right)\Big] +$$
$$\tfrac{1}{45}\Big[22\kappa_n^2\kappa_m^2 - (\kappa_n-\kappa_m)^4 + \kappa_n^3\tfrac{s_n}{s_m}\left(\tfrac{4\kappa_n^2+10\kappa_n\kappa_m+5\kappa_m^2}{\kappa_n+\kappa_m}\right) + \kappa_m^3\tfrac{s_m}{s_n}\left(\tfrac{4\kappa_m^2+10\kappa_n\kappa_m+5\kappa_n^2}{\kappa_n+\kappa_m}\right)\Big] +$$
$$\tfrac{1}{3}a_1(\kappa_n+\kappa_m)\Big[\kappa_n^3\left(1-2\tfrac{s_n}{s_m}\right) + \kappa_m^3\left(1-2\tfrac{s_m}{s_n}\right) - \kappa_n^2\kappa_m\left(1+3\tfrac{s_n}{s_m}\right) - \kappa_m^2\kappa_n\left(1+3\tfrac{s_m}{s_n}\right)\Big] +$$
$$\beta_1(\kappa_n+\kappa_m)^4\Big\} \tag{2.116c}$$

The sub-harmonic transfer function is again obtained simply by changing the sign of the quantities $(\omega_m, k_m, \kappa_m)$ in Eqs (2.115a), (2.115b) and (2.115c). Fig. 2.12 shows the ratio between the transfer function given by Eq. (2.113) for MS98 model and the target transfer function shown in Fig. 2.10 by adopting the values $(\alpha_1, \beta_1) = \left(\frac{1}{9}, \frac{1}{945}\right)$ in Eqs (2.116) as presented above. This figure also includes a 10% error square for which the side length is $\Omega_S = 0.208$ corresponding to $\kappa \approx 1.80$. Madsen and Schäffer (1998) presented similar solutions for the traditional Boussinesq equations of order $O(\sigma^2, \varepsilon)$ enhanced to Padé [2,2] dispersion characteristics and the lower order model by Madsen and Sørensen (1993) expressed in terms of the depth-integrated velocity. These solutions lead to side lengths $\Omega_S = 0.078$ and $\Omega_S = 0.071$ for the 10% error squares respectively.

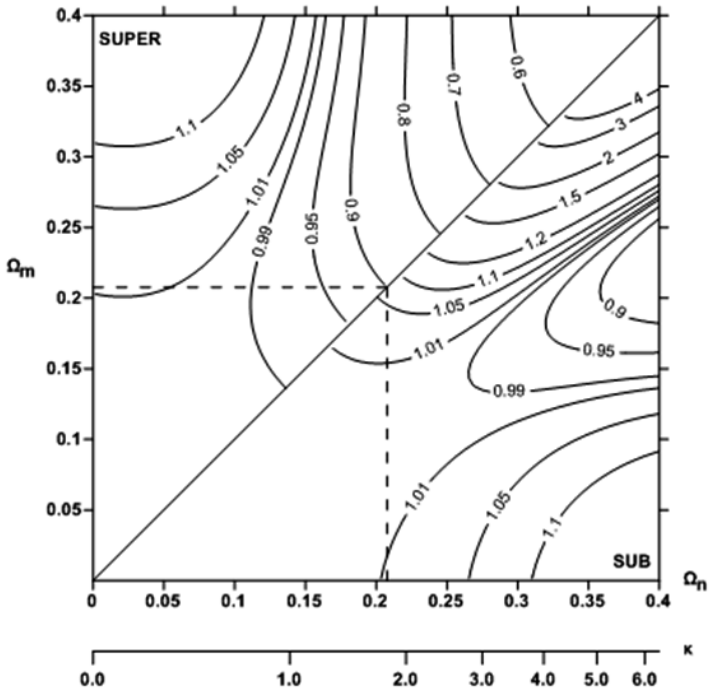

Fig. 2.12. Ratio of second-order transfer functions, $G_\zeta / G_\zeta^{Stokes}$, where G_ζ is given by Eq. (2.113) for MS98 model. Results for super-harmonics are shown above the diagonal; results for sub-harmonics are shown below it. The dashed square indicates a 10% error.

The transfer function analysis was also applied to KM09 and KM09em models. The coefficients of the linear system (2.112) for the weakly nonlinear model are written for the case of super-harmonic

$$\left.\begin{array}{c} m_{11}^{(2)} = \omega_p,\ m_{12}^{(2)} = -k_p d, \\ m_{21}^{(2)} = -k_p \frac{\tanh(\kappa_p)}{\kappa_p},\ m_{22}^{(2)} = \omega_p \end{array}\right\} \tag{2.117a}$$

$$F_1^+ = \frac{1}{2} k_p \left(\frac{\omega_n}{k_n} + \frac{\omega_m}{k_m}\right) \tag{2.117b}$$

$$F_2^+ = \frac{1}{2} k_p \frac{\omega_n \omega_m}{d k_n k_m} \tag{2.117c}$$

The sub-harmonic transfer function is again obtained simply by changing the sign of the quantities $(\omega_m, k_m, \kappa_m)$ in Eqs (2.117a), (2.117b) and (2.117c). Fig. 2.13 shows the ratio between the transfer function given by Eq. (2.113) for KM09 weakly nonlinear model and the target transfer function shown in Fig. 2.10. The figure also includes a 10% error square for which the side length is $\Omega_S = 0.051$ corresponding to $\kappa \approx 0.33$ which is slightly greater than the limit between shallow and intermediate water. Thus the results of KM09 for the second-order transfer function are very poor, similarly to the weakly nonlinear model of $O(\sigma^2, \varepsilon)$

presented by Madsen and Schäffer (1998) as well as to the lower order model by Madsen and Sørensen (1993). The super-harmonic transfer for KM09 weakly nonlinear model is too large and this leads to too peaky wave profiles for shoaling waves.

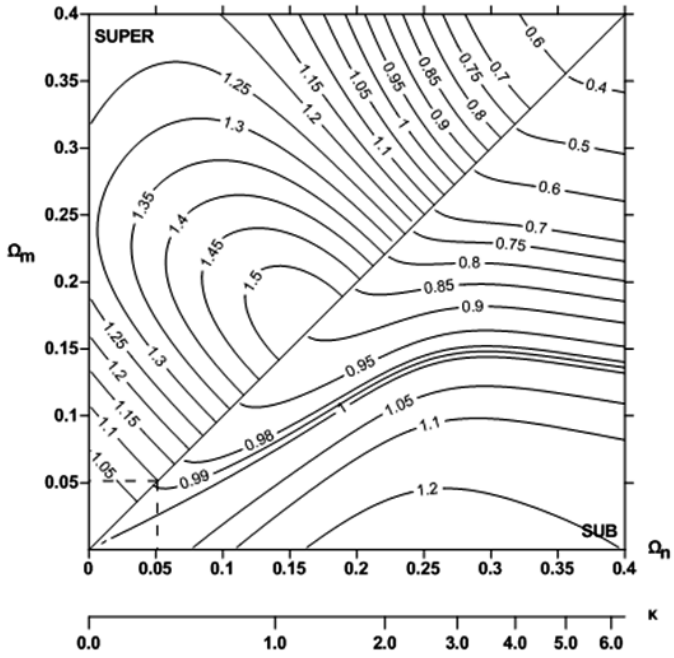

Fig. 2.13. Ratio of second-order transfer functions, $G_\zeta / G_\zeta^{Stokes}$, where G_ζ is given by Eq. (2.113) for KM09 model. Results for super-harmonics are shown above the diagonal; results for sub-harmonics are shown below it. The dashed square indicates a 10% error.

The coefficients of the linear system (2.112) for KM09em model are written for the case of super-harmonic

$$m_{11}^{(2)} = \omega_p,\ m_{12}^{(2)} = -k_p d,\ \ m_{21}^{(2)} = -1$$

$$m_{22}^{(2)} = \frac{1}{k^2 k_p}\{k^2 + [-1 + \kappa\coth(\kappa)]k_m^2 + 2[-1 + \kappa\coth(\kappa)]k_m k_n + [-1 + \kappa\coth(\kappa)]k_n^2\}\omega_p \tag{2.118a}$$

$$F_1^+ = \frac{1}{2}k_p\left(\frac{\omega_n}{k_n} + \frac{\omega_m}{k_m}\right) \tag{2.118b}$$

$$F_2^+ = \frac{1}{16}\frac{\omega_n\omega_m}{dkk_nk_m}\mathrm{csch}^2(\kappa)\{8k\sinh^2(\kappa) + (\kappa_m^2 + \kappa_n^2)[2\kappa\cosh(\kappa) - \sinh(2\kappa)] + 2k_m\kappa_n[-4\kappa + 2\kappa\cosh(\kappa) + \sinh(2\kappa)]\} \tag{2.118c}$$

Again simple change of the sign of the quantities $(\omega_m, k_m, \kappa_m)$ in Eqs (2.118a), (2.118b) and (2.118c) leads to the sub-harmonic transfer function solution. Fig. 2.14 shows the ratio

between the transfer function given by Eq. (2.113) for KM09em model and the target transfer function shown in Fig. 2.10. The specific model embeds the wavenumber k as a free parameter in the momentum equation similarly to Li's (2008) model. In the case of regular waves k can be obtained from linear dispersion equation since the model is fully linear dispersive. However, for irregular waves a representative value for the wavenumber should be adopted. A numerical investigation of the model's behaviour showed a very weak sensitivity on this parameter. For the bichromatic wave of the present transfer function analysis, k is considered to be the wavenumber corresponding through the linear dispersion equation to frequencies $\omega_m + \omega_n$ and $\omega_n - \omega_m$ for the super-harmonic and sub-harmonic, respectively. This is not a quite accurate assumption since these sub- and super-harmonics are bound waves that do not satisfy the linear dispersion equation. The sub-harmonic transfer function is significantly underestimated for high values of both Ω_n and Ω_m and even a difference of sign occurs between the model's results and the target solution. In addition, the blank domain in the graph is due to a singularity that refers to sub-harmonic transfer function for simultaneous high and low values of Ω_n and Ω_m, respectively.

Figure 2.14 also includes a 10% error square with side length $\Omega_S = 0.05$ corresponding to $\kappa \approx 0.32$ which is approximately the limit between shallow and intermediate water. These values are slightly lower than the ones for KM09 weakly nonlinear model. However, in intermediate and deep water where the extra terms of order $O(\varepsilon\sigma^2)$ become significant, the KM09em model behaves more accurately than the weakly nonlinear version. Nevertheless the nonlinear response of KM09 models is quite poor as deduced from both the Stokes-type Fourier analysis and the sub- and super-harmonic analysis.

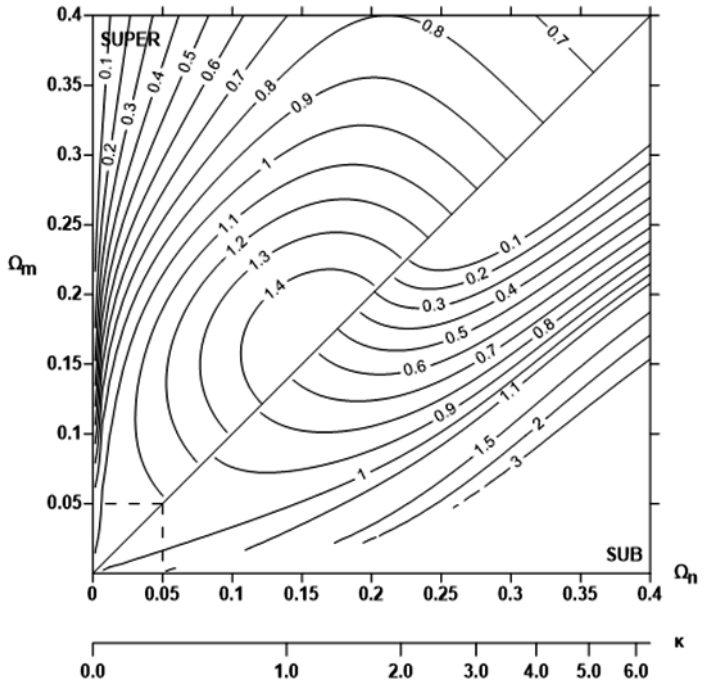

Fig. 2.14. Ratio of second-order transfer functions, $G_\zeta / G_\zeta^{Stokes}$, where G_ζ is given by Eq. (2.113) for KM09em model. Results for super-harmonics are shown above the diagonal; results for sub-harmonics are shown below it. The dashed square indicates a 10% error.

2.5 Validation and inter-comparison of Boussinesq-type models

To verify KK02, KK02e, KM09, and KM09em, the 1DH version of each model was applied to simulate the propagation of regular and irregular waves over a submerged trapezoidal bar. For all the models the differential equations were solved numerically using a finite difference scheme on a non-staggered grid. As described in chapter 3, the numerical scheme adopted in the presented thesis relies on a generalization of the Adams-Bashforth-Moulton predictor-corrector scheme proposed by Wei and Kirby (1995). However, in these preliminary tests described in the present chapter the original ABM scheme was employed. In this scheme the field evolution in time was accomplished by an Adams-Bashforth third order predictor, followed by an Adams-Moulton fourth order corrector arrangement. Terms involving first-order spatial derivatives were differenced to $O(\Delta x^4)$, while second and higher-order spatial derivatives were differenced to $O(\Delta x^2)$. This was chosen in order to reduce the truncation errors to a small size relative to all the retained terms in the equations. In all the test cases studied in the following a fairly dense grid of about 75 – 100 points per wavelength in the offshore was chosen. Thus no grid size impact was observed and good numerical stability was ensured.

The models were first applied to a submerged trapezoidal bar for non-breaking monochromatic waves (T = 2.02 s and H = 2.00 cm). The experiments, as described in Dingemans (1994a,b), were carried out in the wave flume of the Department of Civil Engineering, Delft University of Technology, with an overall length of 37.7 m, width 0.8 m and height 0.75 m. The bottom profile, as described in Beji and Battjes (1993, 1994) (see also Battjes and Beji, 1991), is shown in Fig. 2.15. The water depth in the horizontal bottom region was 0.4 m and reduced to 0.1 m in the shallowest region above the horizontal part of the bar. The upward slope of the submerged mound was 1:20 and the downward 1:10.

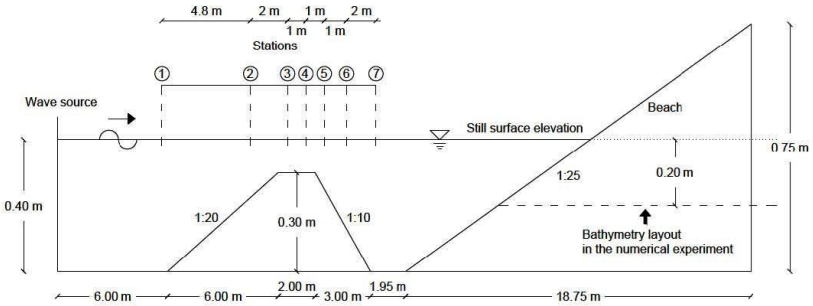

Fig. 2.15. Definition sketch of wave flume and location of wave gauges in Beji and Battjes's experiment.

Figure 2.16 shows time domain comparisons of the measured and computed surface displacement for regular waves at gauges 1 to 7. It can be seen that in general the tested models behave adequately in this experiment. For a more comprehensive analysis a comparison with Gobbi and Kirby's (1999) model, referred to as GK99, is also shown. The latter is a Boussinesq-type model of order $O((kd)^4)$, i.e. of the same level of nonlinearity with MS98. All KK02, KK02e and GK99 models behave quite accurately over the submerged bar. KK02 and KK02e show almost identical performance. They represent well the nonlinear steepening on the upwave slope of the bar and the enhancement and decomposition into higher free harmonics over the crest and the downslope as well. The same comparison is shown in Fig. 2.17 for KM09 and KM09em models. KM09em model gives more accurate results than the basic (weakly nonlinear) version of KM09 model.

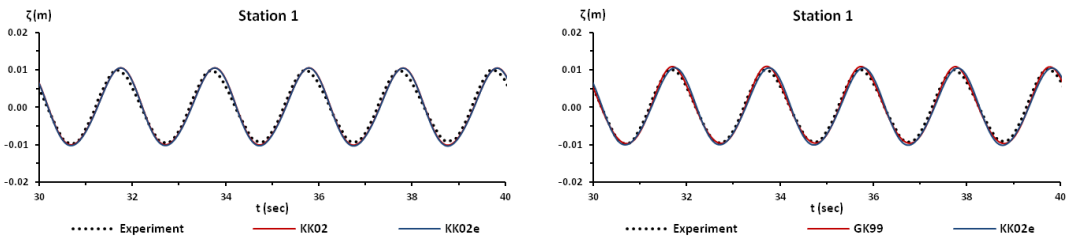

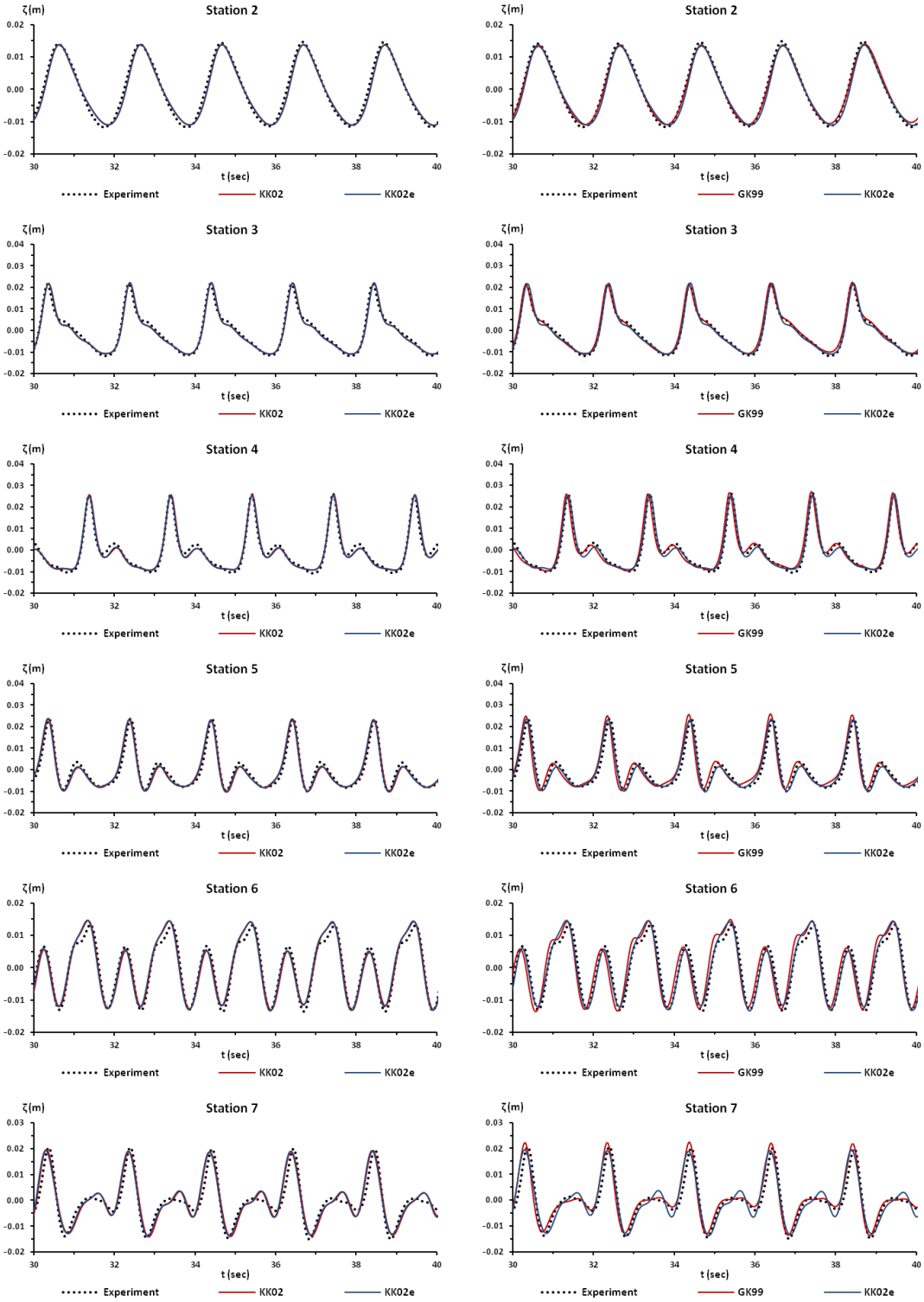

Fig. 2.16. Measured and computed by KK02, KK02e and GK99 models time series of surface elevation.

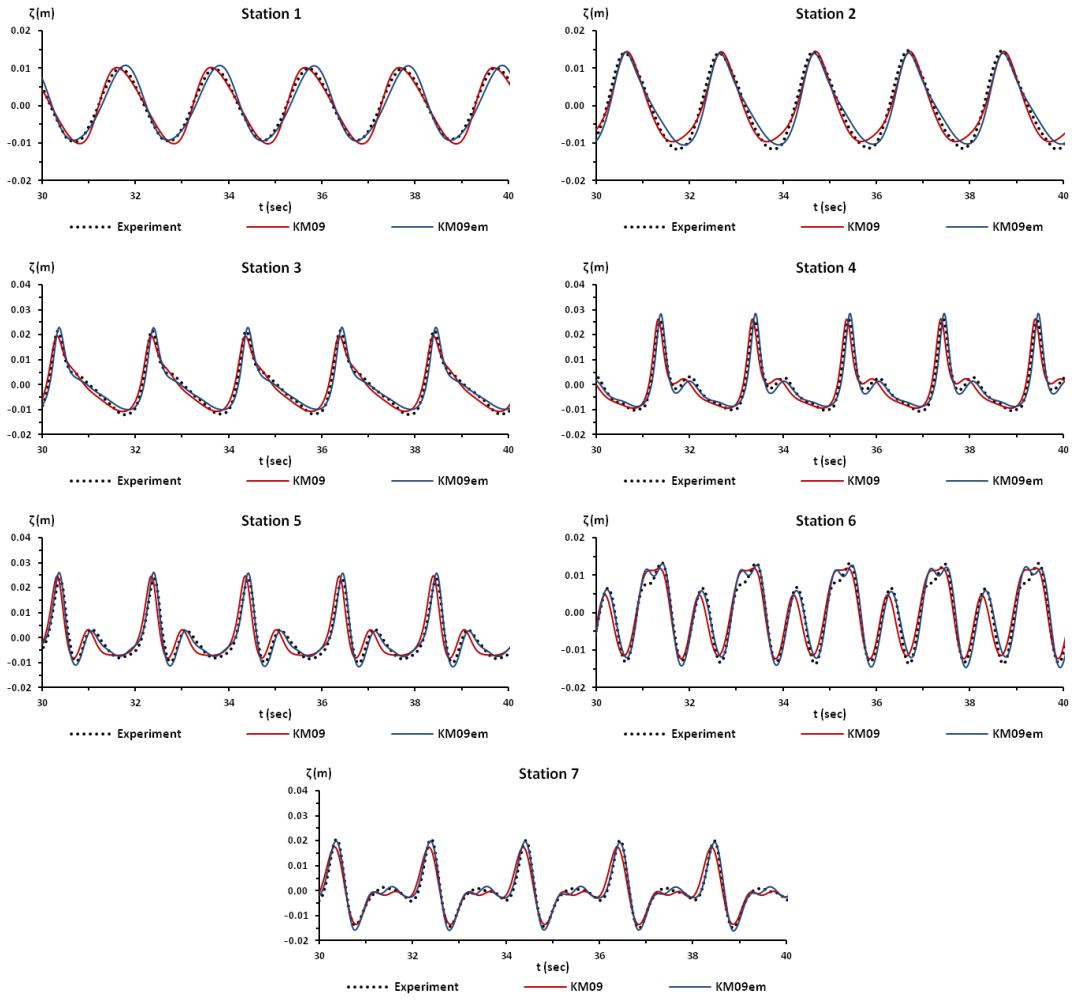

Fig. 2.17. Measured and computed by KM09 and KM09em models time series of surface elevation.

The second test involves irregular non-breaking incident JONSWAP waves with peak frequency f_p = 0.5 Hz and significant wave height H_s = 1.8 cm. Experimental results are presented in Beji and Battjes (1994) who used the same setup shown in Fig. 2.15. Fig. 2.18 provides time series of measured and computed by KK02, KK02e, KM09 and KM09em models surface elevation at six stations. The time series shown extend over a time span of 20 s, i.e. 40 s-60 s from start. Here an improved behaviour of model KM09 over the other models is observed, especially at the most demanding locations, those of Stations 5, 6 and 7, where nonlinearities are more pronounced. The nonlinear wave interactions are quite well represented by KK02 and KK02e models too, which again show almost identical response.

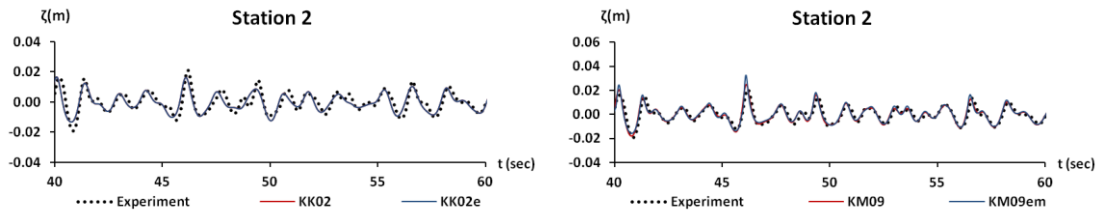

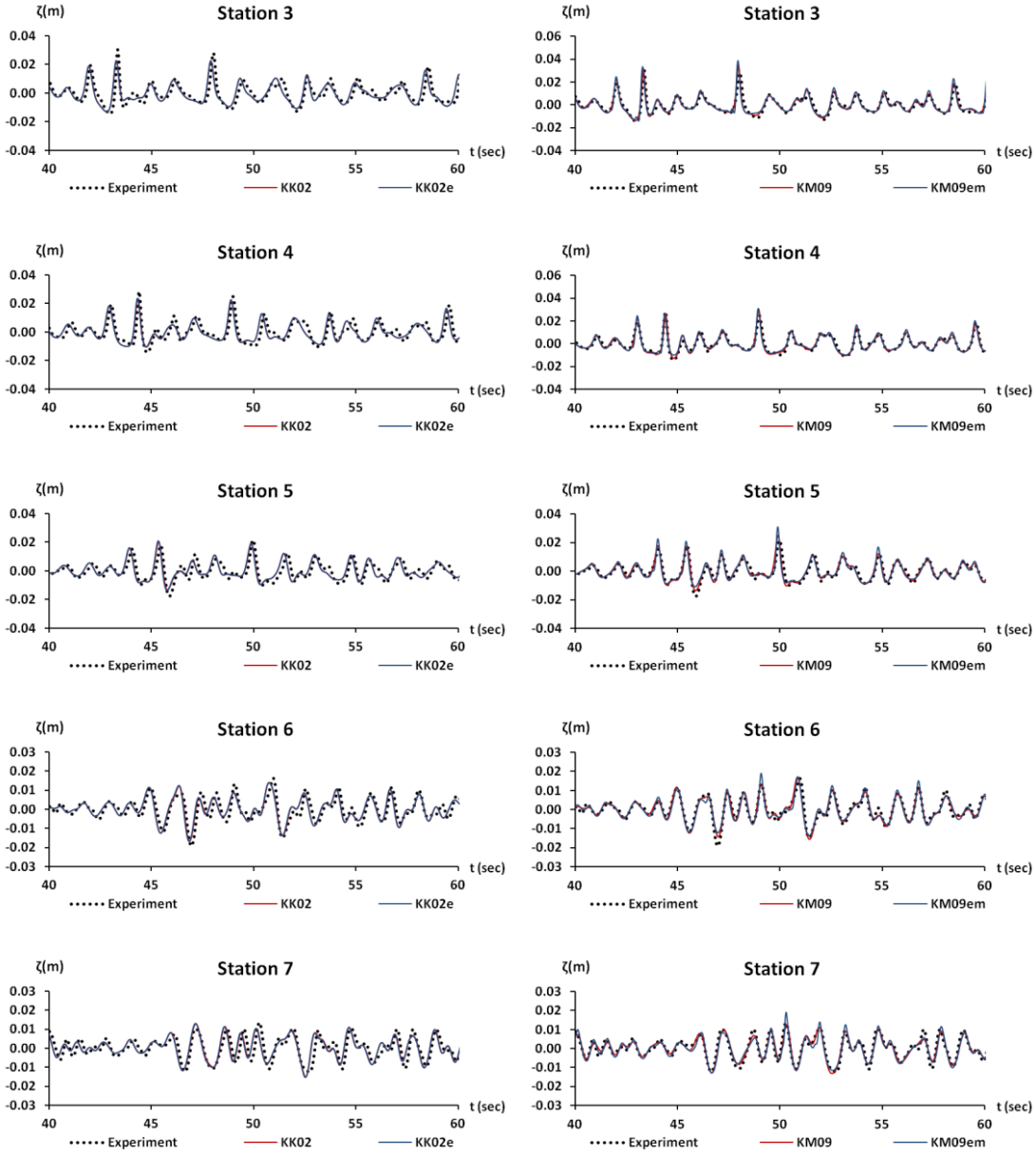

Fig. 2.18. Time series of irregular surface elevation.

In addition to the time series comparisons, wave spectra were also computed from the experimental and the studied models' data. Results are shown in Fig. 2.19 for stations 2 to 7. The computational procedure is the one followed by Beji and Nadaoka (1999). Each record contained 21000 data points but only its part after approximately 10 wave peak periods was used in order to avoid possible contamination of the data due to transients (Ohyama *et al.*, 1994). The remaining 20480 data were divided into 10 segments of 2048 points each as proposed by Beji and Nadaoka (1999). Then each segment was transformed through a Fast Fourier Transform. No tapering technique was applied since the spectral leakage was not significant. The final spectra were obtained after ensemble averaging all the realizations and

frequency smoothing over five neighbouring components. Each spectrum then had 100 degrees of freedom and the statistical error was 14.1%.

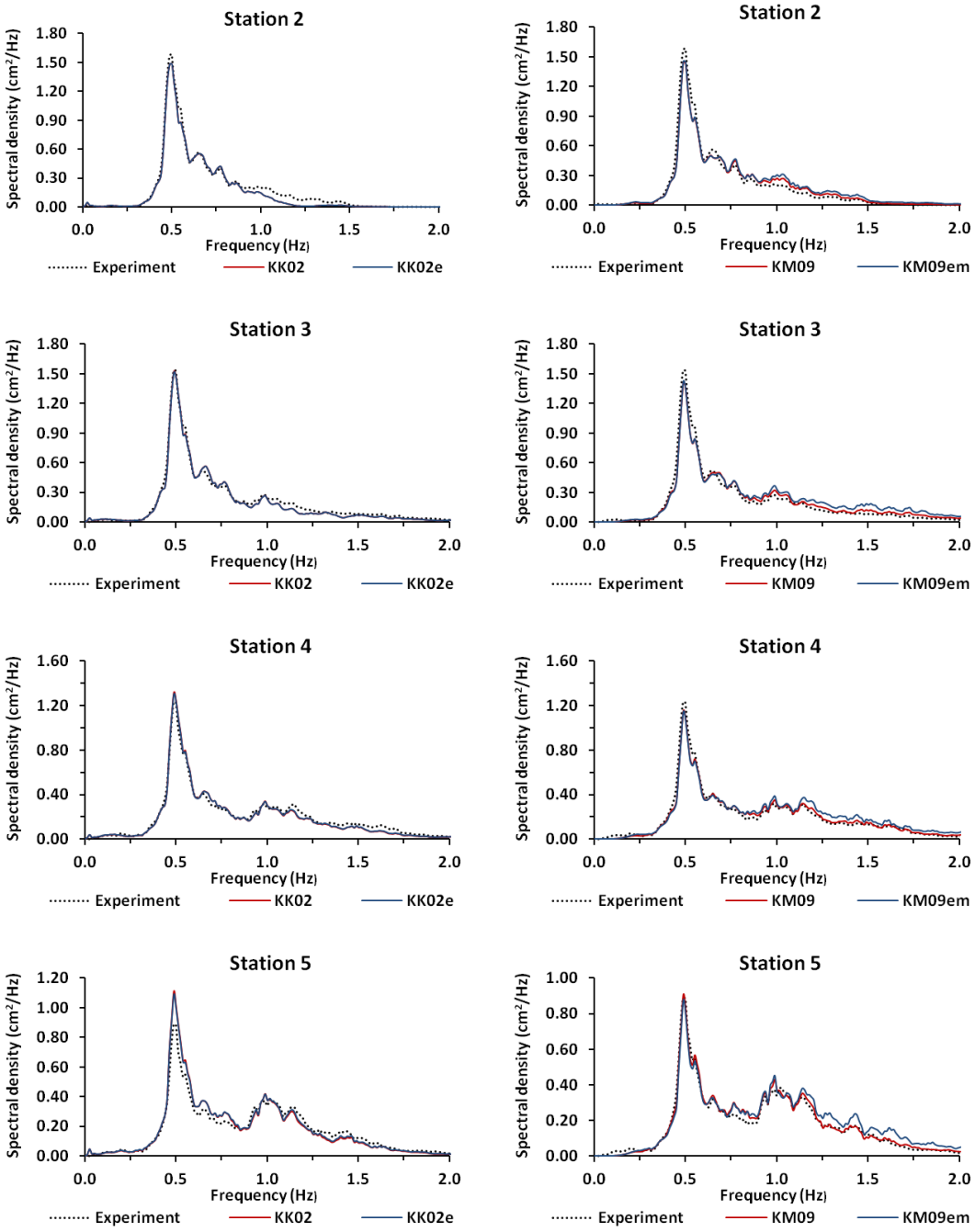

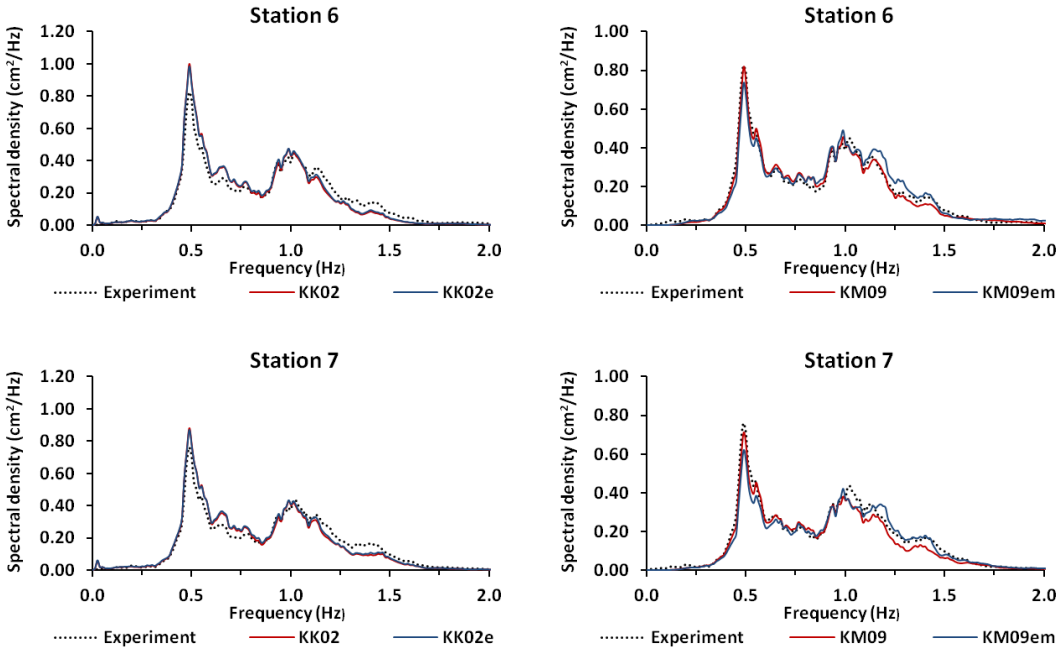

Fig. 2.19. Spectra from measured and computed time series of surface elevation.

The overestimation of the second and higher order transfer functions in shallow water for both versions of KM09 model, along with some spurious low-frequency oscillations produced an overestimation of the spectral density at low frequencies. For this reason a Butterworth third-order high-pass filter was applied considering a half-power point cutoff frequency of f_c = 0.25 Hz. It can be said that in general the computations simulate well the spectral density capturing its transformations along the wave propagation over the obstacle and the nonlinear wave interactions are quite well represented.

2.6 Discussion on higher order models

In traditional Boussinesq equations the nonlinearity is considered weak under the assumption $\varepsilon = O(\sigma^2)$. With this assumption, higher order terms, e.g. of $O(\varepsilon^2\sigma^2)$, are comparable to $O(\sigma^6)$ and are thus neglected. Madsen and Schäffer (1998) allowed the nonlinearity to be stronger and specifically $\varepsilon \sim O(\sigma)$. Their derivation relies on a Taylor expansion of velocity potential with respect to the dispersion parameter σ^2. Since high order terms, up to $O(\varepsilon\sigma^4)$, are retained, the resulting nonlinear characteristics of the equations are very accurate as shown in the above analysis. On the other hand Karambas and Koutitas (2002) followed a similar derivation but terms only up to $O(\varepsilon\sigma^2)$ were retained. Thus inclusion of terms of $O(\varepsilon^2\sigma^2)$ in the extended model KK02e does not increase the order of the resulting higher harmonics solutions with respect to $\kappa = \sigma kd$. Hence, the application field of KK02e equations with regard to higher harmonics is not extended further to deeper water.

On the other hand, these enhanced equations offer an obvious improvement on the nonlinear amplitude dispersion.

The above were verified further in the previous section 2.5, where an almost identical response was found for KK02 weakly and strongly nonlinear models for the simulation of regular wave propagation over a bar. In order to have a clear insight in the level of nonlinear enhancement of KK02e as compared to KK02, an analysis of the various terms of different order in Eq. (2.26) (in dimensional form) was performed. In particular a profile of the maximum absolute value of each term was obtained and is depicted in Fig. 2.20. It is noted that $O(1)$ refers to the term $g\frac{\partial \zeta}{\partial x}$.

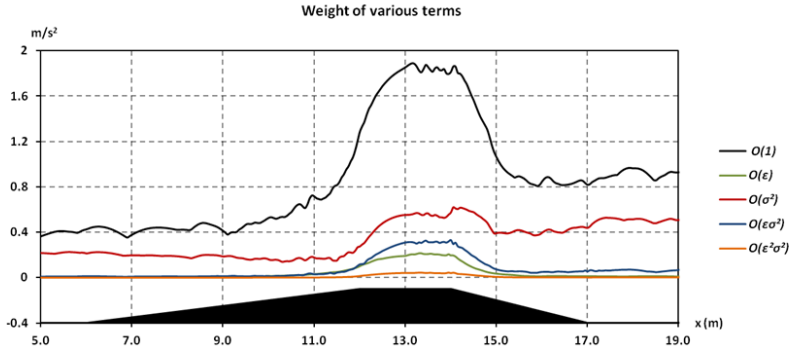

Fig. 2.20. Weight of various terms of different order in KK02e momentum equation in Beji and Battjes's (1994) test.

The lowest-order linear term of $O(1)$ is, as expected, by far the most significant one, about three times the term of $O(\sigma^2)$ and forty times the terms of $O(\varepsilon^2\sigma^2)$. The nonlinear terms are pronounced over the crest and the downslope of the bar, as expected. The contribution of the extra terms of KK02e model of $O(\varepsilon^2\sigma^2)$ is about 14% of the term of $O(\varepsilon\sigma^2)$ and 1.5% of the sum of all terms that already exist in the original model version, KK02.

A similar analysis was also performed for KM09em model and is presented in Fig. 2.21. Here the term of $O(1)$ is about two times the term of $O(\sigma^2)$ and thirty times the terms of $O(\varepsilon\sigma^2)$. The contribution of the extra terms of KM09em model of $O(\varepsilon\sigma^2)$ is about 7% of the term of $O(\sigma^2)$ and 2% of the sum of all terms that already exist in the weakly nonlinear model version, KM09.

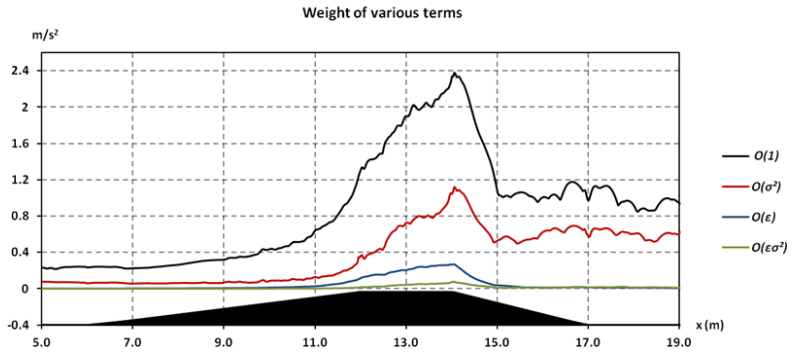

Fig. 2.21. Weight of various terms of different order in KM09em momentum equation in Beji and Battjes's (1994) test.

Despite the previous analysis, it should be mentioned that, in general, the relative height of the various terms may vary in different test cases, e.g. deep water, highly nonlinear waves, etc. In particular, the specific experimental setup refers to a depth range $k'd'$ from 0.32 to 0.67, which corresponds to depths close -from the offshore- to the boundary between intermediate and shallow water, and to a nonlinearity parameter $\varepsilon = 0.05$. However, strongly nonlinear waves can easily be present in intermediate and deep water, that is why such conditions were checked numerically. In these cases the parameters ε and σ^2 have both high values leading to significant terms of $O(\varepsilon^2\sigma^2)$, comparable to those of $O(\varepsilon\sigma^2)$ or even of $O(\sigma^2)$. Zou (1999) examined such a case of near-breaking highly nonlinear waves. Nevertheless, the waves studied herein propagate in deeper water where no breaking due to depth limitation occurs.

In order to further examine the impact of the extra nonlinear terms of order $O(\varepsilon^2\sigma^2)$, three different cases were simulated through KK02 weakly and strongly nonlinear models. All three cases refer to regular waves of period $T = 8$ s propagating over a mildly sloping bed in deep and intermediate water. Fig. 2.22 shows a snapshot of surface elevation for almost linear waves of height $H_0 = 2.0$ m in deep water with nonlinearity parameter $\varepsilon = 0.04$. Due to the low value of ε, terms of order $O(\varepsilon^2\sigma^2)$ are negligible as compared to $O(\varepsilon\sigma^2)$ terms. Hence the results for KK02 weakly and strongly nonlinear models are almost identical.

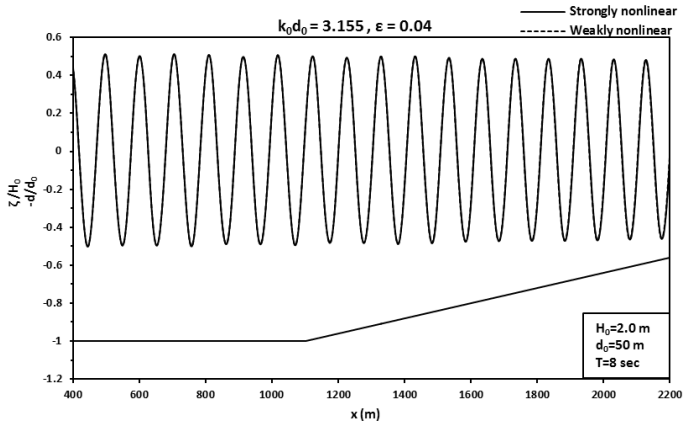

Fig. 2.22. Free surface elevation for KK02 weakly and strongly nonlinear models with nonlinearity parameter $\varepsilon = 0.04$.

Figure 2.23 shows a snapshot for waves of height $H_0 = 7.5$ m. The nonlinearity in this case is higher, $\varepsilon = 0.15$, leading to a slight difference in the results of the two models. The most obvious difference refers to the nonlinear dispersion reported in subsection 2.4.1 too, that produces an increasing shift between the two profiles as shown in this figure.

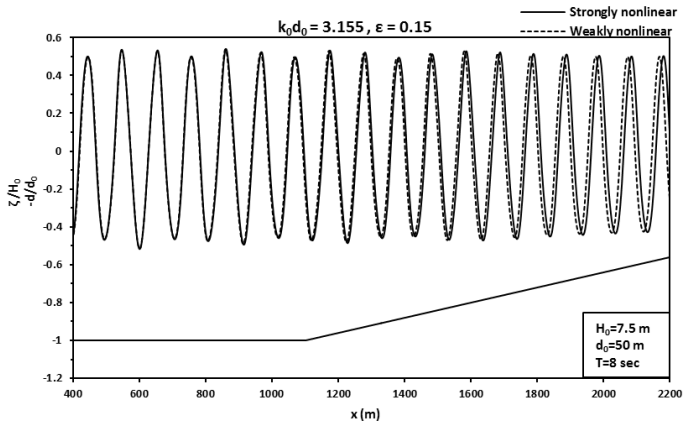

Fig. 2.23. Free surface elevation for KK02 weakly and strongly nonlinear models with nonlinearity parameter $\varepsilon = 0.15$.

Figure 2.24 refers to strongly nonlinear waves with nonlinearity parameter $\varepsilon = 0.24$. In this case the terms of $O(\varepsilon^2\sigma^2)$ are comparable to those of $O(\varepsilon\sigma^2)$, leading to more significant differences between the two versions. Here the shift between the two profiles is more obvious and the differences due to nonlinear dispersion appear to even deeper water than in the previous cases.

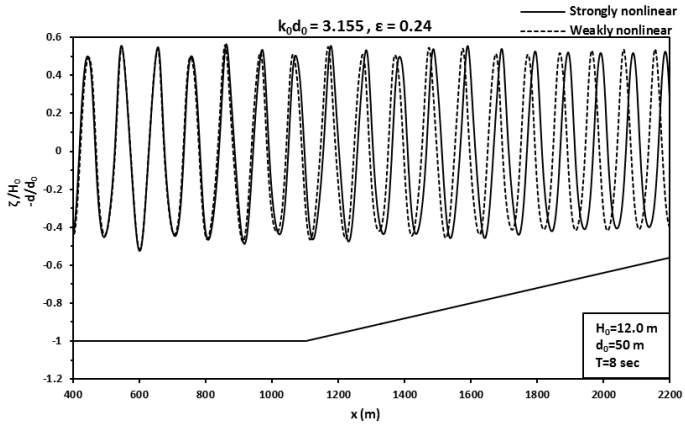

Fig. 2.24. Free surface elevation for KK02 weakly and strongly nonlinear models with nonlinearity parameter $\varepsilon = 0.24$.

On the other hand, terms of $O(\varepsilon\sigma^2)$ are comparable to the ones of $O(\sigma^2)$ in intermediate and deep water for any value of the nonlinearity parameter ε. Hence, the nonlinear characteristics of Karambas and Memos's (2009) original model are not quite representative in deeper water conditions where $\varepsilon\sigma^2 \sim \sigma^2$. Consequently, the results of the modified enhanced nonlinear version of KM09 model differ significantly from the ones of the weakly nonlinear version as presented in the previous analysis and also shown in the verification section. Despite this fact, the nonlinear characteristics of both versions of KM09 model remain quite poor and this is due to the adoption of a linear solution of the Laplace equation. Nevertheless, the validity of Stokes theory as being a target solution for indicating the nonlinearity impact could be a matter of discussion, bearing in mind that, depending on wave parameters, Stokes waves may not be suitable for application in small water depths. Such a reservation would equally apply to the target dispersion relation, since this is a Stokes theory result.

Apart from accuracy, the required computational time is a serious issue when evaluating wave models. Fig. 2.25 shows the ratio of the computational time of KK02 strongly and weakly nonlinear models as a function of the number of time steps. In the same figure the ratio of the computational time of KM09 modified enhanced nonlinear model version to the weakly nonlinear version is also depicted. The models' applications were performed on a quad-core Intel Core i5 processor at 3.33 GHz without parallel computing and the compiler was Microsoft FORTRAN PowerStation 4.0. It is deduced that the extra nonlinear terms of KK02 model increase the computational time by approximately 19%, while the modified enhanced nonlinear version of KM09 requires less than 7% more computational time than its weakly nonlinear counterpart. It should be noted that the curves of Fig. 2.25 are not directly comparable since either weakly or strongly nonlinear models are not of the same degree of nonlinearity. Moreover, for most practical one-dimensional applications, e.g. for a 10 min

simulation, the deviations between the various models correspond to an insignificant difference of only a few seconds in absolute time. On the other hand, in the two-dimensional version of KM09 model the evaluation of the convolution integral increases significantly the computational cost compared to KK02 model, despite the latter's mathematical complexity (see Karambas and Memos, 2009). In brief, the computational time of the aforementioned models is expected somewhat increased compared to lower order models that employ similar numerical schemes (Nwogu, 1993; Wei and Kirby, 1995).

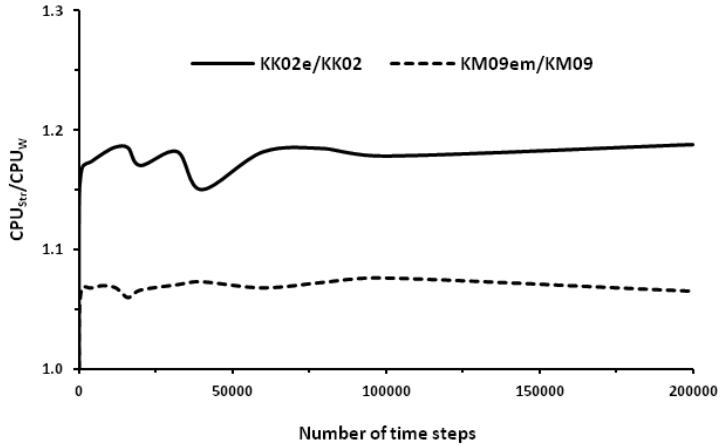

Fig. 2.25. Comparison of computational time for KK02, KK02e, KM09, and KM09em models.

In the light of the discussion about the nonlinear response of the presented models an important aspect refers to their behaviour in conjunction to a wave breaking model. Although wave breaking due to depth limitation takes place in shallower water, thus the dispersion parameter σ has locally low values, close to incipient wave breaking the conditions are highly nonlinear. Hence the nonlinear parameter ε may take values close to unity or even higher. Consequently, the nonlinear terms of $O(\varepsilon, \varepsilon\sigma^2, \varepsilon^2\sigma^2)$ or higher have an important impact on the models' accuracy. In the absence of these terms the breaking initiation may be erroneously estimated. Extension to the surf zone has been accomplished for KM09 model relying on either the surface roller or the eddy viscosity concept and both approaches gave similar results (Chondros *et al*., 2011; Klonaris *et al*. 2013). Additionally, wave breaking has been incorporated in KK02 model by Karambas and Koutitas (2002) based on the surface roller concept. All these models have shown fairly good response.

The original range of applicability of Boussinesq equations provides for mild nonlinearity. However, several enhancements of the nonlinear characteristics were achieved during the past couple of decades. These modifications proved to work well, although they were actually violating the underlying assumptions of the original equations. Nevertheless, extension of the nonlinear features of the said equations is not a straightforward procedure. Through the

presented investigation it can be concluded that there is no clear-cut answer whether nonlinear upgrading offers notable enhancements affording a wider range of applicability. Thus, it can be reasonably argued that not any strengthening of nonlinearity is bound to pay off the extra time and effort required, induced mainly by the many complications introduced by the, sometimes very many, extra terms included in the formulation of the model equations. Also, it should be underlined that the details of the numerical treatment may play a significant role in the quality of the associated results. However, in general, it can be said that each one of the presented nonlinear enhancements offers its potential over a specific range of conditions.

From the nonlinear analysis presented in this chapter, it can be argued that KK02e model offers an improvement over KK02 with respect to nonlinear dispersion and under highly nonlinear conditions, e.g. close to the surf zone. This result is further confirmed in chapter 3. However, there is a wide range of conditions under which KK02e does not show any significant improvement over KK02 model. On the other hand, KM09em does not represent appreciable advances over its counterpart of weak nonlinearity. In some of the cases studied herein even the opposite result was true. In addition, in the two-dimensional version of KM09 model the evaluation of the convolution integral increases significantly the computational cost compared to KK02e model, despite the latter's mathematical complexity, as mentioned above. Moreover, retaining terms of higher order than the ones in KK02e model would go beyond the objective of the present thesis, in addition to the increase of the computational complexity and the possibility of numerical instabilities. Thus, KK02e model and its two-dimensional counterpart were chosen to form the basis of the compound model developed in the present thesis.

References

Abbott, M. B., McCowan, A. D., and Warren, I. R. (1984). "Accuracy of short-wave numerical model." *J. Hydr. Eng.*, 110(10), 1287-1301.

Agnon, Y., Madsen, P. A., and Schäffer, H. A. (1999). "A new approach to high-order Boussinesq models." *J. Fluid Mech.*, 399, 319-333.

Airy, G. B. (1845). "Tides and waves." *Encycl. Metrop.*, Art. 192, 241-396.

Antuono, M., and Brocchini, M. (2013). "Beyond Boussinesq-type equations: Semi-integrated models for coastal dynamics." *Phys. Fluids*, 25, 016603, 21 pp.

Battjes, J. A., and Beji, S. (1991). "Spectral evolution in waves traveling over a shoal." *Proc. Nonlinear Water Waves Workshop*, D. H. Peregrine, ed., University of Bristol, 11-19.

Beji, S., and Battjes, J. A. (1993). "Experimental investigation of wave propagation over a bar." *Coast. Eng.*, 19(1-2), 151-162.

Beji, S., and Battjes, J. A. (1994). "Numerical simulation of nonlinear wave propagation over a bar." *Coast. Eng.*, 23(1-2), 1-16.

Beji, S., and Nadaoka, K. (1996). "A formal derivation and numerical modelling of the improved Boussinesq equations for varying depth." *Ocean Eng.*, 23(8), 691-704.

Beji, S., and Nadaoka, K. (1999). "A spectral model for unidirectional nonlinear wave propagation over arbitrary depths." *Coast. Eng.*, 36(1), 1-16.

Benjamin, T. B., Bona, J. L., and Mahony, J. J. (1972). "Model equations for long waves in non-linear dispersive systems." *Phil. Trans. R. Soc. Lond. A*, 272(1220), 47-78.

Benjamin, T. B., and Feir, J. E. (1967). "The disintegration of wave trains on deep water. Part 1. Theory" *J. Fluid Mech.*, 27(3), 417-430.

Berkhoff, J. C. W. (1972). "Computation of combined Refraction – Diffraction." *Proc. 13th Int. Conf. on Coastal Engineering*, ASCE, Vancouver, Canada, 471-490.

Bingham, H. B., and Agnon, Y. (2005). "A Fourier–Boussinesq method for nonlinear water waves." *Eur. J. Mech. B/Fluids*, 24(2), 255-274.

Boussinesq, J. (1871). "Théorie de l' intumescence liquede appelée onde solitaire ou de translation, se propageant dans un canal rectangulaire." *Comptes Rendus de l' Academie des Sciences*, 72, 755-759.

Boussinesq, M. J. (1872). "Théorie des ondes et des remous qui se propagent le long d' un canal rectangulaire horizontal, en communiquant au liquide contenu dans ce canal des vitesses sensiblement pareilles de la surface au fond." *J. Math. Pures Appl.*, Deuxième Série, 17: 55-108.

Brocchini, M. (2013). "A reasoned overview on Boussinesq-type models: the interplay between physics, mathematics and numerics." *Proc. R. Soc. A*, 469(2160), 20130496.

Broer, L. J. F. (1974). "On the Hamiltonian theory of surface waves." *Appl. Sei. Res.*, 30, 430-446.

Broer, L. J. F. (1975). "Approximate equations for long water waves." *Appl. Sei. Res.*, 31, 377-395.

Broer, L. J. F., van Groesen, E. W. C., and Timmers, J. M. W. (1976). "Stable model equations for long water waves." *Appl. Sei. Res.*, 32, 619-636.

Chen, Q. (2006). "Fully nonlinear Boussinesq-type equations for waves and currents over porous beds." *J. Eng. Mech.*, 132 (2), 220-230.

Chen, Q., Kirby, J. T., Dalrymple, R. A., Shi, F., and Thornton, E. B. (2003). "Boussinesq modeling of longshore currents." *J. Geophys. Res.*, 108 (C11), 3362, doi: 10.1029/2002JC001308.

Chen, Y., and Liu, P. L.-F. (1995). "Modified Boussinesq equations and associated parabolic models for water wave propagation." *J. Fluid Mech.*, 288, 351-381.

Chester, W. (1968). "Resonant oscillations of water waves. I. Theory." *Proc. R. Soc. Lond. A*, 306(1484), 5-22.

Chondros, M. K., Koutsourelakis, I. G., and Memos, C. D. (2011). "A Boussinesq-type model incorporating random wave breaking." *J. Hydraul. Res.*, 49 (4), 529–538.

Chondros, M. K., and Memos, C. D. (2014). "A 2DH nonlinear Boussinesq-type wave model of improved dispersion, shoaling, and wave generation characteristics." *Coast. Eng.*, 91, 99-122.

Dingemans M. (1973). "Water waves over an uneven bottom; a discussion of long-wave equations." *Technical Report*, R729, part 2, Delft Hydraulics, Delft, The Netherlands.

Dingemans, M. W. (1994a). "Comparison of computations with Boussinesq-like models and laboratory measurements." *MAST-G8M note*, H1684, Delft Hydraulics, 32 pp.

Dingemans, M. W. (1994b). "Water wave propagation over uneven bottoms." Ph.D. thesis, Delft University of Technology.

Fang, K., Liu, Z., Gui, Q., Zou, Z., and Yin, J. (2013). "Alternative forms of enhanced Boussinesq equations with improved nonlinearity." *Mathematical Problems in Engineering*, vol. 2013, Article ID 160749, Hindawi Publishing Corporation, doi: 10.1155/2013/160749.

Fang, K. Z., and Zou, Z. L. (2010). "Boussinesq-type equations for nonlinear evolution of wave trains." *Wave Motion*, 47(1), 12-32.

Fuhrman, D. R., and Madsen, P. A. (2009). "Tsunami generation, propagation, and run-up with a high-order Boussinesq model." *Coast. Eng.*, 56(7), 747-758.

Galan, A., Simarro, G., Orfila, A., Simarro, J., and Liu, P. L.-F. (2012). "Fully nonlinear model for water wave propagation from deep to shallow waters." *J. Waterway, Port, Coastal, Ocean Eng.*, 10.1061/(ASCE)WW.1943-5460.0000143, 362-371.

Gobbi, M. F., and Kirby, J. T. (1999). "Wave evolution over submerged sills: tests of a high-order Boussinesq model." *Coast. Eng.*, 37(1), 57-96.

Gobbi, M., Kirby, J. T., and Kennedy, A. B. (2000a). "On the consistency of fully nonlinear Boussinesq models and their ability to predict vertical vorticity fields." *Proc. 27th Int. Conf. on Coastal Engineering*, B. L. Edge, ed., Sydney, Australia, 1321-1334.

Gobbi, M. F., Kirby, J. T., and Wei, G. (2000b). "A fully nonlinear Boussinesq model for surface waves. Part 2. Extension to $O(kh)^4$." *J. Fluid Mech.*, 405, 181-210.

Green, A. E., Laws, N., and Naghdi, P. M. (1974). "On the theory of water waves." *Proc. R. Soc. Lond. A*, 338(1612), 43-55.

Green, A. E., and Naghdi, P. M. (1976). "A derivation of equations for wave propagation in water of variable depth." *J. Fluid Mech.*, 78(2), 237-246.

Infeld, E., and Rowlands, G. (1990). *Nonlinear waves, Solitons and Chaos*, Cambridge University Press, 423 pp.

Karambas, Th. V. (1999). "A unified model for periodic non-linear dispersive waves in intermediate and shallow water." *J. Coast. Res.*, 15(1), 128-139.

Karambas, Th. V., and Karathanassi, E. K. (2004). "Longshore sediment transport by nonlinear waves and currents." *J. Waterw. Port Coast. Ocean Eng.*, 130(6), 277-286.

Karambas, Th. V., and Koutitas, C. (2002). "Surf and swash zone morphology evolution induced by nonlinear waves." *J. Waterway, Port, Coastal, Ocean Eng.*, 10.1061/(ASCE)0733-950X(2002)128:3(102), 102-113.

Karambas, Th. V., and Memos, C. D. (2009). "Boussinesq model for weakly nonlinear fully dispersive water waves." *J. Waterway, Port, Coastal, Ocean Eng.*, 10.1061/(ASCE)0733-950X(2009)135:5(187), 187-199.

Kennedy, A. B., Kirby, J. T., Chen, Q., and Dalrymple, R. A. (2001). "Boussinesq-type equations with improved nonlinear performance." *Wave Motion*, 33(3), 225-243.

Kirby, J. T. (1997). "Nonlinear, dispersive long waves in water of variable depth." In: Gravity Waves in Water of Finite Depth, J. N. Hunt, ed., *Advances in Fluid Mechanics*, vol. 10, pp. 55-125, Computational Mechanics Publications.

Kirby, J. T. (2003). "Boussinesq models and applications to nearshore wave propagation, surf zone processes and wave-induced currents." *Advances in Coastal Modelling*, V. C. Lakhan, ed., pp. 1-41, Elsevier.

Kirby, J. T. (2016). "Boussinesq models and their application to coastal processes across a wide range of scales." *J. Waterw. Port Coast. Ocean Eng.*, 10.1061/(ASCE)WW.1943-5460.0000350, 03116005.

Kirby, J. T., Shi, F., Tehranirad, B., Harris, J. C., and Grilli, S. T. (2013). "Dispersive tsunami waves in the ocean: Model equations and sensitivity to dispersion and Coriolis effects." *Ocean Model.*, 62, 39-55.

Klonaris, G. Th., Memos, C. D., and Karambas, Th. V. (2013). "A Boussinesq-type model including wave-breaking terms in both continuity and momentum equations." *Ocean Eng.*, 57, 128-140.

Korteweg, D. J., and Vries, G. de (1895). "On the change of form of long waves advancing in a rectangular canal, and on a new type of long stationary waves." *Phil. Mag.*, Series 5, 39 (240), 422-443.

Lamb, H. (1932). *Hydrodynamics* (6th ed.), University Press, Cambridge, 738 pp.

Li, B. (2008). "Wave equations for regular and irregular water wave propagation." *J. Waterway, Port, Coastal, Ocean Eng.*, 10.1061/(ASCE)0733-950X(2008)134:2(121), 121-142.

Lighthill, J. (1978). *Waves in fluids*, Cambridge University Press, 504 pp.

Liu, Z., and Fang, K. (2015). "Two-layer Boussinesq models for coastal water waves." *Wave Motion*, 57, 88-111.

Lynett, P., and Liu, P. L.-F. (2004a). "A two-layer approach to wave modelling." *Proc. R. Soc. Lond. A*, 460(2049), 2637-2669.

Lynett, P., and Liu, P. L.-F. (2004b). "Linear analysis of the multi-layer model." *Coast. Eng.*, 51(5-6), 439-454.

Ma, G., Shi, F., and Kirby, J. T. (2012). "Shock-capturing non-hydrostatic model for fully dispersive surface wave processes." *Ocean Model.*, 43-44, 22-35.

Madsen, P. A., Bingham, H. B., and Liu, H. (2002). "A new Boussinesq method for fully nonlinear waves from shallow to deep water." *J. Fluid Mech.*, 462, 1-30.

Madsen, P. A., Bingham, H. B., and Schäffer, H. A. (2003). "Boussinesq-type formulations for fully nonlinear and extremely dispersive water waves: derivation and analysis." *Proc. R. Soc. Lond. A*, 459(2033), 1075– 1104.

Madsen, P. A., and Fuhrman, D. R. (2010). "High-order Boussinesq-type modelling of nonlinear wave phenomena in deep and shallow water." In: Advances in numerical simulation of nonlinear water waves, Q. Ma, ed., *Advances in Coastal and Ocean Engineering*, vol. 11, pp. 245-285, World Scientific.

Madsen, P. A., Fuhrman, D. R., and Wang, B. (2006). "A Boussinesq-type method for fully nonlinear waves interacting with a rapidly varying bathymetry." *Coast. Eng.*, 53(5-6), 487-504.

Madsen, P. A., Murray, R., and Sørensen, O. R. (1991). "A new form of the Boussinesq equations with improved linear dispersion characteristics." *Coast. Eng.*, 15(4), 371-388.

Madsen, P. A., and Schäffer, H. A. (1998). "Higher-order Boussinesq-type equations for surface gravity waves: derivation and analysis." *Phil. Trans. R. Soc. Lond. A*, 356(1749), 3123-3184.

Madsen, P. A., and Schäffer, H. A. (1999). "A review of Boussinesq-type equations for gravity waves." *Advances in Coastal and Ocean Engineering*, P. L.-F. Liu, ed., vol. 5, pp. 1-95, World Scientific.

Madsen, P. A., and Sørensen, O. R. (1992). "A new form of the Boussinesq equations with improved linear dispersion characteristics. Part 2. A slowly-varying bathymetry." *Coast. Eng.*, 18(3-4), 183-204.

Madsen, P. A., and Sørensen, O. R. (1993). "Bound waves and triad interactions in shallow water." *Ocean Eng.*, 20(4), 359-388.

McLean, J. W., Ma, Y. C., Martin, D. U., Saffman, P. G., and Yuen, H. C. (1981). "Three-dimensional instability of finite-amplitude water waves." *Phys. Rev. Lett.*, 46(13), 817–820.

Mei, C. C., and Le Méhauté, B. (1966). "Note on the equations of long waves over an uneven bottom." *J. Geophys. Res.*, 71(2), 393-400.

Mei, C. C. (1989). *The Applied Dynamics of Ocean Surface Waves*, World Scientific, 740 pp.

Memos, C. D., Karambas, Th. V., and Avgeris, I. (2005). "Irregular wave transformation in the nearshore zone: experimental investigations and comparison with a higher order Boussinesq model." *Ocean Eng.*, 32(11-12), 1465-1485.

Memos, C. D., Klonaris, G. Th., Chondros, M. K. (2016). "On higher order Boussinesq-type wave models." *J. Waterw. Port Coast. Ocean Eng.*, 142 (1), 04015011.

Nwogu, O. (1993). "Alternative form of Boussinesq equations for nearshore wave propagation." *J. Waterway, Port, Coastal, Ocean Eng.*, 10.1061/(ASCE)0733-950X(1993)119:6(618), 618-638.

Ohyama, T., Beji, S., Nadaoka, K., and Battjes, J. A. (1994). "Experimental verification of numerical model for nonlinear wave evolutions." *J. Waterway, Port, Coastal, Ocean Eng.*, 10.1061/(ASCE)0733-950X(1994)120:6(637), 637-644.

Ottesen-Hansen, N. E. (1978). "Long period waves in natural wave trains." *Progress report*, No. 46, Institute of Hydrodynamics and Hydraulic Engineering, Technical University of Denmark, pp. 13-24.

Peregrine, D. H. (1967). "Long waves on a beach." *J. Fluid Mech.*, 27 (4), 815-827.

Radder, A. C. (1992). "An explicit Hamiltonian formulation of surface waves in water of finite depth." *J. Fluid Mech.*, 237, 435-455.

Rego, V. S., and Neves, C. F. (1997). "A Boussinesq-type wave model with vertical shear." *Ocean Wave Measurement and Analysis: Proceedings of the Third International Symposium Waves 97*, edited by B. L. Edge *et al*., ASCE, Reston, Va., 446-460.

Sand, S. E., and Mansard, E. P. D. (1986). "Reproduction of higher harmonics in irregular waves." *Ocean Eng.*, 13(1), 57-83.

Schäffer, H. A. (2004a). "Another step towards a post-Boussinesq wave model." *Proc. 29th Int. Conf. on Coastal Engineering*, J. M. Smith, ed., Lisbon, Portugal, 132-144.

Schäffer, H. A. (2004b). "Accurate determination of internal kinematics from numerical wave model results." *Coast. Eng.*, 50(4), 199-211.

Schäffer, H. A. (2006). "Progress on a convolution method for nonlinear, dispersive wave transformation over gently varying bathymetry." *Proc. 30th Int. Conf. on Coastal Engineering*, J. M. Smith, ed., San Diego, California, U.S.A., 149-156.

Schäffer, H. A. (2009). "A fast convolution approach to the transformation of surface gravity waves: Linear waves in 1DH." *Coast. Eng.*, 56(5-6), 517-533.

Schäffer, H. A. (2012). "Towards wave disturbance in ports computed by a deterministic convolution-type model." *Proc. 33rd Int. Conf. on Coastal Engineering*, P. Lynett and J. M. Smith, eds, Santander, Spain, 1(33), waves.7. doi:10.9753/icce.v33.waves.7.

Schäffer, H. A., and Madsen, P. A. (1995). "Further enhancements of Boussinesq-type equations." *Coast. Eng.*, 26(1-2), 1-14.

Schröter, A., Mayerle, R., and Zielke, W. (1994). "Optimized dispersion characteristics of the Boussinesq wave equations." *Proc. Waves-Physical and Numerical Modelling*, M. Isaacson and M. Quick, eds, University of British Columbia, Vancouver, Canada, 416-425.

Seabra-Santos, F. J., Renouard, D. P., and Temperville, A. M. (1987). "Numerical and experimental study of the transform of a solitary wave over a shelf or isolated obstacle." *J. Fluid Mech.*, 176, 117-134.

Serre, F. (1953) "Contribution à l' étude des écoulements permanents et variables dans les canaux." *Houille Blanche*, 3, 374-385.

Shen, C. Y. (2001). "Constituent Boussinesq equations for waves and currents." *J. Phys. Oceanogr.*, 31(3), 850– 859.

Shi, F., Dalrymple, R. A., Kirby, J. T., Chen, Q., and Kennedy, A. B. (2001). "A fully nonlinear Boussinesq model in generalized curvilinear coordinates." *Coast. Eng.*, 42(4), 337–358.

Shi, F., Kirby, J. T., Harris, J. C., Geiman, J. D., and Grilli, S. T. (2012). "A high-order adaptive time-stepping TVD solver for Boussinesq modeling of breaking waves and coastal inundation." *Ocean Model.*, 43-44, 36-51.

Simarro, G., Galan, A., Minguez, R., and Orfila, A. (2013). "Narrow banded wave propagation from very deep waters to the shore." *Coast. Eng.*, 77, 140-150.

Skjelbreia, L., and Hendrickson, J. (1960). "Fifth order gravity wave theory." *Proc. 7th Int. Conf. on Coastal Engineering*, J. W. Johnson, ed., Vol. 1, The Hague, Netherlands, 184-196.

Tsutsui, S., Suzuyama, K., and Ohki, H. (1998). "Model equations of nonlinear dispersive waves in shallow water and an application of its simplified version to wave evolution on the step-type reef." *Coast. Eng. J.*, 40(1), 41-60.

Ursell, F. (1953). "The long-wave paradox in the theory of gravity waves." *Proc. Camb. Philos. Soc*., 49(4), 685-694.

Veeramony, J., and Svendsen, I. A. (2000). "The flow in surf-zone waves." *Coast. Eng.*, 39(2-4), 93-122.

Wei, G., and Kirby, J. T. (1995). "Time-dependent numerical code for extended Boussinesq equations." *J. Waterway, Port, Coastal, Ocean Eng.*, 10.1061/(ASCE)0733-950X(1995)121:5(251), 251-261.

Wei, G., Kirby, J. T., Grilli, S. T., and Subramanya, R. (1995). "A fully nonlinear Boussinesq model for surface waves. Part 1. Highly nonlinear unsteady waves." *J. Fluid Mech.*, 294, 71-92.

Whitham, G. B. (1974). *Linear and nonlinear waves*, Wiley-Interscience, 636 pp.

Witting, J. M. (1984). "A unified model for the evolution of nonlinear water waves." *J. Comput. Phys.*, 56(2), 203-236.

Wu, T. Y. (1999). "Modelling nonlinear dispersive water waves." *J. Eng. Mech.*, 125(7), 747-755.

Wu, T. Y. (2001). "A unified theory for modelling water waves." *Adv. Appl. Mech.*, 37, 1-88.

Zhang, Y., Kennedy, A. B., Donahue, A. S., Westerink, J. J., Panda, N., and Dawson, C. (2014). "Rotational surf zone modeling for $O(\mu^4)$ Boussinesq–Green–Naghdi systems." *Ocean Model.*, 79, 43-53.

Zou, Z. L. (1999). "Higher order Boussinesq equations." *Ocean Eng.*, 26(8), 767-792.

Zou, Z. L. (2000). "A new form of higher order Boussinesq equations." *Ocean Eng.*, 27(5), 557-575.

Zou, Z. L., and Fang, K. Z. (2008). "Alternative forms of the higher-order Boussinesq equations: Derivations and validations." *Coast. Eng.*, 55(6), 506-521.

Zou, Z. L., Liu, Z. B., and Fang, K. Z. (2009). "Further improvements to the higher-order Boussinesq equations: Bragg reflection." *Coast. Eng.*, 56(5-6), 672-687.

Chapter 3

Integrating nearshore dynamics with the Boussinesq-type wave model

3.1 Introduction

Since Peregrine (1967) derived the "classical" Boussinesq equations for water waves assuming weak dispersion and weak nonlinearity, many models of this type have been presented to extend the range of applicability further offshore. This was achieved by introducing different kinds of modifications to the original assumptions, and these models are hence loosely referred to as Boussinesq-type models. A thorough review of existing Boussinesq-type wave models was presented in chapter 2.

The main scope of the research concerning Boussinesq-type models has been the enhancement of their dispersive and nonlinear character in order to be applicable to more and more deep water and finally face no limitation with respect to depth. Aiming at upgrading the linear and nonlinear properties, different formulations have been proposed based on the depth-integrated velocities (Abbott *et al*., 1984; Madsen *et al*., 1991), the depth-averaged velocities (Beji and Nadaoka, 1996; Zou, 1999; Memos *et al*., 2005) or the velocities at an arbitrary level (Nwogu, 1993, Wei and Kirby, 1995). Further on, even more upgraded equations have been derived by retaining higher order terms or applying linear enhancement techniques (Wei *et al*., 1995; Schäffer and Madsen, 1995; Madsen and Schäffer, 1998; Gobbi *et al*., 2000a). More recently, some advanced post-Boussinesq models have been presented to achieve high accuracy in both dispersion and nonlinear characteristics (Madsen *et al*., 2002; Lynett and Liu, 2004; Karambas and Memos, 2009).

Modelling satisfactorily the combined physical processes present throughout the entire coastal zone, from offshore to the shoreline, is a crucial point for a variety of applications ranging from sedimentation studies to the design of coastal defences. Hence, extending the applicability inshore has been another challenge for the Boussinesq modelling community,

maybe even harder than extending offshore, since complex phenomena such as surf and swash zone dynamics have to be adequately reproduced.

Boussinesq-type models have been extended into the surf zone by mainly three different techniques to simulate wave breaking. The first one relies on the eddy viscosity concept that introduces extra dissipative terms (Zelt, 1991; Karambas and Koutitas, 1992; Kennedy *et al*., 2000). The second one is based on the surface roller approach (Svendsen, 1984; Deigaard, 1989; Brocchini *et al*., 1991, 1992; Schäffer *et al*., 1992, 1993). Both techniques have been proven to give similar results in most of the cases (Chondros *et al*., 2011). A combination of the two techniques was applied by Karambas and Tozer (2003). Also, Cienfuegos *et al*. (2010) and Klonaris *et al*. (2013) combined the two methods by introducing an extra dissipative term into the mass equation. The last approach employs the vorticity transport model (Veeramony and Svendsen, 2000; Briganti *et al*., 2004; Musumeci *et al*., 2005; Kim *et al*., 2009). More recently, another approach turns off the dispersive terms in the vicinity of the breaking roller and allows the dissipative nature of shallow water bores to remove energy from waves while conserving momentum (Tonelli and Petti, 2009; Roeber *et al*., 2010; Shi *et al*., 2012; Tissier *et al*., 2012; Gallerano *et al*., 2014). This shallow water bore concept requires shock-capturing numerical schemes to ensure stability at the bore front but is relatively simple to implement.

Simulating the complete nearshore wave transformation requires treatment of the moving shoreline. Extending Boussinesq-type models to the swash zone is a quite hard numerical task. Three major groups of computational procedures have been developed. The first one is based on coordinate transformation techniques following the water edge (Pedersen and Gjevik, 1983; Özkan and Kirby, 1995). The second approach relies on the grid draining and filling (Liu *et al.*, 1995; Militello *et al.*, 2004). A direct comparison between coordinate-transformation techniques and the more common wetting and drying method can be found in Brocchini *et al*. (2002). The third approach includes techniques that treat the entire computational field as active fluid domain. An example in this category is the slot method (Tao, 1983; Madsen *et al*., 1997). Also, the pioneering work by Bellotti and Brocchini (2001) provides shoreline boundary conditions by means of techniques valid for hyperbolic systems. Some other moving boundary techniques have been also proposed such as Lynett *et al*.'s (2002) linear extrapolation method. Finally, the Finite Volume approach has been also successfully applied to define the wet/dry interface through the implementation of suitable Riemann solvers. Examples of different types of FV techniques in combination with Boussinesq equations can be found in Roeber *et al*. (2010), Roeber and Cheung (2012), Shi *et al*. (2012), and Kazolea *et al*. (2012).

An important factor in coastal modelling is the wave-induced current field. The classical procedure for describing wave-driven depth-averaged currents relies on a decoupled approach. Firstly, the wave field is determined by a linear wave model and then the currents are computed from the depth-integrated flow equations including radiation stresses, bottom friction and viscosity. However, one of the advantages of nonlinear Boussinesq-type models is that they can estimate the wave-induced depth-averaged current field without the need to decouple the wave and current motion. This capability was firstly stated by Basco (1983) and is of great importance, not only because the application of a single numerical model is required only, but also because the wave-current interaction is "internally" taken into account. However, besides the correct parameterization of the energy dissipation due to breaking and bottom friction, the correct Doppler shift for wave-current interaction needs to be enforced (Yoon and Liu, 1989; Chen *et al*., 1998). The interaction between wave groups and low-frequency motions can also be described by nonlinear Boussinesq-type models in addition to the steady circulation. Pure hydrostatic models based on the nonlinear shallow water equations (NSWE) can also partly describe the wave-induced currents but they are unable to describe the wave dispersion. Thus, the combined effects of wave-wave and wave-current interaction are insufficiently reproduced in intermediate water, resulting to inaccuracies in the computation of the underlying current field. Non-hydrostatic models based on NSWE overcome this problem by introducing vertical velocity terms to account for weakly dispersive waves (Stelling and Zijlema, 2003; Yamazaki *et al*., 2011). Although, higher-order Boussinesq-type models embed enhanced nonlinear characteristics, the performance of non-hydrostatic NSWE models with regard to wave-induced currents is in many cases comparable. In recent years a number of applications of Boussinesq wave models computing the associated current field are reported in the international literature (Sørensen *et al*., 1998, 2004; Chen *et al*., 1999, 2003; Shi *et al*., 2012; Geiman and Kirby, 2013; Feddersen, 2014; Choi *et al*., 2015).

Apart from the different mathematical formulations, the efficiency and special features of the various Boussinesq-type models originate also from their numerical implementation. A variety of discretization methods employing finite differences, finite elements, finite volumes or hybrid methods have been proposed on cartesian or curvilinear coordinate systems. Each of them is accompanied by a specific solution algorithm. These range diversely, including explicit forward marching solutions, Alternating Direction Implicit (ADI) algorithms and predictor-corrector-iteration schemes. It is of general acceptance that numerics are at least of the same importance for the efficiency of Boussinesq models as the mathematical background itself, especially in terms of computational effort, time and stability.

In this chapter the Boussinesq-type wave model used in this study is extended to the surf and swash zones, including the description of the wave-induced current field. In addition, the adopted numerical scheme is described in detail. Finally, a number of validation tests, both in one and two horizontal dimensions, are presented to check the wave model's performance.

3.2 Theoretical background and mathematical formulation

As concluded in chapter 2, the adopted Boussinesq model in the present thesis relies on the basic Eqs (2.27) and (2.28) in the 1DH case and Eqs (2.16), (2.17) and (2.18) in the 2DH case, respectively. The model is of $O(\varepsilon^2\sigma^2)$ and the parameters B and B_2 are set equal to $\frac{1}{15}$ and 0.0653, respectively, in order to optimize linear dispersion and linear shoaling, as already discussed in chapter 2.

However, in order to simulate the wave propagation in the entire nearshore zone a number of physical processes have also to be modelled and included in the main model. First of all, the range of applicability is extended into the surf zone by incorporating wave breaking following the eddy viscosity concept. Extension to the swash zone requires a method to simulate the moving shoreline. This is achieved here through the application of an improved version of the permeable-seabed or slot technique, originally proposed by Tao (1983, 1984). Inclusion of bottom friction is based on either the conventional quadratic law or a probabilistic analysis (Kobayashi *et al*., 2007). A Smagorinsky-type subgrid model is also applied to account for the unresolved small-scale motions (Chen *et al*., 1999; Zhan *et al*., 2003).

The higher order of nonlinearity of the wave model allows for an internal computation of the wave-induced current field: longshore, cross-shore and rip currents. However, due to the use of depth-averaged velocities, the estimation of the undertow (defined herein in the potential part of the water column) requires a computation of the surface roller area where water is carried shoreward in the surf zone. Hence, a geometrical determination of the surface roller is applied although the wave breaking model itself is based on the eddy viscosity concept. A part of the work described herein can be also found in Klonaris *et al*. (2015, 2016) and Klonaris and Memos (2015).

3.2.1 Wave breaking

Surf zone dynamics is of great interest for coastal engineers since description of currents, sedimentation and erosion requires an accurate analysis of breaking waves. Thus the wave model has to be extended to account for breaking waves too.

Wave breaking in Boussinesq models has been modelled using a variety of techniques. The two major of them are the eddy viscosity formulation and the surface roller concept. The former was originally introduced by Heitner and Housner (1970) to capture the shock across a tsunami bore. Tao (1983) and Abbott *et al*. (1983) expressed the eddy viscosity in terms of a mixing length related to the water depth, and a velocity scale related to the instantaneous level of turbulent kinetic energy. The variation of this energy was determined by solving a time-domain transport equation for it, but no prediction or criteria for the start of breaking was included. A similar, but more sophisticated, approach was used by Karambas *et al*. (1990), Zelt (1991), and Karambas and Koutitas (1992). The surface roller approach attributed to Deigaard (1989), Brocchini *et al*. (1991, 1992) and Schäffer *et al*. (1992, 1993) is based on the roller concept introduced by Svendsen (1984). The roller approach was further developed by Madsen et al. (1997a) and was even applied to irregular wave propagation (Madsen *et al*., 1997b; Ozanne *et al*., 2000).

Both techniques have some advantages and drawbacks. The surface roller approach relies on a more realistic physical background than the eddy viscosity technique that assumes the breaking terms to be of the diffusive form. However, the surface roller technique may cause numerical instabilities in the two-dimensional case as the toe of the roller becomes a curve, hence its geometrical determination more complex. Instabilities may also be caused when the roller direction is determined interactively from the instantaneous wave field. Herein the eddy viscosity model presented by Kennedy *et al*. (2000) and Chen *et al*. (2000a) is used to simulate wave breaking. The method yields extra diffusive terms, $\vec{F}_{br} = (F_{br}, G_{br})$, in the x- and y-momentum equations, respectively:

$$F_{br} = \frac{1}{d+\zeta}\left\{\{v_{br}[(d+\zeta)U]_x\}_x + \frac{1}{2}\{v_{br}[(d+\zeta)U]_y + v_{br}[(d+\zeta)V]_x\}_y\right\} \tag{3.1}$$

$$G_{br} = \frac{1}{d+\zeta}\left\{\{v_{br}[(d+\zeta)V]_y\}_y + \frac{1}{2}\{v_{br}[(d+\zeta)V]_x + v_{br}[(d+\zeta)U]_y\}_x\right\} \tag{3.2}$$

where v_{br} is the eddy viscosity, which is a function of both space and time given by

$$v_{br} = B_{br}\delta_b^2(d+\zeta)\zeta_t \tag{3.3}$$

where δ_b is a mixing length coefficient with an empirical value of $\delta_b = 1.2$ and the quantity B_{br} varies smoothly from 0 to 1 in order to avoid an impulsive start of breaking and consequently a possible instability. It is given by

$$B_{br} = \begin{cases} 1, & \zeta_t \geq 2\zeta_t^* \\ \frac{\zeta_t}{\zeta_t^*} - 1, & \zeta_t^* < \zeta_t < 2\zeta_t^* \\ 0, & \zeta_t \leq \zeta_t^* \end{cases} \tag{3.4}$$

A similar expression to Eq. (3.3) for the eddy viscosity coefficient was initially proposed by Zelt (1991) based on the observation that a bore width is generally several times the local water depth (Rajaratnam, 1976).

The parameter ζ_t^* determines the onset and cessation of breaking. Use of ζ_t as a breaking initiation variable ensures that the dissipation is concentrated on the front face of the breaking wave. A breaking event begins when ζ_t exceeds some initial threshold value, but, as breaking evolves, the wave may continue breaking even if ζ_t drops below this value. The magnitude of ζ_t^* therefore, decreases in time from some initial value $\zeta_t^{(I)}$ to a terminal one $\zeta_t^{(F)}$. This decrease is assumed to follow a linear relation:

$$\zeta_t^* = \begin{cases} \zeta_t^{(F)}, & t - t_0 \geq T^* \\ \zeta_t^{(I)} + \frac{t-t_0}{T^*}\left(\zeta_t^{(F)} - \zeta_t^{(I)}\right), & 0 \leq t - t_0 < T^* \end{cases} \tag{3.5}$$

where $T^* = 5\sqrt{d/\mathrm{g}}$ is the transition time from breaking initiation to a fully developed bore and t_0 is the time that breaking was initiated. The typical value of $\zeta_t^{(F)}$is $0.15\sqrt{\mathrm{g}d}$ and the parameter $\zeta_t^{(I)}$ varies between $(0.35 \div 0.65)\sqrt{\mathrm{g}d}$. The lower limit of the coefficient $\zeta_t^{(I)}$ is more suitable for simulating wave breaking over bar/trough beaches while the upper for monotonic sloping beaches. In order to compute the value of the parameter ζ_t^*, the age, $t_0 - t$, of each breaking event has to be estimated. This requires the calculation of the wave incidence angle, θ, in order to track the breaking history along the wave ray. By applying the Sommerfeld condition for a progressive wave field on a locally constant water depth ($\zeta_t + \vec{c} \cdot \nabla\zeta = 0$, $\vec{c}$ the wave celerity), the model can make an intrinsic estimation for the angle θ (Chen *et al*., 2000a; Sørensen *et al*., 2004):

$$\theta = \tan^{-1}\left(\frac{\zeta_y}{\zeta_x}\right) \tag{3.6}$$

3.2.2 Wave run-up

In order to extend the model's application into the swash zone the land-water interface has to be represented realistically. The present wave model simulates the wave motion in the swash zone following the procedure described by Kennedy *et al*. (2000) and Chen *et al*. (2000a). This is basically a modification of the slot method originally proposed by Tao (1983, 1984). The main idea is that, instead of tracking the moving boundary, the entire computational domain is considered active, but wherever there is very little or no water covering the land, modified equations are solved. These equations assume that, instead of being solid, the beach contains narrow 'slots', so it is possible for the water level to be below

the beach elevation. Hence the shoreline is at any instant determined by the intersection of the water surface and the sea bed.

Madsen *et al*. (1997a,b) applied a similar technique assuming a porous beach. However, a comparison with the analytical solution of wave run-up on a solid beach (Carrier and Greenspan, 1958) indicated about 10% under-prediction of the maximum run-up. This was because water has to fill at first the slot before covering a previously dry area, leading to a decrease of the overall water volume available for run-up.

This motivated Kirby *et al*. (1998) and Kennedy *et al*. (2000) to propose a slight modification, adopted here, in order to conserve mass. Their formulation ensures that, there is no net fluid loss at a specific location when water is above the top of the slot. However, some small, but much reduced, mass loss still exists when water level is below the top of the slot.

Figure 3.1 (reproduced from Kennedy *et al*., 2000) shows a schematic of a wave flume with a sloping bottom in the presence of a narrow slot.

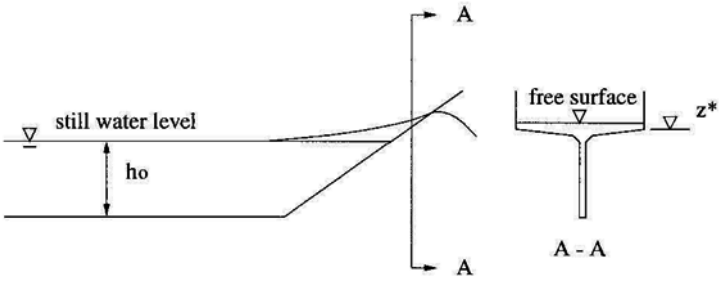

Fig. 3.1. Schematic of wave flume with presence of narrow slot (from Kennedy *et al.*, 2000).

The width of the wave flume is defined by:

$$b(\zeta) = \begin{cases} 1, & \zeta > z^* \\ \delta + (1-\delta)e^{\lambda(\zeta - z^*)/h_o}, & \zeta \le z^* \end{cases} \tag{3.7}$$

where δ is the slot width relative to a unit width of the beach, λ is the shape parameter that controls the smooth transition of the cross-sectional area from a unit width to a narrow slot, z^* denotes the elevation of the sea bed where $b = 1$ and h_o is a reference water depth that must be deeper than the water depth at the lowest limit of the swash zone. In the applications presented herein h_o was defined at the toe of the slope. Thus the cross-sectional area can be expressed as:

$$A(\zeta) = \begin{cases} (\zeta - z^*) + \delta(z^* + h_o) + \frac{(1-\delta)h_o}{\lambda}\left[1 - e^{-\lambda(1+z^*/h_o)}\right], & \zeta > z^* \\ \delta(\zeta + h_o) + \frac{(1-\delta)h_o}{\lambda}e^{\lambda(\zeta - z^*)/h_o}\left[1 - e^{-\lambda(1+\zeta/h_o)}\right], & \zeta \le z^* \end{cases} \tag{3.8}$$

Omitting the effect of a narrow slot on the vertical distribution of the fluid particle velocity, the two-dimensional mass equation for a permeable sea bed is written:

$$\beta \frac{\partial \zeta}{\partial t} + \nabla \cdot \left(\Lambda \vec{U} \right) = 0 \tag{3.9}$$

where $\beta = b(\zeta)$ and $\Lambda = A(\zeta)$. In the absence of the slot scheme, $\beta = 1$, and $\Lambda = d + \zeta$, where d the still water depth, and Eq. (3.9) reduces to Eq. (2.16). On the other hand, the presence of the slots does not alter the momentum Eqs (2.17) and (2.18).

In Tao's (1984) and Madsen *et al.*'s (1997a) formulations, it was chosen $z^* = -d$ leading to an effective loss of mass during run-up. In the formulation by Kennedy *et al.* (2000), adopted here, z^* is defined so that, when the water level is above the top of the slot, the overall volume will be identical to the one without the existence of the slot. Taking into account that $\delta << 1$ and $\lambda >> 1$, the resulting z^* is:

$$z^* = \frac{-d}{1-\delta} + \mathrm{h_o} \left(\frac{\delta}{1\text{-}\delta} + \frac{1}{\lambda} \right) \tag{3.10}$$

In any case the slot width should be as small as possible in order to avoid a distortion of the mass balance. On the other hand, too small values lead to numerical instabilities. The opposite is true for the shape parameter λ. In all the applications presented in the following it was chosen $\lambda = 80$ and $\delta = 0.001\text{-}0.01$.

3.2.3 Bottom friction

Bottom friction is not very significant for most shore-normal applications concerning short waves, while it may be important for modelling long wave transformation. However, in the two-dimensional case a steady current field can only be generated if the radiation stress's forcing is balanced by bottom friction and mixing processes. Thus, an accurate modelling of the bed friction is of high importance.

The model offers two options for computing the bed shear stresses. The first one is using a quadratic resistance law for the instantaneous stresses:

$$\vec{\tau}_b = \left(\tau_{bx}, \tau_{by} \right) = \frac{1}{2} f_{cw} \vec{U} \left| \vec{U} \right| \tag{3.11}$$

where f_{cw} is the bed friction coefficient which is typically a function of both the wave and the current fields. In order to represent the effect of turbulent interaction of the oscillatory boundary layer and the mean flow Ribberink's (1998) wave-current bottom friction factor is employed:

$$f_{cw} = \left(\frac{\left| \vec{U} \right|}{\left| \vec{U} \right| + u_{ow-max}} \right) f_c + \left(1 - \frac{\left| \vec{U} \right|}{\left| \vec{U} \right| + u_{ow-max}} \right) f_w \tag{3.12}$$

where $\vec{\overline{U}} = (\overline{U}, \overline{V})$ is the depth-averaged current velocity field described in subsection 3.2.5, f_c is the current friction factor and f_w is the wave friction factor. The model's equations rely on the assumption of a uniform velocity profile over depth. Thus the near-bottom velocity, $\vec{u}_o = (u_o, v_o)$, is taken equal to $\vec{U}$ and u_{ow-max} is the amplitude of its oscillatory component, $\vec{u}_{ow} = \vec{u}_o - \vec{\overline{U}}$. This amplitude is obtained by taking the mean value of the amplitudes of the oscillatory components of the near-bottom velocities of the previous waves. A typical range of values for the bed friction factor is $f_{cw} \approx$ 0.001-0.01 and besides the aforementioned analysis, a constant value lying in this range could also be employed for simplicity leading to acceptable results.

Based on an implicit relation derived by Jonsson (1966), Swart (1974) proposed the following formula for the wave friction factor:

$$f_w = \begin{cases} \exp\left[-5.977+5.213(K_N/A_b)^{0.194}\right] & \text{for} \quad K_N/A_b < 0.63 \\ 0.3 & \text{for} \quad K_N/A_b \geq 0.63 \end{cases} \tag{3.13}$$

where A_b is the water particle amplitude of the near-bottom oscillation ($A_b = u_{ow-max}/\omega$, where ω is the angular frequency, corresponding to the peak of the spectrum in the case of irregular waves) and K_N is the bed roughness given from Eq. (3.14a) for regular waves and Eq. (3.14b) for irregular waves (Nielsen, 1992). Eq. (3.13) was employed although it refers to the near-bed oscillatory motion, while the model equations are expressed in terms of the depth-averaged horizontal velocities.

$$K_N = 170\sqrt{\theta_{2.5} - 0.05}d_{50} + 8{\eta_r}^2/\lambda_r \tag{3.14a}$$

$$K_N = 73\sqrt{\theta_{2.5} - 0.05}d_{50} + 3.5{\eta_r}^2/\lambda_r \tag{3.14b}$$

where $\theta_{2.5}$ is the Shields parameter based on an equivalent roughness $K_N{}' = 2.5d_{50}$ given by

$$\theta_{2.5} = \frac{1}{2} f_{2.5}\psi \tag{3.15}$$

where $f_{2.5}$ is given from Eq. (3.13) for $K_N = K_N{}'$ and the mobility number

$$\psi = \frac{u_{ow-max}^2}{(s-1)\mathrm{g}d_{50}} \tag{3.16}$$

where d_{50} is the median grain diameter and $s = \rho_s/\rho$ is the relative density of sediments (ρ_s is the sediment's density and ρ the water density).

The bed ripple height, η_r, and the ripple steepness, η_r/λ_r (with λ_r the ripple length), are given from the following formulae proposed by Nielsen (1992) for regular waves:

$$\eta_r = \left(0.275 - 0.022\psi^{0.5}\right)A_b \quad \text{for} \quad \psi < 156 \tag{3.17a}$$

$$\eta_r/\lambda_r = 0.182 - 0.24{\theta_{2.5}}^{1.5} \tag{3.17b}$$

For irregular waves the following formulae were used (Nielsen, 1992):

$$\eta_r = 21A_b\psi^{-1.85} \quad \text{for} \quad \psi > 10 \tag{3.18a}$$

$$\eta_r/\lambda_r = 0.342 - 0.34\sqrt[4]{\theta_{2.5}} \tag{3.18b}$$

The current friction factor is calculated following Ribberink (1998) from

$$f_c = \frac{2\mathrm{g}}{C_c^2} \tag{3.19}$$

where C_c is the Chezy friction coefficient given by

$$C_c = 18\log\left[\frac{12(d+\bar{\zeta})}{K_N}\right] \tag{3.20}$$

where $\bar{\zeta}$ is the mean value of the free surface elevation.

The alternative formulation relies on the more sophisticated probabilistic analysis by Kobayashi *et al.* (2007). The instantaneous depth-averaged velocities can be expressed as

$$(U,V) = (\bar{U} + U_T\cos\theta\,, \bar{V} + U_T\sin\theta) \tag{3.21}$$

where U_T is the depth-averaged oscillatory horizontal velocity with zero mean in the wave propagation direction approximated by

$$U_T = [\mathrm{g}/(d+\bar{\zeta})]^{0.5}(\zeta - \bar{\zeta}) \tag{3.22}$$

Equations (3.21) and (3.22) rely on the assumption of linear shallow water theory and they yield

$$\sigma_U = \sigma_T\cos\theta\,,\ \sigma_V = \sigma_T\sin\theta\,,\ \sigma_T = [\mathrm{g}(d+\bar{\zeta})]^{0.5}\sigma_*,\ \sigma_* = \frac{\sigma_\zeta}{d+\bar{\zeta}} \tag{3.23}$$

where σ_U, σ_V, σ_T and σ_ζ are the standard deviations of U, V, U_T and ζ, respectively.

Assuming the equivalency of time and probabilistic averaging, as well as the Gaussian distribution of U_T, the bed stresses can be approximated as:

$$\vec{\tau}_b = \left(\tau_{bx},\tau_{by}\right) = \frac{1}{2}f_{cw}\sigma_T^2\left(G_{bx},G_{by}\right) \tag{3.24}$$

where f_{cw} is the same as in Eq. (3.11) and $\left(G_{bx},G_{by}\right)$ are given by the improper integrals

$$G_{bx} = \int_{-\infty}^{\infty} F_U F_\alpha f(r) dr \quad \text{and} \quad G_{by} = \int_{-\infty}^{\infty} F_V F_\alpha f(r) dr \tag{3.25}$$

and

$$F_U = \frac{\bar{U}}{\sigma_T} + r\cos\theta, F_V = \frac{\bar{V}}{\sigma_T} + r\sin\theta \quad \text{and} \quad F_\alpha = \sqrt{{F_U}^2 + {F_V}^2} \tag{3.26}$$

with

$$f(r) = \frac{1}{\sqrt{2\pi}} \exp\left(-\frac{r^2}{2}\right) \tag{3.27}$$

where the mean and the standard deviation of the Gaussian variable $r = U_T/\sigma_T$ are zero and unity, respectively.

However, the simplified expressions by Feddersen *et al.* (2000) are used here leading to acceptable deviations, as also discussed by Kobayashi *et al*. (2007):

$$G_{bx} = \frac{\bar{U}}{\sigma_T}\left[1.16^2 + \left(\frac{\bar{U}}{\sigma_T}\right)^2\right]^{0.5} \quad \text{and} \quad G_{by} = \frac{\bar{V}}{\sigma_T}\left[1.16^2 + \left(\frac{\bar{V}}{\sigma_T}\right)^2\right]^{0.5} \tag{3.28}$$

For the applications presented here both the quadratic and the probabilistic formulations led to quite similar results. Hence no clear evidence occurred proving the superiority of either approach.

3.2.4 Subgrid turbulent mixing

Wave breaking typically generates eddies and turbulent flow in the surf zone. Due to the complex three-dimensional nature of the turbulence an approximation was made. In particular, as this Boussinesq model is based on vertically integrated mass and momentum equations and the grid size is usually smaller than the typical depth, the effects of unresolved small-scale motions are parameterized using the approach of the large eddy simulation on the horizontal plane. The wave breaking terms account for the energy dissipation due to breaking and are usually strongly localized on the front face of the breaking wave. Additionally, the subgrid turbulent processes causing the Reynolds-like stresses have also to be taken into account. In the absence of such a subgrid model for the turbulence contribution from the mean flow, the underlying wave-induced current field may become chaotic. A Smagorinsky-type subgrid model (Smagorinsky, 1963) was adopted which yields extra terms in the momentum equations (Chen *et al.*, 1999; Zhan *et al.*, 2003). The extra eddy viscosity terms, $\vec{F}_{\text{eddy}} = \left(F_{\text{eddy}}, G_{\text{eddy}}\right)$, in the x- and y-momentum equations, respectively, are

$$F_{\text{eddy}} = \frac{1}{d+\zeta}\left\{\{v_e[(d+\zeta)U]_x\}_x + \frac{1}{2}\left\{v_e[(d+\zeta)U]_y + v_e[(d+\zeta)V]_x\right\}_y\right\} \tag{3.29}$$

$$G_{\text{eddy}} = \frac{1}{d+\zeta}\left\{\left\{v_e[(d+\zeta)V]_y\right\}_y + \frac{1}{2}\left\{v_e[(d+\zeta)V]_x + v_e[(d+\zeta)U]_y\right\}_x\right\} \tag{3.30}$$

where v_e is the eddy viscosity coefficient due to the subgrid turbulence estimated by

$$v_e = \mathrm{c_s}\,\mathrm{d}x\,\mathrm{d}y\left[\bar{U}_x{}^2 + \bar{V}_y{}^2 + \frac{1}{2}\left(\bar{U}_y + \bar{V}_x\right)^2\right]^{1/2} \tag{3.31}$$

in which $\mathrm{c_s}$ is the mixing coefficient with a default value of 0.25 and dx and dy are the grid spacing in the x and y directions, respectively.

3.2.5 Wave-induced currents

The traditional treatment of nearshore dynamics requires splitting of the total flow field into a current and a wave problem. The concept of the radiation stresses introduced by Longuet-Higgins and Stewart (1961) and the pioneering work by Bowen (1969a,b) and Longuet-Higgins (1970a,b) offer some robust tools for the understanding of nearshore circulation. The decoupled and phase-averaged approach includes the computation of the radiation stresses from a wave model and the solution of the nonlinear shallow water equations for the mean flow driven by gradients in the radiation stress field. This practice constitutes a quite reliable method for calculating current patterns and long waves in the surf zone, but is limited with respect to the resolution of phenomena happening at the wave-by-wave level, i.e. wave-wave interaction, run-up, etc.

Hence, the decoupled procedure is not needed for a nonlinear Boussinesq-type model when it has been extended to the surf and swash zones (Basco, 1983). These models can automatically include the combined effects of wave-wave and wave-current interactions, inherently, without the need of explicit formulation for the radiation stresses. In this study, the presented nonlinear wave model is applied to calculate the integrated system of wave-induced longshore, cross-shore and rip currents.

The total horizontal velocity can be written as the sum of a mean velocity, $\vec{\bar{U}} = (\bar{U}, \bar{V})$, assumed uniform over depth, and an oscillatory component, $\vec{u}_w$:

$$\vec{u} = \vec{\bar{U}} + \vec{u}_w \tag{3.32}$$

The depth-averaged mean horizontal velocity is introduced in such a way that multiplied by the mean water depth gives the mean mass flux (Mei, 1983; Dingemans, 1994). In particular, if $\overline{(\,)}$ denotes the time-average, one gets

$$\vec{\bar{U}} = \frac{1}{d+\bar{\zeta}} \overline{\int_{-d}^{\zeta} \vec{u}\, \mathrm{d}z} \tag{3.33}$$

It follows from Eq. (3.32) that $\overline{\int_{-d}^{\zeta} \vec{u}\, \mathrm{d}z} = (d+\bar{\zeta})\vec{\bar{U}} + \overline{\int_{-d}^{\zeta} \vec{u}_w\, \mathrm{d}z}$. It should be mentioned that the mean quantities vary also in time following slow temporal scales. This dependence is ignored here (see also Dingemans, 1994). Thus with the definition of Eq. (3.33) it follows that

$$\overline{\int_{-d}^{\zeta} \vec{u}_w\, \mathrm{d}z} = 0 \tag{3.34}$$

It is stressed that the horizontal mean velocity, $\vec{\bar{U}}$, so defined has actually two components, the wave-induced current field plus the effect of the mass flux due to the wave motion.

All the time-averaged quantities in the aforementioned analysis are computed following a procedure similar to the one by Rakha *et al.* (1997). For regular wave propagation the quantities involved were time-averaged over each wave period and the results were averaged over the number of periods. For irregular wave trains, all the time series were divided into N_c time cycles each consisting of N time steps. The variables were time-averaged over the N steps of each cycle and then the results were averaged over the number of cycles. Typically, each cycle had a length of 20-30 times the mean wave period.

The aforementioned analysis focuses on the depth-averaged wave-driven currents. However, in order to estimate sediment transport a detailed three-dimensional velocity structure is needed up to the shoreline. This concerns both the primary wave-induced longshore currents and the secondary cross-shore currents.

In the surf zone there is an onshore directed flow due to two mechanisms, the wave drift and the breaking surface rollers carrying water shorewards. This shoreward discharge caused by the waves must be compensated by a current in the offshore direction, the so-called undertow (Fredsøe and Deigaard, 1992). The undertow has its maximum in the lower part of the water column and is confined within the surf zone, because outside the surf zone there are no surface rollers to transport water, and also because the energy dissipation in the near-bed wave boundary layer is too weak to cause shear stresses outside that layer.

Although in the present model wave breaking is simulated using the eddy viscosity concept, an estimation for the surface roller is required in order to compute the near-bed return flow under a breaking waveform. In order to do so, the vertical profile of the horizontal velocity proposed by Schäffer *et al.* (1992) and Madsen *et al.* (1997a) is employed. The main idea is that the surface roller is considered as a volume of water being carried with the wave celerity, $\vec{c} = \left(c^{(x)}, c^{(y)}\right)$. Below the surface roller the velocity profile is considered uniform with a value of $\vec{U}_o = (U_o, V_o)$ as shown in Fig. 3.2. Outside the surf zone the surface rollers are not present and $\vec{U}_o$ is equal to $\vec{U}$.

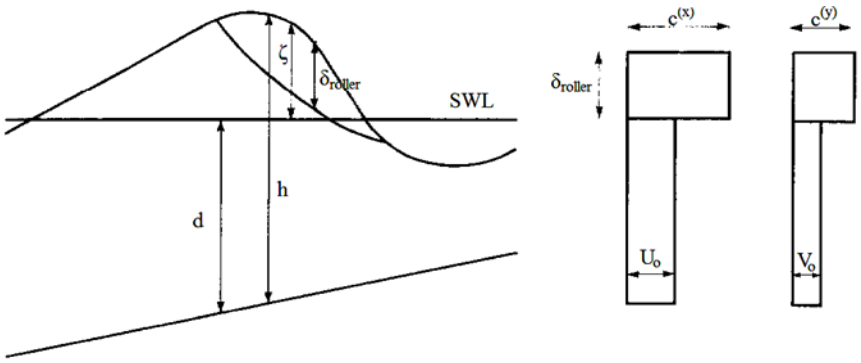

Fig. 3.2. Cross-section of a breaking wave and vertical profile of the horizontal particle velocity components (from Madsen *et al.*, 1997a, modified).

Since the surface roller concept is not used inherently in the model equations, the wave breaking nodes are determined using the eddy viscosity concept and by assuming an equivalency between the two breaking models, the surface roller thickness, δ_{roller}, can be estimated at each node. The celerity of the surface roller is estimated following Sørensen *et al.* (2004) as:

$$\vec{c} = \left(c^{(x)}, c^{(y)}\right) = 1.3\sqrt{gd}(\cos\theta\,, \sin\theta) \tag{3.35}$$

This result is in agreement with the experiments presented by Stive (1980) showing that a characteristic point at the front of a broken wave (such as the crest or the trough) moves with a celerity which is 20-30% higher than the linear shallow water celerity.

Once the roller thickness has been determined, the depth-averaged undertow, $\vec{\bar{U}}_o = (\bar{U}_o, \bar{V}_o)$, can be estimated, where $\vec{U}_o$ is defined by

$$\vec{U}_o = (U_o, V_o) = \frac{(d+\zeta)\vec{U} - \vec{c}\delta_{roller}}{d+\zeta-\delta_{roller}} \tag{3.36}$$

This is a rather crude approximation for the undertow but has proved to give quite accurate results (see Madsen *et al.*, 1997a), definitely better when compared to the procedure ignoring altogether the roller effect.

The near bottom undertow velocity, U_b, is computed from the 1DH (the 2DH extension is straightforward) analytical expression proposed by Putrevu and Svendsen (1993), which is valid both inside and outside the surf zone:

$$\frac{U_b}{\sqrt{g(d+\bar{\zeta})}} = \left[\frac{\bar{U}_o}{\sqrt{g(d+\bar{\zeta})}} - \frac{A}{6} + \frac{\tau_{sb}(d+\bar{\zeta})}{2\rho\nu_{tz}\sqrt{g(d+\bar{\zeta})}}\right](1+R_1)^{-1} \tag{3.37}$$

where ρ is the water density, τ_{sb} is a steady streaming term, ν_{tz} is the eddy viscosity coefficient outside the bottom boundary layer, and A and R_1 are coefficients. Effectively:

$$\tau_{sb} = \frac{1}{2}\rho v_{tg}\beta_1 \frac{u_{ow-max}^2}{c^{(x)}} \quad \text{with} \quad \beta_1 = \sqrt{\frac{\omega}{2v_{tg}}} \tag{3.38}$$

$$A = \frac{\alpha_1 (d+\bar{\zeta})^2}{v_{tz}\sqrt{g(d+\bar{\zeta})}} \quad \text{with} \quad \alpha_1 = g\frac{\partial \bar{\zeta}}{\partial x} + \frac{1}{2}\frac{\partial \overline{u_{ow}^2}}{\partial x} \tag{3.39}$$

$$R_1 = \frac{f_w u_{ow-max}(d+\bar{\zeta})}{\pi v_{tz}} \tag{3.40}$$

where v_{tg} is the eddy viscosity coefficient inside the bottom boundary layer, u_{ow-max} is the amplitude of the oscillatory component of the near bottom velocity u_{ow}, defined above as $u_{ow} = U_o - \bar{U}_o$, ω is the wave angular frequency and f_w is the bed friction coefficient due to waves.

Following de Vriend and Stive (1987) the eddy viscosity coefficient outside the bottom boundary layer is given by

$$v_{tz} = 0.025(d + \bar{\zeta})\left(\frac{\overline{D}}{\rho}\right)^{1/3} \tag{3.41}$$

where D is the wave energy dissipation per unit area due to breaking derived by $D = \rho g c^{(x)} \delta_{roller} \beta_D$, with β_D a function of the angle of inclination of the roller taken here equal to 0.1 (Deigaard *et al*., 1991; Dally and Brown, 1995; Madsen *et al*., 1997a). Outside the surf zone v_{tz} is taken equal to 20% of its value at the breaking point.

Inside the bottom boundary layer the relation by Staub *et al*. (1996) was adopted for the eddy viscosity coefficient:

$$v_{tg} = \frac{1}{6}\kappa u_* \delta_w \tag{3.42}$$

where κ is the von Karman constant (κ = 0.4), u_* is the friction velocity (Staub *et al*., 1996) and δ_w is the wave boundary layer thickness, which was taken equal to $\sqrt{vT/\pi}$ with v the kinematic viscosity of the water and *T* the wave period.

3.3 Numerical aspects

3.3.1 Numerical scheme

It is convenient for the numerical calculations to rewrite the model's Eqs (3.9), (2.17), (2.18) as follows:

$$\zeta_t = E(\zeta, U, V) + f_s(x, y, t) \tag{3.43}$$

$$U'_t = F(\zeta, U, V) + [F_1(V)]_t + F_2(\zeta, U, V) + F_{br} - \frac{\tau_{bx}}{d+\zeta} + F_{\text{eddy}} + F_{\text{sp}} \tag{3.44}$$

$$V'_t = G(\zeta, U, V) + [G_1(U)]_t + G_2(\zeta, U, V) + G_{br} - \frac{\tau_{by}}{d+\zeta} + G_{\text{eddy}} + G_{\text{sp}} \tag{3.45}$$

where:

$$E = -\frac{1}{\beta}\left[(\Lambda U)_x + (\Lambda V)_y\right] \tag{3.46}$$

$$U' = U - \left(\mathrm{B} + \tfrac{1}{3}\right) d^2 U_{xx} - (2\mathrm{B}_2 + 1) d d_x U_x \tag{3.47}$$

$$V' = V - \left(\mathrm{B} + \tfrac{1}{3}\right) d^2 V_{yy} - (2\mathrm{B}_2 + 1) d d_y V_y \tag{3.48}$$

$$F = -\mathrm{g}\zeta_x - \left(UU_x + VU_y\right) \tag{3.49}$$

$$G = -\mathrm{g}\zeta_y - \left(UV_x + VV_y\right) \tag{3.50}$$

$$F_1(V) = \left(\mathrm{B} + \tfrac{1}{3}\right) d^2 V_{xy} + \left(\mathrm{B}_2 + \tfrac{1}{2}\right) d d_x V_y + \left(\mathrm{B}_2 + \tfrac{1}{2}\right) d d_y V_x \tag{3.51}$$

$$G_1(U) = \left(\mathrm{B} + \tfrac{1}{3}\right) d^2 U_{xy} + \left(\mathrm{B}_2 + \tfrac{1}{2}\right) d d_y U_x + \left(\mathrm{B}_2 + \tfrac{1}{2}\right) d d_x U_y \tag{3.52}$$

and F_2, G_2 include all the remaining terms of $\psi_I^{(x)}, \psi_{II}^{(x)}, \psi_{III}^{(x)}$ and $\psi_I^{(y)}, \psi_{II}^{(y)}, \psi_{III}^{(y)}$, respectively, that are functions of ζ, U, V and their spatial and temporal derivatives. The term $f_s(x, y, t)$ is the source function for wave generation and F_{sp}, G_{sp} provide for wave absorption at the model boundaries. These terms are described in the subsection 3.3.2.

The differential Eqs (3.43), (3.44), (3.45) are solved numerically using a finite difference scheme on a non-staggered cartesian Arakawa A-grid (Arakawa and Lamb, 1977). Since a consistent numerical scheme was employed the truncation error would be eliminated in the limit as $\Delta x \to 0$, $\Delta y \to 0$, and $\Delta t \to 0$. However, if a low-order discretization was employed, the error terms may have the same magnitude as the actual dispersive terms of the model using typical grid resolutions. In this case a back substitution of the truncation terms should be performed in order to obtain an accurate performance. For this reason, terms involving first-order spatial derivatives were differenced to $O(\Delta x^4)$, while second and third-order spatial derivatives were differenced to $O(\Delta x^2)$. This was chosen in order to reduce the truncation errors to a small size relative to all the retained terms in the equations. The spatial finite

differences were central in the interior of the computational domain and forward/backward at the boundary nodes.

Time integration is performed using a generalized multi-step predictor-corrector scheme proposed by Zlatev *et al.* (1984). The predictor formula is of third order, followed by a fourth-order corrector arrangement. In the following, level (n+1) refers to the new time step at which values of ζ, U and V are to be obtained. Level (n) refers to the present time step at which information is known. Levels (n-1) and (n-2) are the last past time steps at which all information is also known. Using the explicit predictor formula, new values for the three variables at the node (i,j) are obtained by:

$$\zeta_{i,j}^{(n+1)} = \alpha\zeta_{i,j}^{(n)} + (1-\alpha)\zeta_{i,j}^{(n-1)} + \Delta t\left[p_1(E')_{i,j}^{(n)} + p_2(E')_{i,j}^{(n-1)} + p_3(E')_{i,j}^{(n-2)}\right] \quad (3.53)$$

$$[U']_{i,j}^{(n+1)} = \alpha[U']_{i,j}^{(n)} + (1-\alpha)[U']_{i,j}^{(n-1)} + \Delta t\left[p_1(F')_{i,j}^{(n)} + p_2(F')_{i,j}^{(n-1)} + p_3(F')_{i,j}^{(n-2)}\right] + \Delta t\left[p_1[(F_1)_t]_{i,j}^{(n)} + p_2[(F_1)_t]_{i,j}^{(n-1)} + p_3[(F_1)_t]_{i,j}^{(n-2)}\right] \quad (3.54)$$

$$[V']_{i,j}^{(n+1)} = \alpha[V']_{i,j}^{(n)} + (1-\alpha)[V']_{i,j}^{(n-1)} + \Delta t\left[p_1(G')_{i,j}^{(n)} + p_2(G')_{i,j}^{(n-1)} + p_3(G')_{i,j}^{(n-2)}\right] + \Delta t\left[p_1[(G_1)_t]_{i,j}^{(n)} + p_2[(G_1)_t]_{i,j}^{(n-1)} + p_3[(G_1)_t]_{i,j}^{(n-2)}\right] \quad (3.55)$$

where:

$$E' = E + f_s(x, y, t) \quad (3.56)$$

$$F' = F + F_2 + F_{br} - \frac{\tau_{bx}}{d+\zeta} + F_{\text{eddy}} + F_{\text{sp}} \quad (3.57)$$

$$G' = G + G_2 + G_{br} - \frac{\tau_{by}}{d+\zeta} + G_{\text{eddy}} + G_{\text{sp}} \quad (3.58)$$

Δt is the time step, α is a real free parameter and the coefficients $p_1(\alpha), p_2(\alpha), p_3(\alpha)$ were chosen based on α to obtain a third order relation.

In order to obtain the predicted values for $U_{i,j}^{(n+1)}$ and $V_{i,j}^{(n+1)}$ two tridiagonal linear systems have to be solved. Hence, the algorithm is really semi-implicit in terms of U and V. The two linear systems are solved through the application of Thomas (1949) algorithm in x and y directions consecutively. After the predicted values are evaluated, the following implicit corrector formulation is applied:

$$\zeta_{i,j}^{(n+1)} = \alpha^*\zeta_{i,j}^{(n)} + (1-\alpha^*)\zeta_{i,j}^{(n-1)} + \Delta t\Big[c_1(E')_{i,j}^{(n+1)} + c_2(E')_{i,j}^{(n)} + c_3(E')_{i,j}^{(n-1)} + c_4(E')_{i,j}^{(n-2)}\Big] \tag{3.59}$$

$$[U']_{i,j}^{(n+1)} = \alpha^*[U']_{i,j}^{(n)} + (1-\alpha^*)[U']_{i,j}^{(n-1)} + \Delta t\Big[c_1(F')_{i,j}^{(n+1)} + c_2(F')_{i,j}^{(n)} + c_3(F')_{i,j}^{(n-1)} + c_4(F')_{i,j}^{(n-2)}\Big] + \Delta t\Big[c_1[(F_1)_t]_{i,j}^{(n+1)} + c_2[(F_1)_t]_{i,j}^{(n)} + c_3[(F_1)_t]_{i,j}^{(n-1)} + c_4[(F_1)_t]_{i,j}^{(n-2)}\Big] \tag{3.60}$$

$$[V']_{i,j}^{(n+1)} = \alpha^*[V']_{i,j}^{(n)} + (1-\alpha^*)[V']_{i,j}^{(n-1)} + \Delta t\Big[c_1(G')_{i,j}^{(n+1)} + c_2(G')_{i,j}^{(n)} + c_3(G')_{i,j}^{(n-1)} + c_4(G')_{i,j}^{(n-2)}\Big] + \Delta t\Big[c_1[(G_1)_t]_{i,j}^{(n+1)} + c_2[(G_1)_t]_{i,j}^{(n)} + c_3[(G_1)_t]_{i,j}^{(n-1)} + c_4[(G_1)_t]_{i,j}^{(n-2)}\Big] \tag{3.61}$$

with $\alpha^* \in [0,2)$ and the coefficients $c_1(\alpha^*)$, $c_2(\alpha^*)$, $c_3(\alpha^*)$, $c_4(\alpha^*)$ were chosen based on α^* to obtain a fourth-order relation. After solving Eqs (3.59), (3.60) and (3.61) the values of ζ, U and V at the time level (n+1) are obtained.

It should be mentioned that the time derivatives of the quantities U, V, F_1 and G_1that appear in the right-hand side of Eqs (3.54), (3.55), (3.60) and (3.61) are approximated following Wei *et al.* (1995) and Wei and Kirby (1998). In particular, for the predictor stage, the corresponding time derivatives are evaluated as:

$$(w_t)_{i,j}^{(n)} = \frac{1}{2\Delta t}\left(3w_{i,j}^{n} - 4w_{i,j}^{n-1} + w_{i,j}^{n-2}\right) + O\left(\Delta t^2\right) \tag{3.62a}$$

$$(w_t)_{i,j}^{(n-1)} = \frac{1}{2\Delta t}\left(w_{i,j}^{n} - w_{i,j}^{n-2}\right) + O\left(\Delta t^2\right) \tag{3.62b}$$

$$(w_t)_{i,j}^{(n-2)} = -\frac{1}{2\Delta t}\left(w_{i,j}^{n} - 4w_{i,j}^{n-1} + 3w_{i,j}^{n-2}\right) + O\left(\Delta t^2\right) \tag{3.62c}$$

For the corrector stage:

$$(w_t)_{i,j}^{(n+1)} = \frac{1}{6\Delta t}\left(11w_{i,j}^{n+1} - 18w_{i,j}^{n} + 9w_{i,j}^{n-1} - 2w_{i,j}^{n-2}\right) + O\left(\Delta t^3\right) \tag{3.63a}$$

$$(w_t)_{i,j}^{(n)} = \frac{1}{6\Delta t}\left(2w_{i,j}^{n+1} + 3w_{i,j}^{n} - 6w_{i,j}^{n-1} + w_{i,j}^{n-2}\right) + O\left(\Delta t^3\right) \tag{3.63b}$$

$$(w_t)_{i,j}^{(n-1)} = -\frac{1}{6\Delta t}\left(w_{i,j}^{n+1} - 6w_{i,j}^{n} + 3w_{i,j}^{n-1} + 2w_{i,j}^{n-2}\right) + O\left(\Delta t^3\right) \tag{3.63c}$$

$$(w_t)_{i,j}^{(n-2)} = -\frac{1}{6\Delta t}\left(-2w_{i,j}^{n+1} + 9w_{i,j}^{n} - 18w_{i,j}^{n-1} + 11w_{i,j}^{n-2}\right) + O\left(\Delta t^3\right) \tag{3.63d}$$

The corrector step was iterated until the relative error, Δf, between two successive results reached an acceptable limit. The relative error is defined as (Long and Kirby, 2006):

$$\Delta \mathrm{f} = \max\left\{\frac{\sum_{i,j}\left|\zeta_{i,j}^{(n+1)} - \zeta_{i,j}^{(n+1)^*}\right|}{\sum_{i,j}\left|\zeta_{i,j}^{(n+1)}\right|},\ \frac{\sum_{i,j}\left(\left|U_{i,j}^{(n+1)} - U_{i,j}^{(n+1)^*}\right| + \left|V_{i,j}^{(n+1)} - V_{i,j}^{(n+1)^*}\right|\right)}{\sum_{i,j}\left(\left|U_{i,j}^{(n+1)}\right| + \left|V_{i,j}^{(n+1)}\right|\right)}\right\} \tag{3.64}$$

where $(\,)^*$ denotes the preceding estimate. The corrector step was iterated if Δf exceeded 0.001. For weakly nonlinear cases the scheme required typically no iterations, unless problems arose from boundaries. However, for strong nonlinear cases, more iterations were required. Moreover, the iterated results appeared to oscillate around the desired solution. In order to increase the convergence rate, a relaxation technique was applied at the corrector stage. The adjusted relaxed value, $f_{i,j}^r$, was:

$$f_{i,j}^r = \mathrm{R} f_{i,j} + \left(1 - \mathrm{R}\right) f_{i,j}^* \tag{3.65}$$

where R is the relaxation coefficient in the interval (0,1), $f_{i,j}$ and $f_{i,j}^*$ are the current and the preceding iterated values, respectively. In all the computational cases a value of R=0.7-0.8 gave satisfactory results.

By assuming $(\alpha, \alpha^*) = (1,1)$ the predictor and corrector stages reduce to the Adams-Bashforth third-order and Adams-Moulton fourth-order formulae, respectively. This ABM fourth-order scheme was initially proposed by Wei and Kirby (1995) for a weakly nonlinear Boussinesq-type model based on Nwogu's (1993) equations and was later extended to the higher order models by Wei *et al.* (1995) and Gobbi and Kirby (1999). The numerical scheme adopted here is a generalization of ABM scheme, offering better numerical stability properties (Zlatev *et al.*, 1984; Banijamali, 1998).

3.3.2 Boundary conditions

Source function

The desired waves are generated inside the computational domain by introducing a source term, $f_s(x, y, t)$, in the continuity equation. An analytical expression for this source function was obtained following the work by Wei *et al.* (1999). The basic idea behind this method is the distribution of the source function over a certain neighborhood of the source in order to avoid the generation of spurious noise around the source point.

The source's neighborhood is assumed to be a 2D region of constant depth and, without losing generality the source itself is considered parallel to the y-axis, with x_s its central

location in the x direction. A smooth Gaussian distribution is considered and the source function can be written:

$$f_s(x, y, t) = F_s(y, t) \exp\left[-\beta_s (x - x_s)^2\right] \tag{3.66}$$

where β_s is the shape coefficient. The time series for a wave train, along the y-axis, composed by N_s frequencies and M_s directional components is given by:

$$F_s(y, t) = \sum_{i=1}^{N_s} \sum_{j=1}^{M_s} D_{s_{i,j}} \cos\left(\omega_i t - k_i y \sin\varphi_j + \varepsilon_{i,j}\right) \tag{3.67}$$

where ω_i and k_i are the angular frequency and the wavenumber of the i-th frequency component, respectively, φ_j is the angle between the wave propagation direction and the x-axis for the j-th directional component and $\varepsilon_{i,j}$ is a random phase within the range of [0, 2π). Following Wei *et al*'s. (1999) method applied to the linearized version of the present model, the magnitude of the source function, D_s, for a monochromatic wave or a single wave component of a random wave train with wave amplitude ζ_0 is determined by:

$$D_s = \frac{2\zeta_0\left(\omega^2 + \mathrm{B}gk^4 d^3\right)\cos\varphi}{\omega I k\left[1 + \left(\mathrm{B} + \frac{1}{3}\right)(kd)^2\right]} \tag{3.68}$$

with I defined by

$$I = \sqrt{\frac{\pi}{\beta_s}} \exp\left[-\frac{(k\cos\varphi)^2}{4\beta_s}\right] \tag{3.69}$$

As far as the shape coefficient is concerned, large β_s values are generally preferred since then the source region is narrower. However, a too narrow source region may lead to a poor finite difference representation. In most of the computations here a value of $\beta_s = 80/(\delta_s L)^2$ was adopted, with L the target wavelength and $\delta_s = 0.3$.

It is stressed that the source function method is theoretically derived for the linear version of the Boussinesq-type model. Thus, some discrepancies from the target solution may occur due to the nonlinear terms. In most of the cases these deviations are insignificant (Wei and Kirby, 1998). However, for very strongly nonlinear waves the source function theory fails to generate the desired wave forms.

Reflective boundaries

For a reflective boundary with an outward normal vector $\vec{n}$, three conditions were imposed :

$$\vec{U}\cdot\vec{n}=0\ ,\ \nabla\zeta\cdot\vec{n}=0\ ,\ \frac{\partial\vec{U}_T}{\partial\vec{n}}=0\ ,\ \forall\ \vec{x}\in\partial\Omega \tag{3.70}$$

where Ω is the fluid computational domain, $\partial\Omega$ is the associated domain reflective boundary, $\vec{x}$ is a position in the domain and $\vec{U}_T$ is the velocity component tangent to the boundary.

It should be mentioned that the first two relations of Eq. (3.70) specify completely the kinematic boundary condition. The third one, though not inconsistent with the inviscid flow assumed, is actually not required by the kinematic constraints (Wei and Kirby, 1995).

Absorbing boundaries

At the upwave and downwave limits of the computational domain, absorbing boundary conditions were imposed. In particular, in order to avoid wave reflection at the boundaries damping layers were applied to absorb the energy of the outgoing waves. The energy damping is achieved by adding the artificial damping terms F_{sp} and G_{sp} to the right-hand side of the x and y-momentum equations, respectively. These terms are defined by (Israeli and Orszag, 1981; Wei and Kirby, 1995):

$$F_{sp}=-w_1(x,y)U-w_2(x,y)\left(U_{xx}+U_{yy}\right) \tag{3.71a}$$

$$G_{sp}=-w_1(x,y)V-w_2(x,y)\left(V_{xx}+V_{yy}\right) \tag{3.71b}$$

where w_1 and w_2 are functions of two different kinds of damping mechanisms, Newtonian cooling and viscous damping, respectively. Assuming one sponge layer, i.e., from $x=x_{\text{sp}}$ to $x=x_{\text{L}}$ (computational domain from $x=0$ to $x=x_{\text{L}}$), then:

$$w_1(x)=\begin{cases}0, & x<x_{\text{sp}}\\ \alpha_1\omega f(x), & x\geq x_{\text{sp}}\end{cases} \tag{3.72a}$$

$$w_2(x)=\begin{cases}0, & x<x_{\text{sp}}\\ \alpha_2 v_{\text{sp}} f(x), & x\geq x_{\text{sp}}\end{cases} \tag{3.72b}$$

where α_1 and α_2 are constants to be determined for each specific run, v_{sp} is the viscous coefficient and ω is the frequency of the wave to be damped. The relaxation function is given by

$$f(x)=\frac{\exp\left[\left(\frac{x-x_{\text{s}}}{x_{\text{L}}-x_{\text{s}}}\right)^2\right]-1}{\exp(1)-1} \tag{3.73}$$

The width of the damping layers was taken to be three times the corresponding wavelength.

3.3.3 Numerical investigation

Compared to backward-differencing formulae, the ABM formulae are more accurate but less stable for the same order of accuracy in Δt. Increasing the order of ABM formulae corresponds to a reduction of the stable range of Courant numbers resulting in most ABM formulae being weakly unstable. The numerical scheme to discretize the enhanced nonlinear equations is quite complex. To gain some insight into the model, von Neumann's linear stability analysis was applied, for the case of constant water depth and one-dimensional flow only. A similar analysis was also performed by Wei and Kirby (1998) for Nwogu's (1993) equations. Under the aforementioned simplifications, the linearized version of the basic equations reads

$$\zeta_t = E = -dU_x \tag{3.74a}$$

$$U'_t = F = -\mathrm{g}\zeta_x + \mathrm{B}\mathrm{g}d^2\zeta_{xxx} \tag{3.74b}$$

The stability ranges for the predictor stage alone and the corrector stage alone are not the same. It also varies according to the number of the iterations used in each time step. For simplicity, the following stability analysis will be performed for the case which corresponds to using only one iteration in the corrector stage for each time step. This is the most common case when applying the linear model version on a horizontal bottom.

By applying von Neumann's analysis, ζ and U can be written at the j-node and n^{th} time step by their Fourier components as:

$$\zeta_j^n = \zeta_o \exp[i(kj\Delta x - \omega n\Delta t)] \tag{3.75a}$$

$$U_j^n = U_o \exp[i(kj\Delta x - \omega n\Delta t)] \tag{3.75b}$$

where $i = \sqrt{-1}$ is the imaginary unit, k and ω are the corresponding wavenumber and angular frequency. Thus, the discretization results to

$$(U')_j^n = U_j^n - \left(\mathrm{B} + \frac{1}{3}\right) d^2 \frac{U_{j+1}^n - 2U_j^n + U_{j-1}^n}{\Delta x^2} \tag{3.76a}$$

$$(U_x)_j^n = \frac{U_{j-2}^n - 8U_{j-1}^n + 8U_{j+1}^n - U_{j+2}^n}{12\Delta x} \tag{3.76b}$$

$$(\zeta_x)_j^n = \frac{\zeta_{j-2}^n - 8\zeta_{j-1}^n + 8\zeta_{j+1}^n - \zeta_{j+2}^n}{12\Delta x} \tag{3.76c}$$

$$(\zeta_{xxx})_j^n = \frac{-\zeta_{j-2}^n+2\zeta_{j-1}^n-2\zeta_{j+1}^n+\zeta_{j+2}^n}{2\Delta x^3} \tag{3.76d}$$

Since only one iteration is considered here for each time step, the discretized values are inserted into the linearized one-dimensional version of Eqs (3.53) and (3.54) and the resulting predicted values $\zeta_j^{(n+1)*}$ and $U_j^{(n+1)*}$ are inserted into the linearized one-dimensional version of Eqs (3.59) and (3.60) to directly obtain the desired values $\zeta_j^{(n+1)}$ and $U_j^{(n+1)}$. By applying Twizell's (1984) method for multiple time step schemes, the resulting discretized equations for the corrector step can be combined into a single matrix equation as

$$Z^{n+1} = AZ^n \tag{3.77}$$

where Z^{n+1} and Z^n are six element vectors defined as

$$Z^{n+1} = \left\{\zeta_j^{n+1}, U_j^{n+1}, \zeta_j^n, U_j^n, \zeta_j^{n-1}, U_j^{n-1}\right\}^T \tag{3.78a}$$

$$Z^n = \left\{\zeta_j^n, U_j^n, \zeta_j^{n-1}, U_j^{n-1}, \zeta_j^{n-2}, U_j^{n-2}\right\}^T \tag{3.78b}$$

and A is the 6x6 amplification matrix. The stability range can be determined by the condition that the modulus of all the six eigenvalues of A, λ_i $(i = 1, 2,.., 6)$, should not be greater than 1. These eigenvalues are a function of the ratio of water depth to the grid size $d/\Delta x$, the Courant number $C_r = \sqrt{gd}\Delta t/\Delta x$, and the dimensionless wavenumber $k\Delta x$. The lengthy analytical expressions of $|\lambda_i|$ are not given here. Instead of this, the variation of $|\lambda_i|$ for $d/\Delta x = 1$, $C_r \in [0, 2]$, and $k\Delta x \in [0, \pi]$ is depicted in Fig. 3.3. The specific figure refers to the standard ABM formulae proposed by Wei and Kirby (1995), and thus $(\alpha, \alpha^*) = (1,1)$. It can be observed that only the first two of the eigenvalues have moduli that can exceed one for certain values of $d/\Delta x$, C_r, and $k\Delta x$. These two eigenvalues are complex conjugate and therefore their moduli are exactly the same. Thus, it is sufficient to study the variation of $|\lambda_1|$ for different values of $d/\Delta x$, C_r, and $k\Delta x$ in greater detail.

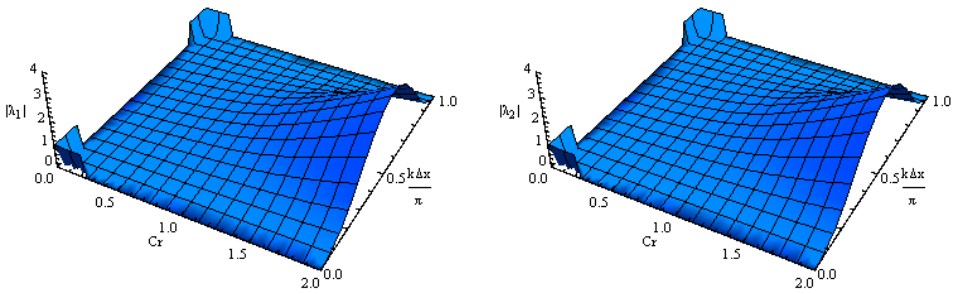

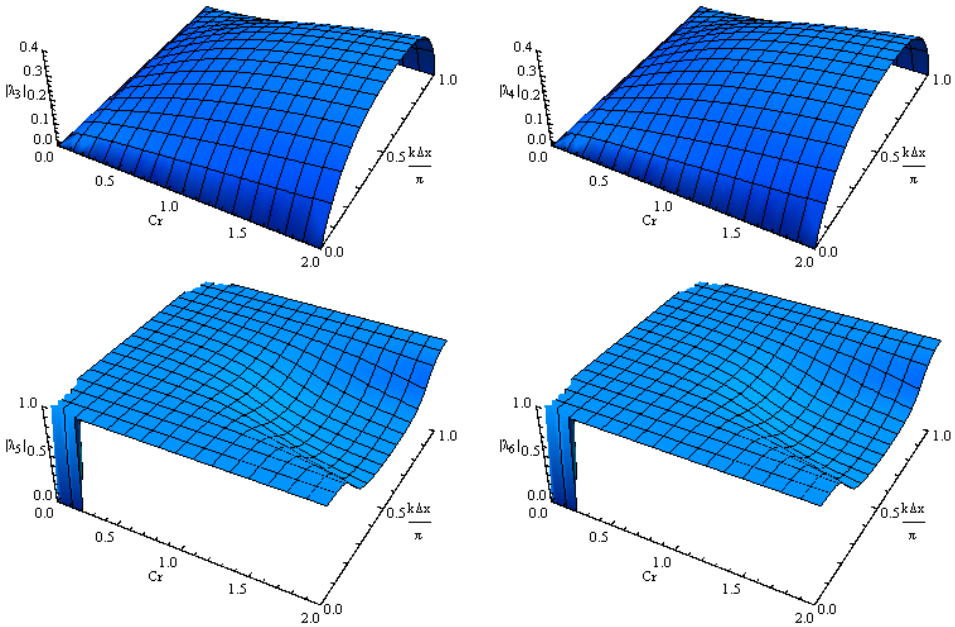

Fig. 3.3. Variation of the six eigenvalues' moduli $|\lambda_i|$ $(i = 1, 2, 3, 4, 5, 6)$ with Courant number, C_r, and dimensionless wavenumber, $k\Delta x$, for a fixed value of $d/\Delta x = 1$.

For a more detailed analysis of the stability range, five cross sections corresponding to $k\Delta x = \nu\frac{\pi}{10}$ $(\nu = 1, 2, 3, 4, 5)$ were chosen from Fig. 3.3 to plot the diagrams in Figs 3.4 and 3.5. From Fig. 3.4 it can be concluded that for fixed values of C_r and $d/\Delta x$, the maximum value of $|\lambda_1|$ is reached at $k\Delta x = \frac{\pi}{2}$. Therefore, the numerical scheme will be linearly stable if $|\lambda_1| \leq 1$ at $k\Delta x = \frac{\pi}{2}$. Fig. 3.5 shows the variation of $|\lambda_1|$ with C_r for a fixed value $k\Delta x = \frac{\pi}{2}$ and several values of $d/\Delta x$. It seems that $|\lambda_1|$ is a decreasing function of the ratio $d/\Delta x$. However, further analysis showed that the value of the eigenvalue's modulus for $d/\Delta x = 0.01$ is very close to the corresponding one for $d/\Delta x = 0.1$. Therefore, it can be concluded from the aforementioned analysis and the relevant figures that the numerical scheme using one predictor and one corrector stage is linearly stable if $C_r \leq 0.88$, regardless the values of $d/\Delta x$ and $k\Delta x$.

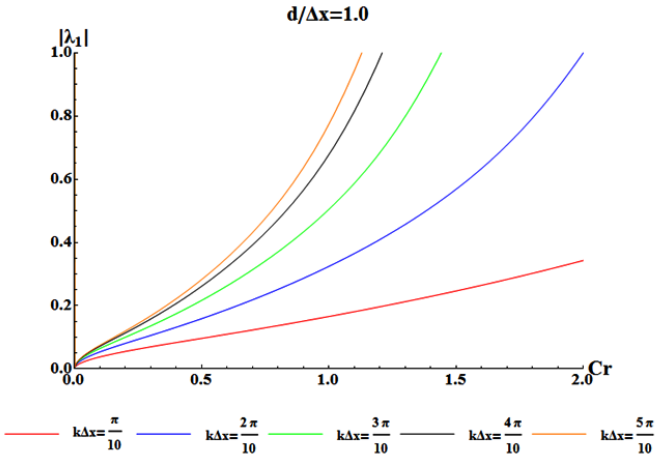

Fig. 3.4. Variation of the eigenvalue's modulus $|\lambda_1|$ with Courant number, C_r, for various values of the dimensionless wavenumber, $k\Delta x$, and for a fixed value of $d/\Delta x = 1$ [Wei and Kirby's (1995) scheme with $(\alpha, \alpha^*) = (1,1)$].

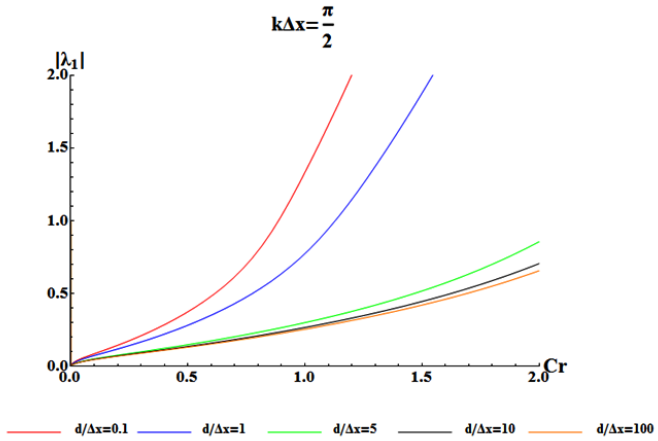

Fig. 3.5. Variation of the eigenvalue's modulus $|\lambda_1|$ with Courant number, C_r, for various values of the ratio $d/\Delta x$, and for a fixed value of $k\Delta x = \frac{\pi}{2}$ [Wei and Kirby's (1995) scheme with $(\alpha, \alpha^*) = (1,1)$].

The generalized multistep predictor-corrector formula introduced by Zlatev *et al*. (1983, 1984) extends the linear stability range of the standard ABM formula through the insertion of the free parameters (α, α^*) (Banijamali, 1998). Application of the values $(\alpha, \alpha^*) = (-0.85, 1.80)$ derived by Zlatev *et al*. (1983) for a third-order predictor followed by a fourth-order corrector step results to Figs 3.6 and 3.7. These values offer an extension of the linear stable region to $C_r \leq 1.28$, regardless the values of $d/\Delta x$ and $k\Delta x$.

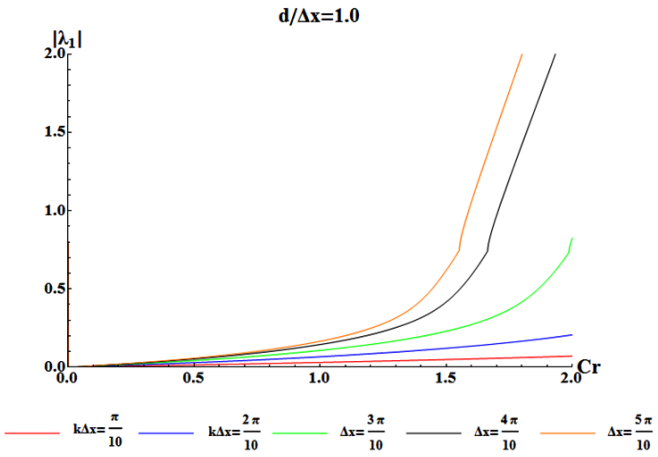

Fig. 3.6. Variation of the eigenvalue's modulus $|\lambda_1|$ with Courant number, C_r, for various values of the dimensionless wavenumber, $k\Delta x$, and for a fixed value of $d/\Delta x = 1$ [generalized multistep predictor-corrector scheme with $(\alpha, \alpha^*) = (-0.85, 1.80)$].

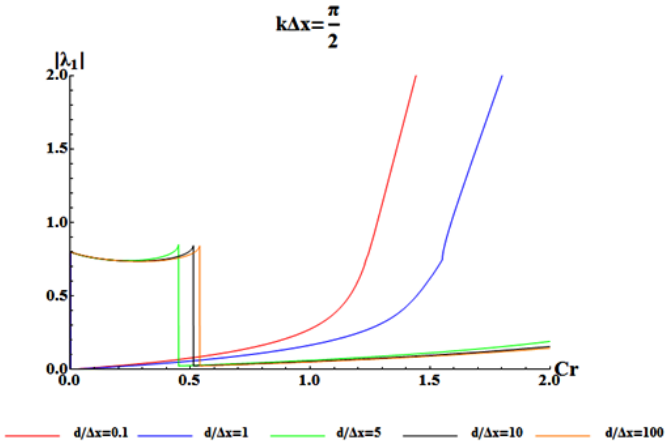

Fig. 3.7. Variation of the eigenvalue's modulus $|\lambda_1|$ with Courant number, C_r, for various values of the ratio $d/\Delta x$, and for a fixed value of $k\Delta x = \frac{\pi}{2}$ [generalized multistep predictor-corrector scheme with $(\alpha, \alpha^*) = (-0.85, 1.80)$].

It should be mentioned that the stability properties described above refer to only one iteration at the corrector stage. If more than one iterations are executed, the stability range is modified. In addition, the aforementioned analysis refers to linear stability over a horizontal bottom which is a strong simplification. However, most of the numerical instabilities, even of the linear type, occur on a sloping bottom where the sloping terms amplify the spurious forms. Moreover, in most of the real model applications the nonlinear effects are not negligible, and the criterions for linear stability evaluated above do not guarantee the overall numerical stability of the scheme.

In most of the cases studied in the present thesis a very low, and even more negative, value of the free parameter α resulted to a low rate of convergence of the numerical scheme. Hence,

in all the computations the parameters α and α^* were considered in the range 0.8-1.2 and linear stability was ensured, even for very long runs, by keeping the Courant number around 0.30-0.35. However, in some cases nonlinear instability occurred under strongly nonlinear conditions or close to the boundaries. In these cases short spurious waves were generated by higher order nonlinear terms, infected the solutions and led shortly to unstable results. In most of these computations the application of a low-pass fourth-order Shapiro (1970) numerical filter was enough to remove the spurious noise. The analytical expression for this one-dimensional 9-point filter is given by

$$Z_i^* = \frac{1}{256}[186Z_i + 56(Z_{i+1} + Z_{i-1}) - 28(Z_{i+2} + Z_{i-2}) + 8(Z_{i+3} + Z_{i-3}) - (Z_{i+4} + Z_{i-4})] \tag{3.79}$$

where $Z_i = \{\zeta_i, U_i\}$ represents the original values which consists of both long and short waves, and Z_i^* represent the new values with short waves being filtered out. It is straightforward to obtain an expression for the corresponding two-dimensional filter. However, this would be a very complex formula involving 9 x 9 = 81 neighboring points for each filtered point. Instead of this, the 1-D formula was applied twice, firstly in the x direction and subsequently in the y direction to account for the two dimensional case. This simplified approach is very convenient although it introduces some inaccuracies concerning artificial numerical anisotropy in the wave propagation. The response function, R^*, is expressed by the ratio of the smoothed to unsmoothed amplitudes:

$$R^* = \left[1 - \sin^8\left(\frac{\pi\Delta x}{L_x}\right)\right]\left[1 - \sin^8\left(\frac{\pi\Delta y}{L_y}\right)\right] \tag{3.80}$$

where L_x and L_y denote the wavelengths in the x and y directions, respectively. Fig. 3.8 depicts the variation of the response function with respect to the ratio of the wavelength to the grid size for both the one- and two-dimensional cases. The 1-D diagram also shows the variation of the response function with respect to the order N of the Shapiro (1970) filter used. Waves with wavelength twice of the grid size are completely filtered out. As the wave length increases, the value of R^* also increases. Thus, the effect of filtering decreases for longer waves.

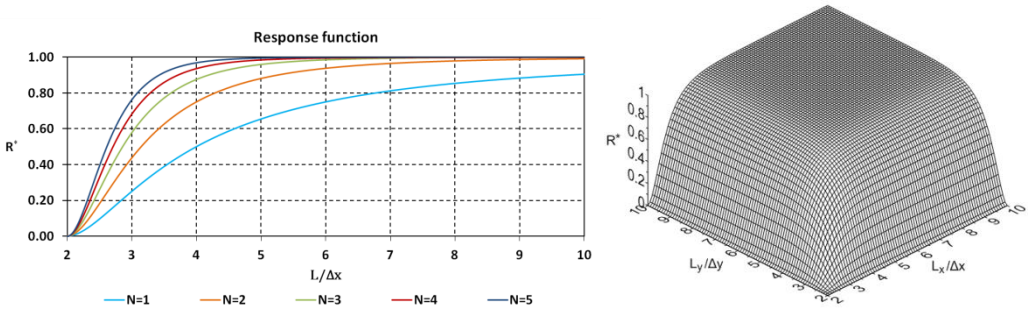

Fig. 3.8. Response function for various orders of the 1-D numerical filter (at left) and 2-D filter (at right).

Every time the low-pass filter is applied, a fraction of the long wave energy is also undesirably damped. Moreover, it is apparent from Fig. 3.8 that the efficiency of the filter increases as the order increases, leading, though, to larger inaccuracies. The fourth-order filter appears as a good option since it is a quite light filter, almost imperceptible for wavelengths longer than 5-6 times the grid size. Nevertheless in some runs the application of an extra localized numerical filter was required in order to completely remove the instabilities in areas of intense nonlinearity, such as close to breaking initiation or in the swash zone.

For wave propagation simulations, the accuracy can often pose more stringent requirements than stability, and thus Courant numbers near the stability limit are not generally encouraged. The accuracy with the respect to the order of discretization has been commented above. In addition, a grid sensitivity analysis is also performed for the cnoidal wave test presented in subsection 3.4.1. In general, the linear properties of a propagating wave are adequately reproduced if 10 grid points are used per wavelength (Banijamali, 1998). However, in order to describe the characteristics of highly nonlinear waves, 40-80 points per wavelength are required. The spatial discretization errors are more often the dominant source of errors in comparison to time discretization errors. This is further pronounced due to the presence of higher-order spatial derivatives compared to only first-order time-derivatives.

Another issue with regard to accuracy refers to numerical refraction in two horizontal dimensions. Finite resolution causes preferred directions of propagation (anisotropy). The numerical isotropy of wave propagation is checked herein through a benchmark ring test. A Gaussian symmetrical hump was generated in the center of a square tank 10 x 10 m. The tank had a uniform depth of 0.5 m and was surrounded by fully reflective vertical walls. The initial Gaussian-shaped free surface elevation was given by

$$\eta_o(x,y) = 0.1\exp\{-0.4[(x-5)^2 + (y-5)^2]\} \tag{3.81}$$

Due to gravitational forcing, the wave was generated and propagated out of the center and then it was reflected back in the domain by the four side walls. Since no sponge layers were

used and there was no wave breaking and bottom friction, there should be no energy loss. Fig. 3.9 shows contour plots of surface elevation at various times.

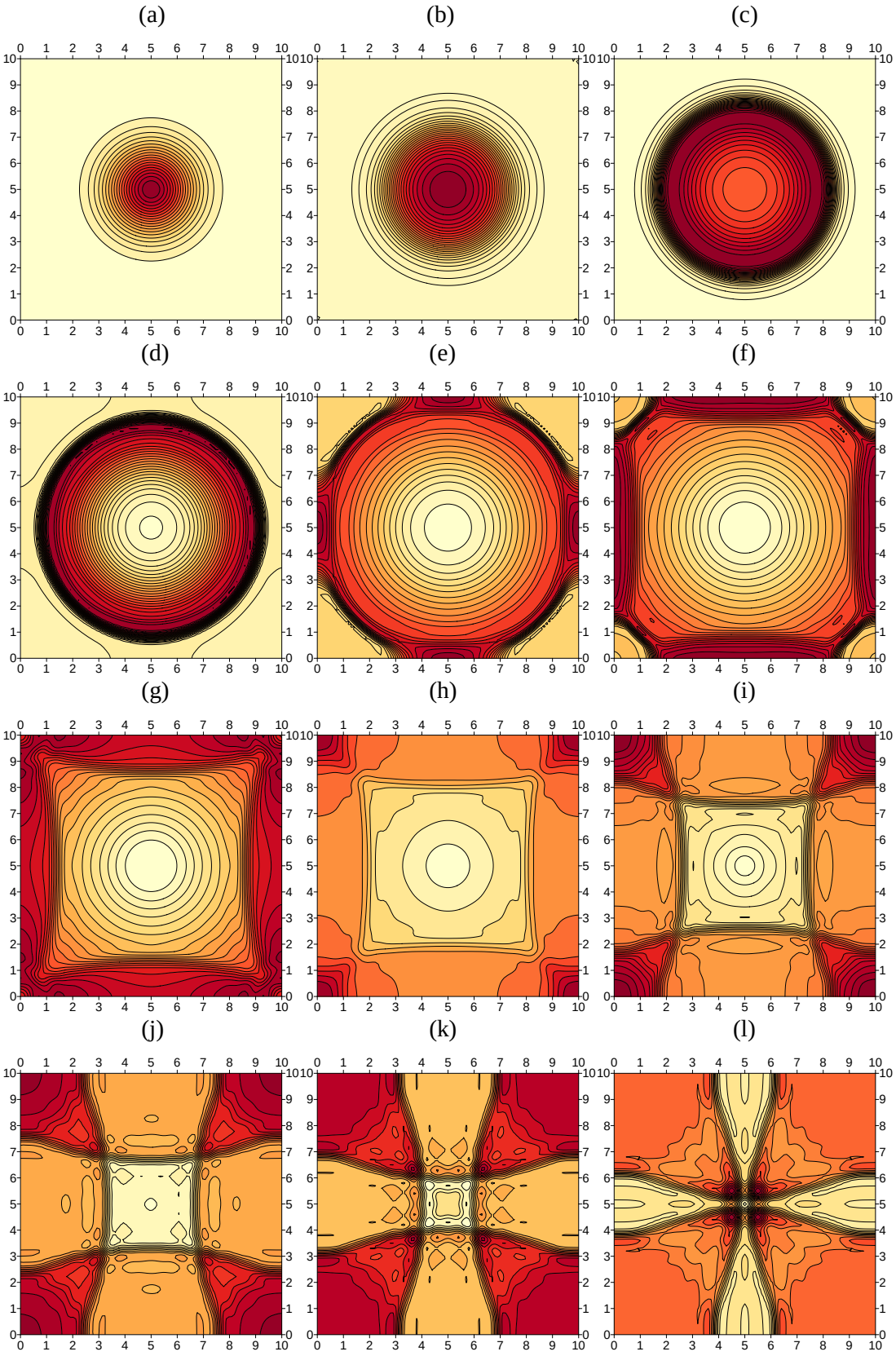

Fig. 3.9. Contour plots of free surface elevation at time (a) $t = 0$; (b) $t = 1$; (c) $t = 2$; (d) $t = 3$; (e) $t = 4$; (f) $t = 5$; (g) $t = 6$; (h) $t = 7$; (i) $t = 8$; (j) $t = 9$; (k) $t = 10$; (l) $t = 11$;

The grid size was $\Delta x = \Delta y = 0.1$ m and the time step $\Delta t = 0.02$ sec. It can be observed that the symmetric characteristics of the tank and initial conditions result to almost perfectly symmetric wave patterns. Thus, the spurious numerical anisotropy introduced by the numerical scheme is negligible. Since a source function is not applied here to generate waves and the four wall boundaries around the basin are fully reflective, the water volume should remain constant. Fig. 3.10 depicts the timeseries of the relative error of the water volume in the entire tank defined by

$$Er(t) = \frac{V(t) - V(0)}{V(0)} \tag{3.82}$$

where $V(t)$ is the total water volume with respect to the still water level ($V(t) = 0$ when the water is calm) and $V(0)$ is the initial volume of the Gaussian hump. As shown in Fig. 3.10, the relative error of the water volume is less than 1% and hence the numerical scheme conserves the mass and the boundary conditions are well posed.

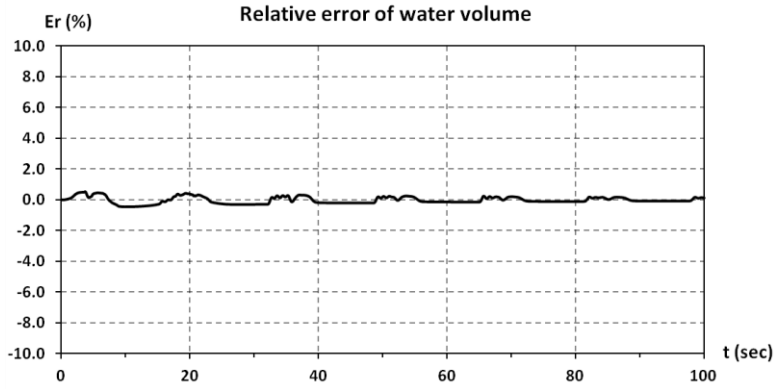

Fig. 3.10. Timeseries of the relative error E of the water volume in the tank.

Apart from accuracy, the required computational time is a serious issue when evaluating wave models. Boussinesq-type wave models imply reduced computational time compared to fully 3-D models but they are more time-consuming compared to phase-averaged wave models, especially when dealing with two-horizontal dimensional applications. The numerical solution of Boussinesq equations involves large matrices, e.g. 500x500, 1000x1000, etc. and thus have computations. Hence, the PC used for the simulations should have some requirements of high standards, i.e. high processor frequency, low ratio of processor frequency to FSB (Front Side Bus), Large L2 Cache memory, and a minimum of available RAM, say 1GB.

In order to check the Boussinesq model's computational cost, it was run on four different PCs to simulate the ring test described above. All of them included multi-cored processors and parallel computing was used to accelerate the computations. The technical characteristics

of the processors are given in table 3.1. The compiler used in all the computations was Intel Visual Fortran 11.1.051.

Table 3.1. Technical characteristics of the PCs used in simulations.

Processors	Cores	Frequency	RAM
Intel Core 2 Duo T9600	2	2.80 GHz	6 GB
Intel Core i7-2670QM	4	2.20 GHz	4 GB
Intel Core i7-4770	8	3.40 GHz	16 GB
Intel Xeon E5-2620v2	12	2.10 GHz	8 GB

A comparison of the variation of the computational time with the number of time steps for the various processors is depicted in Fig. 3.11. The diagram at left refers to the test described above which includes 301x301 grid points. It can be seen that, in general, the increase of the number of cores offers significant acceleration of the computations when parallel computing is used. However, the 8-cored processor appears to be faster than the 12-cored. This is explained by the higher frequency of the former's (3.40 GHz) compared to latter's (2.10 GHz). In addition, parallel computing implies some time consumption because of the communication of the different cores. It should be also mentioned that some delay in computations also appears because the 12-cored processor consists actually of two 6-cored processors and thus their inter-processor communication requires some extra time. However, if the ring test is applied on a much larger domain including 1001x1001 grid points, then the 12-cored processor is faster, though slightly, than the 8-cored, since the computational strain corresponding to each core is much increased. Consequently, the superiority of the one over the other processor depends on their frequency, the number if cores when parallelization is used, and also the size of the computational domain.

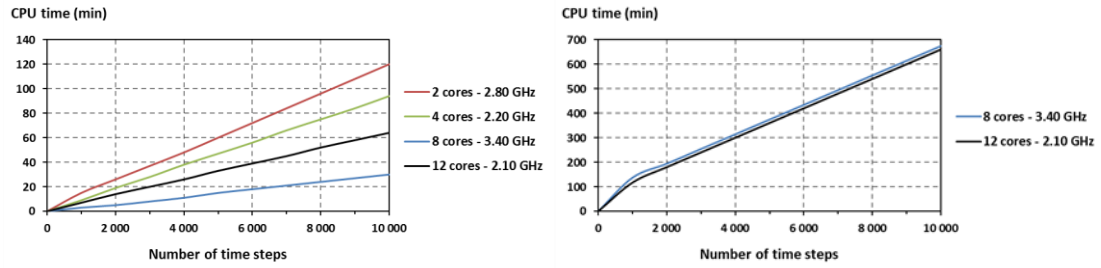

Fig. 3.11. Computational time for four different processors for 301x301 grid points (at left) and two different processors for 1001x1001 grid points (at right).

The significance of the parallelization in computations is pronounced in Fig. 3.12 where the ratio of the computational time required without using parallel computing to the corresponding time when using parallelization is depicted for the 8- and 12-cored processors.

It can be observed that for the domain including 301x301 points the parallelization offers a speed-up of about 2.5 times for the 8-cored processor and about 2 times for the 12-cored. The reasons for this limited gain of time were explained above and they are attributed to inter-procedural delays during the communication of the different cores. However, if the large domain of the 1001x1001 points is considered, the speed-up for the 8-cored processor is still 2.5 times, while for the 12-cored it is increased to 4 times.

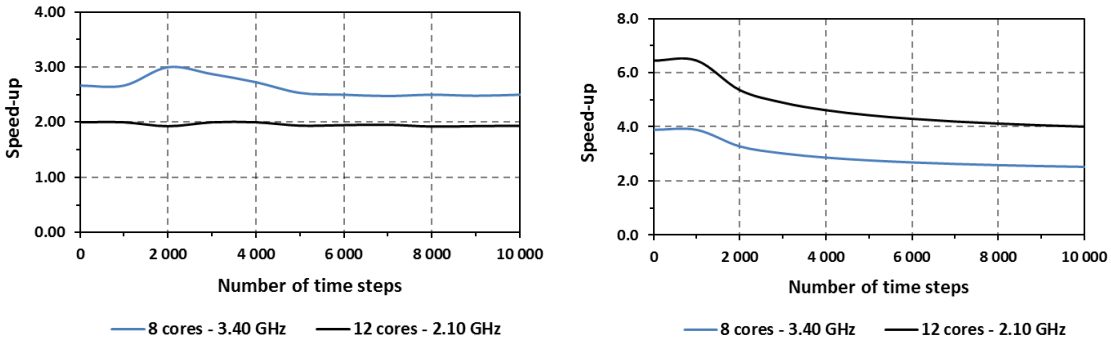

Fig. 3.12. Speed-up due to parallelization for 301x301 grid points (at left) and 1001x1001 grid points (at right) for 8-cored and 12-cored processors.

As a practical conclusion, it can be said that simulation of 20 min of wave propagation in a domain of a coastal zone with dimensions 1 km x 1 km would require about 1 day of computational time on an 8-cored PC similar to the one described above. These computational times are not prohibitive anymore with the more and more increased power of computers. Moreover, the recently introduced GPU technology offers a powerful and promising tool for the application of two-dimensional phase-resolving wave models in larger computational domains even on personal PCs.

3.4 Model validation

In order to check the model's ability to simulate nearshore dynamics, both its 1DH and 2DH versions were validated through a number of experimental tests. Both regular and irregular wave propagation over plane beaches, submerged shoals and a rip channel were studied. The results were compared to laboratory measurements involving time domain data, wave spectra, phase-averaged wave parameters and current fields. Some of the tests are very demanding since they combine a number of physical processes such as shoaling, depth refraction, diffraction, breaking, wave run-up, overtopping, nonlinear energy transfer and interactions with the wave-induced current field.

3.4.1 1DH validation

Regular breaking waves on a planar beach

The first set of comparisons refers to the data by Hansen and Svendsen (1979). Their experiments were conducted in a wave flume involving shoaling and breaking regular waves. The waves were generated on a horizontal bottom at a depth of 0.36 m, followed by a planar beach of slope 1:34.26. Measurements of the surface elevation were taken at a large number of stations using an automated, continuously moving trolley. Due to a considerable scatter of the measured values the measurements were smoothed somewhat following Kennedy *et al*. (2000).

The entire data set covers a variety of different breaking conditions. In the present study two cases were chosen to be checked. The first one, case No. 051041, involved spilling breaking waves with a period of T = 2.0 s and incoming wave height H_o = 0.036 m. The second one, case No. 031041, referred to plunging breaking waves with T = 3.33 s and H_o = 0.043 m. The breaker types were distinguished based on a surf similarity analysis. A comparison between the measured and the computed wave height and wave setup for the two cases is shown in Figs 3.13, 3.14, 3.15 and 3.16. The grid step and the time step were 0.02 m and 0.004 s, and 0.03 m and 0.006 s for test cases No. 051041 and No. 031041, respectively. Both for the spilling and plunging cases the parameters for breaking initiation and cessation were set to $\zeta_t^{(I)} = 0.65\sqrt{gd}$ and $\zeta_t^{(F)} = 0.15\sqrt{gd}$, respectively. A sensitivity analysis showed that both the wave height and wave setup are sensitive to the value of $\zeta_t^{(I)}$, while no significant sensitivity to the value of $\zeta_t^{(F)}$ was observed. However, the default values described in subsection 3.2.1 for breaking on a plane beach were applied. The mixing length coefficient δ_b was set after calibration to 1.0 and 1.2 for the spilling and plunging tests, respectively.

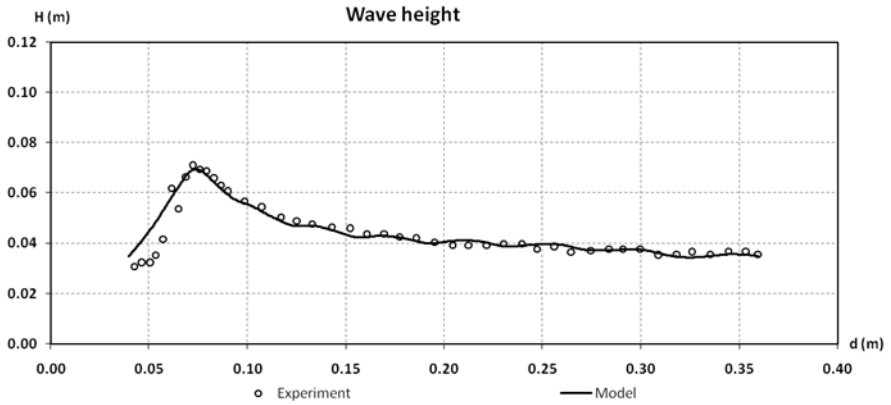

Fig. 3.13. Computed and measured wave height for spilling breaker case No. 051041.

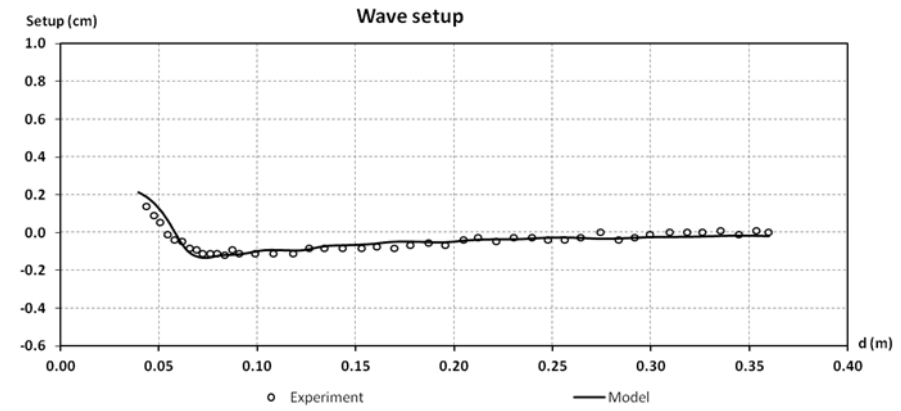

Fig. 3.14. Computed and measured wave setup for spilling breaker case No. 051041.

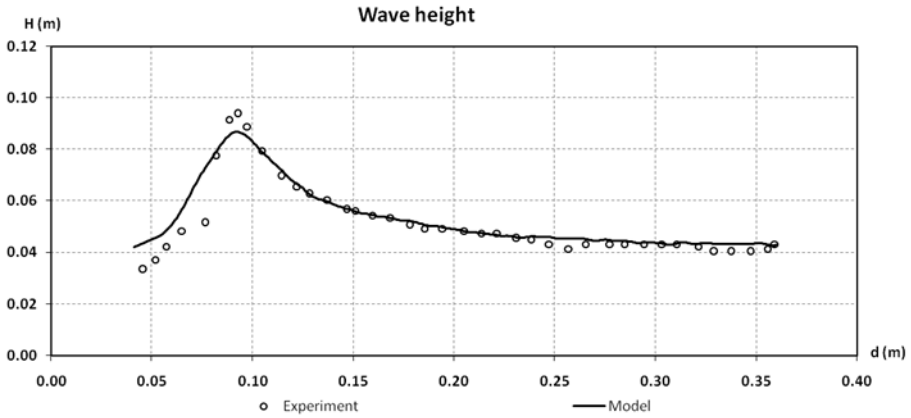

Fig. 3.15. Computed and measured wave height for plunging breaker case No. 031041.

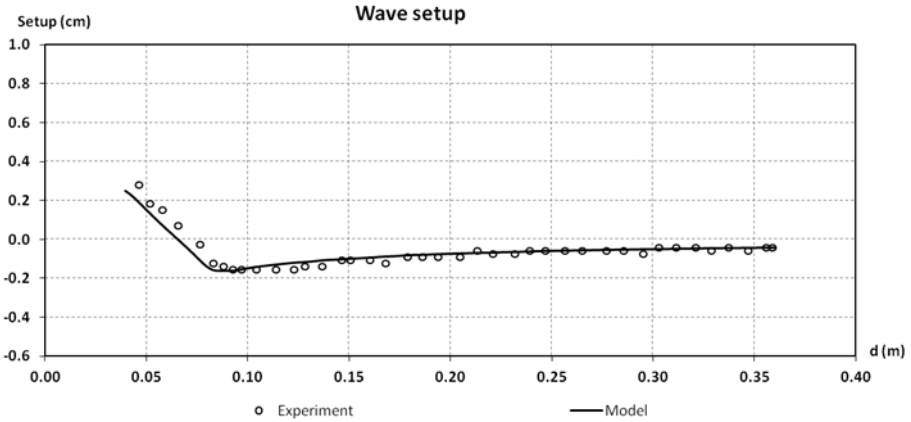

Fig. 3.16. Computed and measured wave setup for plunging breaker case No. 031041.

The dimensionless wavenumbers in the source region for the spilling and the plunging breaking tests were kd = 0.64 and 0.37, respectively. Thus both cases lie in the range of applicability of the present model. The comparison for the spilling case is very good. Both the breaking height and the initiation of breaking are well-predicted. There is only a slight over-prediction of wave height and setup in the inner surf zone. This has been also observed in

other Boussinesq-type models simulating wave breaking by using the eddy viscosity concept (Kennedy *et al*., 2000). Simulating plunging breaking is a difficult task due to the intense and rapid energy dissipation. However, the comparison herein is quite reasonable. The position of breaking initiation is predicted accurately but the maximum wave height is underestimated, with an error of about 7.5%. In this test, the over-prediction of the wave height in the inner surf zone is more pronounced.

For the spilling breaking test case the mass balance was studied in order to evaluate the efficiency of the slot technique. For a long wave surging up a gentle slope, where numerical diffusion is small, the moving boundary is important for the conservation of the total mass. A reference water volume was considered extended from the toe of the sloping beach to 1 m downwave of the still shoreline. The ratio of error introduced in the mass balance equation to the initial water volume inside the frame of reference was computed and is presented in Fig. 3.17. This relative error is very small, proving the efficiency of the model to conserve the total mass.

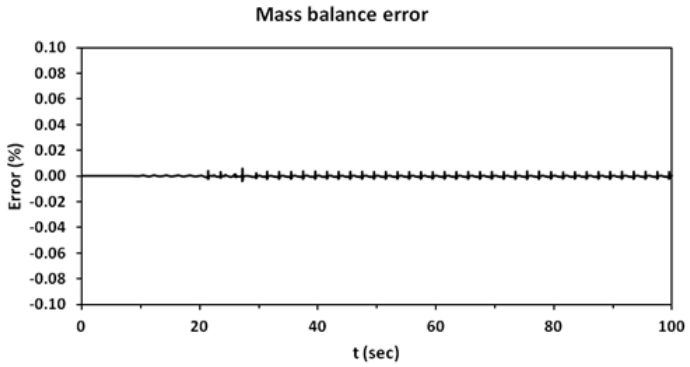

Fig. 3.17. Time evolution of relative error in mass balance.

Apart from the two cases described above, an extra test concerning regular wave breaking was also employed to check the model's ability to estimate the depth-averaged undertow. This test is reported by Hansen and Svendsen (1984) and was performed using the same experimental layout as the one described above. It involves waves of period T = 2.0 s and incoming wave height H_o = 0.12 m. This is a strongly nonlinear waveform since ε = 0.33 and the dimensionless wave number at the horizontal bed is kd = 0.64. The breaker is of spilling type. The spatial step was $\Delta x = 0.02$ m and the time step Δt = 0.004 s. Figs 3.18, 3.19, and 3.20 depict the wave height, the wave setup and the depth-averaged undertow variation respectively, with x = 0 at 2.7 m offshore of the toe of the slope (15 m from the still water shoreline).

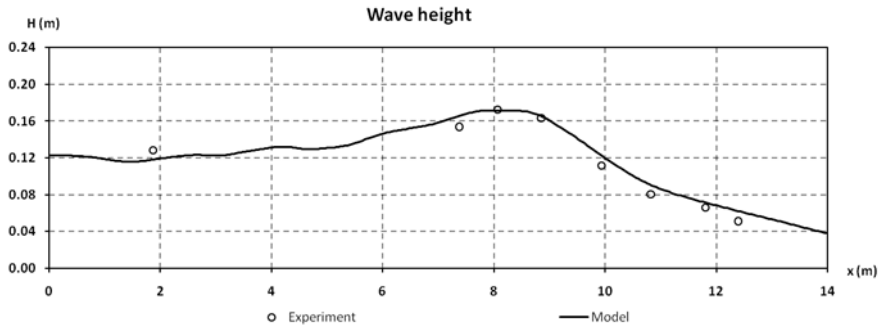

Fig. 3.18. Computed and measured wave height in Hansen and Svendsen's (1984) test.

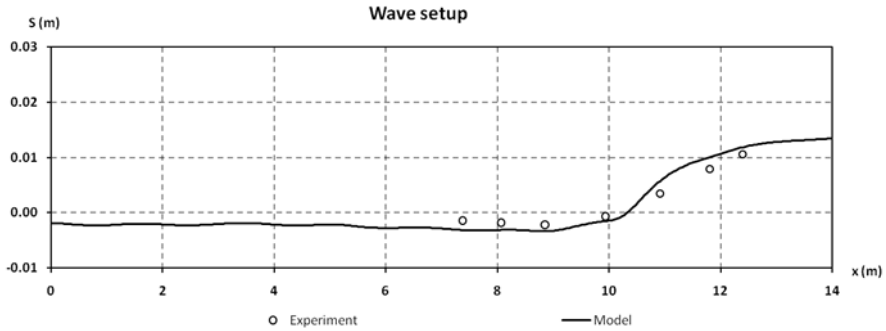

Fig. 3.19. Computed and measured wave setup in Hansen and Svendsen's (1984) test.

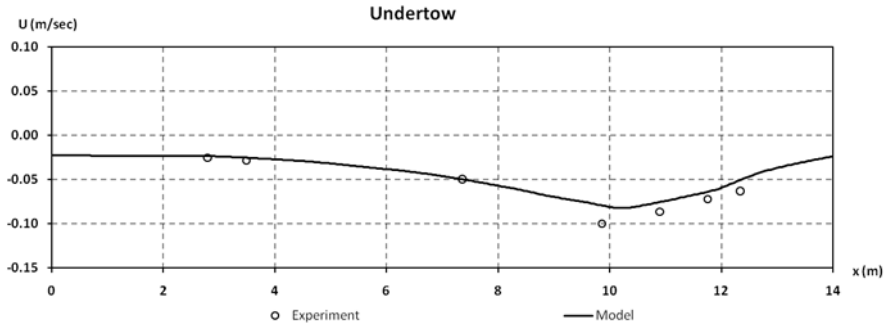

Fig. 3.20. Computed and measured depth-averaged undertow in Hansen and Svendsen's (1984) test.

Despite the strongly nonlinear conditions, all three variables tested are well-predicted, proving the significance of the enhanced nonlinear character of the model. The tendency and the position of the extremes are acceptably predicted. Thus, it can be said, in general, that the flow properties in the surf zone can be modelled with reasonable accuracy.

Another, more demanding, test for checking the model's response to regular wave breaking of weak plunging type was the one corresponding to Stansby and Feng's (2005) experiment. Shorenormal waves with height H_o = 0.105 m and period T = 2.42 s were generated at a constant depth region of d = 0.34 m and then propagated on a constant slope 1:20. A spatial step of 0.04 m and a time step of 0.005 s were chosen. A comparison between the measured and computed by the model wave height and wave setup are shown in Fig. 3.21.

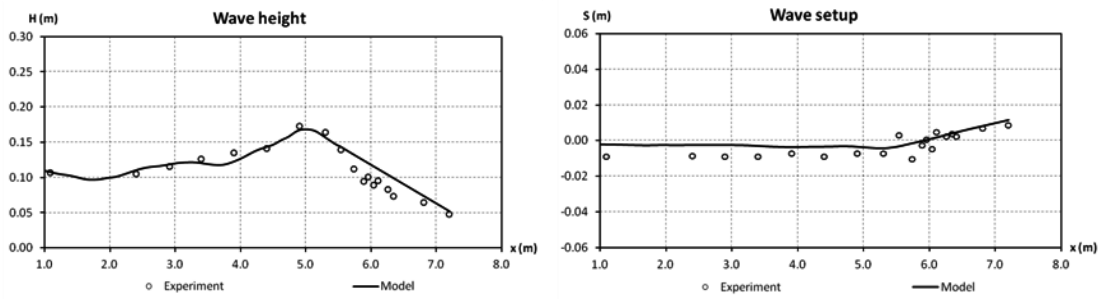

Fig. 3.21. Measured and computed wave height (left) and wave setup (right) for Stansby and Feng's (2005) experiment.

Wave breaking initiation was observed at about x = 4.95 m. The model over-estimates the wave height in the inner surf zone. However, it should be noted that the specific experimental test hardly lies in the range of applicability of the specific Boussinesq-type model due to the high Ursell number, Ur = 48.19, much higher than 32 which is approximately a typical limit for the original Boussinesq theory. In addition, plunging breaking is difficult to be simulated by a Boussinesq model because total flow disruption and intense foaming take place. Thus, despite the discrepancies observed in Fig. 3.22 the overall response of the Boussinesq-type model to this demanding test was acceptable. A comparison with the results of an SPH model (Makris *et al*., 2015, 2016) for the specific test case can be found in Klonaris *et al*. (2015).

Cnoidal breaking waves

The one-dimensional model version was further validated against the benchmark test by Ting and Kirby (1994). The experiments were conducted in the 40 m long wave tank of the Ocean Engineering Laboratory at the University of Delaware. The experimental layout is shown in Fig. 3.22. Both spilling and plunging cnoidal waves were examined. The waves were generated by a bulkhead wave generator over a constant depth of 0.4 m and were then shoaled on a plywood false bottom creating a uniform slope of 1:35. The test case chosen here involves spilling breaking of cnoidal waves of period T = 2.0 s and incoming wave height H_o = 0.125 m.

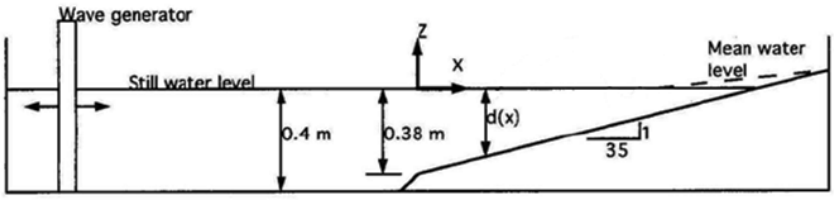

Fig. 3.22. Layout of Ting and Kirby's (1994) experiment (from Ting and Kirby, 1994, modified).

Periodic waves were generated for a minimum of 20 minutes before data were taken. Thus a steady-state condition was established. The still water depth at the twenty one measurement stations is given in Table 3.2. The grid spacing was $\Delta x = 0.04$ m and the time step $\Delta t = 0.004$ s.

Table 3.2. Still water depth at the locations of measurements.

Stations	1	2	3	4	5	6	7
Still water depth (m)	0.400	0.400	0.367	0.338	0.314	0.290	0.247

Stations	8	9	10	11	12	13	14
Still water depth (m)	0.221	0.207	0.196	0.193	0.177	0.163	0.150

Stations	15	16	17	18	19	20	21
Still water depth (m)	0.138	0.124	0.106	0.089	0.077	0.063	0.049

A comparison between the measured and the computed time series of the free surface elevation at various stations is shown in Fig. 3.23. Results for both the present model and its weakly nonlinear counterpart of $O(\varepsilon\sigma^2)$ are depicted. The model's response is quite accurate, succeeding in describing the wave form steepening due to shoaling. The breaking point was measured at depth d_b = 0.196 m (station 10) and the breaking height H_b = 0.1625 m. Both the present model and its weakly nonlinear counterpart embed similar linear characteristics since they differ only by the terms of $O(\varepsilon^2\sigma^2)$. Thus, they can both describe linear dispersion very accurately up to kd = 3. A slight superiority of the enhanced nonlinear model over the weakly nonlinear one is confirmed by the presented comparison. This concerns mainly the nonlinear dispersion, as already discussed in chapter 2. Although the target solution for the amplitude dispersion relation in Fig. 2.6 is the one given for Stokes theory, still the phase error was found larger for the weakly nonlinear model version applied to cnoidal waves.

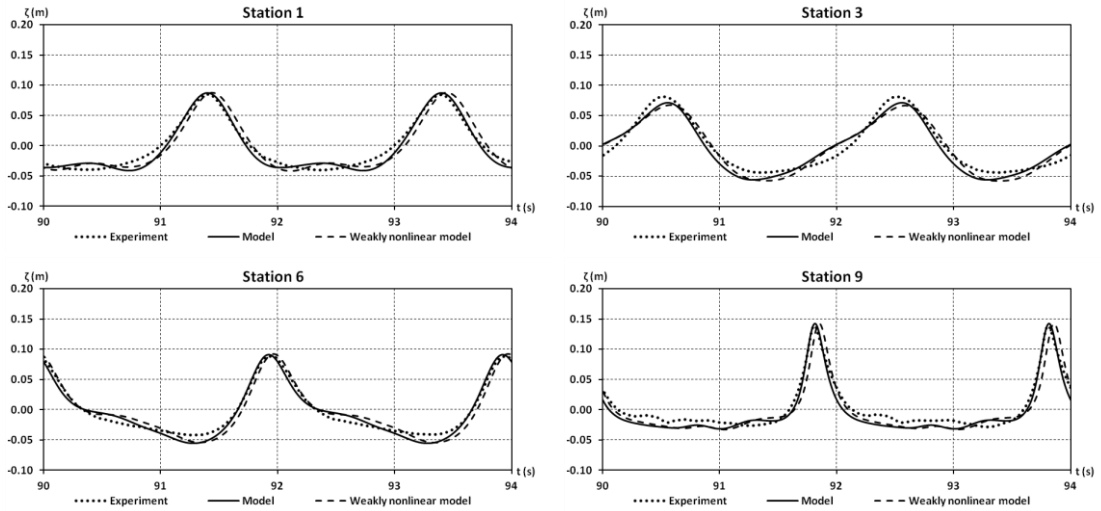

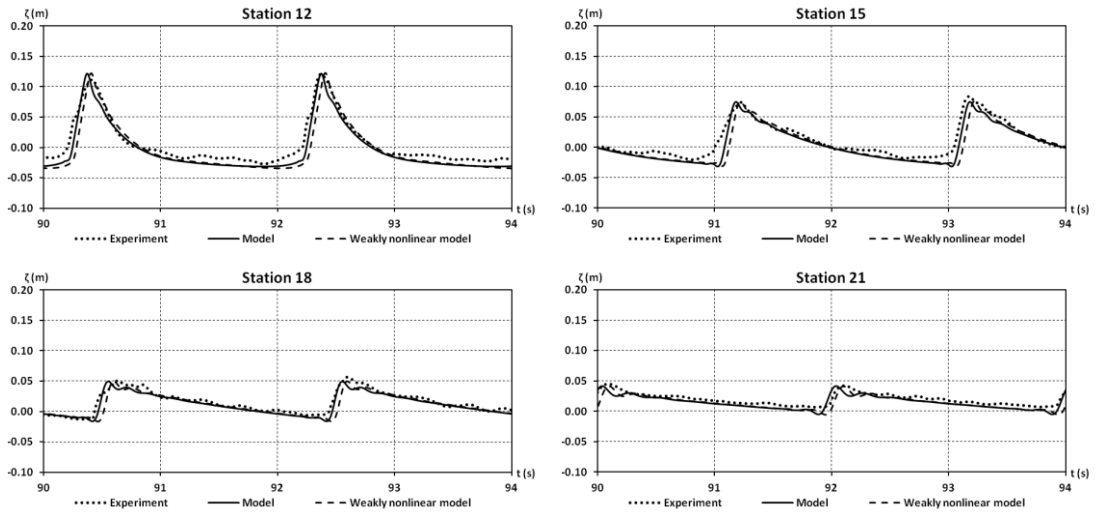

Fig. 3.23. Time series of free surface elevation at various stations in Ting and Kirby's (1994) experiment.

In order to get a more clear insight of the model's nonlinearity, a grid sensitivity analysis was applied in the specific test case. Both the enhanced and the weakly nonlinear model versions were run for four different grid sizes, Δx = 0.02, 0.03, 0.04 and 0.08 m and an inter-comparison at station 9 is depicted in Fig. 3.24. The specific station is located slightly upwave of the breaking point where the conditions are highly nonlinear with $\varepsilon \approx 0.80$.

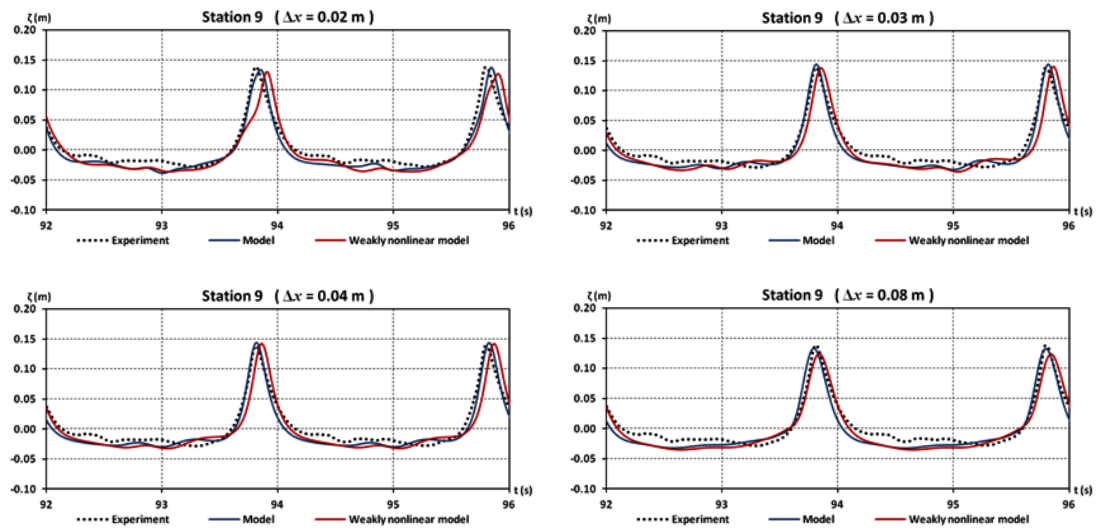

Fig. 3.24. Time series of free surface elevation at station 9 in Ting and Kirby's (1994) experiment for various grid sizes.

The discrepancies between the two model versions seem independent of the grid size as the present model is more accurate with respect to nonlinear dispersion in all cases. Moreover, for such highly nonlinear conditions the applied discretization with Δx = 0.04 m, leading to approximately 70 grid points per wavelength close to the breaking point, is adequate. A

similar result was observed for the rest of the test cases studied in the present thesis. A very fine resolution of Δx = 0.02 m seems to produce an over-pronounced asymmetry of the wave form, while even finer resolutions led to numerical instabilities. On the other hand, a coarser resolution of Δx = 0.08 m tends to flatten the wave forms. Nevertheless, for the range of values studied here the results did not show a strong sensitivity on the grid size. Thus, for such highly nonlinear waves 40-80 points per wavelength adequately reproduce the wave's nonlinearity.

Fig. 3.25 shows the comparison between the measured and computed distribution of wave amplitudes and mean water level. The distance x is measured positive shoreward from the toe of the slope. The mean surface elevation is denoted by ζ_{mean} and the maximum and minimum surface elevation by ζ_{max} and ζ_{min}, respectively. Breaking point is captured well by the model, along with the wave height decay in the surf zone. The quite accurate computation of both positive and negative amplitudes supports the model's capability to describe the nonlinear crest-trough asymmetry. Wave set-down and setup are also acceptably predicted but for a slight underestimation in the outer surf zone. However, the general tendency and the decrease of the setup slope in the inner surf zone are correctly reproduced.

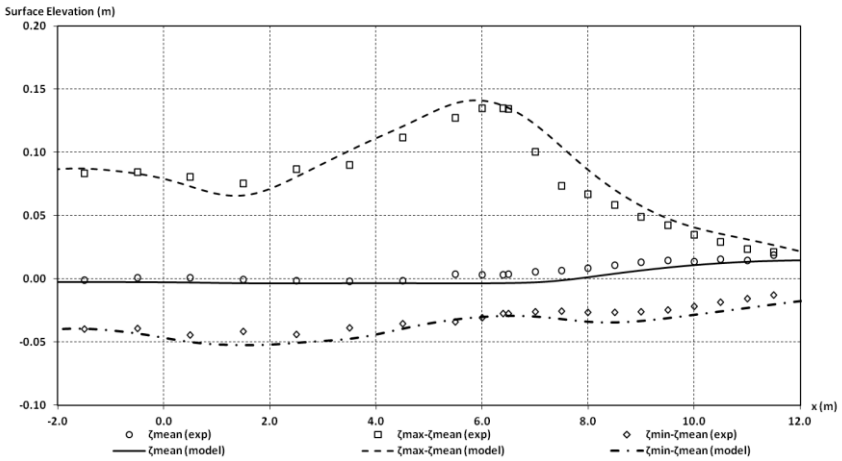

Fig. 3.25. Distribution of wave amplitudes and mean water level.

In general the results presented here are satisfactory and indicative of the model's ability to simulate accurately the nearshore conditions, where cnoidal waves are typically present.

Solitary wave breaking and run-up

In order to further check the model's response in the surf and swash zones the experiment by Synolakis (1987) was simulated. This corresponds to the propagation and breaking of a solitary wave on a laboratory beach of constant slope 1:19.85. The experiment was performed in the W. M. Keck Laboratories of the California Institute of Technology. The wave tank had

glass sidewalls and dimensions 37.73 m × 0.61 m × 0.39 m. Waves were generated at a distance 14.68 m offshore from the toe of the slope. The beach consisted of a ramp made out of anodized aluminium panels with a hydrodynamically smooth surface. Thus, in the numerical simulations a low friction coefficient of 0.005 was assigned. A similar range of friction coefficients was adopted in the National Tsunami Hazard Mitigation Program (NTHMP) report (2012). The still water depth in the constant depth region was d = 0.2 m and the wave height H = 0.056 m giving a ratio H/d=0.28. The profile of the solitary wave centred at $x = \mathrm{X}_1$ is given by:

$$\zeta(x, 0) = H\mathrm{sech}^2[\gamma(x - \mathrm{X}_1)] \tag{3.83}$$

where $\gamma = (3H/4d^3)^{1/2}$.

The grid size was Δx = 0.01 m and the time step Δt = 0.001 s. In Fig. 3.26 a comparison is shown between experimental data and snapshots of the non-dimensional surface elevation ζ/d as computed from the model at different non-dimensional times $t' = t\sqrt{g/d}$.

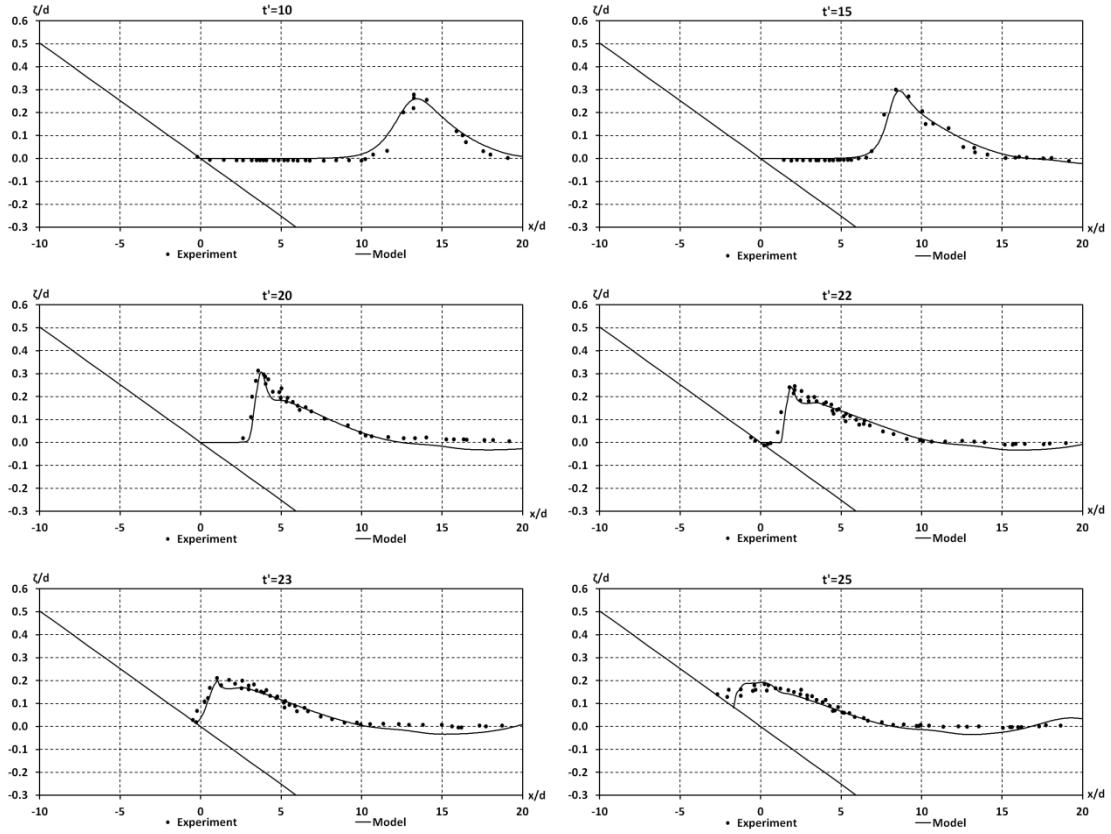

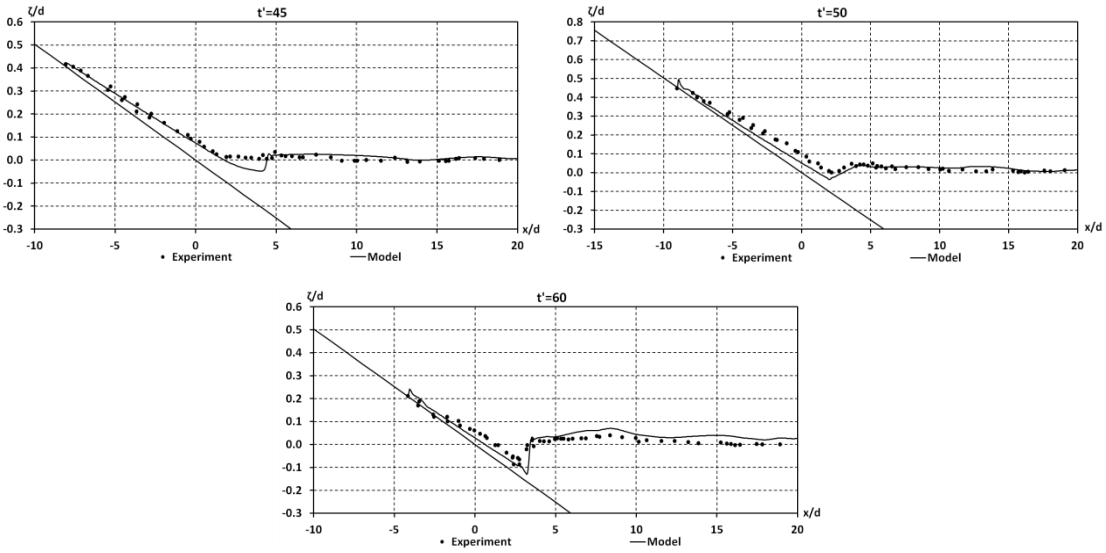

Fig. 3.26. Measured and computed snapshots of the solitary wave propagation in Synolakis's (1987) experiment.

The specific test was simulated in order to mainly check the moving shoreline concept described above, along with the wave breaking module. The model's performance to this demanding test was fairly good both in the surf and swash zones. The nonlinear steepening is well-reproduced until the inception of breaking, i.e. around t′=20. The almost vertical wave front is very accurately described, and so is the breaking wave form in the surf zone. In addition, the moving shoreline concept is fairly well activated, except for a slightly thinner wave tongue during the downwash as expected (see disscusion in subsection 3.2.2). Also, the maximum run-up is well predicted. Without the inclusion of the bottom friction an over-estimation of about 8% of the maximum run-up was observed. In general, the simulation of run-up and run-down stages are acceptable.

Irregular wave breaking on a plane beach

The 1DH version was further validated for random wave propagation and breaking on a gentle slope of 1:20. The experiment was performed by Mase and Kirby (1992) and the experimental setup is depicted in Fig. 3.27. Waves were generated on a constant depth of 0.47 m from a Pierson-Moskowitz spectrum with a peak frequency of 1.0 Hz.

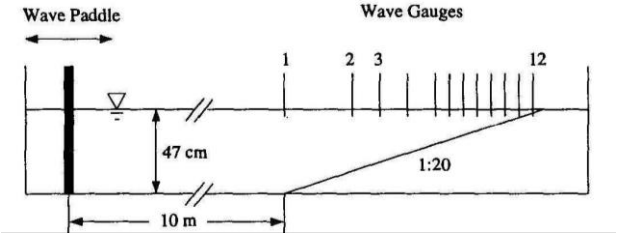

Fig. 3.27. Layout of Mase and Kirby's (1992) experiment (Wei and Kirby, 1995).

Time series of surface elevation were obtained at twelve wave gauges at depths d = 47, 35, 30, 25, 20, 17.5, 15, 12.5, 10, 7.5, 5 and 2.5 cm. The value of kd for the peak wave frequency was about 2.0, representing a severe test for a Boussinesq-type model to simulate deeper water conditions. The dominant breaking type was spilling and most waves started breaking at about d = 0.15m. The model was run for about 12 minutes. The spatial step was 0.02 m and the time step 0.004 s. Fig. 3.28 shows a comparison between measured and computed surface elevation time series at six gauges for an interval of 20 s. Some discrepancies concerning small phase and height errors are observed. However, the agreement is quite good and wave shoaling, breaking and nonlinear interaction are described well.

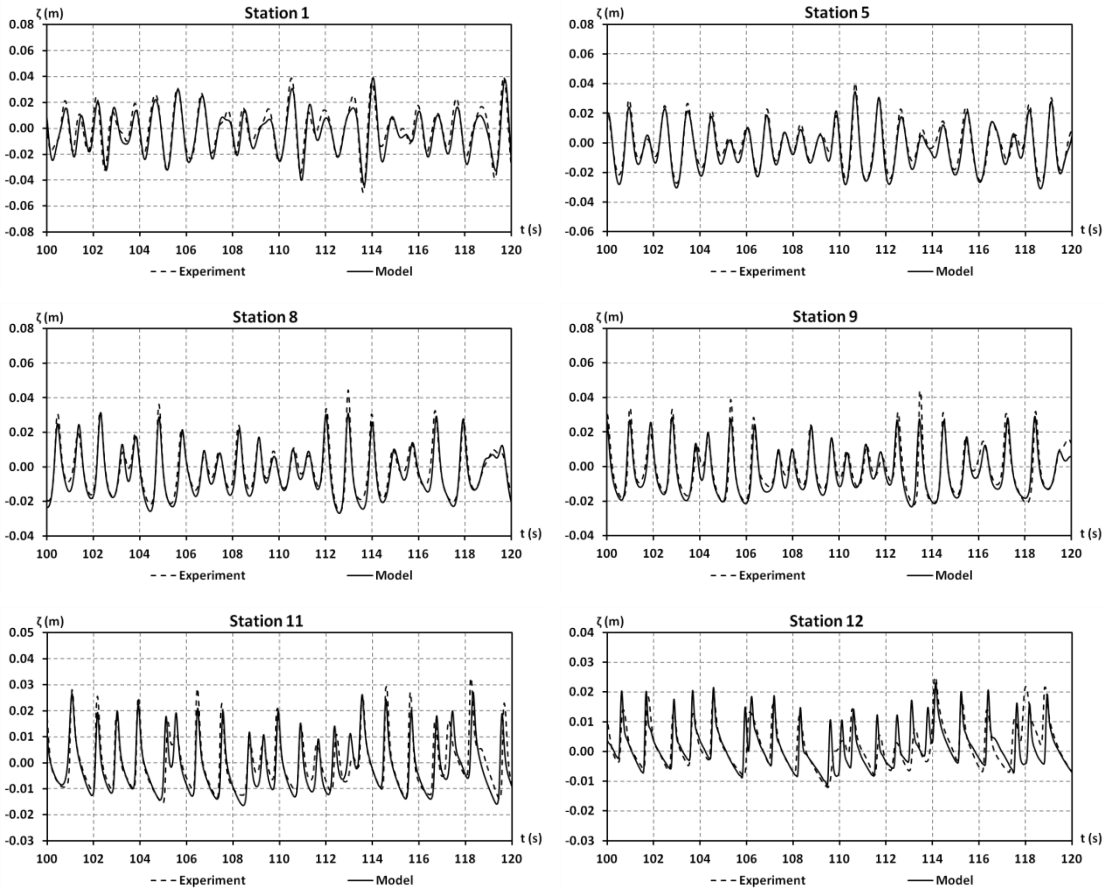

Fig. 3.28. Measured and computed free surface elevation time series at various wave gauges for Mase and Kirby's (1992) experiment.

A comparison between wave spectra computed from the model's and the measured surface elevation time series was also performed. The results at the same wave stations are shown in Fig. 3.29. In order to compute the wave spectra each time record containing 10240 data was split into 10 segments of 1024 points each with time interval 0.05 s. The energy spectrum of each segment, computed through a Fast Fourier Transform (FFT), was summed up and

averaged. The ensemble averaged spectrum was smoothed by averaging three points. Thus the degree of freedom was 60, and the resolution frequency 0.02 Hz.

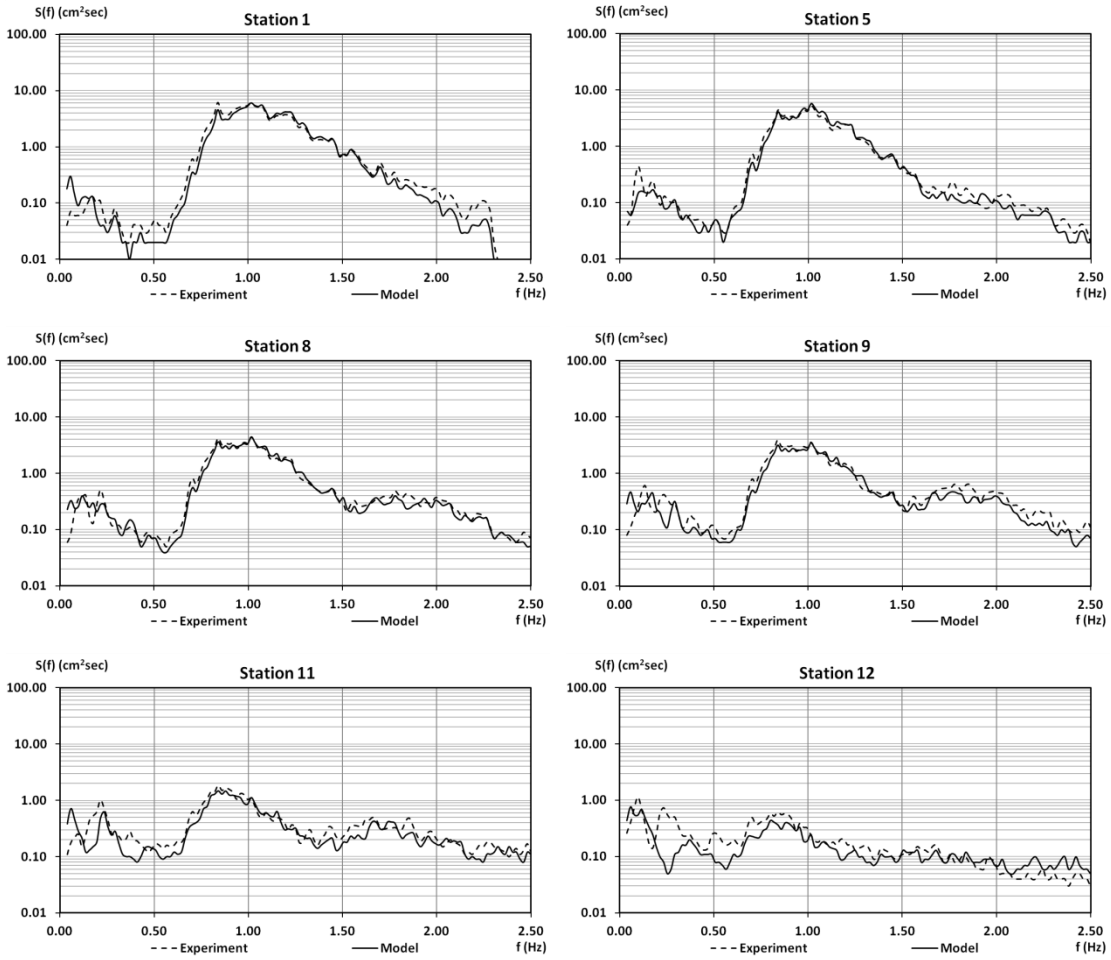

Fig. 3.29. Measured and computed wave spectra at various wave gauges for Mase and Kirby's (1992) experiment.

The agreement is fairly good, especially for the main part of the spectra around the peak frequency. Some deviations in the low-frequency domain are observed and can be attributed to an inaccurate computation of bound sub-harmonics, discrepancies in modelling the surf beat mechanism and reflections of the released long waves to the shoreline. Inaccuracies of bound sub-harmonics appear both because of not applying a second order incidence boundary condition and due to the nonlinear properties of the Boussinesq equations themselves. On the other hand, some discrepancies at the high frequencies can be attributed to a poor finite difference representation of very short waves and to inherent limitations of the Boussinesq equations (see discussion in chapter 2). For example, linear dispersion is accurate for the present model up to kd =3. Hence an accurate representation of free waves at 2.0 Hz (two times the peak frequency) requires the water depth to be less than 0.2 m. Finally, some energy

is also damped due to the low-pass numerical filter, though weak, applied to ensure the numerical stability, as discussed in the subsection on the numerical scheme.

Fig. 3.30 shows the variation of the significant wave height, H_{m_0}, as calculated from the wave spectra, and the wave setup. The significant wave height is well-predicted both outside and inside the surf zone. The agreement for mean water level is reasonably good, but for a slight over-estimation of the maximum set-down. However, the tendency of the setup is described quite accurately.

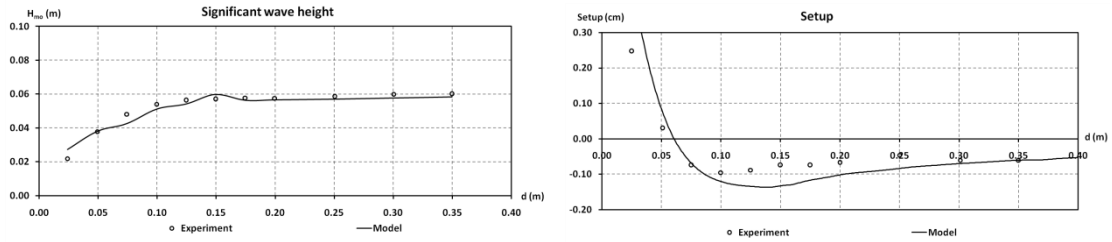

Fig. 3.30. Measured and computed significant wave height (left) and wave setup (right) for Mase and Kirby's (1992) experiment.

Wave propagation over a fringing reef

Wave transformation in fringing reef environments has recently received a lot of attention. Two series of flume experiments were conducted at Oregon State University in 2007 and 2009. The experiments were described by Roeber (2010) and referred to solitary wave propagation over different reef configurations. Among the 198 test cases in total, the one simulated here is the one presented also in Roeber and Cheung (2012). This is a very challenging test since it reveals whether the numerical model is capable of handling nonlinearity, dispersion, wave breaking, overtopping, bore propagation, and sheet flow. The effective length of the flume was 83.7 m and the water depth was $d = 2.5$ m submerging the reef flat by 0.14 m. The reef slope was 1:12 with a crest 0.065 m above the water level. The generated solitary wave had a height of 0.75 m, giving a dimensionless wave height of $H/d = 0.30$. The grid spacing was $\Delta x = 0.05$ m and the time step $\Delta t = 0.005$ s. A comparison between experimental data and snapshots of the non-dimensional free surface in different non-dimensional times is shown in Fig. 3.31.

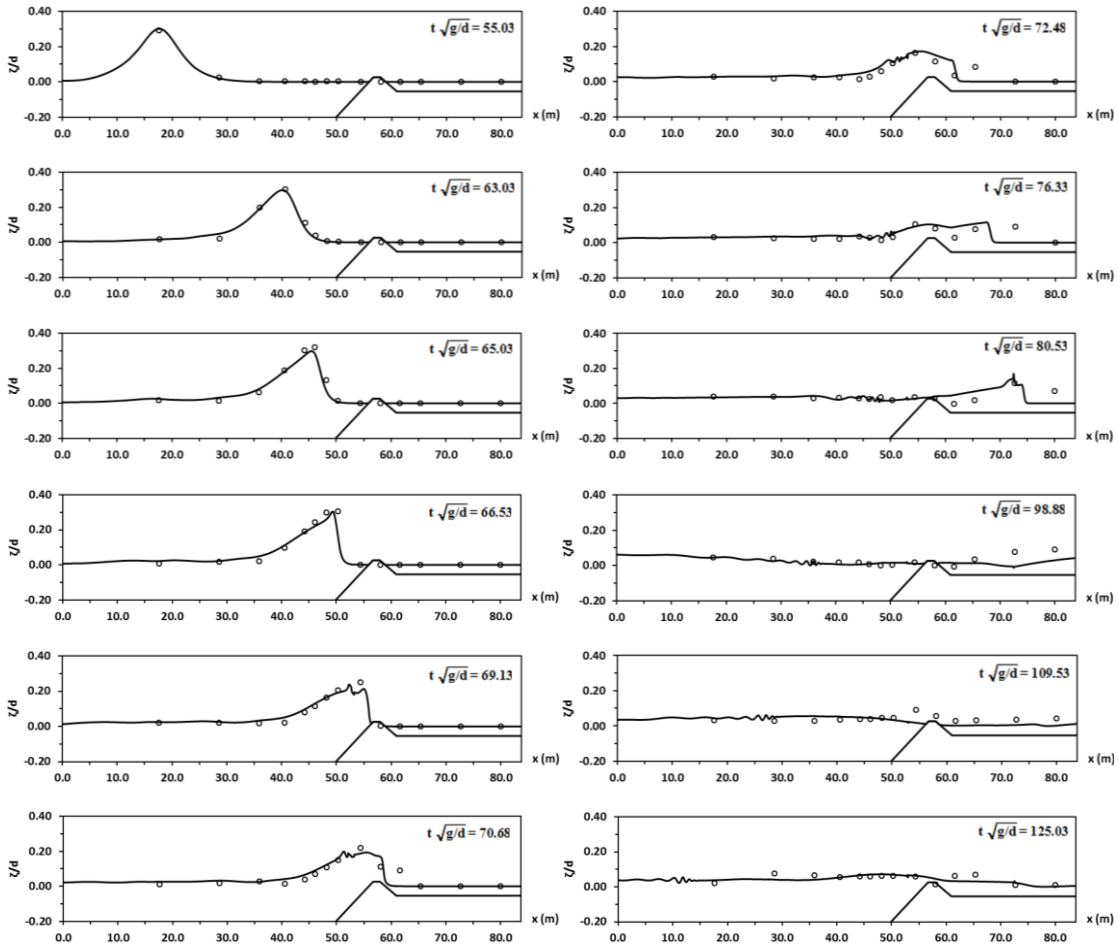

Fig. 3.31. Snapshots of the solitary wave propagation in the fringing reef test.

The solitary wave shoals over the slope, develops into a plunging breaker and splashes-up around $t\sqrt{g/d} = 69$. The comparison shows a good agreement for the shoaling solitary wave as the steepened front face is quite accurately described. Also, the computed overturning of the free surface due to breaking seems reasonable. The phenomenon resembles a hydraulic jump and transition from subcritical flow, upwave of the sloping reef, to supercritical flow with a turbulent bore propagating in the initially calm water of the lagoon. The overtopping and the propagation of the bore are adequately reproduced. A comparison between the measured and computed time series of the non-dimensional free surface at various gauges is shown in Fig. 3.32. The axis origin is located at the position of the wave maker, 25.9 m upwave of the sloping beach toe. Some discrepancies are observed at the wave gauges 13 and 14 since the formation of the second peak is underestimated as the bore travels in longer distances.

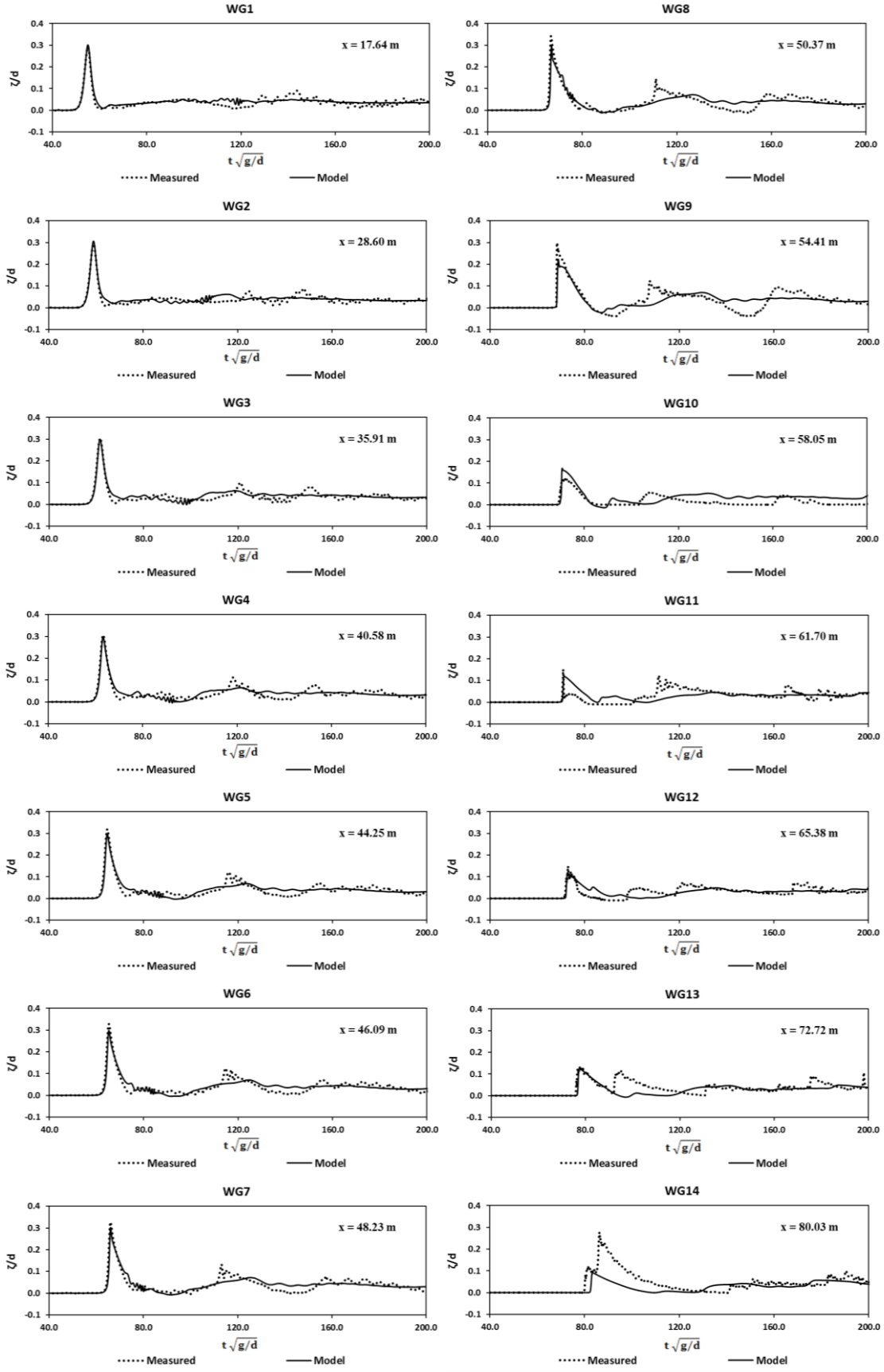

Fig. 3.32. Measured and computed non-dimensional free surface elevation time series at various wave gauges for the fringing reef test.

It should be mentioned that the governing equations are formulated based on physical variables, i.e. *U* and *V*. This formulation holds for subcritical flows but is not generally adequate for supercritical flow regimes. The introduction of the breaking eddy viscosity terms improves numerical stability but also ensures correct propagation speed and height of the broken wave. Roeber *et al*. (2010) have addressed this issue and suggested the use of variables $(d+\zeta)\vec{U}$, which are conservative for both sub- and supercritical flow.

Irregular wave breaking over a submerged bar

The last test for the verification of the one-dimensional model corresponds to irregular waves propagating and breaking over a submerged trapezoidal bar. The experiment was carried out in the wave-flume of the Department of Civil Engineering, Delft University of Technology. The flume had a length of 37.7 m and width of 0.8 m. The experimental layout was the one presented by Beji and Battjes (1994) and is depicted in Fig. 3.33. The specific test simulated here corresponds to random waves of a Jonswap spectrum, generated on a horizontal bottom of depth 0.4 m. The peak period was T_p = 2 s and the dominant breaker over the bar was of the spilling type. The critical value for breaking initiation was reduced to $0.35\sqrt{gd}$ due to the presence of the bar, as already discussed in subsection 3.2.1.

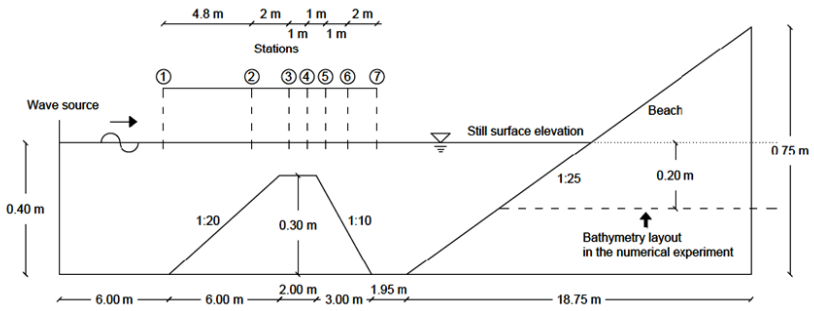

Fig. 3.33. Layout of Beji and Battjes's (1994) experiment.

The dimensionless wavenumber corresponding to the peak frequency was *kd* = 0.68 on the horizontal bottom and *kd* = 0.32 on the top of the shoal, where the free board was 0.10 m. As mentioned above, the linear dispersion is well-represented by the model up to *kd* = 3. This leads to the conclusion that only the wave components with frequencies up to 1.36 Hz and 2.72 Hz, on the horizontal bed and the top of the bar respectively, can be described very accurately. In addition, a nonlinear transfer function analysis (see subsection 2.4.3) showed that for the present Boussinesq-type wave model, the limit for an accurate estimation of the second-order energy transfer (error up to 10%) is *kd* = 1.16. This means that nonlinear wave interactions can be adequately reproduced only for frequencies less than 0.77 Hz and 1.54 Hz, on the horizontal bed and the top of the bar respectively. The grid size was chosen Δx = 0.05

m, leading to 73 points per wavelength for the peak frequency on the horizontal bed and 38 on the top of the shoal, and the time step was Δt = 0.0025 s. The model was run for about 14 minutes.

Wave spectra were computed from both the measured and the model's surface elevation time series. A comparison between the two is shown in Fig. 3.34 at the seven wave gauges. The computational procedure is briefly described in the following. Each record contained 21000 data points but only its part after approximately 10 wave peak periods was used in order to avoid possible contamination of the data due to transients (Ohyama *et al.*, 1994). The remaining 20480 data were divided into 10 segments of 2048 points each. Then each segment was transformed through a Fast Fourier Transform. No tapering technique was applied since the spectral leakage was not significant. The final spectra were obtained after ensemble averaging of all the realizations and frequency smoothing over five neighboring components. Each spectrum then had 100 degrees of freedom and the statistical error was 14.1%.

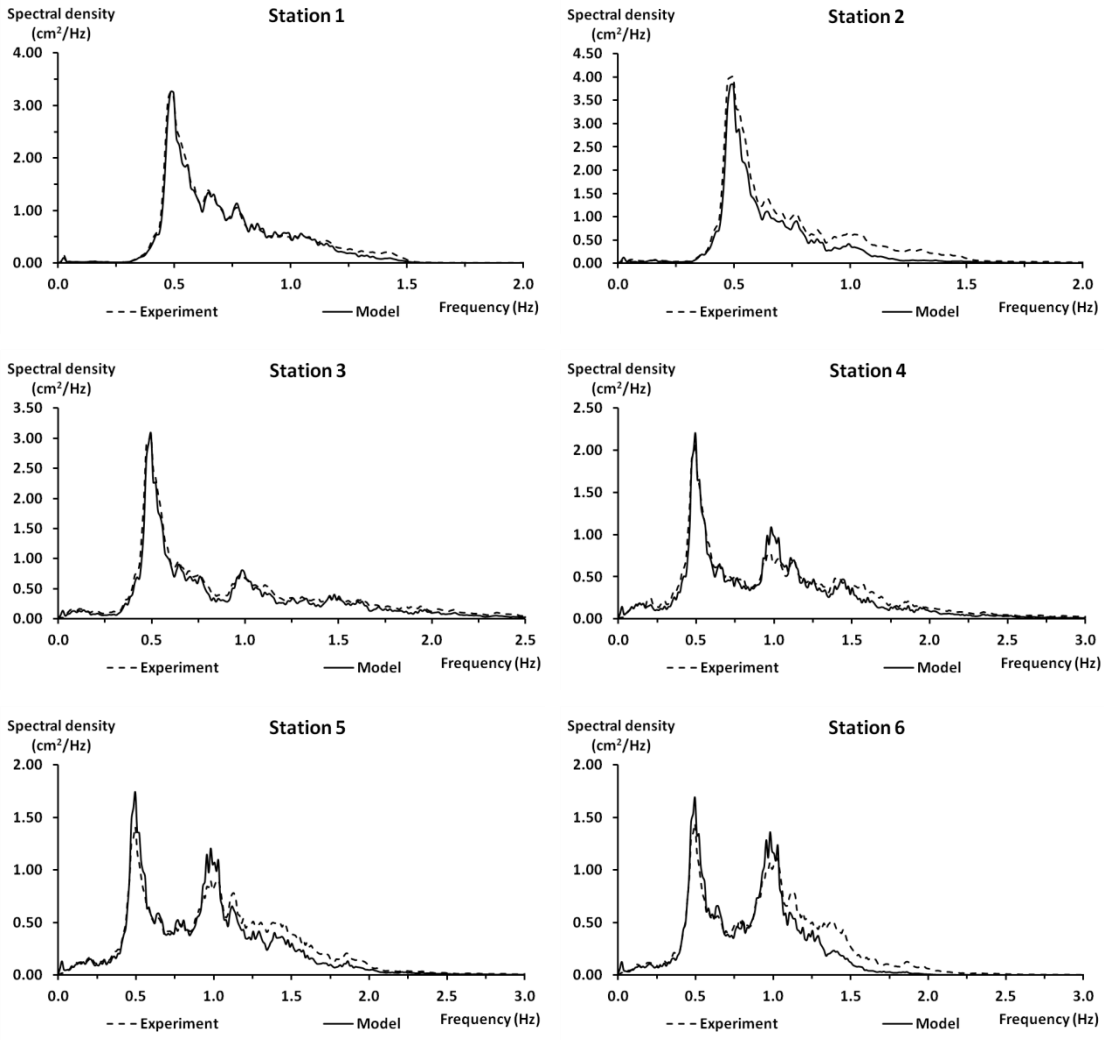

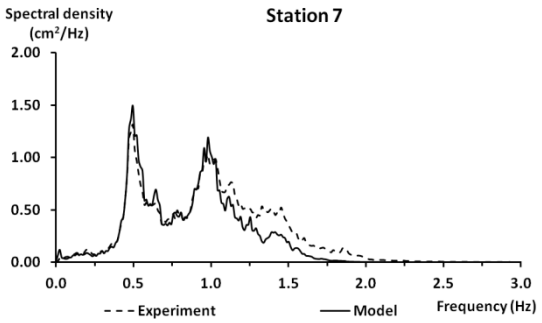

Fig. 3.34. Measured and computed wave spectra at various wave gauges for Beji and Battjes's (1994) experiment.

Although this is a quite demanding test, the model's response is reasonably good. Spectral transformation due to shoaling is very accurately reproduced for the main part of the spectrum around the peak frequency. The bound super-harmonics generation is slightly under-estimated at the up-wave slope, as already discussed. The energy dissipation due to breaking seems reasonably predicted as the spectrum shape is described correctly and a secondary peak is formed. However, both the primary and the secondary peaks are over-estimated at stations 5 and 6. On the other hand, the spectral density is under-predicted at the high-frequency domain. On the contrary, both the bound sub-harmonics and the released long waves due to the surf beat mechanism are computed quite accurately. Thus it can be said in general that irregular wave group propagation and breaking over the bar is adequately simulated.

3.4.2 2DH validation

Regular wave propagation over an elliptic shoal

The first test for checking the validity of the two-dimensional model is the benchmark test by Berkhoff *et al.* (1982). Their experiment referred to monochromatic wave propagation over an elliptic shoal and combined a number of physical processes, like shoaling, refraction, diffraction and nonlinear dispersion. Nonbreaking regular waves of period T = 1.0 s and wave height H_o = 0.0464 m are generated in a constant depth region of d = 0.45 m and propagate over an uneven bottom. The experimental layout and the bathymetry are shown in Fig. 3.35 (at left). The bathymetry displays an elliptic shoal resting on a 1:50 plane sloping seabed. The entire slope is turned at an angle of -20° with respect to the wave paddles.

The computational domain was the same as in Fig. 3.35, except for two sponge layers sitting behind the wave-maker and at the end of the beach. Since only nonbreaking waves were considered, instead of shoreline boundary, a minimum depth of 0.07 m was used in the model. The two vertical side walls at x = ±10 m were treated numerically as fully reflective

boundaries. The grid steps were $\Delta x = \Delta y = 0.05$ m and the time step 0.01 s. The computed wave field reached a stable state after $t = 30$ s.

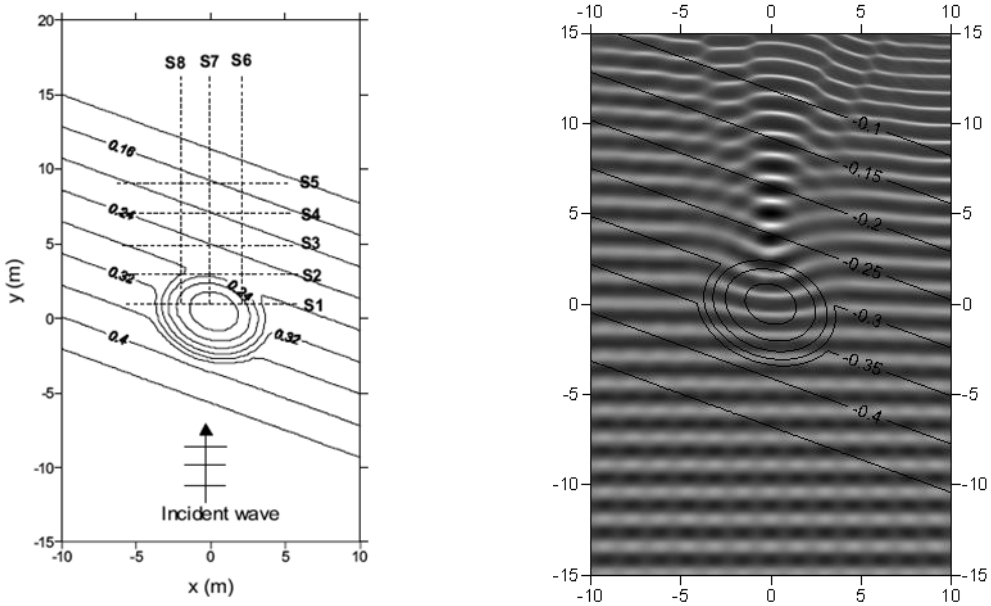

Fig. 3.35. Left: Experimental layout and bathymetry of Berkhoff *et al.*'s (1982) experiment (contours in meters). Right: Snapshot of the free surface elevation, viewed in plan.

A snapshot of the free surface elevation at $t = 40$ s is also depicted in Fig. 3.35 (at right) from a plan view. The light and dark shade regions correspond to positive and negative values of ζ, respectively, while the solid lines denote the bottom topography. Strong energy focus is observed behind the shoal, pronouncing the large effect of wave diffraction.

The wave height along eight transects (S1-S8) near the shoal was measured in the experiment. Fig. 3.36 shows the comparison between the measured and computed by the model wave heights along these sections.

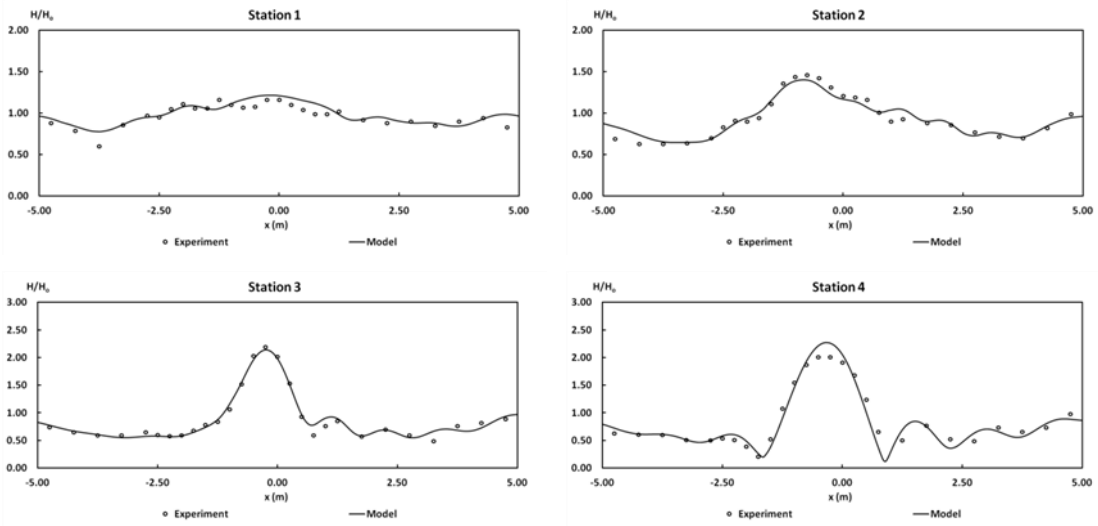

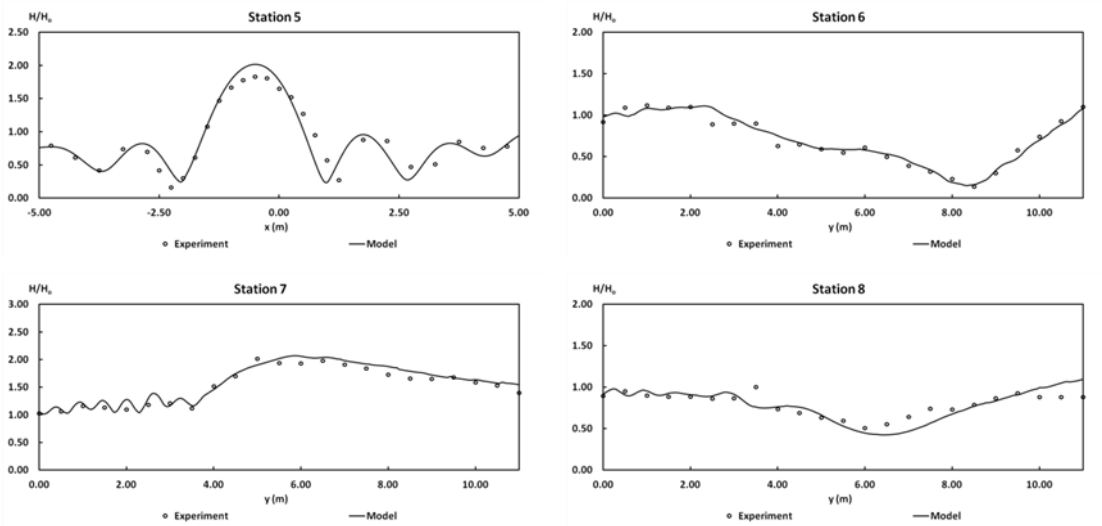

Fig. 3.36. Computed and measured relative wave heights along Section S1 to Section S8 in Berkhoff *et al.*'s (1982) experiment.

The computed results for the wave height agree quite well with the measured ones along both directions, parallel and normal to wave incidence. The combined effects of refraction and diffraction are described adequately and wave focusing behind the shoal produces a maximum wave height of approximately 2.2 times the incident one. The quite large values of the dimensionless wavenumber ($kd \approx 1.9$ close to the wavemaker) prove the model's ability to reproduce fairly good the nonlinear dispersion effect.

Regular breaking waves over a circular shoal

Another test case for checking the model's ability to reproduce the combined effects of refraction, diffraction and breaking is the one by Chawla *et al.* (1996). The experiments were conducted in the wave basin at the Center for Applied Coastal Research in the University of Delaware. The basin's dimensions were 18.2 m × 20 m and a circular shoal with radius of 2.57 m was built on a flat bottom. A schematic view of the experimental set-up is shown in Fig. 3.37. (reproduced, modified from Kirby *et al.*, 1998). The center of the shoal was located at x = 5 m and y = 8.98 m. Thus, there was some small asymmetry in the y-direction. The water depth of the horizontal bottom was d = 0.395 m and the one on the submerged shoal was given by

$$d = 9.125 - \sqrt{82.81 - (x-5)^2 - (y-8.98)^2} \tag{3.84}$$

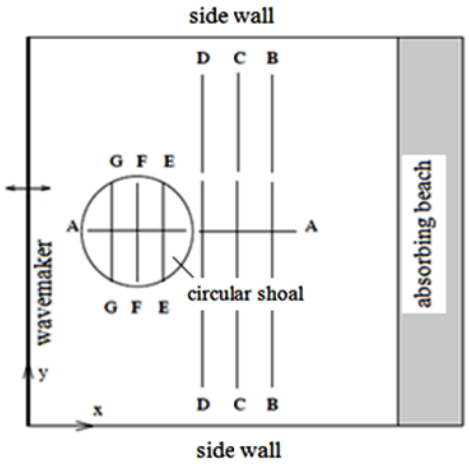

Fig. 3.37. Schematic view of the set-up in Chawla *et al.*'s (1996) experiment (from Kirby *et al.*, 1998, modified).

Near the eastern wall (the wall on the right in Fig. 3.37) of the numerical wave basin, a 4.4 m wide sponge layer was used to represent a sloping stone beach in the physical experiment. The test case simulated here refers to breaking monochromatic waves of period T = 1 s and wave height H_o = 0.02 m. The grid size in the x direction was 0.025 m in order to resolve the very steep breaking front face. Thus, a number of about 20 grid points per wavelength was considered on the top of the shoal. On the other hand, the grid size in the y direction was taken Δy = 0.05 m. The different grid size for the two directions may insert some artificial anisotropy and an error in simulating accurately the wave refraction. However, it is worth allowing a small inaccuracy when considering the decrease of the computational time when applying such a coarser numerical domain. Fig. 3.38 shows a comparison between the measured and the computed relative wave heights at six transects.

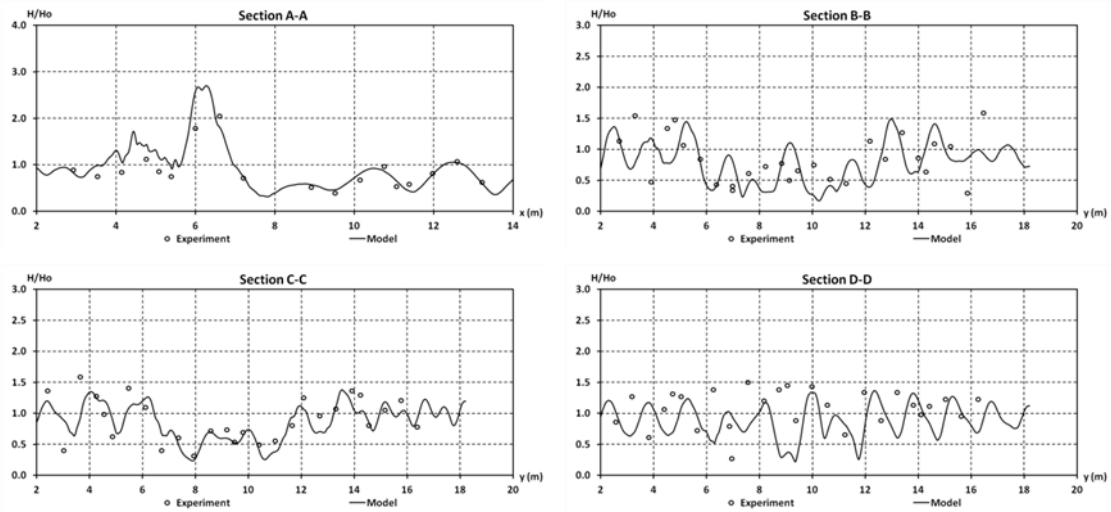

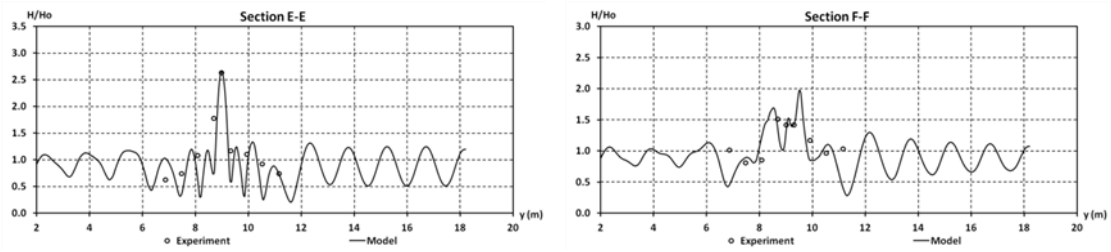

Fig. 3.38. Computed and measured relative wave heights at various transects in Chawla *et al.*'s (1996) experiment.

The experiment showed that the wave height does not reach the maximum on top of the shoal but on the downward slope instead. This is attributed to the energy focusing due to wave refraction on the shoal. The focusing effect is well-predicted by the Boussinesq model (transect E-E). Behind the shoal some discrepancies are observed. However, one can say that the defocusing and the diffraction of the broken waves are reasonably described.

A snapshot of the numerical wave field is shown in Fig. 3.39 (at left). The gray areas represent the wave crests, while the dark areas are the wave troughs. Wave crests become very peaky on the top of the shoal due to nonlinear shoaling effects. Wave refraction and diffraction are clearly shown by the bending of the wave crests and their variation in the transverse direction respectively. Secondary crests are generated behind the shoal due to the release of the super-harmonics.

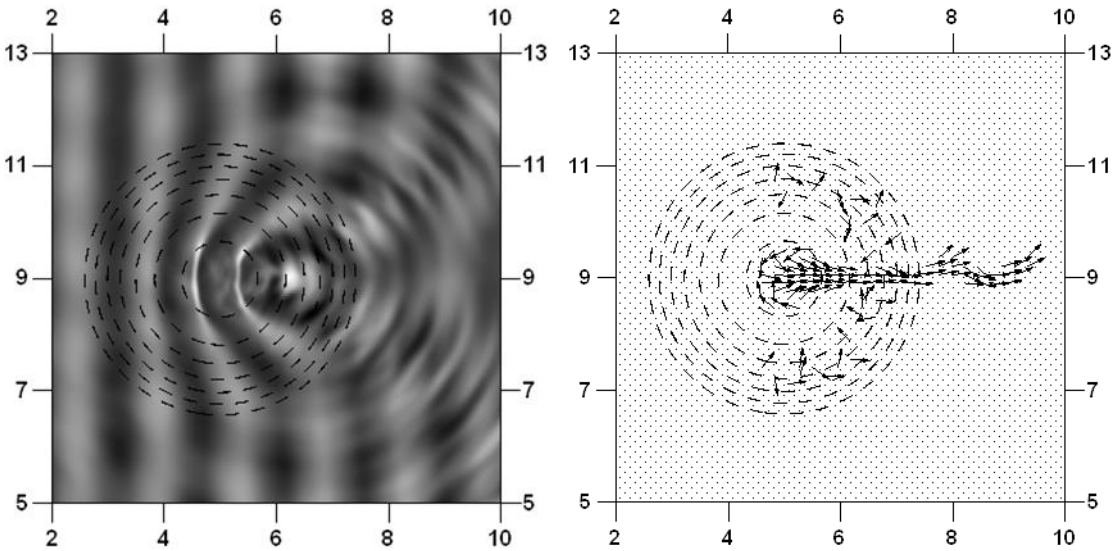

Fig. 3.39. Left: Snapshot of the free surface elevation, viewed in plan. Right: modelled underlying current field. Dashed lines represent contours of water depth.

The underlying wave-induced current field estimated by the Boussinesq model is also depicted in Fig. 3.39 (at right). Although there were no measurement of breaking-induced circulation in Chawla *et al.*'s (1996) experiment, a strong jet associated with wave breaking on the top of the shoal was visually observed (Kirby *et al.*, 1998; Chen *et al.*, 2000a). In the

simulation of the wave-induced currents, a constant bottom friction coefficient of f_{cw} = 0.001 and a subgrid mixing model were used. It should be mentioned that the asymmetry in the *y* axis of the wave height distribution due to the slightly off-centered shoal position and the reflective walls assumed is well-represented by the model. This asymmetry has also some small effect on the jet-like current field.

A rip channel

A very demanding test is the laboratory experiment reported by Hamm (1992a,b). It was conducted at the Laboratoire d' Hydraulique de France in Grenoble and the wave tank measured 30 m × 30 m. The bathymetry was a plane sloping beach of 1:30 with a rip channel excavated along the centerline as shown in Fig. 3.40.

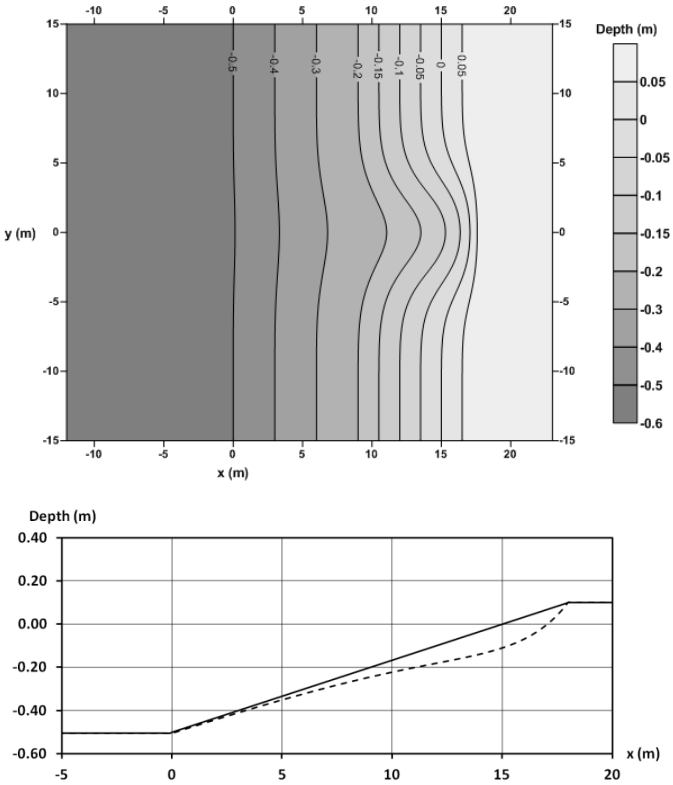

Fig. 3.40. Model topography for the rip channel test. Above: contour plot of the bathymetry. Below: bathymetry profiles along a plane beach section (solid line) and along the rip channel (dashed line).

The test aims at validating the model's efficiency to describe the wave-induced current field. The test case studied here refers to normal incidence of regular waves with a period of 1.25 s and a wave height of 0.07 m offshore, where the horizontal bed is approximately 0.50 m deep. Due to symmetry, a reflective boundary condition was considered at the centerline of the rip channel and only half of the physical wave tank was employed in the numerical computations. The grid step was taken 0.05 m, the time step 0.01 s and the simulation period was 600 s

corresponding to 480 wave periods. The bottom friction coefficient was taken f_{cw} = 0.012 (after calibration) and the Smagorinsky coefficient c_s = 0.25. A varying f_{cw} was also examined but the results were quite similar (see subsection 3.2.3).

Due to increased depth and refraction by the rip channel, the inception of breaking along the centerline occurred quite closer to the shoreline as compared to the plane beach away from the channel. Thus a significant variation of the wave setup appeared along the y direction. This alongshore gradient of the mean water elevation drove a current towards the centerline and due to symmetry the flow from both sides joined there to form a rip current. A steady state for the wave-induced current field was reached after about 150 s. A contour plot of the wave setup as computed by the model is shown in Fig. 3.41.

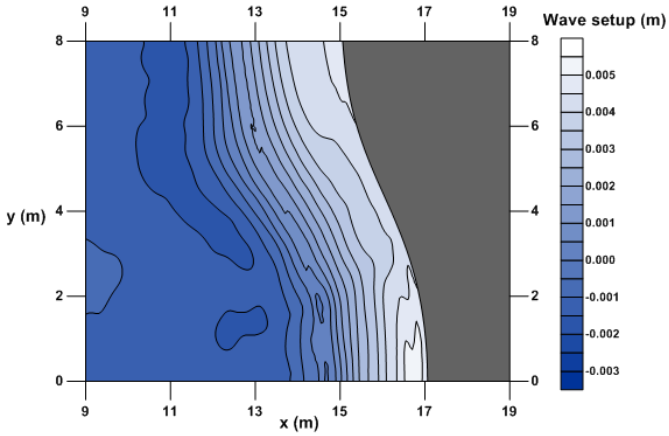

Fig. 3.41. Contour plot of the computed setup.

A comparison between the computed and the measured wave height along a plane beach and the rip channel is depicted in Fig. 3.42. The agreement is fairly good and the refraction due to the opposing current along the rip channel leads to an increase of the wave height. This mechanism along with the shoaling counteract the decrease of the wave height due to depth refraction and their balance defines the breaking point, which is accurately predicted.

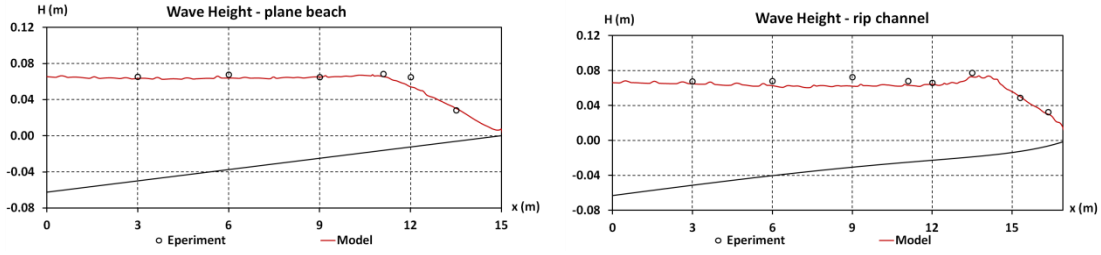

Fig. 3.42. Comparison between computed and measured wave height along a plane beach section (left) and along the rip channel (right).

A vector plot of the underlying current field is shown in Fig. 3.43 after steady state is reached. The represented velocities are the mean values of depth-averaged velocities below

the surface roller, $\vec{\bar{U}}_o$. Thus the effect of the depth-averaged undertow is also taken into account and at the plane beach the current field is directed seawards in the surf zone. A pronounced rip current is observed along the centerline of the channel and some small eddies can also be identified.

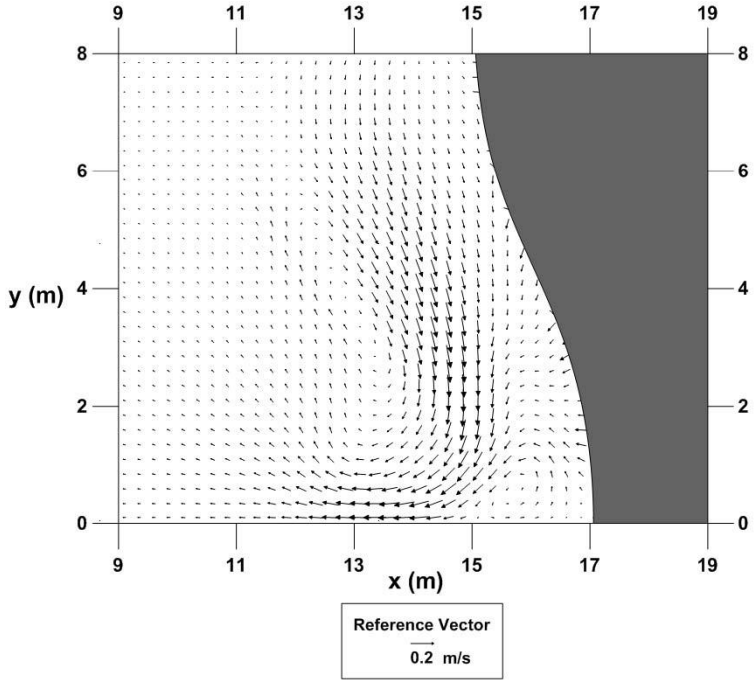

Fig. 3.43. Vector plot of the wave-induced current field.

A comparison between the computed and the measured rip current velocity is depicted in Fig. 3.44. By imposing the reflective boundary condition along the centerline, the computed rip current was bound to be directed strictly parallel to the channel's axis. However, in the experiment significant deviations from this direction were observed. Thus for consistency reasons, the current's velocity component parallel to the channel's centerline is shown and compared to the computed one. The agreement between the measured, 0.17 m/s, and computed, 0.19 m/s, maximum values is acceptable while for the total near bottom current velocity a maximum value of 0.25 m/s was measured (Hamm, 1992b). However, a discrepancy in the position of this maximum value is observed. This could be attributed to instabilities of the rip current, also noted by Hamm (1992b) in his report, and possible imperfections in the experimental layout that was supposed to be symmetrical but unexpected lateral asymmetries were actually measured. Similar to the present model's results for the rip current were given by other Boussinesq-type models (Sørensen *et al*., 1998). The uniformity of the experimental measurements of the monochromatic wave tests was commented by Hamm (1992b) as rather poor. A similar test case with the same significant wave height, H_s = 0.07 m, and peak period, T_p =1.25 s, but referring to normal, unidirectional irregular waves of

a Jonswap spectrum, was also checked in the laboratory. This test's results were more uniform. For comparison reasons, the measured rip current velocity in this latter test is also included in Fig. 3.44.

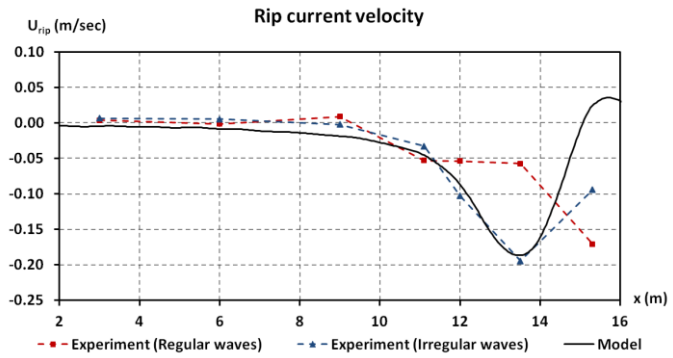

Fig. 3.44. Measured and computed rip current velocity along the rip channel.

Despite the application of the eddy viscosity breaking model, the flow is still modelled as being potential. However, in reality, strong vorticity is produced by the breaking process. This aspect has been included in some Boussinesq-type wave models accounting for partially rotational flow (Veeramony and Svendsen, 2000; Shen, 2001; Chen, 2006; Kim *et al*., 2009). Herein, the generation and transportation of the vortices observed in Fig. 3.43 inside the surf zone can be explained by the vorticity equation derived from the momentum Eqs (3.44) and (3.45). Taking the curl of these equations leads to:

$$\vec{\Omega}_t + (\vec{U}\cdot\nabla)\vec{\Omega} = -\vec{\Omega}(\nabla\cdot\vec{U}) + \nabla\times\vec{F}_{br} + \nabla\times\vec{F}_{\text{eddy}} - \nabla\times\left(\frac{\vec{\tau}_b}{d+\zeta}\right) + O(\sigma^2) \qquad (3.85)$$

where $\vec{\Omega} = \nabla\times\vec{U} = (0, 0, V_x - U_y)$ is the vorticity vector. Vector $\nabla\times\vec{F}_{br}$ is the source of vorticity caused by the longshore variation of wave breaking, while the bottom friction and the subgrid mixing are dissipation agents (Chen *et al*., 1999). The first term on the right-hand side of Eq. (3.85) results in the vortex stretching, while the second on the left-hand side in the vortex advection.

A snapshot of a subdomain of the wave pattern after the establishment of the steady state is shown in Fig. 3.45.

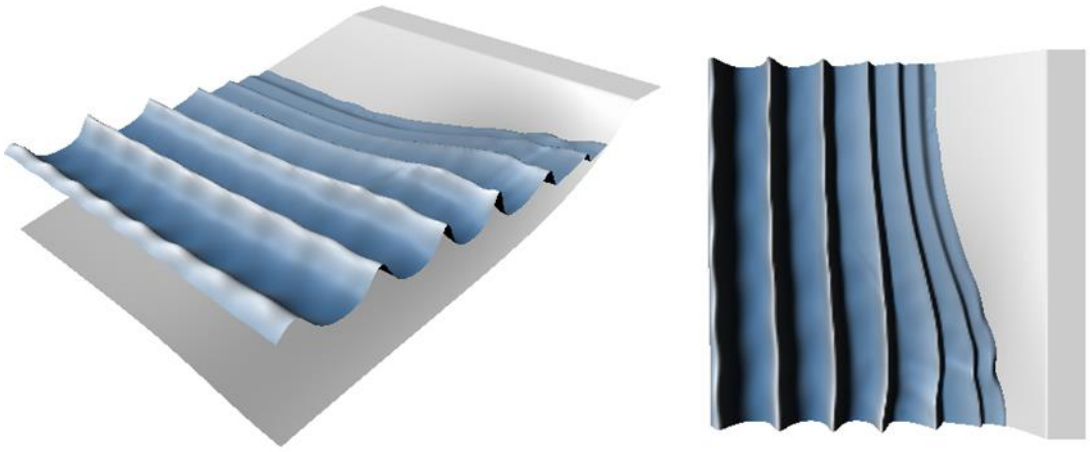

Fig. 3.45. Snapshot of the surface elevation from a bird's-eye view (at left) and from a plan view (at right).

The wave-induced current field and especially the rip current affect and modify the wave field. Apart from the increase of the wave height described above, the opposing rip current also causes a small local bend in the wave crests, as it can be seen in Fig. 3.45.

The subgrid turbulent processes may become an important factor influencing the flow pattern of the wave-induced current field. The Smagorinksy-type mixing terms aim at parameterizing these effects based on the wave-induced current field that extends both inside and outside the surf zone. On the other hand, the breaking terms are of similar type but their role is different, since they are strictly localized on the front face of a broken wave to account for energy dissipation due to the breaking process. The model's sensitivity to the eddy coefficient due to subgrid turbulence, c_s, was studied for the specific test.

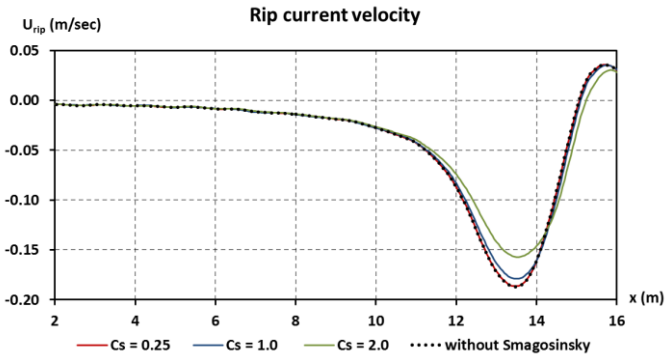

Fig. 3.46. Computed rip current velocity along the rip channel for various Smagorinsky coefficients.

A comparison of the rip current velocity along the centerline of the channel for different values of the mixing coefficient is depicted in Fig. 3.46. Some dependency on that coefficient is identified, especially in the zone of the strongest current. However, in general, the sensitivity was rather weak for the typical value range 0.25-1.0 of the Smagorinsky coefficient. A similar behavior was also observed in the other two-dimensional tests.

Oblique long-crested irregular waves

The last validation test refers to the laboratory experiments performed in the U.K. Coastal Research Facility at HR Wallingford (Memos, 2002; Memos *et al.*, 2005), aimed at studying various aspects of random wave propagation in shallow water. The basin of the facility, with overall dimensions 27 m × 54 m (Fig. 3.47), contained a narrow strip of horizontal bed and a rigid beach sloping uniformly at 5%. The water depth over the horizontal bed was 0.80 m. The bed was constructed rough, everywhere but for the part of the horizontal bottom between the left lateral wall and the dashed line in Fig. 3.47, where the bed was considered smooth.

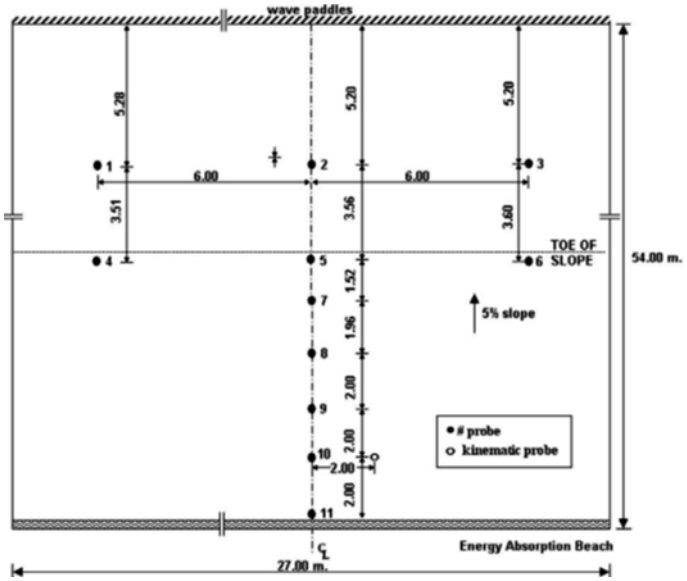

Fig. 3.47. Plan of the experimental setup at HR Wallingford.

The test case simulated herein corresponds to oblique long-crested irregular waves of a Jonswap spectrum with enhancement factor $\gamma = 3.3$, peak period $T_p = 1.2$ s and significant wave height at the wave paddles $H_s = 0.09$ m. The angle of incidence was 15° to the shore. Time series of the surface elevation were measured at the eleven wave gauges indicated in Fig. 3.47 with a sampling rate of 25 Hz.

In order to avoid in the numerical model undesired disturbance due to reflection from the side wall in the source region, instead of generating waves at the target angle, the oblique incidence was reproduced by rotating the entire topography at an angle of -15° and then considering normal incidence of the desired waves. This is a rather simpler computational procedure since the lateral boundaries were used as guiding walls for the long-crested waves on the horizontal bottom. The grid size was taken 0.03 m and the time step 0.005 s. Since no data were available at the wave paddles' location, the experimental surface elevation time series at the probe 2 was used as an input. The bed friction coefficient on the rough parts of the bottom was taken constant $f_{cw} = 0.01$.

The model was run for approximately 6.5 minutes which corresponds to 325 peak periods. The energy spectra were estimated from the computed time series at the eleven probes. A number of 48640 points, corresponding to a time length of 389.12 s, was employed for this calculation. Then an interpolation technique was applied to obtain 9728 data points with a time step of 0.04 s, identical to the experimental one. This set of data was divided into 19 segments of 512 points each. Then each segment was transformed through a Fast Fourier Transform. The final spectra were obtained after ensemble averaging all the realizations and no smoothing over neighboring components was applied. Each spectrum then had 38 degrees of freedom.

A comparison between the wave spectra estimated from the measured and the computed surface elevation time series is depicted in Fig. 3.48.

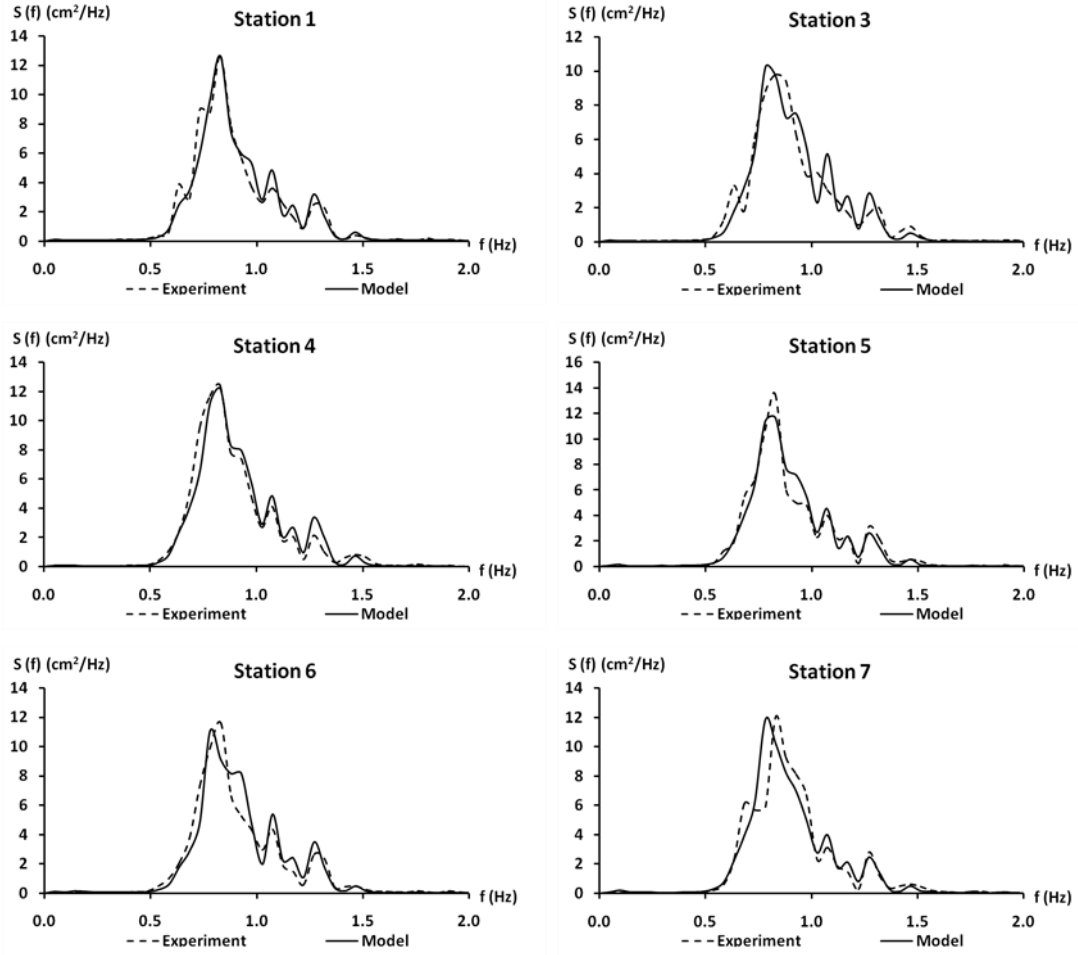

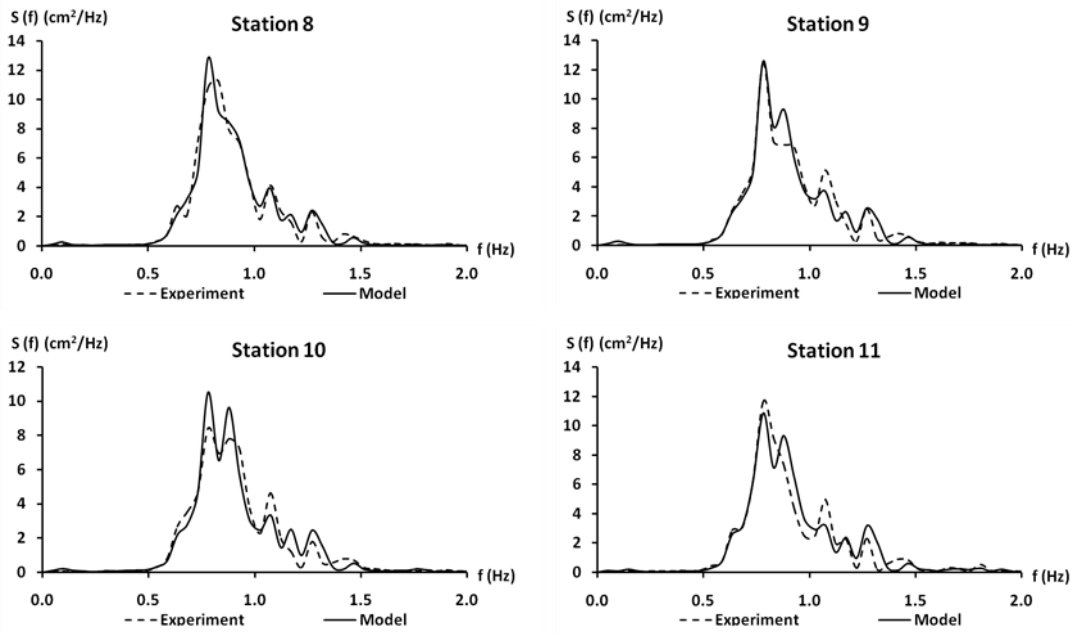

Fig. 3.48. Measured and computed wave spectra at various wave gauges of the experiment at HR Wallingford.

The agreement seems adequately good over a wide depth range since the corresponding to the peak frequency dimensionless wavenumber at the source area is $kd \approx 2.3$ whereas at station 11 $kd \approx 1.1$. The main part of the spectra around the peak is quite accurately predicted and so is the spectrum shape all over the wave tank. The effect of energy transfer to higher frequencies is evident and it is simulated reasonably well by the present Boussinesq-type model. Despite some discrepancies, the 2DH model seems, in general, able to simulate a long-crested irregular wave field under oblique incidence, incorporating nearshore physical processes such as shoaling, refraction, breaking and nonlinear interactions.

3.5 Discussion on Boussinesq-type wave model

In the previous chapter different Boussinesq-type equations for the description of wave propagation were derived. A nonlinear analysis and an inter-comparison of these Boussinesq-type models led to the choice of the most suitable one for the present study. Regarding the basic equations , apart from the linear dispersion, which is correctly modelled up to the limit of deep water, $kd = 3$, the nonlinear amplitude dispersion can be also computed more accurately to deeper water compared to their counterparts of weaker nonlinearity.

Keeping always in mind that the final scope is to compute the coastal sediment transport, the wave model itself should integrate correctly the nearshore dynamics. In order to make it suitable for practical applications the major coastal physical processes had to be modelled realistically and extend the model's applicability all the way from offshore to the swash zone.

This integration was presented in detail in this chapter. However, a thorough approach to this integration should also include a fair criticism to the adopted computational procedures.

At first, extension to the surf zone relies on the applied eddy viscosity concept. This is a very simple approach that is easily calibrated. On the other hand, both the surface roller technique and the vorticity model rely on a more realistic physical background. The former's application in 2DH cases is more complex and often imports numerical instabilities, while the latter requires the solution of an extra equation for the vorticity transport which encumbers the numerical solution. As noted by Kennedy *et al*. (2000), the largest disadvantage of the eddy viscosity breaking concept is that, in some special cases, such as stationary hydraulic jumps, the criterion may be Doppler-shifted to the point where breaking initiation is not recognized. In addition, it was shown that the specific breaking module sometimes over-estimates the wave height in the inner surf zone. In essence, even the form of the breaking initiation criterion is somewhat arbitrary. A criterion based on a critical slope of the free surface would be closer to the underlying physics for waves breaking when crests overturn but it has been proven in practice that both criteria are equivalent. Despite the aforementioned disadvantages, the eddy viscosity concept was finally chosen due to its simplicity and its good stability properties.

Recently, shock-capturing techniques have been proposed for simulating wave breaking by a Boussinesq-type model (Roeber *et al*., 2010; Shi *et al*., 2012). These techniques are usually associated with Godunov-type schemes based on Riemann solvers. They describe breaking waves as bores and conserve flow volume and momentum across discontinuities. The efficiency of such a scheme was confirmed by Roeber and Cheung (2012) for the fringing reef test where the propagation of the bore is very accurately described all over the supercritical flow domain, even at the most downwave gauges far from the reef. However, these techniques rely on Finite Volume approaches which may be more efficient for complex geometries but they are more cumbersome when dealing with higher-order derivatives that are present in nonlinear equations, especially when the latter are expressed in their non-conservative form. Consequently, in the present thesis the more classical finite difference approach was chosen to deal with higher-order equations. Hence, the eddy viscosity breaking module was a realistic choice for the model's extension to the surf zone.

Extension to the swash zone relies on a modified slot technique. The first application of the permeable-seabed technique yielded run-up errors (Madsen *et al*., 1997). However, herein the modified version proposed by Kennedy *et al*. (2000) and Chen *et al*. (2000a) was applied. This modification ensures the water mass conservation when water is above the top of the slot. Nevertheless, some small mass loss still exists when water level is below the top of the slot. In subsection 3.4.1 the mass balance was examined and was found to be adequately

fulfilled. Another, disadvantage of the slot technique is the induction of numerical noise, especially if too narrow slots are employed. On the other hand, too wide slots result to an increased mass loss because z^* deviates from the value given by Eq. (3.10). Thus, the values of the empirical coefficients that govern this technique arise from a case-sensitive compromise. However, the range of values applied here was found to work quite well, in agreement with other researchers.

Another alternative for simulating wave run-up and run-down could be the wetting and drying techniques. These techniques are, generally, easy to implement but they are known to be related to violation of mass conservation and numerical instabilities (Leendertse, 1987; Balzano, 1998). The aforementioned Finite Volume approach has been also successfully applied to define the wet/dry interface through implementation of suitable Riemann solvers. However, the modified slot technique associated with the adopted finite difference scheme on a fixed grid was favoured as a choice.

Apart from the wave phenomena, the nonlinear model estimates quite successfully the wave-induced current field by applying a suitable time-averaging of the total velocities. In addition, the wave-current field interaction seems to be well-reproduced. This is a significant result since the traditional decoupled process of running consecutively the wave and the hydrodynamic models, apart from being time-consuming, ignores also the aforementioned interaction. However, it is worth mentioning that not all of the nonlinear Boussinesq-type models are able to model wave-induced currents. Apart from accurate parameterizing the energy dissipation due to wave breaking and bottom friction, the correct Doppler shift for wave-current interaction needs to be enforced (Yoon and Liu, 1989; Chen *et al*. 1998). This property is connected with the current refraction, a phenomenon that most Boussinesq-type equations fail to model. The present model is capable of reproducing the correct Doppler shift as it can be derived following the analysis by Madsen and Schäffer (1998). In particular, the linear version of the model over a horizontal bottom coincides with the corresponding one of their equations at $O(\sigma^2)$. Following their analysis, the total depth-averaged velocity is considered to consist of two parts, a wave orbital velocity and a current velocity assumed uniform over depth and allowed to be as strong as the phase celerity of the wave. The temporal variation of the current is typically orders of magnitude slower than that of the waves, while the spatial variation is closely related to the variation of the bottom bathymetry. Thus, following a similar Fourier analysis as the one in chapter 2 for a constant depth, the resulting dispersion relation in non-dimensional form reads

$$\frac{(\omega - kU_c)^2}{k^2 d} = \frac{1 + \mathrm{B}\kappa^2}{1 + \left(\mathrm{B} + \frac{1}{3}\right)\kappa^2} \tag{3.86}$$

where $U_c = U_c'/\sqrt{gd_o'}$ is the non-dimensional current velocity, U_c' the dimensional current velocity, and the non-dimensional variables ω, k, d and κ are given in section 2.3.

Eq. (3.86) is the Padé [2,2] expansion of the Stokes linear solution for the combined wave-current action. Consequently, the model provides the correct form of the Doppler shift.

Another issue concerning the correct description of the wave-current interaction refers to the transport of the vertical vorticity associated with surf zone currents (Chen *et al*., 2000b, 2003; Gobbi *et al*., 2000b; Chen, 2006). Similarly to most Boussinesq-type models, the presented model was originally derived under the assumption of potential flow. However, Eq. (3.85) gives a quite accurate description of the generation and transport of the vertical vorticity, including its advection and stretching. Moreover, the terms of $O(\sigma^2, \varepsilon\sigma^2, \varepsilon^2\sigma^2)$ enhance the representation of the vertical component of vorticity compared to lower order models. However, formally, the order of the computed vertical vorticity is not exactly consistent with the order of the wave motion itself described by the Boussinesq equations. This slight inconsistency is present in almost all Boussinesq-type wave models derived for potential flows. Shen (2001) was the first to retain both the vertical and horizontal components of vorticity in his Boussinesq-type equations for weakly non-hydrostatic stratified flows and surface waves over an impermeable bottom. Chen (2006) proposed a methodology of consistently recovering the vertical vorticity at the leading order of accuracy of the Boussinesq equations by extending them to describe quasi-rotational wave-current motions in the nearshore. This issue is open for further investigation in the future.

The undertow effect was also taken into account by combining the eddy viscosity and the surface roller breaking concepts. It should be mentioned though that a rather crude approximation of the depth-averaged undertow is made by the model. On the other hand, a fully three-dimensional sediment transport calculation would require the variation of the undertow velocity over depth and consequently the solution of an extra equation, as the one in the models by Rakha *et al*. (1997) and Rakha (1998). In this case, two boundary condition are required, one at the surface associating the shear stress with the instantaneous energy dissipation due to breaking (Deigaard, 1993), and one at the bottom requiring an iterative procedure for the streaming at the boundary layer (Brøker and Fredsøe, 1984; Deigaard and Fredsøe, 1989). Moreover, the undertow's profile depends also on the variation of the eddy viscosity whose computation requires another iterative procedure and the solution of an extra equation for the turbulent kinetic energy (Deigaard *et al*., 1986). Nevertheless, as will be shown in chapter 4, a depth-integrated advection-diffusion equation will be solved for the suspended sediment and thus such a detailed description of the variation of the undertow velocity is not necessary. Hence, in order to avoid the above iterative processes and the solution of the extra equations, the aforementioned approximation was made for the depth-

averaged undertow and the formula by Putrevu and Svendsen (1993) was employed to obtain an estimation of the near bottom undertow. However, it should be mentioned that by doing this simplification the effect of the wave-current boundary layer is not taken into account by the presented model. The near bottom wave-current interaction is only, partly, taken into account in the estimation of the compound friction factor.

The numerical model relies on a generalized multi-step predictor-corrector scheme which offers fourth-order accuracy. As analyzed above, this scheme embeds improved numerical stability properties compared to the Adams-Bashforth-Moulton predictor-corrector scheme. However, compared to other recently used techniques in Boussinesq-type models, such as high-order Runge-Kutta time-stepping, hybrid TVD-type schemes and shock-capturing methods (Roeber *et al*., 2010; Shi *et al*., 2012; Kirby *et al*., 2013), the high nonlinearity and the slot technique introduce in some cases increased grid-based noise which is removed through the application of high-order filters. Some numerical noise is also introduced due to the use of the non-staggered Arakawa A-grid. The use of a staggered Arakawa C-grid, which is probably the most common in CFD modelling, would offer better stability and higher accuracy. However, staggered grids increase the computational complexity when higher order nonlinear terms are involved. Another convenient alternative could be the use of depth-integrated velocities instead of the depth-averaged ones (Abbott *et al*., 1978; Madsen *et al*., 1997a). This flux-formulation offers similar linear properties but it is more convenient for solving the equations in their conservative form (Madsen *et al*., 1991; Madsen and Sørensen, 1992). An analysis of the nonlinear properties of that formulation would be required for final assessment in conjunction with other issues involved.

For weakly nonlinear cases the numerical scheme requires typically no iterations, unless problems arose from boundaries. For strong nonlinear cases, more iterations may be required. The convergence rate is associated with the residue of the iterations. In practice, this residue depends on the basic predictor-corrector arrangement, the special treatment of the cross-terms, especially the ones involving time-derivatives, treated differently than the rest of the terms, and the relative magnitude of the nonlinear terms. The model's convergence depends also on the adopted criterion for the cessation of iterations. A number of different criteria have been proposed ranging from milder (Wei and Kirby, 1995; Wei *et al*., 1995) to more stringent (Gobbi *et al*., 2000a; Long and Kirby, 2006). It should be also mentioned that the adopted criterion influences the stability properties of the numerical scheme too. In any case, the applied relaxation technique described above increases the convergence rate to acceptable levels.

Until recently, the high computational time when dealing with 2DH applications, along with the associated numerical instabilities, have been the main disadvantages of Boussinesq-type

models as compared to phase-averaged wave models. However, the more and more increased power of computers can now suppress significantly the CPU time required for common applications. Moreover, as discussed above, computer parallelization reduces significantly the computational time and makes 2DH applications of Boussinesq models workable, even on personal PCs. For example, as already discussed the simulation of 20 min of wave propagation in a domain of a coastal zone with dimensions 1 km x 1 km would require about 1 day of computational time, or a 300 m x 300 m domain would take about 2 hours of simulation. It should be also mentioned that the recently developed GPU (Graphics Processing Unit) technology is expected to further reduce very impressively the CPU time when introduced to Boussinesq modelling. Indicatively, it is mentioned that speed-up of more than 100 times has been reported when applying the GPU computing in other 2DH models.

Waves are generated by applying the efficient source function technique, adapted to the specific Boussinesq-type equations and the outgoing energy is absorbed by suitable damping layers. The source function has been derived on the basis of linear equations. In weakly nonlinear cases, the generation of first-order waves will unintentionally introduce spurious free second- and higher-order waves in addition to bound second-order waves, which are phase-locked to the first order waves. To avoid the release of such spurious waves, a second- or higher-order correction should be applied based on the transfer functions derived in chapter 2 (see also Madsen and Sørensen, 1993). This aspect is open for further research. However, under strongly nonlinear conditions, the source function technique fails to generate the desired waves.

Both the one and two-dimensional versions of the model were validated by using a variety of different experimental tests. Both regular and irregular wave propagation and breaking over plane beaches and submerged shoals were quite successfully simulated. The 1DH model was applied for a cnoidal wave test and the model's performance was very accurate even at the inner surf zone. The superiority of the present model over its weaker nonlinear counterpart was evidenced. Breaking and run-up of a solitary wave was also simulated fairly well, proving the efficiency of the moving shoreline treatment. Run-up and overtopping were also simulated for a solitary wave propagating over a fringing reef. This simulation tested the model's efficiency to describe the transition from sub- to super-critical flow and the propagation of the bore. A very demanding two-dimensional test including a rip channel was employed to check the model's ability to reproduce combined coastal processes. The results were reasonably good. Finally, long-crested irregular waves of oblique incidence were simulated. Despite some discrepancies, the agreement between the computed and the measured data was acceptable.

Some of the validation tests combined a number of physical processes such as shoaling, depth and current refraction, diffraction, breaking, wave run-up, overtopping, nonlinear energy transfer and interactions with the wave-induced current field. Reasonable agreement has been found between the measurements and the computed results in these stringent tests. Hence it can be claimed that the presented compound model is a quite robust tool for studying wave-induced nearshore phenomena and a reliable basis for proceeding to the sediment transport computations presented in the next chapter.

References

Abbott, M. B., Larsen, J., Madsen, P. A., Tao, J. (1983). "Simulation of wave breaking and runup." Seminar on Hydrodynamics of waves in coastal areas, vol. 7. Moscow, 146-149.

Abbott., M. B., McCowan, A. D., and Warren, I. R. (1984). "Accuracy of short-wave numerical models." J. *Hydraul. Eng*., 110 (10), 1287-1301.

Abbott, M. B., Petersen, H. M., and Skovgaard, O. (1978). "On the numerical modelling of short waves in shallow water." *J. Hydraul. Res*., 16 (3), 173-203.

Arakawa, A., and Lamb, V. R. (1977). "Computational design of the basic dynamical processes of the UCLA general circulation model." *Methods in Computational Physics: Advances in Research and Applications*, 17 (ed. J. Chang). Academic Press, New York, pp. 173-265.

Balzano, A. (1998). "Evaluation of methods for numerical simulation of wetting and drying in shallow water flow models." *Coast. Eng*., 34 (1-2), 83–107.

Banijamali, B. (1998). "A study of enhanced, higher-order Boussinesq-type equations and their numerical modelling." *Series Paper*, 17, Aalborg University and ICCH, Danish Hydraulic Institute, Hørsholm, Denmark, 201 pp.

Basco, D. R. (1983). "Surfzone currents." *Coast. Eng*., 7 (4), 331-355.

Beji, S., and Battjes, J. A. (1994). "Numerical simulation of nonlinear wave propagation over a bar." *Coast. Eng*., 23 (1-2), 1-16.

Beji, S., and Nadaoka, K. (1996). "A formal derivation and numerical modelling of the improved Boussinesq equations for varying depth." *Ocean Eng.*, 23 (8), 691-704.

Bellotti, G., and Brocchini, M. (2001). "On the shoreline boundary conditions for Boussinesq-type models." *Int. J. Num. Meth. Fluids*, 37 (4), 479-500.

Berkhoff, J. C. W., Booij, N., and Radder, A. C. (1982). "Verification of numerical wave propagation models for simple harmonic linear water waves." *Coast. Eng*., 6 (3), 255–279.

Bowen, A. J. (1969a). "The generation of longshore currents on a plane beach." *J. Mar. Res*., 27, 206-215.

Bowen, A. J. (1969b). "Rip currents. 1. Theoretical investigations." *J. Geophys. Res*., 74 (23), 5467-5478.

Briganti, R., Musumeci, R. E., Bellotti, G., Brocchini, M., and Foti, E. (2004). "Boussinesq modeling of breaking waves: description of turbulence." *J. Geophys. Res.*, 109, C07015.

Brocchini, M., Cherubini, P., and Iovenitti, L. (1991). "An extension of Boussinesq type model to the surf zone." In: Computer Modeling in Ocean Engineering, A.S. Arcilla, M. Pastor, O.C. Zienkiewicz, B.A. Schrefler, Eds., Balkema, Rotterdam, pp. 349-359.

Brocchini, M., Drago, M., and Iovenitti, L. (1992). "The modeling of short waves in shallow waters. Comparisons of numerical models based on Boussinesq and Serre equations." *Proc. 23rd Int. Conf. on Coastal Engineering*, B. L. Edge, ed., ASCE, Venice, Italy, pp. 76-88.

Brocchini, M., Svendsen, I. A., Prasad, R. S., and Belloti, G. (2002). "A comparison of two different types of shoreline boundary conditions." *Comput. Methods Appl. Mech. Engrg*., 191 (39-40), 4475-4496).

Brøker, I., and Fredsøe, J. (1984). "Resulting sediment transport due to non-linear effects in waves." ISVA (Inst. Hydrodyn. Hydraul. Eng.), Technical University, Lyngby, *Progr. Rep.* 61, pp. 55-66.

Carrier, G. F., and Greenspan, H. P. (1958). "Water waves of finite amplitude on a sloping beach." *J. Fluid Mech*., 4 (1), 97–109.

Chawla, A., Özkan-Haller, H. T., and Kirby, J. T. (1996). "Experimental study of breaking waves over a shoal." *Proc. 25th Int. Conf. on Coastal Engineering*, B. L. Edge, ed., ASCE, Orlando, Florida, U.S.A., pp. 2-15.

Chen, Q. (2006). "Fully nonlinear Boussinesq-type equations for waves and currents over porous beds." *J. Eng. Mech.*, 132 (2), 220-230.

Chen, Q., Dalrymple, R. A., Kirby, J. T., Kennedy, A. B., and Haller, M. C. (1999). "Boussinesq modeling of a rip current system." *J. Geophys. Res*., 104 (C9), 20617-20637.

Chen, Q., Kirby, J. T., Dalrymple, R. A., Kennedy, A. B., and Chawla, A. (2000a). "Boussinesq modeling of wave transformation, breaking and runup. II: 2D." *J. Waterw. Port Coast. Ocean Eng*., 126 (1), 48-56.

Chen, Q., Kirby, J. T., Dalrymple, R. A., Kennedy, A. B., Thornton, E. B., and Shi, F. (2000b). "Boussinesq modelling of waves and alongshore currents under field conditions." *Proc. 27th Int. Conf. on Coastal Engineering*, B. L. Edge, ed., Sydney, Australia, 651–663.

Chen, Q., Kirby, J. T., Dalrymple, R. A., Shi, F., and Thornton, E. B. (2003). "Boussinesq modeling of longshore currents." *J. Geophys. Res*., 108 (C11), 3362, doi: 10.1029/2002JC001308.

Chen, Q., Madsen, P. A., Schäffer, H. A., and Basco, D. R. (1998). "Wave-current interaction based on an enhanced Boussinesq approach." *Coast. Eng*., 33 (1), 11–39.

Choi, J., Kirby, J. T., and Yoon, S. B. (2015). "Boussinesq modeling of longshore currents in the SandyDuck experiment under directional random wave conditions." *Coast. Eng*., 101, 17–34.

Chondros, M. K., Koutsourelakis, I. G., and Memos, C. D. (2011). "A Boussinesq-type model incorporating random wave breaking." *J. Hydraul. Res*., 49 (4), 529–538.

Cienfuegos, R., Barthélemy, E., and Bonneton, P. (2010). "Wave-breaking model for Boussinesq-type equations including roller effects in the mass conservation equation." *J. Waterw. Port Coast. Ocean Eng*., 136 (1), 10-26.

Dally, W. R., and Brown, C. A. (1995). "A modeling investigation of the breaking wave roller with application to cross-shore currents." *J. Geophys. Res*., 100 (C2), 24873-24883.

Deigaard, R. (1989). "Mathematical Modelling of Waves in the Surf Zone." *Prog. Report*, 69. ISVA, Technical University of Denmark, Lynghy, pp. 47-59.

Deigaard, R. (1993). "A note on the three-dimensional shear stress distribution in a surf zone." *Coast. Eng*., 20 (1-2), 157-171.

Deigaard, R., and Fredsøe, J. (1989). "Shear stress distribution in dissipative water waves." *Coast. Eng*., 13 (4), 357-378.

Deigaard, R., Fredsøe, J., and Brøker, I. (1986). "Suspended sediment in the surf zone." *J. Waterw. Port Coast. Ocean Eng*., 112 (l), 115-128.

Deigaard, R., Justesen, P., and Fredsøe, J. (1991). "Modelling of undertow by an one-equation turbulence model." *Coast. Eng*., 15 (5-6), 431–458.

De Vriend, H. J., and Stive, M. J. F. (1987). "Quasi-3D modelling of nearshore currents." *Coast. Eng*., 11 (5-6), 565–601.

Dingemans, M. W. (1994). "Water wave propagation over uneven bottoms." Ph.D. thesis, Delft University of Technology.

Feddersen, F. (2014). "The generation of surfzone eddies in a strong alongshore current." *J. Phys. Oceanogr*., 44 (2), 600-617.

Feddersen, F., Guza, R. T., Elgar, S., and Herbers, T. H. C. (2000). "Velocity moments in alongshore bottom stress parameterizations." *J. Geophys. Res*., 105 (C4), 8673-8686.

Fredsøe, J., and Deigaard, R. (1992). "Mechanics of coastal sediment transport." *Advanced Series on Ocean Engineering*, World Scientific Publishing, Singapore, vol. 3, 369 pp.

Gallerano, F., Cannata, G., and Villani, M. (2014). "An integral contravariant formulation of the fully non-linear Boussinesq equations." *Coast. Eng.*, 83, 119–136.

Geiman, J. D., and Kirby, J .T. (2013). "Unforced oscillation of rip-current vortex cells." *J. Phys. Oceanogr*., 43 (3), 477-497.

Gobbi, M. F., and Kirby, J. T. (1999). "Wave evolution over submerged sills: tests of a high-order Boussinesq model." *Coast. Eng.*, 37(1), 57-96.

Gobbi, M. F., Kirby, J. T., and Wei, G. E. (2000a). "A fully nonlinear Boussinesq model for surface waves. Part 2. Extension to $O(kh)^4$." *J. Fluid Mech*., 405, 181-210.

Gobbi, M., Kirby, J. T., and Kennedy, A. B. (2000b). "On the consistency of fully nonlinear Boussinesq models and their ability to predict vertical vorticity fields." *Proc. 27th Int. Conf. on Coastal Engineering*, B. L. Edge, ed., Sydney, Australia, 1321-1334.

Hamm, L. (1992a). "Directional nearshore wave propagation over a rip channel: an experiment." *Proc. 23rd Int. Conf. on Coastal Engineering*, B. L. Edge, ed., ASCE, Venice, Italy, pp. 226-239.

Hamm, L. (1992b). "Random wave propagation in the nearshore zone: experiments in a directional wave basin." *Internal report*, MAST-G6M, SOGREAH.

Hansen, J. B., and Svendsen, I. A. (1979). "Regular waves in shoaling water, experimental data." Inst. Hydrodyn. Hydr. Eng., *Series Paper*, 21.

Hansen, J. B., and Svendsen, I. A. (1984). "A theoretical and experimental study of undertow." *Proc. 19th Int. Conf. on Coastal Engineering*, B. L. Edge, ed., ASCE, Houston, Texas, U.S.A., pp. 2246-2262.

Israeli, M., and Orszag, S. A. (1981). "Approximation of radiation boundary conditions." *J. Comput. Phys*., 41 (1), 115-135.

Jonsson, I.G. (1966). "Wave boundary layers and friction factors." *Proc. 10th Int. Conf. on Coastal Engineering*, J. W. Johnson, ed., ASCE, Tokyo, Japan, pp. 127-148.

Karambas, Th. V., and Koutitas, C. (1992). "A breaking wave propagation model based on the Boussinesq equations." *Coast. Eng*., 18 (1-2), 1-19.

Karambas, Th. V., Krestenitis, Y., Koutitas, C. (1990). "A numerical solution of Boussinesq equations in the inshore zone." *Hydrosoft*, 3 (1), 34-37.

Karambas, Th. V., and Memos, C. D. (2009). "Boussinesq model for weakly nonlinear fully dispersive water waves." *J. Waterw. Port Coast. Ocean Eng*., 135 (5), 187-199.

Karambas, Th. V., and Tozer, N. P. (2003). "Breaking waves in the surf and swash zone." *J. Coast. Res.*, 19 (3), 514-528.

Kazolea, M., Delis, A. I., Nikolos, I. K., and Synolakis, C. E. (2012). "An unstructured finite volume numerical scheme for extended 2D Boussinesq-type equations." *Coast. Eng*., 69, 42-66.

Kennedy, A. B., Chen, Q., Kirby, J. T., and Dalrymple, R. A. (2000). "Boussinesq modeling of wave transformation, breaking and runup. I: 1D." *J. Waterw. Port Coast. Ocean Eng*., 126 (1), 39-47.

Kim, D. H., Lynett, P. J., and Socolofsky, S. A. (2009). "A depth-integrated model for weakly dispersive, turbulent, and rotational fluid flows." *Ocean Model*., 27 (3-4), 198-214.

Kirby, J. T., Wei, G., Chen, Q., Kennedy, A. B., and Dalrymple, R. A. (1998). "FUNWAVE 1.0. Fully nonlinear Boussinesq wave model. Documentation and user's manual." *Report CACR-98-06*, Center for Applied Coastal Research, Department of Civil and Environmental Engineering, University of Delaware, 80 pp.

Kirby, J. T., Shi, F., Tehranirad, B., Harris, J. C., and Grilli, S. T. (2013). "Dispersive tsunami waves in the ocean: Model equations and sensitivity to dispersion and Coriolis effects." *Ocean Model*., 62, 39-55.

Klonaris, G., and Memos, C. (2015). "A Boussinesq-type model simulating wave and wave-induced current fields". EGU General Assembly, 12-17 April, Vienna, Austria, id. 563.

Klonaris, G. Th., Memos, C. D., and Drønen, N. K. (2016). "High-order Boussinesq-type model for integrated nearshore dynamics." *J. Waterw. Port Coast. Ocean Eng*., 142 (6), 04016010.

Klonaris, G. Th., Memos, C. D., and Karambas, Th. V. (2013). "A Boussinesq-type model including wave-breaking terms in both continuity and momentum equations." *Ocean Eng*., 57, 128-140.

Klonaris, G. Th., Memos, C. D., and Makris, C. V. (2015). "Nearshore compound simulation by a Boussinesq-type wave model." IAHR/COPRI Symposium 'Long Waves and Relevant Extremes', *E-proceedings of the 36th IAHR World Congress*, The Hague, the Netherlands, 28 June - 3 July, 2015.

Kobayashi, N., Agarwal, A., and Bradley, D. J. (2007). "Longshore current and sediment transport on beaches." *J. Waterw. Port Coast. Ocean Eng*., 133 (4), 296-304.

Leendertse, J. J. (1987). ''Aspects of SIMSYS2D, a system for two dimensional flow computation.'' *R-3752-USGS*, Rand, Santa Monica, CA, 80 pp.

Liu, P. L.-F., Cho, Y. S., Briggs, M. J., Kanoglu, U., and Synolakis, C. E. (1995). "Runup of solitary waves on a circular island." *J. Fluid Mech*., 302, 259-285.

Long, W., and Kirby, J. T. (2006). "Boussinesq modeling of waves, currents and sediment transport." *Report CACR-06-02*, Center for Applied Coastal Research, Ocean Engineering Laboratory, University of Delaware, 323 pp.

Longuet-Higgins, M. S. (1970a). "Longshore currents generated by obliquely incident sea waves, 1." *J. Geophys. Res*., 75 (33), 6778– 6789.

Longuet-Higgins, M. S. (1970b). "Longshore currents generated by obliquely incident sea waves, 2." *J. Geophys. Res*., 75 (33), 6790– 6801.

Longuet-Higgins, M. S., and Stewart, R. W. (1961). "The changes in amplitude of short gravity waves on steady non-uniform currents." *J. Fluid Mech*., 10 (4), 529–549.

Lynett, P., and Liu, P. L.-F. (2004). "A two-layer approach to wave modelling." *Proc. R. Soc. Lond. A*, 460, 2637-2669.

Lynett, P., Wu, T.-R., and Liu, P. L.-F. (2002). "Modeling wave runup with depth-integrated equations." *Coast. Eng*., 46 (2), 89–107.

Madsen, P. A., Bingham, H. B., and Hua Liu (2002). "A new Boussinesq model for fully nonlinear waves from shallow to deep water." *J. Fluid Mech*., 462, 1-30.

Madsen, P. A., Murray, R., and Sørensen, O. R. (1991). "A new form of the Boussinesq equations with improved linear dispersion characteristics." *Coast. Eng.*, 15 (4), 371-388.

Madsen, P. A., and Schäffer, H. A. (1998). "Higher-order Boussinesq-type equations for surface gravity waves: derivation and analysis." *Philos. Trans. R. Soc. Lond*., A 356, 3123-3181.

Madsen, P. A., and Sørensen, O. R. (1992). "A new form of the Boussinesq equations with improved linear dispersion characteristics. Part 2. A slowly-varying bathymetry." *Coast. Eng*., 18 (3-4), 183-204.

Madsen, P. A., and Sørensen, O. R. (1993). "Bound waves and triad interactions in shallow water." *Ocean Eng*., 20(4), 359-388.

Madsen, P. A., Sørensen, O. R., and Schäffer, H. A. (1997a). "Surf zone dynamics simulated by a Boussinesq type model. Part I. Model description and cross-shore motion of regular waves." *Coast. Eng*., 32 (4), 255-287.

Madsen, P. A., Sørensen, O. R., and Schäffer, H. A. (1997b). "Surf zone dynamics simulated by a Boussinesq type model. Part II: surf beat and swash oscillations for wave groups and irregular waves." *Coast. Eng*., 32 (4), 289–319.

Makris C. V., Krestenitis Y. N., and Memos C. D. (2015). "SPH modelling of coherent structures and intermittent events in the surf zone of weak plungers." *E-proceedings of the 36th IAHR World Congress*, The Hague, the Netherlands, 28 June - 3 July, 2015.

Makris C. V., Memos C. D., and Krestenitis Y. N. (2016). "Numerical modeling of surf zone dynamics under weak plunging breakers with SPH method." *Ocean Model.*, 98, 12-35.

Mase, H., and Kirby, J. T. (1992). "Hybrid frequency-domain KdV equation for random wave transformation." *Proc. 23rd Int. Conf. on Coastal Engineering*, B. L. Edge, ed., ASCE, Venice, Italy, pp. 474-487.

Mei, C. C. (1983). *The Applied Dynamics of Ocean Surface Waves*. J. Wiley and Sons, New York, 740 pp. (Corrected reprint, World Scientific, 1989).

Memos, C. (2002). "Stochastic description of sea waves." *J. Hydraul. Res*., 40 (3), 1–10.

Memos, C. D., Karambas, Th. V., and Avgeris, I. (2005). "Irregular wave transformation in the nearshore zone: experimental investigations and comparison with a higher order Boussinesq model." *Ocean Eng*., 32 (11-12), 1465-1485.

Militello, A., Reed, C. W., Zundel, A. K., and Kraus., N. C. (2004). "Two-Dimensional Depth-Averaged circulation model M2D: version 2.0, Report 1, technical documentation and user's guide." US Army Corps of Engineers, ERDC/CHL TR-04-2.

Musumeci, R., Svendsen, I., and Veeramony, J. (2005). "The flow in the surf zone: a fully nonlinear Boussinesq-type approach." *Coast. Eng*., 52 (7), 565–598.

National Tsunami Hazard Mitigation Program [NTHMP] (2012). "Proceedings and Results of the 2011 NTHMP Model Benchmarking Workshop." *NOAA Special Report*, U.S. Department of Commerce/ NOAA/NTHMP, 436 p.

Nielsen, P. (1992). "Coastal bottom boundary layers and sediment transport." *Advanced Series on Ocean Engineering*, World Scientific Publishing, Singapore, vol. 4, 324 pp.

Nwogu, O. (1993). "Alternative form of Boussinesq equations for nearshore wave propagation." *J. Waterw. Port Coast. Ocean Eng.*, 119 (6), 618-638.

Ohyama, T., Beji, S., Nadaoka, K., and Battjes, J. A. (1994). "Experimental verification of numerical model for nonlinear wave evolutions." *J. Waterw. Port Coast. Ocean Eng*., 120 (6), 637-644.

Ozanne, F., Chadwick, A., Huntley, D., Simmonds, D., and Lawrence, J. (2000). "Velocity predictions for shoaling and breaking waves with a Boussinesq-type model." *Coast. Eng*., 41 (4), 361–397.

Özkan, H. T., and Kirby, J. T. (1995). "Finite amplitude shear wave instabilities." *Proc. Coastal Dynamics '95*, Gdansk, Poland, pp. 465-476.

Pedersen, G., and Gjevik, B. (1983). "Run-up of solitary waves." *J. Fluid. Mech*., 135, 283-299.

Peregrine, D. H. (1967). "Long waves on a beach." *J. Fluid Mech.*, 27 (4), 815-827.

Putrevu, U., and Svendsen, I. A. (1993). "Vertical structure of the undertow outside the surf zone." *J. Geophys. Res.*, 98 (C12), 22707–22716.

Rajaratnam, N. (1976). *Hydraulic jumps*. Advances in Hydroscience 4, V.T. Chow, ed. Academic Press, New York, pp. 197-280.

Rakha, K. A. (1998). "A Quasi-3D phase-resolving hydrodynamic and sediment transport model." *Coast. Eng*., 34 (3-4), 277–311.

Rakha, K. A., Deigaard, R., and Brøker, I. (1997). "A phase-resolving cross-shore transport model for beach evolution." *Coast. Eng*., 31 (1-4), 231-261.

Ribberink, J. S. (1998). "Bed-load transport for steady flows and unsteady oscillatory flows." *Coast. Eng*., 34 (1-2), 59–82.

Roeber, V. (2010). "Boussinesq-type model for nearshore wave processes in fringing reef environment." Ph.D. thesis, University of Hawaii at Manoa, Honolulu, HI.

Roeber, V., and Cheung, K. F. (2012). "Boussinesq-type model for energetic breaking waves in fringing reef environments." *Coast. Eng*., 70, 1-20.

Roeber, V., Cheung, K. F., and Kobayashi, M. H. (2010). "Shock-capturing Boussinesq-type model for nearshore wave processes." *Coast. Eng*., 57 (4), 407-423.

Schäffer, H. A., Deigaard, R., and Madsen, P. A. (1992). "A two-dimensional surf zone model based on the Boussinesq equations." *Proc. 23rd Int. Conf. on Coastal Engineering*, B. L. Edge, ed., ASCE, Venice, Italy, pp. 576-590.

Schäffer, H. A., and Madsen, P. A. (1995). "Further enhancements of Boussinesq-type equations." *Coast. Eng*., 26 (1-2), 1-14.

Schäffer, H. A., Madsen, P. A., and Deigaard, R. (1993). "A Boussinesq model for waves breaking in shallow water." *Coast. Eng*., 20 (3-4), 185-202.

Shapiro, R. (1970). "Smoothing, filtering, and boundary effects." *Rev. Geophys. and Space Phys*., 8 (2), 359-386.

Shen, C. Y. (2001). "Constituent Boussinesq equations for waves and currents." *J. Phys. Oceanogr.*, 31 (3), 850-859.

Shi, F., Kirby, J. T., Harris, J. C., Geiman, J. D., and Grilli, S. T. (2012). "A high-order adaptive time-stepping TVD solver for Boussinesq modeling of breaking waves and coastal inundation." *Ocean Model.*, 43-44, 36-51.

Smagorinsky, J. (1963). "General circulation experiments with the primitive equations. I. The basic experiment." *Mon. Weather Rev*., 91, 99–165.

Sørensen, O. R., Schäffer, H. A., and Madsen, P. A. (1998). "Surf zone dynamics simulated by a Boussinesq type model. III. Wave-induced horizontal nearshore circulations." *Coast. Eng*., 33 (2-3), 155-176.

Sørensen, O. R., Schäffer, H. A., and Sørensen, L. S. (2004). "Boussinesq-type modelling using an unstructured finite element technique." *Coast. Eng*., 50 (4), 181-198.

Stansby P. K., and Feng, T. (2005). "Kinematics and depth-integrated terms in surf zone waves from laboratory measurements." *J. Fluid Mech.*, 529, 279–310.

Staub, C., Jonsson, I.G., and Svendsen, I. A. (1996). "Sediment suspension in oscillatory flow: measurements of instantaneous concentration at high shear." *Coast. Eng*., 27 (1-2), 67–96.

Stelling, G. S., and Zijlema, M. (2003). "An accurate and efficient finite-difference algorithm for non-hydrostatic free-surface flow with application to wave propagation." *Int. J. Numer. Methods Fluids*, 43 (1), 1-23.

Stive, M. J. F. (1980). "Velocity and pressure field of spilling breakers." *Proc. 17th Int. Conf. on Coastal Engineering*, B. L. Edge, ed., ASCE, Sydney, Australia, pp. 547-566.

Svendsen, I. A. (1984). "Wave heights and setup in a surf zone." *Coast. Eng*., 8 (4), 303-329.

Swart, D. (1974). "Offshore sediment transport and equilibrium beach profiles." *Tech. Rep*., Delft Hydraulics Lab. Publ. No. 131, Delft, The Netherlands.

Synolakis, C. E. (1987). "The runup of solitary waves." *J. Fluid Mech*., 185, 523–545.

Tao, J. (1983). "Computation of wave run-up and wave breaking." *Internal Report*, Danish Hydraulic Institute, 40 pp.

Tao, J. (1984). "Numerical modelling of wave runup and breaking on the beach." *Acta Oceanol. Sin*., 6(5), 692-700, in Chinese.

Thomas, L. H. (1949). *Elliptic Problems in Linear Differential Equations over a Network*. Watson Sci. Comput. Lab Report, Columbia University, New York.

Ting, F., and Kirby, J. (1994). "Observation of undertow and turbulence in a laboratory surf zone." *Coast. Eng*., 24 (1-2), 51-80.

Tissier, M., Bonneton, P., Marche, F., Chazel, F., and Lannes, D. (2012). "A new approach to handle wave breaking in fully non-linear Boussinesq models." *Coast. Eng.*, 67, 54–66.

Tonelli, M., and Petti, M. (2009). "Hybrid finite volume-finite difference scheme for 2DH improved Boussinesq equations." *Coast. Eng*., 56 (5-6), 609–620.

Twizell, E. H. (1984). *Computational Methods for Partial Differential Equations*. Ellis Horwood Limited, West Sussex, England, 276pp.

Veeramony, J., and Svendsen, I. A. (2000). "The flow in surf-zone waves." *Coast. Eng.*, 39 (2-4), 93-122.

Wei, G., and Kirby, J. T. (1995). "Time-dependent numerical code for extended Boussinesq equations." *J. Waterw. Port Coast. Ocean Eng.*, 121 (5), 251-261.

Wei, G., and Kirby, J. T. (1998). "Simulation of water waves by Boussinesq models." *Report CACR-98-02*, Center for Applied Coastal Research, Ocean Engineering Laboratory, University of Delaware, 202 pp.

Wei, G., Kirby, J. T., Grilli, S. T., and Subramanya, R. (1995). "A fully non-linear Boussinesq model for surface waves. Part 1. Highly non-linear unsteady waves." J. *Fluid Mech*., 294, 71–92.

Wei, G., Kirby, J. T., and Sinha, A. (1999). "Generation of waves in Boussinesq models using a source function method." *Coast. Eng.*, 36 (4), 271-299.

Yamazaki, Y., Cheung, K. F., and Kowalik, Z. (2011). "Depth-integrated, non-hydrostatic model with grid nesting for tsunami generation, propagation, and run-up." *Int. J. Numer. Methods Fluids*, 67, 2081-2107.

Yoon, S. B. and Liu, P. L.-F. (1989). "Interaction of currents and weakly nonlinear water waves in shallow water." *J. Fluid Mech*., 205, 397-419.

Zelt, J. A. (1991). "The run-up of nonbreaking and breaking solitary waves." *Coast. Eng*., 15 (3), 205-246.

Zhan, J. M., Li, Y. S., and Wai, O. W. H. (2003). "Numerical modeling of multi-directional irregular waves incorporating 2-D numerical wave absorber and subgrid turbulence." *Ocean Eng*., 30 (1), 23-46.

Zlatev, Z., Berkowicz, R., Prahm L. P. (1983). "Stability restrictions on time-stepsize for numerical integration of first-order partial differential equations." *J. Comput. Phys*., 51 (1), 1-27.

Zlatev, Z., Berkowicz, R., Prahm L. P. (1984). "lmplementation of a variable stepsize variable formula method in the time-integration part of a code for treatment of long-range transport of air pollutants." *J. Comput. Phys*., 55 (2), 278-301.

Zou, Z. L. (1999). "Higher order Boussinesq equations." *Ocean Eng*., 26 (8), 767-792.

Chapter 4

Sediment transport model

4.1 Introduction

Understanding the nearshore hydrodynamic and morphodynamic processes is of great importance for solving coastal engineering problems. In particular, the vast diversity of nature and human activity throughout the coastal zone leads to the challenging, but also urgent, need for accurate and reliable predictions of the above physical processes. However, the interaction of waves and nearshore currents, the corresponding sediment transport and, eventually, the beach morphology evolution form a very complicated system, difficult to be modelled. This dynamic system becomes even more complex under the presence of coastal structures interacting with the natural environment. Thus, proper design of such man-made structures and activities (detached emerged and submerged breakwaters, groynes, seawalls, dredging, beach nourishment) requires the use of advanced mathematical models. In addition, the more and more increasing computational efficiency of computers offers nowadays the possibility of developing such efficient numerical tools.

The beach profile evolution is a complex problem influenced by a number of factors and can be studied in a large range of time and space scales. Roelvink and Brøker (1993) classified broadly the available cross-shore profile models into four classes depending on their theoretical background. The newest class of the "process-based" or "deterministic" profile models take explicitly into account the different processes contributing to profile development. However, most of the available sediment transport and morphological models use phase-averaged wave models and thus the effects of long waves and wave asymmetry can only be included in an approximate manner (Roelvink, 1991). On the other hand, models relying on the "energetic approach" may calculate the intra-wave variation of the sediment transport but neglect any lag effects in the development of the sediment concentration profile.

A number of detailed intra-wave sediment transport models has been developed assuming a wave theory to describe the intra-wave water motion (Fredsøe *et al*., 1985; Brøker Hedegaard

et al., 1991). Moreover, only a restricted number of phase-resolving wave models combined with detailed intra-wave sediment transport models have been reported in the international literature. Watanabe (1994) combined such a wave model based on the Boussinesq equations with an energetics sediment transport model. Boussinesq-type models have the advantage of being able to incorporate the nonlinear and dispersive wave characteristics from deep to shallow water and the swash zone. Thus, they can provide to the sediment transport models all the required information such as, wave breaking induced turbulence, wave asymmetry, bound long waves, wave-induced currents and swash zone hydraulic modelling. Nevertheless, not many examples of coupling either one horizontal dimensional (1DH) (Rakha *et al*., 1997; Karambas and Koutitas, 2002; Long and Kirby, 2003; Long *et al*., 2006; van Dongeren *et al*., 2006) or two horizontal dimensional (2DH) (Rakha, 1998; Karambas and Karathanassi, 2004; Drønen and Deigaard, 2011; Wenneker *et al*., 2011; Karambas, 2012; Rahman *et al*., 2013; Karambas and Samaras, 2014) Boussinesq-type wave models with a sediment transport and a morphological model have been presented.

Accurately estimating coastal sediment transport is a very hard task due to the complexity of the environment and the dependence of the result on a large number of factors. Most of these factors are difficult to be predicted in a robust way. The scientific interest was focused in computing the sediment transport rates along rivers and uniform flows much earlier than drawing attention to the coastal zone. Hence, a number of simple sediment transport formulae were developed for inland waters (du Boys, 1879; Schoklitsch, 1934; Kalinske, 1947; Meyer-Peter and Müller, 1948; Einstein, 1950). In the early years, the application of some of these formulae was extended to coastal water. However, the sediment's motion in the sea environment is much different due to reversing directionality and the combined action of waves and currents.

Since then a large variety of simplified mathematical formulae has been proposed for computing the coastal sediment transport rates in terms of bed, suspended or total loads. At first, the bed load under the action of a uniform current was studied (Yalin, 1963; Ashida and Michiue, 1972; Wilson, 1966; Madsen, 1991; Nielsen, 1992; Parker and Kovacs, 1993; Cheng, 2002). Among these the pioneer work by Bagnold (1963, 1966) introduced the energetics model in which the main idea is that the transport rate for steady flows is a function of the stream power. His approach relies on considerations of energy balance and mechanical equilibrium.

Within the coastal environment the stirring up of the sediment is caused mainly by the wave action. Thus, research focused on estimating the bed load under the wave action itself or the combination of waves and currents (Swart, 1974; Madsen and Grant, 1976; Fernandez Luque and van Beek, 1976; Sleath, 1978; Willis, 1978; van de Graaff and van Overeem, 1979;

Hallermeier, 1982; Nielsen, 2002; Hoefel and Elgar, 2003; Nielsen and Callaghan, 2003; Gonzalez-Rodriguez and Madsen, 2007). Ribberink (1998) proposed a quasi-steady model for bed load transport under the combined wave-current action. Regarding the suspended sediment, a number of models and empirical formulae have been developed (Bakker, 1974; Deigaard *et al*., 1986a; Briand and Kamphuis, 1993; Huynh-Thanh and Temperville, 1991; O'Connor and Nicholson, 1995; Ribberink and Al-Salem, 1995).

Mathematical formulae have been also proposed for the total sediment loads under current (Engelund and Hansen, 1972; Ackers and White, 1973), wave (Sato and Horikawa, 1986; Sawamoto and Yamashita, 1986; Ahilan and Sleath, 1987; Trowbridge and Young, 1989) or combined wave-current effect (Grass, 1981; van Rijn, 1989; Soulsby, 1997; van Rijn 2007a,b). A commonly used formulation in engineering applications was proposed by Bijker (1968) and forms a wave-current extension of Frijlink's (1952) formula. Engelund and Fredsøe (1976) derived a semi-empirical law for the total load assuming that only a certain fraction of the particles in a single bed layer is transported. Bailard (1981) derived a formula for the total load directly from Bagnold's approach. It takes into account the wave-current instantaneous velocity profiles. Roelvink and Stive (1989) modified Bailard's (1981) formula to take into account the additional stirring of sediment by the surface breaking-induced turbulence.

An interesting formulation was proposed by Dibajnia and Watanabe (1992, 1998) and Dibajnia *et al*. (2001) for sheet flow conditions and bed ripples. This model takes into account the unsteady aspects of sediment transport by incorporating the phase-lag effect of the suspended particles. Thus, it can adequately describe the sediment transport under nonlinear and irregular waves. Camenen and Larson (2005, 2006, 2007) proposed a sophisticated unified model for the total load which takes into account the phase-lag effects under combined waves and currents.

The longshore sediment transport is closely associated to the wave-driven currents and several longshore sediment transport formulae have been based on arguments that the sediment is stirred up by the waves and then transported along the coast by the wave-driven longshore current (Longuet-Higgins, 1972; Inman and Bagnold, 1963). Bijker (1971) developed a detailed longshore sediment transport model for combined waves and currents on a beach with constant slope. Moreover, a number of models for longshore transport have been proposed based on the energetics approach (Komar, 1971, 1977; Thornton, 1972; Bowen, 1981; Bailard and Inman, 1981) or a traction approach (Swart, 1976; Madsen and Grant, 1976). Komar and Inman (1970) also performed a number of filed measurements concerning the longshore sediment transport to evaluate Inman and Bagnold's (1963) formula. Deigaard *et al*. (1986b) developed a model which includes a longshore current model for arbitrary

coastal profiles. The flow resistance in their current model is calculated from the combined wave-current boundary layer and is consistent with the sediment transport description. Their model was further extended by Deigaard *et al*. (1988) to include the effects of irregular waves, wind shear stress and coastal currents.

With regard to longshore sediment transport, the CERC (1984) formula is the most widely used method to estimate the total transport rate across the width of the surf zone. The CERC-formula was originally derived for sandy beaches and it has only the characteristics of the incoming waves as input. This is not realistic, as the sediment transport must be expected to depend also on the sediment and on the coastal profile. Dean *et al*. (1982) showed the dependence of the longshore sediment transport on the grain size by calibrating the leading coefficient in the CERC-formula. Ozasa and Brampton (1980), Kamphuis *et al*. (1986), and Kamphuis (1991) proposed modifications to the CERC-formula by taking into account the grain size of the sediment, the beach slope, higher-order wave theories, and the along-shore variation of wave height. Damgaard and Soulsby (1996) derived a physics-based formula for bed load longshore sediment transport for both shingle and sandy beaches. More recently, a number of 2DH sediment transport models have been developed which include the computation of the longshore transport rate (Karambas and Karathanassi, 2004; Kobayashi *et al*., 2007; Karambas and Samaras, 2014).

Prediction of the coastal morphological evolution is the final and probably the most important issue in coastal engineering problems. Gradients in the transport rates cause deposition or erosion of sediment leading to topography changes. Thus, the accurate estimation of the sediment transport load plays a key role in the correct prediction of bathymetry. Also, the theoretical background of the geomorphological model itself is also crucial. The descriptive models rely on the classification of various beaches and the transition from one beach state to another (Sonu, 1973; Short, 1978; Lippmann and Holman, 1990). On the other hand, equilibrium profile models rely on the concept that beach profiles tend towards an equilibrium (Bruun, 1954; Dean, 1977; Vellinga, 1982). Empirical profile models describe in an empirical way the evolution towards equilibrium (N-line models, Bakker, 1968).

Predicting detailed morphological changes in coastal areas of complex topography requires rather the application of advanced process-based morphodynamic models. Such models have been developed over the last decades (Dally and Dean, 1984; Stive and Battjes, 1984; Stive, 1986; Watanabe and Dibajnia, 1988; Nairn, 1990; Steetzel, 1990; Brøker Hedegaard *et al*., 1991; Sato and Mitsunobu, 1991). Comparisons between various cross-shore profile models can be found in Roelvink and Brøker (1993) and Brøker Hedegaard *et al*. (1992). The process-based models rely on a more realistic background since their applicability is governed

by processes rather than by geography. In particular, phase-resolving wave models can incorporate intra-wave sediment transport processes and, thus, offer more accurate estimations of the instantaneous sediment loads compared to phase-averaged models. On the other hand, the former models require much higher computational effort compared to other simpler models. Consequently, at least regarding the phase-resolving wave models, it is mainly cross-shore cases that have been studied, even for short-term simulations referring to individual storms with duration of some hours. However, morphological processes in nature are much more complex, involving significant variability in the longshore direction of large coastal cells. The application of some recent morphodynamic techniques (Roelvink, 2006), in combination with the increased power of modern computers allow longer-term simulations for larger coastal areas, up to the order of some days for phase-resolving models and months or years when phase-averaged wave models are at play. In this way, the gap between the different time scales of hydrodynamic and morphodynamic processes is bridged.

In this chapter a sediment transport and a corresponding geomorphological model are developed and combined with the presented Boussinesq-type wave model. The significance of this work is that it introduces a 2DH integrated model combining a phase-resolving wave model with a sediment transport model and a geomorphological model, relying on advanced sediment transport formulae in both the surf and swash zones. In addition, extensive one and two-dimensional validation has been performed. A restricted number of other Boussinesq models combined with sediment transport computations have been presented in the past but they are based on cruder sediment formulae, while extensive verification has not been presented, especially against two horizontal dimensional tests. A sensitivity analysis for the main parameters of the sediment transport and morphological models is also performed.

4.2 Mechanisms of sediment transport

The two major agents of coastal sediment transport are the breaking and run-up of waves and the wave-induced currents. The dynamics at the grain scale is very difficult to be studied due to the small scale and the high level of uncertainty. The various components acting on the surface of the grains consist of the normal and shear stresses due to the water motion, the ground reaction from neighboring grains, the hydrodynamic subpressure due to infiltration, and the collision with other grains. This force balance decides the initiation of a sediment grain's movement. For very fine sediments, clays or mud, molecular cohesive forces also act making the moving initiation harder, especially when advanced solidification is at play. However, in the present thesis only non-cohesive sediments have been studied.

Usually, the wave action is the main factor of the grains' agitation and then the various currents are responsible for their transport in great horizontal distances. The turbulence due to the combined wave-current action contributes, along with the orbital velocities, to the vertical diffusion of the suspended sediments. Thus, a part of the wave energy is consumed for the bed material's agitation and its vertical diffusion, while the turbulent kinetic energy of the current also contributes to this diffusion and the horizontal advection. From a hydrodynamic point of view the main mechanisms of sediment transport can be classified as (Sorensen, 2006; Karambas *et al*., 2016):

- The longshore current generated by the oblique incidence and wave breaking transports sediments parallel to the shore. Also, variations in the alongshore distribution of wave breaker heights will cause alongshore variations in the surf zone wave setup and the generation of currents from areas of high waves to area of low waves. The balance of these two mechanisms establishes a longshore current. In most cases, the former mechanism predominates. In addition, in some parts of a coast where longshore currents have been established, they may be often interrupted by seaward flows, known as rip currents, which move the sediment in the offshore direction. The system of the nearshore currents is schematically shown in Fig. 4.1. Sediment transport due to longshore and rip currents in a sandy beach are shown in Fig. 4.2.

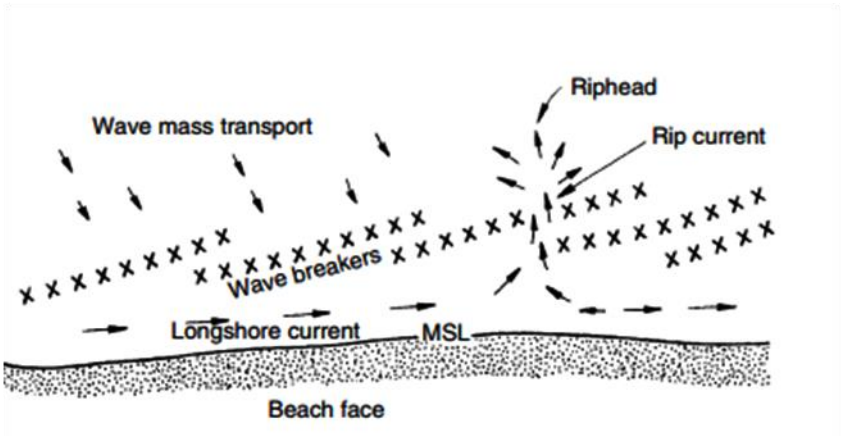

Fig. 4.1. Typical wave-generated nearshore circulation (from Sorensen, 2006).

Fig. 4.2. Sand transport due to longshore and rip currents in Newport Beach, California, 2009 (photo: Tom Cozad).

- As a wave propagates shoreward in the nearshore zone there is an asymmetry in the horizontal water particle velocities at the sea bed. According to nonlinear wave theories (Stokes, Cnoidal, Stream Function, etc.), the orbital velocities under the wave crests directed onshore are higher and despite having shorter duration than the ones below the wave troughs, directed offshore, induce a net inshore effect. This is due to the fact that the shear stress exerted on a bottom sand grain depends on the water particle velocity squared. Thus, a larger onshore bed stress is followed by a significantly lower offshore stress. Consequently, the net sediment transport due to this mechanism is directed onshore. This onshore transport further increases due to the fact that a certain threshold stress must be exceeded for a bottom particle to move.
- Gravity is a major agent for sediment transport, acting downslope and in a generally seaward direction for a monotonic profile. However, for the case of a barred profile, gravity can act in the shoreward direction over portions of the profile. Gravity tends to smooth any irregularities that occur in the profile. However, it can also serve as a stabilizing force, since sediment particles cannot be mobilized from the bed, unless: (a) upward-directed forces associated with fluid turbulence can exceed the submerged weight of the sediment, and/or (b) slope-parallel fluid shear forces can exceed the frictional resistance of sediment.
- Sediment transport also takes place due to secondary currents. As described in chapter 3, the three-dimensional undertow counteracts close to the shoreline the onshore mass transport and causes an offshore directed sediment transport.
- Another agent for sediment transport is the current generated in the wave bottom boundary layer. Due to the viscous shear stresses inside this layer the water velocities are lower than the ones over the rest over the water column. The aforementioned secondary current is parallel to the wave propagation direction.

- The turbulence due to wave breaking results in the suspension of the sediment grains, which are transported by the three-dimensional wave-induced current. The net transport of sand will be controlled by the net time-integrated horizontal flow velocity during the interval of sediment suspension. This mechanism may transport sediment in either the onshore or offshore direction.
- Onshore winds exert an onshore stress on the water surface and a consequent return flow at the bottom. On the other hand, seaward winds result in an onshore near bottom flow. This wind-induced near bed flow forms another mechanism of sediment transport.

The above description pronounces the complexity of the mechanism driving coastal sediment transport and littoral geomorphology. It should be also mentioned that the relative effect of these processes varies with the wave climate, water depth and the morphology of the coastal area.

Once the sediment is mobilized, it is very common to split the study of its transport into three modes:

- Bed load
- Suspended load
- Wash load

The wash load consists of imported very fine particles that are transported by water and are normally not represented in the bed. Thus, it is difficult to predict the wash load rate from the properties of the bed material. Consequently, this part of the sediment transport is neglected when the total sediment load is estimated.

The total load is divided into the bed load and the suspended load. No precise definition for these two terms has been given so far and their distinction is not always clear and meaningful. However, this splitting up relies on the different mechanisms that are effective during the two transport modes.

The bed load is the part of the total load that is in more or less continuous contact with the bed during transport. The grain movements include rolling, sliding or jumping along the bed. The intergranular collision forces and the effective bed shear stresses acting directly on the sand surface are the main physical mechanisms for this type of sediment transport that takes place in a layer with thickness less than, say, 10 times the median grain diameter d_{50}. On the other hand, the suspended load is the part of the total load that is moving all over the water column without continuous contact with the bed. In this case, the main mechanism for the sediment's movement is the agitation of fluid turbulence that is produced close to the bottom due to bed friction or/and close to the water surface due to wave breaking.

Sheet flow is another, intermediate transport mode referring to a layer with thickness (10÷100) d_{50} and large sediment concentrations (> 5-10 vol. %) which is transported along the bed (Ribberink, 1998). In this high-concentration layer the grains do not only roll or slide, but intergranular and extra pressure forces due to grain-water interactions also play a key role. This mode appears quite often in storm surges and under high waves, over flat beds when the bed ripples have already disappeared.

4.3 Sediment properties

The natural beaches usually consist of inorganic material with various physical properties which affect the sediment transport processes. The sediments are primarily formed by the physical and chemical disintegration of rocks from the earth's crust. According to their mineral composition, the predominant materials are quartz mineral and clay minerals. Based on their genetic origin they can be classified as lithogeneous, biogeneous, and hydrogeneous.

The sediment transported in the coastal zone usually contains particles ranging from gravels down to clays or even colloidal size fragments. These terms refer to the size of the sediment particle. Table 4.1 represents the grain size scale of the American Geophysical Union. This scale is based on powers of 2 mm by using the phi-parameter defined as $\varphi = -\log_2 d$ (with d the particle's diameter in mm).

Table 4.1. Grain size scale according to the American Geophysical Union (from van Rijn, 1993, modified).

Class name	**Millimeters**	**Micrometers**	**φ - values**
Boulders	> 256		< -8
Cobbles	256 - 64		-8 to -6
Gravel	64 - 2		-6 to -1
Very coarse sand	2.0 – 1.0	2000 – 1000	-1 to 0
Coarse sand	1.0 – 0.5	1000 – 500	0 to +1
Medium sand	0.5 – 0.25	500 - 250	+1 to +2
Fine sand	0.25 – 0.125	250 - 125	+2 to +3
Very fine sand	0.125 – 0.062	125 - 62	+3 to +4
Coarse silt	0.062 – 0.031	62 - 31	+4 to +5
Medium silt	0.031 – 0.016	31 - 16	+5 to +6
Fine silt	0.016 – 0.008	16 - 8	+6 to +7
Very fine silt	0.008 – 0.004	8 - 4	+7 to +8
Coarse clay	0.004 – 0.0020	4 - 2	+8 to +9
Medium clay	0.0020 – 0.0010	2 - 1	+9 to +10
Fine clay	0.0010 – 0.0005	1 – 0.5	+10 to +11
Very fine clay	0.0005 – 0.00024	0.5 – 0.25	+11 to +12
Colloids	< 0.00024	< 0.24	> +12

In the present thesis only non-cohesive sediments have been studied. This covers usually the particles in the range from sand (0.06 mm to 2 mm) to gravel (2mm to 20 mm). Based on their mineral and chemical composition, the sands can be distinguished in:

- silicate sands
- carbonate sands
- gypsum sands

Silicate sands mainly consist of quartz and feldspar minerals, which are extremely insoluble in the water. On the other hand, carbonate sands are much more soluble in the water. They originate from shells and corals and consist of calcium-carbonite ($CaCO_3$). Gypsum sands consist of crystal forms of gypsum ($CaSO_4.2H_2O$), which is a moderately soluble mineral.

From a hydraulic point of view, the most important sediment properties are related to the size, shape and specific gravity. The most usual and convenient method for the analysis of the particle size distribution is the sieve analysis, which is applicable for particle sizes not smaller than 0.06 mm. An adequate number of representative sediment samples is analyzed, and the result is presented as a frequency curve or a cumulative frequency curve. The most representative measure of the grain size is the median particle diameter, d_{50}, which corresponds to the median of the distribution curve, i.e. 50% by weight being finer.

Most of the sand particles on the face of the earth are more or less rounded because their edges and corners are smoothed by abrasion as running water or wind moves the sand particles from their origin to their resting place. In coastal zones, where sand moves in and out with each wave, sand particles are more or less rounded. The shape of particles is generally represented by the (modified) Corey (1949) shape factor and the rollability parameter (Winkelmolen, 1971).

The density of quartz and clay minerals is approximately $\rho_s = 2650$ kg/m^3 and the relative density is defined as the ratio of the sediment density (or specific gravity) to the water density:

$$s = \rho_s/\rho \tag{4.1}$$

For natural sediments, s is usually very close to 2.65.

The porosity, n_p, of the sediment is often related to the deposition history of the bed's sediment. Random packing of the grains yields porosity ranges from 0.36 to 0.40. Natural sediments with particles of various sizes have relatively small porosity values because the smaller particles can occupy the large void spaces. A poorly sorted coarse sand has a porosity of about 0.40, while a well sorted fine sand has a porosity of about 0.45. Mud deposits containing clay, silt, sand and organic material can have a large porosity factor, up to 0.80.

The settling or fall velocity, W_s, of a grain is defined as the terminal velocity attained when the grain is settling in an extended fluid under the action of gravity. It depends on several parameters, the most important of which are the grain size, the specific gravity, the grain shape, and the dynamic viscosity of the fluid. Considering the settling of a single spherical particle of diameter d, the terminal fall velocity is the fall velocity when the fluid drag force on the particle is in equilibrium with the gravity force, giving

$$W_s = \left[\frac{4(\mathrm{s}-1)\mathrm{g}d}{3\mathrm{C_D}}\right]^{0.5} \tag{4.2}$$

where $\mathrm{C_D}$ is the drag coefficient, which is a function of the Reynolds number $\mathrm{Re} = W_s d/v$, with v the kinematic viscosity of the fluid, and the shape factor (Albertson, 1952). For low values of the Reynolds number (Re < 1) the Stokes' (1851) law is applied and the drag coefficient is given by $\mathrm{C_D} = 24/\mathrm{Re}$, yielding

$$W_s = \frac{(\mathrm{s}-1)\mathrm{g}d^2}{18v} \tag{4.3}$$

Outside the Stokes region there is no simple expression for the drag coefficient. The value of $\mathrm{C_D}$ decreases rapidly and becomes nearly constant for $10^3 < \mathrm{Re} < 10^5$. This constant value is approximately 0.39 for spherical particles and varies from 1 to 1.3 for natural sediment particles.

Many semi-empirical formulae have been developed to estimate the settling velocity for weak concentrations based on these two asymptotic behaviors (Hallermeier, 1981; van Rijn, 1993; Koutitas, 1994; Julien, 1995; Cheng, 1997; Ahrens, 2000; Kamphuis, 2000; Guo, 2002; Jimenez and Madsen, 2003; Camenen, 2007). Soulsby (1997) proposed a simple relationship:

$$W_s = \frac{v}{d_{50}}\left(\sqrt{10.36^2 + 1.049 d_*^3} - 10.36\right) \tag{4.4}$$

where $d_* = \left[\frac{(\mathrm{s}-1)\mathrm{g}{d_{50}}^3}{v^2}\right]^{1/3}$ is the dimensionless grain size.

If the suspended concentration of sediment increases, the settling velocity of individual particles decreases because of the return flow induced by neighboring particles. Based on experimental data, Richardson and Zaki (1954) included the effect of high concentrations in the estimation of the settling velocity. Soulsby (1997) modified his own formula to include the effect of concentration:

$$W_s = \frac{v}{d_{50}}\left[\sqrt{10.36^2 + 1.049(1-\mathrm{c})^{4.7} d_*^3} - 10.36\right] \tag{4.5}$$

where c is the sediment's volume concentration.

The shape of the grains and the temperature also influence the fall velocity. The effect of the temperature is taken into account by the kinematic viscosity coefficient. The settling velocity is usually defined in still water. However, various researchers have investigated the effect of an oscillatory flow (Ho, 1964; Hwang, 1985; Nielsen, 1979, 1984). The major mechanism governing the fall velocity reduction in an oscillating flow is the drag-nonlinearity effect. Such effects are also associated with turbulence. Moreover, the intensive eddy production close to the bed induce upward motions which may reduce the fall velocity until the eddies dissolve at higher levels. These lift-up motions compete with downward velocities and the overall asymmetric fluid motion in the vertical direction may finally result in a slight increase of the settling velocity (Jobson and Sayre, 1970).

The angle of repose, also referred to as the angle of internal friction, φ_m, is a characteristic angle related to the particle stability on a horizontal or sloping bed. This parameter is a function of size, shape and porosity. It increases with decreasing roundness and it usually lies in the range 30° to 40° for sandy materials.

4.4 Threshold of motion

Particle movement will initiate when the instantaneous fluid force on a particle is larger than the instantaneous resting force related to the submerged particle weight and the friction coefficient. The driving forces are strongly related to the local near-bed velocities. However, the turbulent fluctuations, along with the randomness of particle size, shape and position, make the initiation of grain's movement a rather stochastic process.

Early works on the initiation of movement were done by Brahms (1753), who proposed a sixth power relationship between the flow and the required weight of a stone to be stable, and by Dubuat (1786) who introduced the concept of the critical bed-shear stress. These early works refer to the incipient motion under a current's action. Sternberg (1875) and Hjulström (1935) derived some well-known relationships between the critical depth-averaged current velocity and the particle diameter. More recently, van Rijn (1984a,b,c) and Soulsby (1997) proposed also some formulae for the critical depth-averaged current speed based on the critical bed-shear stress concept.

The critical bed-shear stress give a precise measure of the threshold of motion. This concept relies on the mobility (Shields) parameter, the critical value of which for the initiation of movement of a single particle with diamater d is given by

$$\theta_{\mathrm{cr}} = \frac{\tau_{\mathrm{b,cr}}}{\mathrm{g}(\rho_{\mathrm{s}}-\rho)d} \tag{4.6}$$

where $\tau_{b,cr}$ is the threshold bed-shear stress.

The critical mobility parameter depends on the hydraulic conditions near the bed, the particle shape and particle position relative to other particles. The hydraulic conditions near the bed can be expressed by the grain Reynolds number $\mathrm{Re}_* = u_{*,cr}d/v$, where $u_{*,cr}$ is the critical bed friction velocity defined by $u_{*,cr} = \sqrt{\tau_{b,cr}/\rho}$. Shields (1936) conducted a number of experiments on a flat bottom and presented graphically the dependence of θ_{cr} from Re_* in the case of a steady current. This diagram is depicted in Fig. 4.3.

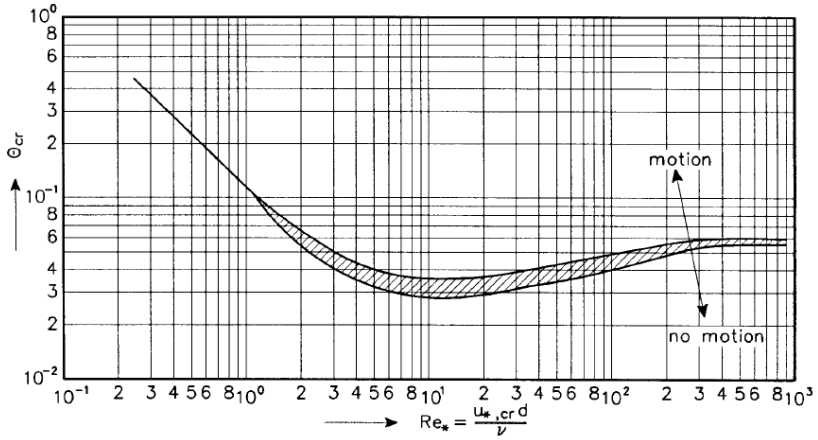

Fig. 4.3. θ_{cr} as a function of Re_* for a current over a plane bed (from van Rijn, 1993).

Using the median particle diameter d_{50} as a characteristic particle diameter, van Rijn (1993) expressed the Shields curve as

$$\theta_{cr} = \begin{cases} 0.24d_*^{-1} & \text{for} \quad 1 < d_* \leq 4 \\ 0.14d_*^{-0.64} & \text{for} \quad 4 < d_* \leq 10 \\ 0.04d_*^{-0.1} & \text{for} \quad 10 < d_* \leq 20 \\ 0.013d_*^{0.29} & \text{for} \quad 20 < d_* \leq 150 \\ 0.055 & \text{for} \quad d_* > 150 \end{cases} \tag{4.7}$$

Under waves, a number of formulae have been proposed for the initiation of motion on a plane bed but none of them is generally accepted (Bagnold, 1947; Manohar, 1955; Vincent, 1957; Goddet (1960); Eagleson and Dean, 1961; Ishihara and Sawaragi, 1962; Bonnefille and Pernecker, 1965; Carstens *et al*., 1967; Rance and Warren, 1968). Among these formulae, the one by Komar and Miller (1975) is probably the most widely used for the critical bottom orbital velocity. An increase of this critical velocity with the wave period is indicated by the theoretical relationships, although the various experimental data only weakly support this conclusion. Shields' (1936) original work referred to steady unidirectional currents. However, it has been shown that it can be reasonably extended for waves or combined waves and currents (van Rijn, 1993; Soulsby, 1997; Soulsby and Whitehouse, 1997). The critical Shields

parameter by a number of factors, such as the shape, gradation and size of the grains, the presence of bed forms, the presence of cohesive material, and the transverse and longitudinal bed slope (Fredsøe and Deigaard, 1992; van Rijn, 1993; Soulsby, 1997).

4.5 Bed features

A universal characteristic of erodible seabeds is their tendency not to remain stable but form a variety of bed features. This broad topic shall not be discussed in great extend because it would go beyond the objective of the present thesis. However, these bed waves will be presented briefly since they have a significant influence on the flow and sediment patterns.

Figure 4.4 shows the most important bed forms formed by a steady current. When the tractive form is increased to the point where sediment transport starts, the bed will be unstable. In the case of fine sediment, ripples are formed, while coarse sediments will usually form dunes. Ripples are small triangular sand waves that are usually not longer than about 0.6 m, and not higher than about 60 mm. Under hydraulically smooth conditions a viscous sublayer is formed, which is thicker than the sediment size. Under these conditions bed ripples are formed if the critical tractive force just is surpassed. On the other hand, dunes are formed if the bed is hydraulically rough. The ripple length depends on a number of factors, such as the sediment size, but is essentially independent of the water depth. Three-dimensional ripples have been discussed by Raudkivi (1976) and Sleath (1984).

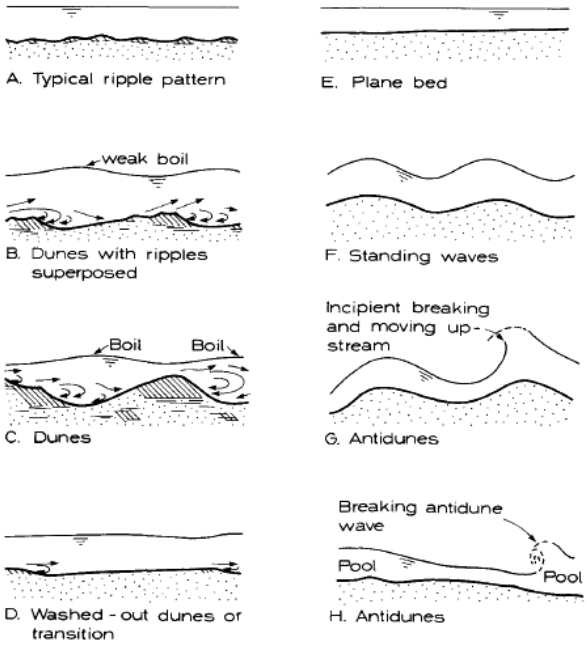

Fig. 4.4. Typical bed forms in order of increased stream power of a steady current (from Simons and Richardson, 1961).

Dunes are large, irregular sand waves usually formed in natural streams. The longitudinal profile is roughly triangular, with a mildly curved upstream surface and a downstream slope approximately equal to the angle of repose. Flow separation occurs at the crest and reattachment in the trough. At the upper part of the dune violent free turbulence is formed, which moves the sediment particles near the zone of reattachment, even when the local shear stress is below its critical value (Raudkivi, 1963). For increased stream power the dunes tend to wash out and this means a rather drastic reduction of both hydraulic resistance and water depth. Further increase of the stream power leads from the plane bed to the so-called antidunes whose longitudinal profile is nearly sinusoidal. The above transition from the initially plane bed to the various bed forms is depicted in Fig. 4.5.

In the case of wave action, the shape of the bed forms is quite different from those found in unidirectional flows. Because of changes in the strength and direction of the flow the shape of the bed is also unsteady and will change during the wave period. For short periodic waves, the volume of the sediment moved back and forth during one wave period is usually small compared to the volume of sand in a bed wave. Thus, the shape can be considered nearly steady, with only small fluctuations during the wave period. This is not the case for long periodic waves or very fine sediment. In this case, the mean bed profile is more elongated.

Bagnold (1946) defined two types of wave ripples: two-dimensional ripples related to rolling grains and three-dimensional vortex ripples related to eddy motions. The former are formed at low Shields numbers, not much larger than two times the critical value, while the latter are higher ripples formed at higher Shields numbers. The vortices formed in this latter case move considerable amount of sediment away from the bed which results to an increased suspended sediment transport.

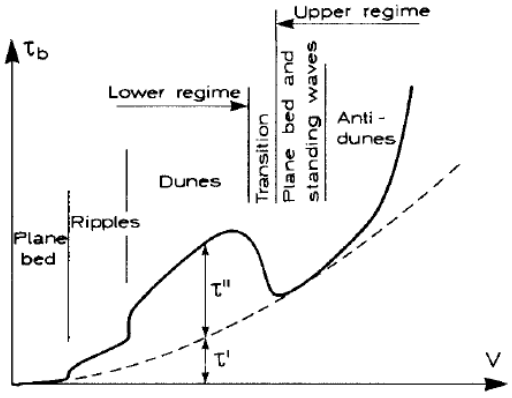

Fig. 4.5. Relation between total bed shear stress and flow velocity of a steady current for different bed forms (from Fredsøe and Deigaard, 1992).

In the case of upper flow regime, the wave ripples are washed out and sheet flow on a plane bed takes place (Dingler and Inman, 1976; Horikawa *et al*., 1982). According to Wilson

(1989), sheet flow regime is present for Shields parameters greater than 0.8. Generally, these conditions are assumed to be present in the surf zone where breaking waves are dominant.

Another bed form related to wave action consists of surf zone bars or longshore bars. These bars have their orientation parallel to the coastline and our found near the breaker line. The basic mechanism behind their formation is the net onshore-directed velocities seaward of the breaker line, and the net offshore-directed velocities (undertow) in the surf zone. In the case of high-energy coasts consisting of fine material (0.2-0.3 mm) two or more parallel bars are generated, while no bars are generated in the case of low-energy coasts of relatively coarse sediment (> 0.5 mm). Longshore variation in the bar shape and dimensions may be affected by the interaction of swell and edge waves.

For combined waves and currents various bed features may be formed (symmetrical and asymmetrical ripples, large sand waves, furrows, ribbons, ridges, banks, etc.) depending on the relative strength of currents and waves. A detailed discussion on this issue can be found in van Rijn (1993).

4.6 Suspended sediment

With regard to sand suspension, the settling of the grains towards the bed is counterbalanced by diffusion of sand upwards due to the turbulent water motions near the bed. The vertical eddy diffusivity of sediments, ε_v, depends on the turbulence in the flow and on the height above the bed. However, the mixing of sediment is not completely analogous to the mixing of water. The vertical eddy diffusivity of sediments is related to the vertical eddy viscosity, ν_T, through the Schmidt number σ:

$$\varepsilon_v = \sigma \nu_T \tag{4.8}$$

In principle, σ should be constant and equal to unity. However, deviations from this value have been observed and they can be attributed to three different processes. At first Sumer and Deigaard (1981) and van Rijn (1984b) explained that the centrifugal force in a fluid eddy causes sediment grains to be thrown outside of the eddy, which increases σ. Secondly, Fredsøe and Deigaard (1992) explained that the sediment's settling out of the surrounding water may take place before the water loses its earlier composition by mixing. Thirdly, Rose and Thorne (2001) argued that the value of σ may be affected by the settling velocity, which varies because of the presence of turbulence. Based on measurements by Coleman (1981), van Rijn (1984b) proposed the expression:

$$\sigma = 1 + 2\left(\frac{W_s}{u_*}\right)^2 \quad \text{with} \quad 0.1 < \frac{W_s}{u_*} < 1 \tag{4.9}$$

where u_* is the bottom friction velocity.

In the case of a steady current, different assumptions about the eddy diffusivity lead to different expressions for the concentration profile. If the eddy diffusivity is assumed to increase linearly with height above the bed, z, the corresponding concentration profile is the power-law profile:

$$\mathrm{C}(z) = \mathrm{C_a}\left(\frac{z}{z_\mathrm{a}}\right)^{-\frac{W_s}{\kappa u_*}} \tag{4.10}$$

where κ (= 0.40) is the von Karman constant, z_a is a reference height near the seabed, usually taken equal to $2d_{50}$, and $\mathrm{C_a}$ is a sediment reference concentration at the height z_a. The ratio $W_s/\kappa u_*$is referred to as the Rouse parameter and determines the shape of the suspended sediment profile.

If the eddy diffusivity is assumed to vary parabolically with height above the bed, the Vanoni-distribution is obtained:

$$\mathrm{C}(z) = \mathrm{C_a}\left(\frac{h-z}{z}\frac{z_\mathrm{a}}{h-z_\mathrm{a}}\right)^{\frac{W_s}{\kappa u_*}} \tag{4.11}$$

where h is the water depth.

Van Rijn (1984b) assumed the eddy diffusivity to vary parabolically with height in the lower half, and be constant with height in the upper half, of the water column. His profile probably corresponds better to currents alone in the sea (Soulsby, 1997).

The reference concentration is an important parameter for the accurate estimation of suspended sediment load. Thus, a number of formulae have been proposed for its calculation in the case of a steady current (Engelund and Fredsøe, 1976; Smith and McLean, 1977; Itakura and Kishi, 1980; Celik and Rodi, 1984; van Rijn, 1984b; Akiyama and Fukushima, 1986; Nielsen, 1992; Briand and Kamphuis, 1993; Zyserman and Fredsøe, 1994).

In a pure oscillatory flow, the turbulence is restricted to the thin wave boundary layer. The flow in this case is unsteady and thus it is necessary to apply the complete continuity equation for the suspended sediment:

$$\frac{d\mathrm{C}}{dt} = W_s\frac{\partial \mathrm{C}}{\partial z} + \frac{\partial}{\partial z}\left(\varepsilon_\mathrm{v}\frac{\partial \mathrm{C}}{\partial z}\right) + \nabla(\varepsilon_\mathrm{h}\nabla \mathrm{C}) \tag{4.12}$$

where ε_h is the horizontal eddy diffusivity of sediments.

The last term on the r.h.s. of Eq. (4.12) can usually be neglected, because the vertical gradient of C is much larger than the horizontal one. Furthermore, the convective terms on the l.h.s. of Eq. (4.12) are higher order terms which can normally be neglected. By applying these simplifications, and assuming the vertical eddy diffusivity to be time-invariant and having a

known vertical variation, an analytical solution for the time-averaged (in one wave period) sediment concentration, $\overline{C}$, can be obtained. This solution usually consists of an exponential profile of $\overline{C}$ over depth.

However, the assumption that ε_v is time-invariant is usually an oversimplification. Moreover, for unsteady flows, the suspended sediment does not react instantaneously to the velocity field. In particular, the instantaneous amount of sediment in suspension is not determined by the instantaneous value of the bed shear stress, because the sediment takes some time to settle after being picked-up from the bed. This means that the time-averaged sediment transport must be determined from the instantaneous quantities by:

$$\vec{q}_{ss} = \frac{1}{T}\int_0^T \int_0^h \vec{u} C \, dz dt \tag{4.13}$$

with T the wave period and $\vec{u} = (u\ , v)$ the instantaneous horizontal velocity.

Due to the aforementioned unsteady effects, the correct approach for solving the vertical distribution of suspended sediment in unsteady flows is to solve the complete version of Eq. (4.12). The numerical solution of this equation requires the application of three boundary conditions . The first one is that C must be periodic in time, the second implies that there must be no vertical flux at the water surface, and the third one is related to the bed concentration of suspended sediment. The latter one, still does not have a completely satisfactory solution. Some researchers are in favour of relating the bed concentration to the Shields parameter (Engelund and Fredsøe, 1976; Zyserman and Fredsøe, 1994), while others prefer the use of a so-called 'pick-up function'. This latter method relies on the idea that the vertical flux of sediment just above the bed must be equal to the amount of sediment eroded from the bed into the fluid, minus the amount of sediment deposited from the fluid into the bed.

Fredsøe *et al*. (1985) and Fredsøe and Deigaard (1992) studied the variation of the sediment's concentration within the wave period. Just above the bed, the maximum concentration occurs at the same time as the maximum bed shear stress, with a phase-lag compared to the maximum wave velocity outside the boundary layer. However, as the distance from the bed increases, the maximum concentration lags more and more behind the maximum bed shear stress. This happens because it takes some time for the sediment to settle after it has been picked up from the bed. Moreover, the time variation of C is asymmetric. This pattern is attributed both to the asymmetry of the near bed velocity and to the fact that the rise in the concentration is very rapid when the sediment is brought into suspension and pushed away from the bed during periods of large bed shear stresses, while the fall is simply due to the settling velocity, with almost no turbulence present.

For combined waves and currents, the turbulence is present over the whole flow depth. In this case, the unsteady advection-diffusion Eq. (4.12) should be solved. However, the variation of the eddy diffusivity should be similar to the current alone case in the outer region, and time-dependent and similar to the wave alone case within the boundary layer. The expression for the bed reference concentration by Zyserman and Fredsøe (1994) can be extended for combined waves and currents, while van Rijn (1993) extended his current-only concentration profile to include the effect of waves.

Downwave of the breaker line, the turbulence generated due to wave breaking results in much higher level of turbulent kinetic energy. This leads to a significant increase of the amount of suspended sediment. The breaking-induced turbulence must be taken into account by modifying the eddy diffusivity parameter (Battjes, 1983; de Vriend and Stive, 1987; Kraus and Larson, 2001; Camenen and Larson, 2007). The transition region from the breaking to fully developed broken waves has not been satisfactorily described. However, in the inner part of the surf zone, the broken waves are more or less transformed to hydraulic bores and the eddy viscosity can be related to the turbulent kinetic energy which can be calculated by an one-equation turbulence model. Such models, combined with sediment transport models, form the most advanced methods for calculating suspended sediment concentrations. They describe the wave-current boundary layer combined with some form of turbulent energy closure. Such models have been presented by Huynh Thanh *et al*. (1994), Ribberink and Al-Salem (1995), and Li and Davies (1996).

Perhaps the most well-established model of this class is the Danish 'STP' model. This model consists of two parts: a hydrodynamic module and a sediment transport module. The former describes the turbulent boundary layer under combined waves and current, using Fredsøe's (1984) theory. The sediment transport module is based on the work by Engelund and Fredsøe (1976) and Fredsøe *et al*. (1985). Deigaard *et al*. (1986a) extended the model to include the effect of wave breaking. The sediment transport module calculates the time-varying bed load and sediment concentration profile from the time-varying bed shear-stress and the eddy-diffusivity profile obtained by the hydrodynamic module. The resulting loads are found as the time average of their instantaneous values. The model applies for both plane and rippled beds and it has been updated periodically to include new processes and features. The STP model has been also combined with morphological models to describe the coastal profile (Deigaard *et al*., 1988; Brøker Hedegaard *et al*., 1991). These compound models relied on empirical relations for the variation of wave height across the profile (Andersen and Fredsøe, 1983; Deigaard *et al*., 1986b). Some years later, Rakha *et al*. (1996, 1997) incorporated the STP method into a 1DH Boussinesq-type model to combine the advantages of a phase-resolving model and an intra-wave sediment transport approach. The model could also describe the bed

morphological changes through an iterative process. Rakha (1998) extended this model to two horizontal dimensions offering both good hydrodynamic and sediment transport results. However, no morphological module was included in this later model version. Recently, Drønen and Deigaard (2007) and Drønen *et al*. (2011) combined the STP method with a spectral wave model for achieving quasi-3D modelling of longshore bars and the description of the long term response of a shoreline to the presence of coastal structures. Similar hybrid quasi-2DH shoreline models were also developed by Kaergaard and Fredsøe (2013a,b) and Kristensen *et al*. (2013) by combining a spectral wave model with the STP method for sediment transport.

4.7 Sediment transport formulae

As already discussed in subsection 4.1, a large number of formulae have been proposed for estimating the coastal sediment transport. These formulae refer to the bed load, the suspended load or the total load for currents, waves or combined currents and waves. Some commonly used among them are described in the following. The one-dimensional version of the formulae is only presented, while the two-dimensional extension is straightforward.

4.7.1 Meyer-Peter and Müller's formula

Meyer-Peter and Müller (1948) conducted a number of experiments in a laboratory flume involving both uniform and mix-sized particle grains. Based on their measurements and the critical shear stress concept, they proposed the following formula for the bed load under currents only:

$$\Phi_b = 8(\theta - \theta_{\mathrm{cr}})^{1.5} \tag{4.14}$$

where

$$\Phi_b = \frac{q_{sb}}{\sqrt{(\mathrm{s}-1)\mathrm{g}d_{50}{}^3}} \tag{4.15}$$

is the non-dimensional bed load transport rate and q_{sb} is the dimensional volumetric bed load rate per unit width. The Shields parameter $\theta = \tau_b/[(\mathrm{s}-1)\rho \mathrm{g} d_{50}]$ is constant over time since the bed shear stress, τ_b, is only due to a steady current.

Their experiments included relatively coarse material and they estimated the critical mobility parameter as $\theta_{\mathrm{cr}} = 0.047$. Obviously, if $\theta < \theta_{\mathrm{cr}}$ no sediment transport takes place.

4.7.2 Bijker's formula

Based on Frijlink's (1952) formula for a current only, Bijker (1968) derived a sediment transport formulation for both the bed load and suspended load under combined waves and currents. The bed load, q_{sb}, and the suspended load, q_{ss}, are given by the following formulae:

$$q_{sb} = \mathrm{C}_b d_{50} \sqrt{\frac{\mu_\mathrm{c}\tau_\mathrm{c}}{\rho}} \exp\left[-0.27 \frac{\mathrm{g}(\rho_\mathrm{s} - \rho) d_{50}}{\mu_\mathrm{c}\tau_\mathrm{cw}}\right] \tag{4.16a}$$

$$q_{ss} = 1.83 q_{sb}\left[I_1 \ln\left(\frac{33h}{\delta_\mathrm{c}}\right) + I_2\right] \tag{4.16b}$$

where h is the water depth; μ_c is the ripple parameter given by $\mu_\mathrm{c} = (f_\mathrm{ct}/f_\mathrm{c})^{3/2}$, with f_ct the total friction coefficient and f_c the skin friction coefficient due to current; τ_c is the shear stress due to current only; τ_cw is the shear stress due to wave-current interaction; I_1 and I_2 are the Einstein (1950) integrals for the suspended load; δ_c=$100 d_{50}/h$ is the dimensionless thickness of the bed load layer; and C_b is a breaking wave parameter defined by:

$$\mathrm{C}_b = \begin{cases} 2 & \text{if} \quad H_\mathrm{w}/h < 0.05 \\ 2 + 3(H_\mathrm{w}/h - 0.05) & \text{if} \quad 0.05 \le H_\mathrm{w}/h < 0.4 \\ 5 & \text{if} \quad 0.4 \le H_\mathrm{w}/h \end{cases} \tag{4.17}$$

with H_w the wave height.

The shear stress due to wave-current interaction is computed following the method proposed by Bijker (1967) introducing a suspension factor:

$$\tau_\mathrm{cw} = \left[1 + 0.5\left(\xi_\mathrm{B}\frac{U_\mathrm{w}}{U_\mathrm{c}}\right)^2\right]\mu_\mathrm{c}\tau_\mathrm{c} \tag{4.18}$$

where $\xi_\mathrm{B} = \sqrt{f_\mathrm{wt}/f_\mathrm{ct}}$ is a parameter due to the wave-current interaction; f_wt is the total friction coefficient due to waves; U_w is the peak value of the wave orbital velocity at the bottom; and U_c is the mean current velocity.

The Einstein (1950) integrals for the suspended load are given by:

$$I_1 = \int_{\delta_\mathrm{c}}^{1}\left(\frac{1-y}{y}\right)^A dy \quad \text{and} \quad I_2 = \int_{\delta_\mathrm{c}}^{1}\left(\frac{1-y}{y}\right)^A \ln y dy \tag{4.19}$$

where $A = W_s/\left[\kappa(\tau_\mathrm{cw}/\rho)^{0.5}\right]$, with κ the von Karman constant as above.

4.7.3 Engelund and Fredsøe's formula

Fernandez Luque (1974) and Fernandez Luque and Beek (1976) have argued against some of Bagnold's (1963, 1966) ideas and they developed a consistent theory for the transport of bed load on a plane bed considering the motion of individual particles. His theory was supported by a series of careful experimental observations. A basic idea of his theory is that close to incipient particle motion only the topmost grains will be eroded, and the bed load will not effectively reduce the fluid part of the turbulent shear stress. Relying on this approach, Engelund and Fredsøe (1976) developed a bed load formula containing time-averaged quantities rather than an exact description of the forces, which have a fluctuating character. The main assumption that was made was that the bed load is the transport of a certain fraction p (probability) of the particles that may be in one single layer.

$$\Phi_b = 5p\left(\sqrt{\theta'} - 0.7\sqrt{\theta_{\mathrm{c}}}\right) \tag{4.20}$$

where Φ_b is given by Eq. (4.15), θ' is the Shields parameter due to skin friction only and it is given by

$$\theta' = \theta_{\mathrm{c}} + \frac{\pi}{6}\mu_d p \tag{4.21}$$

where $\mu_d = \tan\varphi_d$ represents the dynamic friction, with φ_d the dynamic friction angle for the bed load sediment. The fraction p is given by the expression

$$p = \left[1 + \left(\frac{\frac{\pi}{6}\mu_d}{\theta' - \theta_{\mathrm{c}}}\right)^4\right]^{-\frac{1}{4}} \tag{4.22}$$

The critical value θ_{c} usually lies in the range $0.04 \div 0.06$. In their original work, Engelund and Fredsøe (1976) used the value $\theta_{\mathrm{c}} = 0.05$.

Following Einstein's (1950) ideas, the suspended load, q_{ss}, is evaluated as

$$q_{ss} = 11.6U_f'\mathrm{C_a}z_{\mathrm{a}}\left[I_1 \ln\left(\frac{30h}{K_N{}'}\right) + I_2\right] \tag{4.23}$$

where h is the water depth, U_f' is the shear velocity related to skin friction, $K_N{}' = 2.5d_{50}$ is Nikuradse's equivalent roughness, $z_{\mathrm{a}} = 2d_{50}$ is the bed reference level, I_1 and I_2 are given by Eq. (4.19), and the bed reference concentration is given by

$$C_a = \frac{0.65}{(1 + 1/\lambda)^3} \tag{4.24}$$

where

$$\lambda = \sqrt{\frac{\theta' - \theta_c - \frac{\pi}{6} p\mu_d}{0.027 s\theta'}} \quad \text{if} \quad \theta' > \theta_c + \frac{\pi}{6} p\mu_d \tag{4.25}$$

Engelund and Fredsøe (1982) studied the bed material's motion also in the case of a transverse slope. The original work by Engelund and Fredsøe (1976) referred to a current. Fredsøe (1984) presented a hydrodynamic module describing the turbulent boundary layer under combined waves and current. Based on this work, Fredsøe *et al*. (1985) developed a sediment transport module describing the distribution of suspended sediment under combined wave-current motion. Deigaard *et al*. (1986a) introduced the effect of wave breaking in the computation of suspended sediment load. As described above, the combination of the aforementioned works forms the Danish STP model, which has been updated with new feature since then. Based on experimental data sets, Zyserman and Fredsøe (1994) proposed a different formulation for the reference concentration:

$$C_a = \frac{0.331(\theta' - \theta_c)^{1.75}}{1 + 0.72(\theta' - \theta_c)^{1.75}} \quad \text{if } \theta' > \theta_c \tag{4.26}$$

with $\theta_c = 0.045$.

4.7.4 Bailard's formula

Based on Bagnold's (1963) energetics approach for sediment transport in streams, Bailard (1981) developed a total load model for time varying sediment transport over a plane sloping bed. In both the bed load and the suspended load, the transport rate vectors are composed by a velocity-induced component directed parallel to the instantaneous velocity vector and a gravity-induced component directed down slope. Bagnold (1963) also developed a related sediment transport equation for oscillatory flows. In this case, the wave motion acted to move the sediment back and forth in an amount proportional to the local rate of energy dissipation. Although no net transport results from this linear wave motion, a steady current of arbitrary strength, when superimposed on the wave motion, is free to transport the sediment in the steady current's direction. Relying on this concept Bailard (1981) proposed the following formula for the time-averaged total load under combined waves-current, although better agreement has been reported for wave-dominated conditions (Soulsby, 1997):

$$\vec{q}_{sb} = \frac{c_f \varepsilon_B}{(s-1) g \tan\varphi_m}\left(\langle|\vec{u}|^2\vec{u}\rangle - \frac{\tan\beta}{\tan\varphi_m}\langle|\vec{u}|^3\rangle\right) \tag{4.27a}$$

$$\vec{q}_{ss} = \frac{c_f \varepsilon_s}{(s-1) g W_s}\left(\langle|\vec{u}|^3\vec{u}\rangle - \frac{\varepsilon_s \tan\beta}{W_s}\langle|\vec{u}|^5\rangle\right) \tag{4.27b}$$

where c_f is the bed friction coefficient such as $\vec{\tau}_b = \rho c_f |\vec{u}|\vec{u}$; $\vec{u}$ is the instantaneous near-bottom velocity due to combined waves and currents; $\tan\beta$ is the bed slope; φ_m is the internal friction angle; $\varepsilon_B = 0.10$ and $\varepsilon_s = 0.02$ (Bailard, 1982); and $<\cdot>$ denotes averaging over the wave period.

Bailard's (1981) formulation obviously ignores the effect of the additional stirring of sediment by the surface breaking-induced turbulence which penetrates towards the bottom. Roelvink and Stive (1989) included this additional effect and modified Bailard's (1981) formula for the suspended load as:

$$\vec{q}_{ss} = \frac{c_f \varepsilon_s}{(s-1) g W_s}\left(\langle|\vec{u}|^3\vec{u}\rangle - \frac{\varepsilon_s \tan\beta}{W_s}\langle|\vec{u}|^5\rangle\right) + \frac{\varepsilon_s \langle|\vec{u}|\rangle b D_b}{(s-1) g W_s} \tag{4.28}$$

where D_b is the dissipation of turbulent kinetic energy, $D_b = \rho b_d \bar{k}^{3/2}$, with $b_d \approx 1$ and $\bar{k}$ is the depth- and time-averaged turbulent kinetic energy; $b = \left[\exp\left(\bar{h}/H_{rms}\right) - 1\right]^{-3/2}$, with $\bar{h}$ the mean water depth.

4.7.5 Soulsby and van Rijn's formula

Van Rijn (1984a,b,c) derived a theory for sediment transport in rivers combining fundamental physics and empirical results. Van Rijn (1989) adapted this initial current-alone formula to account for combined waves and currents. The bed load is given by

$$q_{sb} = 0.25 d_{50} d_*^{-0.3} \sqrt{\frac{\mu_c \alpha_{cw} \tau_c}{\rho}}\left(\frac{\tau_{cw} - \tau_{cr}}{\tau_{cr}}\right)^{1.5} \tag{4.29}$$

where α_{cw} is a coefficient due to the presence of waves (which can affect the mean shear stress), τ_{cr} is the critical shear stress, τ_{cw} is the bed shear stress due to combined waves and current, and μ_c is a shape factor related to ripples.

The suspended load is obtained by solving the following equation for the mean concentration $\bar{C}$:

$$\frac{d\overline{\mathrm{C}}}{dz} = -\frac{(1-\overline{\mathrm{C}})^5 \overline{\mathrm{C}} W_s}{\varepsilon_{\mathrm{scw}}} \tag{4.30}$$

where $\varepsilon_{\mathrm{scw}}$ is the mixing coefficient for the case of wave-current interaction, and then evaluating the flux:

$$q_{ss} = \int_{z_{\mathrm{a}}}^{h} \overline{u}(z)\overline{\mathrm{C}}(z)dz \tag{4.31}$$

where $\overline{u}(z)$ is the mean velocity at level z, and $z_{\mathrm{a}} = \max\{k_{\mathrm{sct}}, k_{\mathrm{swt}}\}$ is the reference level, with k_{sct} and k_{swt} the total roughness due to current and waves, respectively. The aforementioned analysis forms the basis of the computer program TRANSPOR and it is described in detail by van Rijn (1993).

Soulsby (1997) proposed another modification of the original van Rijn's (1984a,b,c) formula to account for combined waves and current. The total load is given by

$$q_{tot} = (A_{sb} + A_{ss})\left[\left(\overline{U}^2 + \frac{0.018}{\mathrm{C_D}} U_{\mathrm{rms}}^2\right)^{1/2} - \overline{U}_{\mathrm{cr}}\right]^{2.4} (1 - 1.6\tan\beta) \tag{4.32}$$

where $\overline{U}$ is the depth-averaged current velocity; U_{rms} is the root-mean-square wave orbital velocity; $\overline{U}_{\mathrm{cr}}$ is the threshold current velocity given by van Rijn (1984a); $\tan\beta$ is the bed slope; $\mathrm{C_D}$ is the drag coefficient due to current alone; and A_{sb} and A_{ss} account for the bed load and the suspended load, respectively. They are given by the expressions:

$$A_{sb} = \frac{0.005h(d_{50}/h)^{1.2}}{[(\mathrm{s}-1)\mathrm{g}d_{50}]^{1.2}} \tag{4.33a}$$

$$A_{ss} = \frac{0.012 d_{50} d_*^{-0.6}}{[(\mathrm{s}-1)\mathrm{g}d_{50}]^{1.2}} \tag{4.33b}$$

with h the water depth.

4.7.6 Dibajnia and Watanabe's formula

A very interesting sediment transport formula is the one proposed by Dibajnia and Watanabe (1992) and Dibajnia (1995). The formula was initially derived for sheet flow conditions but was later extended to cover suspended load over ripples, as well as bed load transport (Dibajnia *et al*., 1994). It was further extended to handle mixed-size sands (Dibajnia and Watanabe, 1996) and also to irregular sheet flow conditions (Dibajnia and Watanabe,

1998; Dibajnia *et al*., 2001). The specific formulation breaks down the sediment transport into two half-cycles due to the presence of waves. During the first half-cycle the sediment moves in the direction of the wave and during the second half-cycle in the opposite direction. An important aspect of this approach is that it takes into account a possible quantity of sand still in suspension after each half-cycle, and hence moving in the opposite direction. This phase-lag phenomenon was firstly described by Dohmen-Janssen (1999). Thus, the formula can estimate the sediment transport under nonlinear waves. The volumetric transport rate is given by

$$\vec{q}_s = \alpha_{dw} W_s d_{50} \frac{\vec{u}_c T_c \left(\Omega_c + \Omega_t^{'}\right) + \vec{u}_t T_t \left(\Omega_t + \Omega_c^{'}\right)}{(T_c + T_t)\sqrt{(\mathrm{s}-1)\mathrm{g}d_{50}}} \tag{4.34}$$

where $\vec{u}_c$ and $\vec{u}_t$ are representative velocity amplitudes for the positive and negative portions of the total velocity profile including wave-current interaction, $\vec{u} = u\vec{\imath}$ (see Fig. 4.6), with T_c and T_t being their corresponding duration, respectively, $\vec{\imath}$ the unity vector, and $\alpha_{dw} = 0.0019$.

$$|\vec{u}_c|^2 = \frac{2}{T_c}\int_{t_0}^{t_0+T_c} |\vec{u}|^2 dt \quad \text{and} \quad |\vec{u}_t|^2 = \frac{2}{T_t}\int_{t_0+T_c}^{t_0+T} |\vec{u}|^2 dt \tag{4.35}$$

It should be mentioned that Eq. (4.34) is the latest update of the described formulation and was presented by Dibajnia *et al*. (2001). It is slightly different than the previous versions to better account for irregular waves involving low frequency components and strong steady currents.

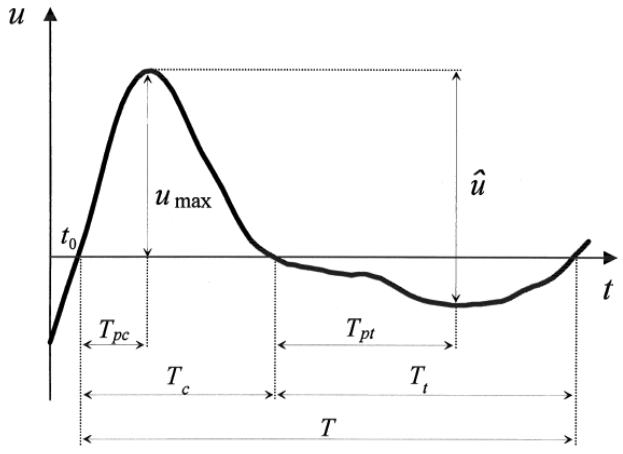

Fig. 4.6. Time evolution of total velocity u and definition of parameters (from Dibajnia *et al*., 2001).

Values of Ω are obtained as:

$$\begin{cases} \text{if } \omega_j \le \omega_{\text{cr}} & \begin{cases} \Omega_j = \omega_j T_j \sqrt{\dfrac{(\text{s}-1)\text{g}}{d_{50}}} \\ \Omega_j^{'} = 0 \end{cases} \\ \text{if } \omega_j > \omega_{\text{cr}} & \begin{cases} \Omega_j = \left[\omega_{\text{cr}} + (1-\gamma_j)(\omega_j - \omega_{\text{cr}})\right] T_j \sqrt{\dfrac{(\text{s}-1)\text{g}}{d_{50}}} \\ \Omega_j^{'} = \gamma_j (\omega_j - \omega_{\text{cr}}) T_j \sqrt{\dfrac{(\text{s}-1)\text{g}}{d_{50}}} \end{cases} \end{cases} \tag{4.36}$$

with the condition for Ω_j (and not for $\Omega_j^{'}$) that

$$\text{if } \Psi_j < \Psi_{\text{sheet}} : \ \Omega_j = \left(\frac{\Psi_j - \Psi_{\text{cr}}}{\Psi_{\text{sheet}} - \Psi_{\text{cr}}}\right)^3 \Omega_j \tag{4.37}$$

where $\Psi_j = (1/2) f_{\text{w}} u_j^2 / [(\text{s}-1)\text{g}d_{50}]$ and

$$\omega_j = (\theta_j - \theta_{\text{cr}}) \frac{d_{50}}{W_s T_j} \quad \text{and} \quad \theta_j = \Psi_j / f_{\text{w}} \tag{4.38}$$

where f_{w} is the wave friction factor and the subscript j should be replaced by either c or t, i.e. crest or trough. The parameter $\gamma_j$is given by $\gamma_j = \beta_j^* \beta_j' \beta_j''$, where the three factors account for the wave asymmetry, whether the velocity in the next half-cycle is high enough to carry the suspended sand delivered by the current half-cycle or not, and additional sediment exchange between the two half-cycles due to possibly different angles of vectors $\vec{u}_c$ and $\vec{u}_t$ (see Dibajnia *et al*., 2001; Karambas and Karathanassi, 2004).

The critical values for the mobility numbers were set: $\Psi_{\text{cr}} = 0.05$ and $\theta_{\text{cr}} \approx 5$. Ψ_{sheet} is the critical Shields number for initiation of sheet flow. Eq. (4.37) indicates that over a flat bed when $\Psi_j < \Psi_{\text{sheet}}$, the bed load motion may not be as intensive as that under fully developed sheet flow conditions. Comparison with Dibajnia and Watanabe's (1992) and Ribberink and Al-Salem's (1995) sheet flow data showed that $\Psi_{\text{sheet}} = 0.8$ and $\omega_{\text{cr}} = 1.2 - 1.17\sqrt{\Lambda}$, with Λ a parameter taking into account the presence of bed ripples (Dibajnia, 1995).

4.7.7 Ribberink's formula

Based on Meyer-Peter and Müller's (1948) bed-shear concept, Ribberink (1998) proposed a quasi-steady formula for bed load transport under combined waves and currents. His formulation assumes that the instantaneous solid flux is proportional to a function of the

difference between the actual time-dependent bed shear stress and the critical bed shear stress. The specific formula was calibrated against a large set of experimental data including wave-current interactions in plane regime (suspended load negligible) and field measurements. The bed load rate is given by

$$\vec{q}_{sb} = 11\left\langle \left(\left|\vec{\theta}'(t)\right| - \theta_{\mathrm{cr}}\right)^{1.65} \frac{\vec{\theta}'(t)}{\left|\vec{\theta}'(t)\right|} \right\rangle \tag{4.39}$$

where

$$\vec{\theta}'(t) = \frac{\vec{\tau}_b'(t)}{\mathrm{g}\left(\rho_{\mathrm{s}} - \rho\right)d_{50}} = \frac{\frac{1}{2}\rho f_{\mathrm{cw}}'|\vec{u}_b(t)|\vec{u}_b(t)}{\mathrm{g}\left(\rho_{\mathrm{s}} - \rho\right)d_{50}} \tag{4.40}$$

with f_{cw}' the wave-current skin friction factor, computed following Madsen and Grant (1976), and $\vec{u}_b(t)$ is the instantaneous near-bottom total (wave + current) velocity. The critical Shields parameter is given from Eq. (4.7).

Ribberink's (1998) formula was not validated in the regime of fully developed vortex ripples. In this case significant time-dependent suspended transport occurs, which cannot be modelled in a quasi-steady way. Even the validity of the bed load formula has not been examined under such conditions.

4.8 Model description

The morphological changes vary at a much slower rate as compared to the short-term variations of hydrodynamics. One key issue for practical engineering applications is to bridge the gap between these two different time scales and consequently allow longer simulation periods. Lesser *et al*. (2004) and Roelvink (2006) introduced the powerful concept of the morphological acceleration factor (Morfac), f_{MOR}, which enables researchers to simulate the morphological evolution in coastal areas at longer time scales.

This efficient concept was adopted in the present model. The main idea behind this approach is that the speed of the changes in the morphology is scaled up to a rate that has not a significant impact on the waves and other hydrodynamic processes. The implementation of the Morfac is achieved by simply multiplying the bed level changes by a non-unity factor (Morfac) after each time step, Δt, of the wave model. Thus, the computation of the sediment transport and morphological changes is performed simultaneously with the hydrodynamics.

In particular, the morphology is updated over the morphological time step, Δt_{mor}, and for each update simulations by four modules are performed: a wave module, a hydrodynamic

module, a sediment transport module, and a bathymetry updating module. This process is repeated as many times is required to reach a preset final time period. The relevant flow chart is depicted in Fig. 4.7.

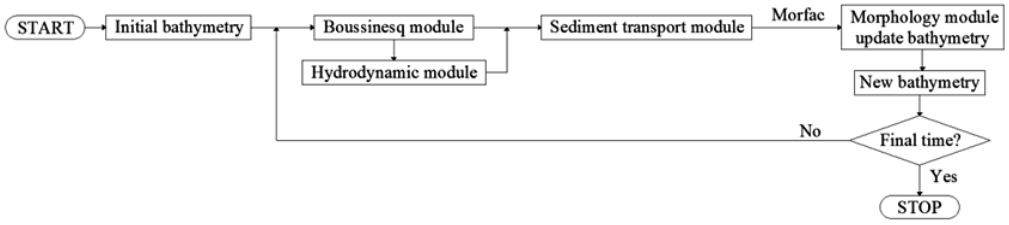

Fig. 4.7. Flow chart of wave-current, sediment transport and morphology models.

The wave module is the Boussinesq-type model that was presented in detail in chapter 3. It is a phase-resolving model that can simulate the wave propagation from deep to shallow water, including surf and swash zones. The Boussinesq-type model due to its nonlinear character offers an inherent estimation of the wave-induced depth-averaged current field, as also presented in chapter 3. However, the associated hydrodynamic module cannot predict the near bed steady streaming generated by the phase shift in orbital motions caused by bottom boundary layer mechanisms, such as the viscosity effects. This drift motion is more frequently shoreward in the offshore regions. Nevertheless, inside the surf zone, where sediment transport is more intense, the above mechanism is suppressed by both the turbulence and the undertow acting in the middle layer. Thus, the wave drift should be directed offshore. These latter two mechanisms have been incorporated in the hydrodynamic module by calculating the near bottom undertow velocity. The hydrodynamic module was described in detail in subsection 3.2.5.

The sediment transport rates are calculated as the sum of the bed and suspended loads for non-cohesive sediment in the offshore region and inside the surf zone. On the other hand, inside the swash zone, Larson and Wamsley's (2007) formula is applied, relying on the ballistic theory. The instantaneous intra-wave sediment transport rates are time-averaged to obtain the final transport rates.

Finally, the bathymetry is updated by solving the equation for conservation of sediment based on the time-averaged sediment transport rates. However, the morphological time step is different from the time step Δt of the Boussinesq wave model due to the application of the morphological acceleration factor technique. Thus:

$$\Delta t_{\text{mor}} = f_{\text{MOR}} \cdot \Delta t \tag{4.41}$$

while the spatial step, Δx, is common for all models.

4.8.1 Sediment transport module

The output from the wave and hydrodynamic modules is used as input in the sediment transport module for the computation of the time-averaged sediment transport loads. Offshore and inside the surf zone, the sediment movement is usually divided into bed load and suspended load. The increasing magnitude of the wave orbital velocity starts mobilizing the bed sediment and then a part of it is suspended in the vicinity of the bed ripples. Then, typically, as waves approach the breaker line the sheet-flow movement is favored. Inside the surf zone, the strong stirring up due to the wave breaking causes intense suspension of the sediment which is mainly transported by the wave-induced currents. In the swash zone, sediment moves mainly as sheet flow during the up-rush and down-rush. These mechanisms have been included in the sediment transport module, similarly to the work by Nam *et al*. (2009, 2010) which, however, is based on a spectral phase-averaged wave model.

Offshore and surf zone

(i) Bed load

For the computation of the bed load per unit width, $\vec{q}_{sb}$, the semi-empirical formulation by Camenen and Larson (2005, 2006, 2007) was applied. This sophisticated formula is based on Meyer-Peter and Müller's (1948) bed-shear stress concept and is valid under the combined action of asymmetric waves and currents. Effectively:

$$\frac{q_{sb,w}}{\sqrt{(s-1)\mathrm{g}{d_{50}}^3}} = \alpha_\mathrm{w} \frac{\theta_\mathrm{cw,net}}{\sqrt{|\theta_\mathrm{cw,net}|}} \theta_\mathrm{cw,m} \exp\left(-\mathrm{b}\frac{\theta_\mathrm{cr}}{\theta_\mathrm{cw}}\right) \tag{4.42a}$$

$$\frac{q_{sb,n}}{\sqrt{(s-1)\mathrm{g}{d_{50}}^3}} = \alpha_\mathrm{n} \frac{\theta_\mathrm{cn}}{\sqrt{|\theta_\mathrm{cn}|}} \theta_\mathrm{cw,m} \exp\left(-\mathrm{b}\frac{\theta_\mathrm{cr}}{\theta_\mathrm{cw}}\right) \tag{4.42b}$$

where the subscripts w and n correspond, respectively, to the wave direction and the direction normal to the waves, α_w, α_n and b are empirical coefficients to be given in the following. In the general case of combined waves and currents at an arbitrary angle, φ, between them (see Fig. 4.8) the instantaneous Shields parameter due to wave and current, respectively, are defined as:

$$\vec{\theta}_\mathrm{w}(\mathrm{t}) = \frac{\frac{1}{2}\mathrm{f_w}|\vec{\mathrm{U}}_\mathrm{w}(\mathrm{t})|\vec{\mathrm{U}}_\mathrm{w}(\mathrm{t})}{(\mathrm{s}-1)\mathrm{g}\mathrm{d}_{50}} \quad \text{and} \quad \vec{\theta}_\mathrm{c} = \frac{\frac{1}{2}\mathrm{f_c}|\vec{\mathrm{U}}_\mathrm{c}|\vec{\mathrm{U}}_\mathrm{c}}{(\mathrm{s}-1)\mathrm{g}\mathrm{d}_{50}} \tag{4.43}$$

with $\vec{U}_{\mathrm{w}}(t)$ and $\vec{U}_{\mathrm{c}}$ the near bed instantaneous oscillatory and current velocities, respectively, and f_{w} and f_{c} the bed friction coefficients due to waves and current, respectively. However, it should be reminded that the orbital velocity is assumed uniform over depth. In Eqs (4.42a,b) the mean absolute Shields parameter, $\theta_{\mathrm{cw,m}}$, and the maximum Shields parameter, θ_{cw}, due to wave-current interaction are obtained by vector addition:

$$\theta_{\mathrm{cw,m}} = \left(\left|\vec{\theta}_{\mathrm{c}}\right|^2 + \left|\vec{\theta}_{\mathrm{w,m}}\right|^2 + 2\left|\vec{\theta}_{\mathrm{w,m}}\right|\left|\vec{\theta}_{\mathrm{c}}\right|\cos\varphi\right)^{1/2} \tag{4.44}$$

$$\theta_{\mathrm{cw}} = \left(\left|\vec{\theta}_{\mathrm{c}}\right|^2 + \left|\vec{\theta}_{\mathrm{w}}\right|^2 + 2\left|\vec{\theta}_{\mathrm{w}}\right|\left|\vec{\theta}_{\mathrm{c}}\right|\cos\varphi\right)^{1/2} \tag{4.45}$$

with $\vec{\theta}_{\mathrm{w,m}}$ and $\vec{\theta}_{\mathrm{w}}$ the mean wave and maximum wave Shields numbers, respectively. The Shields parameter in the direction normal to the wave direction is only due to current and is defined by:

$$\theta_{\mathrm{cn}} = \frac{\frac{1}{2} f_{\mathrm{c}} \left|\vec{U}_{\mathrm{c}}\right|^2 |\sin\varphi| \sin\varphi}{(s-1)\mathrm{g}d_{50}} \tag{4.46}$$

The last exponential term in Eqs (4.42a,b) was introduced in order to account for the effect of the critical Shields parameter, θ_{cr}, which, similarly to experimental observations, allows low sediment transport even when the instantaneous Shields parameter is slightly lower than the critical value (Camenen and Larson, 2005). The critical Shields value corresponds to the critical velocity for the inception of sheet flow, $U_{\mathrm{w,crsf}}$. Thus, the exponential term also allows a possible error on the estimation of $U_{\mathrm{w,crsf}}$ given by:

$$U_{\mathrm{w,crsf}} = 8.35\sqrt{(s-1)\mathrm{g}\sqrt{d_{50}\delta_{\mathrm{w}}}}(1+r_{\mathrm{w}}) \tag{4.47}$$

where r_{w} is the wave symmetry coefficient, $r_{\mathrm{w}} = U_{\mathrm{w,max}}/U_{\mathrm{w}} - 1$, with $U_{\mathrm{w,max}}$ being the maximum value of the instantaneous near bed wave velocity, $U_{\mathrm{w}}(t)$, as shown in Fig. 4.8.

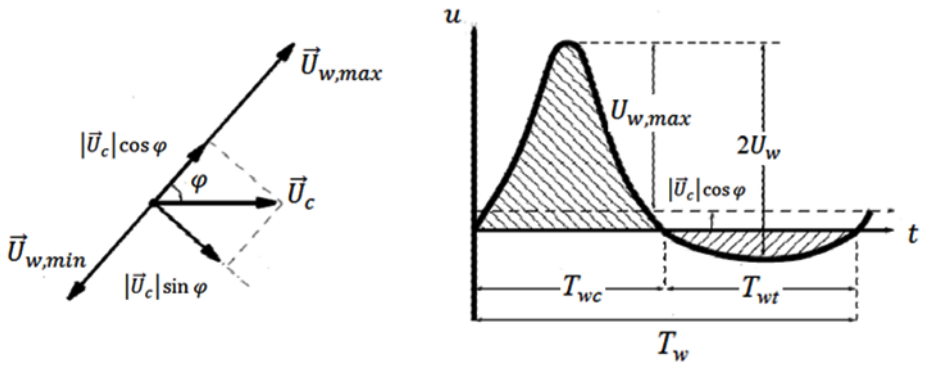

Fig. 4.8. Left: Wave and current interaction. Right: Typical velocity variation over wave period in the direction of wave propagation including current effect (from Camenen and Larson, 2007, modified).

The parameters α_w, α_n and b were set equal to $\alpha_w = 6 + 6|\vec{\theta}_c|/(|\vec{\theta}_c| + |\vec{\theta}_w|)$, $\alpha_n = 12$ and $b = 4.5$ (Camenen and Larson, 2007).

Similarly to the formula by Dibajnia and Watanabe (1992), and in order to take into account the unsteady effects of the sediment's movement a typical wave cycle is divided in two half periods, one with onshore movement, T_{wc}, and one with offshore movement, T_{wt} (see Fig. 4.8). These unsteady effects are caused by a time lag between velocity and sediment concentration, resulting in negative wave-related transport rates and thus smaller total net rates than without these effects. The mean Shields parameters during the onshore (> 0) and the offshore (< 0) half periods are defined as:

$$\theta_{\mathrm{cw,onshore}} = \frac{1}{T_{wc}} \int_0^{T_{wc}} \frac{\frac{1}{2} f_{\mathrm{cw}} \left(U_{\mathrm{w}}(t) + |\vec{U}_{\mathrm{c}}| \cos\varphi\right)^2}{(s-1)\mathrm{g}d_{50}} dt \tag{4.48}$$

$$\theta_{\mathrm{cw,offshore}} = \frac{1}{T_{wt}} \int_{T_{wc}}^{T_w} \frac{\frac{1}{2} f_{\mathrm{cw}} \left(U_{\mathrm{w}}(t) + |\vec{U}_{\mathrm{c}}| \cos\varphi\right)^2}{(s-1)\mathrm{g}d_{50}} dt \tag{4.49}$$

The phase-lag is introduced through the coefficient $\alpha_{pl,b} = \alpha_{on} - \alpha_{off}$, with:

$$\alpha_j = \frac{v^{0.25} U_{\mathrm{cw,j}}^{0.5}}{W_s T_{wj}^{0.75}} \exp\left[-\left(\frac{U_{\mathrm{w,crsf}}}{U_{\mathrm{cw,j}}}\right)^2\right] \tag{4.50}$$

where W_s is the settling velocity according to Camenen and Larson (2007) and the subscript j refers to either the onshore or offshore movement. $U_{\mathrm{cw,j}}$ is the root-mean-square value of the velocity over the half period T_{wj}. The characteristic values of the Shields parameter are modified due to the lag effects for both half periods. Thus, the net Shields parameter involved in Eq. (4.42a) is expressed as:

$$\theta_{\mathrm{cw,net}} = (1 - \alpha_{\mathrm{pl,b}})\theta_{\mathrm{cw,onshore}} + (1 + \alpha_{\mathrm{pl,b}})\theta_{\mathrm{cw,offshore}} \tag{4.51}$$

The presented formula for the bed load is one of the few formulae that take into account the aforementioned unsteady effects. A comparison with several existing popular formulations against a large set of available experimental data showed the overall best performance of the above relation (Camenen and Larson, 2005; 2006) and thus it was selected herein.

(ii) Suspended load

If the bed shear stress is sufficiently large, the particles can be lifted, put in suspension, and transported mainly by the current. In the marine environment, the process of sediment transport is complex due to the interaction between steady and oscillatory flows. In the general case, the wave-related part of the suspended load includes unsteady effects both due to the wave asymmetry and a possible phase-lag between the pulses of the instantaneous velocity and concentration. Due to this non-coincident reaction of the sediment to the velocity field, the sediment transport module solves the advection-diffusion equation (AD-equation) for the depth-averaged sediment concentration, C_{ave}:

$$\frac{\partial(C_{ave}h)}{\partial t}+\frac{\partial(C_{ave}hU)}{\partial x}+\frac{\partial(C_{ave}hV)}{\partial y}=\frac{\partial}{\partial x}\left(K_x h\frac{\partial C_{ave}}{\partial x}\right)+\frac{\partial}{\partial y}\left(K_y h\frac{\partial C_{ave}}{\partial y}\right)+P_r-D_r \quad (4.52)$$

where $h=d+\zeta$ is the total instantaneous depth, $K_x=K_y=5.93u_{*,c}h$ are the diffusion coefficients with $u_{*,c}$ the friction velocity due to current only, P_r and D_r are the sediment pick-up and deposition rates, respectively, equal to:

$$P_r=c_R W_s \quad \text{and} \quad D_r=\frac{C_{ave}}{\beta_d}W_s \quad (4.53)$$

where c_R is the near-bottom sediment reference concentration and β_d is a coefficient calculated from (Camenen and Larson, 2008):

$$\beta_d=\frac{\varepsilon}{W_s h}\left[1-\exp\left(-\frac{W_s h}{\varepsilon}\right)\right] \quad (4.54)$$

where ε is the sediment diffusivity given by:

$$\varepsilon=\left(\frac{k_b^3 D+k_c^3 D_c+k_w^3 D_w}{\rho}\right)^{1/3}h \quad (4.55)$$

where D is the energy dissipation per unit area due to wave breaking, D_c and D_w are the energy dissipation per unit area from the bed friction due to current and wave, respectively, and k_b, k_c and k_w are coefficients. Typically, $D>D_w>D_c$, and, in many cases, only the largest dissipation needs to be considered. The parameter k_b was considered constant and equal to 0.01, although its value depends on the breaker type. The other two parameters were estimated according to Camenen and Larson (2007):

$$k_w=\frac{\kappa}{3\pi}\begin{cases}0.15+1.5\sin^2\left(\frac{\pi}{2}\frac{W_s}{u_{*,w}}\right) & \text{if} \quad \frac{W_s}{u_{*,w}}\le 1\\ 1.0+0.65\sin^2\left(\frac{\pi}{2}\frac{u_{*,w}}{W_s}\right) & \text{if} \quad \frac{W_s}{u_{*,w}}>1\end{cases} \quad (4.56)$$

$$k_{\mathrm{c}} = \frac{\kappa}{6}\begin{cases} 0.4 + 3.5\sin^2\left(\frac{\pi}{2}\frac{W_s}{u_{*,\mathrm{c}}}\right) & \text{if} \quad \frac{W_s}{u_{*,\mathrm{c}}} \leq 1 \\ 1.0 + 2.9\sin^2\left(\frac{\pi}{2}\frac{u_{*,\mathrm{c}}}{W_s}\right) & \text{if} \quad \frac{W_s}{u_{*,\mathrm{c}}} > 1 \end{cases} \tag{4.57}$$

where $u_{*,\mathrm{w}}$ is the friction velocity due to waves only and κ (= 0.40) is, as above, the von Karman constant.

The near-bottom reference concentration is a very important parameter for the correct estimation of the suspended load, as discussed in subsection 4.6. Herein Camenen and Larson's (2007) formula was adopted:

$$c_R = A_{\mathrm{cr}}\theta_{\mathrm{cw,m}}\exp\left(-\mathrm{b}\frac{\theta_{\mathrm{cr}}}{\theta_{\mathrm{cw}}}\right) \tag{4.58}$$

Based on the analysis of a large data set Camenen and Larson (2007) proposed the default value:

$$A_{\mathrm{cr}} = 3.5{\cdot}10^{-3}\exp(-0.3d_*) \tag{4.59}$$

However, analysis of the available data that yield the numerical factors of Eq. (4.59) gives a significant variability of A_{cr}.

The sediment transport rate is often large near the shoreline because of swash uprush and backwash processes. On the other hand, most of the available formulae tend to yield sediment transport that decreases too rapidly from the swash zone towards the offshore and thus the interaction between the swash zone and the inner surf zone is not accurately described. In order to deal with this difficulty the modification by Nam *et al*. (2009) was adopted. In particular, the sediment transport at the still-water shoreline obtained from the swash computations and described in the following was used as a boundary condition for Eq. (4.52). In addition, the pick-up and deposition rates were modified as following:

$$\tilde{P}_r = P_r\left[1 + \tilde{\theta}\frac{V_{\mathrm{long}}}{v_o}\exp\left(-\tilde{\mu}\frac{h}{R}\right)\right] \tag{4.60}$$

$$\tilde{D}_r = \frac{D_r}{1 + \tilde{\theta}\frac{V_{\mathrm{long}}}{v_o}\exp\left(-\tilde{\mu}\frac{h}{R}\right)} \tag{4.61}$$

where V_{long} is the average longshore current across the surf zone, R is the run-up height as computed by the model, v_o is a scaling velocity which is obtained from swash zone computations and is described in the following, and $\tilde{\theta}$ and $\tilde{\mu}$ are non-negative coefficients with values 9.3 and 2.4, respectively (Nam *et al*., 2009).

From the solution of Eq. (4.52) and after time-averaging, the net suspended load per unit width can be computed:

$$\vec{q}_{ss} = \left(\overline{\mathrm{C_{ave}} h - K_x h \frac{\partial \mathrm{C_{ave}}}{\partial x}} \, , \overline{\mathrm{C_{ave}} h - K_y h \frac{\partial \mathrm{C_{ave}}}{\partial y}} \right) \tag{4.62}$$

Besides the AD-equation, the sediment transport module offers a simple alternative for the estimation of the suspended load following Camenen and Larson (2008). Assuming a steady state, an exponential profile of the sediment concentration over depth is obtained and thus the suspended load under the combined action of waves and current is computed as:

$$q_{ss,w} = \left(U_{\mathrm{cw,onshore}} - U_{\mathrm{cw,offshore}} \right) c_R \frac{\varepsilon}{W_s} \left[1 - \exp\left(- \frac{W_s h}{\varepsilon} \right) \right] \tag{4.63a}$$

$$q_{ss,n} = \left| \vec{U}_c \right| \sin\varphi \; c_R \frac{\varepsilon}{W_s} \left[1 - \exp\left(- \frac{W_s h}{\varepsilon} \right) \right] \tag{4.63b}$$

Equations (4.63a,b) give the suspended load above the bed reference level and assume no significant vertical variation of the velocity above this level. For the applications studied herein both formulations for the suspended load led to quite similar results, as also shown in the sensitivity analysis section.

Swash zone

The mechanisms of sediment transport in the swash zone have received in the past less attention than those in the surf zone. This can be attributed partly to the very complex processes taking place in the swash zone and partly to the difficulties in performing reliable field and laboratory measurements. However, due to the high engineering interest, significant progress has been made during the last years concerning the hydrodynamics and sediment transport in the swash zone (Butt and Russell, 2000; Elfrink and Baldock, 2002; Larson *et al*., 2004).

A number of formulae and techniques have been proposed for calculating the sediment transport rates in the swash zone (Larson, 1996; Leont'yev , 1996; Larson *et al*., 2001). Most of them mainly deal with aspects of cross-shore transport. Only little attention has been paid to the longshore direction although longshore sediment transport in the swash zone may account for up to the half of the total longshore transport (Kamphuis, 1991). Herein the formulae by Larson and Wamsley (2007) have been adopted for the computation of the net transport rates in the cross-shore and longshore directions. Effectively:

$$q_{bc,\text{net}} = K_c \frac{\tan\varphi_m}{\tan^2\varphi_m - \left(\frac{dd}{dx}\right)^2} \frac{u_o^3}{\text{g}} \left(\frac{dd}{dx} - \tan\beta_e\right) \frac{t_o}{T} \tag{4.64}$$

$$q_{bl,\text{net}} = K_l \frac{\tan\varphi_m}{\tan^2\varphi_m - \left(\frac{dd}{dx}\right)^2} \frac{u_o^2 v_0}{\text{g}} \frac{t_o}{T} \tag{4.65}$$

where φ_m is the internal friction angle ($\approx 30^o$), u_0, v_0 and t_o are scaling velocities and time, respectively, T is the swash duration (assumed equal to the incidence wave period), d is the still water depth, $\tan\beta_e$ is the foreshore equilibrium slope, and K_c and K_l are empirical coefficients. Based on field measurements, Larson *et al*. (2004) proposed $K_c = 0.001$ and Larson and Wamsley (2009) assumed that $K_l \approx K_c$. Nam *et al*. (2009) used the value 0.0008 for both coefficients in their model. However, in the present thesis a significant variability of the values of these two coefficients was observed through calibration with laboratory measurements. Further investigation on this issue is required since the computed sediment transport loads in the swash zone are sensitive to the value of these parameters. The required swash zone hydrodynamics were derived based on the ballistic theory. For more details concerning the derivation see Larson and Wamsley (2007) and Larson *et al*. (2004).

The transformation of the waves as they travel up and down the foreshore is quite complex. However, it has been shown that the speed of the wave front as it propagates up the foreshore may be reasonably well described using simple theory in which the front is regarded as a slug of water moving under the action of gravity and friction. By applying this analogy with the ballistic theory, the scaling time is given by:

$$\frac{t_o}{T} = \sqrt{1 - \frac{z_o}{R}} \tag{4.66}$$

where z_o is the vertical distance from the reference level.

Assuming that the wave front has a speed of u_s at the start of the uprush and that it is oriented at an angle α_s with respect to the y-axis which is assumed to be parallel to the shoreline, the scaling velocities are given by

$$u_o = u_s \cos\alpha_s \sqrt{1 - \frac{z_o}{R}} \quad and \quad v_o = u_s \sin\alpha_s \tag{4.67}$$

The local equilibrium slope is given by (Larson *et al*., 1999):

$$\tan\beta_e = \frac{I_U - I_B}{I_U + I_B}\tan\varphi_m \tag{4.68}$$

where

$$I_U = \frac{1}{T}\int_{t_s}^{t_m}\left[\frac{|\vec{\tau}_b(t)|}{(s-1)\rho g d_{50}}\right]^{3/2} dt \tag{4.69a}$$

$$I_B = \frac{1}{T}\int_{t_m}^{t_e}\left[\frac{|\vec{\tau}_b(t)|}{(s-1)\rho g d_{50}}\right]^{3/2} dt \tag{4.69b}$$

with $\vec{\tau}_b(t)$ the bed shear stress, t_s and t_e the start and end time of the swash, respectively, and t_m the time when uprush changes to backwash.

Overall, the total net sediment transport load per unit width, $\vec{q}_{tot} = \left(q_{x,tot}, q_{y,tot}\right)$, equals the sum of the bed load and suspended load, $\vec{q}_{sb} + \vec{q}_{ss}$, in the surf zone and offshore, while it is reduced to the swash zone net transport load, $\vec{q}_{sz}$, further onshore. The components of $\vec{q}_{sz}$ along the cross-shore and longshore directions are given by Eqs (4.64) and (4.65), respectively.

4.8.2 Morphology module

The morphology module yields the bathymetry update by solving the sediment mass conservation equation:

$$\frac{\partial d}{\partial t} = \frac{1}{1-n_p}\nabla\cdot\vec{q}'_{tot} \tag{4.70}$$

where n_p is the sediment porosity (≈ 0.4). Following Watanabe (1988) and Johnson and Zyserman (2002), the effect of the bed slope has been included resulting in the effective total loads:

$$q'_{x,tot} = q_{x,tot} + \varepsilon_{xx}\left|q_{x,tot}\right|\frac{\partial d}{\partial x} + \varepsilon_{xy}\left|q_{x,tot}\right|\frac{\partial d}{\partial y} \tag{4.71a}$$

$$q'_{y,tot} = q_{y,tot} + \varepsilon_{yx}\left|q_{y,tot}\right|\frac{\partial d}{\partial x} + \varepsilon_{yy}\left|q_{y,tot}\right|\frac{\partial d}{\partial y} \tag{4.71b}$$

where ε_{xx}, $\varepsilon_{xy} = \varepsilon_{yx}$, and ε_{yy} are empirical coefficients, introducing diffusion and cross-terms to the bed level evolution equation. They help to dampen the spurious short waves

generated from the numerical solution of Eq. (4.70). These diffusivity parameters have not been studied in depth and typically they can be used as tuning parameters (Watanabe, 1988). However, too high values may lead to unrealistic over-damping of the bed features, while too low values may lead to numerical instabilities. In the applications presented herein, a typical range 2-5 was considered for ε_{xx} and ε_{yy}, while ε_{xy} was set around unity.

For the numerical solution of Eq. (4.70) the model offers two options. The first one is the second order Warming-Beam upwind scheme (Long and Kirby, 2006). The second one is a modified second order Lax-Wendroff scheme (Deigaard *et al*., 1988; Rakha *et al*., 1997). Both schemes are conditionally stable but require the estimation of the celerity of bed disturbances, $\frac{1}{1-n_p}\frac{\partial \vec{q}'_{tot}}{\partial d}$, that its expression cannot be soundly treated numerically.

An important aspect in the morphological model is the smoothing of the calculated transport. As described by Fredsøe and Deigaard (1992), in the case of regular waves the calculated sediment transport may have a discontinuity at the point of wave-breaking. This is unrealistic, as the undertow profile needs some distance before it becomes fully developed. In order to solve this inconsistency, the calculated sediment transport load is slightly smoothed using a three-point running average filter before it is inserted in Eq. (4.70). When studying the evolution of coastal profiles, this smoothing causes the maximum of the offshore-directed transport to be shifted shoreward of the breaking point and thus influences the formation of a trough inshore of the resulting bar. Moreover, the offshore-directed transport starts slightly offshore of the breaking point which smooths out the front face of the formed bar. Brøker Hedegaard *et al*. (1991) studied the effect of different filters on the resulting coastal profiles.

As described above, the morphological acceleration factor technique was applied in order to have longer simulations and thus practical applications of the model. The simulations are time consuming compared to typical Boussinesq wave model applications with no morphology update. However, by an appropriate choice of f_{MOR} reliable short-term morphological simulations (of the order of several hours) can be performed with no prohibitive computational effort. Nevertheless, care must be taken not to exaggerate with the value of the morphological factor in order to be able to describe realistically the interaction of the wave, hydrodynamic and morphology modules. In addition, large morphological time steps, Δt_{mor}, may lead to instabilities in the solution of Eq. (4.70). In the present thesis f_{MOR} was varied in the range 1-20 with no significant impact on the wave model's results.

4.9 Model validation

In order to check the compound model's ability to simulate nearshore dynamics, sediment transport and morphology evolution, both its 1DH and 2DH versions were validated through a

number of experimental tests. Both regular and irregular wave propagation over initially plane beaches, complex bathymetries and a detached breakwater were studied. The results were compared to laboratory measurements involving hydrodynamic parameters, sediment transport loads and short-term bathymetry changes.

4.9.1 1DH validation

In all the 1DH laboratory experiments presented here the net time-averaged sediment transport rate distributions, $Q_{meas}(x)$, were calculated from successive beach profile measurements using the sediment conservation law and a known boundary condition ($Q_{meas}(x) = 0$) at the landward or seaward end of the profile. Thus:

$$Q_{meas}(x_i) = Q_{meas}\left(x_{i\text{-}1}\right) - \int_{x_{i\text{-}1}}^{x_i} \mathrm{M}\frac{\Delta z_b}{\Delta t'}\,dx \tag{4.72}$$

where $Q_{meas}(x_i)$ is the integral volume of sediment transport at position i, Δz_b is the difference in bed elevation between measurement intervals, $\Delta t'$ is the time difference between measurement intervals and M is the solid fraction of the gross sediment volume, approximately 0.6 for the laboratory sand as described in Baldock *et al*. (2011).

CRIEPI Test - Initially plane beach

The first set of comparisons refers to the data by Kajima *et al*. (1982) and Shimizu *et al*. (1985). Their experiments were conducted in CRIEPI's Large Wave Flume in Japan. The flume was 205 m long, 3.4 m wide and 6 m deep and cross-shore hydrodynamics, sediment transport and beach change processes were investigated. The case studied here is Test 3-2 including sand of median diameter d_{50}= 0.27 mm. The initial bathymetry consisted of a horizontal bottom of 4.5 m depth followed by a uniform slope of 1:20. Regular waves were generated at the uniform depth section with period T = 6.0 s and wave height H_o = 1.00 m. The overall duration of the experiment was 98.1 hrs.

A spatial grid spacing of Δx = 0.3 m and a time step of Δt = 0.02 s were used in the Boussinesq model, while a morphological factor f_{MOR} = 20 was employed leading to a morphological step of Δt_{mor} = 0.4 s. A comparison between the measured and the computed by the model wave height, total sediment transport load and beach profile is depicted in Figs 4.9, 4.10 and 4.11, respectively. The sediment loads were measured and computed, respectively, after two hours of wave incidence while the morphology profiles after 7 hours. The sloping beach starts at x = 40 m.

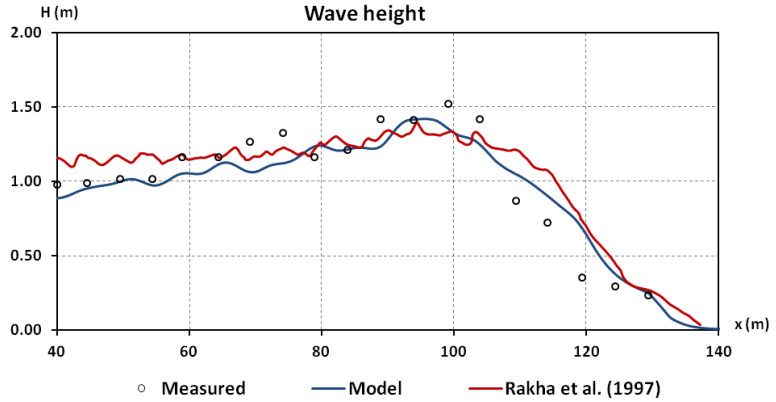

Fig. 4.9. Computed and measured wave height for test case 3-2 (CRIEPI).

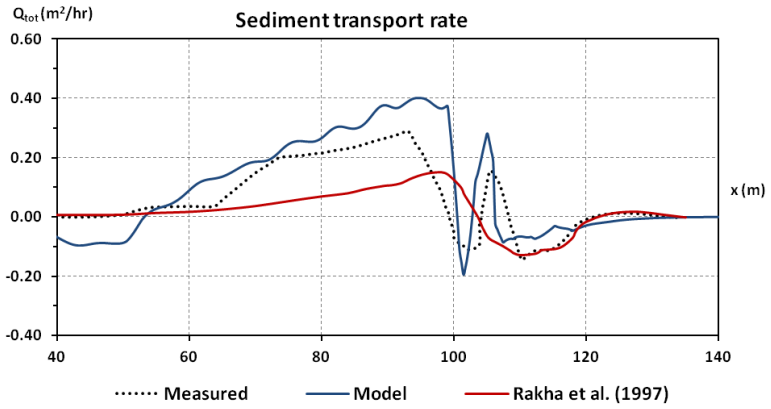

Fig. 4.10. Computed and measured total sediment transport rate after 2 hrs of wave incidence for test case 3-2 (CRIEPI).

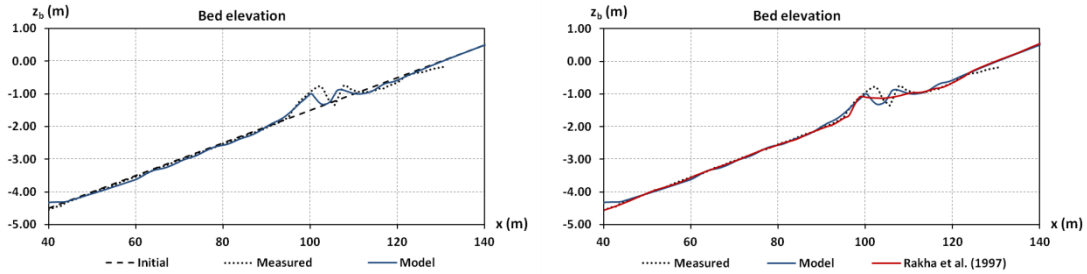

Fig. 4.11. Computed and measured beach profile after 7 hrs of wave incidence for test case 3-2 (CRIEPI).

The specific test case refers to erosive conditions close to the shoreline. This was also expected since Dean's (1973) expression gives $F_o = H_o/(W_s T)$ ~ 4.3. Dean (1973) claimed that $F_o > 1$ corresponds to erosive conditions, while $F_o < 1$ to accretive. However, in recent literature higher values are proposed based on field measurements, e.g. Hanson and Kraus (2011) proposed $F_o > 4.0$ for erosion and $F_o < 2.40$ for accretion.

Good results were obtained for the main bar formation. However, an under-prediction of the down-wave part of the bar is observed. This can be attributed to the computed secondary peak

of the sediment load at the outer surf zone which is more abrupt than the measured one. Nevertheless, the inner secondary bar is fairly accurately predicted, as well as the slight erosion further onshore. Two consecutive breaking events take place just after x = 100 m leading to the formation of the inner bar. This double incidence of breaking results to a steep offshore-directed suspended load distribution and, consequently, to the sharp dip in the modelled total load rate just after x = 100 m. The diffusivity parameter ε_{xx} was set equal to 5 and no significant sensitivity to this value was observed for the specific test case.

The above figures also include a comparison with the results from the model by Rakha *et al*. (1997). The present model computes more accurately the wave height due to its higher order of nonlinearity. In addition, it reproduces adequately the secondary peak of the sediment load distribution, proving the capability of the applied sediment transport formulae to satisfactorily capture the effect of the wave asymmetry. Finally, both models describe reasonably well the formation of the main bar but this is valid only for the present model when the secondary inner bar is concerned.

Irregular bathymetry – Erosive conditions

The second test refers to the experiments performed in the CIEM large wave flume at UPC in Barcelona as part of the SUSCO experiment (Baldock *et al*., 2011). The flume was 100 m long, 3 m wide and 5 m high. The experimental layout consisted of a horizontal bottom of 2.5 m depth followed by an irregular beach profile of an overall mean gradient of approximately 1:15. The beach was covered by a medium sand of d_{50}= 0.25 mm.

A set of fourteen different tests was conducted involving regular, bichromatic and irregular waves. The beach evolution along the centre-line of the wave flume was measured with a semi-automatic mechanical bed profiler with an overall vertical profile accuracy of ±10 mm. Between each test manual reshaping of the beach was performed in order to return to the initial profile. For the erosive tests, this reshaping was performed over the part of the profile between the seaward flank of the breaker bar and the run-up limit.

The case studied here is test M_E referring to the generation and propagation of monochromatic waves with period T = 3.7 s and wave height H_o = 0.41 m over the horizontal bottom. This is an erosive test case and the profile measurements were made after 2 hrs of wave generation.

The model was also run to simulate the test. A spatial grid spacing of Δx = 0.1 m and a time step of Δt = 0.01 s were used in the Boussinesq model, while a morphological factor f_{MOR} = 2 was employed leading to a morphological step of Δt_{mor} = 0.02 s. Figs 4.12, 4.13 and 4.14 show a comparison between the measured and the computed by the model wave height, total

sediment transport load and beach profile after two hours of wave action. It is mentioned that the toe of the sloping bed is at x = 42.5 m.

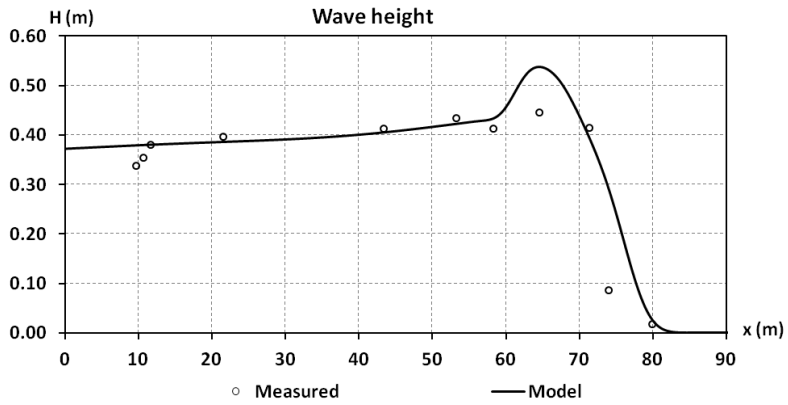

Fig. 4.12. Computed and measured wave height for test case M_E in Baldock *et al*. (2011).

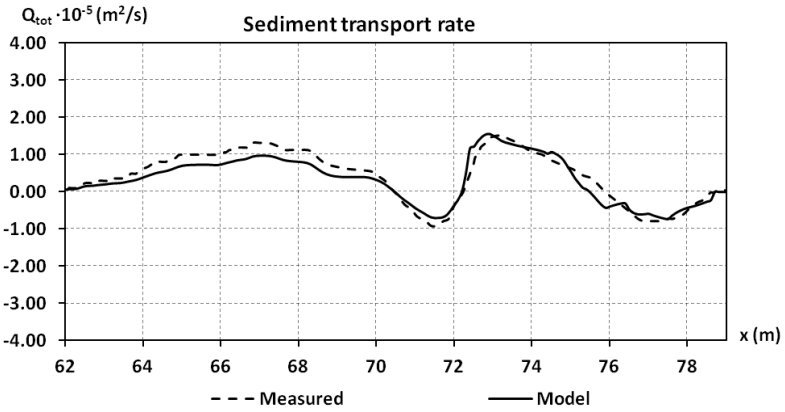

Fig. 4.13. Computed and measured total sediment transport rate after 2 hrs of wave generation for test case M_E in Baldock *et al*. (2011).

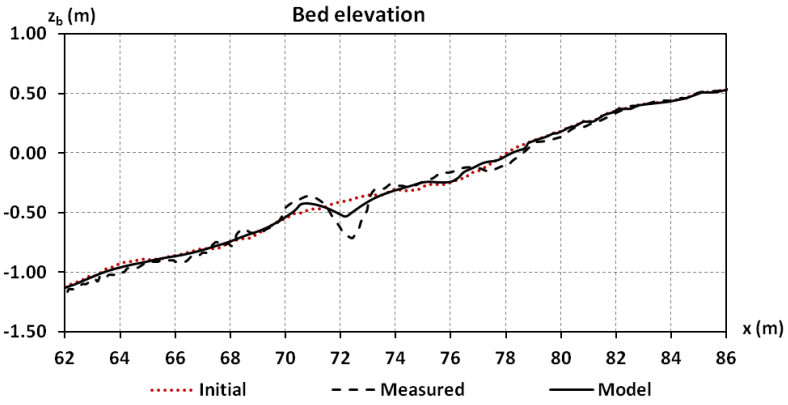

Fig. 4.14. Computed and measured beach profile after 2 hrs of wave generation for test case M_E in Baldock *et al*. (2011).

In overall, the agreement seems reasonable despite an overestimation of the wave height near the breaking point. The initiation of the sediment's movement is quite accurately predicted as well as the overall magnitude of the sediment transport load. In general, the results are acceptable since the main morphological features are described by the model. The position and height of the bar is acceptably predicted, as well as the erosion in the inner surf zone and close to the shoreline.

Irregular bathymetry - Accretive conditions

Another test case of the SUSCO experiment was also simulated by the present model. This is test M_A which refers to accretive conditions. In this case regular waves with period T =4.9 s and wave height H_o = 0.15 m over the horizontal bed of 2.5 m depth were generated. The beach profile was measured after two hours of wave generation similarly to the erosive test.

The spatial step for the model simulation was set Δx = 0.2 m so that the long waves were adequately resolved inside the surf zone, with about 50 points per wavelength near the breaking point. The time step was chosen Δt = 0.02 s and f_{MOR} = 2 yielding a morphological step of Δt_{mor} = 0.04 s. A comparison between the measured and the computed by the model wave height, total sediment transport load and beach profile after two hours of wave action is shown in Figs 4.15, 4.16 and 4.17, respectively.

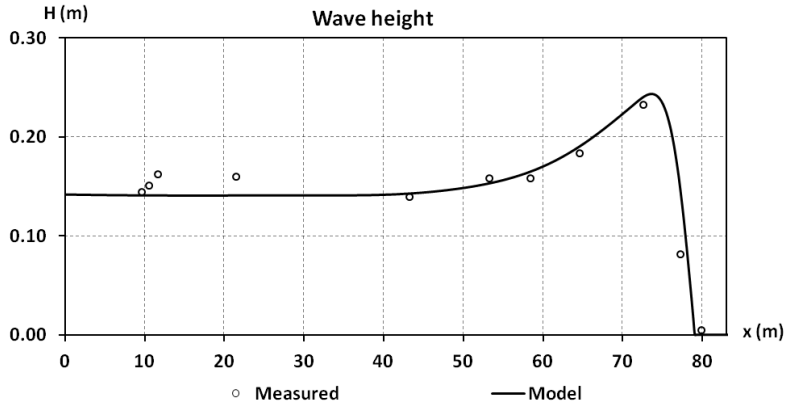

Fig. 4.15. Computed and measured wave height for test case M_A in Baldock *et al*. (2011).

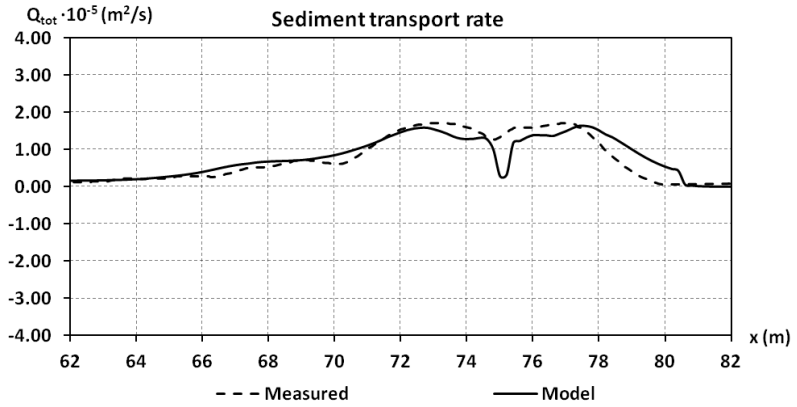

Fig. 4.16. Computed and measured total sediment transport rate after 2 hrs of wave generation for test case M_A in Baldock *et al*. (2011).

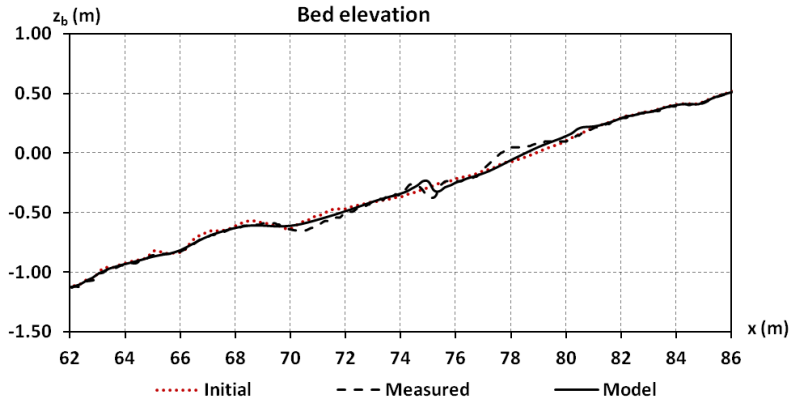

Fig. 4.17. Computed and measured beach profile after 2 hrs of wave generation for test case M_A in Baldock *et al*. (2011).

The agreement for the wave height is very good. Also, the computation of the total sediment transport load is fairly accurate. The inception of the sediment's movement is well captured as well as the shape of the curve of the transport rate with only onshore movement being predicted in accordance with the measured load. However, a deeper tongue is predicted than measured for the transport rate around x = 75 m and this leads to the formation of a slightly more pronounced bar there than actually measured. Moreover, the model computes a milder reduction of the sediment load in the inner surf and swash zones. Thus, although accretion is predicted by the model near the shoreline, it is under-estimated compared to the well-defined swash berm which was observed in the laboratory experiment. Nevertheless, it should be noted that accretive conditions are known to be more demanding tests for numerical models than the erosive ones.

Large Wave Flume experiment

A number of experiments were performed at the Grosser Wellenkanal in Hannover under the EU SAFE project. The flume was 324 m long, 5 m wide and 7 m deep. The purpose of the tests was to study aspects of beach nourishment and offer a benchmark data set for numerical models' validation. Among the tests described in Dette *et al*. (2002), case B2 is reproduced herein. The initial bathymetry consisted of a horizontal bed of 5 m depth followed by the theoretical Bruun equilibrium profile below the water level. Above the water level the beach had a uniform slope of 1:10. The used sand had a median diameter of d_{50}= 0.30 mm. Random waves of a TMA spectrum were generated over the constant depth with peak period T_p = 5.5 s and significant wave height H_{m_o}= 1.20 m. The duration of the test was about 23 hrs and a morphological factor equal to 20 was used in the model simulation.

In Figs 4.18, 4.19 and 4.20 the measured and computed wave height, sediment transport rate and bed elevation are depicted, respectively. The bar formation and the swash zone erosion are reasonably well predicted, although the latter is under-estimated.

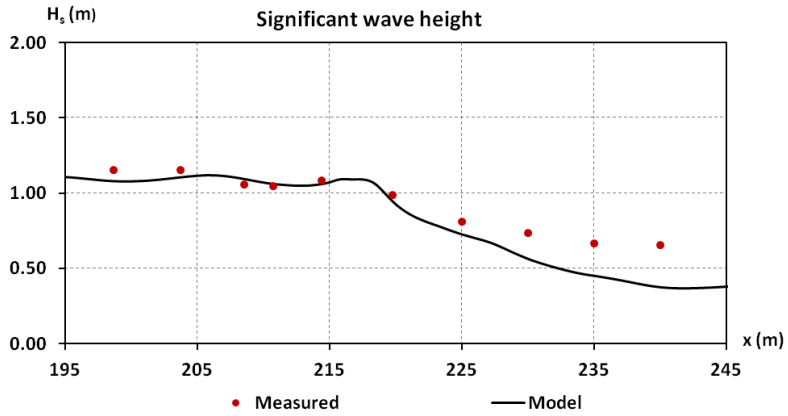

Fig. 4.18. Computed and measured significant wave height for test case B2 in Dette *et al*. (2002).

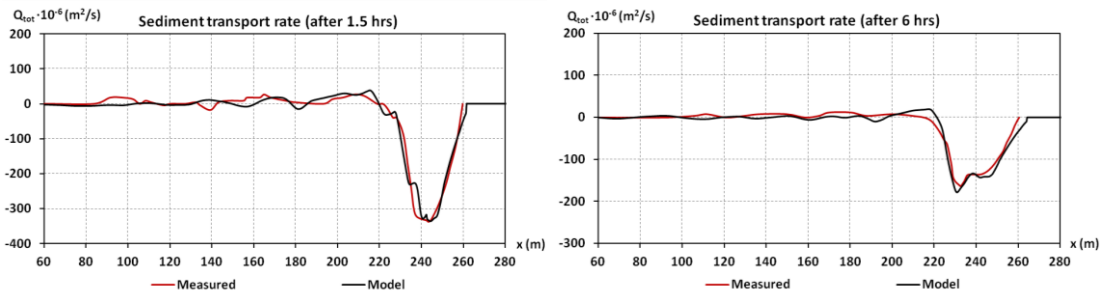

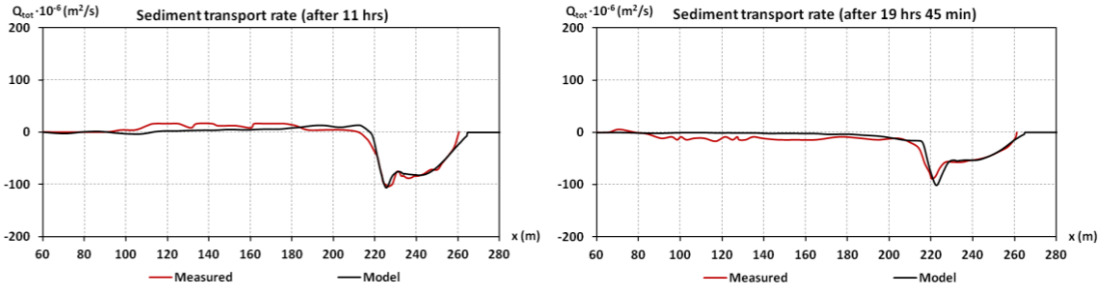

Fig. 4.19. Computed and measured total sediment transport rate at various times for test case B2 in Dette *et al*. (2002).

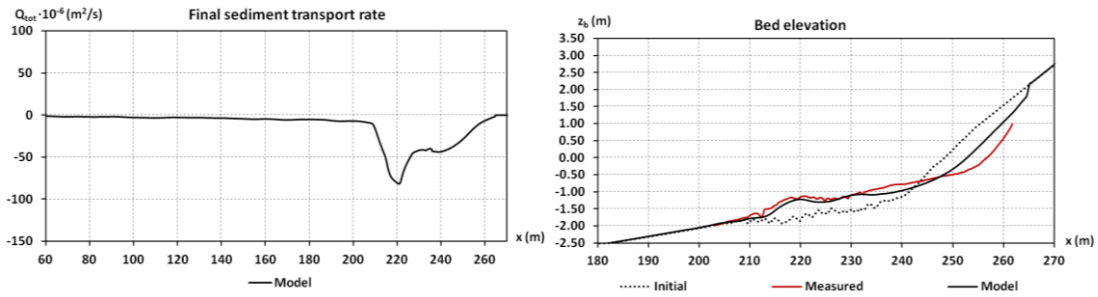

Fig. 4.20. At left: computed final sediment transport rate. At right: computed and measured initial and final beach profiles for test case B2 in Dette *et al*. (2002).

LIP 11D Delta Flume Experiment

The Delta Flume '93 tests were performed at the Delft Hydraulics large-scale wave flume under the EU "Large Installations Plan" in order to provide high-quality data for validating numerical models. The experiments involved hydrodynamics and sediment transport on a beach. The case studied here is Test 1c (Arcilla *et al*., 1994; Roelvink and Reniers, 1995). The initial bathymetry consisted of a horizontal bottom of 4.1 m depth, where waves were generated, followed by an irregular beach profile which was the result of an initially Dean-type beach exposed to preceding erosive wave conditions. Test 1c represented strongly accretive wave conditions including the generation of narrow-banded, random waves with T_p = 8 s and H_{m_o} = 0.60 m. The mean grain size was d_{50} = 0.20 mm and the overall test duration 13 hrs.

The test was reproduced by the model with Δx = 0.5 m and Δt = 0.02 s. A morphological factor f_{MOR} = 20 and thus a morphological step Δt_{mor} = 0.4 s were employed. Figs 4.21 and 4.22 show a comparison between the measured and the computed significant wave height and near bottom undertow velocity, U_b. A comparison with Rakha *et al*.'s (1997) model is also presented. The agreement for both variables is very good for the present model and superior than the previous one's.

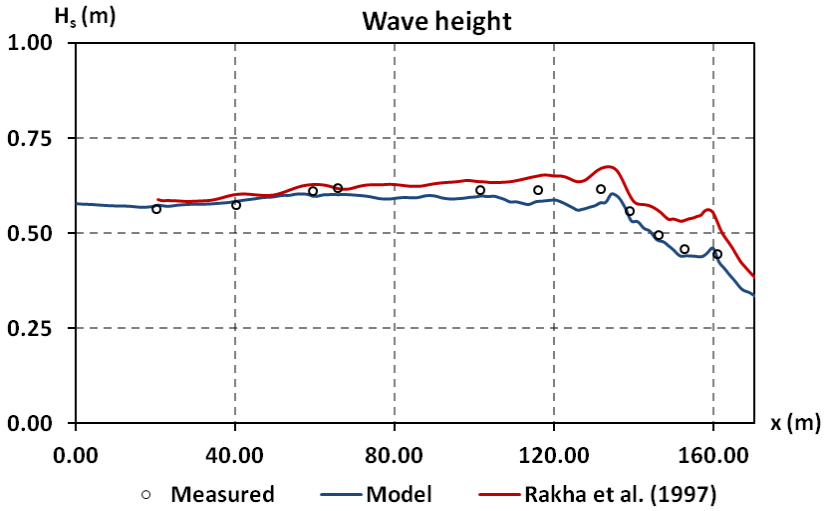

Fig. 4.21. Computed and measured significant wave height for test 1c in LIP 11D.

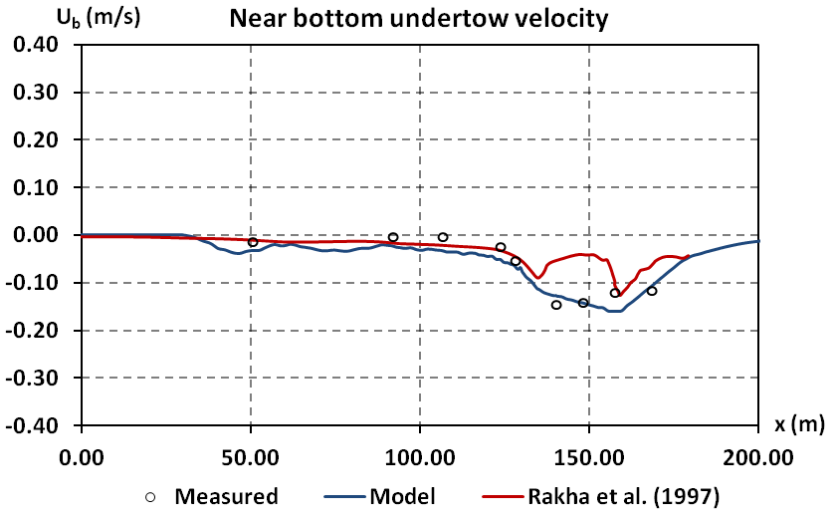

Fig. 4.22. Computed and measured near bottom undertow velocity for test 1c in LIP 11D.

The cross-shore sediment transport rate was calculated from the measured profile change over the first 7 hrs. This rate was compared to the computed by the model and this comparison is depicted in Fig. 4.23. A comparison between the measured and the computed final bed elevation is shown in Fig. 4.24. The results from Rakha *et al.*'s (1997) model are also included in these figures.

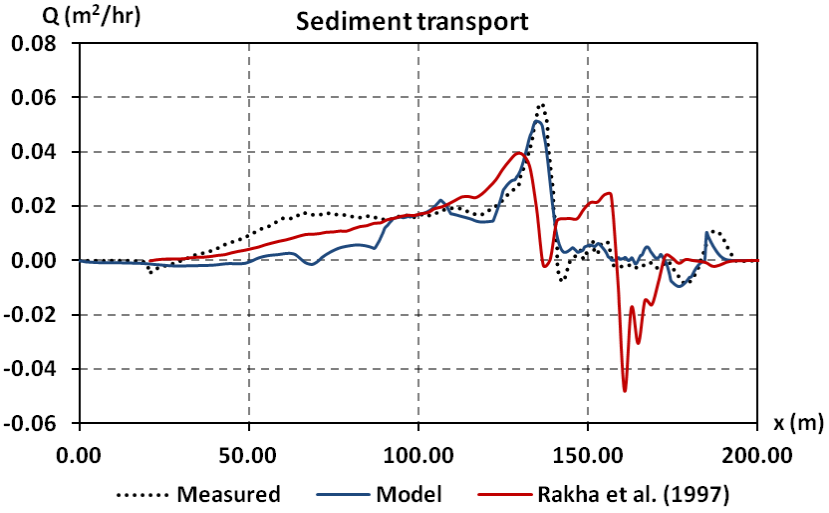

Fig. 4.23. Computed and measured total sediment transport rate after 7 hrs for test 1c in LIP 11D.

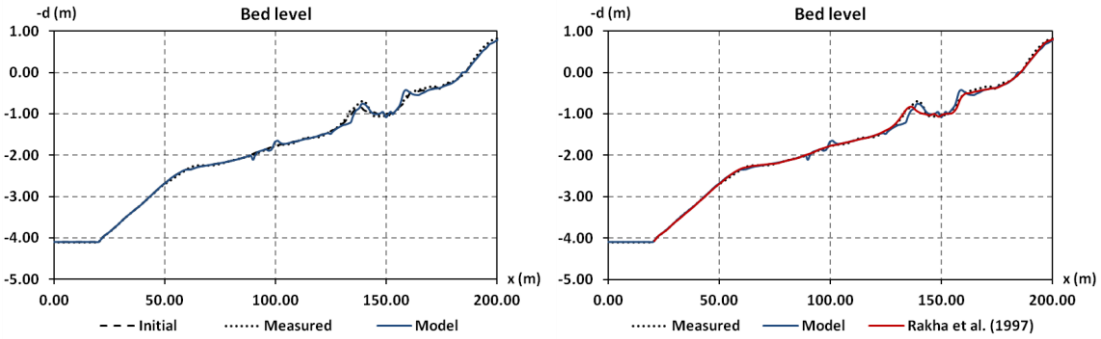

Fig. 4.24. Computed and measured initial and final beach profiles for test 1c in LIP 11D.

The agreement is quite adequate for the present model. The peak of the transport load is only slightly under-predicted and the sediment load in the inner surf and swash zones is quite well described. However, an under-estimation of the sediment transport offshore of the bars is apparent. In general, the computation of the beach morphology evolution is accurate. The main bar height is more accurately computed than in Rakha *et al*. (1997). On the other hand a slightly more peaky berm close to the shoreline is computed by the present model compared to the measurements and Rakha *et al*.'s (1997) results.

4.9.2 2DH validation

Large-Scale Sediment Transport Facility (LSTF) experiment – Oblique waves

The first test for checking the validity of the two-dimensional model refers to the experiments conducted at the Coastal and Hydraulics Laboratory of the U.S. Army Engineer Research and Development Center in Vicksburg (Gravens and Wang, 2007). The dimensions of the basin were 50 m × 30 m × 1.4 m and the experimental layout is depicted in Fig. 4.25. A

movable-bed beach made of quartz sand with d_{50}= 0.15 mm, constructed on top of a concrete fixed bed beach, was located in the central region of the facility. The test reproduced herein is BC1 referring to the oblique incidence of long-crested irregular waves of a TMA spectrum. The wave characteristics over the horizontal bottom of 0.706 m depth were T_p = 1.468 s and H_{m_o} = 0.225 m and the angle of incidence was 10°. The duration of the test was 165 min. The wave-induced longshore current and the sediments were transported towards the 20 flow channels at the downstream end of the facility and then the current through a pumping system was externally re-circulated to the upstream end of the facility.

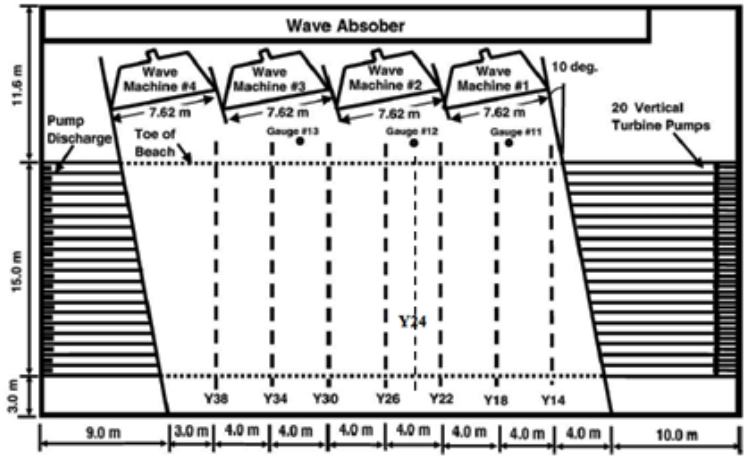

Fig. 4.25. Layout in LSTF experiment (from Nam *et al*., 2009, modified).

In order to avoid in the numerical model undesired disturbance due to reflection from the side wall and artificial diffraction in the source region, instead of generating waves at the target angle, the oblique incidence was reproduced by rotating the entire topography at an angle of -10º and then considering normal incidence of the desired waves. This modified layout requires a rather simpler computational procedure since the lateral boundaries can be used as guiding walls for the long-crested waves on the horizontal bottom. The spatial steps were chosen $\Delta x = \Delta y = 0.08$ m, the time step $\Delta t = 0.01$ s and the morphological factor f_{MOR} = 20. The re-circulation of the longshore current was treated computationally by adding in the momentum equations appropriate sink and source terms across the down-wave and up-wave lateral boundaries, respectively.

The beach topography is fairly uniform in the alongshore direction. In addition, the significant wave height and longshore current did not vary significantly in this direction. Therefore, the comparisons between calculations and measurements are only presented along the Y24 profile which is exactly in the middle of Y26 and Y22 profiles (see Fig. 4.25). Fig. 4.26 depicts a comparison between the measured and computed significant wave height, wave setup, longshore current and longshore sediment transport load, respectively.

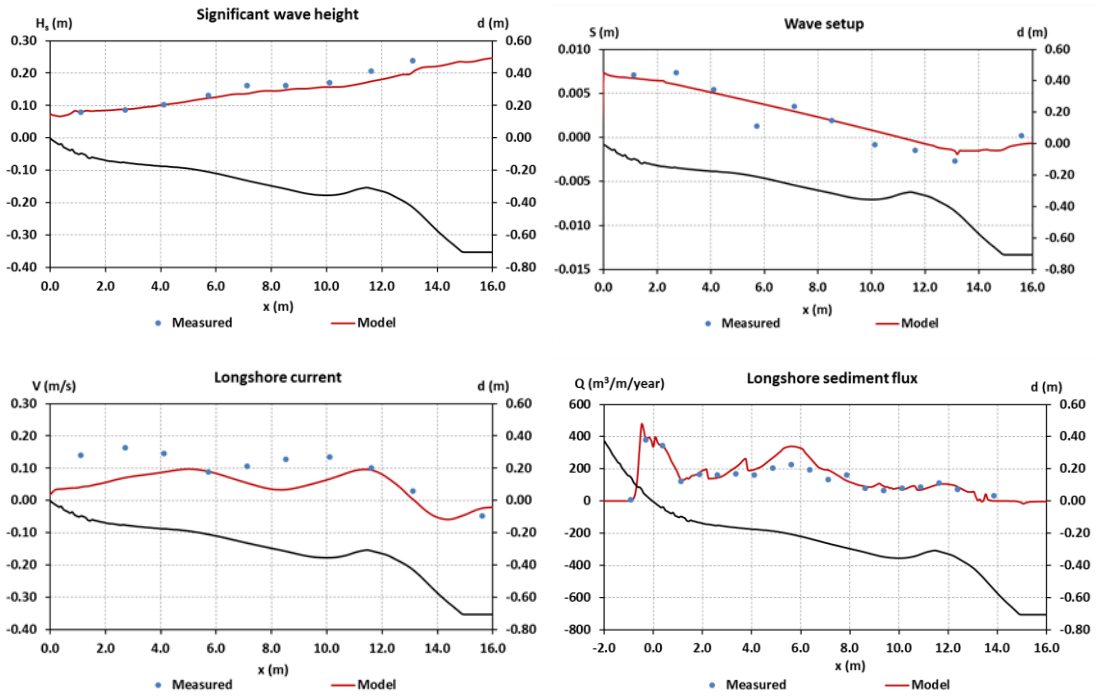

Fig. 4.26. Computed and measured significant wave height, wave setup, longshore current and longshore sediment flux along Y24 profile for Gravens and Wang's (2007) test BC1.

The computed significant wave height agrees quite well with the measured data along the entire beach profile. The results for the mean surface elevation are acceptable as well. However, the minimum set-down is slightly under-estimated and also some cross-shore variations of the setup are not followed by the model, whose results are smoother than the measured ones. The agreement for the longshore current is reasonable despite some under-prediction in the inner surf zone. Finally, the results for the longshore sediment flux are quite accurate apart of a pronounced hump computed at about 20 cm depth.

A snapshot of a subdomain of the wave pattern is shown in Fig. 4.27 and a vector plot of the underlying wave-induced current field appears in Fig. 4.28.

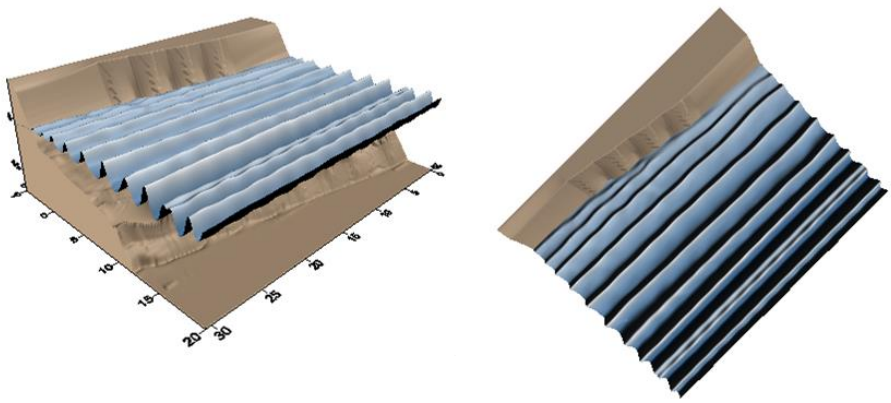

Fig. 4.27. Snapshot of the surface elevation from a bird's-eye view (at left) and on a plan view (at right) for Gravens and Wang's (2007) test BC1.

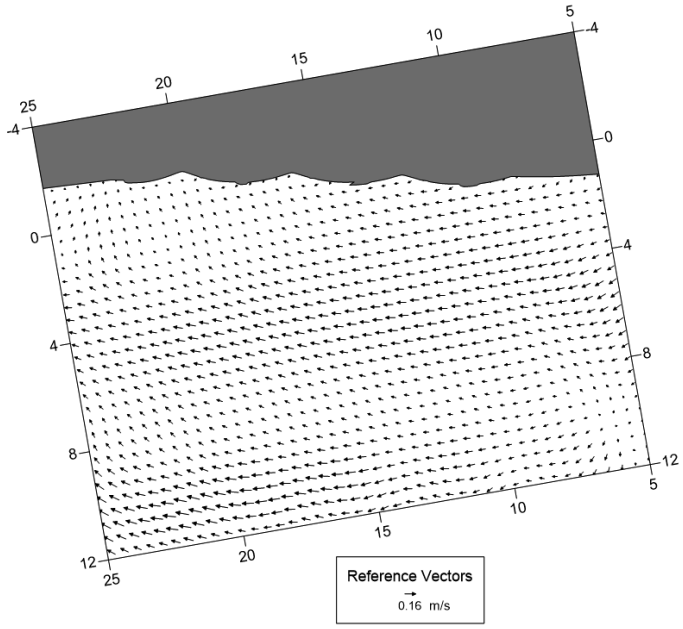

Fig. 4.28. Vector plot of the computed wave-induced current field in Gravens and Wang's (2007) test BC1.

A comparison between the measured and the computed final bed topography is depicted in Fig. 4.29. The initial bathymetry has been also included in the figure. The overall agreement is satisfactory despite some discrepancies mainly appearing at the outer surf zone. However, it should be said that both the measured and the modelled morphological changes are not intense in this test case.

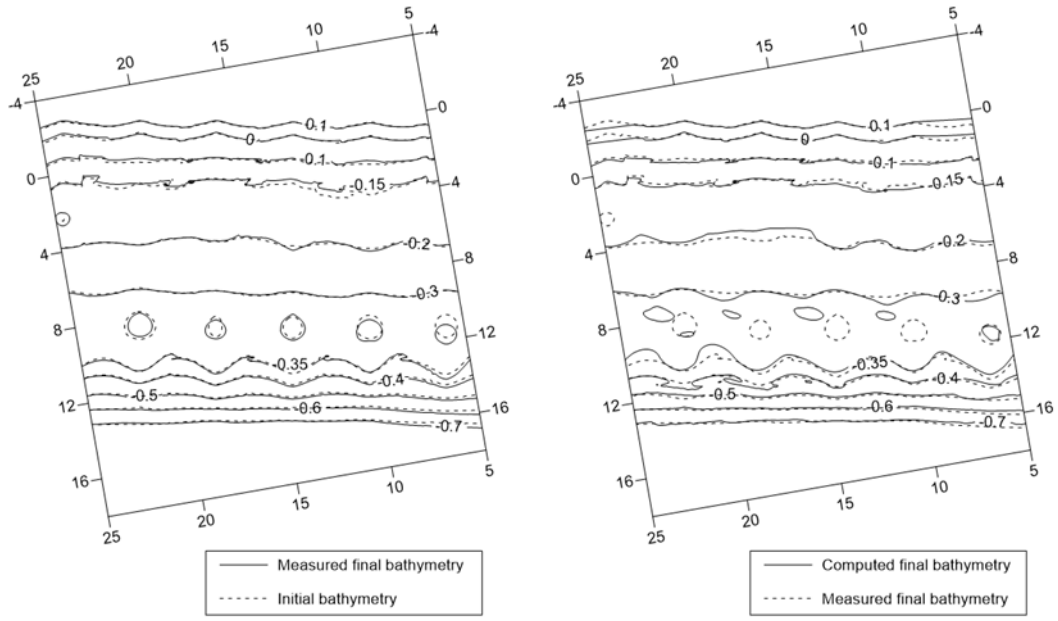

Fig. 4.29. Measured and computed final bathymetry and initial bathymetry in Gravens and Wang's (2007) test BC1.

LSTF experiment – Oblique waves plus external current

Regarding the LSTF experiment, another test case was also simulated by the model. This is test BC2 which involves exactly the same wave conditions as those in case BC1. However, an external longshore current, in addition to the waves and wave-driven longshore current, was imposed across the model beach by re-circulating two times the wave-generated longshore flux of water. In this way, a varying between 5 and 10 cm/s longshore current was imposed across the surf zone. The duration of BC2 test was 150 min and the initially bathymetry was the final bed morphology of test BC1. The numerics for this case were similar to the aforementioned ones. Fig. 4.30 shows a comparison between the measured and computed significant wave height, wave setup, longshore current and longshore sediment transport load along the Y24 profile, respectively.

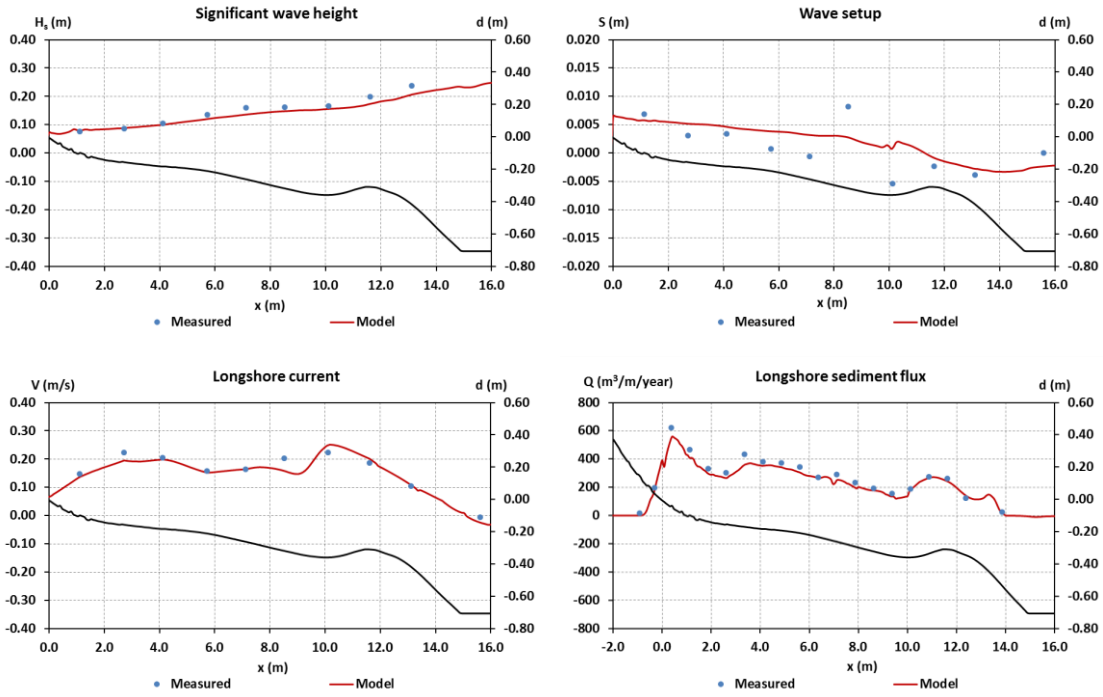

Fig. 4.30. Computed and measured significant wave height, wave setup, longshore current and longshore sediment flux along Y24 profile for Gravens and Wang's (2007) test BC2.

The agreement for the significant wave height and the longshore current is good. The longshore sediment flux is also accurately predicted despite some slight under-estimation in the inner surf zone. Regarding, the mean surface elevation, discrepancies are observed along the profile. Finally, the measured and the computed final bed topography are shown in Fig. 4.31. The overall agreement is reasonable apart from some discrepancies and secondary bars that are computed at around x = 10 m.

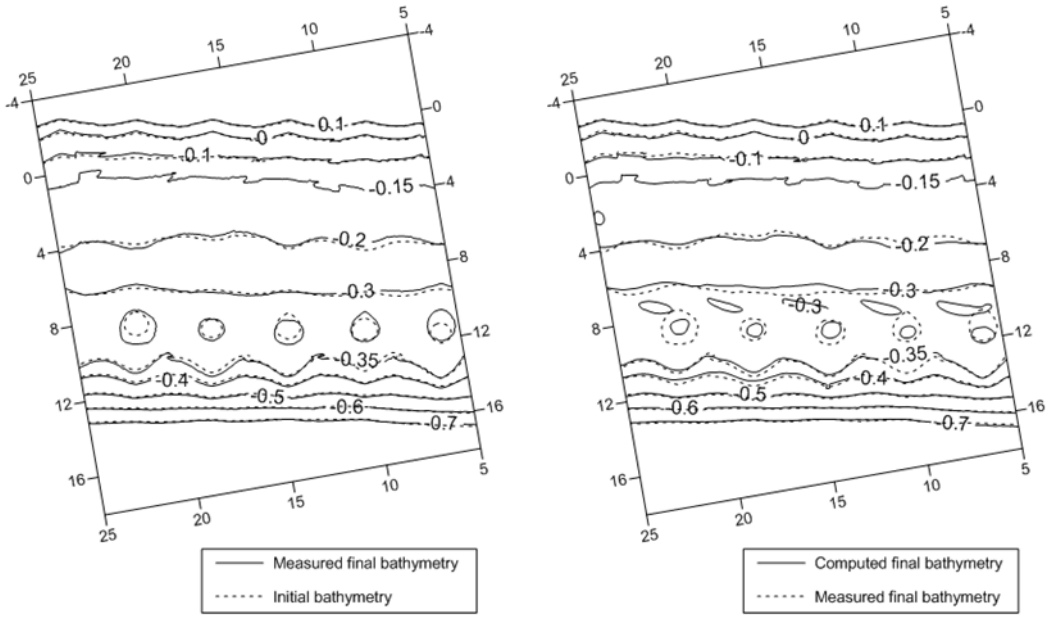

Fig. 4.31. Measured and computed final bathymetry and initial bathymetry in Gravens and Wang's (2007) test BC2.

A detached breakwater – Tombolo

The last test case refers to the shoreline changes behind a detached breakwater. The experiments were conducted in a wave basin that was 10 m long, 5 m wide and 0.7 m high. The experimental layout consisted of a horizontal bottom of 0.335 m depth followed by a uniform sloping bed of about 1:13.71. Eighteen test cases were studied by Ming and Chiew (2000), all involving normal wave incidence. The case simulated herein by the model is test 3 which includes the generation and propagation of regular waves with period T = 0.85 s and wave height H_o = 0.047 m. The beach consisted of sand with median grain size of d_{50}= 0.25 mm. A shore-parallel detached breakwater of 1.50 m length was placed symmetrically to the centerline of the tank at a distance of 0.6 m from the initially straight shoreline. The sediment transport rate in the lee of the breakwater decreases due to the attenuated wave field in the area sheltered by the breakwater. This causes the trapping of sand behind the breakwater and the formation of a tombolo after 18 hours of wave action. The test was reproduced by the model with spatial steps $\Delta x = \Delta y$ = 0.02 m and time step Δt = 0.005 s and snapshots of the tombolo evolution are depicted in Fig. 4.32.

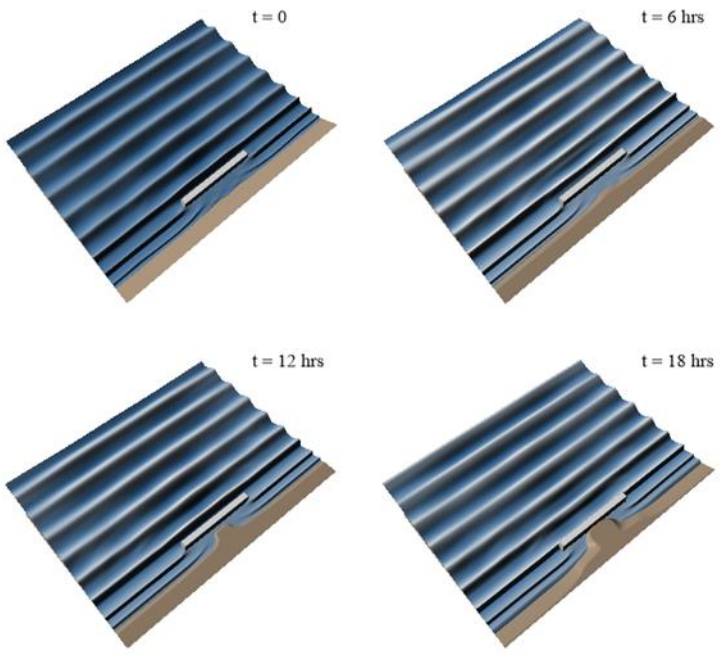

Fig. 4.32. Snapshots of the computed tombolo evolution for test case 3 in Ming and Chiew (2000).

Figure 4.33 shows a comparison between the measured and the computed final shoreline after the tombolo formation. The agreement seems reasonable both concerning the accretion near the centerline of the wave tank and the corresponding erosion at both sides.

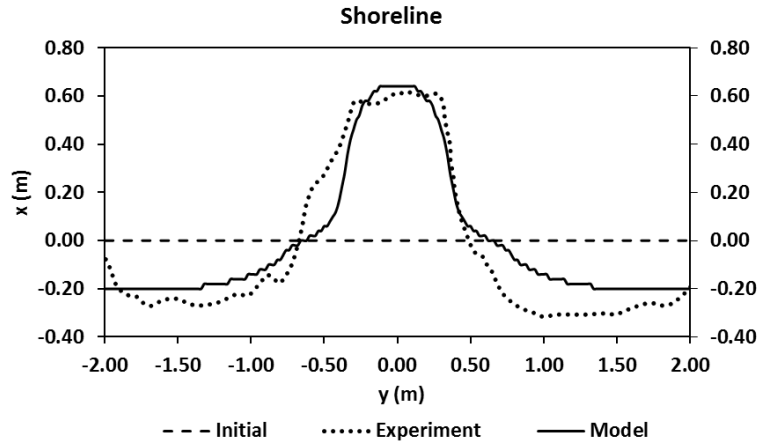

Fig. 4.33. Measured and computed final shoreline and initial shoreline for test case 3 in Ming and Chiew (2000).

4.10 Sensitivity analysis

A number of parameters and coefficients were introduced in the various components of the presented compound model. Some aspects concerning the Boussinesq model and the corresponding hydrodynamics were presented in chapter 3. In this section, aspects referring to

sediment transport and morphology were studied. The analysis was performed for the LID 11D test.

At first, six different sediment transport formulae presented above were compared for their efficiency in calculating the total sediment load. These are the formulae by Bijker (1968), Bailard (1981) as modified by Roelvink and Stive (1989), van Rijn (1993) as modified by Soulsby (1997), Ribberink (1998), Dibajnia *et al*. (2001) and the present model which includes Camenen and Larson's (2007) and Larson and Wamsley's (2007) formulae for the surf and swash zones, respectively. It should be mentioned that Ribberink's (1998) relation is only a bed-load formula and thus the suspended load was calculated by the exponential profile described previously. The comparison is depicted in Fig. 4.34. The formulae by Dibajnia *et al*. (2001) and Camenen and Larson (2007) showed the overall better response. These are the only two formulae, among the ones studied herein, that incorporate the phase-lag effects, proving the significance of this aspect.

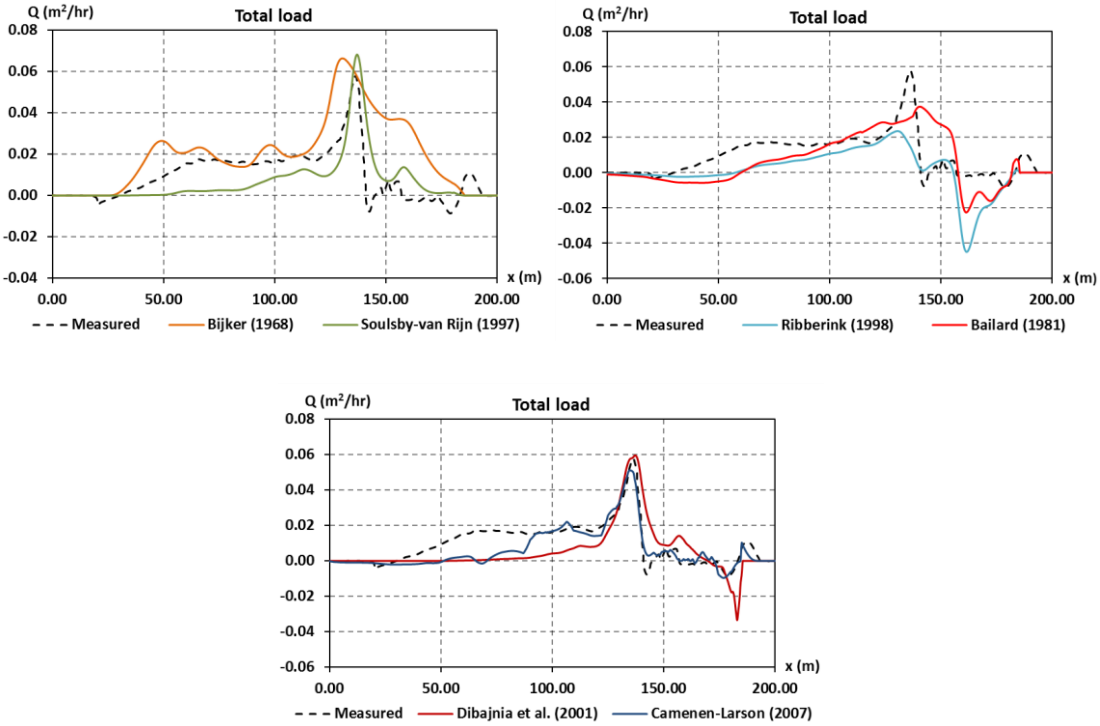

Fig. 4.34. Comparison of various sediment transport formulae for the total load for test 1c in LIP 11D.

The effect of the wave train irregularity was also studied. The model's results for the original test case involving irregular waves were at first compared to the corresponding ones of a regular wave test with $H = H_s$ and secondly to the ones of a regular wave test with $H = H_{\text{rms}}$. In both cases the wave period was considered equal to the peak period of the original test. The comparison is shown in Fig. 4.35. From the analysis it turned out that

between the two cases studied a regular wave with $H = H_{rms}$ offers a better representation of the mean sediment load, although both cases overestimate the transport rates.

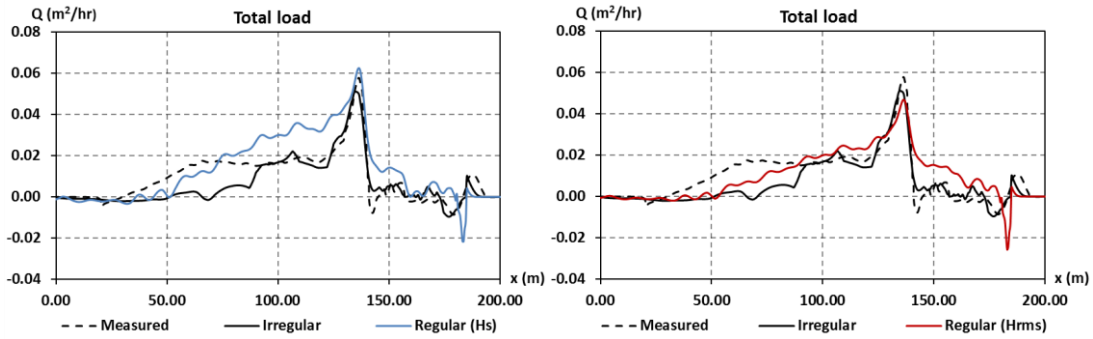

Fig. 4.35. Comparison between irregular and corresponding regular wave tests for LIP 11D experiment.

The effect of the morphological accelerator factor was also studied. A comparison regarding the final bed level is depicted in Fig. 4.36. For the specific test, the model results do not seem very sensitive to this factor, but only up to a limit value, say f_{MOR} = 20. If the value of f_{MOR} becomes large its effect in the hydrodynamics becomes significant and in particular a secondary bar tends to be created offshore of the main one.

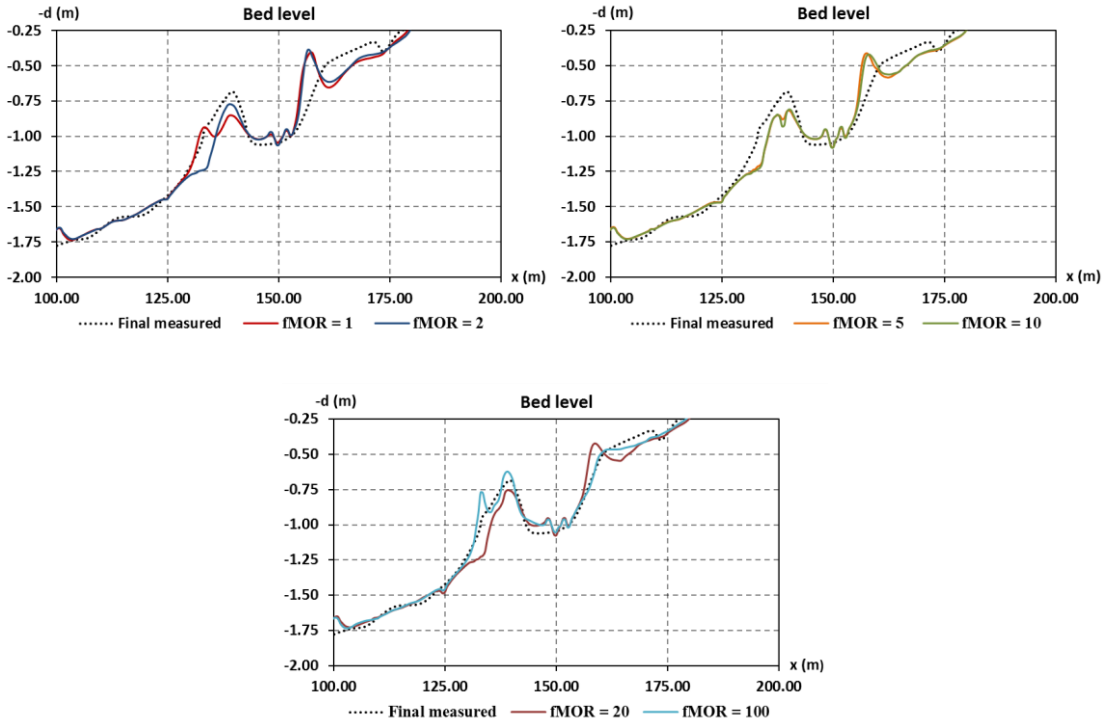

Fig. 4.36. Effect of the morphological factor on the final bed elevation for test 1c in LIP 11D.

The significance of the inclusion of the phase-lag effects in the estimation of the sediment transport rates and the bed morphology can be observed in Fig. 4.37. It appears that exclusion of these unsteady effects may lead to inaccurate, and sometimes even grossly erroneous,

calculation of the sediment transport. Thus, in this particular case, exclusion of these effects leads finally to an inaccurate prediction of the bar.

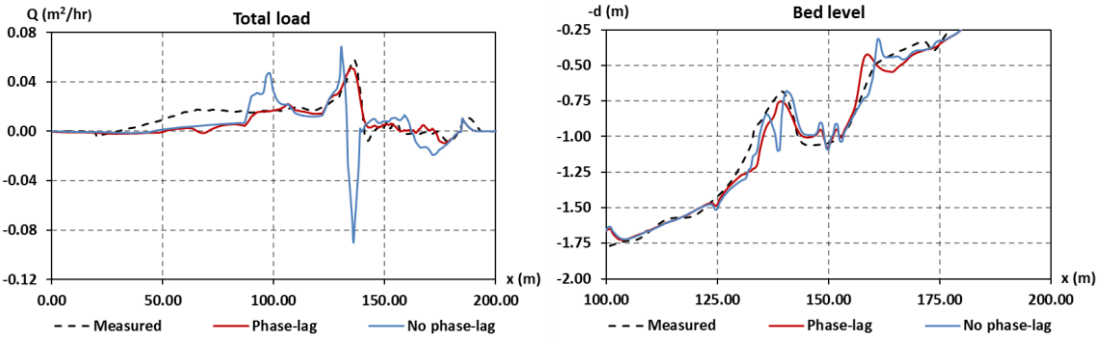

Fig. 4.37. Impact of the phase-lag effects on the sediment total load and the bed elevation for test 1c in LIP 11D.

As presented above, the model offers two options for computing the suspended sediment load. The first one is based on the solution of the AD-equation, while the second one relies on an exponential profile of the suspended sediment. Both techniques were applied in the present analysis and the results are compared in Fig. 4.38. Apparently they show very similar response and only close to the swash zone limit the AD-equation yields better results due to the application of the aforementioned boundary condition. Hence, the nearshore berm is less peaky and more accurately reproduced.

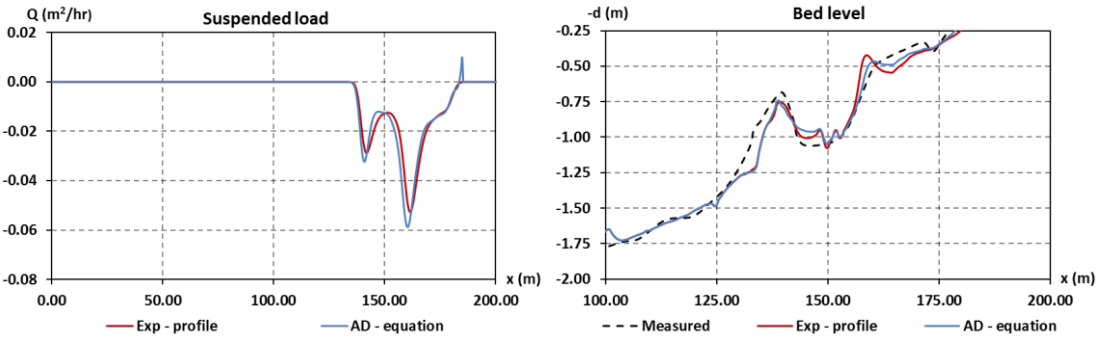

Fig. 4.38. Comparison between an exponential profile and the solution of the AD-equation for test 1c in LIP 11D.

Sensitivity analysis was also performed for some other parameters. The model proved to be sensitive to the value of the reference concentration, c_R. If the leading numerical factor of Eq. (4.59) differs from its default value, $3.5 \cdot 10^{-3}$, say by up to one order of magnitude greater, then the bed load is dominant and the total load is mostly defined by it. Thus, the sensitivity of the total load is restricted. However, if a greater value is employed, then the suspended load starts dominating over the bed load and thus the model results become sensitive to the reference concentration.

Moreover, the morphological model showed a restricted sensitivity to the value of the sediment porosity, n_p, within the range 0.3-0.5. In addition, it proved to be rather non-sensitive to the value of the internal friction angle for the specific test case. Also, the impact of the median grain size d_{50} was found to be significant only for low values ($\leq$ 0.1 mm) where the suspended sediment load becomes more significant.

As already mentioned, the compound model offers two options for solving the Eq. (4.70). These are a modified second order Lax-Wendroff scheme and a second order upwind scheme. A comparison between these two schemes is depicted in Fig. 4.39. Both schemes give similar results downwave of the bar. However, in the region of the bar, the second order upwind scheme seems more accurate. This could be explained by the fact that the Lax-Wendroff scheme suffers from numerical dispersion resulting in spurious oscillations occurring in the numerical results near shocks or steep fronts. Johnson and Zyserman (2002) proposed some filtering techniques to damp these higher harmonics. However, in many cases, the spurious oscillations cannot be eliminated, they are amplified and finally dominate on the numerical results for long computational times (Damgaard and Chesher, 1997; Damgaard, 1998). On the other hand, the upwind schemes are known to be more stable due to their inherent dissipation effects. Moreover, the Warming-Beam scheme employed herein offers a second order accuracy.

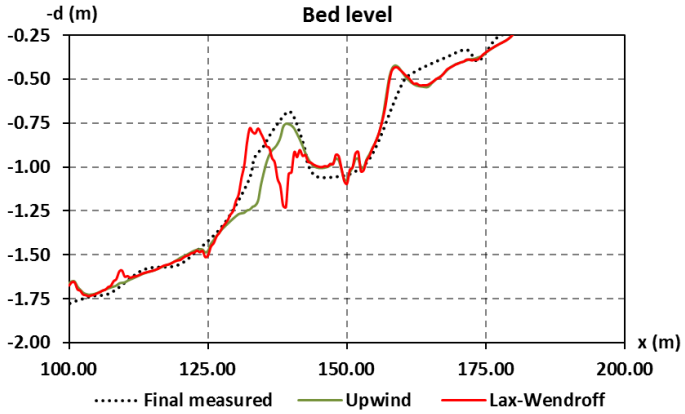

Fig. 4.39. Comparison between two different numerical schemes used in the geomorphological model for test 1c in LIP 11D.

Another interesting aspect was to inspection of the nonlinearity effect on the resulting sediment transport. For this reason, the contribution of the various Boussinesq terms to the computed sediment loads was examined. In particular, the LIP 11D test was simulated by successively retaining terms of $O(1, \varepsilon)$, $O(1, \varepsilon, \sigma^2)$, $O(1, \varepsilon, \sigma^2, \varepsilon\sigma^2)$, $O(1, \varepsilon, \sigma^2, \varepsilon\sigma^2, \varepsilon^2\sigma^2)$ in the Boussinesq-type wave model. The results are depicted in Fig. 4.40.

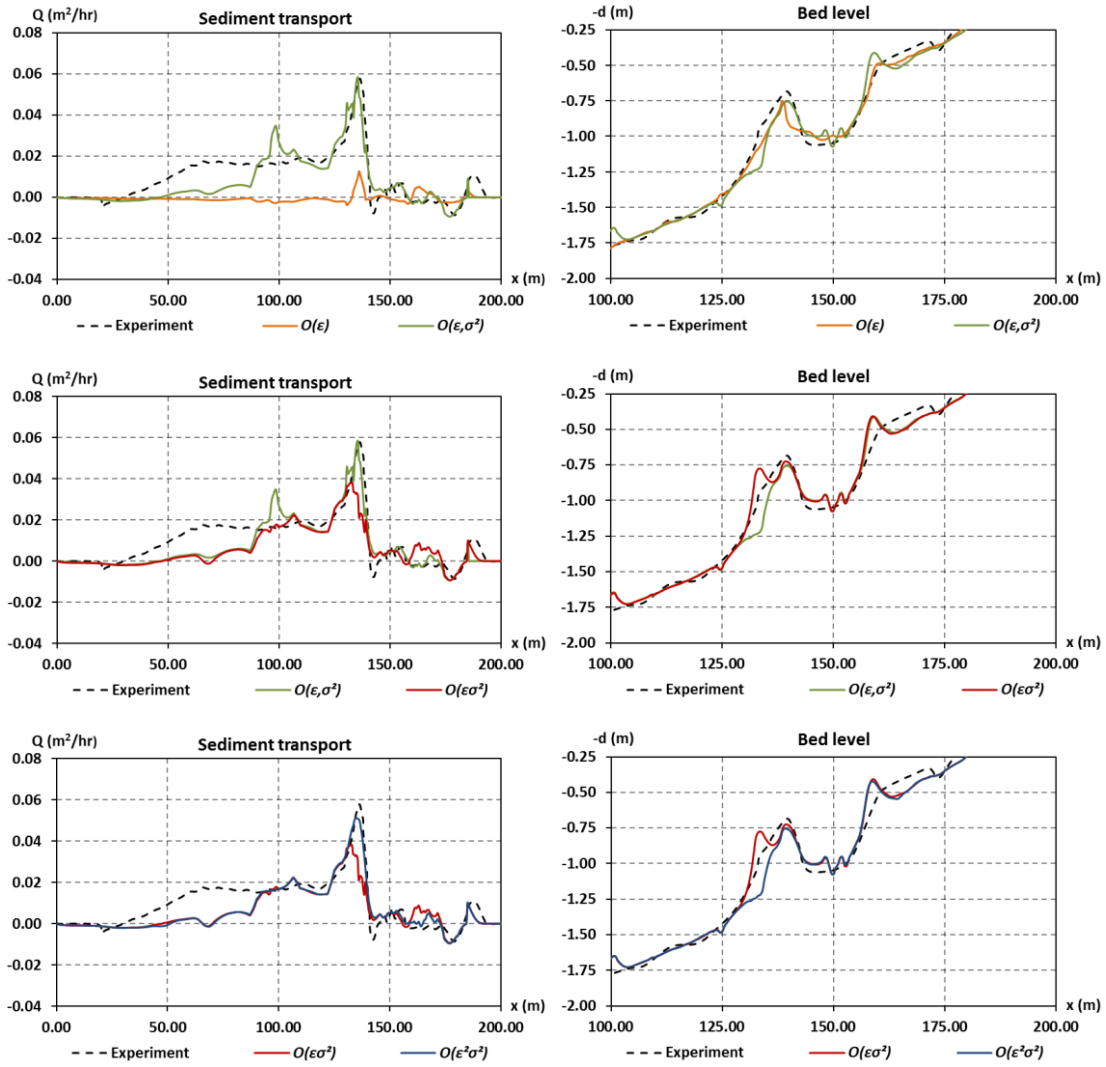

Fig. 4.40. Impact of Boussinesq terms of various order on sediment transport and morphological evolution for test 1c in LIP 11D.

It can be observed that the dispersive terms of $O(\sigma^2)$ notably improve the computed sediment transport load compared to the nonlinear shallow water equations. In particular, these terms seem to have the most significant impact on sediment transport. It is remarkable that inclusion of terms of $O(\varepsilon\sigma^2)$ results to similar, or even less accurate, predictions compared to the case of equations of $O(\sigma^2)$. However, as expected, the higher order Boussinesq equations of $O(\varepsilon^2\sigma^2)$ lead to the most accurate overall predictions.

Finally, with regard to the sediment transport in the swash zone the effect of local equilibrium slope was also studied. In particular, the LIP 11D test was simulated both with including the local equilibrium slope given from Eq. (4.68) and also excluding this term. The results are shown in Fig. 4.41 focusing on the swash zone.

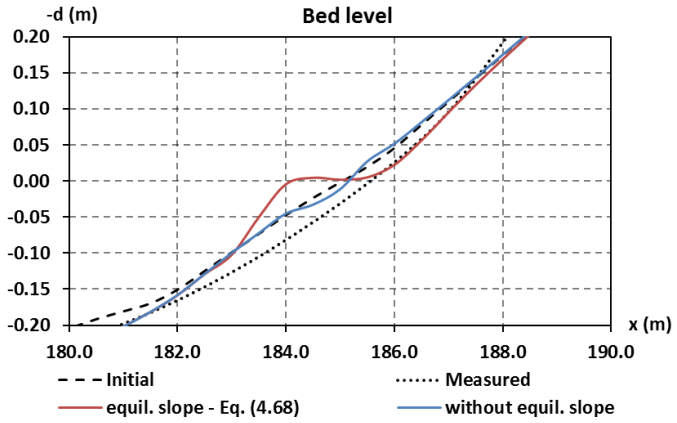

Fig. 4.41. Effect of the local equilibrium slope on the morphological evolution for test 1c in LIP 11D.

The importance of including the local equilibrium slope in the computation of the sediment transport is apparent in the land part of the initial profile (downwave of the initial shoreline). However, in the lower part of the swash zone inclusion of this term results to less accurate predictions since a berm is predicted where erosion actually takes place.

4.11 Discussion on sediment transport model

As already discussed in previous chapters, the main scope of the present thesis is to develop a reliable tool for computing the coastal sediment transport and the corresponding geomorphology. This is a very tough task due to the high level of uncertainty that is inherent in these processes and also due to the lack of an in-depth knowledge of the relative phenomena that take place over a wide range of scales, from large coastal areas and littoral cells down to grain's scale. The complexity and uncertainty of the various processes is so intense that predictions of sediment loads within a factor of 2, or even 5, are generally considered as satisfactory, especially for field measurements. However, nowadays, integrated coastal zone management is practically synonymous to shoreline and sediment management and thus sediment loads have to be estimated realistically, despite the level of uncertainty.

In chapter 3 the Boussinesq-type solver that forms the basis of the developed compound model was presented in detail. Scientific research about wave and hydrodynamic modelling has notably advanced during the last decades. Thus, accurate simulating coastal hydrodynamics is the sine qua non of the correct modelling of coastal sediment transport and geomorphology. However, numerical models for coastal sediment movement have not reached yet a similar level of efficiency. In the light of this effort, Roelvink and Reniers (2012) discuss the philosophy behind coastal sediment transport models. They conclude that for such models with high degree of uncertainty there is no clear-cut answer whether a developer should try to create a 'virtual reality' or a 'realistic analogue' with which one can

investigate processes and effects in relative isolation. Moreover, process-based modelling may be able to explain a variety of short- or medium-term morphological processes, but this is not guaranteed for long-term predictions, for which a data-driven approach may be more suitable. In general, adding more physics to a coastal sediment transport and morphology model improves the ability to represent certain processes but the overall model performance does not necessarily have to improve. This is true because more and more adjustable coefficients may be introduced, for which there is no clear guidance and thus the degree of uncertainty increases. On the other hand, a simpler model with fewer coefficients with a predictable effect on the outcome may be preferable. This idea is also supported in subsection 4.10 where simpler formulae, e.g. Bailard's (1981), gave results of comparable accuracy with other more sophisticated formulae.

Keeping in mind these considerations, three types of coastal morphological models have been developed during the last few decades: coastal profile models, where the focus is on cross-shore processes and the longshore variability is neglected, coastline models, where the cross-shore profiles are assumed to retain their shape even when the coast advances or retreats, and coastal area models. The herein developed model is included in the latter class, where variations in both horizontal dimensions are resolved and a separation between longshore and cross-shore is not employed. The area models are applicable at a range of scales, from small-scale coastal engineering problems to macro-scale evolution of tidal basins.

Coastal morphological area models have been developed since the early '80s (de Vriend *et al*., 1993; Nicholson *et al*., 1997). However, it was only in the late '80s and early '90s that the large European institutes combined in the EU Mast-G6M and G8M projects carried out major developments to their models that are still leading today, such as Delft3D (Deltares, The Netherlands), Mike21 (DHI, Denmark), Telemac (Laboratoire National d' Hydraulique et Environnement, France), PISCES (HR Wallingford, U.K.), University of Liverpool model, STC model (Service Central Technique des Ports Maritimes et des Voies Navigables, France), along with some more alternatives: ADCIRC (U.S. Army Corps of Engineers), ECOMSED (HydroQual, U.S.A.), ROMS-SED (NOPP, U.S.A.), XBeach (Roelvink *et al*., 2009), Wai *et al*. (2004).

Most of the aforementioned models rely on wave-averaged models and hence they cannot predict skewness, asymmetry or bound long waves directly and have to rely on local approximations for these features. On the other hand, as already mentioned in subsection 4.1, only a restricted number of phase-resolving wave models combined with detailed intra-wave sediment transport models have been reported in the international literature, and almost all of them have been checked only with 1DH tests. From this point of view the present compound

model offers original contribution to coastal modelling. Nevertheless, despite this promising approach, similarly to the wave and hydrodynamic modules presented in chapter 3, some criticism should be done on the adopted modelling techniques related to sediment transport in order to illustrate the limitations and potential inaccuracies of the compound model.

The computation of the bed load adopts Meyer-Peter and Müller's (1948) bed shear concept and relies on a semi-empirical formulation. The relationship between the bed load transport and the total Shields parameter to the power 1.5 was first confirmed for steady flows. That formulation was generalized to take into account the combined action of waves and currents. Nevertheless, it should be mentioned that the time-dependent bed load transport is actually treated in a quasi-steady manner using the quadratic value of the instantaneous Shields parameter for the two half-periods of the wave. Despite this simplification, very good agreement with both laboratory and field measurements was observed, better compared to other formulae (Camenen and Larson, 2005). This advantage of the adopted formulation was also verified in subsection 4.10, at least for the test case studied.

An important feature of the bed load formula used is that it takes into account the phase-lag effects. Very few existing formulae, e.g. Dibajnia and Watanabe (1992), embed these unsteady effects which are important in cases of nonlinear waves. This fact was also discussed in the sensitivity analysis section. These phenomena, most probably, explain the different values of the leading coefficients α_w and α_n in the direction of wave propagation and normal to it. Camenen and Larson (2005) calibrated the formula for wave alone and current alone test cases, but the modification of α_w for combined waves-current is rather ad-hoc. However, the data sets were quite extensive and the agreement fairly accurate, despite some scattering.

Another advantage of the adopted formulation is the criterion for the inception of sheet flow which is more accurate than other criteria widely used (Camenen and Larson, 2006). Also, the exponential factor included in the bed load formula offers an accurate estimation of the transport rate near the threshold of movement. Most of other formulae, predict no sediment transport when the Shields parameter is near its critical value, although low transport is often observed. The prediction of the critical Shields parameter incorporates high uncertainty, and the exponential modification somewhat restricts related errors.

It should be mentioned that the presented model cannot predict the near bed steady streaming caused by bottom boundary layer mechanisms, such as the viscosity effects. Thus the wave-current bottom boundary layer is not analytically resolved as in other sediment transport models (Fredsøe *et al.*, 1985). Nevertheless, inside the surf zone, where sediment transport is more intense, the aforementioned mechanisms are suppressed by both the turbulence and the undertow acting in the middle layer. These two mechanisms have been

incorporated in the hydrodynamic module by calculating the near bottom undertow velocity. In addition, the energy dissipation due to bottom friction is also taken into account in the computation of eddy diffusivity of sediments.

The suspended load is obtained either from the solution of the depth-integrated AD-equation for the sediment concentration or by applying a simplified formula relying on an exponential profile of the concentration. When applying the exponential profile two simplifications are applied. The first one and more important is that the unsteady part of the suspended sediment is, at first approximation, neglected. In particular, the r.h.s. of Eq. (4.13) differs from $\frac{1}{T}\int_0^T \int_0^h \vec{u}\mathrm{C}\, dzdt$, where $\vec{u} = \vec{u}(z)$ is the time-averaged (in the wave period) velocity profile. However, this simplification is made when applying the exponential profile approach. Camenen and Larson (2008) observed some underestimation of the computed suspended load for experimental data referring to combined waves and current and in some cases a power law fitted better to the data. Indeed, in some cases, e.g. phase-lag effects over ripples, the unsteady part of the suspended load is also significant (van der Werf and Ribberink, 2004). However, a correction is made in order to take into account the wave-current interaction and the phase-lag effects by dividing the wave-cycle into an onshore and an offshore semi-cycle, see Eq. (4.63a).

The second simplification refers to the use of a uniform profile of the current velocity, i.e. $\vec{u} = \vec{\vec{U}}$, instead of the actual profile. Although the model accounts for the depth-averaged and the near bottom undertow (see subsection 3.2.5), it would be more accurate to compute the actual current velocity profile over depth. Other sediment transport models (Deigaard *et al*., 1988; Rakha *et al*., 1997; Rakha, 1998) resolve the vertical current profile by computing the vertical variation of shear stress and the near bed streaming. This is a feature that could be added to the model in the future. However, Camenen and Larson's (2008) validation against data showed that the use of $\vec{\vec{U}}$ does not introduce significant errors when the measured profiles of sediment's concentration were employed. Thus, the most important assumption is that of the exponential form of the concentration profile.

In any case, the solution of the depth-integrated AD-equation is more theoretically robust. The pick-up and deposition functions are, however, an issue for discussion (see subsection 4.6). Moreover, the formulation adopted for the eddy diffusivity of sediments takes into account the energy dissipation due to wave breaking and wave-current bottom friction. There are other more sophisticated approaches though that relate the eddy diffusivity to the turbulent kinetic energy, k, by implementing (k - ε) models (Deigaard *et al*., 1986a; Rakha *et al*., 1997; Rakha, 1998). Such an approach is left for future investigation that could add another advanced feature to the model.

It is stressed that higher order convective terms are retained in Eq. (4.52) and thus the contribution of the Lagrangian drift to sediment transport is automatically included. Moreover, the Boussinesq wave model, due to its nonlinear character, inherently reproduces the low-frequency oscillations forced by wave groups. However, horizontal advection of sediment clouds due to these long-period oscillations are not accounted for due to the local character of the sediment transport model. Finally, as already mentioned, a very important parameter for the correct calculation of suspended loads is the bed reference concentration. Unfortunately, a high degree of uncertainty is related to the estimation of the value of this parameter, depending also on the reference level used each time. This uncertainty shows once again the difficulty of a strict distinction between suspended and bed loads. A too high value of the bed reference concentration may enhance unrealistically the domination of the suspension as the main transport mechanism. On the other hand, too low a value may lead to the under-estimation of this mechanism.

Another advantage of the present model is the good description it affords of the interaction of inner surf and swash zones with respect to sediment transport loads. The net transport loads in the swash zone are computed based on an analogy to ballistic theory. This concept seems realistic as the wave front can be regarded as a slug of water moving under the action of gravity and friction. A very first formulation of this type was given by Madsen (1991, 1993) for calculating the instantaneous bed load. However, three important issues should be discussed regarding the formulation in the present model. At first, Larson and Wamsley (2007) gave an analytical solution considering both gravity and bottom friction as acting forces. However, the simplified version neglecting bed friction was applied herein both for simplicity and to avoid extra uncertainties due to the more parameters involved. In any case, the important agent of friction is taken into account by the formula through the inherent computation of the wave run-up. Secondly, in the present thesis a significant variability of the values of the leading coefficients K_c and K_l was observed through calibration with laboratory measurements. Thus, further investigation on this issue is required since the computed sediment transport loads in the swash zone are sensitive to the value of these parameters. The third issue refers to the correct estimation of the local equilibrium slope given by Eq. (4.68). The computed sediment transport is sensitive to the value of this parameter whose estimation includes high uncertainty.

With regard to the geomorphological model, it is not straightforward selecting the numerical scheme for the solution of the sediment mass conservation Eq. (4.70). A variety of shock-capturing schemes have been proposed to this effect for simulating the bed level evolution. Johnson and Zyserman (2002) apply a second-order modified Lax-Wendroff scheme. Roelvink and van Banning (1994) and Roelvink *et al*. (1994) use a FTCS explicit scheme

with corrections of the transport rate to compensate negative numerical diffusion. Chesher *et al*. (1993) and Tanguy *et al*. (1993) implement one-step and two-step Lax-Wendroff schemes, respectively. O' Connor and Nicholson (1989, 1995) also use a modified Lax-Wendroff scheme with effects of gravity on the sediment transport rate, while Long and Kirby (2006) use an Euler-WENO scheme. A modified second order Lax-Wendroff scheme is also implemented by the present model. This scheme suffers from spurious oscillations generated near shocks or steep fronts and are related to high wavenumbers. These oscillations grow after long simulation time, degenerate into noise, and finally mask the large-scale morphological features. The inclusion of the bed slope effect in Eqs (4.71a,b) suppresses somewhat these spurious oscillations. On the other hand, the first-order upwind schemes are generally more stable than FTCS schemes due to inherent dissipation effects. However, they have the disadvantage of widening the shock region excessively. Nevertheless, the Warming-Beam scheme that is used by the model offers a second order accuracy. As shown in subsection 4.10, the upwind scheme appears to be a more reliable choice than the Lax-Wendroff scheme, although in most of the rest applications both schemes led to comparable results.

The morphological changes vary at a much slower rate as compared to the short-term variations of hydrodynamics. Thus, for practical engineering applications accelerating methods have to be applied to simulate morphological changes. A number of such strategies have been proposed (tide-averaging, continuity correction, RAM approach, morphological factor approach, parallel online approach) and they are discussed in detail in Roelvink (2006) and Roelvink and Reniers (2012). In the present thesis, the application of the morphological factor technique was proven to be very efficient for the short-term simulations conducted. However, the value of the accelerator factor should be chosen carefully. A very small value is computationally inefficient and not practical for the long time scales involved in the morphological processes, while a very high value affects unrealistically the related hydrodynamics.

The model is tailored for both 1DH and 2DH applications. Due to the high computational effort required for long-term simulations, it is only short-term simulations that have been studied here, up to the order of some hours. For such applications the required computational effort and time are not prohibitive, say about 3 hours for simulating 1 hour of real time with a common computer. However, in order to extend the application of the present compound model based on the Boussinesq equations to long-term simulations powerful computers are required for achieving practical computational times.

In the cross-shore direction the importance of the phase-lag effects has been iterated throughout this study. If this unsteady phenomenon is excluded from the computation of the sediment load then unrealistic rates may be predicted and sometimes even sediment transport

to the reverse direction when compared to the measured one. This inaccuracy affects the correct description of the main morphological features across the beach profile, such as the formation of the wave breaking bar, the trough down-wave of it, the swash berm or the foreshore erosion. However, the sophisticated sediment transport formulae incorporated in this model allow a reasonable prediction of these complex features. It was also shown that in the case of irregular waves, a representative regular wave could be used as input leading to acceptable results. However, for the two representative values of the wave height studied herein, H_s and H_{rms}, an over-prediction of the sediment load was observed proving some dependence on the actual wave-train.

The longshore sediment transport under combined waves and currents was also found to be adequately predicted by the model and a smooth reduction from the swash to the inner surf zone was ensured. Hence, the alongshore variation of the morphology evolution can be reasonably described by the model. This was further supported by a validation test reproducing fairly good the shoreline's response in the lee of a detached breakwater. The tombolo formation due to the trapped sand was described satisfactorily by the model.

The one-dimensional version of the model was also compared to the model by Rakha *et al*. (1997) which likewise combined a Boussinesq-type wave model with a sediment transport and a morphological model. In general, the performance of the former was proved to be superior to the latter. This can be partly attributed to the higher order of nonlinearity of the Boussinesq wave module of the present model compared to the corresponding one in Rakha *et al*. (1997), and partly to the different bed load formulae adopted herein and in Rakha *et al*.'s (1997) model where the formula by Engelund and Fredsøe (1976) was applied.

Combining an intra-wave model, as the one used here, with a sediment transport and a morphological model is a very tough task. Also, the integrated character of the model including both the surf and swash zone sediment computations enhances the reliability of the model, offering thus a robust tool for studying the complex processes of coastal morphology evolution. The next step is to extend the compound model to porous beds in order to study the morphodynamics in the lee of submerged breakwaters, which is the main scope of the present Ph.D. thesis. This extension is presented in chapter 6.

References

Ackers, P., and White, W. R. (1973). "Sediment transport: new approach and analysis." *J. Hydraul. Div.*, ASCE, 99 (HY11), 2041-2060.

Ahilan, R., and Sleath, J. (1987). "Sediment transport in oscillatory flow over flat beds." *J. Hydraul. Eng.*, 113 (3), 308–322.

Ahrens, J. (2000). “A fall-velocity equation.” *J. Waterw. Harbour and Coast. Eng.*,126 (2), 99–102.

Akiyama, J., and Fukushima, Y. (1986). "Entrainment of noncohesive sediment into suspension." *Proc. 3rd Int. Symp. on River Sedimentation*, S. Y. Wang, H. W. Shen, and L. Z. Ding, eds, Univ. of Mississippi, 804-813.

Albertson, M. L. (1952). “Effect of shape on the fall velocity of gravel particles.” *Proc. 5th Hydr. Conf., Bull.*, No 34, J. S. McNown and M. C. Boyer, eds, University of Iowa, U.S.A., pp. 243-262.

Andersen, O. H., and Fredsøe, J. (1983). "Transport of suspended sediment along the coast." *Prog. Rep. 59*, Inst. of Hydrodynamics and Hydraulic Engineering, Techn. Univ. Denmark.

Arcilla, A. S., Roelvink, J. A., O’Conner, B. A., Reniers, A., and Jimenez, J. A. (1994). “The Delta Flume ’93 experiment.” *Proc. Coastal Dyn. ’94*, A. S. Arcilla, S. J. F. Marcel and N.C. Kraus, eds, ASCE, Barcelona, Spain, pp. 488-502.

Ashida, K., and Michiue, M. (1972). “Study on hydraulic resistance and bedload transport rate in alluvial streams.” *Trans. JSCE*, Tokyo, 206, 59-69 (in Japanese).

Bagnold, R. A. (1947). "Sand movement by waves, some small scale experiments with sand by very low density." *Proc. Inst. Civil Engrs*, 27, 447-469.

Bagnold, R. (1963). “An approach of marine sedimentation.” In: *The Sea: Ideas and Observations on Progress in the Study of the Seas*, M. N. Hill, ed., Interscience, New York, vol. 3, pp. 507-528.

Bagnold, R. (1966). “An approach of sediment transport model from general physics.” *Prof. Paper 422-I*, U. S. Geol. Surv., 37 pp.

Bailard, J. (1981). “An energetics total load sediment transport model for a plane sloping beach.” *J. Geophys. Res.*, 86 (C11), 10938–10954.

Bailard, J. A. (1982). “Modeling on-offshore sediment transport in the surfzone.” *Proc. 18th Int. Conf. on Coastal Engineering*, B. L. Edge, ed., Cape Town, South Africa, part II, chapter 87, pp. 1419-1438.

Bailard, J., and Inman, D. L. (1981). “An energetics bedload transport model for a plane sloping beach; local transport.” *J. Geophys. Res.*, 86 (C3), 2035–2043.

Bakker, W. T. (1968). “The dynamics of a coast with a groyne system.” *Proc. 11th Int. Conf. on Coastal Engineering*, ASCE, London, United Kingdom, vol. I, chapter 31, pp. 492-517.

Bakker, W. T. (1974). “Sand concentration in an oscillatory flow.” *Proc. 14th Int. Conf. on Coastal Engineering*, ASCE, Copenhagen, Denmark, vol. I, chapter 66, pp. 1129-1148.

Baldock, T. E., Alsina, J. A., Caceres, I., Vicinanza, D., Contestabile, P., Power, H., and Sanchez-Arcilla, A. (2011). “Large-scale experiments on beach profile evolution and surf and swash zone

sediment transport induced by long waves, wave groups and random waves." *Coast. Eng.*, 58 (2), 214–227.

Battjes, J. (1983). "Surf zone turbulence." *Proc. 20th Congress IAHR*, Moscow, Russia, pp. 137–140.

Bijker, E. W. (1967). "Some considerations about scales for coastal models with movable bed." *Tech. Rep.*, 50, Delft Hydraulics Laboratory, Delft, The Netherlands, 142 pp.

Bijker, E. W. (1968). "Littoral drift as function of waves and current." *Proc. 11th Int. Conf. on Coastal Engineering*, ASCE, London, United Kingdom, vol. I, chapter 26, pp. 415-435.

Bijker, E. W. (1971). "Longshore transport computations." *J. Waterw. Harbour and Coast. Eng.*, ASCE, 97(WW4), 687-701.

Bonnefille, R., and Pernecker, L. (1965). "Début d' entraînement des sédiments par la houle." *Proc. 11th Congress IAHR*, vol. V, pp. 207-208.

Bowen, A. J. (1981). "Simple models of nearshore sedimentation: Beach profiles and longshore bars." In: *Coastline of Canada*, S. B. McCann, ed., pp. 1-11, Geological Survey of Canada, Halifax.

Brahms, A. (1753). *Anfangsgründe der Deich- und Wasserbaukunst*. Aurich, Germany (in german).

Briand, M.-H. G., and Kamphuis, J. W. (1993). "Sediment transport in the surf zone: a quasi 3-D numerical model." *Coast. Eng.*, 20 (1-2), 135-156.

Brøker Hedegaard, I., Deigaard, R., and Fredsøe, J. (1991). "Onshore/Offshore sediment transport and morphological modelling of coastal profiles." *Proc. ASCE Specialty Conf. Coastal Sediments '91*, N. C. Kraus, K. J. Gingerich and D. L. Kriebel, eds, Seattle, WA, U.S.A., pp. 643-657.

Brøker Hedegaard, I., Roelvink, J. A., Southgate, H., Pechon, P., Nicholson, J., and Hamm, L. (1992). "Intercomparison of coastal profile models." *Proc. 23rd Int. Conf. on Coastal Engineering*, B. L. Edge, ed., Venice, Italy, part V, chapter 162, pp. 2108-2121.

Bruun, P. (1954). "Coast erosion and the development of beach profiles." U.S. Army Corps of Engineers, Beach Erosion Board, *Tech. Memo.*, No. 44.

Butt, T., and Russell, P. (2000). "Hydrodynamics and cross-shore sediment transport in the swash-zone of natural beaches: a review." *J. Coast. Res.*, 16 (2), 255– 268.

Camenen, B. (2007). "Simple and general formula for the settling velocity of particles." *J. Hydraul. Eng.*, 133 (2), 229-233.

Camenen, B., and Larson, M. (2005). "A general formula for non-cohesive bed load sediment transport." *Estuar. Coast. Shelf Sci.*, 63 (1-2), 249–260.

Camenen, B., and Larson, M. (2006). “Phase-lag effects in sheet flow transport.” *Coast. Eng.*, 53 (5-6), 531–542.

Camenen, B., and Larson, M. (2007). “A unified sediment transport formulation for coastal inlet application.” *Tech. rep. ERDC/CHL CR-07-1*, U.S. Army Engineer Research and Development Center, Vicksburg, MS, U.S.A., 231 pp.

Camenen, B., and Larson, M. (2008). “A general formula for noncohesive suspended sediment transport.” *J. Coastal Res.*, 24 (3), 615–627.

Carstens, M. R. , Neilson, F. M., and Altinbilek, H. D. (1967). "An analytical and experimental study of bed forms under water waves." Georgia Inst. Tech., *Final Rep. Proj. A-798*.

Celik, I., and Rodi, W. (1984). "A deposition entrainment model for suspended sediment transport." *Report SFB 210/T/6*, Universitat Karlsruhe, Karlsruhe, West Germany.

CERC (1984). *Shore Protection Manual*, vols I to III. US Army Corps of Engineers, Coastal Engineering Research Centre, US Govt Printing Office.

Cheng, N.-S. (1997). “Simplified settling velocity formula for sediment particle.” *J. Hydraul. Eng.*, 123 (2), 149–152.

Cheng, N.-S. (2002). “Exponential formula for bedload transport.” *J. Hydraul. Eng.*, 128 (10), 942-946.

Chesher, T. J., Wallace, H. M., Meadowcroft, I. C., and Southgate, H. N. (1993). “PISCES. A morphodynamic coastal area model. First annual report.” *Report SR 337*, HR Wallingford, Wallingford, Oxfordshire, U.K., 27 pp.

Coleman, N. L. (1981). “Velocity profiles with suspended sediment.” *J. Hydraul. Res.*, 19 (3), 211-229.

Corey, A. T. (1949). “Influence of shape on the fall velocity of sand grains.” MSc thesis, Colorado Agricultural and Mechanical College, Fort Collins, Colorado, USA, 102 pp.

Dally, W. R., and Dean, R. G. (1984). “Suspended sediment transport and beach profile evolution.” *J. Waterw. Port Coast. Ocean Eng.*, 110 (1), 15-33.

Damgaard, J. S. (1998). “Numerical schemes for morphodynamic simulations.” *Report IT 459*, HR Wallingford, Wallingford, Oxfordshire, U.K.

Damgaard. J. S., and Chesher, T. J. (1997). “Morphodynamic simulations of Helwick Bank.” *Report TR 31*, HR Wallingford, Wallingford, Oxfordshire, U.K.

Damgaard. J. S., and Soulsby, R. L. (1996). “Alongshore bed-load transport.” *Proc. 25th Int. Conf. on Coastal Eng.*, B. L. Edge, ed., Orlando, Florida, U.S.A., part IV, chapter 279, pp. 3614–3627.

Dean, R. G. (1973). "Heuristic models of sand transport in the surf zone." *Proc. Conf. Eng. Dynamics in the Surf Zone*, Sydney, Australia, 208-214.

Dean, R. G. (1977). "Equilibrium beach profiles: U.S. Atlantic and Gulf Coasts." Newark (Delaware), Univ. of Delaware, Dept. of Civil Engineering, *Ocean Engineering Rep.*, No. 12, 45 pp.

Dean, R. G., Berek, E. P., Gable, C. G., and Seymour, J. (1982). "Longshore transport determined by an efficient trap." *Proc. 18th Int. Conf. on Coastal Engineering*, B. L. Edge, ed., Cape Town, South Africa, pp. 954-968.

Deigaard, R., Fredsøe, J., and Brøker Hedegaard, I. (1986a). "Suspended sediment in the surf zone." *J. Waterw. Port Coast. Ocean Eng.*, 112 (1), 115-128.

Deigaard, R., Fredsøe, J., and Brøker Hedegaard, I. (1986b). "Mathematical model for littoral drift." *J. Waterw. Port Coast. Ocean Eng.*, 112 (3), 351-369.

Deigaard, R., Fredsøe, J., Brøker Hedegaard, I., Zyserman, J., and Andersen, O. H. (1988). "Littoral drift model for natural environments." *Proc. 21st Int. Conf. on Coastal Engineering*, ASCE, Malaga, Spain, pp. 1603-1617.

Dette, H. H., Larson, M., Murphy, J., Newe, J., Peters, K., Reniers, A., and Steetzel, H. (2002). "Application of prototype flume tests for beach nourishment assessment." *Coast. Eng.*, 47 (2), 137-177.

De Vriend, H. J., and Stive, M. J. F. (1987). "Quasi-3D modelling of nearshore currents." *Coast. Eng.*, 11 (5-6), 565–601.

De Vriend, H. J., Zyserman, J., Nicholson, J., Roelvink, J. A., Péchon, P., and Southgate, H. N. (1993). "Medium-term 2DH coastal area modelling." *Coast. Eng.*, 21 (1-3), 193-224.

Dibajnia, M. (1995). "Sheet flow transport formula extended and applied to horizontal plane problems." *Coastal Eng. Japan*, 38 (2), 179–194.

Dibajnia, M., Moriya, T., and Watanabe, A. (2001). "A representative wave model for estimation of nearshore local transport rate." *Coast. Eng. J.*, 43 (1), 1-38.

Dibajnia, M., Shimizu, T., and Watanabe, A. (1994). "Profile change of a sheet flow dominated beach." *Proc. 24th Int. Conf. on Coastal Engineering*, B. L. Edge, ed., Kobe, Japan, part IV, chapter 140, pp. 1946-1960.

Dibajnia, M., and Watanabe, A. (1992). "Sheet flow under nonlinear waves and currents." *Proc. 23rd Int. Conf. on Coastal Engineering*, B. L. Edge, ed., Venice, Italy, part V, chapter 155, pp. 2015-2028.

Dibajnia, M., and Watanabe, A. (1996). "A transport rate formula for mixed-size sands." *Proc. 25th Int. Conf. on Coastal Eng.*, B. L. Edge, ed., Orlando, Florida, U.S.A., part IV, chapter 293, pp. 3791–3804.

Dibajnia, M., and Watanabe, A. (1998). "Transport rate under irregular sheet flow conditions." *Coast. Eng.*, 35 (3), 167-183.

Dingler, J. R., and Inman, B. L. (1976). "Wave-formed ripples in nearshore sands." *Proc. 15th Int. Conf. on Coastal Engineering*, ASCE, Honolulu, Hawaii, U.S.A., part II, chapter 123, pp. 2109-2126.

Drønen, N., and Deigaard, R. (2007). "Quasi-three-dimensional modelling of the morphology of longshore bars." *Coast. Eng.*, 54 (3), 197–215.

Drønen, N., and Deigaard, R. (2011). "A model for wave induced erosion of sandy barriers." *Proc. 7th IAHR Symp. River, Coastal and Estuarine Morphodynamics (RCEM)*, Beijing, China.

Drønen, N., Kristensen, S., Taaning, M., Elfrink, B., and Deigaard, R. (2011). "Long term modeling of shoreline response to coastal structures." *Proceedings Coastal Sediments 2011*, P. Wang, J. D. Rosati and T. M. Roberts, eds, Miami, Florida, U.S.A, vol. 2, pp. 965-978.

Du Boys, M. P. (1879). "Le Rhône et les rivières à lit affouillable." *Mem. et Doc., Ann. Ponts Chaussées*, ser. 5, vol. XVIII, 141-195 (in french).

Dubuat, L. G. (1786). "Principes d' Hydrauliques et de Pyrodynamique." Paris. Delft Hydraulics, 1992 Scaling tests for calcareous sediments, *Report H1576*, Delft, The Netherlands.

Eagleson, P. S., and Dean, R. G. (1961). "Wave induced motion of bottom sediment particles." *Trans. ASCE*, 126 (1), 1162-1189.

Einstein, H. (1950). "The bed-load function for sediment transportation in open channel flows." U.S. Dep. Agric., *Tech. Bull.*, 1026, 71 pp.

Elfrink, B., and Baldock, T. (2002). "Hydrodynamics and sediment transport in the swash zone: a review and perspectives." *Coast. Eng.*, 45 (3-4), 149–167.

Engelund, F., and Fredsøe, J. (1976). "A sediment transport model for straight alluvial channels." *Nord. Hydrol.*, 7, 293-306.

Engelund, F., and Hansen, E. (1972). *A monograph on sediment transport in alluvial streams* (3rd edition). Technical Press, Copenhagen, Denmark, 62 pp.

Fernandez Luque, R. (1974). "Erosion and transport of bed-load sediment." Ph.D. thesis, Delft University of Technology.

Fernandez Luque, R., and van Beek, R. (1976). “Erosion and transport of bed-load sediment.” *J. Hydraul. Res.*, 14 (2), 127-144.

Fredsøe, J. (1984). "Turbulent boundary layer in wave-current motion." *J. Hydraul. Eng.*, 110 (8), 1103-1120.

Fredsøe, J., Andersen, O. H., and Silberg, S. (1985). “Distribution of suspended sediment in large waves.” *J. Waterw. Port Coast. Ocean Eng.*, 111 (6), 1041-1059.

Fredsøe, J., and Deigaard, R. (1992). "Mechanics of coastal sediment transport." *Advanced Series on Ocean Engineering*, World Scientific Publishing, Singapore, vol. 3, 369 pp.

Frijlink, H. C. (1952). “Discussion des formulas de debit solide de Kalinske, Einstein et Meyer-Peter et Müller compte tenue des measures récentes de transport dans les rivières néerlandaises.” *2ième Journal Hydr.*, Soc. Hydrotechn. de France, Grenoble, France, 98–103 (in french).

Goddet, J. (1960). "Étude du début d' entraînement des matériaux mobiles sous l' action de la houle " La Houille Blanche, No. 2, 122-135 (in french).

Gonzalez-Rodriguez, D., and Madsen, O. S. (2007). “Seabed shear stress and bedload transport due to asymmetric and skewed waves.” *Coast. Eng.*, 54 (12), 914–929.

Grass, A. J. (1981). “Sediment transport by waves and currents.” *Rep. No. FL29*, SERC London Cent. Mar. Technol., London, United Kingdom, 148 pp.

Gravens, M. B., and Wang, P. (2007). “Data report: laboratory testing of longshore sand transport by waves and currents; morphology change behind headland structures.” *Tech. Rep.*, ERDC/CHL TR-07-8, Coastal and Hydraulics Laboratory, U.S. Army Engineer Research and Development Center, Vicksburg, MS, U.S.A.

Guo, J. (2002). “Logarithmic matching and its applications in computational hydraulics and sediment transport.” *J. Hydraul. Res.*, 40 (5), 555–565.

Hallermeier, R. J. (1981). “Terminal settling velocity of commonly occurring sand grains.” *Sedimentology*, 28 (6), 859-865.

Hallermeier, R. J. (1982). “Oscillatory Bed load transport: data review and simple formulation.” *Cont. Shelf Res.*, 1 (2), 159-190.

Hanson, H., and Kraus, N. C. (2011). "Long-term evolution of a long-term evolution model." *J. Coast. Res.*, Special Issue 59, 118 – 129.

Hjulström, F. (1935). *Studies of the morphological activity of rivers as illustrated by the River Fyris Bulletin*, vol. 25, Geological Institute of Upsala, Upsala, Sweden.

Ho, H. W. (1964). “Fall velocity of a sphere in a field of oscillating fluid.” Ph.D. thesis, State Univ. of IOWA, U.S.A.

Hoefel, F., and Elgar, S. (2003). “Wave-induced sediment transport and sandbar migration.” *Science*, 299 (5614), 1885–1887.

Horikawa, K., Watanabe, A., and Katori, S. (1982). “Sediment transport under sheet flow conditions.” *Proc. 18th Int. Conf. on Coastal Engineering*, B. L. Edge, ed., Cape Town, South Africa, vol. II, pp. 1335-1352.

Huynh-Thanh, S., and Temperville, A. (1991). “A numerical model of the rough turbulent boundary layer in combined wave current interaction.” In: *Sand Transport in Rivers, Estuaries and the Sea*, R. L. Soulsby and R. Bettess, eds, Balkema, Rotterdam, pp. 93-100.

Huynh Thanh, S., Tran Thu, T., and Temperville, A. (1994). "A numerical model for suspended sediment in combined currents and waves." In: *Sediment transport mechanisms in coastal environments and rivers*, M. Belorgey, R. D. Rajaona and J. F. A. Sleath, eds, EUROMECH 310, Le Havre, Sept. 1993, World Scientific, Singapore, pp. 122- 130.

Hwang, P. A. (1985). “Fall velocity of particles in oscillating flow.” *J. Hydraul. Eng.*, 111 (3), 485-502.

Inman, O. L., and Bagnold, R. A. (1963). “Littoral processes.” In: *The Sea: Ideas and Observations on Progress in the Study of the Seas*, M. N. Hill, ed., Interscience, New York, vol. 3, pp. 529-533.

Ishihara, T., and Sawaragi, T. (1962). "Fundamental studies of sand drifts." *Coastal Eng. Japan*, 5, 59-65.

Itakura, T., and Kishi, T. (1980). "Open channel flow with suspended sediments." *J. Hydr. Div.*, 106 (8), 1325-1343.

Jobson, H. E., and Sayre, W. W. (1970). “Vertical transfer in open channels.” *J. Hydraul. Div.*, ASCE, 96 (HY3), 703-724.

Johnson, H. K., and Zyserman, J. A. (2002). “Controlling spatial oscillations in bed level update schemes.” *Coast. Eng.*, 46 (2), 109-126.

Julien, P. (1995). *Erosion and sedimentation*. Cambridge University Press, Cambridge, U.K., 390 pp.

Kaergaard, K., and Fredsøe, J. (2013a). "Numerical modeling of shoreline undulations part 1: Constant wave climate." *Coast. Eng.*, 75, 64-76.

Kaergaard, K., and Fredsøe, J. (2013b). "Numerical modeling of shoreline undulations part 2: Varying wave climate and comparison with observations." *Coast. Eng.*, 75, 77-90.

Kajima, R., Shimizu, T., Maruyama, K., and Saito, S. (1982). "Experiments on beach profile change with a large wave flume." *Proc. 18th Int. Conf. on Coastal Engineering*, B. L. Edge, ed., Cape Town, South Africa, part II, chapter 85, pp. 1385-1404.

Kalinske, A. A. (1947). "Movement of sediment as bed load in rivers." *Trans. Amer. Geophys. Union*, 28 (4), 615-620.

Kamphuis, J. W. (1991). "Alongshore sediment transport rate distribution." *Proc. ASCE Specialty Conf. Coastal Sediments '91*, N. C. Kraus, K. J. Gingerich and D. L. Kriebel, eds, Seattle, WA, U.S.A., pp. 170-183.

Kamphuis, J. W. (2000). "Introduction to coastal engineering and management." *Advanced Series on Ocean Engineering*, World Scientific Publishing, Singapore, vol. 16, 437 pp.

Kamphuis, J. W., Davies, M. H., Nairn, R. B., and Sayao, O. J. (1986). "Calculation of littoral sand transport rate." *Coast. Eng.*, 10 (1), 1–21.

Karambas, Th. V. (2012). "Design of detached breakwaters for coastal protection: development and application of an advanced numerical model." *Proc. 33rd Int. Conf. on Coastal Engineering*, P. J. Lynett and J. M. Smith, eds, Santander, Spain, 1(33), pp. 4448-4462.

Karambas, Th. V., and Karathanassi, E. K. (2004). "Longshore sediment transport by nonlinear waves and currents." *J. Waterw. Port Coast. Ocean Eng.*, 130 (6), 277-286.

Karambas, Th. V., and Koutitas, C. (2002). "Surf and swash zone morphology evolution induced by nonlinear waves." *J. Waterway, Port, Coastal, Ocean Eng.*, 10.1061/(ASCE)0733-950X(2002)128:3(102), 102-113.

Karambas, Th., Krestenitis, I., and Koutitas, Ch. (2016). *Coastal Engineering – Shore Protection Structures*. Hellenic Academic Libraries, 156 pp. (in greek).

Karambas, Th. V., and Samaras, A. G. (2014). "Soft shore protection methods: The use of advanced numerical models in the evaluation of beach nourishment." *Ocean Eng.*, 92, 129-136.

Kobayashi, N., Agarwal, A., and Bradley, D. J. (2007). "Longshore current and sediment transport on beaches." *J. Waterw. Port Coast. Ocean Eng.*, 133 (4), 296-304.

Komar, P. D. (1971). "The mechanics of sand transport on beaches." *J. Geophys. Res.*, 76, 713–721.

Komar, P. D. (1977). "Beach sand transport: Distribution and total drift." *J. Waterw. Port Coast. Ocean Div.*, ASCE, 103 (2), 225-239.

Komar, P. D., and Inman, D. L. (1970). "Longshore sand transport on beaches." *J. Geophys. Res.*, 75, 5914–5927.

Komar, P. D., and Miller, M. C. (1975). "The initiation of oscillatory ripple marks and the development of plane-bed at high shear stresses under waves." *J. Sediment Petrol.*, 45 (3), 697-703.

Koutitas, Ch. (1994). *Introduction in coastal techniques and harbor works*. Ziti Publications, Thessaloniki, Greece, 184 pp. (in greek).

Kraus, N., and Larson, M. (2001). "Mathematical Model for Rapid Estimation of Infilling and Sand Bypassing at Inlet Entrance Channels." U.S. Army Corps of Engineers, Coastal and Hydraulics Laboratory, *Technical Note CHETN-IV-35*, Vicksburg, Mississippi, U.S.A, 13 pp.

Kristensen, S. E., Drønen, N., Deigaard, R., and Fredsøe, J. (2013). "Hybrid morphological modelling of shoreline response to a detached breakwater." *Coast. Eng.*, 71, 13–27.

Larson, M. (1996). "Model of beach profile change under random waves." *J. Waterw. Port Coast. Ocean Eng.*, 122 (4), 172-181.

Larson, M., Kraus, N. C., and Wise, R. A. (1999). "Equilibrium beach profiles under breaking and non-breaking waves." *Coast. Eng.*, 36 (1), 59–85.

Larson, M., Kubota, S., and Erikson, L. (2001). "A model of sediment transport and profile evolution in the swash zone." *Proc. Coastal Dyn. '01*, H. Hanson and M. Larson, eds, ASCE, Lund, Sweden, 908–917.

Larson, M., Kubota, S., and Erikson, L. (2004). "Swash-zone sediment transport and foreshore evolution: field experiments and mathematical modeling." *Mar. Geol.*, 212 (1-4), 61–79.

Larson, M., and Wamsley, T. V. (2007). "A formula for longshore sediment transport in the swash." *Proceedings Coastal Sediments '07*, ASCE, New Orleans, U.S.A., pp. 1924–1937.

Leont'yev, I. O. (1996). "Numerical modelling of beach erosion during storm event." *Coast. Eng.*, 29 (1-2), 187-200.

Lesser, G. R., Roelvink, J. A., van Kester, J. A. T. M., and Stelling, G. S. (2004). "Development and validation of a three-dimensional morphological model." *Coast. Eng.*, 51 (8–9), 883– 915 (October).

Li, Z. and Davies, A. G. (1996). "Towards predicting sediment transport in combined wave-current flow." *J. Waterw. Port Coast. Ocean Eng.*, 122 (4), 157-164.

Lippmann, T. C., Holman, R. A. (1990). "The spatial and temporal variability of sand bar morphology." *J. Geophys. Res.*, 95 (C7), 11575–11590.

Long, W., and Kirby, J. T. (2003). "Cross-shore sediment transport model based on the Boussinesq equations and an improved Bagnold formula." *Proc. Coastal Sediments '03*, Clearwater Beach, Florida, U.S.A., May 18-23.

Long, W., and Kirby, J. T. (2006). "Boussinesq modeling of waves, currents and sediment transport." *Report CACR-06-02*, Center for Applied Coastal Research, Ocean Engineering Laboratory, University of Delaware, 323 pp.

Longuet-Higgins, M. S. (1972). "Recent progress in the study of longshore currents." In: *Waves on Beaches*, R. E. Meyer, ed., Academic Press, New York, pp. 203-248.

Madsen, O. S. (1991). "Mechanics of cohesionless sediment transport in coastal waters." *Proc. ASCE Specialty Conf. Coastal Sediments '91*, N. C. Kraus, K. J. Gingerich and D. L. Kriebel, eds, Seattle, WA, U.S.A., pp. 15-27.

Madsen, O. S. (1993). "Sediment transport on the shelf." *Proceedings Sediment Transport Workshop DRP TA1*, 8-9 June, CERC, Vicksburg, Miss., U.S.A.

Madsen, O. S., and Grant, W. D. (1976). "Sediment transport in the coastal environment." *Tech. Rep. 209*, M.I.T., Cambridge, Massachusetts, U.S.A., 105 pp.

Manohar, M. (1955). "Mechanics of bottom sediment movement due to wave action." U.S. Army Corps Engineers, Beach Erosion Board, *Tech. Memo*, No. 75, 122 pp.

Meyer-Peter, E., and Müller, R. (1948). "Formulas for bed-load transport." *Rep. 2nd Meet. Int. Assoc. Hydraul. Struc. Res.*, Stockholm, Sweden, pp. 39–64.

Ming, D., and Chiew, Y.-M. (2000). "Shoreline changes behind detached breakwater." *J. Waterw. Port Coast. Ocean Eng.*, 126 (2), 63-70.

Nairn, R. B. (1990). "Prediction of cross-shore sediment transport and beach profile evolution." Ph.D. thesis, Dept. of Civil Engineering, Imperial College, London.

Nam, P. T., Larson, M., and Hanson, H. (2010). "Modeling morphological evolution in the vicinity of coastal structures." *Proc. 32nd Int. Conf. on Coastal Engineering*, J. M. Smith and P. J. Lynett, eds, Shanghai, China, vol. 3, pp. 2127-2137.

Nam, P. T., Larson, M., Hanson, H., and Hoan, L. H. (2009). "A numerical model of nearshore waves, currents, and sediment transport." *Coast. Eng.*, 56 (11-12), 1084-1096.

Nicholson, J., Broker, I., Roelvink, J. A., Price, D., Tanguy, J. M., and Moreno, L. (1997). "Intercomparison of coastal area morphodynamic models." *Coast. Eng.*, 31 (1–4), 97– 123.

Nielsen, P. (1979). "Some basic concepts of wave sediment transport." Inst. Hydrodyn. Hydr. Eng., *Series Paper*, 20, ISVA, Techn. Univ. Denmark.

Nielsen, P. (1984). "On the motion of suspended sand particles." *J. Geophys. Res.*, 89 (C1), 616–626.

Nielsen, P. (1992). "Coastal bottom boundary layers and sediment transport."*Advanced Series on Ocean Engineering*, World Scientific Publishing, Singapore, vol. 4, 324 pp.

Nielsen, P. (2002). "Shear stress and sediment transport calculations for swash zone modelling." *Coast. Eng.*, 45 (1), 53–60.

Nielsen, P., and Callaghan, D. P. (2003). "Shear stress and sediment transport calculations for sheet flow under waves." *Coast. Eng.*, 47 (3), 347–354.

O'Connor, B. A., and Nicholson, J. (1989). "Modelling changes in coastal morphology." In: *Sediment Transport Modeling*, ASCE, S.S.Y. Wang, ed., pp. 160- 165.

O'Connor, B. A., and Nicholson, J. (1995). "Suspended sediment transport equations." *Rep. No. CE/3/95*, Department of Civil Engineering, University of Liverpool, 11 pp.

Ozasa, H., and Brampton, A. H. (1980). "Mathematical modeling of beaches backed by seawalls." *Coast. Eng.*, 4, 47–63.

Parker, G., and Kovacs, A. (1993). "MYNORCA: a Pascal program for implementing the Kovacs-Parker vectorial bedload transport relation on arbitrarily sloping beds." *Tech. Memo. No. M-233*, St. Anthony Falls Hydr. Lab., University of Minnesota, Minneapolis, U.S.A.

Rahman, S., Mano, A., and Udo, K. (2013). "Quasi-2D sediment transport model combined with Bagnold-type bed load transport." *Proc. 12th International Coastal Symposium*, Plymouth, United Kingdom, vol. 1, pp. 368-373.

Rakha, K. A. (1998). "A Quasi-3D phase-resolving hydrodynamic and sediment transport model." *Coast. Eng.*, 34 (3-4), 277–311.

Rakha, K. A., Deigaard, R., and Brøker, I. (1997). "A phase-resolving cross-shore transport model for beach evolution." *Coast. Eng.*, 31 (1-4), 231-261.

Rakha, K. A., Deigaard, R., Madsen, P. A., Brøker, I., and Rønberg, J. K. (1996). "Simulation of coastal profile development using a Boussinesq wave model." *Proc. 25th Int. Conf. on Coastal Eng.*, B. L. Edge, ed., Orlando, Florida, U.S.A., part IV, chapter 236, pp. 3048–3061.

Rance, P. J., and Warren, N. F. (1968). "The threshold of movement of coarse material in oscillatory flow." *Proc. 11th Int. Conf. on Coastal Engineering*, ASCE, London, United Kingdom, vol. I, chapter 30, pp. 487-491.

Raudkivi, A. J. (1963). "Study of sediment ripple formation." *J. Hydraul. Div.*, ASCE, 89 (HY6), 15-33.

Raudkivi, A. J. (1976). *Loose Boundary Hydraulics* (second edition). Pergamon Press, Oxford, U.K., 397 pp.

Ribberink, J. S. (1998). "Bed-load transport for steady flows and unsteady oscillatory flows." *Coast. Eng.*, 34 (1-2), 59–82.

Ribberink, J. S., and Al-Salem, A. A. (1995). "Sheet flow and suspension in oscillatory boundary layers." *Coast. Eng.*, 25 (3-4), 205–225.

Richardson, J. F., and Zaki, W. N. (1954). "Sedimentation and fluidization: Part I." *Transactions Institution of Chemical Engineers*, 32, 35-53.

Roelvink, J. A. (1991). "Modelling of cross-shore flow and morphology." *Proc. ASCE Specialty Conf. Coastal Sediments '91*, N. C. Kraus, K. J. Gingerich and D. L. Kriebel, eds, Seattle, WA, U.S.A., pp. 603-617.

Roelvink, J. A. (2006). "Coastal morphodynamic evolution techniques." *Coast. Eng.*, 53 (2-3), 277-287.

Roelvink, J. A., and Brøker, I. (1993). "Cross-shore profile models." *Coast. Eng*., 21 (1-3), 163-191.

Roelvink, J. A., and Reniers, A. J. H. M. (1995). "LIP 11D delta flume experiments." *Delta data Rep. H 2130*, Delft Hydraulics , Delft, The Netherlands.

Roelvink, D., and Reniers, A. (2012). "A guide to modeling coastal morphology." *Advances in Coastal and Ocean Engineering*, vol. 12, World Scientific, 274 pp.

Roelvink, D., Reniers, A., van Dongeren, A., van Thiel de Vries, J., McCall, R., and Lescinski, J. (2009). "Modelling storm impacts on beaches, dunes and barrier islands." *Coast. Eng.*, 56 (11-12), 1133-1152.

Roelvink, J. A., and Stive, M. J. F. (1989). "Bar-generating cross-shore flow mechanics on a beach." *J. Geophys. Res.*, 94 (C4), 4785–4800.

Roelvink, J. A., and van Banning, G. K. F. M. (1994). "Design and development of Delft3D and application to coastal morphodynamics." *Hydroinformatics '94*, A. Verwey, A. W. Minns, V. Babovic, and M. Maksimovic, eds, Balkema, Rotterdam, The Netherlands, pp 451-456.

Roelvink, J. A., Walstra, D. J. R., and Chen, Z. (1994). "Morphological modelling of Keta lagoon case." *Proc. 24th Int. Conf. on Coastal Engineering*, B. L. Edge, ed., Kobe, Japan, part V, chapter 232, pp. 3223-3236.

Rose, C. P., and Thorne, P. D. (2001). "Measurements of suspended sediment transport parameters in a tidal estuary." *Cont. Shelf Res.*, 21 (15), 1551-1575.

Sato, S., and Horikawa, K. (1986). "Laboratory studies on sand transport over ripples due to asymmetric oscillatory flows." *Proc. 20th Int. Conf. on Coastal Engineering*, B. L. Edge, ed., Taipei, Taiwan, vol. II, chapter 109, pp. 1481-1495.

Sato, S., and Mitsunobu, N. (1991). "A numerical model of beach profile change due to random waves." *Proc. ASCE Specialty Conf. Coastal Sediments '91*, N. C. Kraus, K. J. Gingerich and D. L. Kriebel, eds, Seattle, WA, U.S.A., pp. 674-687.

Sawamoto, M., and Yamashita, T. (1986). "Sediment transport rate due to wave action." *J. Hydrosci. Hydraul. Eng.*, 4 (1), 1–15.

Schoklitsch, A. (1934). "Der Geschiebetrieb und die Geschiebefracht." *Wasserkraft und Wasserwirtschaft*, 29 (4), 37–43 (in German).

Shields, A. (1936). "Anwendung der Ähnlichkeitsmechanik und der Turbulenzforschung auf die Geshiebebewegung." Preussische Versuchsanstalt fur Wasserbau und Schiffbau, *Heft*, 26, 5-24.

Shimizu, T., Sato, S., Maruyama, K., Hasegawa, H., and Kajima, R. (1985). "Modeling of cross-shore sediment transport rate distributions in a large wave flume." Central Res. Inst. Electr. Power Ind., Tokyo, Japan, *Rep. No. 384028*, 60 pp (in japanese).

Short, A. D. (1978). "Wave power and beach stages - a global model." *Proc. 16th Int. Conf. on Coastal Engineering*, ASCE, Hamburg, Germany, vol. II, chapter 66, pp. 1145-1162.

Simons, D. B., and Richardson, E. V. (1961). "Forms of bed roughness in alluvial channels." *J. Hydraul. Div.*, ASCE, 87 (HY3), 87-105.

Sleath, J. F. A. (1978). "Measurements of bed load in oscillatory flow." *J. Waterw. Port Coast. Ocean Div.*, ASCE, 104 (WW3), 291-307.

Sleath, J. F. A. (1984). *Sea Bed Mechanics*. Wiley, 335 pp.

Smith, J. D., and McLean, S. R. (1977). "Spatially averaged flow over a wavy surface." *J. Geophys. Res.*, 82 (12), 1735-1746.

Sonu, C. J. (1973). "Three-dimensional beach changes." *J. Geol.*, 81 (1), 42-64.

Sorensen, R. M. (2006). *Basic coastal engineering* (third edition). Springer, 324 pp.

Soulsby, R. (1997). *Dynamics of marine sands, a manual for practical applications*. Thomas Telford, H.R. Wallingford, England, 249 pp.

Soulsby, R. L., and Whitehouse, R. S. (1997). "Threshold of sediment motion in coastal environment." *Proc. Conf. on Pacific Coasts and Ports*, University of Canterbury, Christchurch, New Zealand, 149-154.

Steetzel, H. J. (1990). "Cross-shore transport during storm surges." Proc. *22nd Int. Conf. on Coastal Engineering*, B. L. Edge, ed., Delft, The Netherlands, part IV, chapter 145, pp. 1922-1934.

Sternberg, H. (1875). "Untersuchungen über Längen-und querprofil geschiebeführender flüsse." *Zeitschrift für Bauwesen*, 25, 483-506 (in german).

Stive, M. J. F. (1986). "A model for cross-shore sediment transport." Proc. *20th Int. Conf. on Coastal Engineering*, B. L. Edge, ed., Taipei, Taiwan, part II, chapter 114, pp. 1550-1564.

Stive, M. J. F., and Battjes, J. A. (1984). "A model for offshore sediment transport." Proc. *19th Int. Conf. on Coastal Engineering*, B. L. Edge, ed., Houston, Texas, U.S.A., part II, chapter 97, pp. 1420-1436.

Stokes, G. G. (1851). "On the effect of internal friction of fluids on the motion of pendulums." *Trans. Cambridge Philos. Soc.*, IX, pp. 8-106.

Sumer, B. M., and Deigaard, R. (1981). "Particle motions near the bottom in turbulent flow in an open channel. Part 2." *J. Fluid Mech.*, 109, 311-337.

Swart, D. (1974). "Offshore sediment transport and equilibrium beach profiles."*Tech. Rep*., Delft Hydraulics Lab. Publ. No. 131, Delft, The Netherlands.

Swart, D. H. (1976). "Predictive equations regarding coastal transports." *Proc. 15th Int. Conf. on Coastal Engineering*, ASCE, Honolulu, Hawaii, U.S.A., pp. 1113-1132.

Tanguy, J. M., Zhang, B., and Hamm, L. (1993). "A new Lax-Wendroff algorithm to solve the bed continuity equation with slope effect." *Proc. 3rd Int. Conf. on Coastal Estuarine Modeling*, ASCE, M. L. Spaulding, ed., Oak Brook, Illinois, U.S.A., pp. 134-148.

Thornton, E. B. (1972). "Distribution of sediment transport across the surf zone." *Proc. 13th Int. Conf. on Coastal Engineering*, ASCE, Vancouver, Canada, pp. 1049-1068.

Trowbridge, J., and Young, D. (1989). "Sand transport by unbroken water waves under sheet flow conditions." *J. Geophys. Res.*, 94 (C8), 10971-10991.

Van de Graaff, J., and van Overeem, J. (1979). "Evaluation of sediment transport formulae in coastal engineering practice." *Coast. Eng.*, 3, 1–32.

Van der Werf, J., and Ribberink, J. (2004). "Wave induced sediment transport processes in the ripple regime." *Proc. 29th Int. Conf. on Coastal Engineering*, J. M. Smith, ed., Lisbon, Portugal, vol. 2, chapter 139, pp. 1741-1753.

Van Dongeren, A. R., Wenneker, I., Roelvink, D., and Rusdin, A. (2006). "A Boussinesq-type wave driver for a morphodynamical model." *Proc. 30th Int. Conf. on Coastal Engineering*, J. M. Smith, ed., San Diego, U.S.A., vol. 3, pp. 3207-3219.

Van Rijn, L. C. (1984a). "Sediment transport, part I: bed load transport." *J. Hydraul. Eng.*, 110 (10), 1431-1456.

Van Rijn, L. C. (1984b). "Sediment transport, part II: suspended load transport." *J. Hydraul. Eng.*, 110 (11), 1613-1641.

Van Rijn, L. C. (1984c). "Sediment transport, part III: bed forms and alluvial roughness." *J. Hydraul. Eng.*, 110 (12), 1733-1754.

Van Rijn, L. (1989). "Handbook Sediment Transport by Currents and Waves." *Rep. No. H 461*, Delft Hydraulics, Delft, The Netherlands.

Van Rijn, L. (1993). *Principles of Sediment Transport in Rivers, Estuaries and Coastal Seas*. Aqua Publications, Amsterdam, The Netherlands.

Van Rijn, L. C. (2007a). "Unified view of sediment transport by currents and waves. I: Initiation of motion, bed roughness, and bed-load transport." *J. Hydraul. Eng.*, 133 (6), 649-667.

Van Rijn, L. C. (2007b). "Unified view of sediment transport by currents and waves. II: Suspended transport." *J. Hydraul. Eng.*, 133 (6), 668-689.

Vellinga, P. (1982). "Beach and dune erosion during storm surges." *Coast. Eng.*, 6 (4), 361-387.

Vincent, G. E. (1957). "Contribution to the study of sediment transport on a horizontal bed due to wave action." *Proc. 6th Int. Conf. on Coastal Engineering*, J. W. Johnson, ed., Gainesville, Florida, U.S.A., part 2, chapter 20, pp. 326-355.

Wai, O. W. H., Chen, Y., and Li, Y. S. (2004). "A 3-D wave-current driven coastal sediment transport model." *Coast. Eng. J.*, 46 (4), 385-424.

Watanabe, A. (1988) "Modeling of sediment transport and beach evolution." In: *Nearshore Dynamics and Coastal Processes*, K. Horikawa, ed., University of Tokyo Press, Tokyo, Japan, pp. 292– 302.

Watanabe, A. (1994). "A mathematical model of beach processes under sheet-flow condition using nonlinear wave theory." *Int. Symp. on Waves - Physical and Numerical Modelling*, Vancouver, B.C., pp. 1520-1529.

Watanabe, A., and Dibajnia, M. (1988). "Numerical modelling of nearshore waves, cross-shore sediment transport and beach profile change." *Proc. IAHR Symp. on Mathematical Modelling of Sediment Transport in the Coastal Zone*, Copenhagen, Denmark, pp. 166-174.

Wenneker, I., van Dongeren, A., Lescinski, J., Roelvink, D., and Borsboom, M. (2011). "A Boussinesq-type wave driver for a morphodynamical model to predict short-term morphology." *Coast. Eng.*, 58 (1), 66‑84.

Willis, D. H. (1978). "Sediment load under waves and currents." *Proc. 16th Int. Conf. on Coastal Engineering*, ASCE, Hamburg, Germany, vol. II, chapter 97, pp. 1626-1637.

Wilson, K. C. (1966). "An expression for bed-load transportation." *J. Hydraul. Div.*, ASCE, 92 (HY6), 49-59.

Wilson, K. C. (1989). "Friction of wave-induced sheet flow." *Coast. Eng.*, 12 (4), 371‑379.

Winkelmolen, A. M. (1971). "Rollability, a functional shape property of sand grains." *J. Sediment Petrol.*, 41 (3), 701-714.

Yalin, M. S. (1963). "An expression for bed-load transportation." *J. Hydraul. Div.*, ASCE, 89 (HY3), 221–250.

Zyserman, J. A., and Fredsøe, J. (1994). "Data analysis of bed concentration of suspended sediment." *J. Hydraul. Eng.*, 120 (9), 1021-1042.

Chapter 5

Laboratory experiments with submerged breakwaters

5.1 Introduction

Shorelines are naturally dynamic and continuously changing because of the ever-going interaction among sea-level changes, tides, currents, wind, waves, storms, and extreme events. The combined action of these agents results to morphological changes involving accretion or erosion on a continuous basis along the coasts. In addition to natural processes, coastal erosion is intensified by human interventions along the coasts, within river catchments and offshore, raising social, environmental and economic concerns in the long term. This variety of erosion drivers, especially in areas with rapidly rising coastal land value, have led to uncertainties on how to treat the shoreline evolution (Prasetya, 2007; Sharif Ahmadian, 2016).

The engineering interventions to prevent erosion vary from a 'do nothing' approach to 'hard' protection projects. Traditionally, this latter approach has been the most popular including conventional coastal structures to control longshore currents or absorb wave energy and trap the moving sediments. These structures include groynes, breakwaters, seawalls, revetments, dikes, artificial headlands, etc.

In the last decades, alternative 'soft' protection solutions are becoming more and more popular due to the adverse impact of hard works on the beach environmental value, amenity and aesthetics. Such milder interventions include beach nourishment, submerged groynes, submerged breakwaters, beach drainage, sand dune management, or combination of protection measures, e.g. beach replenishment combined with submerged breakwaters, etc. In particular, submerged breakwaters are environmental friendlier and aesthetically superior to conventional emerged breakwaters and, as a result, there is an increased community pressure on coastal management authorities and government agencies to consider the former for beach protection (Evans and Ranasinghe, 2001).

The use of emerged breakwaters is very common in U.S.A. and Europe (Dean and Dalrymple, 2001), and even more in Japan (Seiji *et al*., 1987). In contrast, fully submerged structures have only rarely been adopted for coastal protection. Although natural submerged reefs have been observed to be associated with shoreline salients, and thus provide beach protection (Black and Andrews, 2001), the reported investigations of shoreline response to submerged breakwaters are few in number and many times inconsistent with each other. It should be mentioned that some investigations have shown that submerged breakwaters may result in shoreline erosion in the lee of the structure, which is something that has almost never been reported for emerged breakwaters. Therefore, it is likely that the processes that govern the shoreline response to submerged and emerged breakwaters are different, and thus the well established methods used for the latter may not be accurate for the former (empirical relationships, one-line models). However, until recently, the design of submerged breakwaters (structure length, distance from shoreline, gaps in an array, free board) was rather empirical (Lesser *et al*., 2003) and it was mainly based on the experience with conventional breakwaters (Pilarczyk, 2003). Consequently, in some cases the design was very efficient, while in others it was rather not successful and increased erosion was observed in the lee of the structures. A quite extensive review regarding projects involving submerged breakwaters was presented by Ranasinghe and Turner (2006). A number of such projects are summarized in table 5.1.

Table 5.1. Features of various projects including submerged structures (*B*: length of structure, *S*: distance from undisturbed shoreline, *W*: crest width, *h*: water depth at structure, h_c: water depth at crest of the structure, tanβ: bed slope in the vicinity of the structure, MLW: mean low water, MWL: mean water level, MSL: mean sea level, MLLW: mean lower low water, from Ranasinghe and Turner, 2006, modified).

Location	Reference	Structure type	Shoreline response to structures	Nourishment	Longshore transport rate (m^3/year)	*B* (m)	*S* (m)	*W* (m)	*h* (m)	h_c (m)	tanβ
Delaware Bay, USA	Douglass and Weggel (1987)	Single breakwater +2 end groynes	Erosion	Yes	Negligible	300	75	Not reported	1	At MLW	Not reported
Keino-Matsubara Beach, Japan	Deguchi and Sawaragi (1986)	Single breakwater	Erosion	Yes	Not reported	80	85	20	4	2 m below MLW	0.1 nearshore and 0.03 offshore
Niigata, Japan	Funakoshi *et al*. (1994)	Single breakwater +2 groynes	Erosion	No	Exists, but not quantified	540	400	20	8.5	1.5 m below MWL	0.02
Lido di Ostia, Italy (#1)	Tomassicchio (1996)	Single breakwater	Erosion	Yes	50000	3000	100	15	4	1.5 m below MSL	0.05
Lido di Ostia, Italy (#2)	Tomassicchio (1996)	Single breakwater	Accretion	No	50000	700	50	15	3-4	0.5 m below MSL	0.1
Lido di Dante, Italy	Lamberti and Mancinelli (1996)	Single breakwater	Accretion	Yes	Negligible	770	150	12	3	0.5 m below MSL	0.02

Marche, Italy	Lamberti and Mancinelli (1996)	Multiple segmented breakwaters	Erosion	No	Negligible	Not reported	100-200	10-12	3	0.5 m below MSL	Not reported
Palm Beach, FL, USA	Dean *et al*. (1997)	Single breakwater	Erosion	No	100000	1260	70	4.6	3	0.7 m below MLLW	0.04
Vero Beach, FL, USA	Stauble *et al*. (2000)	Segmented breakwater	Erosion	No	30000	915	85	4.6	2.1-2.7	0.25 – 0.35 m below MLW	0.03
Gold Coast, Australia	Jackson *et al*. (2002)	Multi-function surf reef	Accretion	Yes	500000	350	100-600	2	2-10	1 m below MLW	0.02

It is of particular note that, of the 10 submerged structures presented in table 5.1, net erosion was reported at seven of the sites. In most of these cases structures were accompanied by beach nourishment and no comparisons with previous to construction shoreline response were reported. It was only Tomassicchio (1996), Dean *et al*. (1997) and Stauble *et al*. (2000) that referred to such comparisons. With regard to the larger submerged breakwater in Lido di Ostia, analysis of aerial photographs before and after construction indicated that no detectable benefit was provided, and that erosion rates in the vicinity of the structure remained unchanged. In Palm Beach monitoring indicated that the erosion which occurred in the lee of the structure was twice as much as the background erosion in the area. This was attributed to insufficient wave attenuation over the structure due to the low crest level. Similarly, in Vero Beach the resulting erosion from the construction of the breakwater was greater than at adjacent beaches over the 3-year monitoring period (1996-1999).

Research regarding submerged breakwaters started in recent years and focused on laboratory experiments, numerical models and field measurements in order to investigate their hydrodynamic and morphodynamic impact on coastal zone. The present chapter refers to the laboratory experiments that have been performed during the thesis and thus focuses on the physical modelling of the behaviour of permeable submerged breakwaters. The greatest part of the related research refers to two-dimensional (2D or 1DH) phenomena and mostly to wave transmission, wave reflection and wave setup. In particular, wave transmission is a very important criterion in the design of submerged breakwaters, especially in preliminary stages of design. Although very encouraging 2D design tools have been developed for both impermeable and permeable submerged breakwaters, very few studies have focused on the fully 3D effects. This is an important issue since it has been shown that formulae for 2D wave transmission tend to underestimate the 3D data (Vicinanza *et al*., 2009). In addition, the impact of submerged breakwaters on the sea bed and shoreline evolution has not been yet understood in depth.

The first reported physical experiment on wave transmission behind submerged breakwaters was performed by Stucky and Bonnard (1937) who used a 2D (1DH) trapezoidal section,

while Morison (1949) and Johnson *et al*. (1951) examined rectangular breakwaters. In this latter experiment, steeper waves tended to result in greater energy dissipation as the bar crest became wider, while longer waves were generally less affected. Laboratory experiments with impermeable breakwaters by Goda *et al*. (1967) and Goda (1969) showed that the transmission coefficient K_t is mostly governed by the ratio of the free board (water depth above the bar crest) to the incidence wave height and that generated higher harmonics are present in the transmitted waves.

Since then a number of laboratory experimental studies have been performed to obtain useful results and empirical formulae for various parameters related to both impermeable and permeable, low-crested and submerged breakwaters (Diskin *et al*., 1970; Seelig, 1980; Abdul Khader and Rai, 1980; Allsop, 1983; Powell and Allsop, 1985; Ahrens, 1987; van der Meer, 1988; Davies and Kriebel, 1992; Seabrook and Hall, 1997; Hayakawa *et al*., 1998; Bleck and Oumeraci, 2001; Vidal *et al*., 2002; Lamberti *et al*., 2003; Zanuttigh *et al*., 2003; Zanuttigh and Lamberti, 2006; Tajziehchi and Cox, 2006; Kobayashi *et al*., 2007; Lykke Andersen and Burcharth, 2008). Gourlay (1993; 1996a,b) conducted 2D and 3D laboratory experiments to measure wave transformation, wave-induced setup and current over reefs. They found that both current and setup increase with incident wave height, while submergence depth has respectively direct and inverse effects on current and setup. 2D and 3D laboratory tests were also conducted by Debski and Loveless (1997) and Loveless *et al*. (1998) in a wave flume and a wave basin, respectively, and they observed that the wave-induced setup is significantly smaller in 3D tests as the water level gradient behind the breakwater generates longshore flow. Drei and Lamberti (1999) carried out laboratory experiments under regular and irregular wave attack in a wave flume in the presence of narrow-crested impermeable submerged breakwaters. They demonstrated that wave setup at submerged breakwaters is higher than provided by the setup theory for beaches.

Kriezi and Karambas (2010) studied the wave transmission and reflection in presence of monolithic rectangular submerged breakwaters both experimentally and numerically under breaking and nonbreaking regular and irregular waves. The experiments were conducted in the large-scale facilities of the Universitat Politècnica de Catalunya, Barcelona, Spain. Vanlishout *et al*. (2010) studied the interaction of oblique waves with impermeable rubble-mound submerged breakwaters experimentally and they showed that the permeability has no significant impact on the wave transmission for oblique wave incidence. Del Jesus (2011) carried out 3D laboratory measurements to study the performance of an existing submerged breakwater in Santa Monica (see also Lara *et al*., 2012). Metallinos and Memos (2012) and Metallinos *et al*. (2014, 2016) performed a number of 1DH laboratory experiments in a wave flume in order to study the wave-induced kinematics and porous pressures inside a permeable

submerged breakwater under regular wave action. Based on these measurements Samlidis (2014) calculated the wave transmission coefficient.

Perhaps the most complete database referring to low-crested and submerged breakwaters is the one produced in DELOS project. This database consists of more than 2300 tests (Kramer *et al*., 2005). The data were applied and analyzed to provide new empirical formulae for the wave transmission, the interaction of low-crested structures and oblique wave action, reflection, and 3D effects (van der Meer *et al*., 2005). As part of this project Kramer *et al*. (2003, 2005) conducted a series of 3D experiments in the wave basin at Aalborg University, Denmark, including two submerged breakwaters. They studied the effect of the crest width, the free board and the wave irregularity.

Apart from laboratory experiments, a small number of datasets referring to field measurements around submerged breakwaters have been also reported. Browder and Dean (1996) showed that the erosion of the beach behind a 594 m shoreline-parallel precast concrete submerged breakwater in Palm Beach, Florida, U.S.A., was 2.3 times higher than before the construction of the breakwater. Tomasicchio (1996) investigated the long rubble-mound submerged breakwater at Ostia, Roma, Italy. Apart from the low construction cost, the environmental impact was evaluated as low, and the energy dissipation, sediment transport and shoreline protection were satisfactory. Turner (2006) presented field measurements with regard to the shoreline evolution in the lee of the artificial reef at the norther Gold Coast, Queensland, Australia.

Although a number of laboratory experiments about wave propagation over submerged breakwaters have been conducted, the same is not true for the morphodynamics in the lee of these structures. Such an example is the 3D experiments conducted by Groenewoud *et al*. (1996) in a wave basin which illustrated the effect of the gap length between the segmented submerged breakwaters on the shoreline response. In addition, an analysis of extensive series of laboratory measurements by van der Biezen *et al*. (1997) showed significant sediment loss through the aforementioned gaps. The performance of the artificial reef at Gold Coast was also investigated using a physical model in a wave basin by Turner *et al*. (2001). A view of the artificial reef and Turner *et al*.'s (2001) physical model is depicted in Fig. 5.1 where the formation of a salient in the lee of the structure is apparent. The shape of the reef resembles letter V from a plan view (V-shaped). The 3D morphodynamic effects were also studied experimentally in a wave basin by Ranasinghe *et al*. (2006). An empirical formula for the shoreline response was proposed and the results illustrated the importance of the predominant wave incidence angle, the submergence depth and the distance of the submerged breakwaters from the beach on the resulting erosion or accretion.

Fig. 5.1. Aerial view of the V-shaped artificial reef at the Gold Coast, Australia (at left) and the corresponding physical model at the Water Research Laboratory of University of New South Wales, Australia (at right, from Ranasinghe and Turner, 2006).

The present Ph.D. dissertation included also laboratory experiments referring to morphodynamics in the lee of a permeable submerged breakwater. Hence, this work contributes also to filling a gap in physical modelling projects related to submerged breakwaters, especially with regard to geomorphology. The experiments were performed at the facilities of the Hydraulic Engineering Laboratory of the Civil Engineering Department at the University of Patras, Greece. The present chapter is dedicated to the presentation of the experimental process which is described in detail after some short discussion on general features of submerged breakwaters in subsection 5.2.

5.2 Submerged breakwaters for coastal protection

5.2.1 General features of submerged breakwaters

Recently, submerged breakwaters have become an attractive alternative of soft coastal protection for recreational and residential coastal areas. They form a special case of low-crested breakwaters as their crest is constructed below the mean water level. They are usually made of rock armoured rubble-mound or concrete, similarly to the conventional emerged breakwaters. In some cases concrete blocks of special shape may be used, such as tripods, tetrapods, dolos, reef-balls or geotubes and geocontainers to reduce the danger for swimmers and boats.

During the last years, there is an increasing social reaction against hard engineering structures both along and at a distance from the shoreline. Submerged breakwaters serve as a viable alternative, provided that they are efficiently designed. A single or an array of breakwaters may be constructed. In the latter case the gaps between the structures are of specific length as a result of optimization. Submerged breakwaters can be also constructed in combination with beach fill projects to better retain the nourished sediment. They can be also

used in more complex systems combined with groynes (submerged or not) or/and seawalls in coastal areas of increased erosion. Finally, they can be used as a first defense line to extreme energy regimes before waves approach the main protection structures (Cornett *et al*., 1994).

Submerged breakwaters are permanently underwater, in contrary to sub-aerial low-crested breakwaters whose crest is built close to the high tide level. On the other hand, artificial reefs are usually structures that are built in much deeper water for environmental and fishing purposes, rather than effective energy dissipation. Due to their underwater crest, submerged breakwaters reduce the intensity of the wave action but permit some wave transmission, allowing water circulation in the nearshore zone. This sufficient water exchange results in a nature-friendly beach, providing a calm, sheltered area behind the structure. They are usually placed at depths at least 3-4 m in areas with low tide variation. On the other hand, their effectiveness in coastal areas with large tidal range or intense storm surges is questionable. In these cases they are constructed with a larger crest width resulting in a significant increase of the cost (Pilarczyk, 2003) and they are rather classified as artificial reefs. A sketch of a typical section of a submerged breakwater is shown in Fig. 5.2. A view of a composite coastal intervention in Pallestrina island in Venice, Italy is shown in Fig. 5.3. This project includes nourishment, both emerged and submerged groynes, and submerged breakwaters.

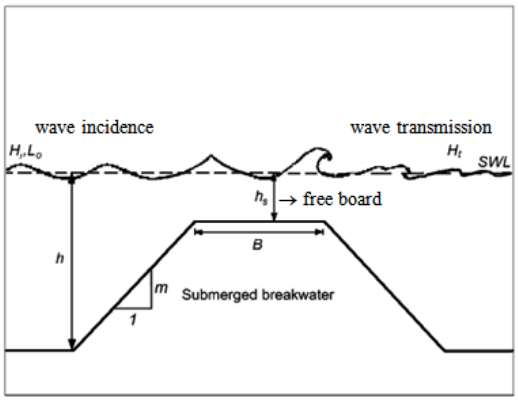

Fig. 5.2. Sketch of a typical section of a submerged breakwater and relevant parameters (from Sharif Ahmadian, 2016, modified).

The advantages of submerged breakwaters over the conventional ones are summarized as follows:

- They are more environmentally friendly since they are less bulky works and thus they imply lower level of nuisance upon the sea bed flora and fauna both during the construction period and after that.
- They allow the circulation and renewal of the water both above their crest and through the gaps between the breakwaters in an array.

- They are superior with respect to aesthetics since they do not interrupt the clear view of the sea from the beach. Consequently they contribute in retaining the touristic value of the coastal area.
- They are generally of lower cost.
- They allow the passage of vessels through the gaps between them.
- Permeable submerged breakwaters support marine life by providing potential habitats to species.

On the other hand, disadvantages are:

- Very low crests may not imply adequate wave energy dissipation and consequently provide ineffective protection against beach erosion, especially in high energy regimes or in areas with high tide levels.
- They may hamper sediment transport under hydrodynamic conditions that would physically result to accretion in the absence of the structures.
- They may imply dangers with regard to the passage of vessels and boats since they are not visible and also due to the high water velocities above their crest. For these reasons the presence of submerged breakwaters should be signed adequately.
- Their construction may result to an abrupt change of the hydrodynamic conditions and possibly to the generation of currents that enhance bed erosion, instead of preventing it. In addition, submerged breakwaters may induce high velocities, especially near the breakwater heads and at the gaps, which may result to scour around the structures or enhanced bed erosion.
- The rip currents through the gaps between the submerged breakwaters are very dangerous for swimmers since they can drift them offshore.
- The inspection of submerged breakwaters is difficult because the entire structures are below the sea water level.
- Although submerged breakwaters are generally of lower cost, in some cases the construction may be costly due to the firm requirement of using barges or other floating equipment.

Fig. 5.3. View of a composite coastal protection project including submerged breakwaters in Pallestrina island in Venice, Italy (photo: DELOS project, www.delos.unibo.it).

Although research concerning submerged breakwaters has significantly advanced during the past years, there are still many issues to be clarified to improve our understanding of the flow around them and thereby produce more effective design methods and tools.

5.2.2 Coastal processes and submerged breakwaters

There are numerous physical processes involved in the wave transformation in the presence of submerged breakwaters, including shoaling, refraction, diffraction, reflection, wave breaking, overtopping, and generation of higher harmonics. A functional design of submerged breakwaters requires accurate prediction of the wave transmission and the wave setup in the sheltered areas. Therefore, the combination and interaction of the aforementioned phenomena have to be taken into account.

As already known from wave theory, shoaling takes place due to both the sloping sea bed and also over the upslope of the submerged breakwater. However, the structure is permeable and thus using the freeboard along its perimeter as water depth for the computation of shoaling is not in principle accurate. Moreover, if the wave incidence is oblique then depth refraction also takes place. In parallel, generation of higher harmonics also occurs (Beji and Battjes, 1993, 1994). This is a process mostly related to long incident waves. As the waves travel upslope, gradually lose their vertical symmetry and obtain a saw-toothed shape. In this phase bound harmonics -primarily of second order- are generated by self-interactions. Over the breakwater crest the waves are virtually non-dispersive, the triplet resonance conditions are nearly satisfied and very rapid energy flow takes place from the primary waves to higher harmonics. This energy transfer coupled with the nonlinear amplitude dispersion results in the formation of dispersive tail waves travelling at nearly the same celerity as the primary waves.

However, their celerity is not exactly the same as the one of the primary waves since it also depends on the wave amplitude which is still larger for the latter components. This explains an increasing phase-lag between the primary and the secondary waves over the crest of the structure. As the wave train moves downslope and de-shoaling takes place, the wave train is decomposed into several smaller amplitude waves of nearly harmonic frequency. This exchange of energy continues at a high rate for several wavelengths down-wave before an equilibrium is reached. This result can be also observed in the simulation of Beji and Battjes's (1994) tests in chapter 2. Again, the permeability of the breakwaters weakens the aforementioned phenomenon.

When the incident waves meet a submerged breakwater a part of the wave energy is reflected offshore, another part is dissipated and a third one is transmitted onshore. The amount of reflection depends mainly on the forward face slope and the submergence depth of the breakwater (Dattari *et al*., 1978; Ahrens, 1987, 1988; van der Meer, 1991) but, in general, it is of the order of 20% for usual structure slopes (Karambas *et al*., 2016). It should be mentioned that reflection may also alter the direction of the incoming waves. Energy dissipation takes place due to mainly three mechanisms shown in Fig. 5.4: wave breaking, friction at the outer surface of the breakwater and flow through the porous medium. When low-crested breakwaters are used the transmitted part of the energy is related also to the overtopping of the structure, while for submerged breakwaters transmission refers to the waves propagating behind the obstacle. Due to the combined aforementioned processes, the transmission coefficient, $K_t = H_t/H_i$, where H_t is the wave height of the transmitted wave and H_i the wave height of the incident wave, depends on a number of factors related to energy dissipation. A number of empirical formulae have been proposed for the estimation of the transmission coefficient relying on geometrical characteristics (free board, crest width, slopes of the breakwater) and wave characteristics (Ahrens, 1987; d' Angremond *et al*., 1996; Calabrese *et al*., 2002; Briganti *et al*., 2003; van der Meer *et al*., 2005). A typical value of the transmission coefficient falls within the range $K_t = 0.3 \div 0.6$, while for conventional emerged breakwaters it is less than 0.10.

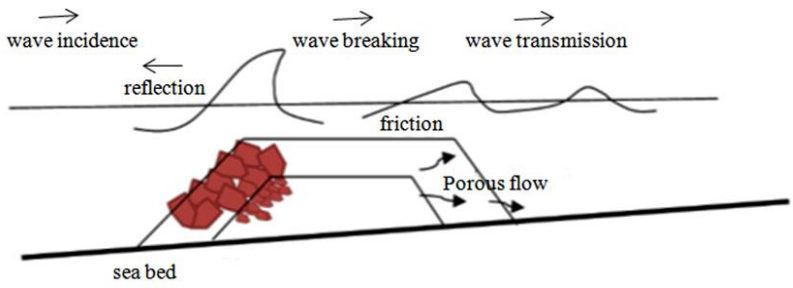

Fig. 5.4. Typical section of a submerged breakwater and mechanisms of energy dissipation (from Karambas *et al*., 2016, modified).

Diffraction also takes place around the heads of the submerged breakwaters. The waves encounter a sudden change in bathymetry and consequently some of their energy will be forced to move along the wave crest. In reality, shoaling, refraction and diffraction all occur simultaneously. Vicinanza *et al*. (2009) studied the wave disturbance behind low-crested breakwaters. The crest of these structures is slightly above the mean water level and, thus, their hydrodynamic behaviour is close to that of submerged breakwaters (Karambas *et al*., 2016). When waves meet a low-crested structure, water may pass over it. This phenomenon is called overtopping and it is often followed by wave transmission at the lee side of the structure. If the breakwaters are permeable, percolation also takes place through their pores. The significance of the effect of three-dimensionality increases with the importance of diffraction and with the reduction of overtopping or permeability of the breakwater or the length of the structure compared to the incident wavelength.

Vicinanza *et al*. (2009) estimated a global transmission coefficient for low-crested breakwaters by summing up the energy contributions due to diffraction and 2D (1DH) overtopping. They ignored the permeability effects because there are indications that these significantly correlate with wave diffraction and overtopping. When permeability increases, the diffracted waves are expected to reduce (Penney and Price, 1952). In particular, the diffraction effect reduces in intensity, thus the diffracted waves become blurred with the main wave field. These considerations were made for low-crested breakwaters, while 3D effects have not yet been studied in depth for submerged breakwaters. However, the aforementioned conclusion was also supported by numerical experiments that were carried out in the present thesis. On the other hand, diffraction and 2D wave transmission were assumed to be uncorrelated and the total transmission coefficient is given by

$$K_{d,t} = \sqrt{{K_d}^2 + {K_t}^2} \tag{5.1}$$

where K_d is the wave diffraction coefficient and K_t is the 2D (or 1DH) transmission coefficient.

A decrease in the mean water level upwave of the breaking line appears as a result of shoaling. Down-wave of the breaking point, the wave energy flux and the radiation stresses decrease due to energy dissipation and consequently an increase of the mean water level takes place. The gradient of the wave-induced setup behind a submerged breakwater causes water to flow along the shoreline resulting to the formation of two vortices of opposite direction. This wave-induced circulation differs from the one behind an emerged breakwater because in the former case the vortices are closer to the shoreline. This difference results from the breaking-induced mass flux that takes place over a submerged breakwater. This mechanism tends to increase the mean water elevation behind the structure resulting to the generation of

offshore-directed rip currents through the gaps of an array of submerged breakwaters. A schematic view of the different expected nearshore circulation patterns behind a system of submerged and emerged breakwaters is depicted in Fig. 5.5. It should be noted that in the case of the submerged breakwaters the shown vortices refer only to the principal circulation due to the onshore mass flux above the bar and the resulting rip currents.

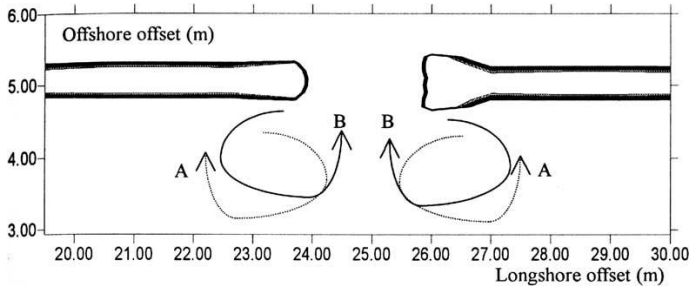

Fig. 5.5. Schematic depiction of the different expected nearshore circulation patterns in the vicinity of emerged (pattern 'A') and submerged (pattern 'B') breakwaters (from Loveless and MacLeod, 1999).

The main scope of submerged breakwaters is to prevent erosion and stabilize the sediments close to the shoreline. Morphodynamic predictions in the lee of submerged breakwaters is a great challenge for coastal engineers due to the high level of uncertainties involved in all the aforementioned complex hydrodynamic processes and also to the lack of systematic knowledge on the related morphological processes. In general, the above described vortices due to the alongshore variation of wave height, along with the waves, tend to transport the sand from the edges of the field towards the center of the shadow of a submerged breakwater creating a salient, but also causing erosion at the side. On the other hand, the rip currents erode the sea bed, especially near the gaps between the breakwaters.

Widely accepted design rules have not been proposed for submerged breakwaters with respect to morphodynamics. In practice, similar guidelines as the ones for emerged breakwaters are followed but also including the transmission coefficient (Pilarczyk, 2003; Burcharth *et al*., 2007; Koutsouvela *et al*., 2007; Karambas *et al*., 2016). Pilarczyk (2003) mentions that a tombolo is formed if a submerged breakwater is constructed very much close to the shoreline. However, in the present thesis, neither the laboratory experiments, nor the numerical ones ever led to such a morphological feature. Thus, reservations are expressed about this issue. A similar skepticism was also presented by Karambas *et al*. (2016). They describe that in this case the mass flux and the rip currents are generated too close to the shoreline, not allowing the formation of the two aforementioned vortices. Consequently, the opposite rip currents transport the sand from the shadow of the breakwater towards the gaps, where it is accreted. This is the inverse process compared to the one formatting the salient.

With regard to their environmental impact, submerged breakwaters are definitely milder interventions compared to the conventional ones. The water quality is not significantly

degraded since they allow the renewal of the water both above their body but also through the gaps. Moreover, the wave breaking on their crest results to an increased oxygenation of the water. However, despite their advantages, submerged breakwaters still are human interventions in the natural ecosystem, imposing an obstacle which interrupts the physical flow from deep to shallow water. This fact has unavoidable environmental impact on the sea-bed flora and fauna. The physical and chemical properties of the water and sediments are modified. The water becomes more hypoxic and hypertrophic resulting to increased concentrations of seaweeds. Also, new species may appear and others disappear because of the 'harder' environment of a breakwater compared to the natural sandy bed. More details about the environmental impact of submerged breakwaters can be found in Kontaxi and Memos (2005) and Koutsouvela (2009). The aforementioned negative effects are generally related to the construction of breakwaters. However, they are mostly attributed to the more bulky emerged breakwaters. In contrary, they are reduced when submerged breakwaters are built and thus these structures are general accepted as being environmentally more friendly than their emergent counterparts.

5.3 Description of laboratory experiments

5.3.1 General description of the facility

In the context of the present Ph.D. thesis laboratory experiments were also performed to study the morphological evolution of a sandy beach in the lee of a permeable submerged breakwater. The objective of the measurements was twofold. Firstly, to better understand the morphological impact of the construction of submerged breakwaters since, to the writer's knowledge, there are no others similar 3D experiments involving this type of structures, and not reefs, in the international literature. Secondly, to offer a validation dataset for the compound numerical model presented in the thesis. In parallel to the described procedure, the vertical profile of the water velocity inside the porous breakwater was also measured. These parallel measurements aimed to validate a different numerical model and they are presented in detail in Metallinos (2016).

The experiments were performed at the facilities of the Hydraulic Engineering Laboratory of the Department of Civil Engineering at University of Patras, in Patras, Greece from May to September 2015. In particular, a rectangular wave basin was used. The basin had a surface area 12 m x 7 m enclosed by vertical walls with height 1.45 m. The walls were made of concrete and had a relatively smooth surface. The maximum workable depth in the wave tank was 1.05 m. The bottom of the tank was horizontal made of concrete. In order to remove

undesired salts the water was softened at the pumping station before filling the basin. Coarse salt was used as softener during this regeneration process. The total water volume in the wave tank during the experiments was approximately 85 m^3. Two long wooden crossbeams were used to move across the wave tank over the water surface. A gantry crane moving on ceiling tracks was used to move these beams and other heavy materials, i.e. bags with sand, stones, etc. A view of the wave tank is shown in Fig. 5.6.

Fig. 5.6. General view of the wave tank before the construction of the sloping bottom.

Close and parallel to the one of the short sides of the rectangular wave tank a 7 m wide wavemaker was placed. It will be described in the following. In all the experiments performed the water depth at the region of the wave source was constant 1.05 m. In order to model shoaling waves a sloping beach was constructed. It consisted of a ramp made out of anodized aluminum panels with a hydrodynamically smooth surface. The ramp was 4 m wide, centered with respect to the width of the wave tank. It was restricted by two lateral vertical plates which acted as driving walls. The plates were also made of hydrodynamically smooth aluminum panels. Consequently, the active area of measurements was actually 4 m wide. The uniform slope of the ramp was measured approximately 1:14.97 and its horizontal length was 9 m. The upwave edge of the ramp had a depth of 0.45 m and it lay at a distance of 1.73 m from the wavemaker. In front of the main ramp, a smaller aluminum ramp with slope 1:2 was also placed for a smooth transition from the region of constant depth 1.05 m to the depth of 0.45 m where the mild sloping bed begins. This smaller ramp, along with the vertical lateral plates contributed also to the stabilization of the main ramp by preventing its oscillations. Views of the described layout before building the submerged breakwater and placing the sand can be seen in Figs 5.7 and 5.8.

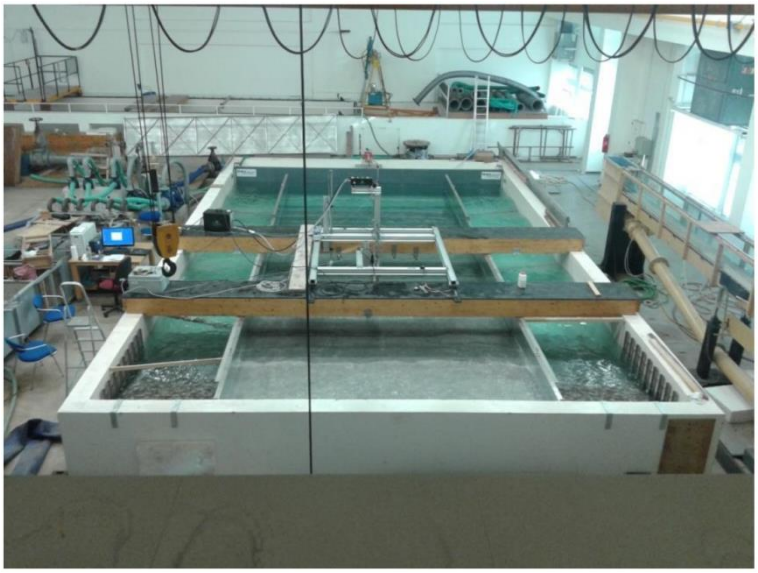

Fig. 5.7. General view of the experimental layout before building the submerged breakwater and placing the sand.

Fig. 5.8. A close view of the experimental layout from upwave.

In order to avoid undesired reflection from the down-wave boundary of the wave basin absorbing layers were placed at both sides of the sloping ramp to absorb the outgoing energy. A view of these layers is shown in Fig. 5.9. They consist of a wire mesh filled with stones of median diameter d_{50} = 0.05 m. The horizontal length of the absorbers was 3.20 m and their slope 1:2.5.

Fig. 5.9. View of the absorbing layer at the down-wave boundary of the wave tank.

5.3.2 Wave generation

The wave tank was equipped with a DHI paddle wavemaker. The paddle was 7 m long and 1 m high and it was installed parallel and next to one of the short sides of the rectangular basin. The installation also included an Active Wave Absorption Control System (AWACS) for wave generation with concurrent absorption of reflected waves approaching the wave paddle. The wavemaker is shown in Fig. 5.10.

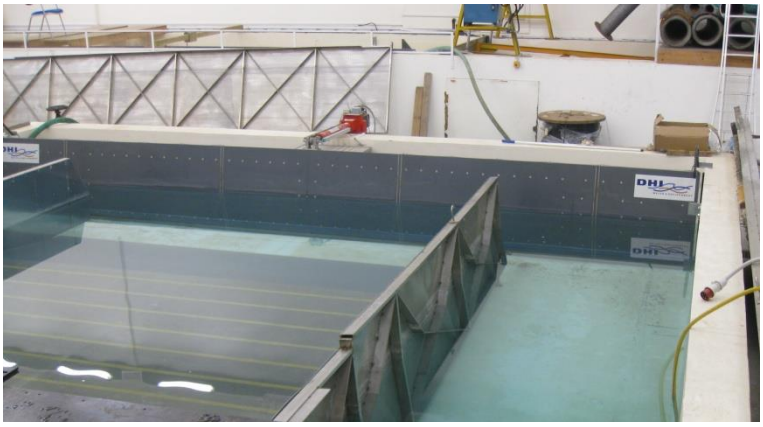

Fig. 5.10. View of the paddle-type wavemaker at the upwave boundary of the wave tank.

An electric actuator moved the wave paddle to produce the desired surface elevations. A side view of the actuator and the edge of the lateral vertical plates are depicted in Fig. 5.11. The plates were extended close to the wave maker to ensure better stability of the sloping ramp by preventing its oscillations. Moreover, the undesired diffraction around their edges

was practically eliminated and thus significant infection of the incoming waves was prevented.

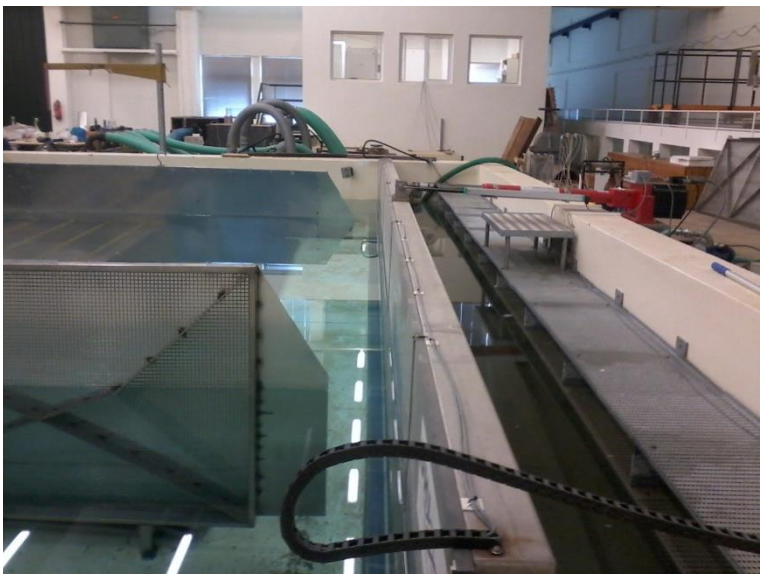

Fig. 5.11. Side view of the wave maker and the electric actuator.

Only normal incidence of the waves was studied because oblique incidence would require much larger basin dimensions for the full wave propagation up to the shoreline. Moreover, larger dimensions would be also required for the full establishment of the wave-induced longshore current and a corresponding recirculation system (Visser, 1991). The movement of the actuator was driven from the control room using the DHI Wave Synthesizer software package. The software accounts for the generation of 1st and 2nd order Stokes waves, irregular waves of a specified wave spectrum and the reproduction of specific timeseries of surface elevation. The maximum frequency permitted by the wavemaker system was 2.5 Hz. In addition, during irregular wave generation the proposed cut-off frequencies were $T_{max} = 2T_p$ and $T_{min} = 0.2T_p$, with T_p being the peak period. Limitations of the produced wave train also existed due to position and speed limitations of the actuator. In practice, the workable range of wave periods was about 0.75 ÷ 2.50 s and the maximum allowed wave height was 0.12 m.

Wave generation relied on the application of Biésel (1951) transfer functions between wavemaker displacement and wave amplitude. Second-order wave generation was also possible based on Schäffer (1993). However, second-order wave generation could not be used together with active wave absorption. In addition, irregular wave trains could be generated basing on a number of different spectrum types (Jonswap, Pierson-Moskowitz, Bretschneider, ISSC, Darbyshire, Scott, TMA). In this case an inverse FFT method with the assignment of random phases for each individual wave component were used for deriving the corresponding time series of surface elevations.

5.3.3 Submerged breakwater and sandy beach

The experiments were conducted to study the evolution of a sandy beach in the lee of submerged breakwaters. Hence, a permeable submerged breakwater was constructed. It consisted of stones of d_{50} = 0.05 m and its porosity was measured approximately $\lambda = 0.52$. In order to measure the porosity the following procedure was applied. A container with specified volume was filled with some stones from the breakwater. Then water was poured into the container in order to completely fill the voids. After that all the stones were removed from the container and the volume of the water was measured. Thus, porosity was given from the ratio of the water volume to the total volume of the container.

The length of the submerged breakwater was 3 m and the gaps between its heads and the left and right vertical plates were 0.5 m each. The lateral plates can be treated computationally as fully reflective boundaries and thus as axes of symmetry. Consequently, the experimental layout was actually representing an array of submerged breakwaters, rather than a single one. The slopes of the breakwater were 1:2, the crest width was 0.5 m and the free board 0.05 m. The toe of the upslope of the breakwater was located 2.25 m down-wave of the toe of ramp of slope 1:15, at a depth of 0.30 m. A sketch of the experimental layout is depicted in Fig. 5.12, while a view of the submerged breakwater is shown in Fig. 5.13. Two holes can be observed, one at the body and one at the head of the breakwater. They were made in order to allow parallel measurements of the velocity profiles inside the porous breakwater. The measurements were related to a different project. They were taken using a ADV equipment and they are described in detail in Metallinos (2016).

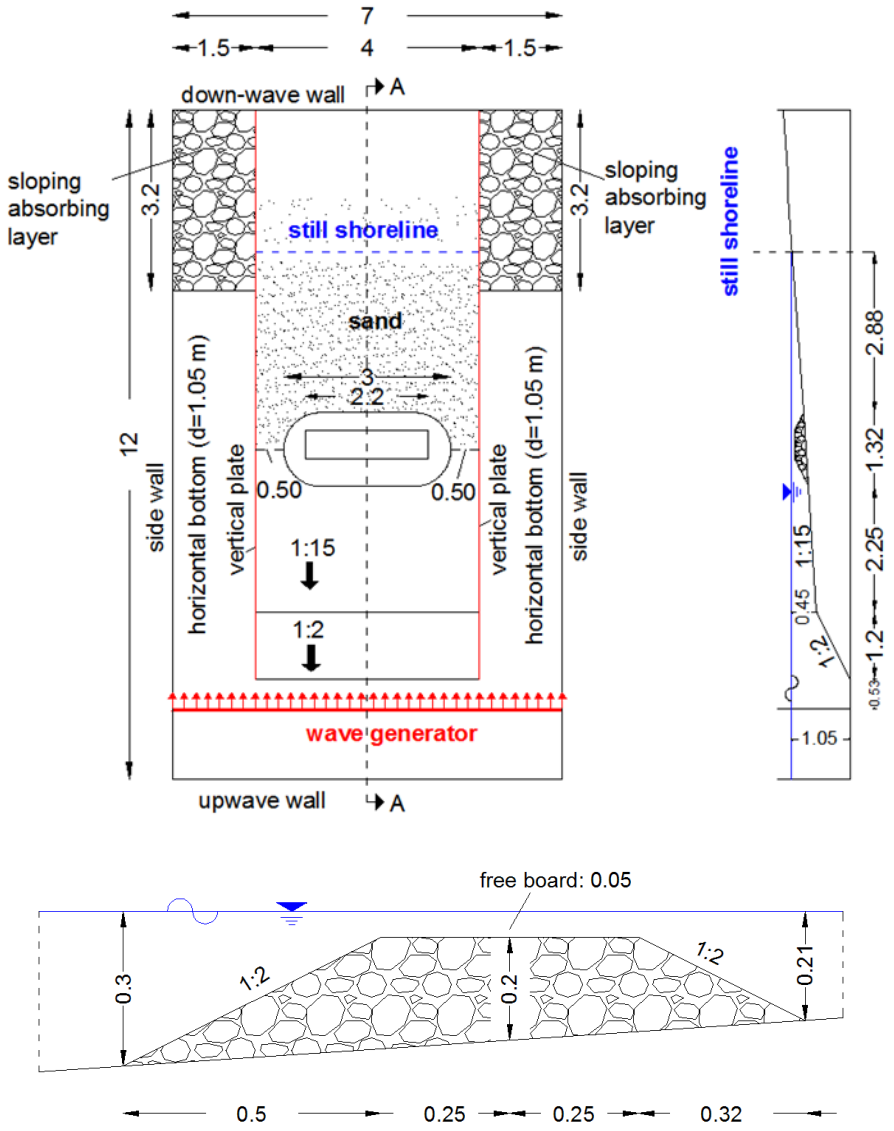

Fig. 5.12. Plan view and central profile of the experimental layout (above) and typical section of the submerged breakwater (below). All dimensions in m.

Fig. 5.13. View of the submerged breakwater.

In the lee of the submerged breakwater sand was placed in order to study the morphology evolution under the wave action. It can be observed in Fig. 5.13 that a piece of naylon was placed below and down-wave of the submerged breakwater and then it was covered with sand. This naylon was used for two reasons. At first, it was rubbed to make its surface rougher and ensure an increased friction force with the sand compared to a direct placement on the smooth surface of the aluminum ramp. Secondly, the piece of naylon helped to collect the sand and remove it at the end of the experiments. The sand was carefully placed and formed a layer with a mean thickness of approximately 4 cm down-wave of the submerged breakwater. The surface of the sandy area was then scratched and flattened to form a plane beach with a uniform slope of about 1:15. A view of the sandy beach during the installation of the layout is shown in Fig. 5.14.

Fig. 5.14. View of the submerged breakwater and the sandy beach.

The total amount of sand in the layout was about 0.8 m^3 and before usage it was kept in 11 bags. In order to examine the properties of the used sand a sieve analysis was performed.

Three independent samples with wet weight of about 0.7 kg each were taken from different bags. The samples were then oven dried for one day at a temperature slightly higher than 60° C. After this, the dry weight of the samples was measured and the sediment was sieved using a sieve vibrator as shown in Fig. 5.15. A sieve analysis was then performed resulting to the sediment grading curve in Fig. 5.16. Some characteristic measures of the sand are shown in table 5.2.

Fig. 5.15. Oven for drying the sediment samples (at left) and sieve vibrator (at right).

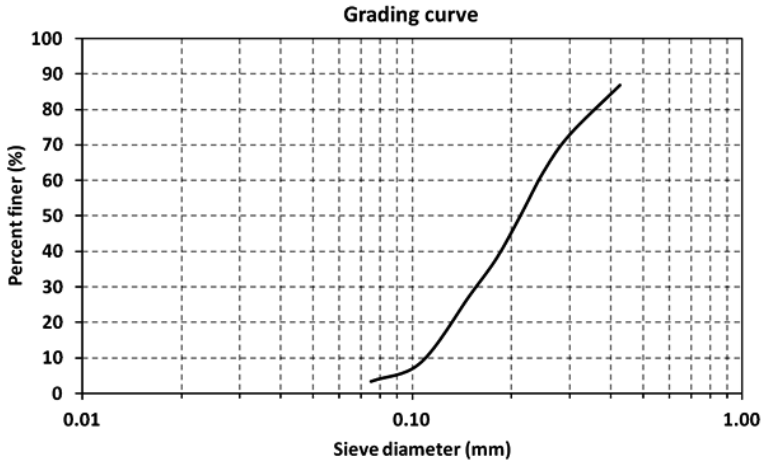

Fig. 5.16. Sediment grading curve.

Table 5.2. Characteristic measures of sediment's distribution.

d_{10} (mm)	0.110
d_{30} (mm)	0.156
d_{50} (mm)	0.210
d_{60} (mm)	0.241
d_{84} (mm)	0.397
Coefficient of uniformity (C_u)	2.19
Coefficient of curvature (C_c)	0.92

The median diameter was d_{50} = 0.21 mm and thus according to the American Geophysical Union the material is classified as fine sand (see table 4.1). The coefficient of uniformity and curvature were C_u = 2.19 < 6 and C_c = 0.92 < 1, respectively. Thus, the material was well-sorted (SP) according to ASTM D-2487. Practically, it consisted of uniform sands with a moisture of about 7 %. A sedimentation test was also performed and showed that silt and clay were contained at a percentage of 7-8 % each. Walkley and Black's (1934) procedure was also applied to estimate the total organic matter included in the soil material. It was found to be very poor in organic matter with a percentage about 0.08 %. As it will be shown in subsection 5.3.4, during the experimental process, especially during the earlier tests, increased foaming and flocculation were observed and colloidal emulsified compounds of ochre color were formed and transported near the water surface throughout the entire basin. Although the content in clay was found to be low, this referred to a particle-size point of view, while the aforementioned foams were, most probably, created by the presence of aluminate compounds in the soil material. In order to prevent this undesired effect, the sediment should have been washed before it was used. However, no suitable facility for this purpose was available. Nevertheless, after the earlier tests and hours of wave propagation, the foaming and flocculation were significantly reduced.

5.3.4 Test cases and data acquisition

The measured data included free surface elevation timeseries at selected locations in the wave tank and initial and final bed elevations of the sandy beach in order to study the morphological evolution. Eight different test cases were studied including regular and irregular (Jonswap spectrum), breaking and non-breaking, long and short waves. It should be noted that the duration of each test depended on the required time for establishing a steady state and a morphological equilibrium. Each test case was finished when no significant morphological evolution was observed anymore. These durations were of the order of some hours. The test cases are summarized in table 5.3.

Table 5.3. Experimental test cases.

Test No.	Wave type	$H_{s,o}$ (m)	T_p (s)	$L_{d=0.45}$ (m)	L_{SB} (m)	Wave breaking	Duration (hrs)
(1)	Regular	0.045	1.25	2.122	1.867	non-breaking	4.0
(2)	Regular	0.045	2.00	3.884	3.258	non-breaking	3.0
(3)	Regular	0.08	1.25	2.122	1.867	breaking	5.0
(4)	Regular	0.08	2.00	3.884	3.258	breaking	4.3
(5)	Irregular	0.045	1.25	2.122	1.867	non-breaking	5.0
(6)	Irregular	0.045	2.00	3.884	3.258	non-breaking	5.0
(7)	Irregular	0.08	1.25	2.122	1.867	breaking	5.0
(8)	Irregular	0.08	2.00	3.884	3.258	breaking	5.0

Four of the tests referred to regular waves and four to irregular waves of a Jonswap spectrum. The third column refers to the wave height at the source line where the depth was 1.05 m, the fourth column is the wave period, the fifth includes the wavelength at the two of the 1:15 sloping bed where the depth was 0.45 m and the sixth column is the wavelength at the toe of the upslope of the submerged breakwater. For the irregular waves the corresponding characteristics are the significant wave height, the peak period and the wavelength that corresponds to the peak period. The seventh column refers to whether wave breaking occurs at the crest of the breakwater or not. A snapshot of the wave propagation during the test No. 3 is depicted at the left in Fig. 5.17, while at the right bed wave ripples close to the gap are shown.

Fig. 5.17. Snapshot of wave propagation (at left) and bed wave ripples close to the gap (at right).

The free surface elevation was measured at seven positions by DHI wave gauges. The timeseries of the surface elevation was also recorded at wave source in order to check if the desired incident wave train was generated. The wave gauges were calibrated before used in the experiments. Measurements were taken for 10 min with a sampling rate of 100 Hz. The location of the wave gauges and a view of the layout are depicted in Figs 5.18 and 5.19, respectively. The coordinates of the wave gauges with respect to the coordinate system shown in Fig. 5.18 are summarized in table 5.4. It is noted that the depth at the stations 2 and 3 is defined as the free water depth above the surface of the submerged breakwater.

Table 5.4. Coordinates and water depth of the wave gauges.

Wave gauges	x (m)	y (m)	depth (m)
1	6.00	2.00	0.420
2	3.30	2.00	0.050
3	3.04	2.00	0.130
4	2.08	2.00	0.124
5	2.48	3.10	0.155
6	2.28	0.90	0.140
7	3.45	0.25	0.250

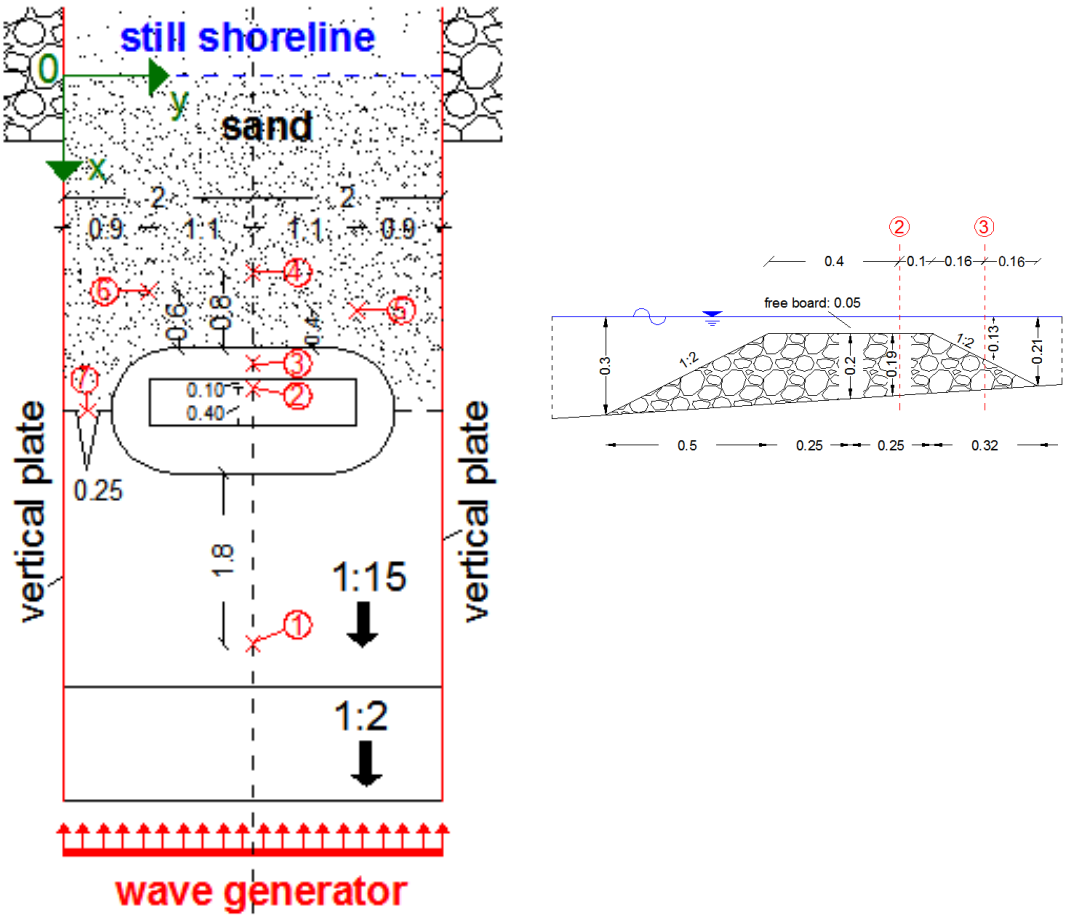

Fig. 5.18. Location of the wave gauges.

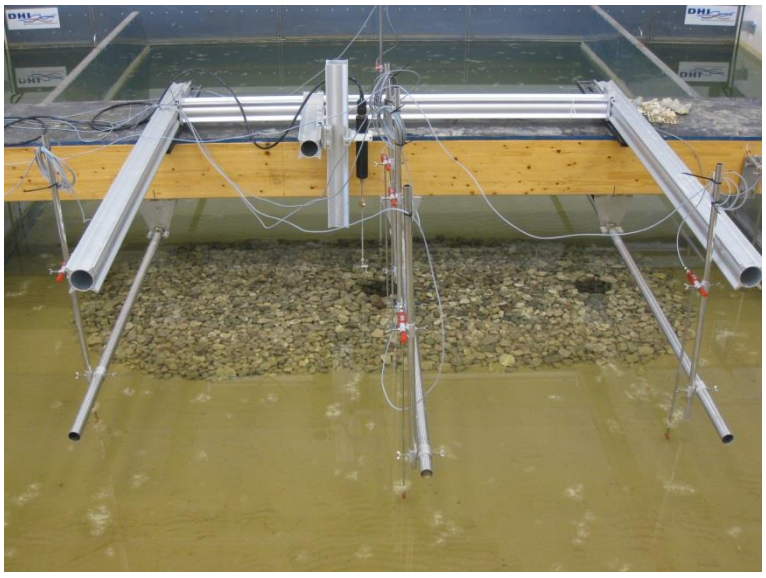

Fig. 5.19. View of the layout including the wave gauges.

Before the initiation of each test the sandy bed was carefully reshaped to a plane beach with a uniform slope of about 1:14. After the end of each test the new bathymetry was measured. The measurements were performed manually using a ruler. A regular grid with a space of

0.10 m was labeled on a rod that could be moved on the lateral vertical plates. Thus, it was placed succesively above and in parallel to each depth contour line and the water depth was measured point by point. In this way, the new bathymetry was recorded all over the distance from the still shoreline to the submerged breakwater. It should be mentioned that measurements were taken over a width of 2 m symetrically to the center line. The measured data both for surface elevations and morphology are presented in chapetr 6, along with the model validation.

5.4 Scale effects

Ideally, a properly designed laboratory model should behave in all respects like a controlled version of the prototype. In a fluid flow model this similar behaviour includes the velocity, acceleration, mass transport of the fluid, and the resultant forces. Similitude is achieved when all major factors influencing reactions are in proportion between prototype and model, while those factors that are not in proportion throughout the model domain are so small as to be insignificant to the process.

A prerequisite for complete similarity is geometric similarity. The prototype-to-model length scale ratio, N_L, is defined as the ratio of a characteristic length in the protype to the corresponding one in the model. Geometric similarity is fulfilled if the length scale ratio is uniform for all geometric dimensions. However, there are distorted models where the horizontal length scale and the vertical length scales are different. Kinematic similarity is also important. It is achieved when the ratio between the components of all vectorial motions, N_V, for the prototype and model is the same for all particles at all times. Kinematic similarity for gravity waves implies the time scale factor:

$$N_T = \sqrt{N_L} \tag{5.2}$$

Dynamic similarity between two geometrically and kinematically similar systems requires that the ratio of all vectorial forces (inertial force, gravitational force, viscous force, surface tension force, elastic compression force, pressure force) in the two systems be the same (Warnock, 1950). Dynamic similarity requires the equality of the Froude number, $\mathrm{Fr} = \frac{V}{\sqrt{gL}}$, and the Reynolds number, $\mathrm{Re} = \frac{VL}{v}$, between the prototype and the model with V, L, and v a characteristic velocity, length, and the fluid kinematic viscosity respectively.

$$\mathrm{Fr}_m = \mathrm{Fr}_p \rightarrow \frac{N_V}{\sqrt{N_L}} = 1 \quad \text{and} \quad \mathrm{Re}_m = \mathrm{Re}_p \rightarrow \frac{N_V N_L}{N_v} = 1 \tag{5.3}$$

where N_v is the ratio of the kinematic viscosities between the prototype and the model. Eq. (5.3) shows that the fluid viscosity in the model should be significantly lower than the viscosity in the prototype. This requirement is very difficult to be fulfilled and consequently the two relations in Eq. (5.3) are inconsistent with each other. Fulfilling the Froude criterion implies a reduced Reynolds number in the model and thus increased scale effects, i.e. laminar flow instead of the fully developed turbulence in the prototype. In order to avoid this undesired effect in Froude-type physical models an increased bed roughness is applied to result in turbulent flow. A very detailed description of scale effects in physical models is presented by Hughes (1993). The experiments performed in the present thesis do not represent a physical model of a predefined prototype. However, they could be seen as a representation of an actual coastal defense project including a submerged breakwater with a geometric scale factor of about $N_L = 10 \div 15$. Thus, the layout represents a submerged breakwater constructed at a depth of about 2.5 – 3.75 m with armor stones with a mean diameter 0.5 – 0.75 m. Hence, the time scale factor could be estimated as $N_T \approx \sqrt{10} \approx 3.2$.

Movable-bed physical model investigations of coastal erosion and sediment transport are probably the most difficult hydraulic models to conduct (Hudson *et al*., 1979). Dean (1985) listed two major requirements for proper physical modeling of sand transport processes: the knowledge of the character of the dominant forces and an understanding of the dominant response mechanisms of the sediment. An important difficulty with respect to movable-bed physical models is that different mechanisms may be governing the sediment transport inside and outside the surf zone. However, Bijker (1967) mentioned that scale laws should be derived with a main requirement of invariability of the scale for the material transport over the entire area of the model concerned.

Physical parameters of the sediment can be combined with some physical properties of the fluid to form a set of dimensionless numbers commonly used for unidirectional flow. According to Kamphuis (1985) these numbers are: the grain size Reynolds number, R_*, the densimetric Froude number, F_*, the relative density, S_s, the relative length, l_s, and the relative fall speed, V_ω. They are given by:

$$R_* = \frac{v_* d_{50}}{v}, F_* = \frac{\rho {v_*}^2}{\gamma_i d_{50}}, S_s = \frac{\rho_s}{\rho}, l_s = \frac{\lambda}{d_{50}} \text{ and } V_\omega = \frac{\omega}{v_*} \tag{5.4}$$

where $v_* = \sqrt{\tau_b/\rho}$ is the shear velocity, γ_i is the submerged sediment specific weight, ρ_s is the sediment density, ρ is the fluid density, λ is a characteristic depth, and ω is the sediment fall speed. For complete similitude in sediment transport, values of all five parameters in Eq. (5.4) must be the same in the model as in the prototype. Generally, this is not possible at

scales other than prototype. However, it has been proven that several useful 'incomplete' similitudes can be formulated.

There are several general similitude difficulties that are common to most proposed scaling criteria. However, practical considerations more often than not limit the modeling choices. For example, the prototype-to-model ratio of fluid density could be manipulated by selection of a model fluid different than water. However, coastal models usually require a large amount of fluid, and water is virtually the only choice (Kamphuis, 1985). Another important aspect refers to the sediment grain size. If the selected scaling criteria requires that grain size be scaled the same as the geometric length scale, there is the possibility that non-cohesive prototype sediments may be scaled to grain diameters that would put the sediment into the cohesive sediment range in the model. If this were to happen, different fundamental sediment transport processes would occur in the model. Despite the difficulties in attaining perfect similitude, Le Méhauté (1976) mentioned that since the only requirement of a movable-bed model is a reproduction of bottom evolution, it is not necessary that this be achieved through exact similitude of water motion.

An important distinction of movable-bed physical models is made between bed load-dominated and suspension-dominated models. Bottom shear stress is an important parameter in bed load-dominated sediment transport and thus physical models must attempt to provide similarity for it. Perfect similitude with respect to all the five dimensionless numbers in Eq. (5.4) is not possible. Kamphuis (1974, 1975) proposed several imperfect similitudes in which two or more of the scale ratios are not maintained. The characteristics of these physical models are summarized in table 5.5. Kamphuis (1975) mentioned two more model types, a model using prototype-sized sand and a 'nothing model' that satisfies none of the criteria.

Table 5.5. Classification of bed load-dominated movable-bed physical models (from Hughes, 1993, modified).

Model Class	R_*	F_*	S_s	l_s	V_ω
Best Model	x	✓	✓	✓	x
Lightweight Model	✓	✓	x_1	x	x
Densimetric Froude Model	x	✓	x_1	x	x
Sand Model	x	x	✓	x	x

✓ Satisfied

x Not satisfied

x_1 Not satisfied but limited to $1.05 < \rho_s/\rho < 2.65$

In steady-flow movable-bed models, similitude of the Shields parameter is considered important if incipient sediment motion is a critical aspect of the modeling effort. On the other hand, researchers disagree on whether the Shields parameter should be conserved in unsteady coastal flows because the processes are much more complex (Oumeraci, 1984; Dean, 1985;

Motta, 1986; Dalrymple, 1989). Similitude of bed forms is also an important issue since it influences the bottom friction. This aspect was studied by Yalin (1972) and Mogridge (1974) who pronounced the importance of matching the grain size Reynolds and the densimetric Froude numbers. Finally, a very important aspect concerning movable-bed physical models is the determination of the morphological time scale. This factor is very subjective and the time scales are best determined by comparing model response time to known prototype response (Kamphuis, 1975). According to Hughes (1993), once the prototype-to-model transport rate scale has been empirically determined, the morphological time scale can be estimated as:

$$N_{t,mor} = \frac{N_L N_z N_{(1-\mathrm{p})}}{N_\mathrm{q}} \tag{5.5}$$

where N_z is the vertical length scale, $N_{(1-\mathrm{p})}$ is the material porosity scale and N_q is the sediment transport scale (per unit width).

In other coastal regimes suspension is the dominant sediment transport mode. In these cases high levels of turbulent water motions lift the sediment grains up into the water column where they are moved by water currents. Suspension-dominated movable-bed physical models require consideration of different physical parameters of the processes. Similarly to the bed load-dominated models, five dimensionless numbers should be retained between the prototype and the model to ensure similitude. These are:

$$R'_* = \frac{\sqrt{\mathrm{g}H_b}d_{50}}{\nu},\ m_b = \frac{\rho \mathrm{g} H_b}{\gamma_i d_{50}},\ S_s = \frac{\rho_\mathrm{s}}{\rho},\ l'_s = \frac{H_b}{d_{50}} \text{ and } V'_\omega = \frac{\omega}{\sqrt{\mathrm{g}H_b}} \tag{5.6}$$

where H_b is the breaking wave height.

Retaining all the aforementioned numbers is again impossible and historical development of scaling criteria for suspension-dominated models primarily aims to satisfy similarity conditions, such as similar beach slopes or particle fall trajectories. A usual distinction of this type of models relies on whether the scale criteria depend on the settling velocity (Valembois, 1960; Le Méhauté, 1970; Dalrymple and Thompson, 1976) or not (Noda, 1971, 1972; Ito and Tsuchiya, 1984; Hallermeier, 1985). As already mentioned in chapter 4, the dimensionless fall speed parameter $H/(\omega T)$, with H the wave height, T the wave period and ω the vertical fall speed of the sediment in the fluid, plays an important role in turbulence-dominated cases (Dean, 1973). Maintaining similarity of the fall speed parameter, and assuming a unity gravitational scale, leads to the similitude condition:

$$N_\omega = \sqrt{N_z} \tag{5.7}$$

with N_ω the settling velocity scale.

In general, preserving the fall speed parameter and fulfilling the Froude criterion for the hydrodynamics results to an accurate reproduction of the surf zone profile in a suspension-dominated model. According to Dean (1985) such a model preserves similarity in wave form, sediment fall path, wave-induced velocities, breaking point, breaker type, and wave decay. However, the bottom shear stress is not correctly scaled because the bottom boundary layer and the ripple formation are not reproduced. This will result in noticeable scale effects when wave breaking turbulence is not the dominant mechanism of sediment transport.

Past experience of suspension-dominated movable-bed models has shown that selecting the sediment size to preserve the Froude number and the settling velocity parameter is more effective in processes that are chiefly erosional in nature, with the erosion occurring inside a turbulence-dominated region such as the surf zone. However, in general, scale effects related to turbulence-dominated models are not as well understood as those arising in bed load-dominated physical models. Outside the surf zone, a higher percentage of sediment transport occurs as bed load and thus the scale effects are more severe for a suspension-dominated physical model that does not typically preserve the Shields parameter. Moreover, the geometric distortion required by some models introduces greater wave reflection from the beach and the longshore bars are not accurately reproduced, influencing also the incoming waves. Finally, the selected initial beach slope and the seafloor permeability have also proved to introduce undesired scale effects. Nevertheless, experience has shown that a beach will still reach the same equilibrium shape inside the surf zone irrespective of the initial slope.

In all the presented experiments the dominant mechanism of sediment transport near the shoreline appeared to be the bed load. This transport mode essentially controlled the shoreline's response to the wave action. On the other hand, in tests 3,4,7 and 8, where breaking occurred above the bar crest, significant sediment suspension appeared down-wave of the submerged breakwater. This mechanism was mainly responsible for the bar formation in the lee of the structure. These morphological features will be further discussed in chapter 6 where the measurements are presented and compared with the model's results. The selected grain diameter was d_{50} = 0.21 mm which is similar to the ones used in other 2DH laboratory experiments under similar geometries and wave conditions (Ming and Chiew, 2000; Turner *et al*., 2001; Wang *et al*., 2002; Gravens and Wang, 2007). As already mentioned, since our understanding about scale effects related to movable-bed physical models is not cleared up, the cumulative international experience offers some practical guidelines.

5.5 Discussion on laboratory experiments

The main scope of the present Ph.D. thesis is to study the bed morphodynamics in the lee of submerged breakwaters. This was done both numerically, as it will be shown in chapters 6 and 7, but also experimentally. These laboratory experiments fill a gap in the international literature. Very few cases of morphodynamic experiments related to submerged breakwaters have been reported and almost all of them refer to either 1DH layouts or, even less, to 2DH physical modelling of artificial reefs. To the best of the author's knowledge there has been no other 3D experimental work including bed evolution behind permeable submerged breakwaters similar and scaled-down to the ones that are constructed in the field by engineers. This is a serious issue, since submerged breakwaters become a popular soft engineering alternative in coastal projects. Thus, besides their interaction with the hydrodynamic and wave fields, whose studying has advanced in the recent years, the related morphodynamics should be also understood. From this point of view, the presented experimental work offers originality in coastal engineering but, similarly to the previous chapters, some weak points should be also addressed to better ground the conclusions that will be drawn.

At first, the active area was 4 m wide, the breakwater was placed at a distance of 3.45 m from the still shoreline and its length was 3 m. Hence, due to the limited horizontal dimensions of the wave tank, lateral spending layers could not be placed. Consequently, oblique incidence of unidirectional waves was not possible since reflection from the lateral plates would significantly infect the wave field. Moreover, the oblique wave generation would require a rotation of the wave paddle resulting to an additional reduction of the active area. Finally, the oblique incidence would generate a longshore current which should be re-circulated in order to establish a steady pattern. The wave tank was not equipped with such a re-circulation system. For all the aforementioned reasons, only normal wave incidence was studied. This is a deficiency of the specific experimental sets and it is left for future research, probably at a larger wave tank. However, this lack of measurements was partly covered by the numerical experiments presented in chapter 7 which include oblique wave incidence.

Despite the normal wave incidence, refraction and diffraction at the heads of the breakwater resulted to some reflection from the lateral plates. However, the infection of the wave field, especially near the shoreline, was not significant. Moreover, the undesired diffraction at the edges of the plates close to the wave generator was also negligible. Due to the basin's limited dimensions the wave paddle had to be placed quite close to the toe of the mild sloping ramp, at a distance of 1.73 m. Hence, a shorter steep ramp had to be placed with a slope of 1:2. This unavoidably led to some reflection of the incoming waves, which was, however, absorbed by the paddle's absorption system.

With regard to the sand, the mean diameter was d_{50} = 0.21 mm. If a geometrical scale factor N_L = 10 is assumed, this would mean that the selected sediment material corresponds to very coarse sand, according to table 4.1. However, the discussion in subsection 5.4 showed that the similitude with respect to sediment transport in a movable-bed model is not well-established and that in most cases a similar to prototype sediment is used. In addition, the grain size used is similar to the one used in the majority of other 2DH experimental works including similar wave conditions and geometries. Moreover, the sediment's bahaviour inside the wave tank (inception of movement, agitation, suspension) corresponded to its actual size of a fine sand. Also, it was not easy to find sediment material finer than the one used in an adequate quantity.

From a particle-size point of view, the sediment's content in clay was found to be low. Despite this, as already discussed, intense emulsification and foaming were observed. They were, most probably, created by the presence of aluminate compounds in the soil material. What should have been done was to wash the sediment before use. However, no suitable facility for this purpose was available. It should be also mentioned that this chemical composition of the material had no serious impact on the sediment transport processes and it was essentially just blurring the water body. In addition, after the earlier tests and hours of wave propagation, the foaming and flocculation were significantly reduced.

Some discussion should be also done on the measuring process. The surface elevations were very accurately measured by the wave gauges. However, the bed morphology was measured manually using a ruler on a regular grid. This fact unavoidably introduces an increased error compared to using a suitable equipment and software, e.g. underwater laser scanner, etc. However, such equipment was not available. An underwater camera was available combined with a Particle Image Velocimetry (PVI) system, but the presence of the suspended sand was blurring the water column and it was reducing dramatically their efficiency. Thus, considering the simplicity and efficiency of manual measurements, this solution was favored, keeping always in mind to get the measurements carefully and accurately. Moreover, before each run the sandy beach was also manually reshaped carefully in order to form a plane bed. Nevertheless, as already discussed, the equilibrium profiles, after hours of wave propagation, were not significantly affected by this.

It should be also mentioned that despite the placement of the piece of naylon under the sandy bed, some loss of sand was taking place through the joints of panels of the lateral vertical plates. Moreover, despite the initial placement of the sand down-wave of the breakwater, the rip currents formed through the two gaps were transporting some sediment to the offshore area.

The submerged breakwater was effectively designed since the wave energy was significantly reduced in most cases. It will be shown in chapter 6 that the shorter waves were

more influenced by its presence rather than the longer ones. Some reflection from the upwave face of the breakwater was observed but it was not high. The mean armor size was 0.05 m, the free board was 0.05 m and the structure height was 0.20 m at its center. The breakwater's porosity was approximately $\lambda = 0.52$, which is a high value, but it should be kept in mind that no core was constructed. According to van der Meer and Daemen (1994) these geometrical characteristics lead to an expected transmission coefficient of about $K_t = 0.5$. However, their analysis refers to breakwaters on a horizontal bottom rather than on a sloping beach.

Although a single submerged breakwater was constructed in the laboratory experiment, the application of the lateral fully reflective plates acted as defining axes of symmetry and thus the experimental layout actually represented an array of submerged breakwaters. This will be also confirmed by the numerical experiments in chapter 7. The ratio of the breakwater's length to its distance from the still shoreline was approximately $B/S \approx 0.90$ and the ratio of the gap length (twice the distance of the head of the breakwater from the vertical plate due to symmetry) to the breakwater's length was $G/B = 1/3$. Hence, from a morphodynamic point of view, salients were formed as expected. However, the morphological response of submerged breakwaters is not yet a well-understood field and this was essentially the motivation for the present Ph.D. thesis. This point will be further discussed in chapter 7.

One last remark is made about the morphological time scale of the experiments. This is a difficult issue to be clarified in movable-bed physical models. Since, there was no prototype for the specific experiments to offer some measurements, it is difficult to decide the accurate times to which the experimental times in table 5.3 would correspond in a real scaled-up case in nature. However, by assuming a reasonable geometrical scale factor of $N_L = 10$ both in horizontal and vertical dimensions (undistorted model) and simplifying Eq. (5.5) gives a morphological time scale $N_{t,mor} \approx \sqrt{10} \approx 3.2$. This means practically that bed morphology in the field prototype is expected to reach an equilibrium after a period whose duration is approximately three times its corresponding value in the physical model.

The measured data from the laboratory experiments will be presented in chapter 6 and they will be compared with the results of the compound numerical model after this has been extended to account for porous beds.

References

Abdul Khader, M. H., and Rai, S. P. (1980). "A study of submerged breakwaters." *J. Hydraul. Res.*, 18 (2), 113-121.

Ahrens, J. P. (1987). "Characteristics of reef breakwaters." *Tech. Rep.*, CERC-87-17, 45 pp.

Ahrens, J. P. (1988). "Reef breakwater response to wave attack." In: Berm breakwaters: unconventional rubble-mound break waters, D. H. Willis, W. F. Baird and O. T. Magoon, eds, ASCE, pp. 22-40.

Allsop, N. W. H. (1983). "Low-crested breakwaters, studies in random waves." *Proc. Coastal Structures '83*, Arlington, Virginia, pp. 94-107.

Beji, S., and Battjes, J. A. (1993). "Experimental investigation of wave propagation over a bar." *Coast. Eng.*, 19(1-2), 151-162.

Beji, S., and Battjes, J. A. (1994). "Numerical simulation of nonlinear wave propagation over a bar." *Coast. Eng.*, 23 (1-2), 1-16.

Biésel, F. (1951). "Les appareils générateurs de houle en laboratoire." *La Houille Blanche*, Vol. 6, Nos 2, 4 et 5 (in french).

Bijker, E. W. (1967). "Some considerations about scales for coastal models with movable bed." *Tech. Rep.*, 50, Delft Hydraulics Laboratory, Delft, The Netherlands, 142 pp.

Black, K., and Andrews, C. (2001). "Sandy shoreline response to offshore obstacles: Part 1. Salient and tombolo geometry and shape." *J. Coast. Res.*, Special Issue 29 Natural and Artificial Reefs for Surfing and Coastal Protection, pp. 82– 93.

Bleck, M., and Oumeraci, H. (2002). "Hydraulic performance of artificial reefs: global and local description." *Proc. 28th Int. Conf. on Coastal Eng.*, J. M. Smith, ed., Cardiff, Wales, U.K., vol. 2, pp. 1778-1790.

Briganti, R., Van der Meer, J. W., Buccino, M., and Calabrese, M. (2003). "Wave transmission behind low crested structures." *Proc. Coastal Structures '03*, ASCE, Portland, Oregon, U.S.A., pp. 580-592.

Browder, A., and Dean, R. G. (1996). "Performance of a submerged breakwater for shore protection." *Proc. 25th Int. Conf. on Coastal Eng.*, B. L. Edge, ed., Orlando, Florida, U.S.A., pp. 2312–2323.

Burcharth, H. F., Hawkins, S. J., Zanuttigh, B., and Lamberti, A. (2007). *Environmental design guidelines for low crested coastal structures*. Amsterdam: Elsevier, 376 pp.

Calabrese, M., Vicinanza, D., and Buccino, M. (2002). "Large-scale experiments on the behavior of low crested and submerged breakwaters in presence of broken waves." *Proc. 28th Int. Conf. on Coastal Eng.*, J. M. Smith, ed., Cardiff, Wales, U.K., pp. 1900–1912.

Cornett, A., Mansard, E. and Funke, E. (1994). "Wave transformation and load reduction using a small tandem reef breakwater-physical model tests." *Ocean Wave Measurement and Analysis*, ASCE, New York, U.S.A., pp. 1008-1023.

Dalrymple, R. A. (1989). "Physical modelling of littoral processes." In: Recent Advances in Hydraulic Physical Modelling, R. Martins, ed., Kluwer Academic Publishers, Dordrecht, The Netherlands, pp. 567-588.

Dalrymple, R. A., and Thompson, W. W. (1976). "Study of equilibrium beach profiles." *Proc. 15th Int. Conf. on Coastal Engineering*, ASCE, Honolulu, Hawaii, U.S.A., part II, chapter 75, pp. 1277-1296.

D' Angremond, K., Van der Meer, J. W., and De Jong, R. J. (1996). "Wave transmission at low-crested structures." *Proc. 25th Int. Conf. on Coastal Eng.*, B. L. Edge, ed., Orlando, Florida, U.S.A., chapter 187, pp. 2418–2427.

Dattari, J., Raman, H., and Shankar, N. J. (1978). "Performance characteristics of submerged breakwaters." *Proc. 16th Int. Conf. on Coastal Engineering*, ASCE, Hamburg, Germany, vol. III, chapter 130, pp. 2153-2171.

Davies, B., and Kriebel, D. L. (1992). "Model testing on wave transmission past low crested breakwaters." *Proc. 23rd Int. Conf. on Coastal Engineering*, B. L. Edge, ed., Venice, Italy, part III, chapter 84, pp. 1115-1128.

Dean, R. G. (1973). "Heuristic models of sand transport in the surf zone." *Proc. Conf. Eng. Dynamics in the Surf Zone*, Sydney, Australia, 208-214.

Dean, R. G. (1985). "Physical modeling of littoral processes." In: Physical modelling in coastal engineering, R. A. Dalrymple, ed., A. A. Balkema, Rotterdam, The Netherlands, pp. 119-139.

Dean, R. G., Chen, R., and Browder, A. E. (1997). "Full scale monitoring study of a submerged breakwater." *Coast. Eng.*, 29 (3-4), pp. 291– 315.

Dean, R. G., and Dalrymple, R. A. (2001). *Coastal Processes with Engineering Applications*. Cambridge University Press, 488 pp.

Debski, D., and Loveless, J. H. (1997). "The design and performance of submerged breakwaters." *Res. Rep.*, University of Bristol, U.K.

Deguchi, I., and Sawaragi, T. (1986). "Beach fill at two coasts of different configuration." *Proc. 20th Int. Conf. on Coastal Engineering*, B. L. Edge, ed., Taipei, Taiwan, pp. 1032-1046.

Del Jesus, M. (2011). "Three-dimensional interaction of water waves with coastal structures." Ph.D. thesis, Universidad de Cantabria, Spain.

Diskin, M. H., Vajda, M. L., and Amir, I. (1970). "Piling-up behind low and submerged permeable breakwaters." *J. Waterw. Harb. Coast. Eng. Div.*, WW2, ASCE, 359-372.

Douglass, L., and Weggel, J. R. (1987). "Performance of a perched Beach-Slaughter Beach, Delaware." *Proc. Coastal Sediments '87*, ASCE, pp. 1385– 1398.

Drei, E., and Lamberti, A. (1999). "Wave pumping effect of a submerged barrier." *Proc. Coastal Structures '99*, ASCE, Santander, Spain, pp. 667-673.

Evans, P., and Ranasinghe, R. (2001). "Artificial surfing reefs: a new paradigm in coastal protection." *Proc. Coasts and Ports '01*, Gold Coast, Australia, IEAust, pp. 128–133.

Funakoshi, H., Shiozawa, T., Tadokoro, T., and Tsuda, S. (1994). "Drifting characteristics of littoral sand around submerged breakwater." *Proc. Int. Conf. on Hydro-technical Eng. for Port and Harbor Construction*, Yokosuka, Japan, pp. 1157–1178.

Goda, Y. (1969). "Re-analysis of laboratory data on wave transmission over breakwaters." *Rep. Port Harbour Res. Inst.*, 18 (3), 3-18.

Goda, Y., Takeda, H., Moriya, Y. (1967). "Laboratory investigation on wave transmission over breakwaters." *Rep. Port Harbour Res. Inst.*, 13, 38.

Gourlay, M. R. (1993). "Wave setup and wave generated currents on coral reefs." *Proc. 11th Australian Conf. on Coastal and Ocean Eng.*, Townsville, Australia, 479-484.

Gourlay, M. R. (1996a). "Wave set-up on coral reefs. 1. Set-up and wave-generated flow on an idealized two dimensional horizontal reef." *Coast. Eng.*, 27 (3-4), 161-193.

Gourlay, M. R. (1996b). "Wave set-up on coral reefs. 2. Set-up on reefs with various profiles." *Coast. Eng.*, 28 (1-4), 17-55.

Gravens, M. B., and Wang, P. (2007). "Data report: laboratory testing of longshore sand transport by waves and currents; morphology change behind headland structures." *Tech. Rep.*, ERDC/CHL TR-07-8, Coastal and Hydraulics Laboratory, U.S. Army Engineer Research and Development Center, Vicksburg, MS, U.S.A.

Groenewoud, M., Van der Graaff, J., Claessen, E., and Van der Beizen, S. (1996). "Effect of submerged breakwater on profile development." *Proc. 25th Int. Conf. on Coastal Eng.*, B. L. Edge, ed., Orlando, Florida, U.S.A., pp. 2428–2441.

Hallermeier, R. J. (1985). "Unified modeling guidance based on a sedimentation parameter for beach changes." *Coast. Eng.*, 9 (1), 37-70.

Hayakawa, N., Hosoyamada, T., Yoshida, S., and Tsujimoto, G. (1998). "Numerical simulation of wave fields around the submerged breakwater with sola-surf method." *Proc. 26th Int. Conf. on Coastal Eng.*, B. L. Edge, ed., Copenhagen, Denmark, vol. 1, pp. 843–852.

Hudson, R. Y., Herrmann, F. A., Sager, R. A., Whalin, R. W., Keulegan, G. H., Chatham, C. E., and Hales, L. Z. (1979). "Coastal Hydraulic Models." *Special Report*, No. 5, US Army Engineer Waterways Experiment Station, Vicksburg, Mississippi, U.S.A.

Hughes, S. A. (1993). "Physical models and laboratory techniques in coastal engineering." *Advanced Series on Ocean Engineering*, World Scientific Publishing, Singapore, vol. 7, 568 pp.

Ito, M., and Tsuchiya, Y. (1984). "Scale-model relationship of beach profile." *Proc. 19th Int. Conf. on Coastal Engineering*, B. L. Edge, ed., Houston, Texas, U.S.A., part II, chapter 95, pp. 1386-1402.

Jackson, L. A., Tomlinson, R., McGrath, J., and Turner, I. (2002). "Monitoring of a multi-functional submerged geotextile reef breakwater." *Proc. 28th Int. Conf. on Coastal Eng.*, J. M. Smith, ed., Cardiff, Wales, U.K., pp. 1923–1935.

Johnson, J. W., Fuchs, R. A., and Morison, J. R. (1951). "The damping action of submerged breakwaters." *Trans. Am. Geophys. Union*, 32 (5), 704-718.

Kamphuis, J. W. (1974). "Practical scaling of coastal models." *Proc. 14th Int. Conf. on Coastal Engineering*, ASCE, Copenhagen, Denmark, vol. III, chapter 121, pp. 2086-2101.

Kamphuis, J. W. (1975). "Coastal mobile bed model - does it work?" *Proc. 2nd Symp. Modeling Techniques*, ASCE, San Francisco, California, U.S.A., vol. 2, pp. 993-1009.

Karambas, Th., Krestenitis, I., and Koutitas, Ch. (2016). *Coastal Engineering – Shore Protection Structures*. Hellenic Academic Libraries, 156 pp. (in greek).

Kobayashi, N., Meigs, L., Ota, T., and Melby, J. (2007). "Irregular breaking wave transmission over submerged porous breakwater." *J. Waterw. Port Coast. Ocean Eng.*, 133 (2), 104-116.

Kontaxi, Ch., and Memos, C. (2005). "Submerged breakwaters as artificial habitats." *Proc. XXXI IAHR Cong.*, Seoul, South Korea, pp. 3967-3975.

Koutsouvela, D. (2010). "Soft shore protection methods against coastal erosion: submerged breakwaters." Ph.D. thesis, University of the Aegean, Greece (in greek).

Koutsouvela, D., Karambas, Th. V., Avgeris, I., and Karathanassi, E. (2007). "Functional design of submerged breakwaters for coastal protection using two wave/morphological models." *Proc. Coastal Structures '07*, Venice, Italy, pp. 1205-1216.

Kramer, M., Zanuttigh, B., Baoxing, W., Van der Meer, J., Lamberti, A., Burcharth, H. (2003). "Wave basin experiments." *Internal Tech. Rep.*, DELOS deliverable D31.

Kramer, M., Zanuttigh, B., Baoxing, W., Van der Meer, J., Vidal, C., Gironella, F. (2005). "Laboratory experiments on low-crested breakwaters." *Coast. Eng.*, 52 (10-11), 867-885.

Kriezi, E., and Karambas, T. (2010). "Modelling wave deformation due to submerged breakwaters." *Proc. of the ICE – Maritime Engineering*, 163-1, 19-29.

Lamberti, A., and Mancinelli, A. (1996). "Italian experience on submerged barriers as beach defence structures." *Proc. 25th Int. Conf. on Coastal Eng.*, B. L. Edge, ed., Orlando, Florida, U.S.A., pp. 2352–2365.

Lamberti, A., Zanuttigh, B., and Tirindelli, M. (2003). "3D hydrodynamic tests with low-crested structures: analysis of overtopping and velocity fields." *Proc. ISOPE 2003*, EA (2003), pp. 562-569.

Lara, J. L., del Jesus, M., and Losada, I. J. (2012). "Three-dimensional interaction of waves and porous coastal structures. Part II: Experimental validation." *Coast. Eng*., 64 (10-11), 26-46.

Le Méhauté, B. (1970). "A comparison of fluvial and coastal similitude." *Proc. 12th Int. Conf. on Coastal Engineering*, J. W. Johnson, ed., ASCE, Washington, D.C., U.S.A., vol. II, chapter 69, pp. 1077-1096.

Le Méhauté, B. (1976). "Similitude in coastal engineering." *J. Waterw. Harb. Coast. Eng. Div.*, 102 (WW3), 317-335.

Lesser, G. R., Vroeg, J. H., Roelvink, J. A., de Gerloni, M., and Ardone, V. (2003). "Modelling the morphological impact of submerged offshore breakwaters." *Proc. Coastal Sediments '03*, World Scientific Publishing Co, Clearwater Beach, Florida, USA, May 18-23, on CD-ROM.

Loveless, J. H., Debski, D., and MacLeod, A. B. (1998). "Sea level set-up behind detached breakwaters." *Proc. 26th Int. Conf. on Coastal Eng.*, B. L. Edge, ed., Copenhagen, Denmark, vol. 2, pp. 1665-1678.

Loveless, J., and MacLeod, B. (1999). "The influence of set-up currents on sediment movement behind detached breakwaters." *Proc. Coastal Sediments* '99, ASCE, Long Island, USA, pp. 2026–2041.

Lykke Andersen, T., and Burcharth, H. (2008). "Three dimensional investigations of wave overtopping on rubble mound structures." *Coast. Eng.*, 56 (2), 180-189.

Metallinos, A. S. (2016). "Hydrodynamic conditions in a submerged porous breakwater." Ph.D. thesis, Dept. of Civil Engineering, National Technical University of Athens, Greece (in greek).

Metallinos, A. S., Emmanouilidou, M.-E. A., and Memos, C. D. (2014). "Wave-induced pore pressures in submerged rubble mound breakwaters simulated by a compound Boussinesq model." *J. Hydraul. Res*., 52 (1), 24–35.

Metallinos, A. S., and Memos, C. D. (2012). "Wave-induced kinematics inside submerged porous structures." *J. Hydraul. Res*., 50 (4), 388-394.

Metallinos, A. S., Repousis, E. G., and Memos, C. D. (2016). "Wave propagation over a submerged porous breakwater with steep slopes." *Ocean Eng.*, 111, 424-438.

Ming, D., and Chiew, Y.-M. (2000). "Shoreline changes behind detached breakwater." *J. Waterw. Port Coast. Ocean Eng.*, 126 (2), 63-70.

Mogridge, G. R. (1974). "Scale laws for bed forms in laboratory wave models." *Proc. 14th Int. Conf. on Coastal Engineering*, ASCE, Copenhagen, Denmark, vol. II, chapter 62, pp. 1069-1085.

Morison, J. (1949). "Model study of wave action on underwater barriers." *Tech. rep.*, *Report HE-116-304*, Inst. Eng. Res., Univ. Calif., Berkeley.

Motta, V. F. (1986). "Scale effects offshore of coastal mobile-bed models." *Proc. Symp. on Scale Effects in Modelling Sediment Transport Phenomena*, IAHR, Toronto, Canada, pp. 460-474.

Noda, E. K. (1971). "Coastal movable-bed scale-model relationship." TETRAT-P-71-191-1, Tetra Tech, Inc., Pasadena, California, U.S.A.

Noda, E. K. (1972). "Equilibrium beach profile scale-model relationship." *J. Waterw. Harb. Coast. Eng. Div.*, WW4, 511-528.

Oumeraci, H. (1984). "Scale effects in coastal hydraulic models." *Proc. Symp. on Scale Effects in Modelling Hydraulic Structures*, H. Kobus, ed., IAHR, Esslingen am Neckar, Germany, pp. 7.10-1 - 7.10-7.

Penney, W., and Price, A. (1952). "The diffraction theory of sea waves and the shelter afforded by breakwaters." *Phil. Trans. R. Soc. Lond. A*, 244 (882), 236-253.

Pilarczyk, K. W. (2003). "Design of low-crested (submerged) structures – an overview –." *6th International Conference on Coastal and Port Engineering in Developing Countries*, Colombo, Sri Lanka.

Powell, K., and Allsop, N. (1985). "Low-crested breakwaters, hydraulic performance and stability." *Tech. rep.* SR 57, HR Wallingford.

Prasetya, G. (2007). "Protection from coastal erosion: thematic paper: the role of coastal forests and trees in protecting against coastal erosion." *Proc. Reg. Tech. Work.*, Regional Office for Asia and the Pacific, Rap Publication, Khao Lak, Thailand, chapter 4, pp. 103-132.

Ranasinghe, R., and Turner, I. L. (2006). "Shoreline response to submerged structures: A review." *Coast. Eng.*, 53 (1), 65-79.

Ranasinghe, R., Turner, I. L., and Symonds, G. (2006). "Shoreline response to multi-functional artificial surfing reefs: A numerical and physical modelling study." *Coast. Eng.*, 53 (7), 589–611.

Samlidis, N. “Wave transmission behind submerged breakwaters.” MSc thesis, National Technical University of Athens (in Greek).

Schäffer, H. A. (1993). "Laboratory wave generation correct to second order." *Proc. Int. Conf. Wave Kinematics and Environmental Forces*, London, United Kingdom, Society for Underwater Technology, pp. 115-139.

Seabrook, S. R., and Hall, K. R. (1997). “Effect of crest width and geometry on submerged breakwater performance.” *Proc. Canadian Coastal Conference*, CCSEA, 58-72.

Seelig, W. N. (1980). “Two-dimensional tests of wave transmission and reflection characteristics of laboratory breakwaters.” *Tech. rep.* No. 80-1, CERC, Fort Belvoir.

Seiji, W. N., Uda, T., and Tanaka, S. (1987). “Statistical study on the effect and stability of detached breakwaters.” *Coastal Eng. Japan*, 30 (1), 121– 131.

Sharif Ahmadian, A. (2016). *Numerical models for submerged breakwaters. Coastal hydrodynamics and morphodynamics.* Butterworth-Heinemann, Elsevier, 362 pp.

Stauble, D. K., Tabar, J. R., and Smith, J. B. (2000). “Performance of a submerged breakwater along a hardbottom influenced coast: Vero Beach, Florida.” *Proc. 13th National Conference on Beach Preservation Technology*, Melbourne, Florida, USA, pp. 175– 190.

Stucky, A., Bonnard, D. (1937). “Contribution to the experimental study of marine rockfill dikesbull.” *Tech. rep.*, Technique de Suizze Romande (also summary in Tech. Memo. 1, Beach Erosion Board, 1940).

Tajziehchi, M., and Cox, R. (2006). “Wave transmission and wave-induced current in presence of submerged breakwaters.” *Proc. 30th Int. Conf. on Coastal Engineering*, J. M. Smith, ed., San Diego, U.S.A., vol. 5, pp. 4970-4982.

Tomassicchio, U. (1996). “Submerged breakwaters for the defence of the shoreline at Ostia: field experiences, comparison.” *Proc. 25th Int. Conf. on Coastal Eng.*, B. L. Edge, ed., Orlando, Florida, U.S.A., pp. 2404–2417.

Turner, I. L. (2006). “Discriminating modes of shoreline response to offshore-detached structures.” *J. Waterw. Port Coast. Ocean Eng.*, 132 (3), 180-191.

Turner, I. L., Leyden, V. M., Cox, R. J., Jackson, L. A., and McGrath, J. (2001). “Physical model study of the gold coast artificial reef.” *J. Coast. Res.*, Special Issue 29, 131–146.

Valembois, J. (1960). "Etude sur modele du transport littoral conditions de similitude." *Proc. 7th Int. Conf. on Coastal Engineering*, J. W. Johnson, ed., Vol. 1, The Hague, Netherlands, 277-307 (in french).

Van der Biezen, S. C., Van der Graaff, J., Schaap., J., Torrini, L. (1997). "Small scale tests and numerical modeling of the hydrodynamic and morphological effects of submerged breakwaters." *Proc. Combined Australian Coastal Engineering and Ports Conf.*, 219-224.

Van der Meer, J. W. (1988). "Rock slopes and gravel beaches under wave attack." Ph.D. thesis, Delft University of Technology, *Delft Hydraulics Rep.* No. 396.

Van der Meer, J. W. (1991). "Stability and transmission at low-crested structures." *Tech. rep.*, No. H 453, *Delft Hydraulics*, 33 pp.

Van der Meer, J. W., Briganti, R., Zanuttigh, B., and Wang, B. (2005). "Wave transmission and reflection at low-crested structures: Design formulae, oblique wave attack and spectral change." *Coast. Eng.*, 52 (10-11), 915-929.

Van der Meer, J. W., and Daemen, I. F. R. (1994). "Stability and wave transmission at low-crested rubble-mound structures." *J. Waterw. Port Coast. Ocean Eng.*, 120 (1), 1-19.

Vanlishout, V., Verhagen, H., and Troch, P. (2010). "Oblique wave transmission through rough impermeable rubble mound submerged breakwaters." *Proc. 32nd Int. Conf. on Coastal Engineering*, J. M. Smith and P. J. Lynett, eds, Shanghai, China, vol. 1, pp. 255-264.

Vicinanza, D., Caceres, I., Buccino, M., Gironella, X., and Calabrese, M. (2009). "Wave disturbance behind low-crested structures: Diffraction and overtopping effects. *Coast. Eng.*, 56 (11-12), 1173-1185.

Vidal, C., Lomónaco, P., Migoya, L., Archetti, R., Turchetti, M., Sorci, M., and Sassi, G. (2002). "Laboratory experiments on flow around and inside LCS structures. Description of tests and data base." *Tech. Rep.*, DELOS European Project, 19 pp.

Visser, P. J. (1991). "Laboratory measurements of uniform longshore currents." *Coast. Eng.*, 15 (5-6), 563-593.

Walkley A., and Black, I. A. (1934). "An examination of the Degtjareff method for determining soil organic matter and a proposed modification of the chromic acid titration method." *Soil Sci.*, 37, pp. 29–38.

Wang, P., Smith, E. R., and Ebersole, B. A. (2002). "Large-scale laboratory measurements of longshore sediment transport under spilling and plunging breakers." *J. Coast. Res.*, 18(1), 118–135.

Warnock, J. E. (1950). "Hydraulic similitude." In: Engineering Hydraulics, H. Rouse, ed., John Wiley & Sons, New York, pp. 136-176.

Yalin, M. S. (1972). "On the geometrically similar reproduction of dunes." *Proc. 13th Int. Conf. on Coastal Engineering*, ASCE, Vancouver, Canada, vol. 2, pp. 1143-1154.

Zanuttigh, B., Guerrero, M., and Lamberti, A. (2003). "3D experimental analysis and numerical simulations of hydrodynamics around low crested structures." *Proc. IAHR Conf.*, Thessaloniki, Greece, 369-376.

Zanuttigh, B., and Lamberti, A. (2006). "Experimental analysis and numerical simulations of waves and current flows around low-crested rubble-mound structures." *J. Waterw. Port Coast. Ocean Eng.*, 132 (1), 10-27.

Chapter 6

Model extension to porous beds

6.1 Introduction

In the previous chapter the behavior of submerged breakwaters was studied through laboratory experiments performed in the context of the present Ph.D. thesis. In addition, a literature review of other experimental research works including submerged structures was presented. However, the technical difficulties in building 3D physical models including arrays of submerged breakwaters, especially when studying geomorphological issues, along with the inherent uncertainty and complexity of the relevant physical processes have resulted to only a restricted number of such experimental works. On the other hand, it is more convenient to study the behavior of submerged structures numerically because it is, generally, less costly and much faster to make a large number of numerical experiments required for studying the effect of various parameters on the hydrodynamics and morphodynamics, such as the breakwater's length, crest width, slopes, porosity, etc. Thus, a significant number of numerical models and methods have been developed, mainly for studying the hydrodynamic behavior of submerged breakwaters. Very few models have been developed though for their geomorphological response. It should be mentioned that submerged breakwaters are permeable structures along their perimeter and consequently they can be studied as special cases by models simulating wave propagation over porous beds.

Longuet-Higgins (1967) presented an analytical formula to calculate the wave setup for submerged breakwaters exposed to non-breaking waves. The mean sea level difference between the two sides of the breakwater was calculated based on the wave height, the water depth and the wavenumber of incident, reflected and transmitted waves. Sollitt and Cross (1972) in their pioneering work presented an analytical approach having as starting point the unsteady equations for flow in the pores of a coarse granular media. Liu (1973) and Liu and Dalrymple (1984) developed a numerical tool for calculating the damping rates for linear dispersive waves on horizontal permeable beds. Madsen (1977) included inertia and

resistance forces, due to the presence of a rectangular porous structure, in his linear wave model.

Massel and Butowski (1980) developed a model for prediction of two-dimensional (1DH) wave transmission and reflection in the presence of porous breakwaters. Numerical models based on the nonlinear shallow water equations and porous flow equations have been used to study the swash motion of nondispersive, long waves on porous beaches and coastal structures by Packwood (1983), Wurjanto and Kobayashi (1993), and Clarke *et al.* (2004). Powell and Allsop (1985) provided empirical curves as design guidelines for the prediction of wave transmission coefficient over low-crested permeable breakwaters with 40% porosity. Kobayashi and Wurjanto (1988) presented a 2D (1DH) numerical model based on the finite amplitude shallow water equations to predict monochromatic wave transmission over an impermeable submerged breakwater. Ahrens (1989) presented a model for predicting the stability of reef breakwaters in terms of reduction in crest height due to wave attack.

Based on the mild-slope equation, Rojanakmthorn *et al*. (1990) developed an elliptic-type numerical model for wave transformation by permeable submerged breakwaters but it underestimated the results in comparison with laboratory measurements. Linear wave propagation over porous seabeds was also investigated theoretically and experimentally by Gu and Wang (1991), extending the analysis by Sollitt and Cross (1972).

Battjes (1994) and Beji and Battjes (1994) developed a weakly nonlinear Boussinesq-type model with improved dispersion characteristics and its application over impermeable submerged breakwaters gave good results. Flaten and Rygg (1991) were the first to employ the Boussinesq approach together with Darcy's law to model weakly dispersive and weakly nonlinear waves over an uneven permeable seabed. Using a perturbation method, Isobe *et al*. (1991) and Cruz *et al*. (1992) derived a set of weakly nonlinear time-dependent equations for 1DH wave transformation over permeable beds. However, due to the inherent weak dispersivity, the frequency-dependent decomposition phenomenon beyond submerged breakwaters cannot be reproduced. Cruz *et al*. (1997) treated this problem by enhancing the dispersion characteristics of the Boussinesq-type equations of the model which were also extended to two horizontal dimensions. Liu and Wen (1997) also incorporated porous flow equations into a 2DH Boussinesq-type model of $O(\varepsilon\sigma^2)$. Kioka *et al*. (1994) derived a 1DH model for porous structures based on the shallow water equations. However, it was only accounting for horizontal solid beds.

Van Gent (1994, 1995) simulated wave interaction with permeable and impermeable coastal structures by developing a 1DH model based on the nonlinear shallow water equations (NSWE) and a two vertical dimensional (2DV) model based on the Reynolds-averaged Navier-Stokes equations (RANS). As part of his work porous media flow was studied both

theoretically and experimentally with emphasis on the resistance of porous media to oscillatory wave motion. Losada *et al*. (1996) developed a model for the prediction of wave transformation of regular waves with oblique incidence over porous submerged breakwaters. Symonds (1994) and Symonds *et al*. (1995) solved the momentum and continuity equations analytically, assuming linear friction with respect to depth-integrated velocity, and presented an equation for current velocity over the reef top.

A number of predictive equations and models for various variables related to submerged breakwaters (transmission coefficient, wave setup, current velocities) have been also proposed (Loveless and Debski, 1997; Seabrook and Hall, 1998; Gironella and Sanchez-Arcilla, 1999; Drei and Lamberti, 1999; Hearn, 1999; González *et al*., 1999; Muñóz-Pérez *et al*., 1999; Mendez *et al*., 2001; Roul and Faedo, 2002; Calabrese *et al*., 2002, 2003; Melito and Melby, 2002; Friebel and Harris, 2004; Roul *et al*., 2004; van der Meer *et al*., 2004, 2005; Gourlay and Colleter, 2005; Buccino and Calabrese, 2007; Christou *et al*., 2008; Goda and Ahrens, 2008; Zanuttigh *et al*., 2008, Soldini *et al*., 2009).

Lin and Liu (1998) developed a RANS model based on the work by Kothe *et al*. (1991). This model was capable of simulating wave-porous structure interactions considering turbulence generation and dissipation mechanisms. However, it was very much time-consuming. Lynett *et al*. (2000) presented a numerical model based on Boussinesq-type equations to simulate solitary wave interaction with porous breakwaters. Lee *et al*. (2002) also studied numerically the linear wave propagation over horizontal permeable seabeds of finite thickness.

Unlike the use of linearized flow resistance inside the porous layer by Flaten and Rygg (1991) and Cruz *et al*. (1997), Hsiao *et al*. (2002) developed a fully nonlinear 2DH Boussinesq-type model for wave propagating over a permeable bed and compared the model results with experimental data for the case of regular waves passing over a submerged breakwater. However, their model is limited to wave motions with rather weak vertical vorticity, or to nearly irrotational flows over a permeable bed. Chen (2006) presented also a fully nonlinear Boussinesq-type model for waves and currents over porous beds. His model was also valid in areas with strong vorticity generated by spatial variations of wave breaking and flow resistance inside the porous beds, including rubble mound coastal structures. Avgeris *et al*. (2004) presented a 2DH Boussinesq-type model for simulating wave propagation over permeable submerged breakwaters based on Karambas and Koutitas (2002) model.

Shen *et al*. (2004) simulated the propagation of cnoidal waves over a submerged breakwater using a two-equation k-ε turbulence model based on the volume of fluid (VOF) method. Garcia *et al*. (2004) developed a 2DV RANS model (COBRAS) based on the decomposition

of the instant velocity and pressure fields into mean and turbulent components in order to calculate the water surface elevation and flow in the presence of permeable low-crested breakwaters for regular breaking waves. The model was extended by Lara *et al*. (2006) for random waves. Johnson *et al*. (2005) and Cáceres *et al*. (2005) applied numerical models to simulate wave and current fields around submerged breakwaters. Van Oosten and Peixó Marco (2005), van Oosten *et al*. (2006), and Panizzo and Briganti (2007) developed artificial neural network models for the prediction of the wave transmission coefficient behind 2D (1DH) submerged structures. Kobayashi *et al*. (2007) developed a time-averaged model to predict the mean and standard deviation of the free surface elevation and horizontal fluid velocities above and inside a porous submerged breakwater. Lin (2006) extended Lin and Li's (2003) model to account for submerged rectangular breakwaters with sudden topography changes. His model is a 3D multiple-layer σ-coordinate model which solves the Navier-Stokes equations for the interaction of water waves with submerged and emerged structures. Liu *et al.* (2013) developed a 2DV model based on Incompressible Smoothed Particle Hydrodynamics (ISPH) to simulate free surface flow in presence of various impermeable coastal structures and its application for predicting wave transmission showed good agreement with experimental data. Sharif Ahmadian and Simons (2014) presented a numerical method to calculate the spatial transmission coefficient and the regular wave field around and behind 3D detached submerged breakwaters. A very detailed review of existing numerical models related to submerged breakwaters can be found in Sharif Ahmadian (2016).

On the other hand, only a restricted number of studies involving numerical models simulating the bed morphology evolution in the lee of submerged breakwaters have been presented. Some of them refer to the shoreline response to the submerged structures (Watanabe *et al*., 1986; Hanson and Kraus, 1990; O'Connor and Nicholson, 1995). Zyserman *et al*. (1999) and Jiménez and Sánchez-Arcilla (2002) analyzed the morphodynamic effects of a detached breakwater considering its geometry and location at the beach in short and long term, respectively.

Van der Biezen *et al*. (1998) presented the results of 2DH numerical modelling of the morphological evolution behind an array of submerged breakwaters. The model used was Delft3D which is based on the nonlinear shallow water equations. The results were compared with experimental measurements (de Later, 1996; van der Biezen *et al*., 1996) referring to normal regular wave incidence. The submerged breakwaters were rubble mound with an impermeable core. The morphodynamic effects of submerged breakwaters were also investigated numerically by Lesser *et al*. (2003) who indicated that an inappropriate design may result to significant erosion at the shoreline.

The hydrodynamic and morphodynamic effects of artificial reefs were studied both experimentally and numerically by Ranasinghe *et al*. (2006). The applied numerical model was MIKE21. In addition, Ranasinghe and Sato (2007) and Ranasinghe *et al*. (2010) simulated the beach morphological evolution behind a single shore-parallel submerged breakwater under normal or oblique wave incidence.

Koutsouvela *et al*. (2007) simulated the bed morphology evolution in the lee of a system of submerged breakwaters based on a mild-slope equation model. Although the results seemed reasonable, no comparison with measurements was given. The bed load was computed from Ribberink's (1998) formula, while the suspended load by assuming an exponential profile for the sediment concentration. Koutsouvela (2010) presented a 2DH compound numerical model for simulating wave propagation, sediment transport and morphological evolution. The wave model relied on enhanced nonlinear Boussinesq-type equations (Beji and Nadaoka, 1996; Karambas and Karathanassi, 2004). Her model was also applied to simulate the bed evolution behind a system of impermeable submerged breakwaters. However, no validation with measurements was presented. Karambas (2012) also presented a model combining the Boussinesq-type wave model by Karambas and Karathanassi (2004) with a sediment transport and a morphological model. The compound model was applied to simulate the cross-shore morphology evolution with and without an artificial reef. This model was also applied by Karambas and Samaras (2014) to simulate in 1DH the bed profile evolution behind a submerged breakwater. The agreement with the measurements by Di Risio *et al*. (2010) was fairly good.

In this chapter the compound numerical model that was presented in chapter 4 is extended to account for porous beds. Then, this final version of the model is validated against the measurements of the laboratory experiments presented in chapter 5 in order to check the model's efficiency to simulate the wave propagation over submerged breakwaters and the bed morphology evolution in the lee of such structures.

6.2 Derivation of model equations for porous beds

In order to simulate the wave propagation over permeable submerged breakwaters and the corresponding bed morphology evolution, the compound model described in chapters 3 and 4 has to be extended to porous beds. The model equations will be derived following Cruz *et al*. (1997). The presented 2DH Boussinesq-type wave model for an impermeable bed consists of Eqs (3.9), (2.17) and (2.18). Herein a porous layer of thickness $h_s(x, y)$ is considered below the free water which has a thickness of $d(x, y)$. Below the porous layer an impermeable

bottom at $z = -h_b(x, y)$ is considered. The rest of the variables involved were defined in chapter 2. The variables and domain of interest are shown in Fig. 6.1.

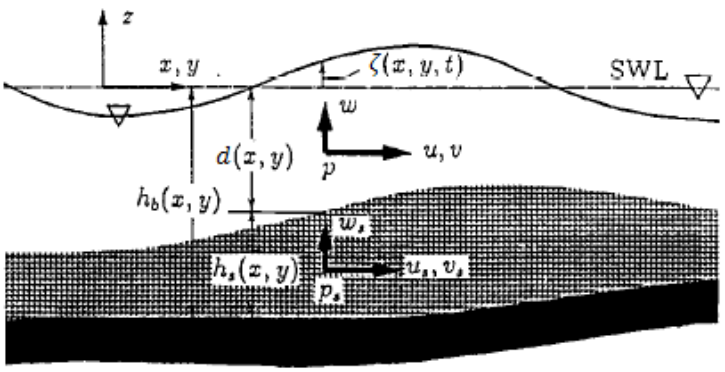

Fig. 6.1. Definition of variables (from Cruz *et al.*, 1997, modified).

The flow is assumed incompressible and irrotational in both layers. The equations of motion inside the porous medium is given by the extended Darcy-Forchheimer equation (Darcy, 1856; Forchheimer, 1901; Polubarinova-Kochina, 1952; van Gent, 1995; Cruz *et al.*, 1997):

$$\lambda\left[\frac{\partial \vec{u}_{s,3}}{\partial t} + (\vec{u}_{s,3} \cdot \nabla_3)\vec{u}_{s,3}\right] + \frac{1}{\rho}\nabla_3(p_s + \rho g z) + \vec{F}_r + \vec{F}_i = \vec{0} \tag{6.1}$$

where λ is the porosity, $\vec{u}_{s,3} = (u_s, v_s, w_s)$ is the seepage velocity vector, ρ is the fluid density, p_s is the pore pressure, $\nabla_3 = \left(\frac{\partial}{\partial x}, \frac{\partial}{\partial y}, \frac{\partial}{\partial z}\right)$ is the three-dimensional gradient operator, $\vec{F}_r$ is the drag resistance term, and $\vec{F}_i$ is the inertial resistance term. The nonlinear resistance term is given by

$$\vec{F}_r = \alpha_1 \vec{u}_{s,3} + \alpha_2 |\vec{u}_{s,3}| \vec{u}_{s,3} \tag{6.2}$$

where the coefficients α_1 and α_2 represent the laminar and turbulent contributions to the flow resistance, respectively. In general, these coefficients depend on the medium and the fluid and their expressions are given in the following. In unsteady flows, an inertial resistance term $\vec{F}_i$ is necessary to account for the divergence and convergence of streamlines in the presence of the solid surfaces. $\vec{F}_i$ is the product of the displaced fluid mass, the virtual mass coefficient and the 1ocal acceleration in the flow direction. Per unit volume of water, this is expressed as

$$\vec{F}_i = (1 - \lambda)(1 + c_m)\frac{d\vec{u}_{s,3}}{dt} \tag{6.3}$$

where c_m is the added mass coefficient which can be evaluated for individual regular shapes but is genereally unknown for randomnly packed granular solids. From Eqs (6.1), (6.2) and (6.3) one gets

$$c_\mathrm{r}\frac{d\vec{u}_{s,3}}{dt}+\frac{1}{\rho}\nabla_3(p_\mathrm{s}+\rho gz)+\alpha_1\vec{u}_{s,3}+\alpha_2\left|\vec{u}_{s,3}\right|\vec{u}_{s,3}=\vec{0} \tag{6.4}$$

where c_r is the inertial coefficient:

$$c_\mathrm{r}=\lambda+(1-\lambda)(1+c_\mathrm{m}) \tag{6.5}$$

Assuming a uniform porosity the mass conservation equation for the porous layer is written:

$$\nabla_3\cdot\vec{u}_{s,3}=0 \tag{6.6}$$

In the overlying water the equations of motion and mass conservation apply:

$$\frac{\partial\vec{u}_3}{\partial t}+(\vec{u}_3\cdot\nabla_3)\vec{u}_3+\frac{1}{\rho}\nabla_3(p+\rho gz)=\vec{0} \tag{6.7}$$

$$\nabla_3\cdot\vec{u}_3=0 \tag{6.8}$$

with $\vec{u}_3=(u,v,w)$ the water particle velocity and p the pressure. At the free surface the dynamic and kinematic conditions are:

$$p=0 \qquad \text{at} \quad z=\zeta(x,y,t) \tag{6.9}$$

$$w=\frac{\partial\zeta}{\partial t}+\vec{u}\cdot\nabla\zeta \qquad \text{at} \quad z=\zeta(x,y,t) \tag{6.10}$$

where $\vec{u}=(u,v)$ is the horizontal velocity vector and $\nabla=\left(\frac{\partial}{\partial x},\frac{\partial}{\partial y}\right)$ is the horizontal gradient operator. At the impermeable bottom, the normal velocity vanishes:

$$w_s=-\vec{u}_s\cdot\nabla h_b \qquad \text{at} \quad z=-h_b(x,y) \tag{6.11}$$

where $\vec{u}_s=(u_s,v_s)$ is the horizontal seepage velocity vector.

Due to the incompressibility assumption, the conservation of the normal mass flux at the interface of the two layers gives:

$$\vec{u}\cdot\nabla d+w=\lambda(\vec{u}_s\cdot\nabla d+w_s) \quad \text{at} \quad z=-d(x,y) \tag{6.12}$$

In addition, there must be equal pressures on both sides of the interface:

$$p=p_\mathrm{s} \qquad \text{at} \quad z=-d(x,y) \tag{6.13}$$

The shear stress on water-porous layer interface and porous layer-bottom interface will set-up boundary layers whose thickness may be comparable to the granule size. However, Sawaragi and Deguchi (1992) have shown that even for the highly nonlinear waves or for the highly porous media, the interface shear stress is small compared to the other terms in Eq. (6.1) or Eq. (6.4). The interface conditions (6.12) and (6.13) do not ensure the continuity of tangential velocities on both sides of the interface. Thus, an additional assumption made is that there is a boundary layer, thick enough to equalize the tangential velocities, but also thin enough not to affect the flows above or below it.

The aforementioned equations refer to dimensional variables, although the primes have been dropped until now. However, in the following the primes denote dimensional variables, while the non-dimensional ones are denoted without primes. Following a similar derivation as the one applied in the subsection 2.3.1 for impermeable beds, the model equations for permeable beds are obtained. The non-dimensionalization applied is the one given in subsection 2.3.1 plus the following scaling for the variables in the porous layer:

$$h_s = \frac{h_s{}'}{d_o{}'}\ ,\ h_b = \frac{h_b{}'}{d_o{}'}\ ,\ \vec{u}_s{}' = \vec{u}_s \varepsilon \sqrt{\mathrm{g} d_o{}'}\ , w_s{}' = w_s \varepsilon \sigma \sqrt{\mathrm{g} d_o{}'}\ , p_s{}' = \varepsilon \rho \mathrm{g} d_o{}' p_s \qquad (6.14)$$

By integrating the continuity Eqs (6.6) and (6.8) and the momentum Eqs (6.4) and (6.7) over depth and applying the boundary conditions (6.9), (6.10), (6.11), (6.12), (6.13), the depth-integrated equations are obtained in terms of the depth-averaged velocity in the free water body, $\vec{U} = (U, V)$, and the depth-averaged velocity in the porous layer, $\vec{U}_s = (U_s, V_s)$. In particular, these velocities are defined by $\vec{U} = \frac{1}{d+\varepsilon\zeta}\int_{-d}^{\varepsilon\zeta} \vec{u}\ \mathrm{d}z$ and $\vec{U}_s = \frac{1}{h_s}\int_{-h_b}^{-d} \vec{u}_s \mathrm{d}z$.

Similarly to chapter 2, the two linear operators given by Eq. (2.15) are applied to the resulting momentum equations in the free water body in order to enhance the linear dispersion and shoaling characteristics. In addition, following Cruz *et al*. (1997), the following linear operator was applied to the momentum equations inside the porous layer:

$$L_\gamma = 1 + \gamma \sigma^2 \nabla [d \nabla \cdot (h_s\, \cdot)] \qquad (6.15)$$

where γ is parameter to be defined.

The resulting equations in non-dimensional form are:

$$\frac{\partial \zeta}{\partial t} + \nabla \cdot \left[\vec{U}(d + \varepsilon\zeta)\right] + \lambda \nabla \cdot \left(h_s \vec{U}_s\right) = 0 \qquad (6.16)$$

$$\vec{U}_t + \varepsilon\left(\vec{U} \cdot \nabla\right)\vec{U} + \nabla\zeta = \sigma^2 \vec{\psi}_I + \varepsilon\sigma^2 \vec{\psi}_{II} + \varepsilon^2 \sigma^2 \vec{\psi}_{III} + \sigma^2\ \frac{\lambda}{2} d \nabla\left[\nabla \cdot \left(h_s \vec{U}_{st}\right)\right] \qquad (6.17)$$

$$
\begin{aligned}
c_{\mathrm{r}}\left[\vec{U}_{st}+\varepsilon\left(\vec{U}_s\cdot\nabla\right)\vec{U}_s\right]+\nabla\zeta+\alpha\vec{U}_s \\
+\sigma^2\left\{\frac{1}{2}\left(c_{\mathrm{r}}\frac{\partial}{\partial t}+a\right)\left[-\frac{2}{3}{h_s}^2\nabla\left(\nabla\cdot\vec{U}_s\right)-h_s\nabla\left(\nabla h_b\cdot\vec{U}_s\right)\right.\right. \\
\left.+h_s\nabla(d-h_s)\nabla\cdot\vec{U}_s+2\nabla d\nabla h_b\cdot\vec{U}_s\right]-\frac{1}{2}\nabla\left[\nabla\cdot\left(d^2\vec{U}_t\right)\right] \\
-(1+\gamma)\lambda\nabla\left[d\nabla\cdot\left(h_s\vec{U}_s\right)\right]-\frac{\gamma}{c_{\mathrm{r}}}\lambda\nabla\left[d\nabla\cdot\left(h_s\nabla\zeta\right)\right] \\
\left.-\frac{\gamma\alpha}{c_{\mathrm{r}}}\lambda\nabla\left[d\nabla\cdot\left(h_s\vec{U}_s\right)\right]\right\}=\vec{0}
\end{aligned}
\tag{6.18}
$$

with $\alpha=\alpha_1+\alpha_2\left|\vec{U}_s\right|$ and $\vec{\psi}_I=\left(\psi_I^{(x)},\psi_I^{(y)}\right)$, $\vec{\psi}_{II}=\left(\psi_{II}^{(x)},\psi_{II}^{(y)}\right)$, and $\vec{\psi}_{III}=\left(\psi_{III}^{(x)},\psi_{III}^{(y)}\right)$ where $\psi_I^{(x)},\psi_I^{(y)},\psi_{II}^{(x)},\psi_{II}^{(y)},\psi_{III}^{(x)},\psi_{III}^{(y)}$ are given from the non-dimensional version of Eqs (2.19), (2.20), (2.21), (2.22), (2.23) and (2.24), respectively.

Equations (6.16), (6.17) and (6.18) are the model's basic equations. It should be mentioned that terms of $O(\varepsilon^2\sigma^2)$ are retained in the momentum Eq. (6.17) in the free water layer, while terms of $O(\varepsilon,\sigma^2)$ are retained in the momentum Eq. (6.18) in the porous medium. This is a difference from other Boussinesq-type models for porous beds which only consider a nonlinear shallow water equation of $O(\varepsilon)$ for the porous medium (Avgeris *et al*., 2004). It will be shown in subsection 6.3 that the additional terms of $O(\sigma^2)$ may be important when simulating short wave propagation. In the absence of the porous layer Eqs (6.16) and (6.17) reduce to Eqs (2.16) and (2.17) - (2.18), respectively.

It was discussed in chapter 2 that the free parameters B and B_2 were set equal to $B=\frac{1}{15}$ and $B_2=0.0653$ in order to optimize the linear dispersion and linear shoaling characteristics of the equations. However, this is valid only for simulating wave propagation over impermeable beds. For a permeable bottom these values, along with the free parameter γ, have to be re-adjusted. In order to compute the new optimal values of these parameters, a Fourier-type analysis is applied, similarly to the one in chapter 2.

The 1DH linearized version of Eqs (6.16), (6.17) and (6.18) is considered over a horizontal bottom overlain by a uniform porous layer. A linear wave over the porous bed is described by

$$
(\zeta,U,U_s)=(\mathrm{a}_1,U_1,U_{s1})e^{\mathrm{i}(kx-\omega t)} \tag{6.19}
$$

where ω is the angular frequency, k is the complex wavenumber, and $\mathrm{a}_1, U_1, U_{s1}$ are the relevant amplitudes. Substitution of Eq. (6.19) into the 1DH linearized horizontal version of Eqs (6.16), (6.17), (6.18) leads to the system of equations:

$$\begin{pmatrix} -\omega & kd & \lambda k h_s \\ k\left(1+\mathrm{B}\kappa^2\right) & -\omega\left[1+\left(\frac{1}{3}+\mathrm{B}\right)\kappa^2\right] & -\frac{1}{2}\lambda\omega\kappa\kappa_s \\ k\left(1+\frac{\gamma}{c_\mathrm{r}}\lambda\kappa\kappa_s\right) & -\frac{1}{2}\omega\kappa^2 & -\omega\varphi \end{pmatrix} \begin{pmatrix} \mathrm{a}_1 \\ U_1 \\ U_{s1} \end{pmatrix} = \begin{pmatrix} 0 \\ 0 \\ 0 \end{pmatrix} \tag{6.20}$$

where

$$\varphi = \left(c_\mathrm{r} + \mathrm{i}\frac{\alpha}{\omega}\right)\left(1+\frac{1}{3}{\kappa_s}^2\right) + \lambda\kappa\kappa_s\left(1+\gamma+\mathrm{i}\frac{\gamma\alpha}{\omega c_\mathrm{r}}\right) \tag{6.21}$$

with $\kappa = \sigma k d$ and $\kappa_s = \sigma k h_s$.

A non-trivial solution exists only if the determinant of the matrix vanishes, leading to:

$$\frac{\omega^2}{k^2 d} = \frac{1+\mathrm{B}\kappa^2}{1+\left(\mathrm{B}+\frac{1}{3}\right)\kappa^2} + \frac{\lambda h_s}{\varphi d}\left(1+\frac{\gamma}{c_\mathrm{r}}\lambda\kappa\kappa_s\right) - \frac{\frac{\lambda\kappa\kappa_s}{2\varphi}\left[\left(1+\frac{\gamma}{c_\mathrm{r}}\lambda\kappa\kappa_s\right) - \kappa^2\frac{\omega^2}{2k^2 d} + \left(1+\mathrm{B}\kappa^2\right)\right]}{1+\left(\mathrm{B}+\frac{1}{3}\right)\kappa^2} \tag{6.22}$$

If $h_s = 0$ or $\lambda = 0$ the dispersion relation Eq. (6.22) reduces to Eq. (2.61) which accounts for impermeable beds. The non-dimensional analytical solution of the linearized problem for porous beds is (Gu and Wang, 1991; Cruz, 1994):

$$\frac{\omega^2}{k^2 d} - \frac{tanh(\kappa)}{\kappa} = -\mathrm{i}R tanh(\kappa_s)\left[\frac{1}{\kappa} - \frac{\omega^2}{k^2 d}tanh(\kappa)\right] \tag{6.23}$$

where R is the non-dimensional permeability given by

$$R = \frac{\lambda\omega}{\alpha_1} \tag{6.24}$$

Since linear analysis has been applied, only the linear part, α_1, of α is retained. According to Sollitt and Cross (1972):

$$\alpha_1 = \frac{\nu\lambda}{K} \quad \text{and} \quad \alpha_2 = \frac{\mathrm{C_f}\lambda^2}{\sqrt{K}} \tag{6.25}$$

where ν is the kinematic viscosity of the fluid and $\mathrm{C_f}$ is a turbulent friction coefficient, which according to Ward (1964) is constant and equal to 0.55. However, van Gent (1995) proposed the following expression:

$$\mathrm{C_f} = \mu\frac{1-\lambda}{\lambda}\frac{\sqrt{K}}{d_{50}} \tag{6.26}$$

where μ is an empirical coefficient with a typical value $\mu = 1.1$ (van Gent, 1995; Avgeris *et al*., 2004).

In the equations above, K is the intrinsic permeability which may be calculated from the following expressions (Engelund, 1953; van Gent, 1995; Burcharth and Andersen, 1995):

$$K = \frac{{d_{50}}^2\lambda^3}{\xi(1-\lambda)^2} \quad \text{and} \quad K = \frac{{d_{50}}^2\lambda^2}{\xi(1-\lambda)^3} \tag{6.27}$$

where ξ is an empirical coefficient. The former expression was adopted in the presented model with a typical value $\xi = 1000$ (van Gent, 1995; Avgeris *et al*., 2004).

An alternative expression for α_2 was proposed by van Gent (1995) based on a Keulegan-Carpenter number for porous media flow, $\mathrm{KC}=\widehat{U}T/(d_{50}\cdot\lambda)$, with $\widehat{U}$ the maximum velocity in the porous medium and T the wave period. In particular:

$$\alpha_2 = \mu\left(1+\frac{7.5}{\mathrm{KC}}\right)\frac{1-\lambda}{d_{50}\lambda^3} \tag{6.28}$$

However, in the present Ph.D. thesis the expression given in Eq. (6.25) was applied for α_2.

From Eqs (6.24) and (6.25) one gets $R = \omega K/\nu$, which is the non-dimensional permeability of $O(10^{-6}) \div O(10^{-2})$ for sands and $O(10^{-1})$ at most for gravels, within the usual range of frequencies (Cruz *et al*., 1997). For consistency between Eqs (6.22) and (6.23) the values $\alpha = \alpha_1$ and $c_r = 1.0$ are used. The real part of the wavenumber, k_r, governs the phase celerity, while the imaginary part, k_i, corresponds to the spatial damping rate. In particular, one may writes: $k = k_r + \mathrm{i}k_i$ and $\kappa = \kappa_r + \mathrm{i}\kappa_i$. Figs 6.2, 6.4 and 6.6 show the ratio of phase celerities c/c^{theor} as a function of κ_r for given values of the porosity $\lambda = 0.50$ and the permeability $R = 0.1$ and for various values of the relative thickness d/h_s. Following Cruz (1994) and Cruz *et al*. (1997) who performed an optimization process, γ was set equal to 0

and 1/15, while three different values, 0, 1/15 and 1/18, were studied for the parameter B. A similar comparison for the ratio k_i/k_i^{theor} which corresponds to the spatial damping rates is depicted in Figs 6.3, 6.5 and 6.7. It is mentioned that c and k_i are obtained from Eq. (6.22), while c^{theor} and k_i^{theor} from Eq. (6.23).

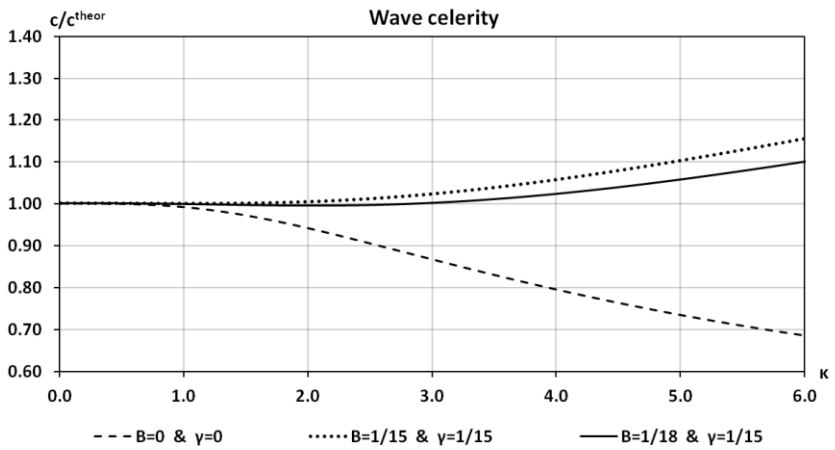

Fig. 6.2. Ratio of phase celerity, c/c^{theor}, where c is determined from Eq. (6.22), c^{theor} from Eq. (6.23), and $\lambda = 0.5$, $R = 0.1$ and $h_s/d = 0.2$.

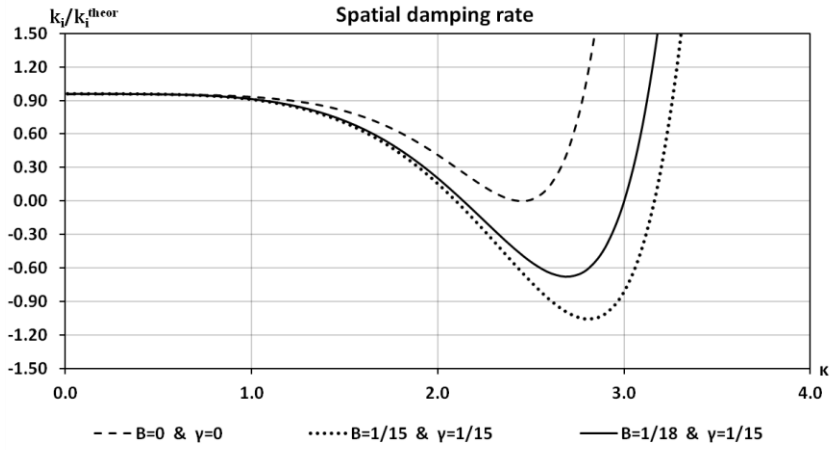

Fig. 6.3. Ratio of porous damping rate, k_i/k_i^{theor}, where k_i is determined from Eq. (6.22), k_i^{theor} from Eq. (6.23), and $\lambda = 0.5$, $R = 0.1$ and $h_s/d = 0.2$.

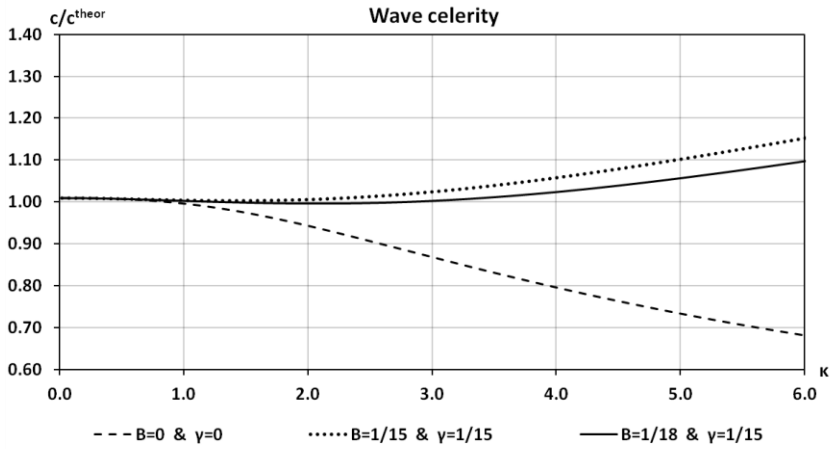

Fig. 6.4. Ratio of phase celerity, c/c^{theor}, where c is determined from Eq. (6.22), c^{theor} from Eq. (6.23), and $\lambda = 0.5$, $R = 0.1$ and $h_s/d = 1.0$.

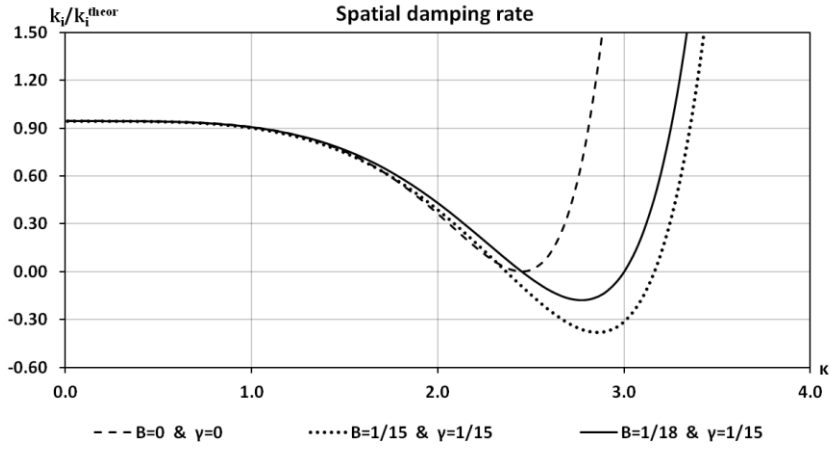

Fig. 6.5. Ratio of porous damping rate, k_i/k_i^{theor}, where k_i is determined from Eq. (6.22), k_i^{theor} from Eq. (6.23), and $\lambda = 0.5$, $R = 0.1$ and $h_s/d = 1.0$.

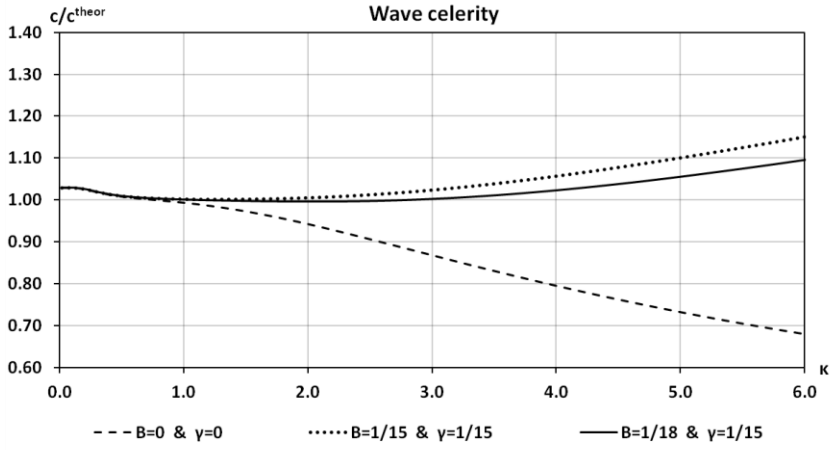

Fig. 6.6. Ratio of phase celerity, c/c^{theor}, where c is determined from Eq. (6.22), c^{theor} from Eq. (6.23), and $\lambda = 0.5$, $R = 0.1$ and $h_s/d = 5.0$.

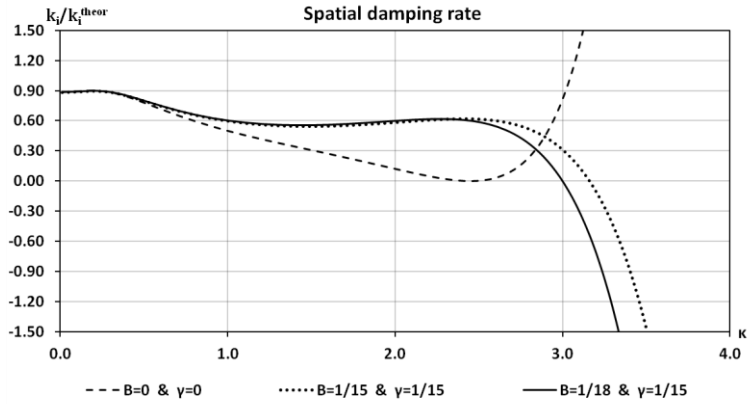

Fig. 6.7. Ratio of porous damping rate, k_i/k_i^{theor}, where k_i is determined from Eq. (6.22), k_i^{theor} from Eq. (6.23), and $\lambda = 0.5$, $R = 0.1$ and $h_s/d = 5.0$.

A similar comparison is depicted in Figs 6.8 and 6.9 in order to highlight the importance of including the terms of $O(\sigma^2)$ in Darcy-Forchheimer Eq. (6.18).

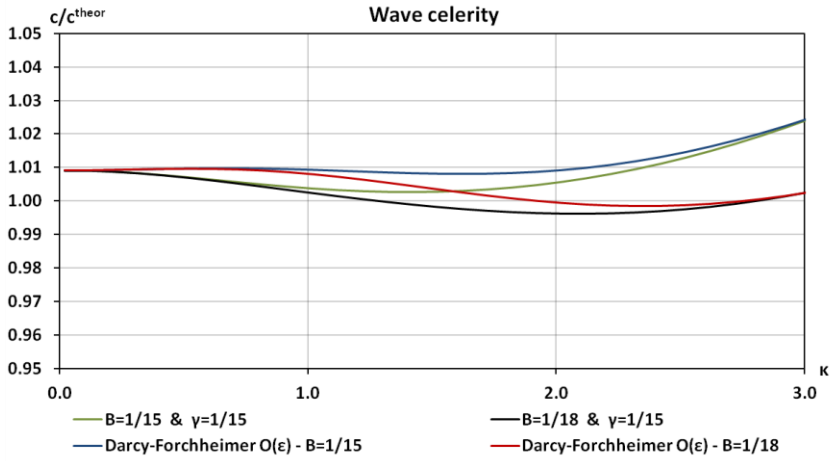

Fig. 6.8. Ratio of phase celerity, c/c^{theor}, for different order of Darcy-Forchheimer Eq. (6.18), i.e. $O(\varepsilon)$ and $O(\varepsilon,\sigma^2)$, and $\lambda = 0.5$, $R = 0.1$ and $h_s/d = 1.0$.

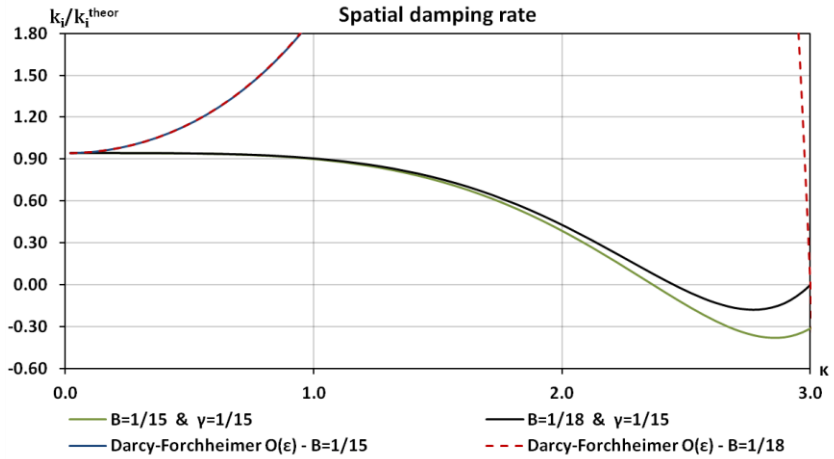

Fig. 6.9. Ratio of porous damping rate, k_i/k_i^{theor}, for different order of Darcy-Forchheimer Eq. (6.18), i.e. $O(\varepsilon)$ and $O(\varepsilon,\sigma^2)$, and $\lambda = 0.5$, $R = 0.1$ and $h_s/d = 1.0$.

From Figs (6.2) to (6.9) it can be observed that adopting the values $(\mathrm{B}, \gamma) = \left(\frac{1}{18}, \frac{1}{15}\right)$ results to an improved model behavior with respect to both the linear dispersion and the linear spatial damping rate compared to the values $(\mathrm{B}, \gamma) = \left(\frac{1}{15}, \frac{1}{15}\right)$ and $(\mathrm{B}, \gamma) = (0, 0)$. However, the prediction of the damping rate remains quite poor in the intermediate and deep water. In addition, the inclusion of terms of $O(\sigma^2)$ in the Darcy-Forchheimer Eq. (6.18) also improves the prediction of the wave celerity compared to the case that only terms of $O(\varepsilon)$ are retained. Although, for the same value of B in both cases, this improvement is not very significant, Fig. 6.9 shows that the nonlinear shallow water equations fail to predict the spatial damping rate in water deeper than approximately $kd \approx 0.5$, which is close to the limit between shallow and intermediate water. Thus, terms of $O(\sigma^2)$ should be retained when simulating wave propagation over permeable submerged breakwaters located in intermediate water. The inclusion of these terms and the modified value of parameter B are two points of novelty of the present model compared to previous counterparts based on Karambas and Koutitas (2002) Boussinesq-type equations (Avgeris *et al*., 2004; Metallinos *et al*., 2014).

It was mentioned above that the added mass coefficient, c_{m}, is generally unknown. In the present model van Gent's (1995) expression was adopted:

$$c_{\mathrm{m}} = \mathrm{q}\frac{1-\lambda}{\lambda} \tag{6.29}$$

with q an empirical coefficient with a typical value of 0.34 (van Gent, 1995; Avgeris *et al*., 2004).

Based on section 3.2 the final dimensional version of the wave model equations for porous beds are written as:

$$\beta\frac{\partial\zeta}{\partial t} + \nabla\cdot\left(\Lambda\vec{U}\right) + \lambda\nabla\cdot\left(h_s\vec{U}_s\right) = 0 \tag{6.30}$$

$$\vec{U}_t + \left(\vec{U}\cdot\nabla\right)\vec{U} + \mathrm{g}\nabla\zeta = \vec{\psi}_I + \vec{\psi}_{II} + \vec{\psi}_{III} + \frac{\lambda}{2}d\nabla\left[\nabla\cdot\left(h_s\vec{U}_{st}\right)\right] + \vec{F}_{br} - \frac{\vec{\tau}_b}{d+\zeta} + \vec{F}_{\mathrm{eddy}} + \vec{F}_{\mathrm{sp}} \tag{6.31}$$

$$
\begin{aligned}
& c_{\mathrm{r}}\left[\vec{U}_{st}+\left(\vec{U}_s\cdot\nabla\right)\vec{U}_s\right]+\mathrm{g}\nabla\zeta+\alpha\vec{U}_s \\
&\quad+\frac{1}{2}\left(c_{\mathrm{r}}\frac{\partial}{\partial t}+a\right)\left[-\frac{2}{3}{h_s}^2\nabla\left(\nabla\cdot\vec{U}_s\right)-h_s\nabla\left(\nabla h_b\cdot\vec{U}_s\right)\right. \\
&\quad\left.+h_s\nabla(d-h_s)\nabla\cdot\vec{U}_s+2\nabla d\nabla h_b\cdot\vec{U}_s\right]-\frac{1}{2}\nabla\left[\nabla\cdot\left(d^2\vec{U}_t\right)\right] \\
&\quad-(1+\gamma)\lambda\nabla\left[d\nabla\cdot\left(h_s\vec{U}_s\right)\right]-\frac{\gamma\mathrm{g}}{c_{\mathrm{r}}}\lambda\nabla[d\nabla\cdot(h_s\nabla\zeta)] \\
&\quad-\frac{\gamma\alpha}{c_{\mathrm{r}}}\lambda\nabla\left[d\nabla\cdot\left(h_s\vec{U}_s\right)\right]=\vec{0}
\end{aligned}
\tag{6.32}
$$

where $\vec{\psi}_I=\left(\psi_I^{(x)},\psi_I^{(y)}\right)$, $\vec{\psi}_{II}=\left(\psi_{II}^{(x)},\psi_{II}^{(y)}\right)$, and $\vec{\psi}_{III}=\left(\psi_{III}^{(x)},\psi_{III}^{(y)}\right)$ are terms of $O(\sigma^2)$, $O(\varepsilon\sigma^2)$, and $O(\varepsilon^2\sigma^2)$, respectively, which are given from Eqs (2.19) - (2.24). $\vec{F}_{br}$ are the breaking terms, $\vec{\tau}_b$ is the bottom friction, $\vec{F}_{\mathrm{eddy}}$ are the Smagorinsky-type terms and $\vec{F}_{\mathrm{sp}}$ are the sponge layer terms. The free parameter B is set equal to $\frac{1}{18}$ and $\frac{1}{15}$ for permeable and impermeable beds, respectively. For impermeable beds Eq. (6.32) vanishes and the model Eqs (6.30) and (6.31) reduce to Eqs (3.9) and (3.44) - (3.45), respectively.

The numerical scheme is the generalized multi-step predictor-corrector scheme described in chapter 3 (Zlatev et al., 1984). At the predictor step, Eq. (6.32) is solved similarly to the momentum Eqs (3.54) and (3.55), while at the corrector similarly to Eqs (3.60) and (3.61). The time derivatives $\vec{U}_{st}$ in Eq. (6.31) and $\vec{U}_t$ in Eq. (6.32) are computed according to Eqs (3.62a,b,c) and (3.63a,b,c,d) at the predictor and corrector stages, respectively. If terms of $O(\sigma^2)$ are retained in Eq. (6.32), two tridiagonal linear systems have to be solved in order to obtain the predicted values for $U_{s_{i,j}}^{(n+1)}$ and $V_{s_{i,j}}^{(n+1)}$. These systems are solved through the application of Thomas (1949) algorithm in x and y directions consecutively. The relative error at the corrector step is generalized to

$$
\Delta\mathrm{f}=\max\left\{\frac{\sum_{i,j}\left|\zeta_{i,j}^{(n+1)}-\zeta_{i,j}^{(n+1)^*}\right|}{\sum_{i,j}\left|\zeta_{i,j}^{(n+1)}\right|},\ \frac{\sum_{i,j}\left(\left|U_{i,j}^{(n+1)}-U_{i,j}^{(n+1)^*}\right|+\left|V_{i,j}^{(n+1)}-V_{i,j}^{(n+1)^*}\right|\right)}{\sum_{i,j}\left(\left|U_{i,j}^{(n+1)}\right|+\left|V_{i,j}^{(n+1)}\right|\right)},\ \frac{\sum_{i,j}\left(\left|U_{s_{i,j}}^{(n+1)}-U_{s_{i,j}}^{(n+1)^*}\right|+\left|V_{s_{i,j}}^{(n+1)}-V_{s_{i,j}}^{(n+1)^*}\right|\right)}{\sum_{i,j}\left(\left|U_{s_{i,j}}^{(n+1)}\right|+\left|V_{s_{i,j}}^{(n+1)}\right|\right)}\right\}
\tag{6.33}
$$

where $( )^*$ denotes the preceding estimate. The corrector step was iterated if Δf exceeded 0.001.

6.3 Model validation

In the previous section the numerical model was extended to account for porous beds. Thus, simulation of wave propagation over permeable submerged breakwaters lies in its range of applicability. In the present section the model is validated against the laboratory measurements described in chapter 5. The validation includes four regular test cases (1 to 4) and four irregular test cases (5 to 8). Their details are summarized in table 5.3 and the position of the 7 wave gauges is shown in Fig. 5.18. All tests refer to normal wave incidence.

6.3.1 Test case No. 1

The first test case refers to relatively short regular waves (strictly speaking intermediate water depth) with period T = 1.25 s and wave height H_o = 0.045 m at the wave source where the depth was constant 1.05 m. Thus, at this depth the wavelength was L_o = 2.419 m leading to a ratio $d_o/L_o \approx 0.43$. At the toe of the sloping ramp of 1:15, where the depth was 0.45 m, the wavelength was 2.122 m and the aforementioned ratio was $d/L \approx 0.21$. The nonlinearity parameter was $\varepsilon = H/d \sim 0.1$ and the corresponding Ursell number was approximately $Ur \approx$ 2.27. The spatial steps were chosen $\Delta x = \Delta y$ = 0.04 m and the time step Δt = 0.008 s. Thus, at the toe of sloping ramp 53 grid points per wavelength were considered, while at the center of the bar crest 21-43 points, since the wavelength lies between 0.857 and 1.747 m, depending on whether the free water depth or the total depth is considered, respectively. In any case, the grid resolution was adequate for reproducing the wave characteristics. The specific test refers to non-breaking waves over the submerged breakwater. Both the wave propagation and the morphological evolution of the bed in the lee of the structure were simulated by the compound model. The simulation period was 4 hrs, similarly to the laboratory experiment.

A comparison between the measured and the computed by the model timeseries of the free surface elevation at the seven wave gauges is depicted in Fig. 6.10.

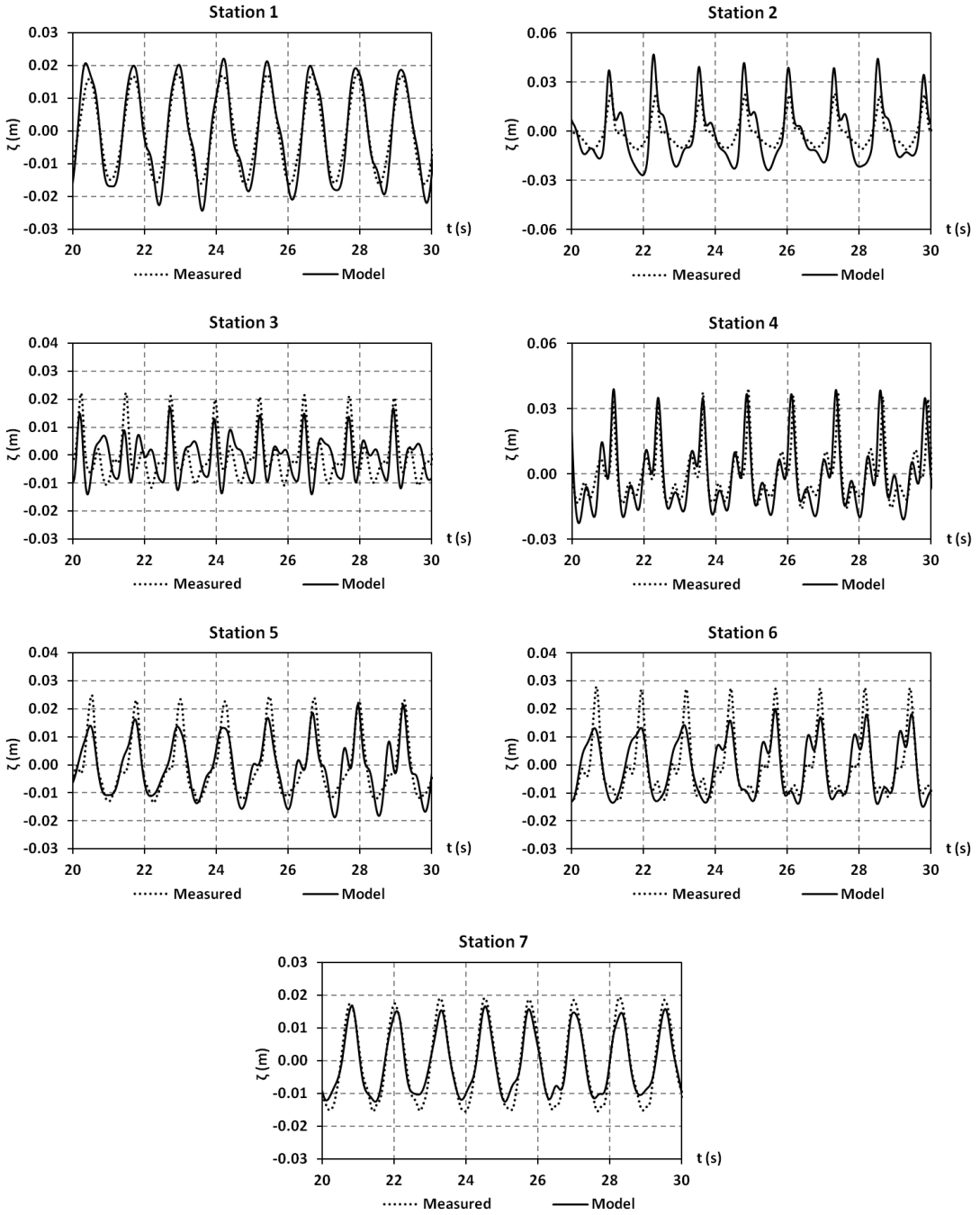

Fig. 6.10. Measured and computed by the model timeseries of free surface elevation for test case 1.

The agreement is generally reasonable. There is an overestimation of the wave height at the station 2 which is located at the bar crest. The free water depth at this point was $d = 0.05$ m and the corresponding non-dimensional wavenumber from linear theory was $kd \approx 0.37$. In addition, the ratio of depths was $h_s/d \approx 3.8$ and by assuming $R = 0.1$ then from Figs 6.5 and 6.7 the damping rate over the permeable structure is underestimated at approximately 80% of its real value. Of course the aforementioned figures have been derived under the assumption of horizontal bed and porous layer which is not the case here. However, the overestimation of wave height at station 2 can be mainly attributed to this inaccuracy. On the other hand, the

surface elevation at the most down-wave gauge 4 is very accurately predicted, proving the model's efficiency to describe the combined phenomena of diffraction and wave transmission over and through the submerged breakwater. The importance of three-dimensionality and, in particular, the diffraction effects are highlighted in Figs 6.11 where the 2DH model results are compared with results of the 1DH model version applied on the central bathymetry profile of the 2D layout. Obviously, the 1DH model underestimates the wave height at station 4.

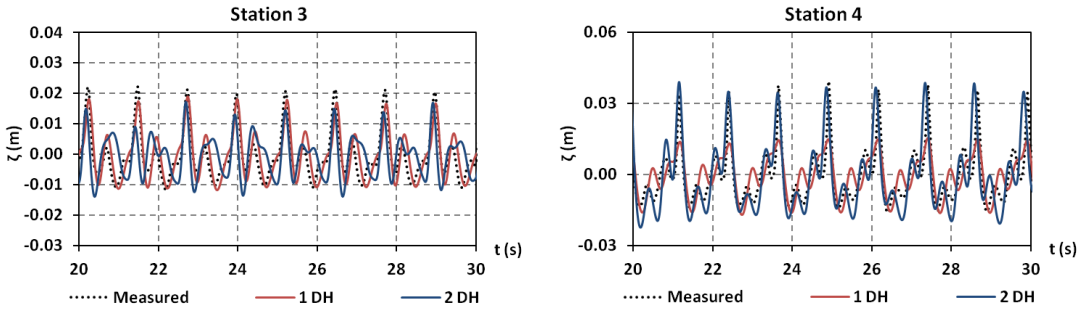

Fig. 6.11. Comparison between the measured free surface elevation and the ones computed by the 2DH and 1DH model versions at wave gauges 3 and 4.

The importance of including terms of $O(\sigma^2)$ in Eq. (6.32) is depicted in Fig. (6.12). It can be observed that retaining only terms of $O(\varepsilon)$ fails to predict the wave height above and down-wave of the breakwater. The under-prediction of the wave height at stations 2 and 3 can be partly explained by the significantly overestimated damping rate by nonlinear shallow water equations in porous layers, as denoted in Fig. 6.9. This figure refers to $h_s/d = 1$, but a similar behavior is valid for a ratio of 3.8. The specific test refers to relatively short waves and the presence of terms of $O(\sigma^2)$ also significantly improves the description of wave diffraction at the head of the breakwater where $kd \approx 0.90$. However, in the case of long waves the significance of terms of $O(\sigma^2)$ is much reduced and retaining only terms of $O(1,\varepsilon)$ led to a similar level of accuracy.

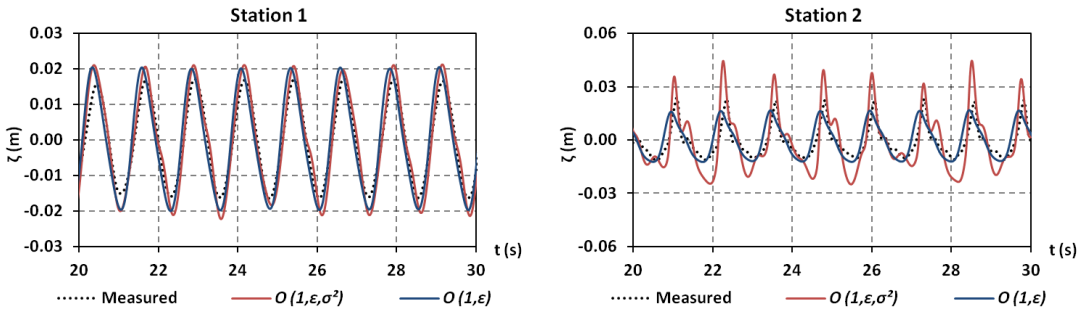

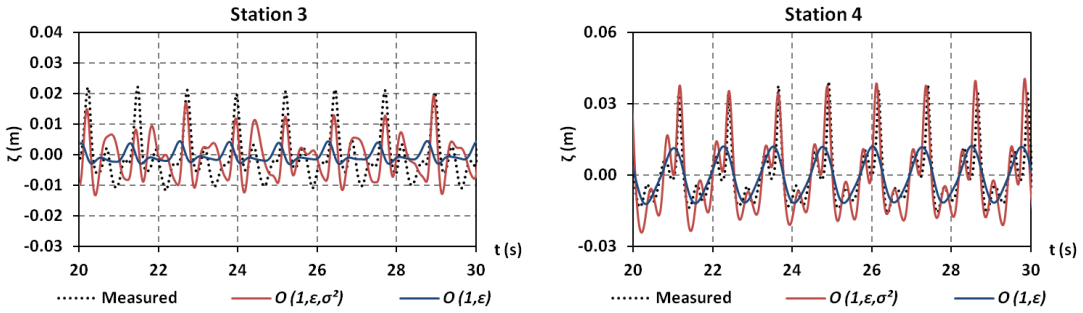

Fig. 6.12. Comparison between the measured free surface elevation and the ones computed by the model when terms of $O(\varepsilon,\sigma^2)$ and $O(\varepsilon)$ are retained in Eq. (6.32).

A snapshot of the computed free surface elevation is depicted in Fig. 6.13. The wave diffraction at the heads of the submerged breakwater is apparent.

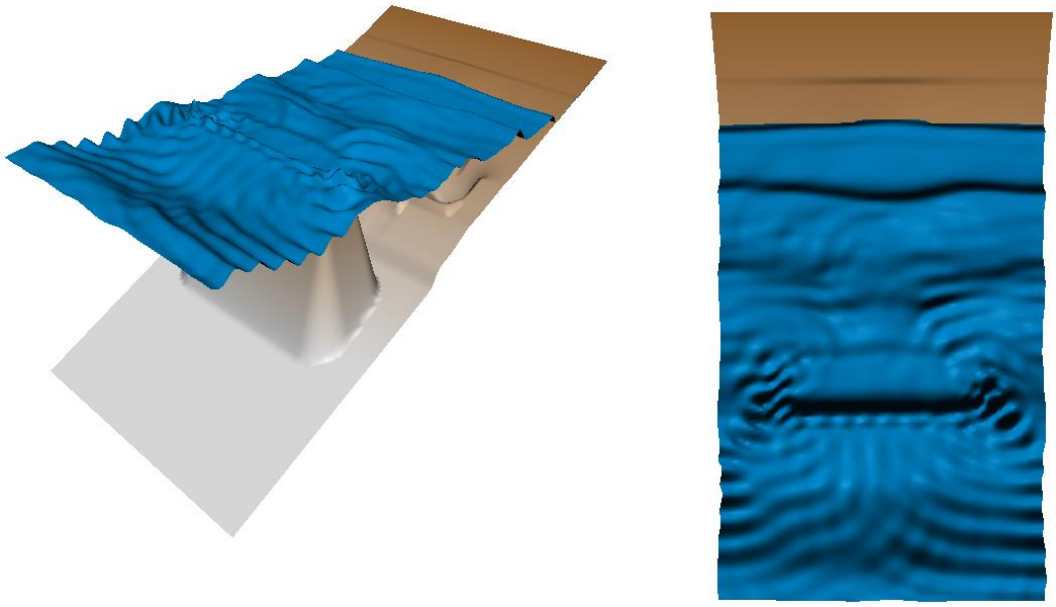

Fig. 6.13. Snapshot of the computed surface elevation from a bird's-eye view (at left) and from a plan view (at right) for test case 1.

Figure 6.14 shows the computed wave-induced current fields both around and inside the submerged breakwater. One can observe the formation of two eddies down-wave of the breakwater and weak rip currents close to the lateral boundaries and across the two symmetric gaps. The velocities in the permeable breakwater appear to be one order of magnitude lower than the currents in the free water body.

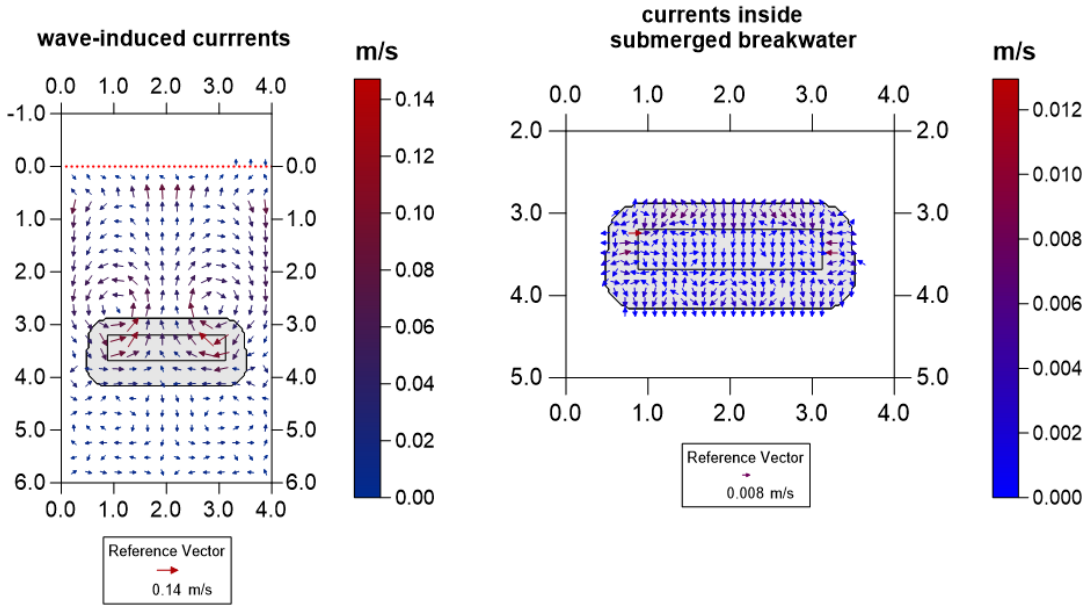

Fig. 6.14. Computed by the model wave-induced current field around and above the submerged breakwater (at left) and inside the breakwater (at right) for test case 1.

The evolution of the sandy bed was also simulated by the compound model for 4 hrs of wave action. A view of the initial and the final shoreline at laboratory is shown in Fig. 6.15.

Fig. 6.15. View of the initial (at left) and final (after 4 hrs of wave action, at right) shoreline for test case 1.

A comparison between the measured and the computed by the model final bed elevation is depicted in Fig. 6.16.

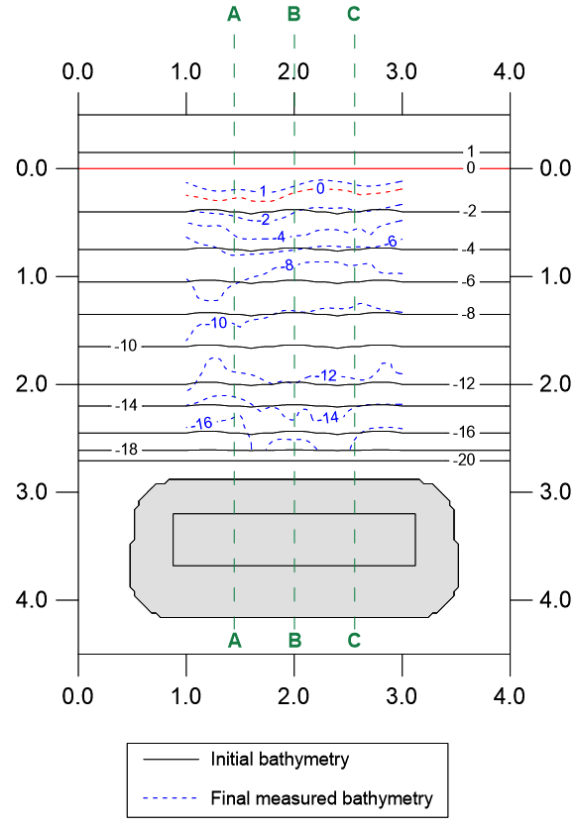

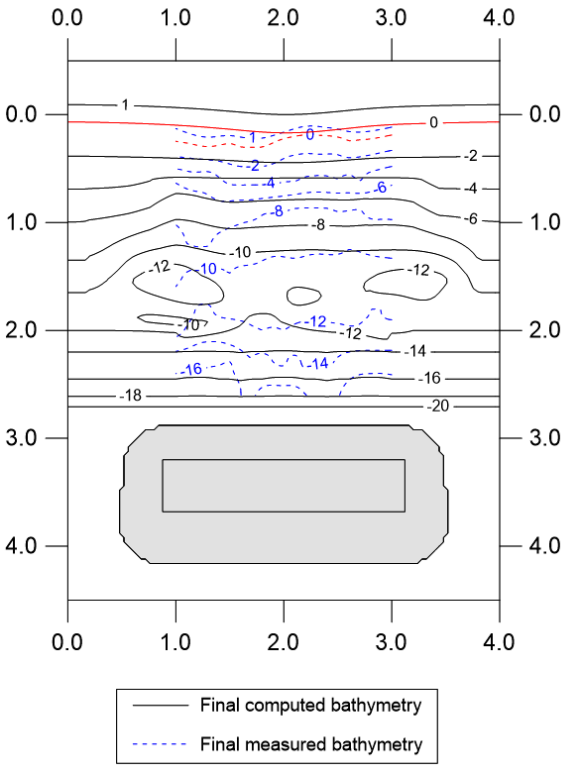

Fig. 6.16. Initial and final measured bathymetries (above) and comparison between final measured and computed bathymetries (below) for test case 1 (depths in cm).

The sediment transport load was not measured during the laboratory experiments. However, an estimation of its magnitude was made along three sections, A, B and C, which are denoted in Fig. 6.16. These sections are located at $y = 1.44, 2$ and 2.56, respectively. The estimation refers only to the cross-shore sediment transport loads and it neglects the longshore transport. Thus, the assumption made is that the sediment transport along every cross-shore profile is independent from the other ones. A similar assumption is made in one-line models and it is very crude but offers an approximation of sediment transport loads in order to have a comparative sense between the model results and the measurements. The estimation relies on the initial and final bathymetries and the solution of Eq. (4.70). In particular, the application of Eq. (4.72) offers the desired loads. A comparison between the estimated from the measurements and the model results sediment transport load is depicted in Fig. 6.17.

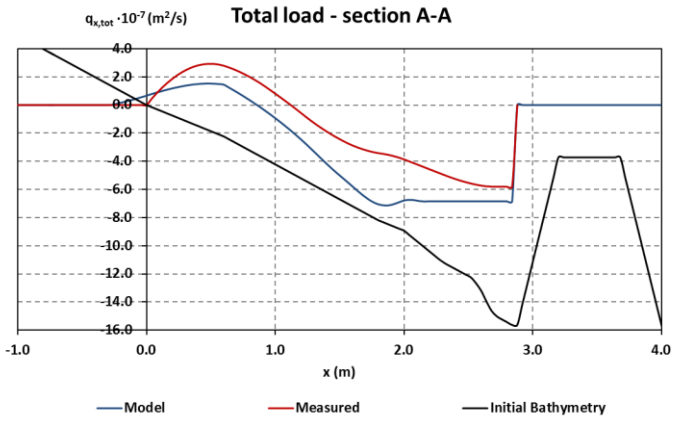

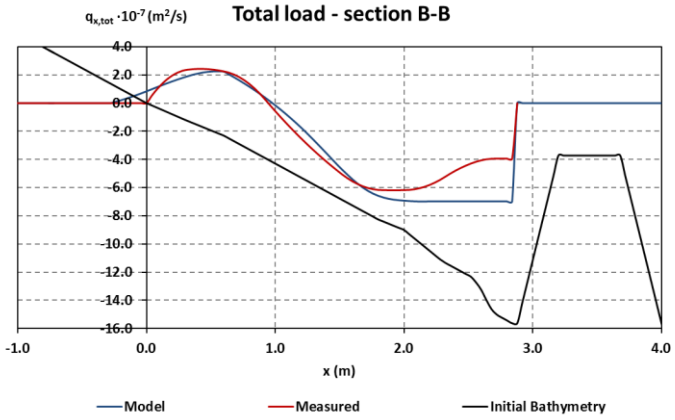

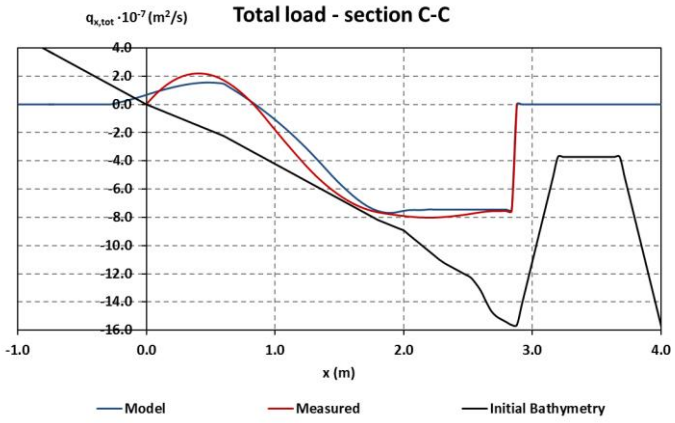

Fig. 6.17. Cross-shore total sediment transport loads as estimated from the measured and computed bathymetry change along 3 sections for test case 1.

The agreement between the sediment transport loads as estimated from the measurements and the model results is reasonable as both the tendency for erosion and accretion are described. However, the simplifying assumptions behind this estimation should be always kept in mind. With regard to bed morphology, the agreement between the model results and the measurements is also reasonable. The formation of the weak salient is described by the model. However, its width is under-estimated compared to the measured one, 20 and 30 cm, respectively, and it is also less flattened than in reality. Near the lateral boundaries the accretion is less intense. However, erosion was not present at the shoreline, neither in the laboratory nor in the model results. Moreover, it was observed during the experiment that sand was transported onshore both along the centerline of the wave tank but also from deeper areas near the lateral walls. At these latter areas and also near the axis of symmetry in the middle of the distance between the breakwater and the shoreline bed erosion was both observed and computed. Finally, it should be mentioned that in all the experimental tests the bed elevation was measured only from $y = 1$ to 3.

6.3.2 Test case No. 2

The second test case refers to relatively longer regular waves (strictly speaking intermediate water depth) with period T = 2.0 s and wave height H_o = 0.045 m at the wave source where the depth was constant 1.05 m. Thus, at this depth the wavelength was L_o = 5.292 m leading to a ratio $d_o/L_o \approx 0.20$. At the toe of the sloping ramp of 1:15, where the depth was 0.45 m, the wavelength was 3.884 m and the aforementioned ratio was $d/L \approx 0.12$. The nonlinearity parameter was $\varepsilon = H/d \sim 0.1$ and the corresponding Ursell number was approximately $Ur \approx 6.94$. The spatial steps were chosen $\Delta x = \Delta y = 0.04$ m and the time step $\Delta t = 0.008$ s. Thus, at the toe of sloping ramp 97 grid points per wavelength were considered, while at the center of

the bar crest 34-75 points, since the wavelength lies between 1.389 and 3.0 m, depending on whether the free water depth or the total depth is considered, respectively. Thus, the grid resolution was adequately fine for reproducing the wave characteristics. The specific test refers to non-breaking waves over the submerged breakwater. Both the wave propagation and the morphological evolution of the bed in the lee of the structure were simulated by the compound model. The simulation period was 3 hrs, similarly to the laboratory experiment.

A comparison between the measured and the computed by the model timeseries of the free surface elevation at the seven wave gauges is depicted in Fig. 6.18.

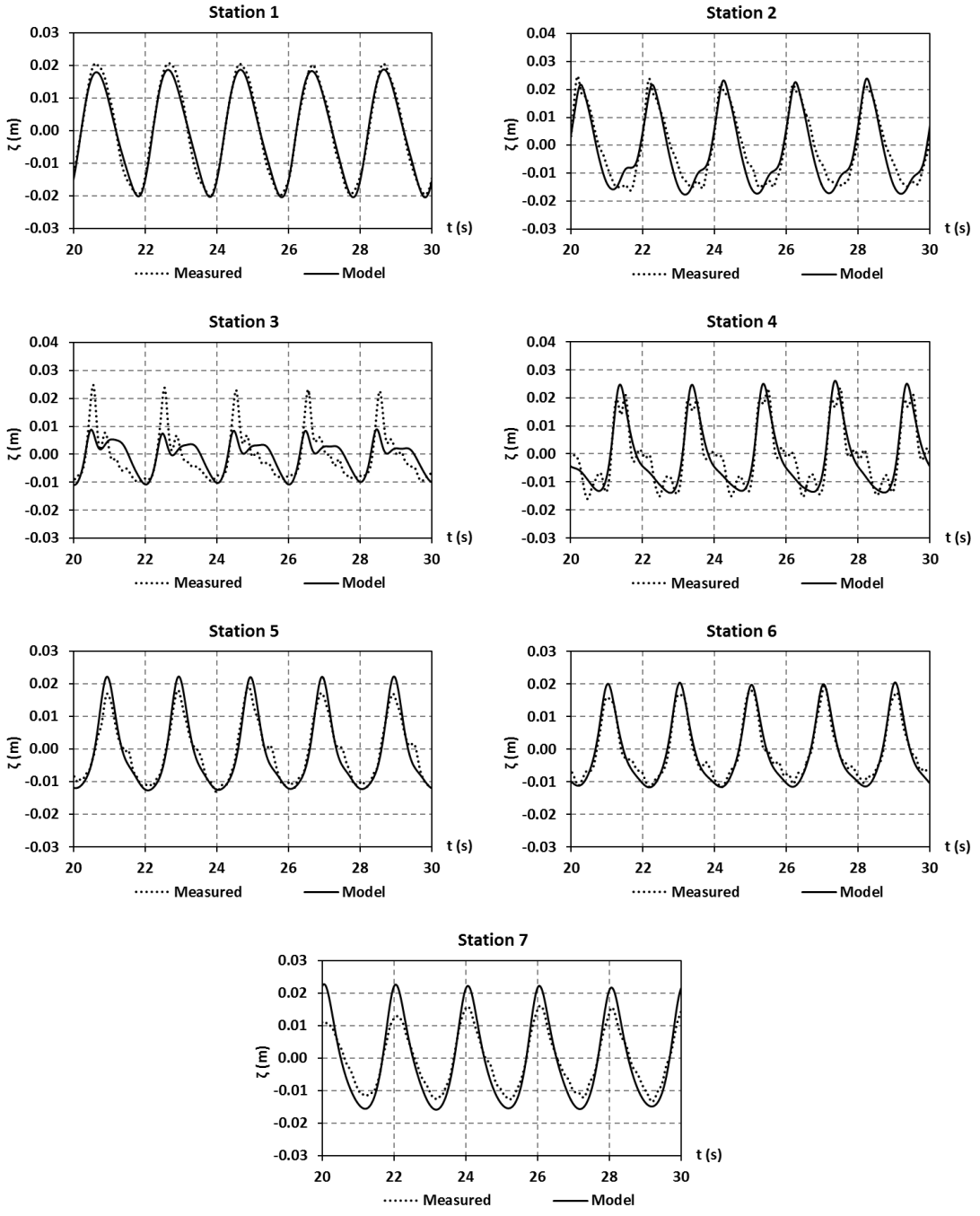

Fig. 6.18. Measured and computed by the model timeseries of free surface elevation for test case 2.

The agreement is generally reasonable, except from an underestimation of the wave height at station 3. The generation of higher harmonics is described by the model but the secondary peaks are more flattened than in reality. The generation and release of higher harmonics is more intense in this test compared to the shorter waves in test case 1 (see also Beji and Battjes, 1993). In order to further explain the discrepancies at this station the nonlinear properties of the model should be studied for porous beds. This issue has been left for future research. In addition, the wave height at station 7, which is located at the gap between the breakwater and one of the two the lateral walls, is over-predicted. On the other hand, the agreement in the lee of the breakwater, at stations 4,5 and 6, is fairly good. A snapshot of the computed free surface elevation is depicted in Fig. 6.19.

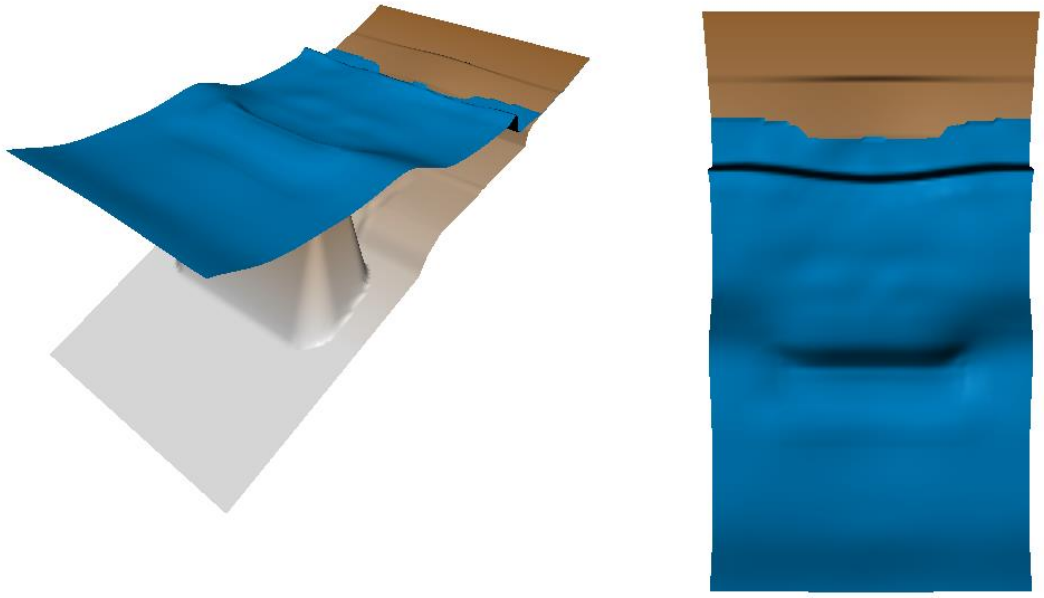

Fig. 6.19. Snapshot of the computed surface elevation from a bird's-eye view (at left) and from a plan view (at right) for test case 2.

Figure 6.20 shows the computed wave-induced current field above and around the submerged breakwater. Two eddies down-wave of the breakwater are observed but they are less pronounced than in test case 1.

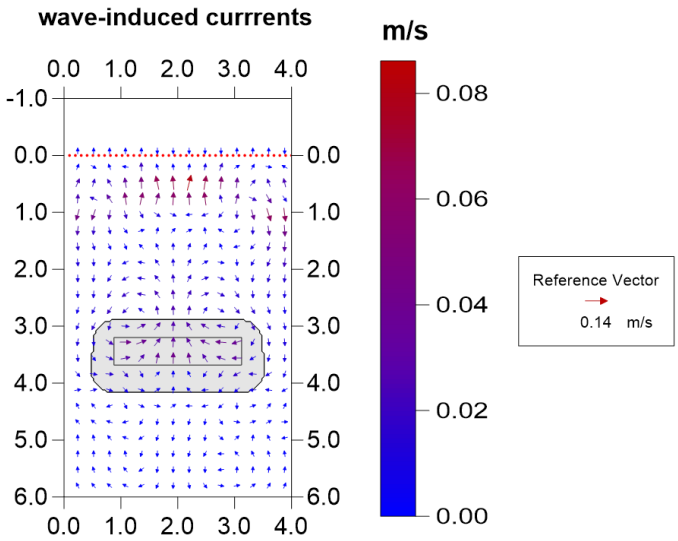

Fig. 6.20. Computed by the model wave-induced current field around and above the submerged breakwater for test case 2.

The evolution of the sandy bed was also simulated by the compound model for 3 hrs of wave action. A view of the initial and the final shoreline at laboratory is shown in Fig. 6.21.

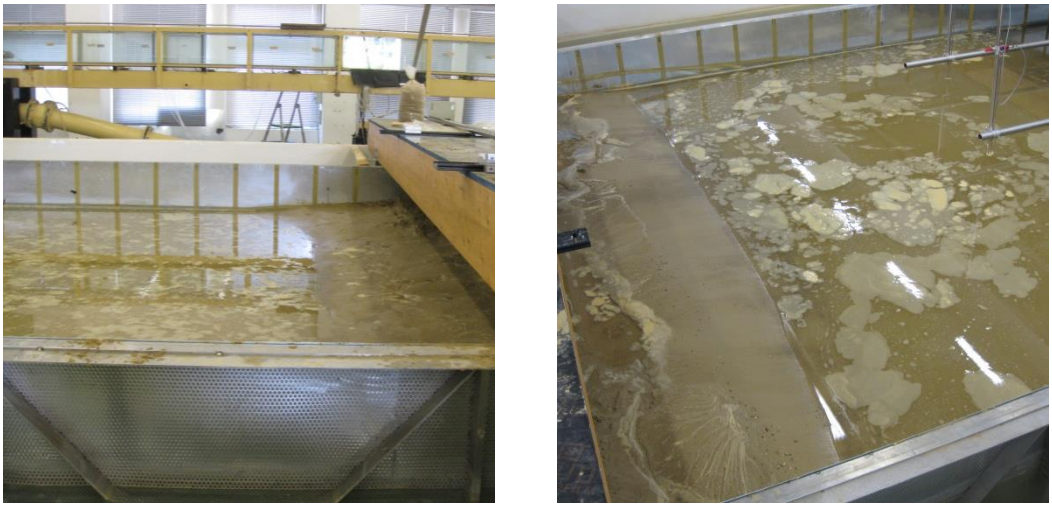

Fig. 6.21. View of the initial (at left) and final (after 3 hrs of wave action, at right) shoreline for test case 2.

A comparison between the measured and the computed by the model final bed elevation is depicted in Fig. 6.22.

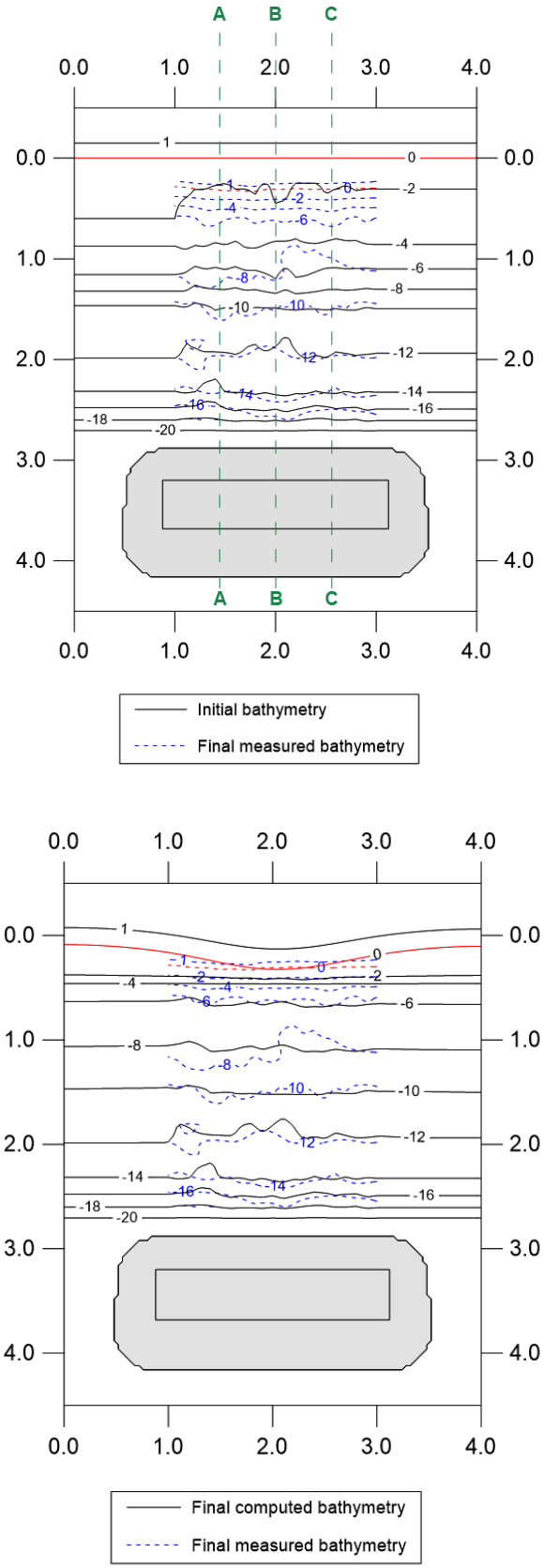

Fig. 6.22. Initial and final measured bathymetries (above) and comparison between final measured and computed bathymetries (below) for test case 2 (depths in cm).

Similarly to test case 1, an estimation of the cross-shore sediment transport rates along sections A, B and C was made from the measured and the computed bathymetry changes. Their comparison is depicted in Fig. 6.23.

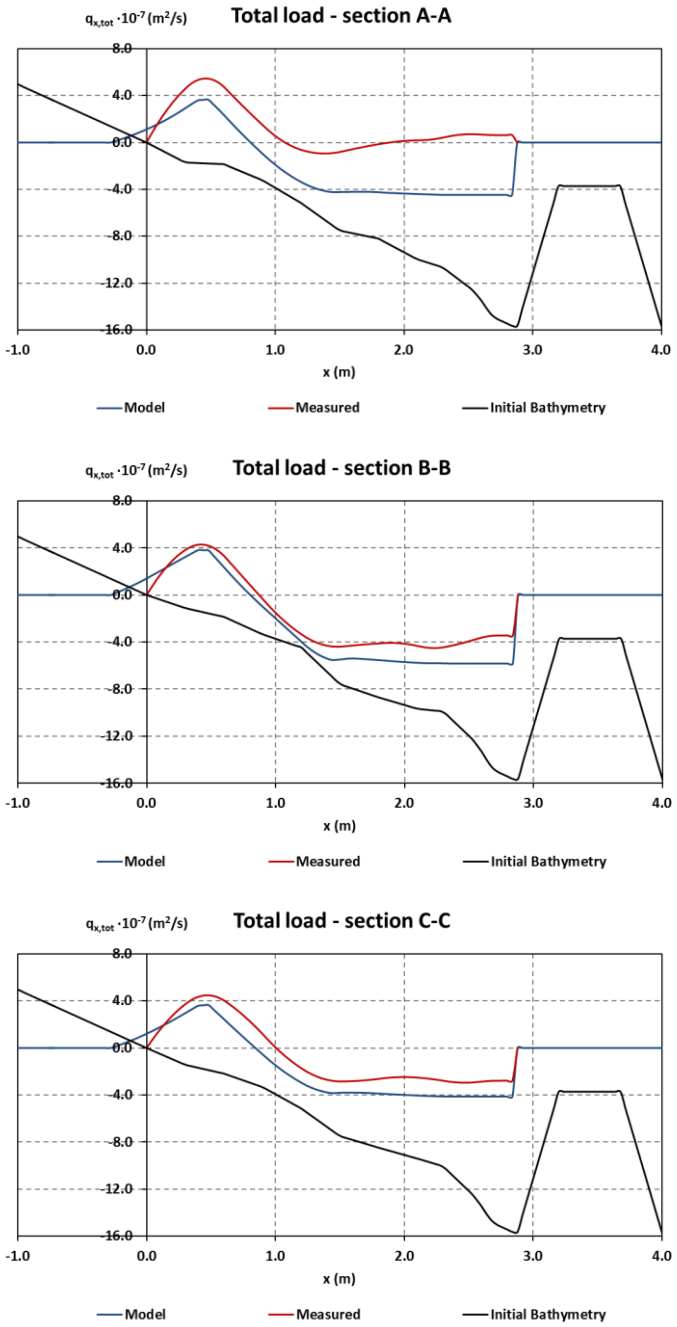

Fig. 6.23. Cross-shore total sediment transport loads as estimated from the measured and computed bathymetry change along 3 sections for test case 2.

The agreement between the sediment transport loads as estimated from the measurements and the model results is quite good along sections B and C. For section A the agreement is reasonable inside the surf zone but there is a discrepancy in deeper water. With regard to bed morphology, the agreement between the model results and the measurements is also

reasonable. The formation of the salient is described by the model and its maximum width of about 30 cm is accurately predicted. However, similarly to test case 1, it is less flattened than in reality. It should be mentioned that during the laboratory performance of test case 2, the wave crests seemed to 'feel' at a lower level the presence of the submerged breakwater than in test case 1. Thus, waves tended to remain long-crested down-wave of the structure compared to the ones in test case 1 where diffraction tended to curve their crests. Consequently, the depth contour lines close to the shoreline had a tendency to move parallel to their initial position, rather than formatting a peaky salient, as it was the case in test No. 1. This behavior resembled mostly to 2D wave propagation, rather than a clear 3D motion and morphology evolution.

6.3.3 Test case No. 3

The first two scenarios referred to waves of the same small wave height, 0.045 m, but different periods in order to get a comparative view of the effect of them on the corresponding morphology evolution. The third test case refers to relatively short regular waves with period T = 1.25 s and wave height H_o = 0.08 m at the wave source where the depth was constant 1.05 m. Thus, similarly to test case 1, the wavelength at the toe of the sloping ramp of 1:15 was 2.122 m and the corresponding depth to wavelength ratio was $d/L \approx 0.21$. However, the nonlinearity parameter was higher, $\varepsilon = H/d \sim 0.18$ and the corresponding Ursell number was approximately $Ur \approx 4.08$. The spatial steps were again chosen $\Delta x = \Delta y = 0.04$ m and the time step Δt = 0.008 s. The specific test refers to breaking waves of spilling type over the submerged breakwater. Both the wave propagation and the morphological evolution of the bed in the lee of the structure were simulated by the compound model. The simulation period was 5 hrs, similarly to the laboratory experiment. A comparison between the measured and the computed by the model timeseries of the free surface elevation at the seven wave gauges is depicted in Fig. 6.24.

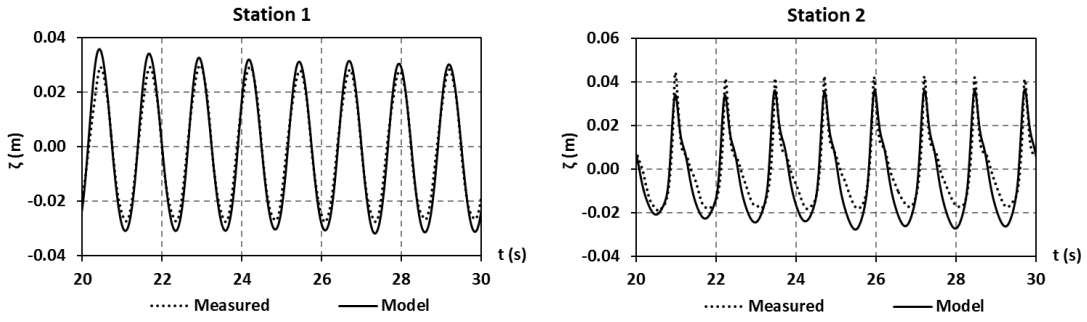

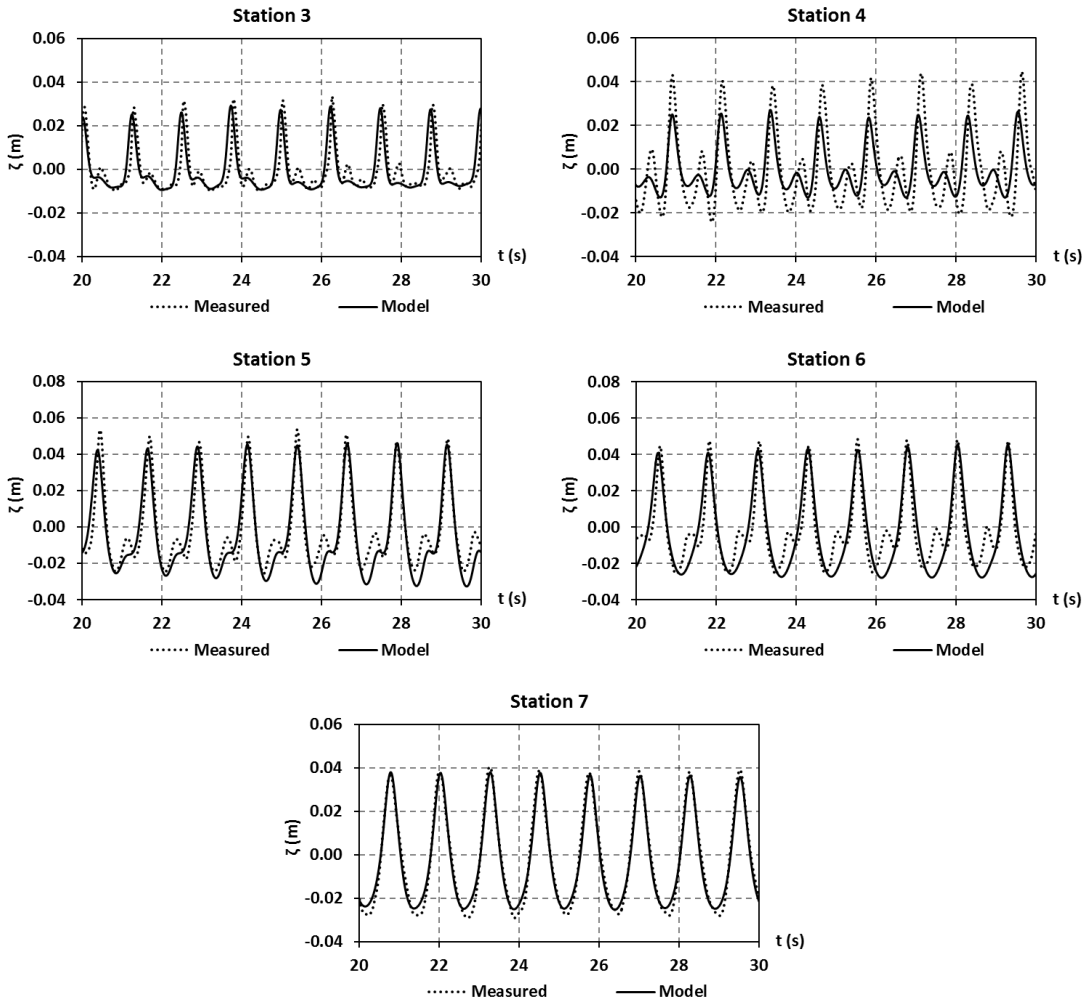

Fig. 6.24. Measured and computed by the model timeseries of free surface elevation for test case 3.

The agreement is fairly good, except form some underestimation of the wave height at the most down-wave station 4. A snapshot of the computed free surface elevation is depicted in Fig. 6.25. The effect of diffraction is apparent on the wave crests. In addition, wave breaking was taking place above the submerged breakwater resulting to a variation of wave height along the wave crests passing over the obstacle. Consequently, the hydraulic gradients resulted to additional curving of the wave crests in the lee of the breakwater. Of course, a surf zone was also formed near the shoreline as waves were breaking again due to depth limitation. The aforementioned complex processes made the accurate prediction of the wave forms at station 4 more difficult compared to test cases 1 and 2.

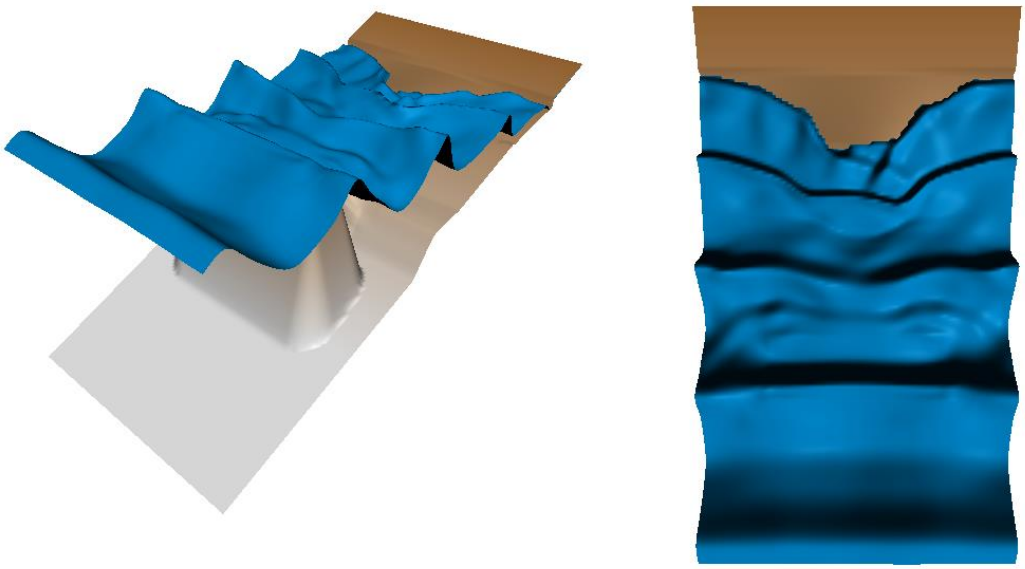

Fig. 6.25. Snapshot of the computed surface elevation from a bird's-eye view (at left) and from a plan view (at right) for test case 3.

The computed wave-induced current field above and around the submerged breakwater is depicted in Fig. 6.26. The two vortices down-wave of the breakwater are more pronounced than in the previous cases. In addition, strong rip currents with a maximum velocity of about 0.23 m/s are formed across the two gaps. Moreover, two eddies of opposite direction are also formed near the shoreline (see also discussion in subsection 5.2.2).

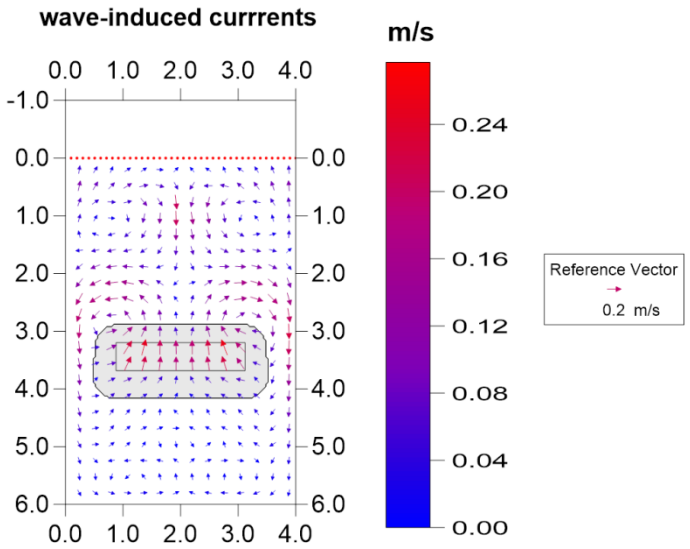

Fig. 6.26. Computed by the model wave-induced current field around and above the submerged breakwater for test case 3.

The evolution of the sandy bed was also simulated by the compound model for 5 hrs of wave action. A view of the initial and the final shoreline at laboratory is shown in Fig. 6.27.

Fig. 6.27. View of the initial (at left) and final (after 5 hrs of wave action, at right) shoreline for test case 3.

A comparison between the measured and the computed by the model final bed elevation is depicted in Fig. 6.28.

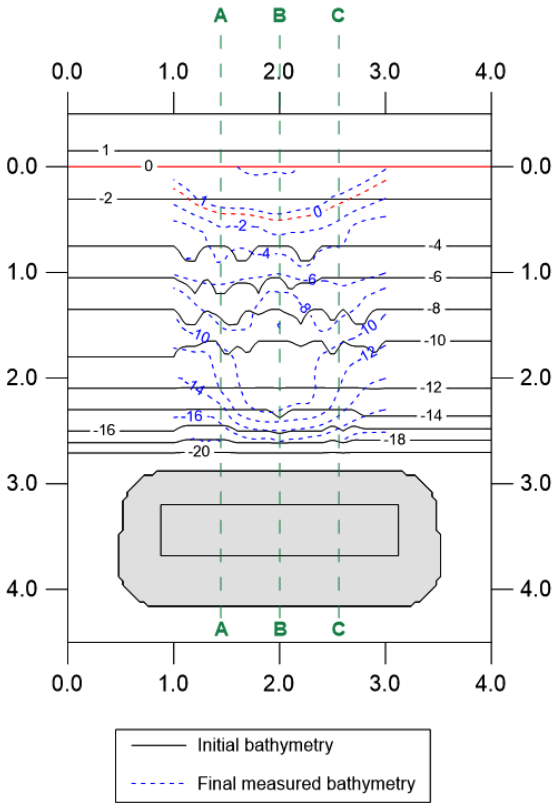

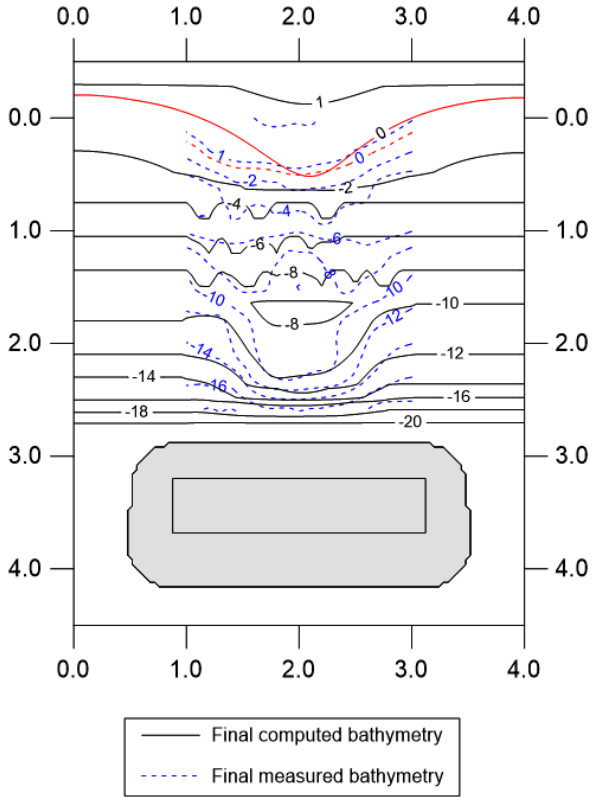

Fig. 6.28. Initial and final measured bathymetries (above) and comparison between final measured and computed bathymetries (below) for test case 3 (depths in cm).

Similarly to the previous test cases, an estimation of the cross-shore sediment transport rates along sections A, B and C was made from the measured and the computed bathymetry changes. Their comparison is depicted in Fig. 6.29.

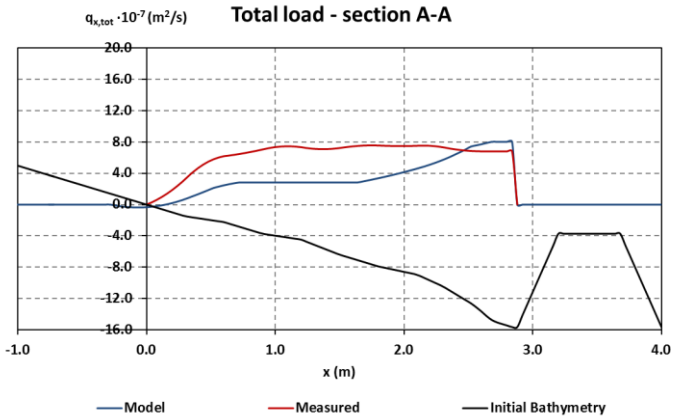

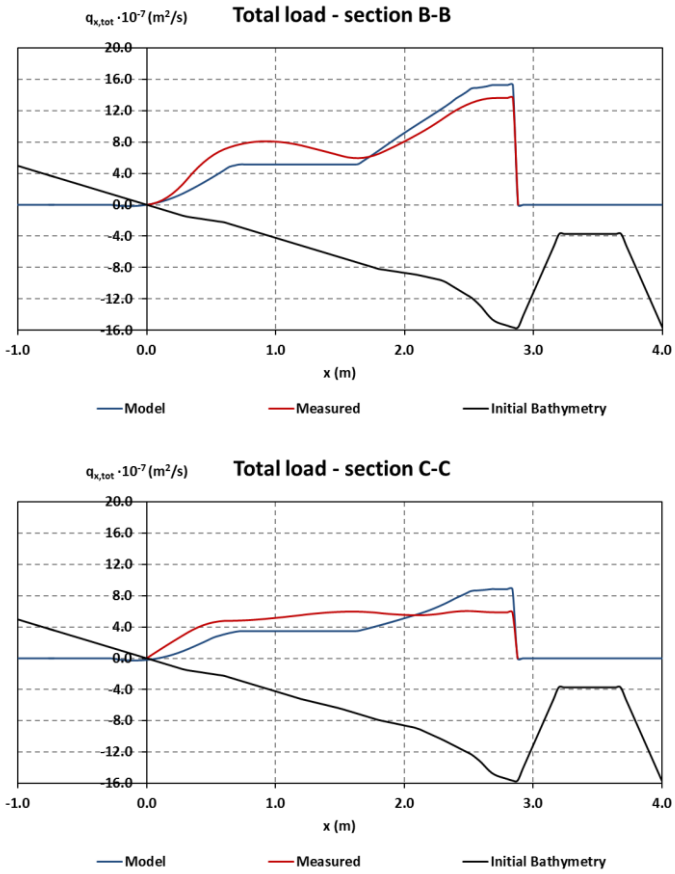

Fig. 6.29. Cross-shore total sediment transport loads as estimated from the measured and computed bathymetry change along 3 sections for test case 3.

The agreement between the sediment transport loads as estimated from the measurements and the model results is reasonable, especially along sections B and C. In contrary, the sediment load along section A is underestimated. However, the correct direction of sediment transport is predicted, as well the tendency for accretion-erosion is, in general, correctly reproduced. Nevertheless, it should be mentioned that test case 3 is clearly dominated by three-dimensional processes and thus the longshore sediment transport is expected to be comparable to the cross-shore. Hence, this estimation is of questionable practical value due to the simplifying assumption behind it.

With regard to the shoreline response, a pronounced salient was both measured and computed. Its maximum width of 0.52 m was accurately computed, although the salient was predicted by the model to be more peaky than in reality. In addition, weak erosion was observed during the experiment behind the two gaps near the shoreline. This tendency was also described by the model. Furthermore, down-wave of the breakwater and near the center of the tank accretion took place and a bar was formed due to wave breaking over the structure. This feature was also described by the compound model.

6.3.4 Test case No. 4

The fourth test case refers to relatively long regular waves with period T = 2.0 s and wave height H_o = 0.08 m at the wave source where the depth was constant 1.05 m. Thus, similarly to test case 2, the wavelength at the toe of the sloping ramp of 1:15 was 3.884 m and the corresponding depth to wavelength ratio was $d/L \approx 0.12$. However, the nonlinearity parameter was higher, $\varepsilon = H/d \sim 0.18$ and the corresponding Ursell number was approximately $Ur \approx 12.5$. The spatial steps were again chosen $\Delta x = \Delta y = 0.04$ m and the time step $\Delta t = 0.008$ s. The specific test refers to breaking waves of spilling type over the submerged breakwater. Both the wave propagation and the morphological evolution of the bed in the lee of the structure were simulated by the compound model. The simulation period was 4.3 hrs, similarly to the laboratory experiment. A comparison between the measured and the computed by the model timeseries of the free surface elevation at the seven wave gauges is depicted in Fig. 6.30.

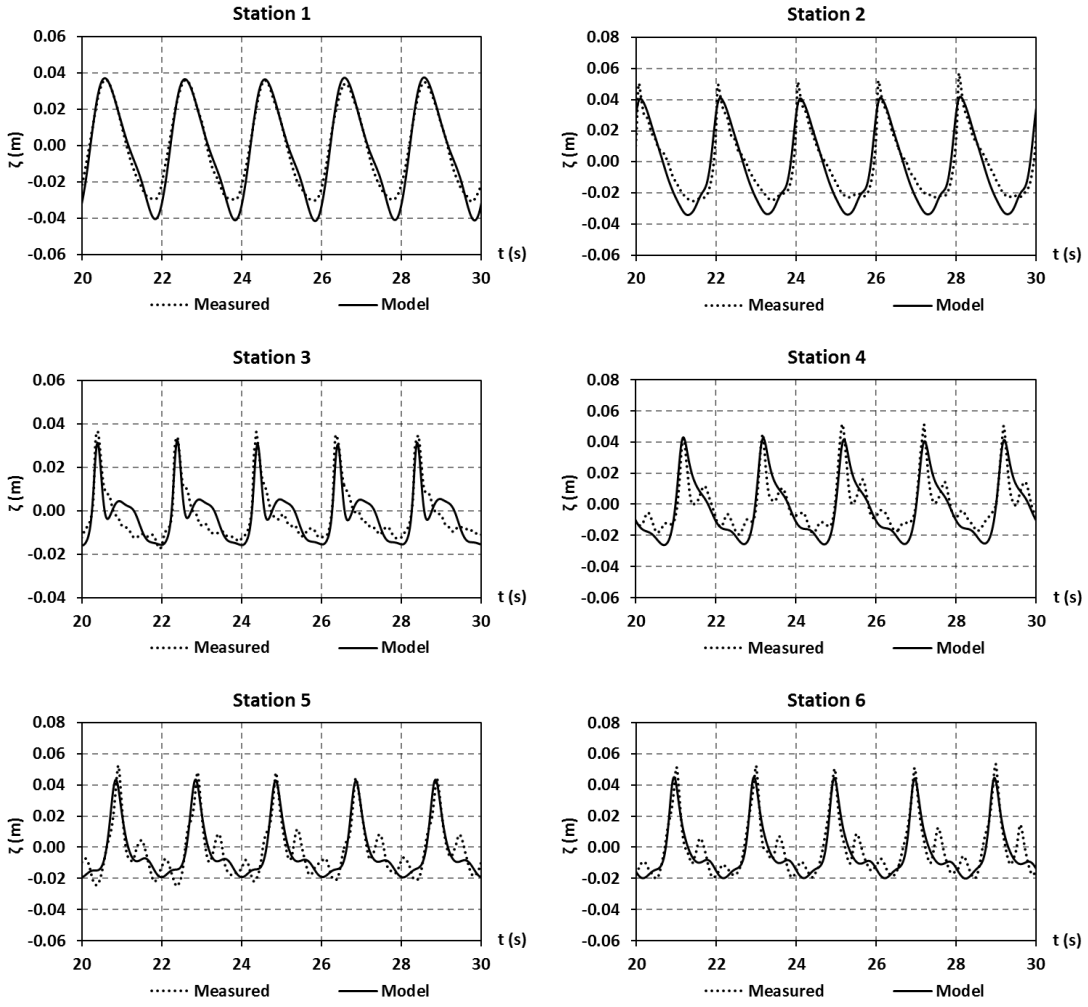

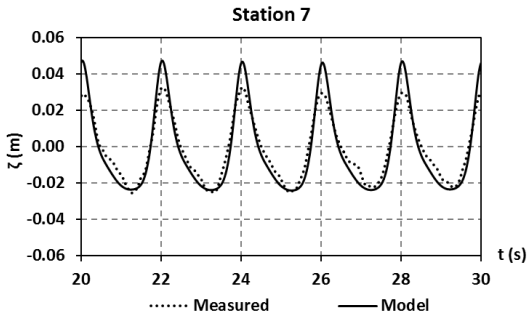

Fig. 6.30. Measured and computed by the model timeseries of free surface elevation for test case 4.

The agreement is fairly good, even at station 3 where there was an under-prediction of the wave height in case 2 which referred to waves of the same period. However, at the specific station the secondary peaks are again over-pronounced. Moreover, the prediction of the wave height at the most down-wave station 4 is accurate, contrary to test case 3 which referred to short waves with similar wave height offshore. Finally, similarly to case 2, a slight overestimation of the wave height is observed at station 7 which is located at the gap between the breakwater and the lateral vertical plate.

A snapshot of the computed free surface elevation is depicted in Fig. 6.31. The wave diffraction is less intense compared to case 3 but wave breaking over the submerged breakwater induced a pronounced variation of wave height along the wave crests. As the waves were propagating in the lee of the breakwater they underwent a second a breaking near the shoreline.

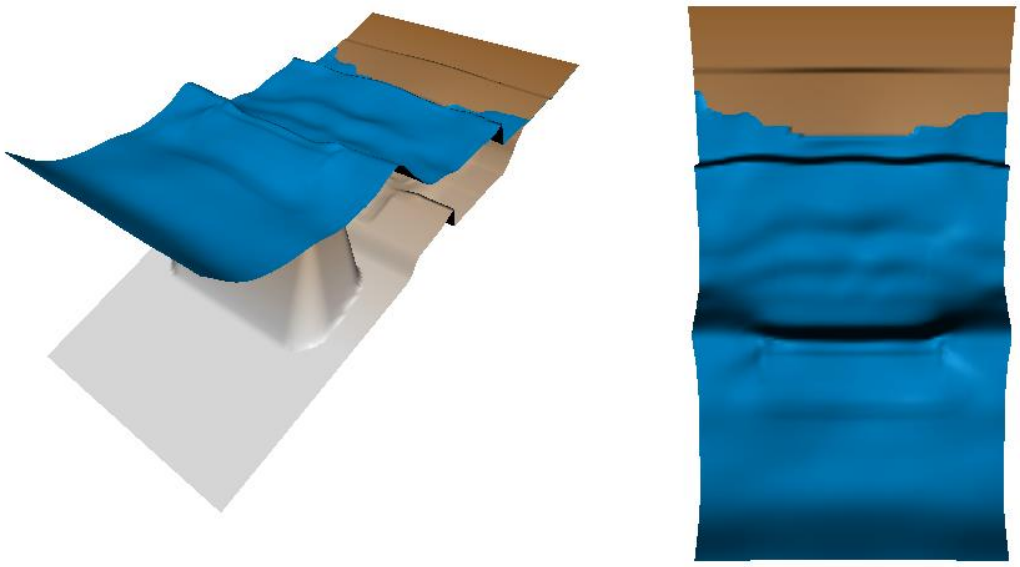

Fig. 6.31. Snapshot of the computed surface elevation from a bird's-eye view (at left) and from a plan view (at right) for test case 4.

The computed wave-induced current field above and around the submerged breakwater is depicted in Fig. 6.32. Similarly to the previous tests, the two vortices down-wave of the breakwater are also formed. The rip currents across the two symmetric gaps are weaker than in test 3, having a maximum velocity of approximately 0.12 m/s.

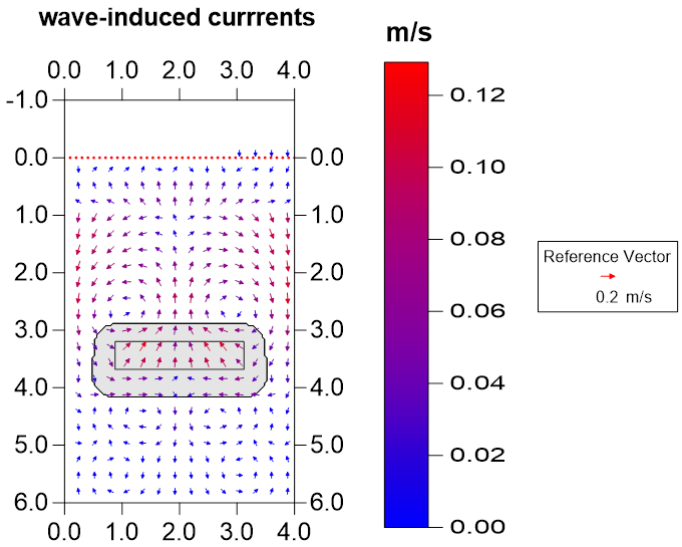

Fig. 6.32. Computed by the model wave-induced current field around and above the submerged breakwater for test case 4.

The evolution of the sandy bed was also simulated by the compound model for 4.3 hrs of wave action. A view of the initial and the final shoreline at laboratory is shown in Fig. 6.33.

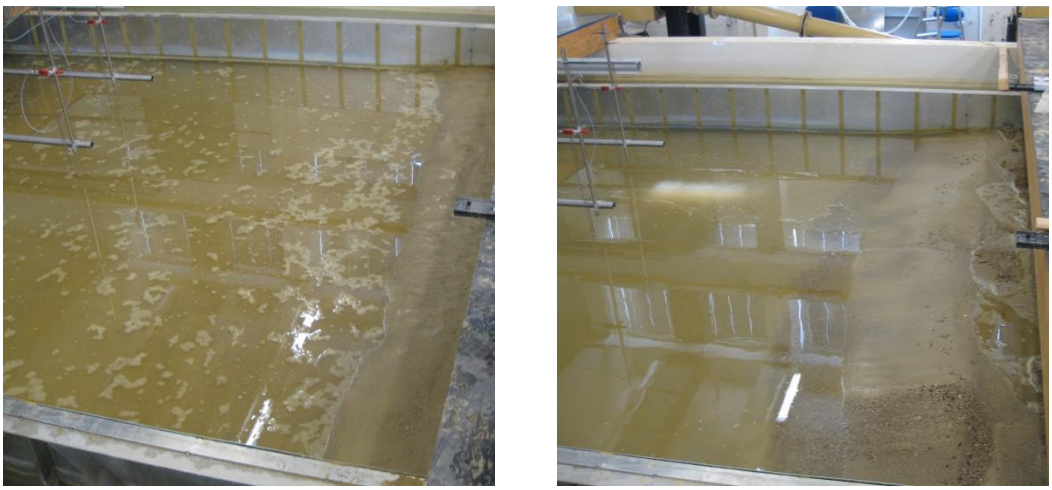

Fig. 6.33. View of the initial (at left) and final (after 4.3 hrs of wave action, at right) shoreline for test case 4.

A comparison between the measured and the computed by the model final bed elevation is depicted in Fig. 6.34.

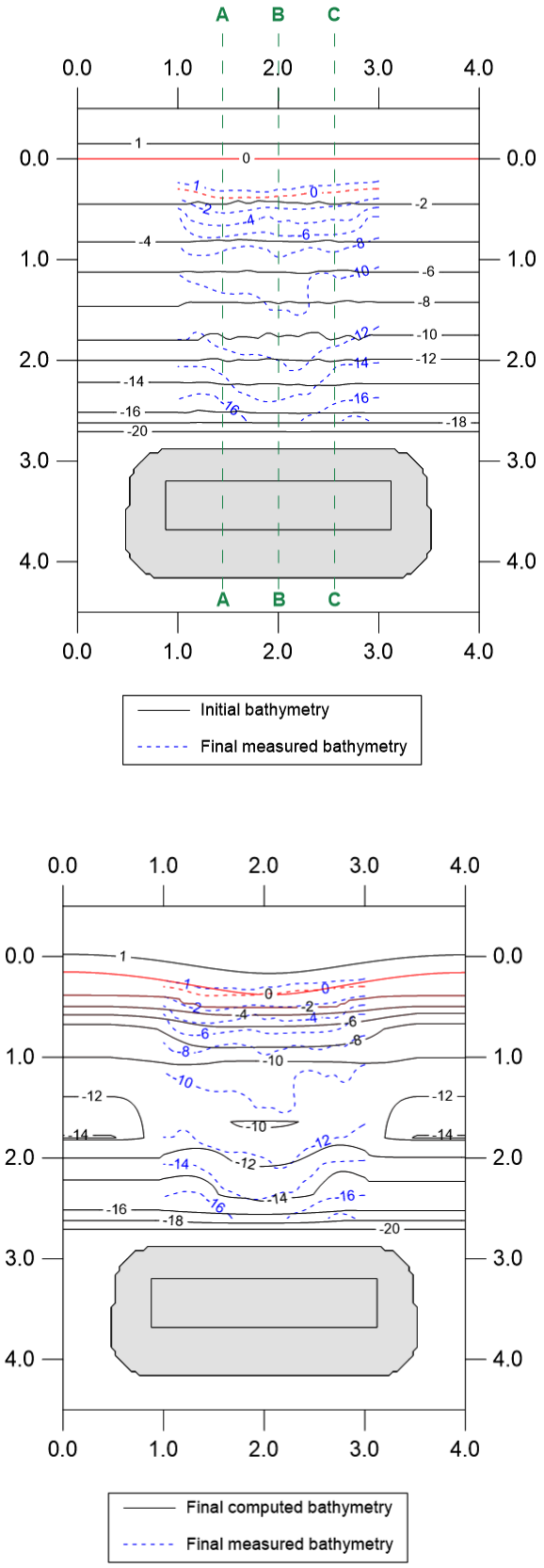

Fig. 6.34. Initial and final measured bathymetries (above) and comparison between final measured and computed bathymetries (below) for test case 4 (depths in cm).

Similarly to the previous test cases, an estimation of the cross-shore sediment transport rates along sections A, B and C was made from the measured and the computed bathymetry changes. Their comparison is depicted in Fig. 6.35.

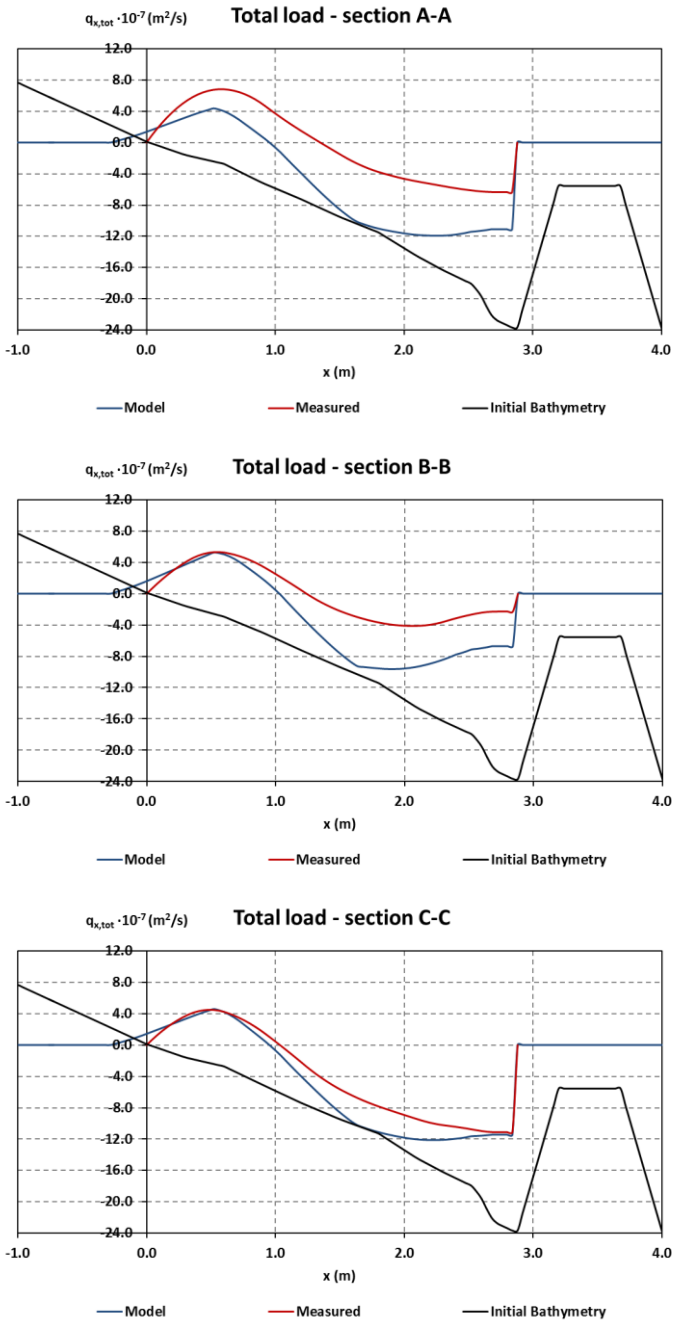

Fig. 6.35. Cross-shore total sediment transport loads as estimated from the measured and computed bathymetry change along 3 sections for test case 4.

The sediment transport rates are reasonably predicted despite some overestimation in the area between the breakwater and the middle point of its distance from the shoreline. The salient is fairly good described, more flattened than in the previous cases. Only the erosion around the middle of the distance of the breakwater from the shoreline is overestimated.

In order to get a clear image of the efficiency of the submerged breakwater, the same test case was simulated by the model without the presence of the submerged breakwater. A comparison of the final bed morphology with and without the structure is depicted in Fig. 6.36. It can be observed that the specific wave conditions would result to weak erosion at the shoreline if the breakwater was not constructed, while its presence leads to accretion and stabilization of an additional dry part of the land.

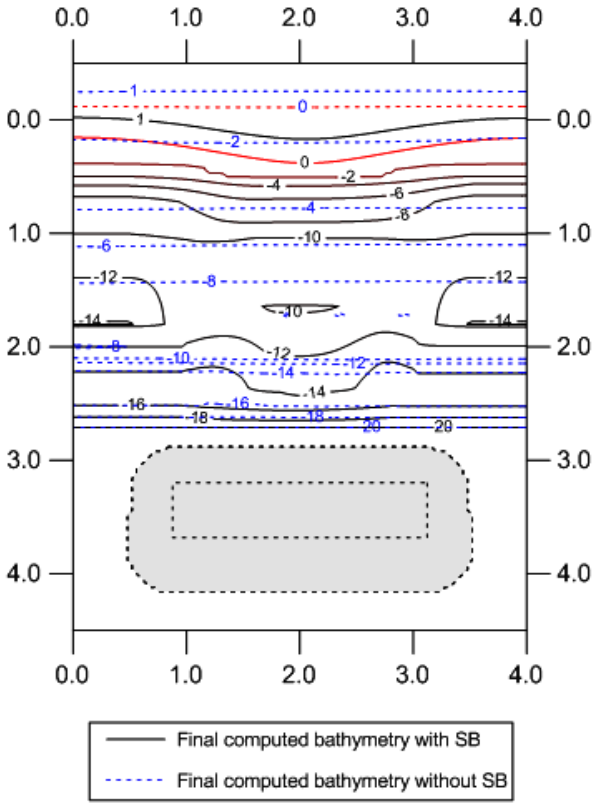

Fig. 6.36. Final computed bathymetry with and without the submerged breakwater for test case 4 (depths in cm).

The sediment transport modelling is associated with a considerable uncertainty. In order to get a better insight of the model results, their sensitivity to the morphological factor was also investigated. The results presented above refered to a morphological factor MF = 50. However, this value was increased and decreased by factors 1.5, 2.0 and 3.0 and an inter-comparison of the computed shorelines is shown in Fig. 6.37. The results were also compared with the measured ones. All the simualtions were performed for the same number of time steps and thus each run corresponded to a different duration. Since no significant morphological change was observed after a specific time when using MF = 50, it comes out that the sandy bed reached its equilibrium. Consequently, the differences appearing when using larger values of the morphological factor are not attributed to a non-equilibrium state but to these large values that have an unrealistic impact on the associated hydrodynamics.

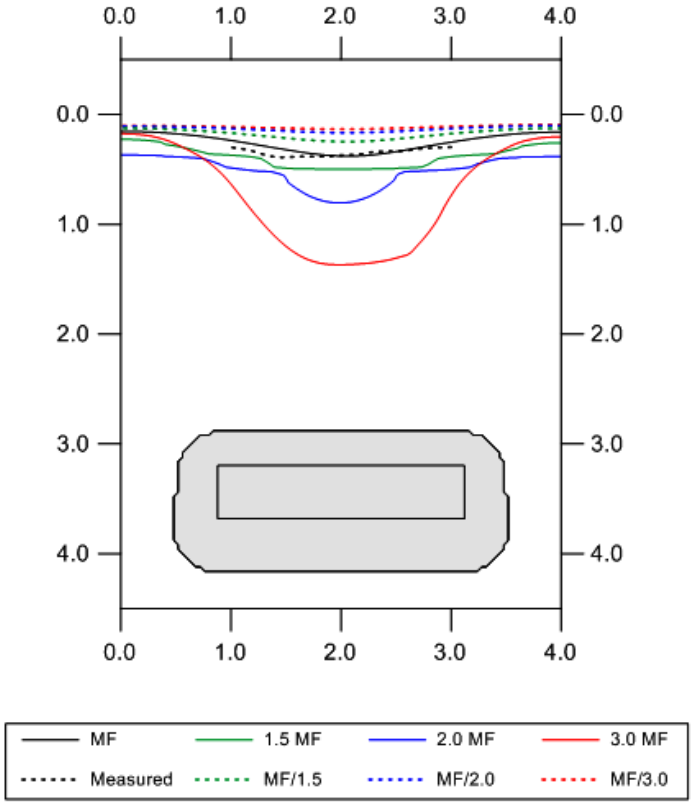

Fig. 6.37. Comparison between the final measured shoreline and the ones computed by the model when using various values of the morphological factor for test case 4.

A thorough discussion about the scale effects in movable-bed physical models was presented in chapter 5. The model validation in the present chapter refers to laboratory scaled measurements and thus a similar discussion can be made concerning the model's ability to simulate morphodynamics at the prototype scale of nature. Due to the absence of field measurements, a first answer, though not thorough, is given by the following procedure. It has been already mentioned that the specific laboratory experiments corresponded to a geometric scale factor of about $N_L \approx 10$ and according to subsection 5.4 this results to a time scale of about $N_T \approx \sqrt{10}$. Although serious considerations have been expressed for the morphological time scale (see subsections 5.4 and 5.5), it was also assumed to be $N_{t,mor} \approx \sqrt{10}$. The final computed bathymetry of the aforementioned simulation was scaled-up by a N_L - factor and the results are shown in Fig. 6.38 as 'scaled-up' curves. In addition, another model run was also performed referring to a scaled-up layout with a factor of N_L for geometric dimensions and N_T for temporal variations. This model layout is mentioned as 'prototype', although no specific prototype actually existed for the laboratory experiments. The results of this run are also depicted in Fig. 6.38. The agreement is impressively good. It should be mentioned that in order to achieve an accurate agreement all length-related quantities had to be scaled-up. For example the mean sand diameter, the diameter of the breakwater stones and the fluid viscosity

are some of them. This is a convenient possibility when working with numerical models, in contrary to physical models where it is difficult to retain the scaling for some parameters, e.g. fluid viscosity, etc. Based on this discussion, there is strong evidence that validating the numerical model with laboratory-scaled measurements can guarantee valid results for field applications too. The validity of this statement is very important for the results presented in chapter 7. Nevertheless, a more in-depth investigation of this issue is required.

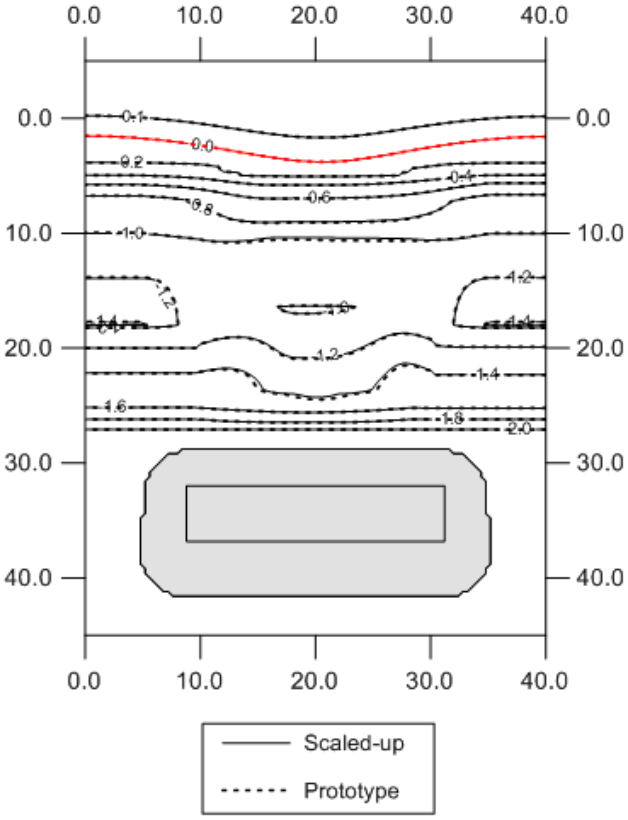

Fig. 6.38. Comparison between the final bathymetry as computed from the scaled-up results of simulation of test case 4 and from a corresponding prototype-scaled layout (depths in m).

6.3.5 Test case No. 5

The first 4 tests referred to regular waves, while tests 5-8 to referred to random waves. In particular, test case 5 involved irregular waves of a Jonswap spectrum with peak period T_p = 1.25 s and significant wave height H_{so} = 0.045 m at the wave source. Hence, this scenario corresponded to test case 1 but for irregular wave propagation. The spatial steps were chosen $\Delta x = \Delta y$ = 0.04 m and the time step Δt = 0.01 s. A negligible percentage of the waves were observed to break over the submerged breakwater. Thus, this was a non-breaking scenario. Both the wave propagation and the morphological evolution of the bed in the lee of the

structure were simulated by the compound model. The simulation period was 5 hrs, similarly to the laboratory experiment.

A comparison between the measured and the computed by the model timeseries of the free surface elevation at the seven wave gauges is depicted in Fig. 6.39. The corresponding comparison for the wave spectra is depicted in Fig. 6.40, while a snapshot of the computed free surface elevation is shown in Fig. 6.41.

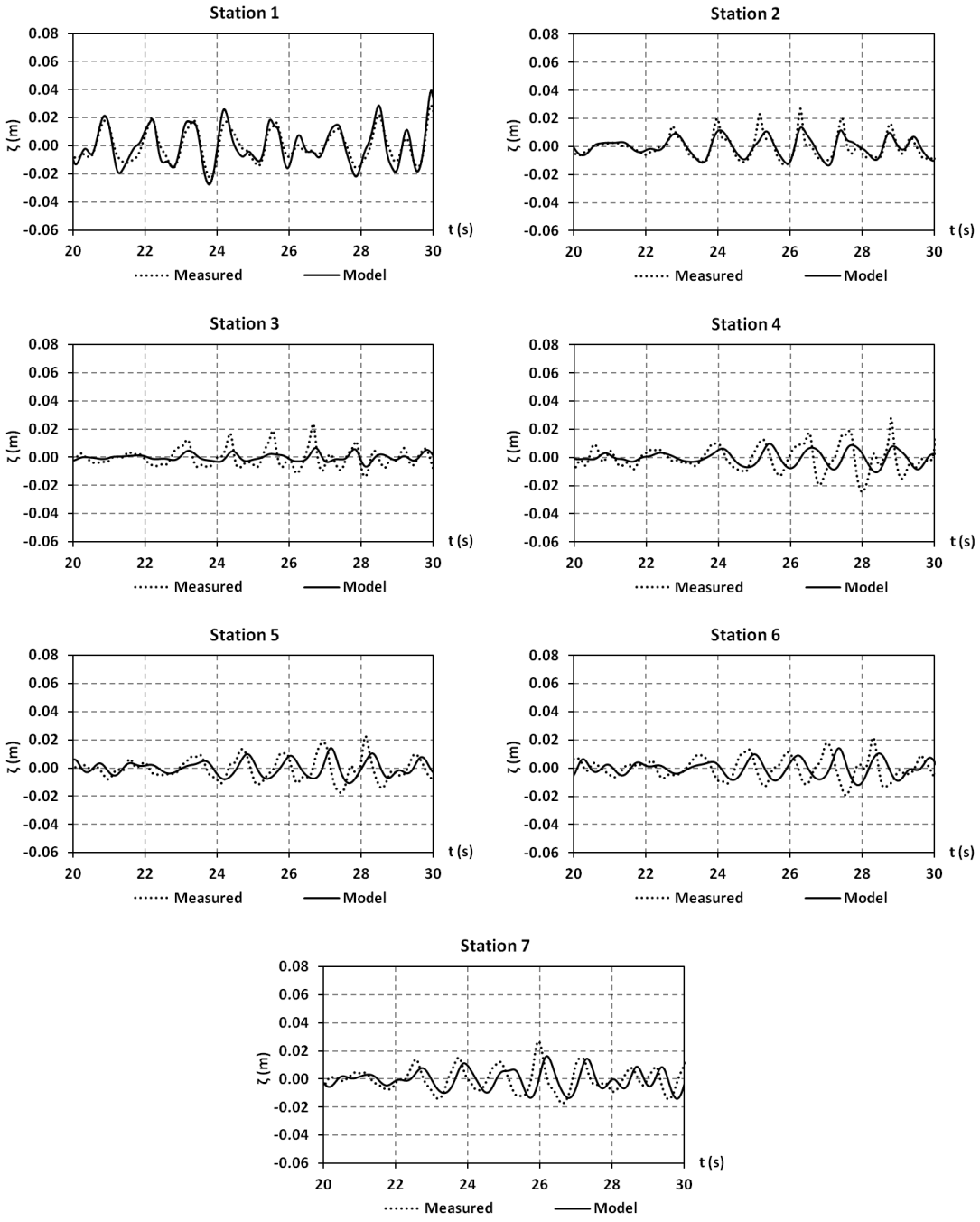

Fig. 6.39. Measured and computed by the model timeseries of free surface elevation for test case 5.

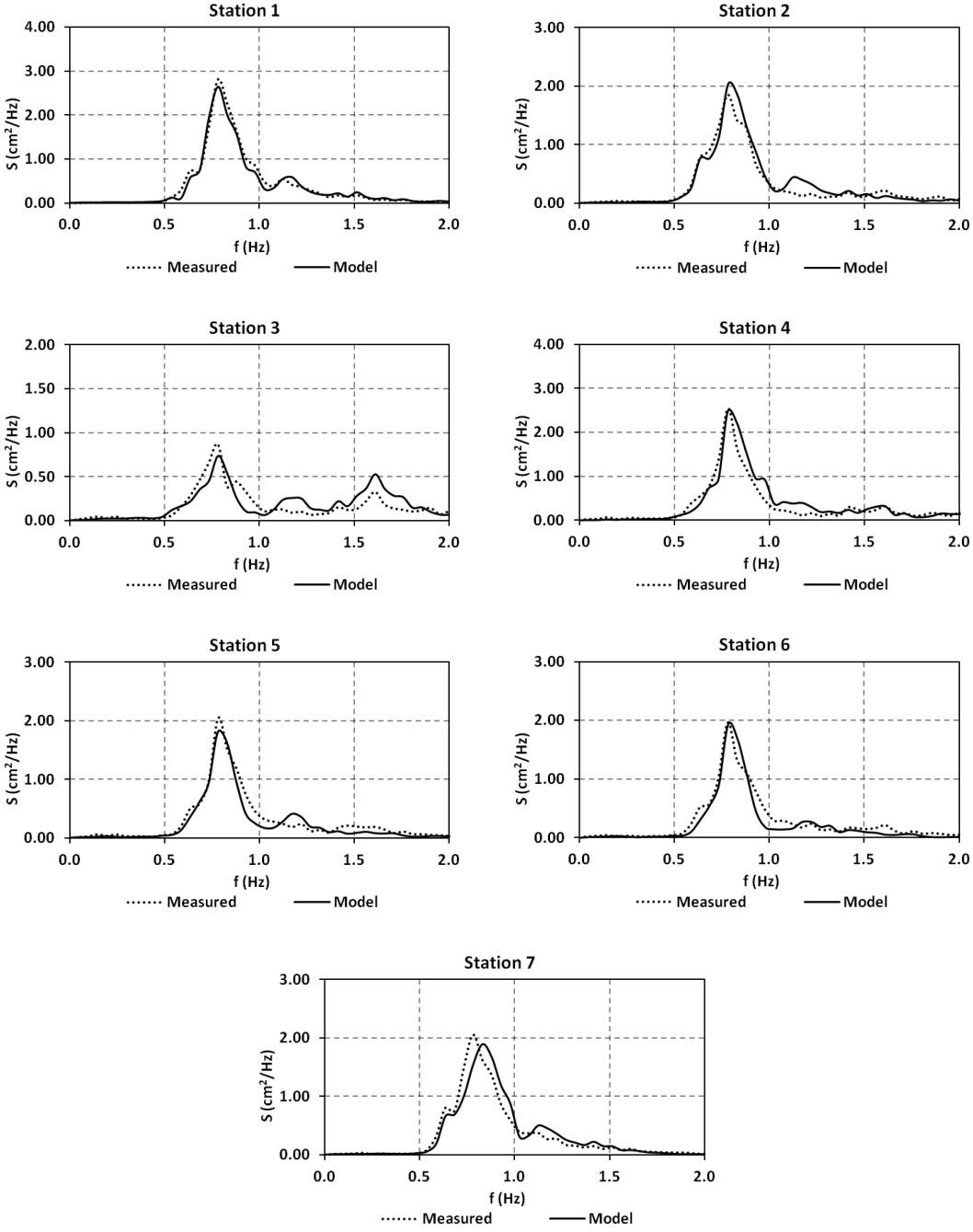

Fig. 6.40. Comparison of wave spectra computed by the measured and simulated by the model timeseries of free surface elevation for test case 5.

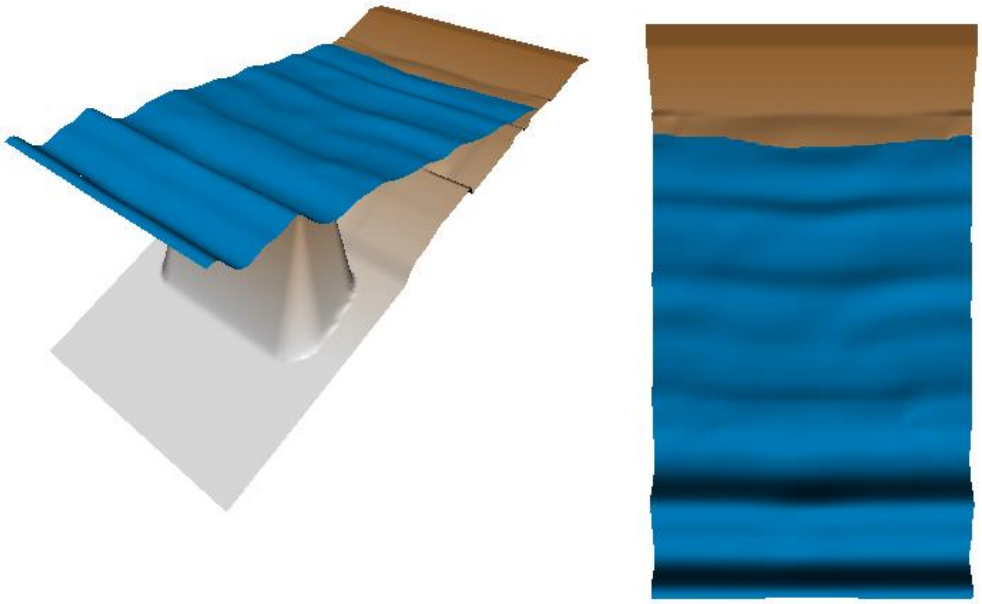

Fig. 6.41. Snapshot of the computed surface elevation from a bird's-eye view (at left) and from a plan view (at right) for test case 5.

The agreement is generally good. Some errors, mainly concerning the wave phases are observed in the timeseries. However, based on Fig. 6.40, it can be claimed that the energy transfer to higher harmonics is adequately described. An underestimation of the energy at the peak frequency and an overestimation at around $kd \sim 1.50$ is observed at station 3. According to the nonlinear analysis performed in chapter 2, an underestimation of the energy density at this nondimensional wavenumber would be expected. However, that analysis referred to impermable beds, while the bottom permeability may have a significant impact, as also shown in subsection 6.2 for the linear properties. In addition, the effect of diffraction should be also kept in mind, although it appears to be less intense than in the corresponding regular test case 1.

Figure 6.42 shows the computed time-averaged velocities both around and inside the submerged breakwater. The velocities are much lower than the ones in the corresponding regular wave test 1 and generally the vector field seems much more irregular. The two vortices down-wave of the breakwater are less pronounced and two additional symmetric eddies are also present upwave of the structure.

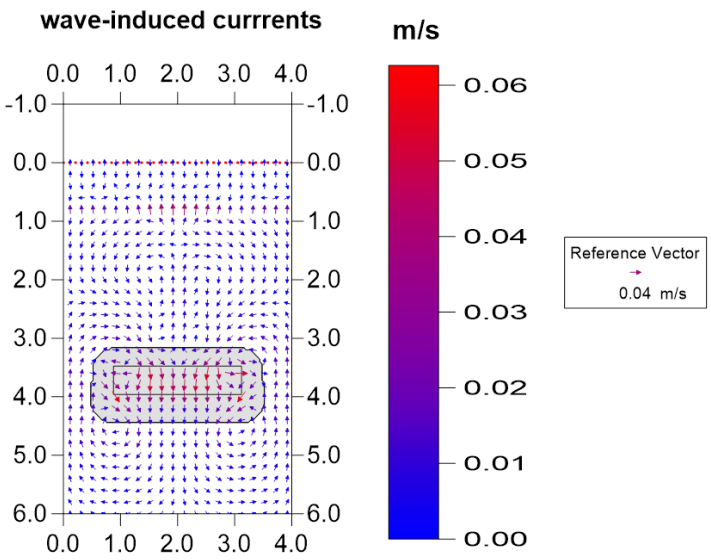

Fig. 6.42. Computed by the model time-averaged velocities around and above the submerged breakwater for test case 5.

The evolution of the sandy bed was also simulated by the compound model for 5 hrs of wave action. A view of the initial and the final shoreline at laboratory is shown in Fig. 6.43.

Fig. 6.43. View of the initial (at left) and final (after 5 hrs of wave action, at right) shoreline for test case 5.

A comparison between the measured and the computed by the model final bed elevation is depicted in Fig. 6.44.

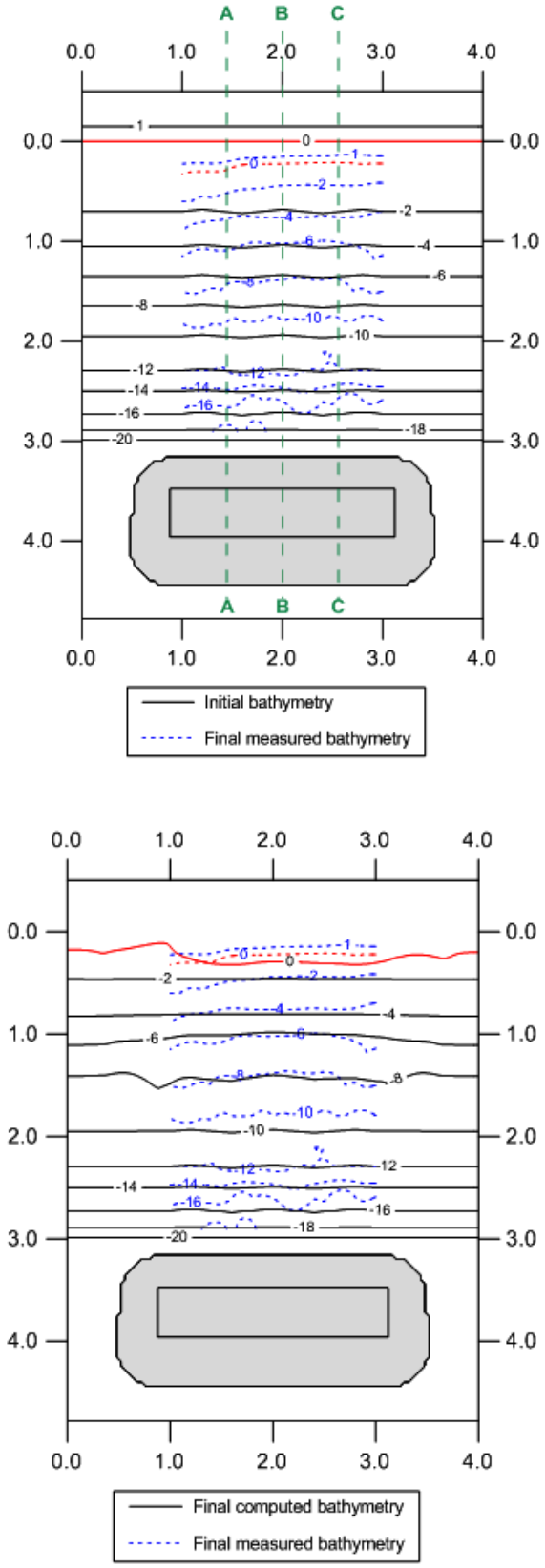

Fig. 6.44. Initial and final measured bathymetries (above) and comparison between final measured and computed bathymetries (below) for test case 5 (depths in cm).

Similarly to the previous test cases, an estimation of the cross-shore sediment transport rates along sections A, B and C was made from the measured and the computed bathymetry changes. Their comparison is depicted in Fig. 6.45.

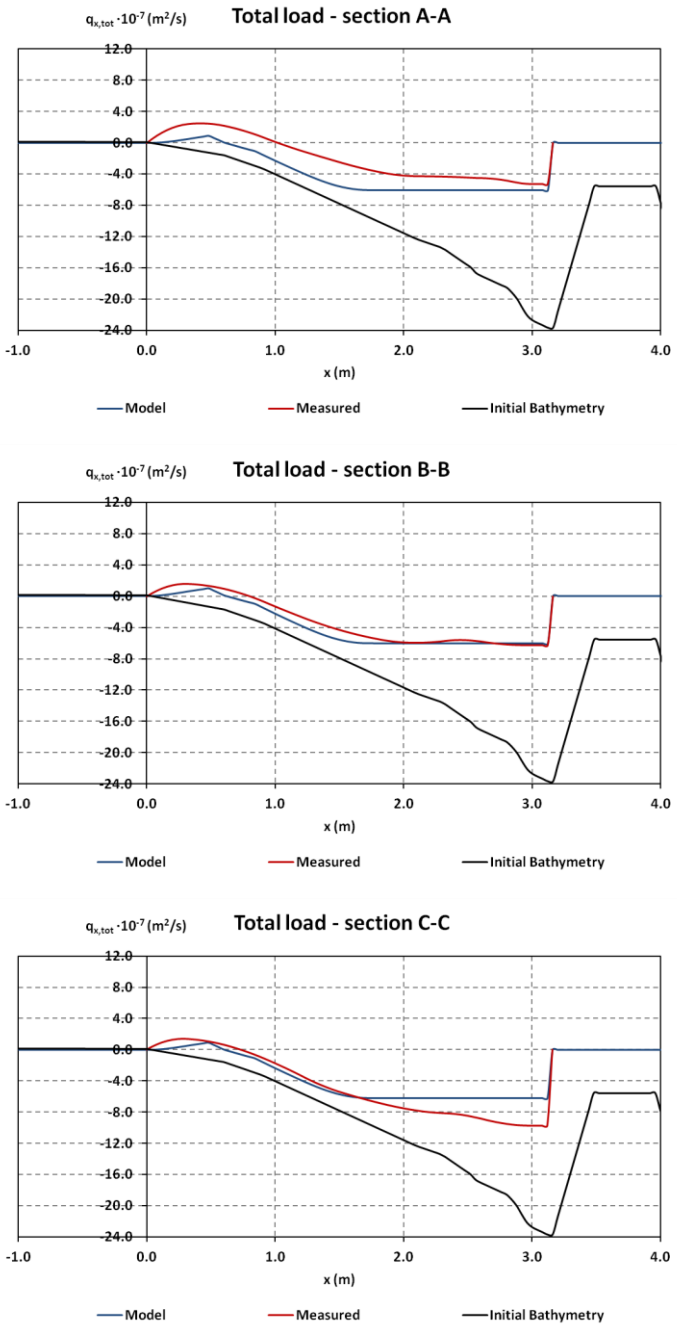

Fig. 6.45. Cross-shore total sediment transport loads as estimated from the measured and computed bathymetry change along 3 sections for test case 5.

The model describes adequately the sediment transport along the three sections, especially in the most onshore area. The bathymetry evolution appears to be milder than in the corresponding regular wave test No. 1. The bathymetry contours seem to be shifted onshore and offshore parallel to their initial position, rather than generating peaky formations. This

behavior resembles of 2D, and not so much 3D, wave propagation. The model, in general, describes these cross-shore bathymetry changes.

6.3.6 Test case No. 6

Test No. 6 involved irregular waves of a Jonswap spectrum with peak period T_p = 2.0 s and significant wave height H_{so} = 0.045 m at the wave source. Hence, this non-breaking scenario corresponded to test case 2 but for irregular wave propagation. The spatial steps were chosen $\Delta x = \Delta y$ = 0.04 m and the time step Δt = 0.01 s. Both the wave propagation and the morphological evolution of the bed in the lee of the structure were simulated by the compound model. The simulation period was 5 hrs, similarly to the laboratory experiment.

A comparison between the measured and the computed by the model timeseries of the free surface elevation at the seven wave gauges is depicted in Fig. 6.46. The corresponding comparison for the wave spectra is depicted in Fig. 6.47, while a snapshot of the computed free surface elevation is shown in Fig. 6.48.

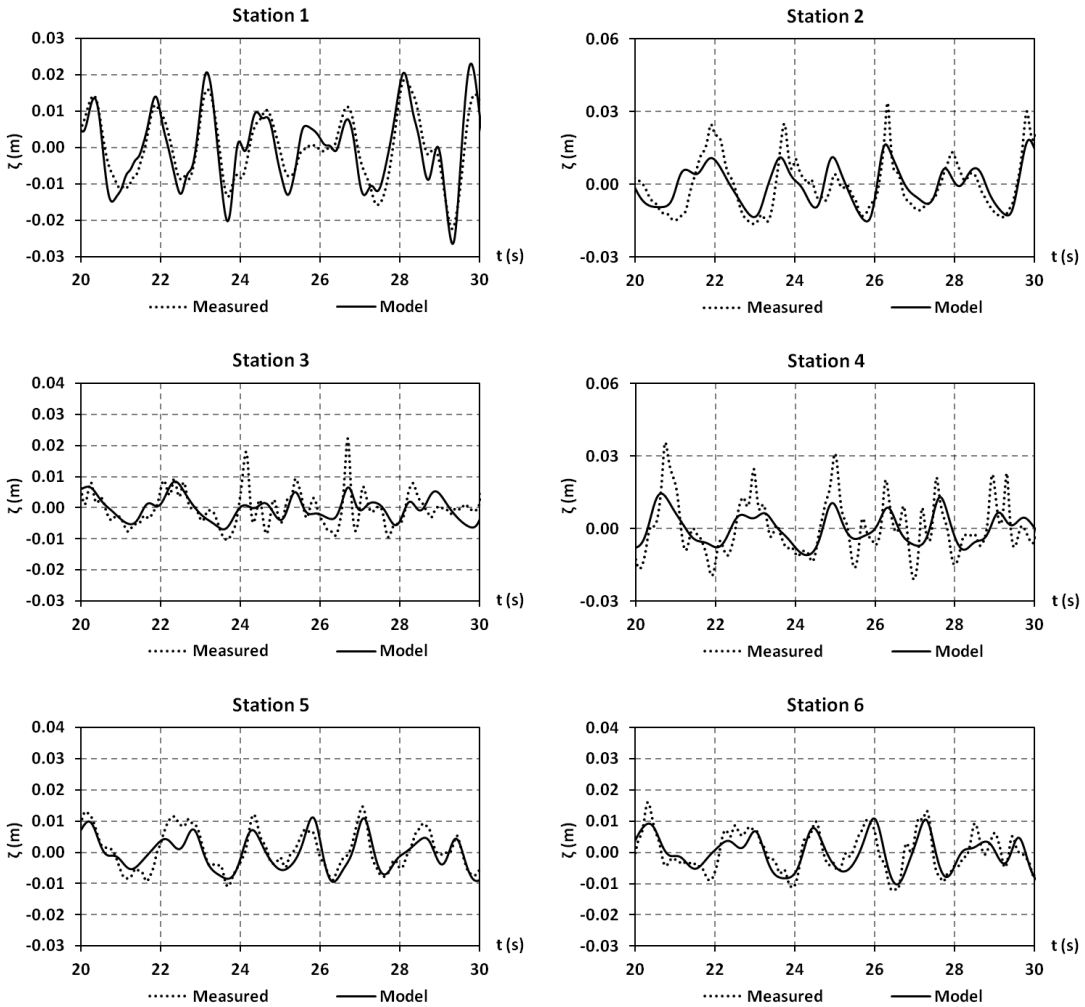

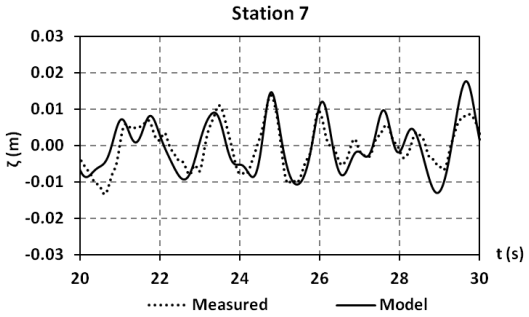

Fig. 6.46. Measured and computed by the model timeseries of free surface elevation for test case 6.

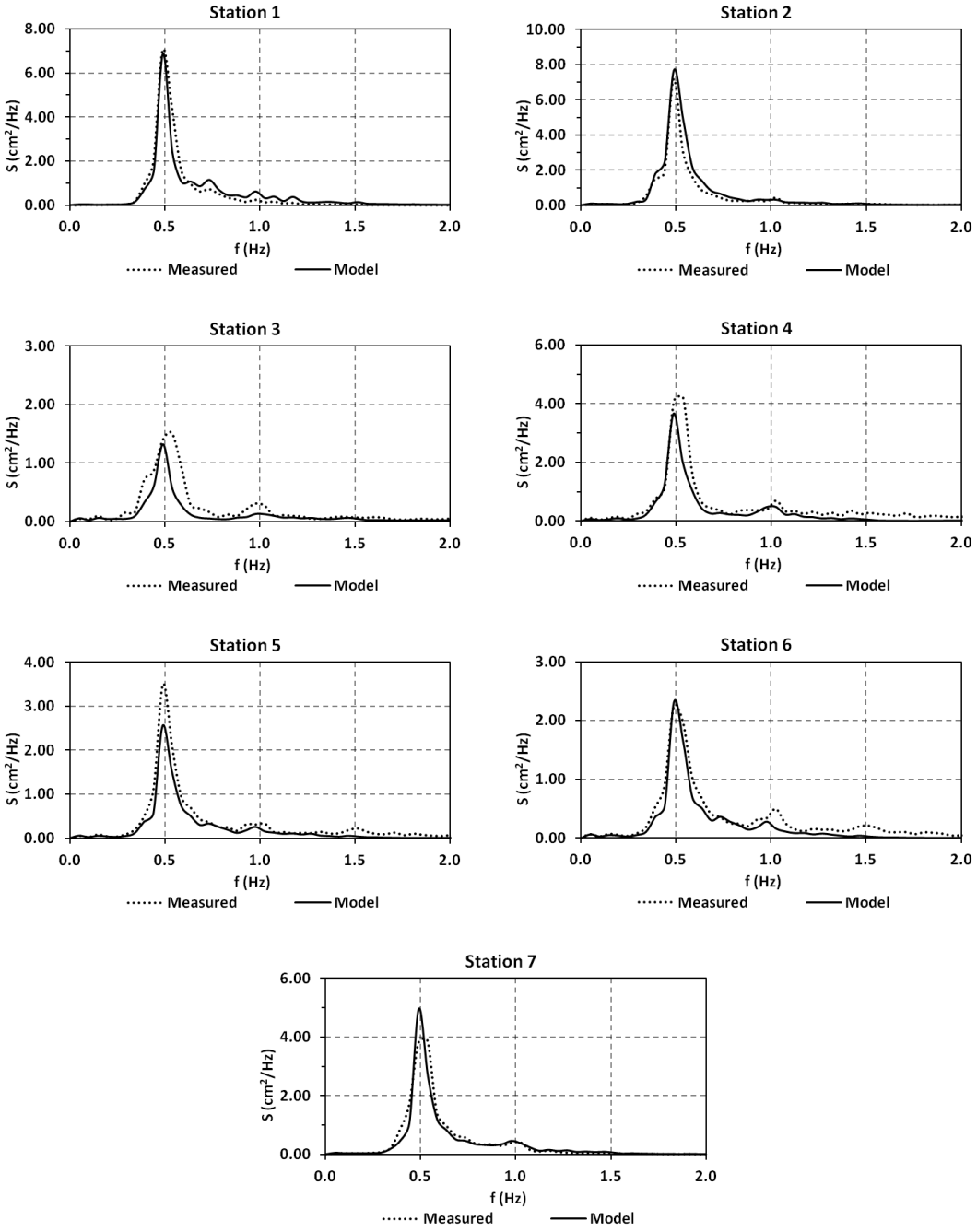

Fig. 6.47. Comparison of wave spectra computed by the measured and simulated by the model timeseries of free surface elevation for test case 6.

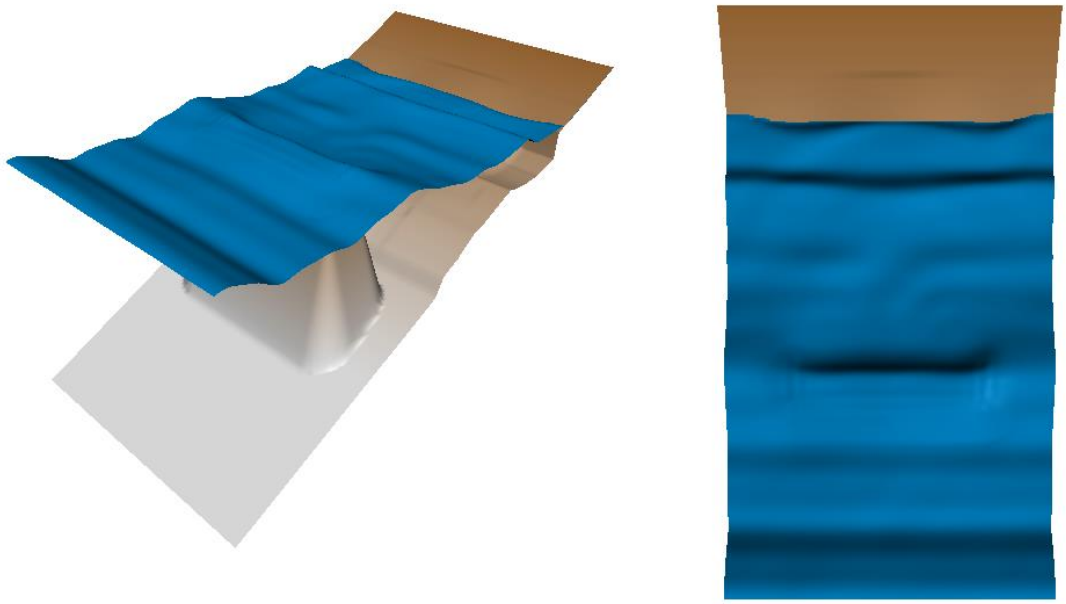

Fig. 6.48. Snapshot of the computed surface elevation from a bird's-eye view (at left) and from a plan view (at right) for test case 6.

The comparison both at the time and the frequency domains show an underestimation of the wave forms and the peak wave energy at stations 3 and 4. However, the spectral shape is reasonably reproduced and the energy transfer to higher harmonics is predicted with acceptable accuracy.

The computed time-averaged velocities both around and inside the submerged breakwater are shown in Fig. 6.49. The two vortices down-wave of the breakwater are more clearly formed than in test case 5 which referred to shorter waves with similar wave height offshore. The velocities are of similar magnitude with the ones in the corresponding regular wave test 2. However, the vortices are more stretched in the present case. Two smaller eddies are also present upwave of the structure and close to its heads.

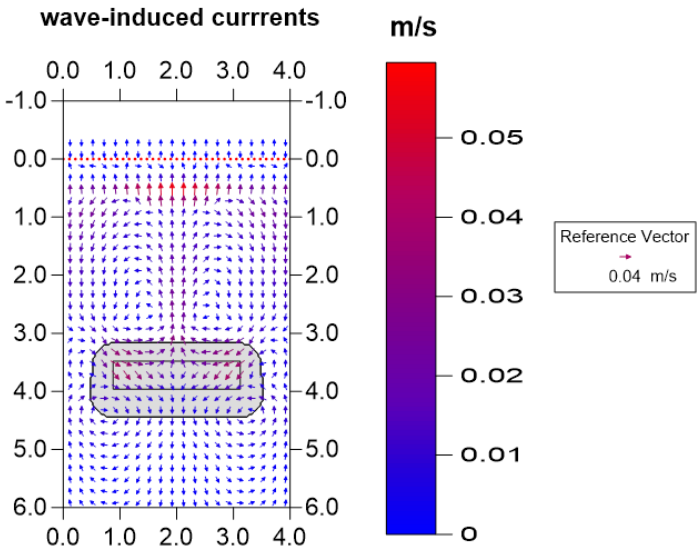

Fig. 6.49. Computed by the model time-averaged velocities around and above the submerged breakwater for test case 6.

The evolution of the sandy bed was also simulated by the compound model for 5 hrs of wave action. A view of the initial and the final shoreline at laboratory is shown in Fig. 6.50.

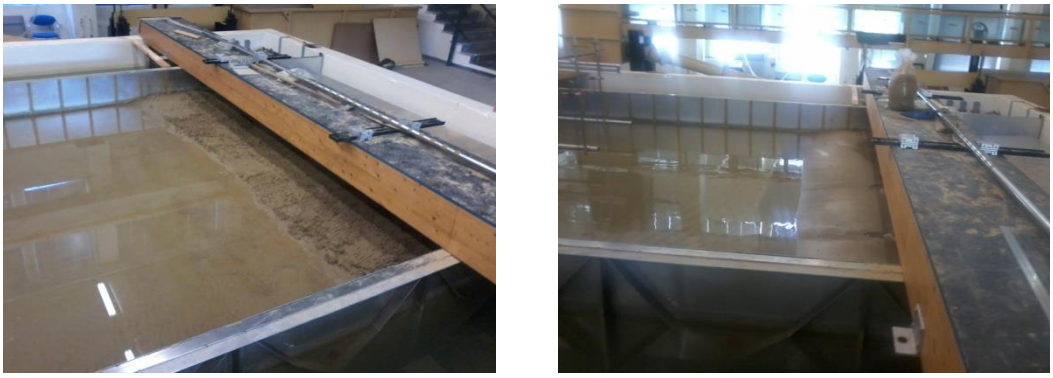

Fig. 6.50. View of the initial (at left) and final (after 5 hrs of wave action, at right) shoreline for test case 6.

A comparison between the measured and the computed by the model final bed elevation is depicted in Fig. 6.51.

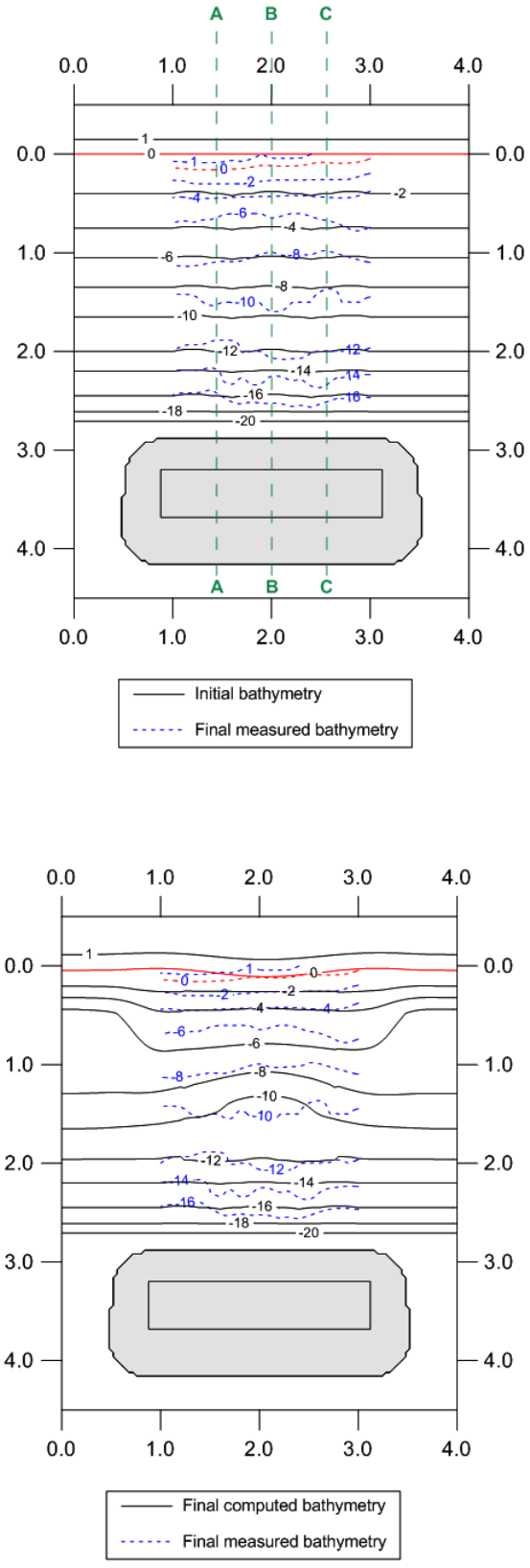

Fig. 6.51. Initial and final measured bathymetries (above) and comparison between final measured and computed bathymetries (below) for test case 6 (depths in cm).

Similarly to the previous test cases, an estimation of the cross-shore sediment transport rates along sections A, B and C was made from the measured and the computed bathymetry changes. Their comparison is depicted in Fig. 6.52.

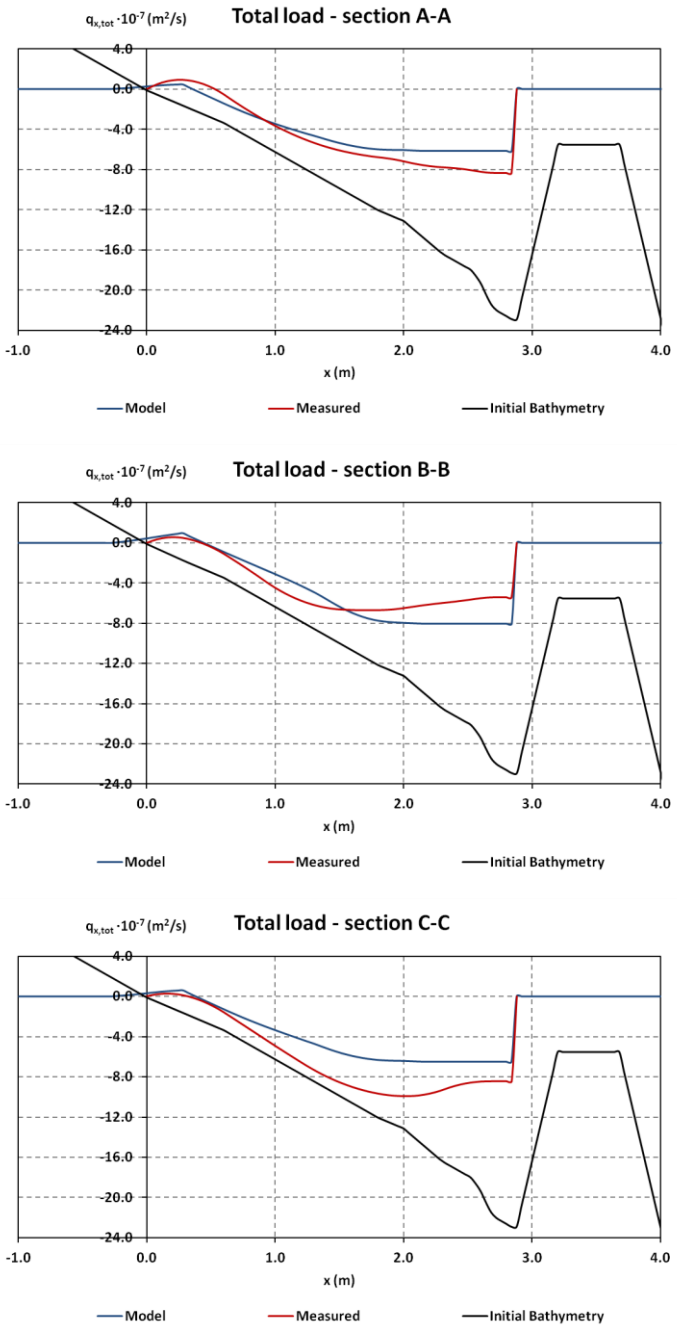

Fig. 6.52. Cross-shore total sediment transport loads as estimated from the measured and computed bathymetry change along 3 sections for test case 6.

The sediment transport is fairly good estimated in the inner zone. In the middle of the wave tank and offshore the model tends to underestimate the transport rates behind the breakwater and towards its heads, while near the centerline the sediment load is over-predicted. However, the evolution of the

shoreline is reasonably predicted and the areas of accretion and erosion are, in generally, correctly described.

6.3.7 Test case No. 7

Test No. 7 included irregular waves of a Jonswap spectrum with peak period T_p = 1.25 s and significant wave height H_{so} = 0.08 m at the wave source. Hence, this scenario corresponded to test case 3 but for irregular wave propagation. This test included breaking waves and the dominant breaking type was spilling. The spatial steps were chosen $\Delta x = \Delta y$ = 0.04 m and the time step Δt = 0.01 s. Both the wave propagation and the morphological evolution of the bed in the lee of the structure were simulated by the compound model. The simulation period was 5 hrs, similarly to the laboratory experiment.

A comparison between the measured and the computed by the model timeseries of the free surface elevation at the seven wave gauges is depicted in Fig. 6.53. The corresponding comparison for the wave spectra is depicted in Fig. 6.54, while a snapshot of the computed free surface elevation is shown in Fig. 6.55.

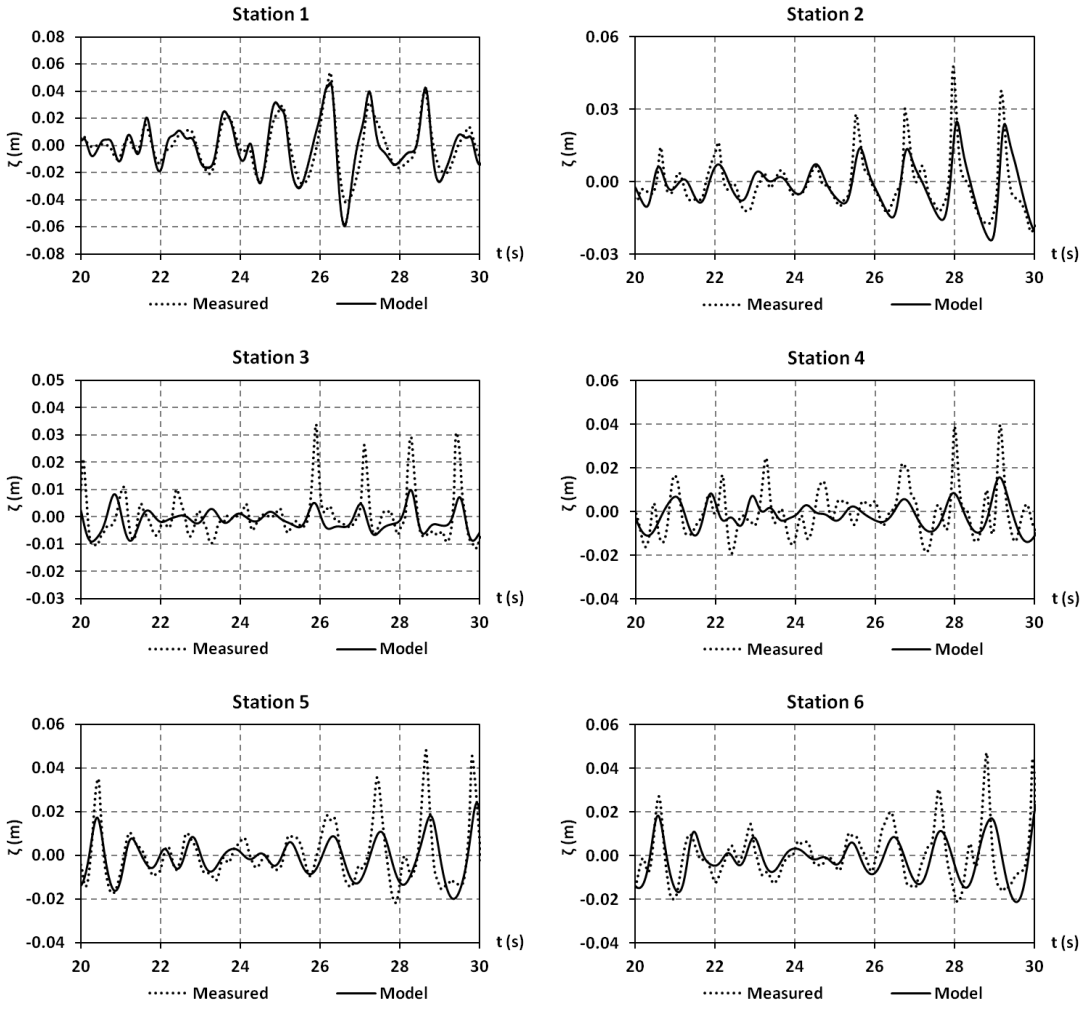

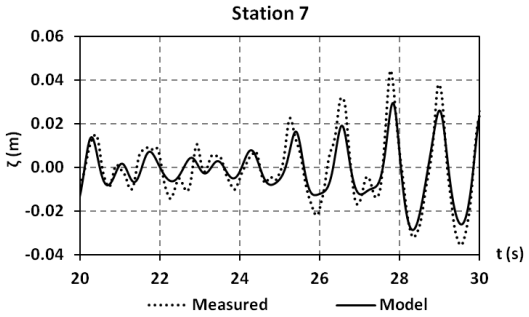

Fig. 6.53. Measured and computed by the model timeseries of free surface elevation for test case 7.

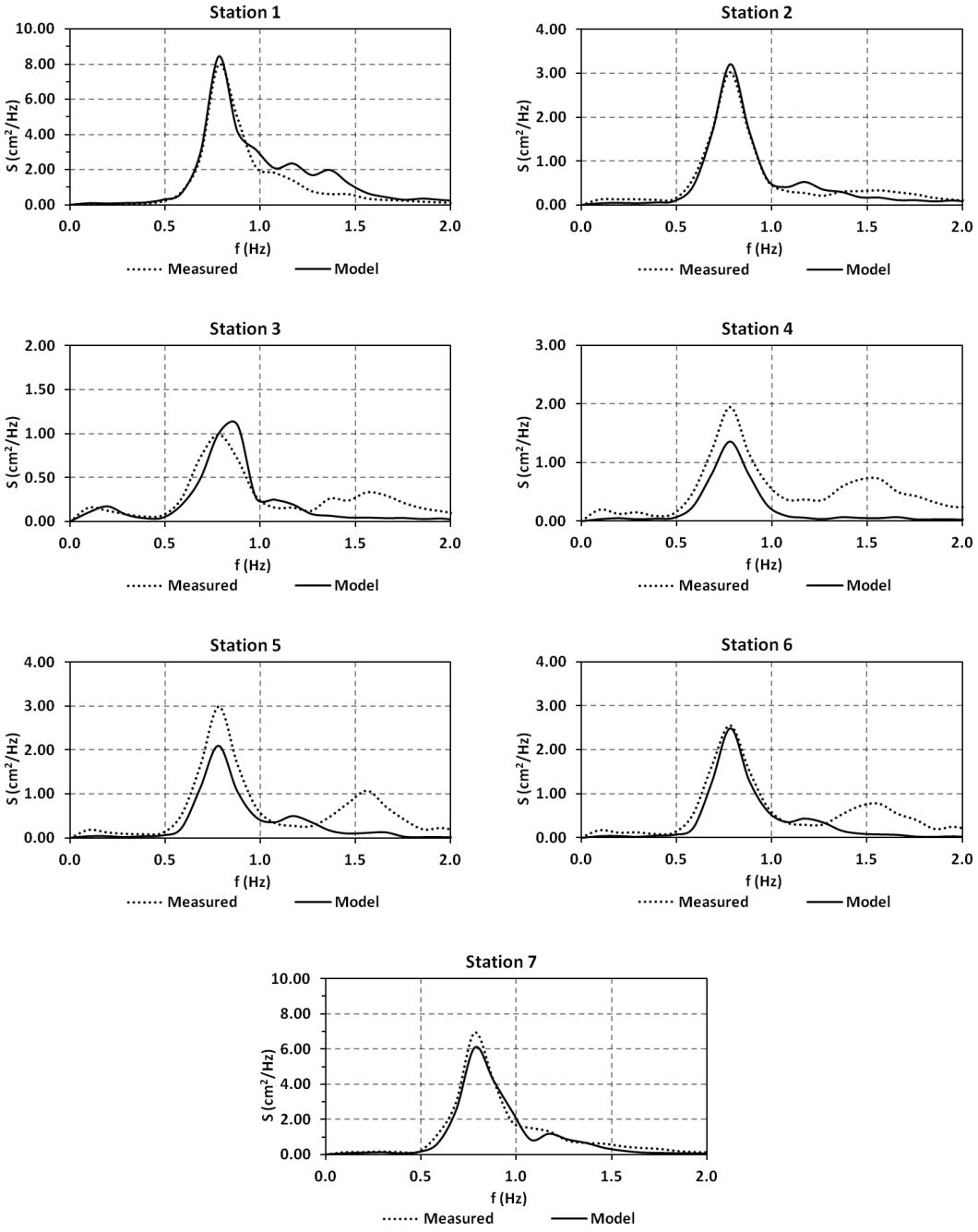

Fig. 6.54. Comparison of wave spectra computed by the measured and simulated by the model timeseries of free surface elevation for test case 7.

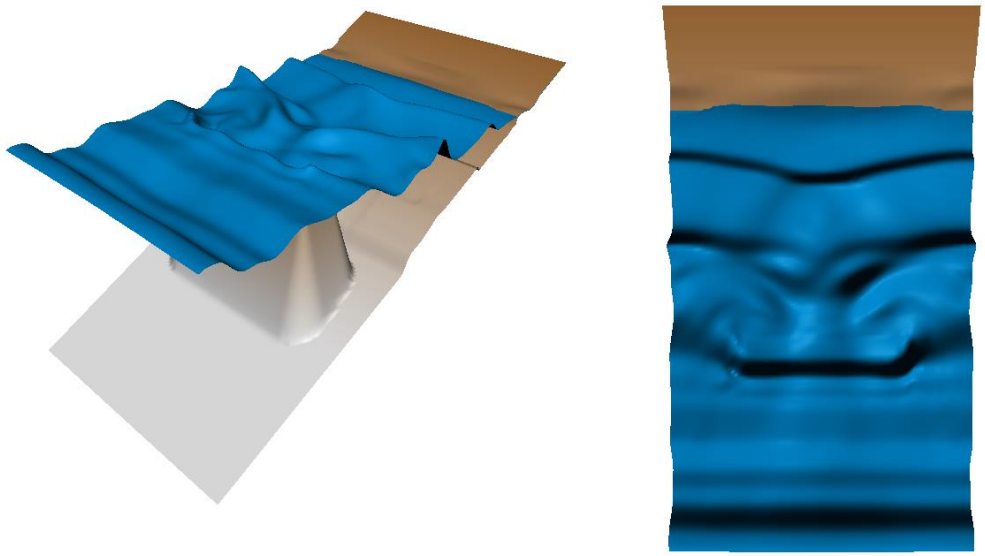

Fig. 6.55. Snapshot of the computed surface elevation from a bird's-eye view (at left) and from a plan view (at right) for test case 7.

The spectral agreement at station 2, which is located at the bar crest is fairly good. Although the generation of higher harmonics is quite well described over the bar crest, at the down-slope of the breakwater the energy transfer to superharmonics is apparently underestimated. Thus, a secondary spectral peak formed around f = 1.5 Hz is not captured by the model. Furthermore, at the most down-wave station 4, the spectrum is significantly under-predicted. This may be attributed to two reasons. At first, an over-pronounced wave breaking by the model over the submerged bar and down-wave of it. Secondly, both visual observations during the laboratory experiments and the model runs revealed significant diffraction, as also shown in Fig. 6.55. The diffracted and refracted waves at the submerged breakwater resulted to significant reflection at the side walls which contaminated the propagating wave field. The combination of these processes is more intense than in the other irregular tests and despite using fully lateral reflective boundaries at the numerical model, the wave forms at station 4 are not very accurately reproduced.

The computed time-averaged velocities both around and inside the submerged breakwater are shown in Fig. 6.56. Compared to the corresponding regular wave test 3, the rip currents and the velocities, in general, are weaker. The two vortices down-wave of the breakwater are also formed but the secondary eddies are not formed here in the inner zone, contrary to test case 3.

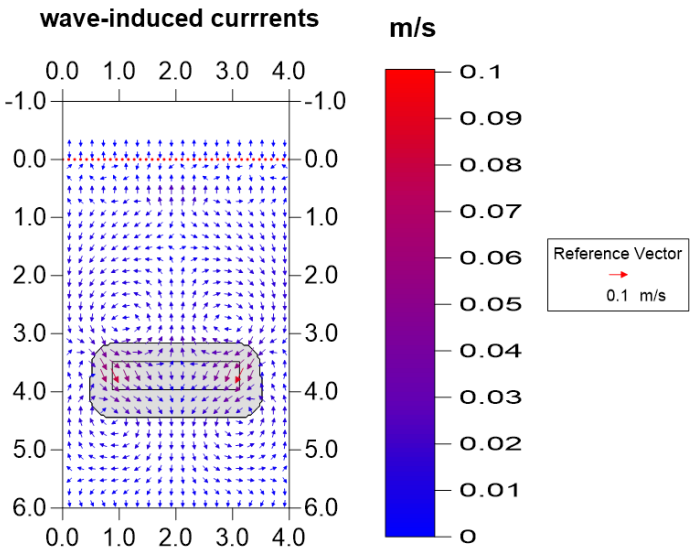

Fig. 6.56. Computed by the model time-averaged velocities around and above the submerged breakwater for test case 7.

The evolution of the sandy bed was also simulated by the compound model for 5 hrs of wave action. A view of the initial and the final shoreline at laboratory is shown in Fig. 6.57.

Fig. 6.57. View of the initial (at left) and final (after 5 hrs of wave action, at right) shoreline for test case 7.

A comparison between the measured and the computed by the model final bed elevation is depicted in Fig. 6.58.

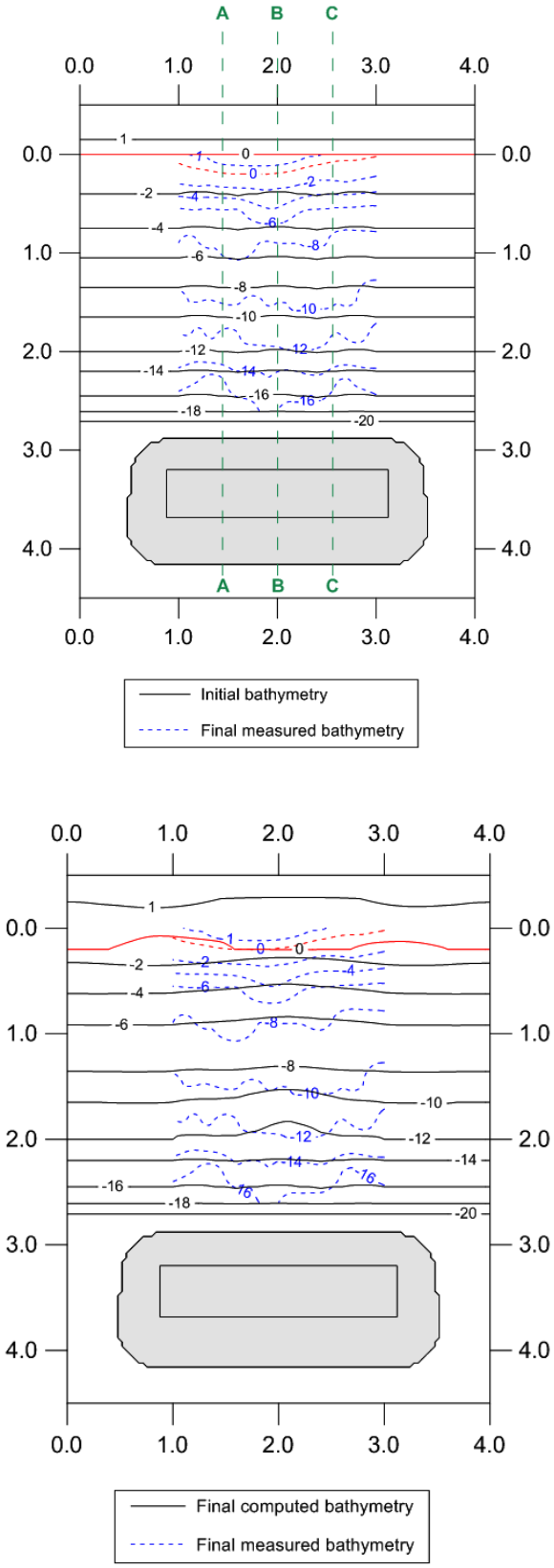

Fig. 6.58. Initial and final measured bathymetries (above) and comparison between final measured and computed bathymetries (below) for test case 7 (depths in cm).

Similarly to the previous test cases, an estimation of the cross-shore sediment transport rates along sections A, B and C was made from the measured and the computed bathymetry changes. Their comparison is depicted in Fig. 6.59.

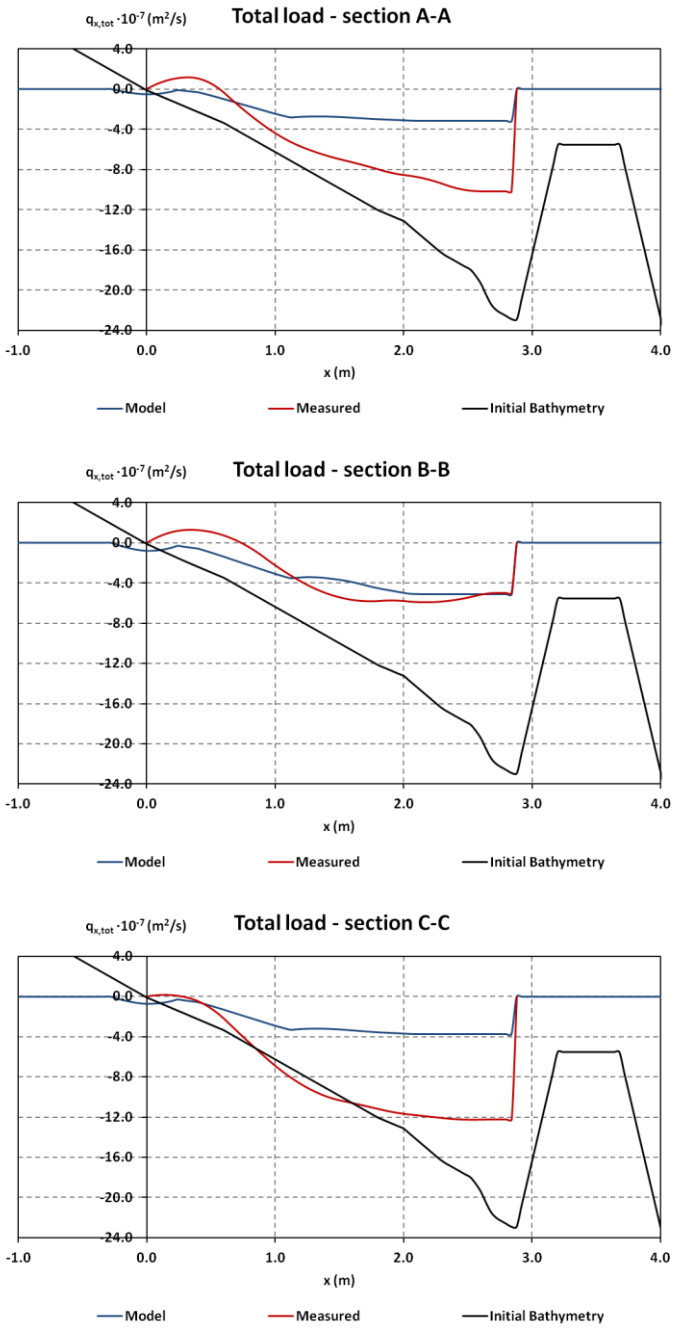

Fig. 6.59. Cross-shore total sediment transport loads as estimated from the measured and computed bathymetry change along 3 sections for test case 7.

The shoreline's response is reasonably predicted, and so is the accretion close to it. However, the erosion in the middle of the distance between the breakwater and the shoreline is significantly underestimated, especially when moving from the centerline towards the heads of the breakwater. This fact is also highlighted in Fig. 6.59 for the sediment transport

rates. Nevertheless, it should be reminded once again that the specific figure refers only to the cross-shore sediment transport by making the assumption that the longshore part is negligible.

6.3.8 Test case No. 8

The last test No. 8 referred to irregular waves of a Jonswap spectrum with peak period T_p = 2.0 s and significant wave height H_{so} = 0.08 m at the wave source. Hence, this scenario corresponded to test case 4, but for irregular wave propagation. This test included breaking waves and the dominant breaking type was spilling. The spatial steps were chosen $\Delta x = \Delta y$ = 0.04 m and the time step Δt = 0.01 s. Both the wave propagation and the morphological evolution of the bed in the lee of the structure were simulated by the compound model. The simulation period was 5 hrs, similarly to the laboratory experiment.

A comparison between the measured and the computed by the model timeseries of the free surface elevation at the seven wave gauges is depicted in Fig. 6.60. The corresponding comparison for the wave spectra is depicted in Fig. 6.61, while a snapshot of the computed free surface elevation is shown in Fig. 6.62.

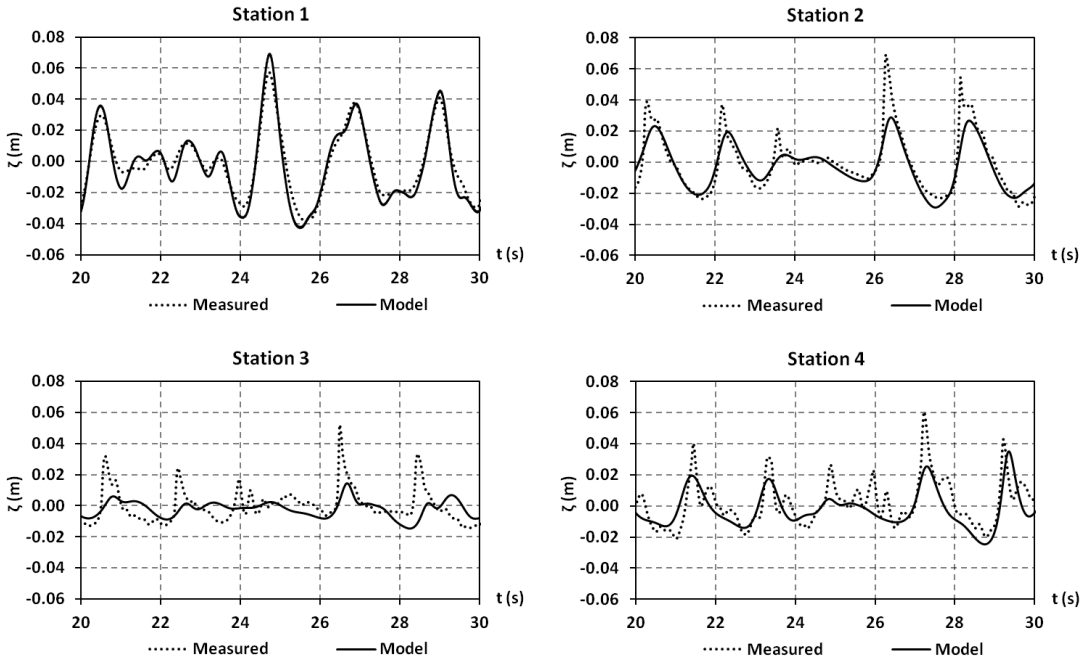

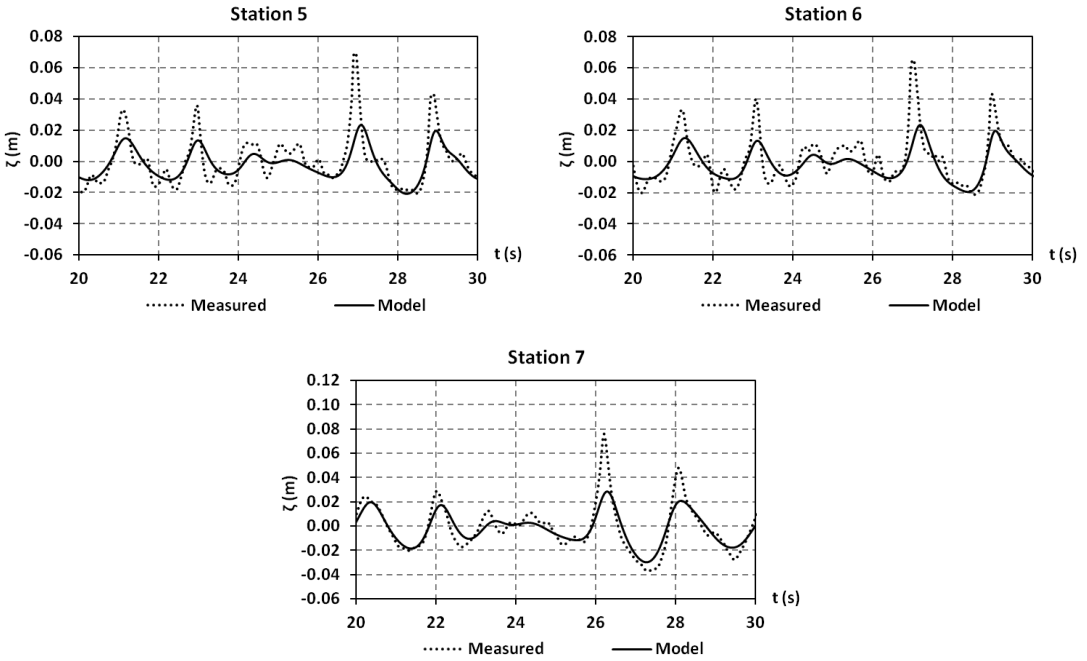

Fig. 6.60. Measured and computed by the model timeseries of free surface elevation for test case 8.

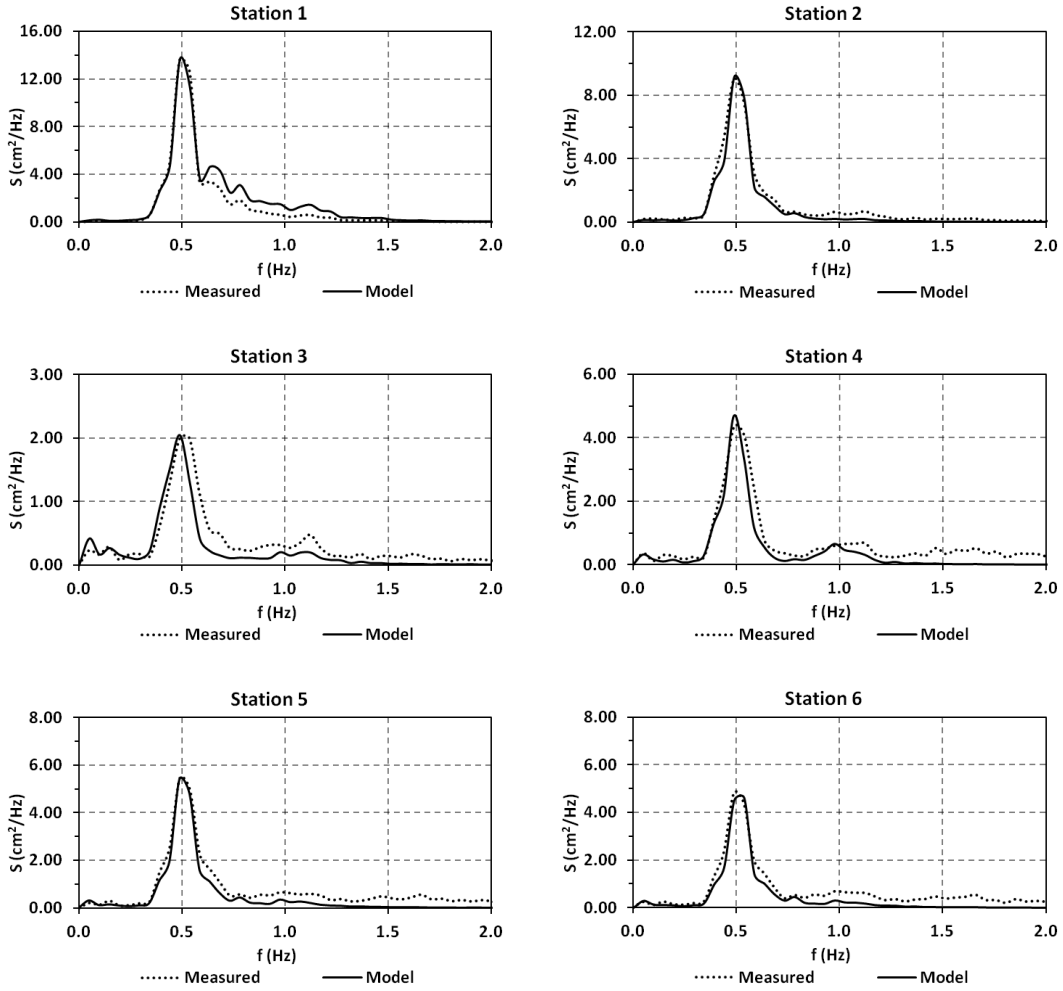

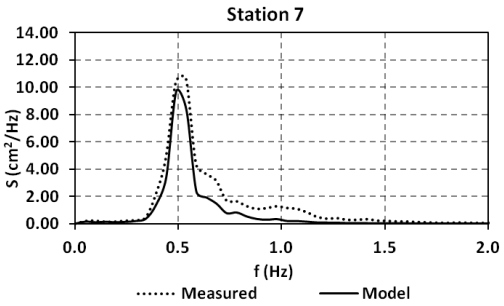

Fig. 6.61. Comparison of wave spectra computed by the measured and simulated by the model timeseries of free surface elevation for test case 8.

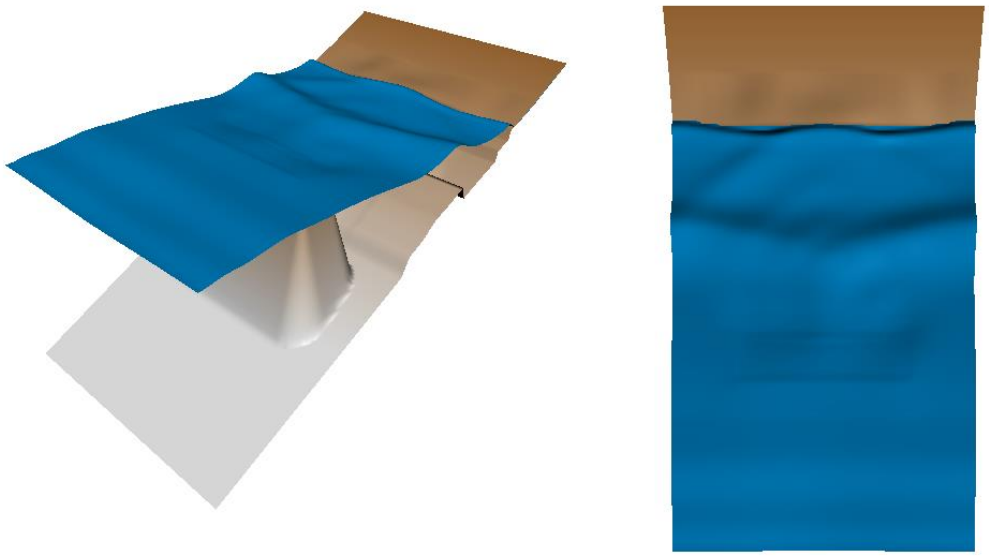

Fig. 6.62. Snapshot of the computed surface elevation from a bird's-eye view (at left) and from a plan view (at right) for test case 8.

The agreement between the measurements and the computed results is better for the specific test than for test No. 8. The peak energy at all wave gauges is accurately described and so is the spectrum shape. Thus, the wave breaking over the permeable structure is also adequately reproduced. An underestimation of the energy transfer to superharmonics is also present, however it is much reduced compared to test No. 7. This was expected, since this latter test referred to shorter waves and the nonlinear properties of the Boussinesq model are more accurate in shallower water (see chapter 2). It should be also mentioned that the diffraction and refraction at the heads of the breakwater are less intense than in test 7 and consequently the reflection from the side walls is also reduced.

The computed time-averaged velocities both around and inside the submerged breakwater are shown in Fig. 6.63. The two eddies down-wave of the breakwater are again present but

they are weaker than in the corresponding regular test case 4. In general, the velocities are lower than in this latter test.

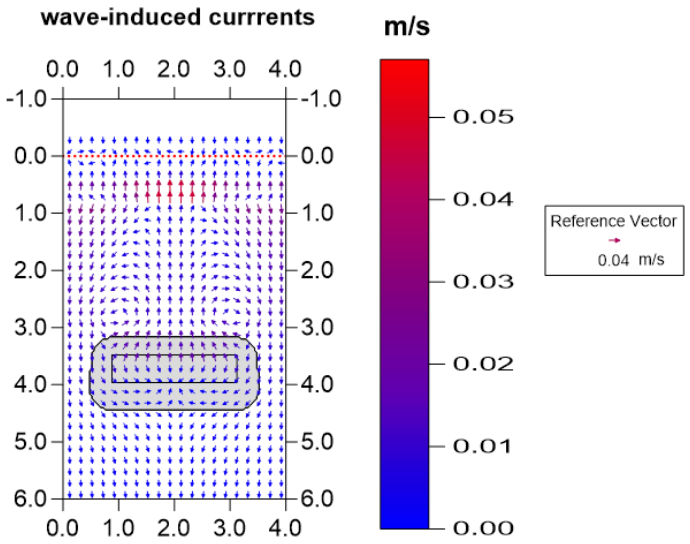

Fig. 6.63. Computed by the model time-averaged velocities around and above the submerged breakwater for test case 8.

The evolution of the sandy bed was also simulated by the compound model for 5 hrs of wave action. A view of the initial and the final shoreline at laboratory is shown in Fig. 6.64.

Fig. 6.64. View of the initial (at left) and final (after 5 hrs of wave action, at right) shoreline for test case 8.

A comparison between the measured and the computed by the model final bed elevation is depicted in Fig. 6.65.

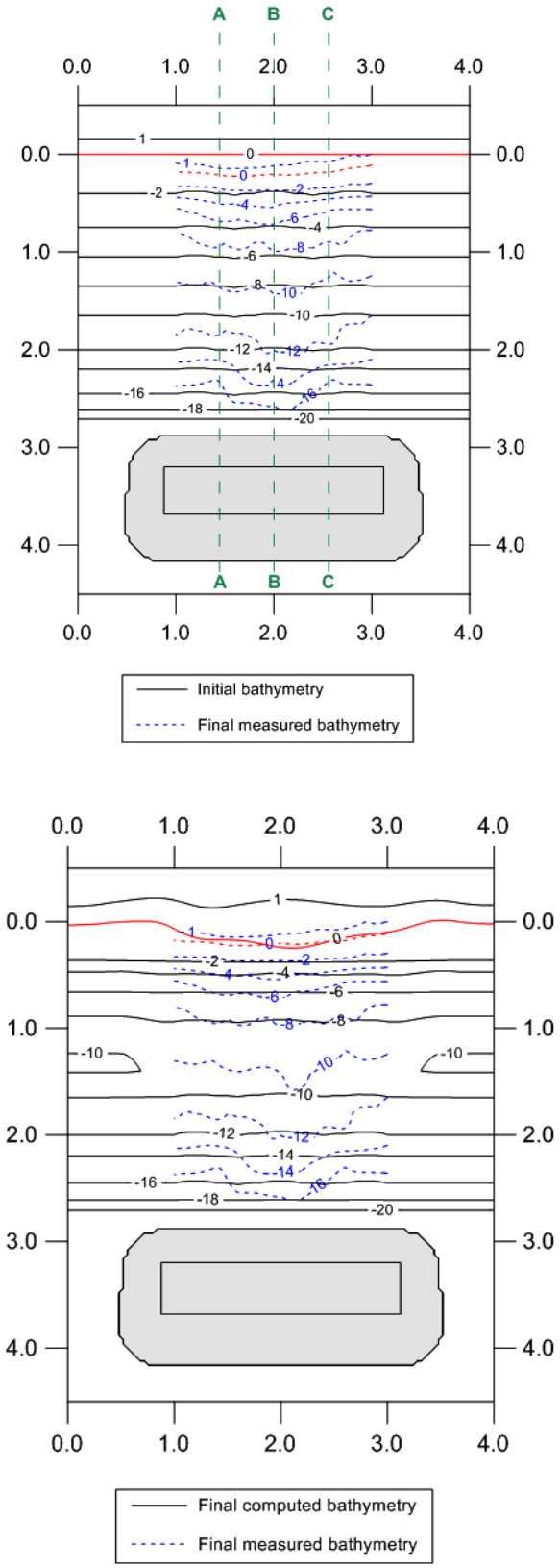

Fig. 6.65. Initial and final measured bathymetries (above) and comparison between final measured and computed bathymetries (below) for test case 8 (depths in cm).

Similarly to the previous test cases, an estimation of the cross-shore sediment transport rates along sections A, B and C was made from the measured and the computed bathymetry changes. Their comparison is depicted in Fig. 6.66.

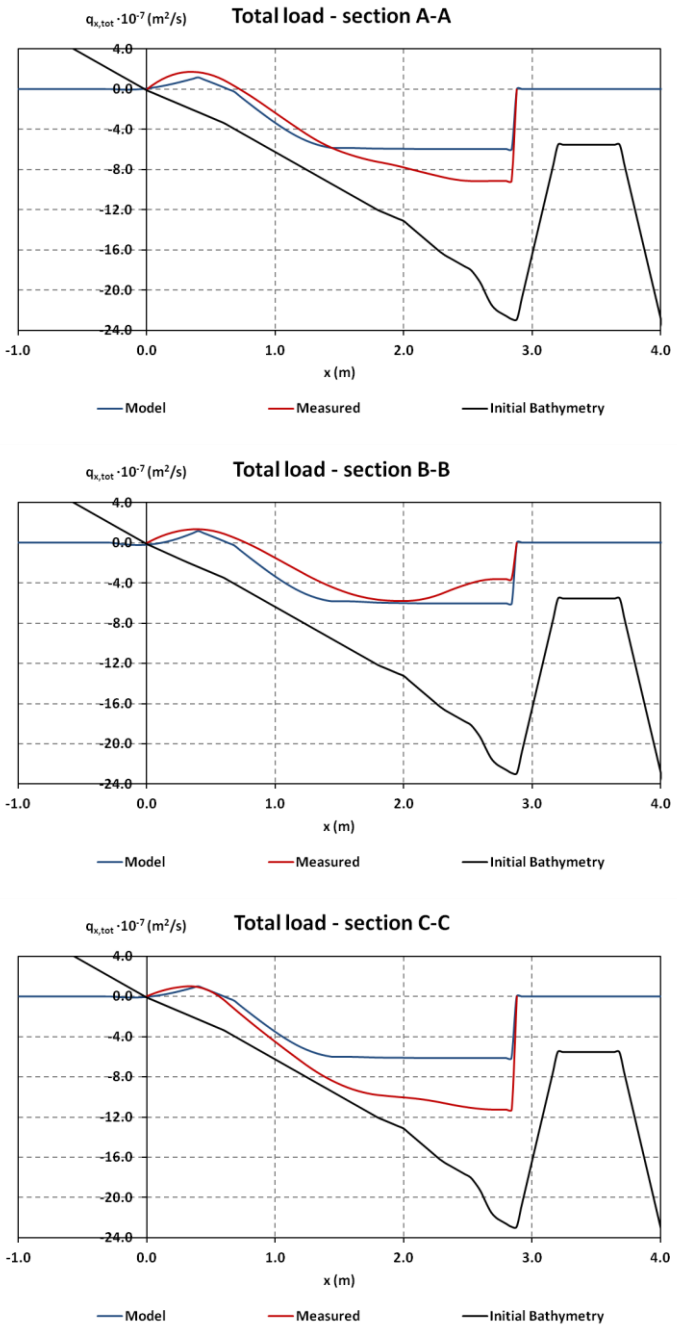

Fig. 6.66. Cross-shore total sediment transport loads as estimated from the measured and computed bathymetry change along 3 sections for test case 8.

The shoreline's response and the formation of the salient are fairly good described by the model. However, the erosion in the middle of the wave tank is underestimated and also a breaking bar that was formed in the laboratory down-wave of the structure is not predicted.

6.4 Discussion on model extension to porous beds

In the present chapter, the compound numerical model described in chapters 3 and 4 was extended to account for porous beds. This extension yielded some extra porosity terms in the continuity and momentum equations and also introduced an additional vectorial Darcy-Forchheimer equation for the flow inside the porous medium. Thus, the final version of the wave module includes five differential equations: the continuity equation, the two momentum equations in x- and y-directions, and the two Darcy-Forchheimer equations in the x- and y-directions, too. For impermeable beds the wave module reduces to that described in chapter 3. The sediment transport and the morphological modules are the ones presented in chapter 4.

The presented extension modifies the linear and nonlinear mathematical properties of the model equations for wave propagation over permeable bottoms. The derivation is based on Cruz *et al*. (1997) and terms of $O(1, \varepsilon, \sigma^2)$ were retained in the Darcy-Forchheimer equation. An enhancement linear operator was also applied in this latter equation, introducing a free parameter γ in addition to the free parameters B and B_2 which were used to optimize the model's linear properties for impermeable beds. A linear analysis was applied for porous bottoms referring to the wave celerity and the damping rate. According to this analysis the optimal value of B is 1/18, instead of 1/15 which was obtained for impermeable beds. Hence, the former value was used herein for porous seafloors. This is an improvement of the presented model compared to its predecessors, which relied on similar, but lower-order Boussinesq-type equations (Avgeris *et al*., 2004; Metallinos *et al*., 2014). A similar analysis can be performed for the linear shoaling characteristics over permeable beds and this may propose a modified optimal value for B_2, different than 0.0653 which was derived for impermeable beds. However, such a linear shoaling analysis was not performed in the present thesis and it is left for future research.

A second improvement of the presented model over its corresponding predecessors is the presence of the additional terms of $O(\sigma^2)$ in the Darcy-Forchheimer equation. According to the linear analysis that was performed, these extra terms improve the result for the wave celerity up to approximately $kd \approx 1.65$. However, with respect to the spatial damping rate, if a 10% error is accepted, the equations of $O(1, \varepsilon, \sigma^2)$ are valid up to $kd \approx 1.0$, while the ones of $O(1, \varepsilon)$ only up to $kd \approx 0.45$, which is only slightly higher than the limit of shallow water. Beyond that limit, the error induced by the nonlinear shallow water equations for a porous medium increases drastically. Thus, this is a significant improvement, especially when simulating wave propagation over permeable submerged breakwaters that are located in intermediate water depths. This conclusion was further supported by the results of the scenarios simulated in the present chapter. In particular, for the test cases including short

waves, the permeable structure lied in the non-dimensional depth range $kd = (0.37 \div 1.00)$. Hence, inclusion of the additional terms of $O(\sigma^2)$ improved the model results. The aforementioned depth range in the long wave test cases was $kd = (0.23 \div 0.58)$ and these terms did not have a significant effect on the results. It should be also mentioned, that the theoretical analysis performed was a linear one, while a non-linear analysis, similar to the one applied in chapter 2 for impermeable beds, is left for future research. Such an analysis is important for better understanding and explaining the energy transfer to super- and sub-harmonics that takes place over permeable submerged bars.

Some discussion should be also made on the validity of the Darcy-Forchheimer equation inside the porous medium. Several researchers have tried to distinguish flow regimes in porous media and define the limits between each other. Typically, the Reynolds number controls the transition from one zone to the other. However, for porous media there is no clear limit for this transition. For example, the nonlinearity experience in non-Darcy flows is not always a result of turbulence but it could be due to the inertial effects, as stated above. Thus, non-Darcy flow is known to occur in porous media also at low Reynolds numbers. According to Dybbs and Edwards (1984) four major regimes can be distinguished:

- Darcy or laminar flow where the flow is dominated by viscous forces and the pressure gradient varies linearly with the flow velocity.
- At increasing Reynolds numbers, a transition zone is observed leading to flow dominated by inertia effects.
- Further increase of the Reynolds numbers results to an unsteady laminar flow with wake oscillations and vortices.
- For high Reynolds numbers, a highly unsteady and chaotic turbulent flow regime appears that is dominated by eddies.

A diagrammatic representation of the flow regimes in a porous medium is depicted in Fig. 6.67 after Basak (1977).

Another issue concerning the correct description of the wave-current interaction refers to the transport of the vertical vorticity associated with surf zone currents. This issue has been discussed in subsection 3.5 for impermeable beds. In addition to this discussion, it should be mentioned that it is also important to retain the vertical vorticity inside the porous medium when simulating breaking waves over a porous bed or a permeable submerged breakwater. However, formally in the present model, the order of the computed vertical vorticity is not exactly consistent with the order of the wave motion itself described by the Boussinesq equations. This slight inconsistency is present in almost all Boussinesq-type wave models for

impermeable beds and it was also present in Hsiao et al.'s (2002) model for porous beds. The methodology introduced by Chen (2006) corrected this inconsistency in the latter model.

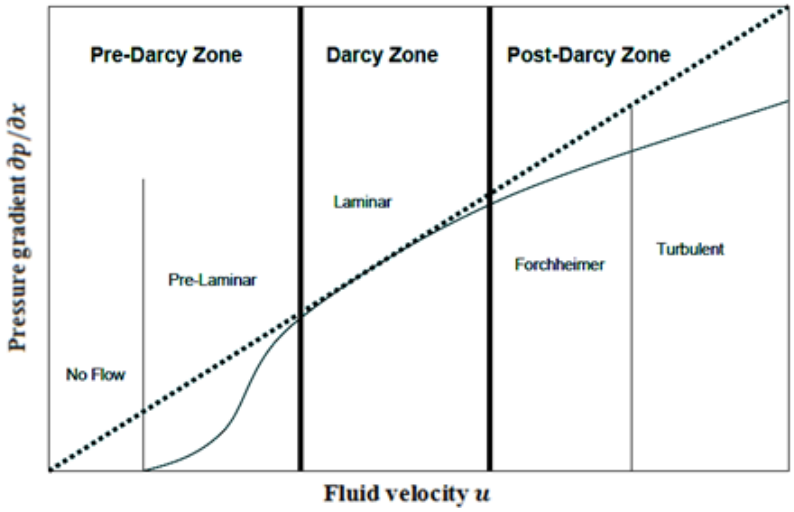

Fig. 6.67. Flow regimes in porous media after Basak (1997) (from Amao, 2007, modified).

The laboratory experiments performed in the context of the present Ph.D. thesis were described in chapter 5. They referred to studying the morphological evolution in the lee of a submerged breakwater. In parallel, the wave characteristics over and around the permeable structure were also studied. The wave transmission coefficients for the eight scenarios are presented in table 6.1. The submerged breakwater was placed on a sloping bed. Thus, the transmission coefficient should be adjusted since the wave height would also change due to shoaling, even in the absence of the structure. Nevertheless, the bed slope was mild, approximately 1:15, and thus the transmission coefficient presented in the table is defined as the ratio of the wave height at the toe of down-slope of the bar to the wave height at the toe of upslope of the bar, defined along the centerline of the wave tank. For completeness, the same ratio for a theoretical situation with no breakwater is also mentioned based on linear theory.

Table 6.1. Wave characteristics and salient width in the various tests.

Test No.	**Wave type**	$H_{s,o}$ **(m)**	T_p **(s)**	$K_t = H_2/H_1$ **(with SB)**	H_2/H_1 **(without SB)**	**X / S** (*)
(1)	Regular	0.045	1.25	0.39	1.03	0.09
(2)	Regular	0.045	2.00	0.61	1.07	0.10
(3)	Regular	0.08	1.25	0.60	1.03	0.15
(4)	Regular	0.08	2.00	0.66	1.07	0.11
(5)	Irregular	0.045	1.25	0.39	1.03	0.07
(6)	Irregular	0.045	2.00	0.65	1.07	0.04
(7)	Irregular	0.08	1.25	0.48	1.03	0.06
(8)	Irregular	0.08	2.00	0.54	1.07	0.07

(*) See Fig. 6.68 for the definition of symbols.

For the irregular test cases, the related wave heights are the significant wave heights. The transmission coefficient varies approximately within the range $0.39 \div 0.65$. It should be kept in mind that the porosity was measured approximately $\lambda = 0.52$, which is a high value. Nevertheless, the efficiency of the breakwater was satisfactory, since the transmitted wave height was averagely about 50% reduced compared to the incident one, while in the absence of the breakwater the former would be 3-7% increased compared to the latter. In addition, it can be deduced that the transmission coefficient is lower for short waves than for longer ones. It was also observed during the laboratory experiments that the longer waves tended to be influenced less by the presence of the submerged obstacle than the shorter ones. Thus, the wave crests of the former remained almost straight during their passing over the bar, while for the latter the diffraction effect was increased resulting to an apparent curving of the wave crests. This result was also expected from the diffraction coefficients given by Wiegel (1962). Consequently, the wave field down-wave of the breakwater was clearly 3D (2DH) for the short wave cases, while for the longer ones the corresponding image resembled 2D (1DH) wave propagation.

With respect to bed morphology evolution, in all the scenarios performed a salient was formed behind the breakwater and its nondimensional width is depicted in table 6.1. In none of them a tombolo was formed. General reservations have been already expressed in chapter 5 for the possibility or not of a tombolo formation behind a submerged breakwater. Besides, the specific geometrical layout with a ratio $B/S = 0.87$ is not expected to result to a tombolo even in the case of an impermeable emerged breakwater, so more for permeable submerged breakwaters. The definition of the various geometrical parameters is given in Fig. 6.68. In the specific layout, the length of the submerged breakwater was $B = 3.0$ m and its distance from the initial shoreline was $S = 3.45$ m. It has been already discussed that the side vertical walls acted as axes of symmetry and thus the layout corresponded to an array of submerged breakwaters. Thus, the distance of the head of the breakwater from the side wall corresponded to half the gap length between two consecutive breakwaters, $G = 1.0$ m.

In the short wave tests, more peaky salients were formed, while the long wave scenarios led to more flattened salients, which seemed like a parallel displacement of the initial almost straight shoreline. Furthermore, wave breaking over the submerged bar resulted to hydraulic gradients along the wave crests and, consequently, to a flow towards the centerline. This fact resulted to an increased peakedness of the corresponding salients in the breaking scenarios. The accretion at the shoreline was increased near the centerline and much reduced near the side walls. Although the bed elevation was not measured close to the vertical plates, shoreline erosion was seldom observed at these areas. Only in test case 3, weak shoreline erosion was observed there. Finally, in the breaking scenarios a bar was always formed just behind the

breakwater near the centerline. Down-wave of the bar bed erosion was present. The required material for the formation of the salient was partly transported from this eroded area, in addition to the one agitated at a second breaking zone closer to the shoreline. A third contribution was from sand moving towards the centerline from onshore areas close to the side walls.

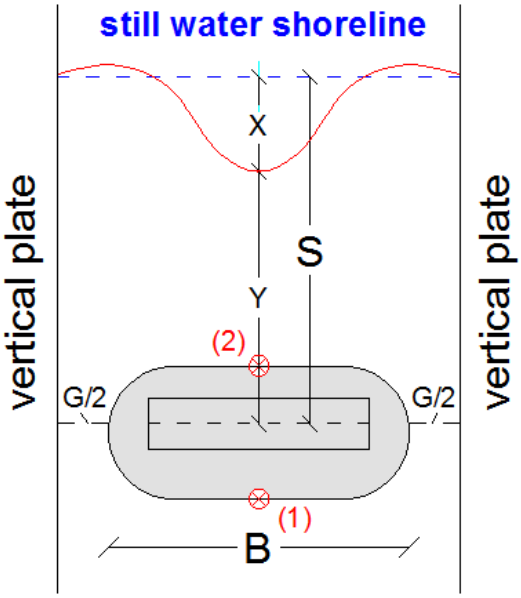

Fig. 6.68. Definition sketch for various geometric parameters.

The compound model was validated against laboratory tests. These tests were very demanding due to the number of complex processes that they combine: wave propagation over and through a permeable breakwater, shoaling, refraction, diffraction, breaking, runup and also the corresponding bed morphological evolution. Thus, given the complexity of the processes, the model behaved, in general, satisfactorily. With regard to wave propagation, two types of inaccuracies mainly appeared. Both of them were mostly related to the short wave tests. The first one appears at the most down-wave station 4 for tests No. 3 and 7. These tests refer to wave breaking of relatively short waves over the submerged breakwater. In these scenarios the most intense diffraction effect is observed resulting to significant reflection from the side walls. It seems that the model fails to accurately predict this reflection, perhaps in addition to some over-estimation of the energy dissipation due to breaking. This result can be attributed both to the non-perfectly smooth surface of the experimental lateral plates and also to the fact that Eq. (3.70) has been derived assuming a linearized version of water equations and, thus, inaccuracies appear for highly nonlinear wave conditions. Consequently, the model under-predicts the wave height at station 4 where the waves have become short-crested.

The second type of discrepancies referred to the energy transfer to higher harmonics over the bar crest and its down-slope. This inaccuracy is also mainly pronounced in test case 7. As already mentioned, the model nonlinear properties have not been studied in detail for permeable beds. However, they are expected to be poorer for higher values of the non-dimensional depth kd which are related to short wave tests. This fact, combined with the increased side reflection due to the significant diffraction, results to the model's inefficiency to reproduce the secondary spectral peak at higher frequencies in test case 7. Most probably, the additional inclusion of terms of $O(\varepsilon\sigma^2)$ in Eq. (6.18) will result in an enhancement of the nonlinear properties of the model for porous beds. This is also left for future research.

With regard to morphodynamics, the model successfully predicted the width of the formed salient at the various test cases. However, the computed salients were in most of the cases less flattened than the measured ones. On the other hand, the erosion around the middle of the distance of the breakwater from the shoreline was in many cases underestimated. The bar created down-wave of the submerged breakwater was predicted by the model in the regular breaking test cases 3 and 4, but not in the irregular tests 7 and 8. It appears that in these latter tests the sediment movement is significantly under-predicted offshore, near the breakwater. This fact may be attributed to the above mentioned underestimation of energy transfer to higher harmonics in these two cases, which results to some components of the wave train not exceeding the critical velocity for sediment movement.

Another point that should be stressed is the significance of the morphological time scale. The usage of a morphological factor with a value up to 50 proved to give accurate results with respect to the shoreline response. Values higher than 50 gave unrealistic growth of the created salient. This issue requires further investigation. Thus, one should be cautious with the selection of the value of the morphological factor, especially when measurements are not available in order to calibrate the model.

In the present chapter the model was extended to account for porous beds and it was validated against the laboratory data obtained from experiments including a permeable submerged breakwater. In chapter 7, the shoreline's response to an array of submerged breakwater is investigated through a number of numerical experiments with the application of the presented compound model.

References

Ahrens, J. P. (1989). "Stability of reef breakwaters." *J. Waterw., Port, Coastal, Ocean Eng.*, 115 (2), 221–234.

Amao, A. M. (2007). "Mathematical model for Darcy Forchheimer flow with applications to well performance analysis." MSc. Thesis, Texas Tech University, Lubbock, Texas, U.S.A.

Avgeris, I., Karambas, Th. V., and Prinos, P. (2004). "Boussinesq modeling of wave interaction with porous submerged breakwaters." *Proc. 29th Int. Conf. on Coastal Eng.*, J. M. Smith, ed., Lisbon, Portugal, 604-616.

Basak, P. (1977). "Non-Darcy flow and its implications to seepage problems." *J. Irrig. Drain. Div.*, ASCE, 103 (4), 459-473.

Battjes, J. A. (1994). "Shallow water wave modelling." *Proc. Waves-Physical and Numerical Modelling*, M. Isaacson and M. Quick, eds, University of British Columbia, Vancouver, Canada, pp. 1-23.

Beji, S., and Battjes, J. A. (1993). "Experimental investigation of wave propagation over a bar." *Coast. Eng.*, 19(1-2), 151-162.

Beji, S., and Battjes, J. A. (1994). "Numerical simulation of nonlinear wave propagation over a bar." *Coast. Eng.*, 23(1-2), 1-16.

Beji, S., and Nadaoka, K. (1996). "A formal derivation and numerical modelling of the improved Boussinesq equations for varying depth." *Ocean Eng.*, 23(8), 691-704.

Buccino, M., and Calabrese, M. (2007). "Conceptual approach for prediction of wave transmission at low-crested breakwaters." *J. Waterw. Port Coast. Ocean Eng.*, 133 (3), 213–224.

Burcharth, H. F., and Andersen, O. H. (1995). "On the one-dimensional steady and unsteady porous flow equations." *Coast. Eng.*, 24 (3-4), 233-257.

Cáceres, I., Sánchez-Arcilla, A., Alsina, J.-M., González-Marco, D., and Sierra, J. P. (2005). "Coastal dynamics around a submerged barrier." *Proc. Coastal Dyn. '05*, A. Sanchez-Arcilla, ed., ASCE, Barcelona, Spain, pp. 1-14.

Calabrese, M., Vicinanza, D., and Buccino, M. (2002). "Large-scale experiments on the behavior of low crested and submerged breakwaters in presence of broken waves." *Proc. 28th Int. Conf. on Coastal Eng.*, J. M. Smith, ed., Cardiff, Wales, U.K., pp. 1900–1912.

Calabrese, M., Vicinanza, D., and Buccino, M. (2003). "Low-crested and submerged breakwater in presence of broken waves." *Proc. 13th ISOPE*, 831-836.

Chen, Q. (2006). "Fully nonlinear Boussinesq-type equations for waves and currents over porous beds." *J. Eng. Mech.*, 132 (2), 220-230.

Christou, M., Swan, C., and Gudmestad, O. (2008). "The interaction of surface water waves with submerged breakwaters." *Coast. Eng.*, 55 (12), 945-958.

Clarke, S., Dodd, N., and Damagaard, J. (2004). "Modeling flow in and above a porous beach." *J. Waterw. Port Coast. Ocean Eng.*, 130 (5), 223–233.

Cruz, E. C. (1994). "Modelling of nonlinear, dispersive transformation around submerged porous breakwaters." Ph.D. thesis, University of Tokyo, Japan.

Cruz, E. C., Isobe, M., and Watanabe, A. (1992). "Nonlinear wave transformation over a submerged permeable breakwater." *Proc. 23rd Int. Conf. on Coastal Engineering*, B. L. Edge, ed., Venice, Italy, part III, chapter 83, pp. 1101-l 114.

Cruz, E. C., Isobe, M., and Watanabe, A. (1997). "Boussinesq equations for wave transformation on porous beds." *Coast. Eng.*, 30 (1-2), 125-156.

Darcy, H. (1856). *Les fontaines publiques de la ville de Dijon*, Dalmont, Paris (in French).

De Later, J. (1996). "Effect of submerged breakwaters on a beach profile exposed to regular waves in a wave basin." MSc.Thesis, Delft University of Technology, The Netherlands.

Di Risio, M., Lisi, I., Beltrami, G. M., and De Girolamo, P. (2010). "Physical modeling of the cross-shore short-term evolution of protected and unprotected beach nourishments." *Ocean Eng.*, 37 (8-9), 777–789.

Drei, E., and Lamberti, A. (1999). "Wave pumping effect of a submerged barrier." *Proc. Coastal Structures '99*, ASCE, Santander, Spain, pp. 667-673.

Dybbs, A., and Edwards, R. V. (1984). "A new look at porous media fluid mechanics - Darcy to turbulent." In: Fundamentals of transport phenomena in porous media, J. Bear and M. Yavuz Corapcioglu, eds, *NATO ASI Series*, vol. 82, Part 1, pp. 199-256.

Engelund, F. A. (1953). "On the laminar and turbulent flows of ground water through homogeneous sand." *Trans. of Danish Academy of Technical Sciences*, no. 3, 153 pp.

Forchheimer, P. (1901). "Wasserbewegung durch bodem." *Z. Ver. Deutsch. Ing.*, vol. 45, 1782-1788 (in german).

Friebel, H., and Harris, L. (2004). "A new wave transmission coefficient model for submerged breakwaters." *Proc. 29th Int. Conf. on Coastal Eng.*, J. M. Smith, ed., Lisbon, Portugal, 19-24.

Garcia, N., Lara, J. L., and Losada, I. J. (2004). "2-D numerical analysis of near-field flow at low-crested permeable breakwaters." *Coast. Eng.*, 51 (10), 991–1020.

Gironella, X., and Sanchez-Arcilla, A. (1999). "Hydrodynamic behaviour of submerged breakwaters. Some remarks based on experimental results." *Proc. Coastal Structures '99*, ASCE, Santander, Spain, pp. 891-896.

Goda, Y., and Ahrens, J. (2008). "New formulation for wave transmission over and through low crested structures." *Proc. 31st Int. Conf. on Coastal Eng.*, J. M. Smith, ed., Hamburg, Germany, 3530-3541.

González, M., Medina, R., and Losada, M. A. (1999). "Equilibrium beach profile for perched beaches." *Coast. Eng.*, 36 (4), 343–357.

Gourlay, M. R., and Colleter, G. (2005). "Wave-generated flow on coral reefs - an analysis for two-dimensional horizontal reef-tops with steep faces." *Coast. Eng.*, 52 (4), 353–387.

Gu, Z., and Wang, H. (1991). "Gravity waves over porous bottoms." *Coast. Eng.*, 15 (5-6), 497–524.

Hanson, H., and Kraus, N. C. (1990). "Shoreline response to a single transmissive breakwater." Proc. *22nd Int. Conf. on Coastal Engineering*, B. L. Edge, ed., Delft, The Netherlands, part V, chapter 154, pp. 2034-2046.

Hearn, C. J. (1999). "Wave-breaking hydrodynamics within coral reef systems and the effect of changing relative sea level." *J. Geophys. Res*., 104 (C12), 30007-30019.

Hsiao, S., Liu, P. L.-F., and Chen, Y., (2002). "Nonlinear water waves propagating over a permeable bed." *Proc. R. Soc. London*, Ser. A, 458, 1291–1322.

Isobe, M., Shiba, K., Ctuz, E. C., and Watanabe, A. (1991). "On the nonlinear deformation of waves due to submerged permeable breakwaters." *Proc. Coastal Eng.*, JSCE, 38 (l), 551-555 (in japanese).

Jiménez, J. A., and Sánchez-Arcilla, A. (2002). "Preliminary analysis of shoreline evolution in the leeward of low-crested breakwaters using one-line models." *Proc. 1st meet. Delos project*, Barcelona, Spain.

Johnson, H. K., Karambas, Th. V., Avgeris, I., Zanuttigh, B., Gonzalez-Marco, D., and Caceres, I. (2005). "Modelling of waves and currents around submerged breakwaters." *Coast. Eng.*, 52 (10-11), 949–969.

Karambas, Th. V. (2012). "Design of detached breakwaters for coastal protection: development and application of an advanced numerical model." *Proc. 33rd Int. Conf. on Coastal Engineering*, P. J. Lynett and J. M. Smith, eds, Santander, Spain, 1(33), pp. 4448-4462.

Karambas, Th. V., and Karathanassi, E. K. (2004). "Longshore sediment transport by nonlinear waves and currents." *J. Waterw. Port Coast. Ocean Eng.*, 130(6), 277-286.

Karambas, Th. V., and Samaras, A. G. (2014). "Soft shore protection methods: The use of advanced numerical models in the evaluation of beach nourishment." *Ocean Eng.*, 92, 129-136.

Kioka, W., Kai, H., and Hiraoka, S. (1994). "Nonlinear shallow water waves over a porous structure." *Proc. Coastal Eng.*, JSCE, 41 (l), 711-715 (in japanese).

Kobayashi, N., Meigs, L., Ota, T., and Melby, J. (2007). “Irregular breaking wave transmission over submerged porous breakwater.” *J. Waterw. Port Coast. Ocean Eng.*, 133 (2), 104-116.

Kobayashi, N., and Wurjanto, A. (1988). “Wave transmission over submerged breakwaters.” *J. Waterw. Port Coast. Ocean Eng.*, 115 (5), 662–680.

Kothe, D. B., Mjolsness, R. C., and Torrey, M. D. (1991). “RIPPLE: A computer program for incompressible flows with free surfaces.” *Rep*., LA-12007-MS, Los Alamos National Laboratory, U.S.A.

Koutsouvela, D. (2010). "Soft shore protection methods against coastal erosion: submerged breakwaters." Ph.D. thesis, University of the Aegean, Greece (in greek).

Koutsouvela, D., Karambas, Th. V., Avgeris, I., and Karathanassi, E. (2007). "Functional design of submerged breakwaters for coastal protection using two wave/morphological models." *Proc. Coastal Structures ’07*, Venice, Italy, pp. 1205-1216.

Lara, J. L., Garcia, N., and Losada, I. J. (2006). “RANS modelling applied to random wave interaction with submerged permeable structures.” *Coast. Eng*., 53 (5-6), 395–417.

Lee, T. C., Tsai, C. P., and Jeng, D. S. (2002). “Ocean waves propagating over a porous seabed of finite thickness.” *Ocean Eng.*, 29 (12), 1577–1601.

Lesser, G. R., Vroeg, J. H., Roelvink, J. A., de Gerloni, M., and Ardone, V. (2003). “Modelling the morphological impact of submerged offshore breakwaters.” *Proc. Coastal Sediments ’03*, World Scientific Publishing Co, Clearwater Beach, Florida, USA, May 18-23, on CD-ROM.

Lin, P. (2006). “A multiple-layer σ–coordinate model for simulation of wave-structure interaction.” *Comput. Fluids*, 35 (2), 147-167.

Lin, P., and Li, C. (2003). “Wave-current interaction with a vertical square cylinder.” *Ocean Eng.*, 30 (7), 55–76.

Lin, P., and Liu, P. L.-F. (1998). “A numerical study of breaking waves in the surf zone.” *J. Fluid Mech.*, 359, 239-264.

Liu, P. L.-F. (1973). “Damping of water waves over porous bed.” *J. Hydraul. Div.*, ASCE, 99 (12), 2263–2271.

Liu, P. L.-F., and Dalrymple, R. A. (1984). “The damping of gravity water-waves due to percolation.” *Coast. Eng.*, 8 (1), 33–49.

Liu, P. L.-F., and Wen, J. (1997). “Nonlinear diffusive surface waves in porous media.” *J. Fluid Mech.*, 347, 119-139.

Liu, X., Xu, H., Shao, S., and Lin, P. (2013). “An improved incompressible SPH model for simulation of wave-structure interaction.” *Comput. Fluids*, 71, 113-123.

Longuet-Higgins, M. S. (1967). “On the wave induced difference in mean sea level between two sides of a submerged breakwater.” *J. Mar. Res.*, 25, 148-153.

Losada, I. J., Silva, R., and Losada, M. A. (1996). “3-D non-breaking regular wave interaction with submerged breakwaters.” *Coast. Eng.*, 28 (1-4), 229–248.

Loveless, J. H., and Debski, D. (1997). "Wave transmission and set-up at detached breakwater." *Proc. Coastal Dyn. ’97*, E. B. Thornton, ed., ASCE, Plymouth, U.K., pp. 674-683.

Lynett, P. J., Liu, P. L.-F., Losada, I. J., and Vidal, C. (2000). “Solitary wave interaction with porous breakwaters.” *J. Waterw. Port Coast. Ocean Eng.*, 126 (6), 314-322.

Madsen, O. S. (1977). “Wave transmission through porous structures.” *J. Waterw. Harb. Coast. Eng. Div.*, 100 (3), 169-188.

Massel, S., and Butowski, P. (1980). “Wind waves transmission through porous breakwater.” *Proc. 17th Int. Conf. on Coastal Engineering*, ASCE, Sydney, Australia, pp. 333-346.

Melito, I., and Melby, J. (2002). "Wave runup, transmission, and reflection for structures armored woth core-loc." *Coast. Eng.*, 45 (1), 33–52.

Mendez, F. J., Losada, I. J., and Losada, M. A. (1999). "Wave-induced mean magnitudes in permeable submerged breakwaters." *J. Waterw. Port Coast. Ocean Eng.*, 127 (1), 7–15.

Metallinos, A. S., Emmanouilidou, M.-E. A., and Memos, C. D. (2014). “Wave-induced pore pressures in submerged rubble mound breakwaters simulated by a compound Boussinesq model.” *J. Hydraul. Res.*, 52 (1), 24–35.

Muñóz-Pérez, J. J., Tejedor, L., and Medina, R. (1999). "Equilibrium beach model for reef protected beaches." *J. Coast. Res.*, 15 (4), 950–957.

O’Connor, B., and Nicholson, J. (1995). "Applications of a coastal area morphodynamic model." *Abstract to MAST. Final Report*, pp. 7-57-7-60.

Packwood, A. R. (1983). “The influence of beach porosity on wave uprush and backwash.” *Coast. Eng.*, 7 (1), 29–40.

Panizzo, A., and Briganti, R. (2007). “Analysis of wave transmission behind low-crested breakwaters using neural networks.” *Coast. Eng.*, 54 (9), 643–656.

Polubarinova-Kochina, P. Ya. (1952). *Theory of groundwater movement*, University Press, Princeton.

Powell, K., and Allsop, N. (1985). "Low-crested breakwaters, hydraulic performance and stability." *Tech. Rep.*, SR 57, HR Wallingford, Wallingford, Oxfordshire, U.K.

Ranasinghe, R., Larson, M., and Savioli, J. (2010). "Shoreline response to a single shore-parallel submerged breakwater." *Coast. Eng.*, 57 (11-12), 1006–1017.

Ranasinghe, R. S., and Sato, S. (2007). "Beach morphology behind single impermeable submerged breakwater under obliquely incident waves." *Coast. Eng. J.*, 49 (1), 1–24.

Ranasinghe, R., Turner, I. L., and Symonds, G. (2006). "Shoreline response to multi-functional artificial surfing reefs: A numerical and physical modelling study." *Coast. Eng.*, 53 (7), 589–611.

Ribberink, J. S. (1998). "Bed-load transport for steady flows and unsteady oscillatory flows." *Coast. Eng*., 34 (1-2), 59–82.

Rojanakamthorn, S., Isobe, M., and Watanabe, A. (1990). "Modeling of wave transformation on submerged breakwater." Proc. *22nd Int. Conf. on Coastal Engineering*, B. L. Edge, ed., Delft, The Netherlands, part I, chapter 80, pp. 1060-1073.

Roul, P., and Faedo, A. (2002). "Physical model study on low-crested structures under breaking wave conditions." *Proc. Int. MEDCOAST Workshop on Beaches of the Mediterranean & the Black Sea*, Kusadasi, Turkey, pp. 83-96.

Roul, P., Faedo, A., and Paris, A. (2004). "Physical model study of water piling-up behind low-crested structures." *Proc. 29th Int. Conf. on Coastal Eng.*, J. M. Smith, ed., Lisbon, Portugal, 4165-4177.

Sawaragi, T., and Deguchi, I. (1992). "Waves on permeable layers." *Proc. 23rd Int. Conf. on Coastal Engineering*, B. L. Edge, ed., Venice, Italy, part III, chapter 117, pp. 1531-1544.

Seabrook, S. R., and Hall, K. R. (1998). "Wave transmission at submerged rubblemound breakwaters." *Proc. 26th Int. Conf. on Coastal Eng.*, B. L. Edge, ed., Copenhagen, Denmark, vol. 2, pp. 2000–2013.

Sharif Ahmadian, A. (2016). *Numerical models for submerged breakwaters. Coastal hydrodynamics and morphodynamics.* Butterworth-Heinemann, Elsevier, 362 pp.

Sharif Ahmadian, A., and Simons, R. R. (2014). "A 3D numerical model of nearshore wave field behind submerged breakwaters." *Coast. Eng.*, 83 (10-11), 190-204.

Shen, Y. M., Ng, C. O., and Zheng, Y. H. (2004). "Simulation of wave propagation over a submerged bar using the VOF method with a two-equation k-ε turbulence modeling." *Ocean Eng.*, 31 (1), 87-95.

Soldini, L., Lorenzoni, C., Brocchini, M., Mancinelli, A. and Cappietti, L. (2009). "Modeling of the wave setup inshore of an array of submerged breakwaters." *J. Waterw. Port Coast. Ocean Eng.*, 135 (2), 38–51.

Sollitt, C. K., and Cross, R. H. (1972). "Wave transmission through permeable breakwaters." *Proc. 13th Int. Conf. on Coastal Engineering*, ASCE, Vancouver, Canada, pp. 1827-1846.

Symonds, G. (1994). "Theory and observation of currents and setup over a shallow reef." *Proc. Coastal Dyn. '94*, A. S. Arcilla, S. J. F. Marcel and N.C. Kraus, eds, ASCE, Barcelona, Spain, pp. 1-13.

Symonds, G., Black, K. P., and Young, I. R. (1995). "Wave-driven flow over shallow reefs." *J. Geophys. Res.*, 100 (C2), 2639-2648.

Thomas, L. H. (1949). *Elliptic Problems in Linear Differential Equations over a Network*. Watson Sci. Comput. Lab Report, Columbia University, New York.

Van der Biezen, S. C, Roelvink, J. A., van de Graaff, J., Schaap, J., and Torrini, L. (1998). "2DH morphological modelling of submerged breakwaters." *Proc. 26th Int. Conf. on Coastal Eng.*, B. L. Edge, ed., Copenhagen, Denmark, vol. 2, pp. 2028–2041.

Van der Biezen, S. C, van de Graaff, J., and de Later, J. (1996). "3D model tests of the influence of submerged breakwaters on a beach profile exposed to regular waves." *Proc. PECS'96*, The Hague, The Netherlands.

Van der Meer, J. W., Briganti, R., Wang, B., and Zanuttigh, B. (2004). "Wave transmission at low-crested structures, including oblique wave attack." *Proc. 29th Int. Conf. on Coastal Eng.*, J. M. Smith, ed., Lisbon, Portugal, 4152-4164.

Van der Meer, J. W., Briganti, R., Zanuttigh, B., and Wang, B. (2005). "Wave transmission and reflection at low-crested structures: Design formulae, oblique wave attack and spectral change." *Coast. Eng.*, 52 (10-11), 915-929.

Van Gent, M. R. A. (1994). "The modelling of wave action on and in coastal structures." *Coast. Eng.*, 22 (3-4), 311–339.

Van Gent, M. R. A. (1995). "Wave interaction with permeable coastal structures." Ph.D. thesis, Delft University of Technology, The Netherlands.

Van Oosten, R. P., and Peixó Marco, J. (2005). "Wave transmission at various types of low-crested structures using neural networks." MSc.Thesis, Delft University of Technology, The Netherlands.

Van Oosten, R. P., Peixó Marco, J., van der Meer, J. W., van Gent, M .R. A., and Verhagen, H. J. (2006). "Wave transmission at low-crested structures using neural networks." *Proc. 30st Int. Conf. on Coastal Eng.*, J. M. Smith, ed., San Diego, California, U.S.A., 4932-4944.

Ward, J. C. (1964). "Turbulent flow in porous media." *J. Hydraul. Div.*, ASCE, 90 (HY5), 1–12.

Watanabe, A., Maruyama, K., Shimizu, T., and Sakakiyama, T. (1986). "Numerical prediction model of three-dimensional beach deformation around a structure." *Coast. Eng. Jpn.*, 29, 179-194.

Wiegel, R. L. (1962). "Diffraction of Waves by Semi-infinite Breakwater." *J. Hydraul. Div.*, ASCE, Vol. 88, No. HY1, pp. 27-44.

Wurjanto, A., and Kobayashi, N. (1993). "Irregular wave reflection and runup on permeable slopes." *J. Waterw. Port Coast. Ocean Eng.*, 119 (5), 537–557.

Zanuttigh, B., Martinelli, L., and Lamberti, A. (2008). "Wave overtopping and piling-up at permeable low crested structures." *Coast. Eng.*, 55 (6), 484–498.

Zlatev, Z., Berkowicz, R., Prahm L. P. (1984). "lmplementation of a variable stepsize variable formula method in the time-integration part of a code for treatment of long-range transport of air pollutants." *J. Comput. Phys*., 55 (2), 278-301.

Zyserman, J. A., Jorgensen, K., and Christensen, E. D. (1999). "Sediment transport and morphology in the vicinity of shore parallel breakwaters." *Proc. Coastal Structures '99*, ASCE, Santander, Spain, pp. 857-863.

Chapter 7

Shoreline response to an array of submerged breakwaters

7.1 Introduction

In chapter 6 the compound model was validated against the laboratory measurements performed in the context of the present Ph.D. thesis. The experiments included the morphological evolution of a sandy beach behind a permeable submerged breakwater. In all the test cases studied the shoreline response led to the formation of a salient. The accurate prediction of the shoreline response is of great importance for a shore protection project. However, the scientific knowledge and understanding of the related complex processes still remain mainly empirical. In particular, a number of practical design rules have been proposed, referring to a single or a system of emergent breakwaters. On the other hand, similar guidelines for the case of submerged breakwaters are almost entirely absent from the international literature. This gap of knowledge was the main motivation for the research conducted in the present chapter. This work is far from offering a comprehensive detailed set of design rules for submerged breakwaters. However, it presents an investigation of the impact of the most important design parameters on the related geomorphological features and can give some general guidelines to the practicing engineer.

Nearshore breakwaters are detached, generally shore-parallel structures that reduce the amount of wave energy reaching a protected area. This reduction of wave energy slows the littoral drift, produces sediment deposition and a shoreline bulge, so-called salient, behind the breakwater. Some longshore sediment transport may continue along the coast behind the breakwater. Tombolo is an extreme form of salient, appearing when the shoreline touches the breakwater. Examples of tombolos and salients are depicted in Fig. 7.1.

(a)

(b)

Fig. 7.1. (a) Tombolo behind a system of emergent breakwaters in Norfolk, England, 2015 (photo: Jonathan Webb) and (b) salient behind an array of emergent breakwaters in Presque Isle, Pennsylvania, U.S.A. (from Mohr, 1994).

A salient is the preferred shoreline response for a variety of coastal projects. It allows longshore sediment transport to continue through the project area to downdrift beaches. Moreover, it provides a recreational swimming environment but limits access for breakwater maintenance compared to a tombolo. Salients are likely to predominate when the breakwaters are sufficiently far from the shore, short relative to incident wavelength, and relatively permeable to waves (low-crested or large gaps with low sediment input). Wave action and longshore currents tend to prevent salients from evolving into tombolos.

Tombolos are likely to form when the breakwaters are close to the shore, long relative to incident wavelength, and relatively impermeable (high crest and small gaps with large sediment input). Tombolos block longshore transport and promote sediment movement offshore by the rip currents formed across the gaps. Although some longshore sediment

transport may occur seaward of the breakwater, the aforementioned interruption may result to starving downdrift beaches of their normal sediment supply, causing erosion.

A number of empirical relationships have been proposed for the design of detached emergent breakwaters in connection to the formation of salients and tombolos. The key variables for this design are: the distance of breakwater from the still shoreline, S, the length of the breakwater structure, B, the gap distance between adjacent breakwater segments, G, and the average depth at the breakwater structure below the mean water level, d_s. The definition of the related key variables is depicted in Fig. 7.2.

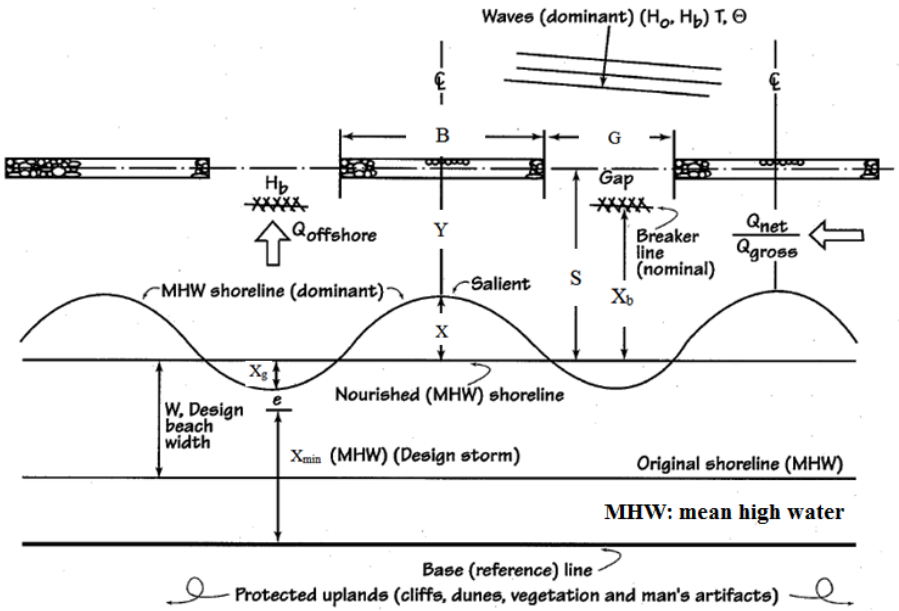

Fig. 7.2. Definition of variables related to shoreline response behind an array of breakwaters (from U.S. Army Corps of Engineers, 2006, modified).

For tombolo formation Dally and Pope (1986) recommended:

$$\frac{B}{S} = 1.5 \text{ to } 2.0 \quad \text{single breakwater} \tag{7.1}$$

$$\frac{B}{S} = 1.5 \qquad L \leq G \leq B \text{ segmented breakwater} \tag{7.2}$$

where L is the wavelength at the structure.

Short breakwaters at greater distance from the shoreline favor salient formation. A wide range of conditions with, generally, $B/S < 1$ is believed to result to a salient behind emergent breakwaters. In particular, Dally and Pope (1986) recommended:

$$\frac{B}{S} = 0.5 \text{ to } 0.67 \tag{7.3}$$

for both single and segmented breakwaters. However, for very long shoreline distances, the recommended ratio for a segmented system in order to ensure that tombolos do not form is (Dally and Pope, 1986):

$$\frac{B}{S} = 0.125 \qquad \text{for long segmented systems} \tag{7.4}$$

Permeable structures (partly submerged, large gaps) allow sufficient wave energy to minimize the chance for tombolo formation. According to Coastal Engineering Manual (U.S. Army Corps of Engineers, 2006), a minimal shoreline response results from a ratio $B/S < (0.125 \div 0.33)$. Ahrens and Cox (1990) defined a beach response index for emergent detached breakwaters:

$$I_s = \exp(1.72 - 0.41B/S) \tag{7.5}$$

where the five types of beach response according to Pope and Dean (1986) give values:

- Permanent tombolo formation: $I_s = 1 \quad \Rightarrow B/S \approx 4.20$
- Periodic tombolos: $I_s = 2 \quad \Rightarrow B/S \approx 2.50$
- Well-developed salients: $I_s = 3 \quad \Rightarrow B/S \approx 1.52$
- Subdued salients: $I_s = 4 \quad \Rightarrow B/S \approx 0.81$
- No sinuosity: $I_s = 5 \quad \Rightarrow B/S \approx 0.27$

These results are preliminary and require verification. The various conditions and the corresponding shoreline features related to emergent breakwaters are summarized in table 7.1.

Table 7.1. Conditions for shoreline response behind emergent breakwaters (from Chasten *et al.*, 1993).

Conditions for the formation of tombolos		
Condition	**Comments**	**Reference**
$B/S > 2.0$		SPM, U.S. Army Corps of Engineers (1984)
$B/S > 2.0$	Double tombolo	Gourlay (1981)
$B/S > 0.67$ to 1.0	Tombolo (shallow water)	Gourlay (1981)
$B/S > 2.5$	Periodic tombolo	Ahrens and Cox (1990)
$B/S > 1.5$ to 2.0	Tombolo	Dally and Pope (1986)

$B/S > 1.5$	Tombolo (multiple breakwaters)	Dally and Pope (1986)
$B/S > 1.0$	Tombolo (single breakwater)	Suh and Dalrymple (1987)
$B/S > 2G/B$	Tombolo (multiple breakwaters)	Suh and Dalrymple (1987)
Conditions for the formation of salients		
$B/S < 1.0$	No tombolo	SPM, U.S. Army Corps of Engineers (1984)
$B/S < 0.4$ to 0.5	Salient	Gourlay (1981)
$B/S = 0.67$ to 1.0	Salient	Dally and Pope (1986)
$B/S < 1.0$	No tombolo (single breakwater)	Suh and Dalrymple (1987)
$B/S < 2G/B$	No tombolo (multiple breakwaters)	Suh and Dalrymple (1987)
$B/S < 1.5$	Well-developed salient	Ahrens and Cox (1990)
$B/S < 0.8$ to 1.5	Subdued salient	Ahrens and Cox (1990)
Conditions for minimal shoreline response		
$B/S \leq 0.17$ to 0.33	No response	Inman and Frautschy (1965)
$B/S \leq 0.27$	No sinuosity	Ahrens and Cox (1990)
$B/S \leq 0.5$	No deposition	Nir (1982)
$B/S \leq 0.125$	Uniform protection	Dally and Pope (1986)
$B/S \leq 0.17$	Minimal impact	Noble (1978)

The ratio G/B is also important for salient or tombolo formation. Large gaps allow more wave energy to reach the shore to promote salient formation. For a given ratio G/B, larger values of S/d_s (or S/X_b) mean that the breakwater is located further offshore to support salient formation. Obviously, breakwaters located far offshore will have reduced effect on the shoreline. Seiji *et al*. (1987) gave conditions on the G/S ratio for no, possible and certain erosion, X_g, opposite of the gap. The magnitude of X_g was not determined, but erosion occurred for $G/S > 0.8$.

Other design factors that influence the functional performance of breakwaters are the crest elevation and width, permeability, slope of front face, and type of construction. Nevertheless, no general guidelines presently exist. In general, low crests allow more energy to penetrate

into the lee of the breakwater to prevent tombolo formation or remove a tombolo by storm waves. On the other hand, wide crests on low structures enhance breaking and the energy reduction encourages tombolo formation. Permeability is also a preventing factor against the formation of tombolos.

All the aforementioned design rules have been proposed for the case of single or systems of emergent detached breakwaters. In contrary, the shoreline response to arrays of submerged breakwaters has not been studied systematically and in depth. Thus, similar functional rules are rather fragmentary and empirical, with almost no field verification at all. Pilarczyk (2003) claimed that the design rules for submerged breakwaters are similar to those of the conventional ones with the additional inclusion of the transmission coefficient, K_t (see also Koutsouvela *et al*., 2007; Burcharth *et al*., 2007; Karambas *et al*., 2016). Effectively:

- For salient formation, the ratio of B to S should be $B/S > (1.0 \div 1.5)/(1.0 - K_t)$. In particular, the value of the ratio should be close to $(1.0 \div 1.5)/(1.0 - K_t)$.
- For an array of submerged breakwaters, it should be $GS/B^2 > 0.5(1.0 - K_t)$ for salients to form.
- Also, in an array of submerged breakwaters, the formation of a salient requires the validity of the double inequality $L \leq G \leq 0.8B$, with L the wavelength at the structure.
- The transmission coefficient should be approximately $K_t = 0.4 \div 0.5$.

The above design rules refer to the formation of salients behind single or systems of submerged breakwaters. Pilarczyk (2003) mentions that a tombolo may be formed behind a submerged breakwater if this is placed very close to the shoreline. However, reservations are expressed about this issue, since in the present thesis, neither the laboratory experiments, nor the numerical ones ever led to such a morphological feature. The justification of this skepticism was presented in subsection 5.2.2 (see also Karambas *et al*., 2016). In overall, it is difficult to derive general design rules without taking into account the morphological processes that take place without the construction of the works, i.e. sediment balance, erosion and accretion.

The very limited number of studies related to the shoreline response to submerged bars mainly refer to natural reefs, rather than submerged structures. Although these reefs are often associated with shoreline salients, the relative few reported investigations are inconsistent. While some investigations suggest that submerged breakwaters may result in larger salients than those that would result from an emergent breakwater of similar size, other investigations indicate that submerged breakwaters may result in shoreline erosion in the lee of the structure. In contrast, erosion is almost never reported in the lee of emergent breakwaters. Therefore, it

is likely that the processes governing shoreline response to submerged and emergent structures are quite different.

Black and Andrews (2001) attempted to quantify the shape and dimensions of salients and tombolos formed in the lee of natural reefs by visual inspection of aerial photographs of 149 coastlines in New Zealand and Australia. Tombolos were observed to form when $B/S > 0.6$, and salients when $B/S < 2.0$. The researchers further extended their analysis to present expressions to predict the salient amplitude (the offshore position of the salient apex) and the geometric shape of the salient. In particular, they proposed the expression

$$\frac{Y}{B} = 0.5\left(\frac{B}{S}\right)^{-1.27} \tag{7.6}$$

where $Y = S - X$ (see Fig. 7.2 for definitions).

Hsu and Silvester (1990) presented a corresponding expression for single emergent breakwaters:

$$\frac{Y}{B} = 0.68\left(\frac{B}{S}\right)^{-1.22} \tag{7.7}$$

The two curves are depicted in Fig. 7.3. At first sight a submerged reef seems to result to larger salients than an emergent breakwater of equal size located in exactly the same offshore location. Therefore, one may conclude that engineered submerged structures must similarly cause enhanced shoreline accretion. However, such a conclusion is counterintuitive, as one would expect a higher degree of wave sheltering in the lee of an emergent breakwater, and therefore less energetic wave conditions, leading to more favourable conditions for salient growth in its lee. Indeed, Ranasinghe *et al*. (2001) critisized on the methodology followed by Black and Andrews (2001) to assess the critical length scales of natural reefs. Their analysis includes several shortcomings that may affect accuarcy. Thus, the results should be treated with increased reservation.

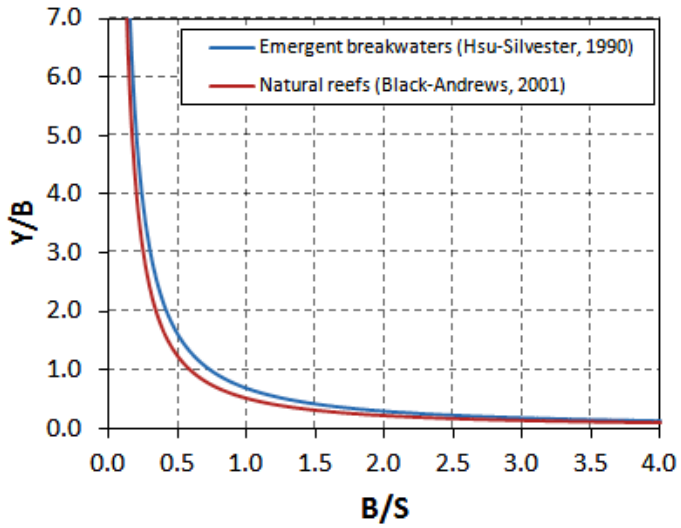

Fig. 7.3. Predictive relationships for salient width behind emergent breakwaters and natural reefs.

A major limitation of the empirical relationship proposed by Black and Andrews (2001) is its inefficiency to clearly differentiate between erosive and accretive shoreline response. However, as described by Ranasinghe and Turner (2006), it is difficult to develop a simple predictive formula which distinguishes between expected erosion or accretion based on geometric and wave characteristics. In particular, field observations have revealed both erosion and accretion behind long as well as short submerged structures. The same is true for submerged structures with small and large freeboard, both narrow- and broad-crested. The shoreline mode (erosion or accretion) also appears to be independent of the magnitude of the longshore sediment transport.

Despite this significant variability of field observations, more consistent results have been reported for laboratory experiments and 2DH numerical models. Ranasinghe and Turner (2006) described that normal wave incidence over submerged structures may lead to both erosion or accretion due to the onshore flow over the structure and the two resulting divergent alongshore currents in its lee. On the other hand, under oblique wave incidence, gradients of the longshore currents due to the presence of the submerged structure favor shoreline accretion. These two different mechanisms are schematically shown in Fig. 7.4.

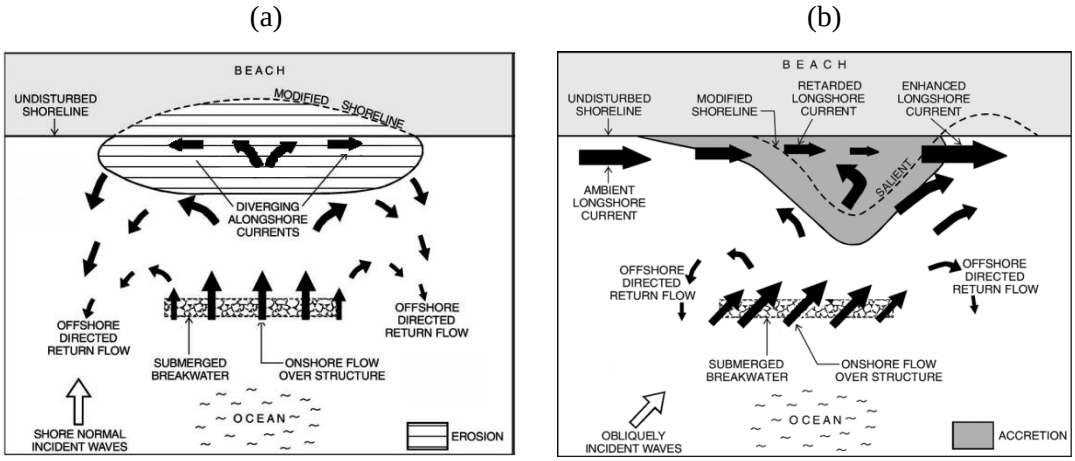

Fig. 7.4. Schematic description of nearshore circulation patterns and associated shoreline erosion/accretion patterns for (a) shore-normal wave incidence and (b) oblique wave incidence (from Ranasinghe and Turner, 2006).

Ranasinghe *et al*. (2006) studied both numerically and experimentally the shoreline response to multi-functional, V-shaped artificial surfing reefs (the shape of the reef resembles letter V from a plan view). Their results indicated that shoreline accretion can be expected when $S/X_b > 1.5$, where X_b is the surf zone width, while erosion can be expected when $S/X_b < 1.0$. In addition, Ranasinghe *et al*. (2010) studied numerically the mode of shoreline response, i.e. shoreline erosion vs shoreline accretion, to a single shore-parallel submerged breakwater. They assumed that the beach follows Dean's (1991) equilibrium profile:

$$h = \mathrm{A}x^{2/3} \tag{7.8}$$

where A is a shape parameter governed by d_{50}. They also included in their analysis the free board, s_b, the total depth at the center of the submerged breakwater, h_b, and the deep water wave height, H_o. The results of their numerical tests with MIKE 21 are shown in Fig. 7.5 using a semi-logarithmic scale. They considered both normal and oblique incidence and a separation between erosive and accretive shoreline response existed. They also examined the effect of the crest width and came to the conclusion that for large free boards it does not affect the mode of shoreline response. In contrary, for small free boards, a wider crest width reduces the risk of shoreline erosion compared to a narrower one. Intuitively, this result makes sense since increased energy dissipation due to wave breaking over the bar is expected in the former case.

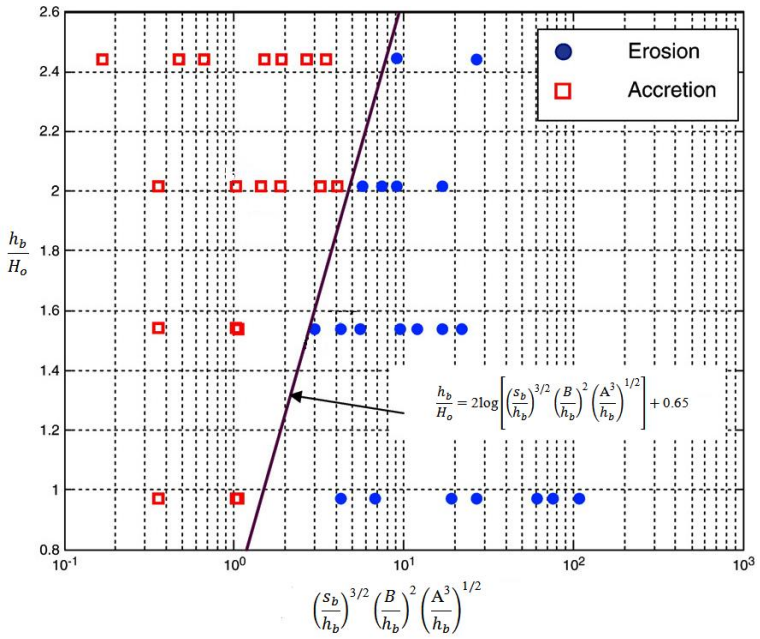

Fig. 7.5. Dependence of the mode of shoreline response from various design parameters for a single shore parallel submerged breakwater (from Ranasinghe *et al*., 2010, modified).

Koutsouvela *et al*. (2007) and Koutsouvela (2010) performed a number of numerical experiments to study the shoreline response to an array of submerged breakwaters. In the former case the wave module was based on the hyperbolic-type mild slope equations, while in the latter on Beji and Nadaoka's (1996) Boussinesq-type equations. They studied the impact of a number of design parameters on the morphology evolution, only for normal wave incidence and impermeable structures.

From the above review, it is evident that a systematic and consistent analysis of the shoreline response to submerged breakwaters has not been yet reported. In the present chapter, a number of numerical experiments is presented in order to study the effect of various design parameters on the shoreline evolution. As already mentioned, this analysis offers an investigation of the morphological response to the change of important related geometrical and wave parameters and not a full set of strict design rules of submerged breakwaters.

7.2 Numerical investigation of shoreline response

A number of numerical experiments were performed in order to study the impact of some important design parameters on the shoreline evolution. An array of five inline, identical permeable submerged breakwaters was considered in all the simulations. Among the validation tests presented in chapter 6, test case 4 was considered as base scenario for the numerical runs performed herein. Thus, the initial bathymetry of test case No. 4 was mirrored

along the axis of symmetry at the center of each gap between two adjacent breakwaters. Consequently, the compound model was already calibrated for the selected wave conditions and the specific initial bathymetry. In addition, it was also validated with respect to the shoreline evolution for one of the geometric layouts of the breakwaters, the one also used in test case No. 4. The effect of the following six different parameters was examined:

- The submerged breakwaters' length – B
- The distance of the breakwaters from the initial shoreline - S
- The length of the gap between two adjacent breakwaters – G
- The porosity of the breakwaters – λ
- The wave period – T
- The angle of wave incidence - θ

In particular, the effect of the first three geometric parameters was studied through modification of the ratios B/S and G/B that are associated with the shoreline response. Five sets of numerical experiments were performed, each one modifying B, S, G, λ, T, respectively. Each test was repeated for 4 different angles of wave incidence, $\theta = 0°$, 15°, 30° and 45°, in order to also study the effect of this wave parameter.

7.2.1 Effect of submerged breakwaters' length

In test case 4 of the laboratory experiments the breakwater length was 3.0 m and its distance from the initial shoreline was 3.45 m, leading to a ratio $B/S = 0.87$. In order to study the effect of the structures' length on the shoreline evolution, 10 different values of the ratio B/S were considered. In particular, the distance $S = 3.45$ m was retained constant and B was modified in each run giving ratios $B/S = 0.30, 0.60, 0.90, 1.20, 1.50, 1.80, 2.10, 2.40, 2.70, 3.00$, respectively. The ratio G/B was kept constant equal to 1/3 and the wave conditions were those of the laboratory test No. 4, i.e. T = 2.0 s, H_o = 0.08 m and the simulation period 4.3 hrs. The final shoreline for the 10 test cases is depicted in Figs 7.6 to 7.15.

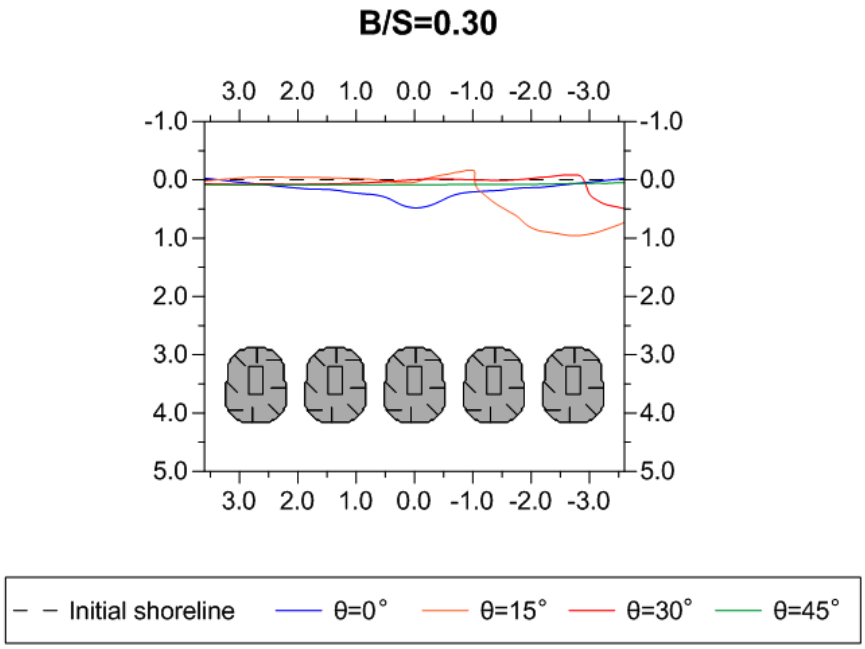

Fig. 7.6. Final computed shoreline for various angles of wave incidence, $B = 1.04$ m and ratio $B/S = 0.30$.

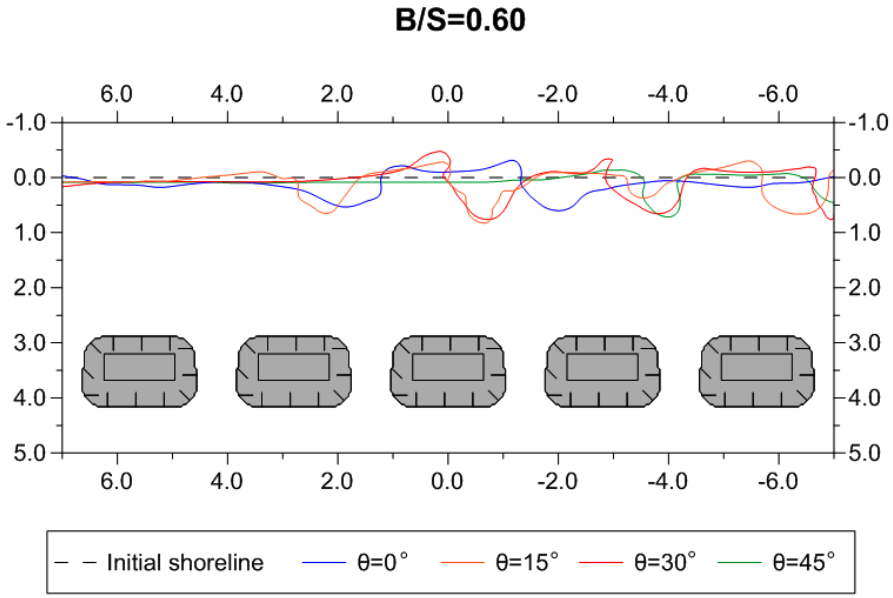

Fig. 7.7. Final computed shoreline for various angles of wave incidence, $B = 2.07$ m and ratio $B/S = 0.60$.

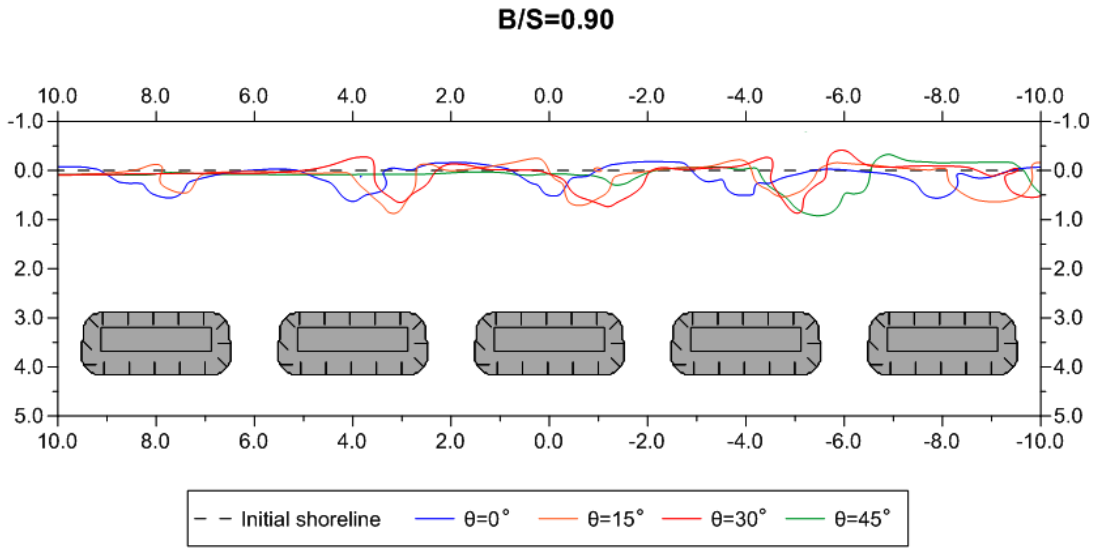

Fig. 7.8. Final computed shoreline for various angles of wave incidence, $B = 3.11$ m and ratio $B/S = 0.90$.

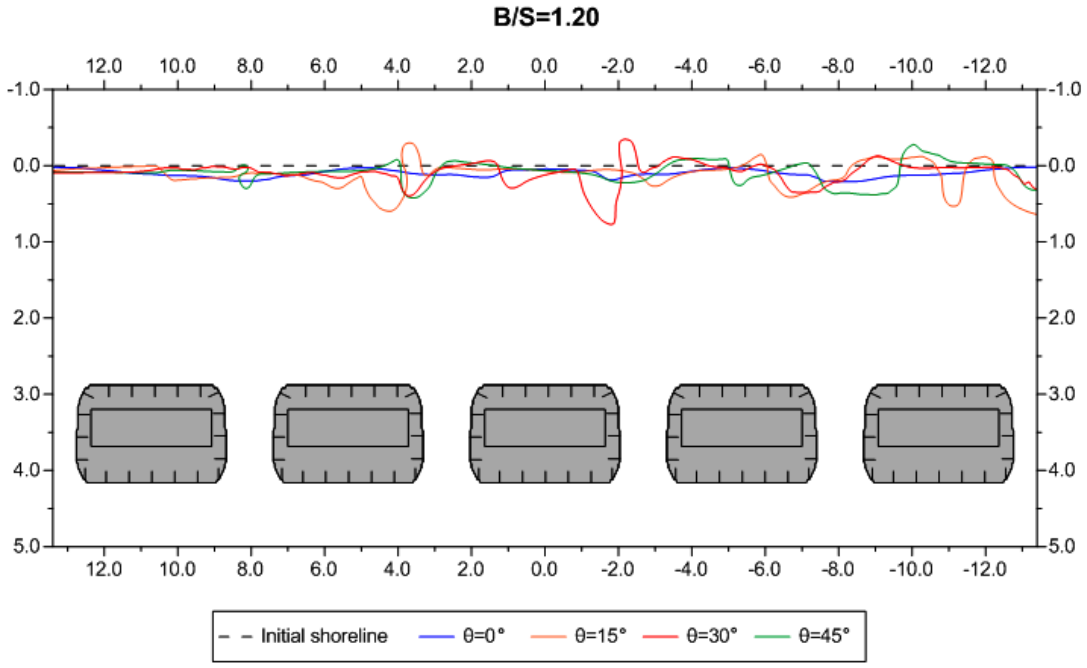

Fig. 7.9. Final computed shoreline for various angles of wave incidence, $B = 4.14$ m and ratio $B/S = 1.20$.

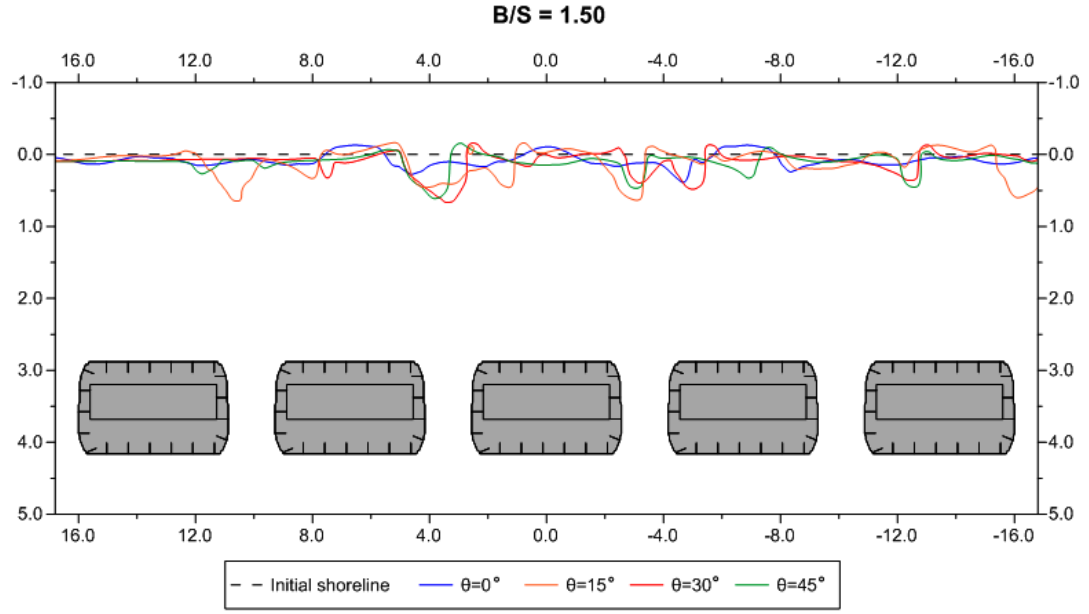

Fig. 7.10. Final computed shoreline for various angles of wave incidence, $B = 5.18$ m and ratio $B/S = 1.50$.

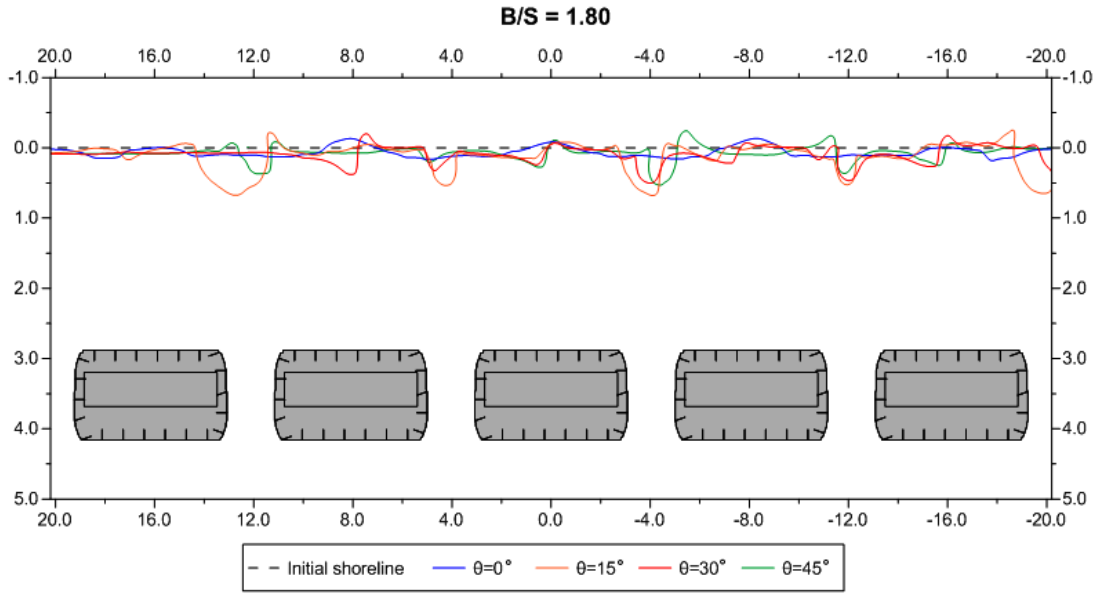

Fig. 7.11. Final computed shoreline for various angles of wave incidence, $B = 6.21$ m and ratio $B/S = 1.80$.

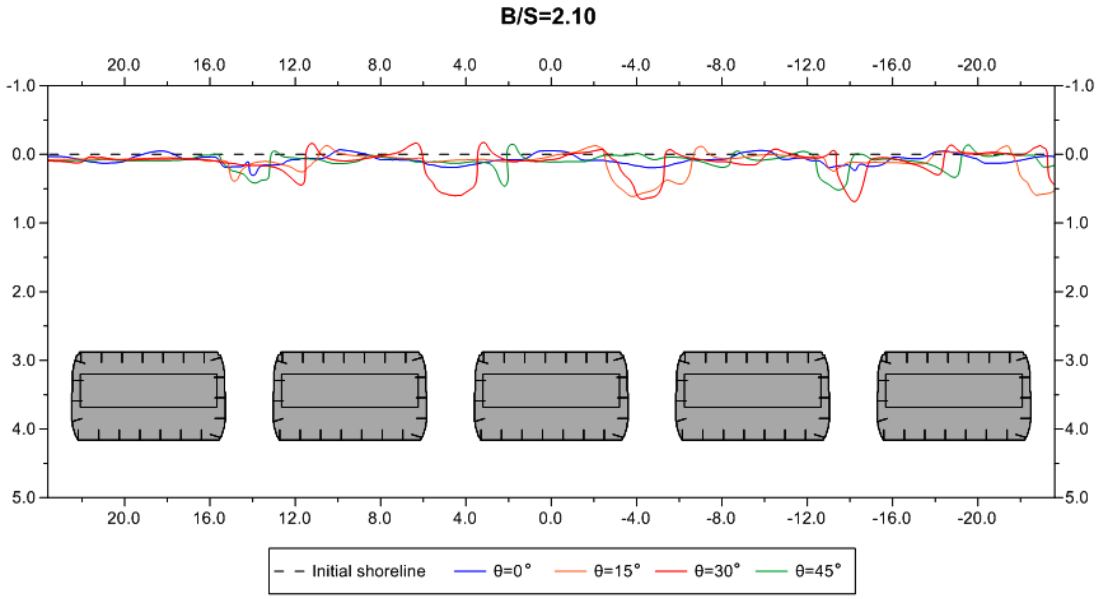

Fig. 7.12. Final computed shoreline for various angles of wave incidence, $B = 7.25$ m and ratio $B/S = 2.10$.

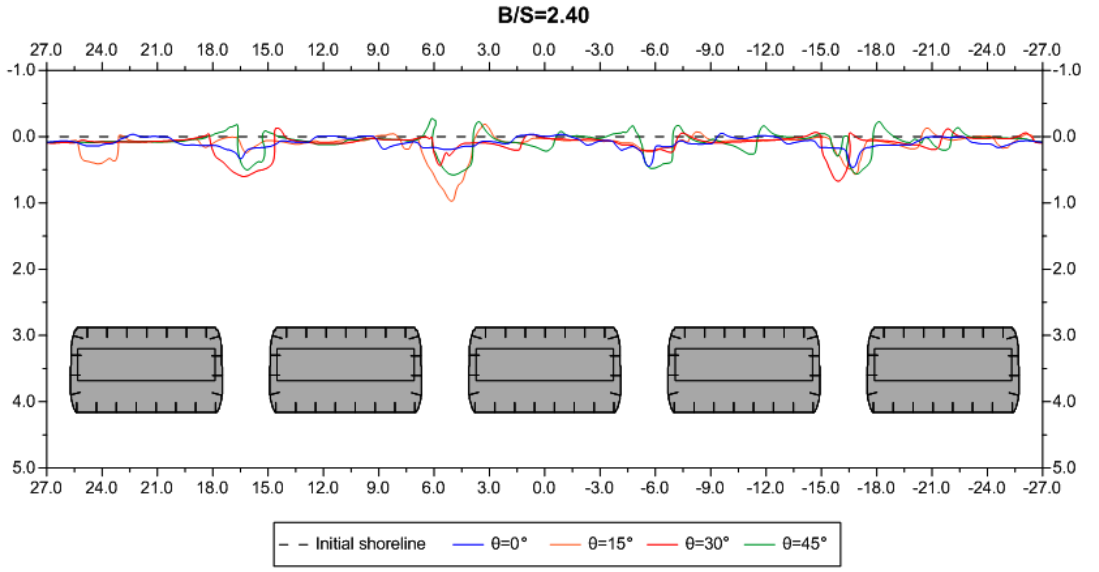

Fig. 7.13. Final computed shoreline for various angles of wave incidence, $B = 8.28$ m and ratio $B/S = 2.40$.

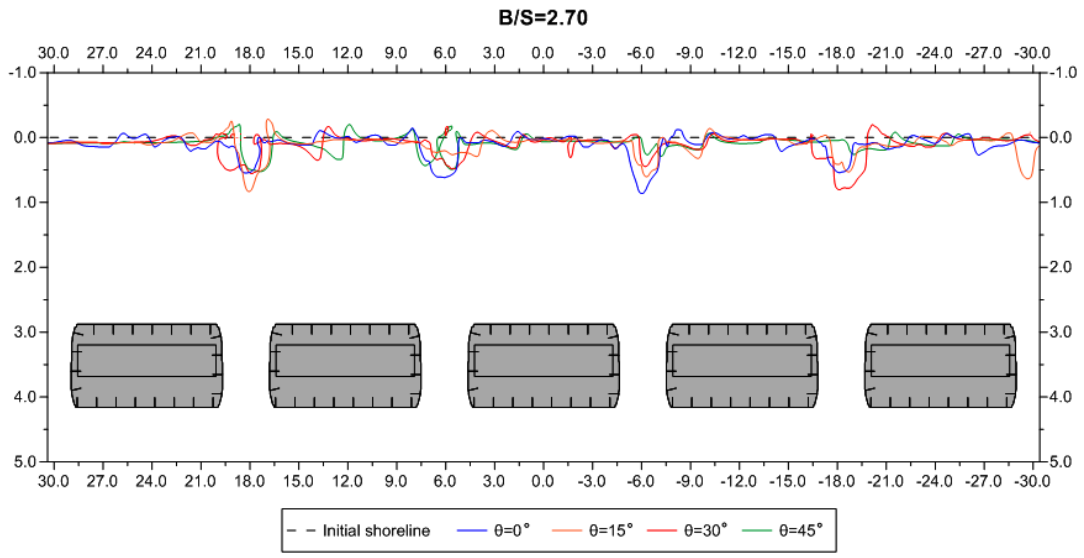

Fig. 7.14. Final computed shoreline for various angles of wave incidence, $B = 9.32$ m and ratio $B/S = 2.70$.

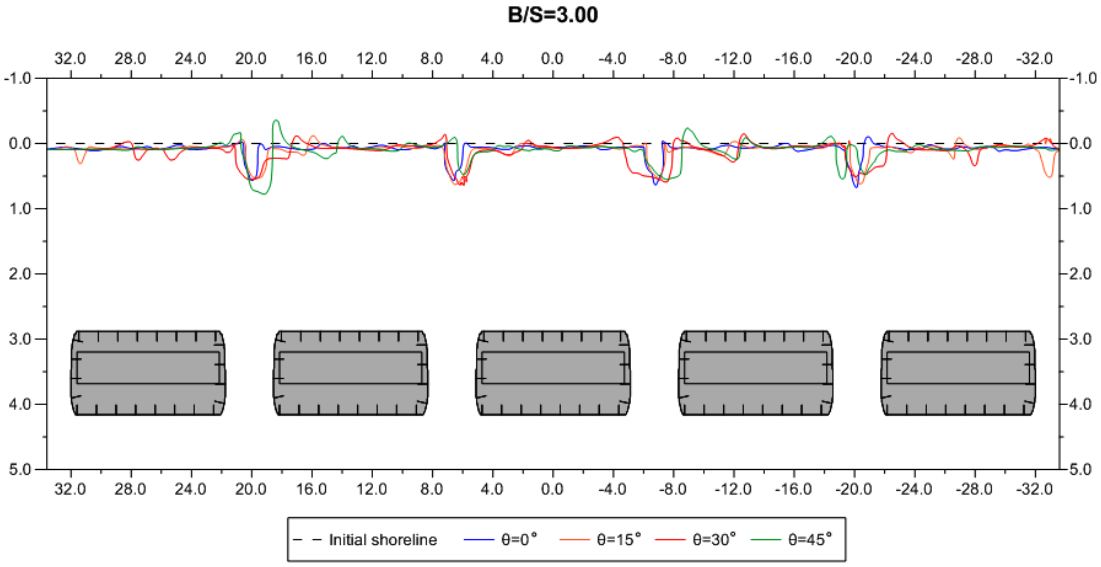

Fig. 7.15. Final computed shoreline for various angles of wave incidence, $B = 10.35$ m and ratio $B/S = 3.00$.

A snapshot of the free surface elevation for various angles of incidence is depicted in Fig. 7.16 for the test case with a ratio $B/S = 3.00$. The above results are summarized in Fig. 7.17, which represents the variation of the non-dimensional salient width, X/S, with the ratio B/S.

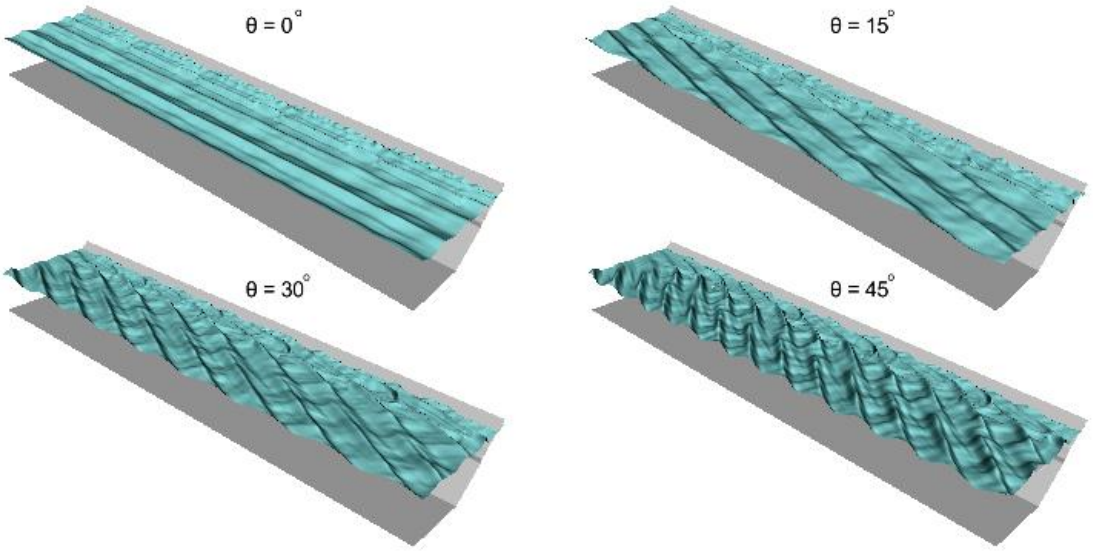

Fig. 7.16. Snapshots of the free surface elevation for various angles of wave incidence, $B = 10.35$ m and ratio $B/S = 3.00$.

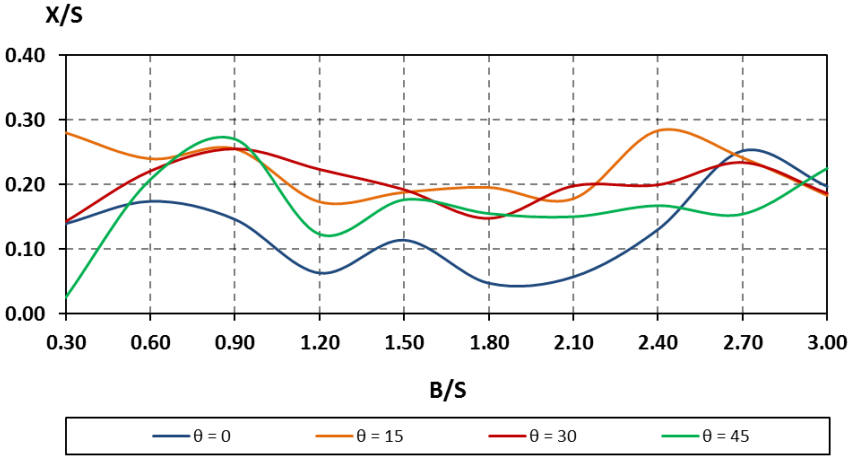

Fig. 7.17. Variation of computed non-dimensional salient width X/S with ratio B/S by modifying B.

From the analysis performed, it can be seen that the salient width is not a monotonically increasing function of the breakwaters length. One may expect longer structures to result to longer salients, and eventually to a tombolo formation. However, this appears not be true. In particular, a tombolo was never formed in the test cases studied, but also longer breakwaters generated longer salients only up to specific limit, approximately $B/S \approx 0.90$. Beyond this limit, increase of B/S results to a reduction of X/S, which is more pronounced for normal wave incidence. This behavior is observed up to about $B/S \approx 2.0$. Further increase of B/S results to a further increase of X/S, but again this oscillating behavior seems to continue beyond $B/S \approx 3.0$, which was the limit studied in the present Ph.D. thesis. The described

shoreline's behavior is observed, more or less, for all the 4 wave angles studied herein. However, as already described in subsection 7.1, the salient width is smaller for shore-normal wave incidence, and the larger ones are observed for $\theta = 15° - 30°$. Nevertheless, in all the test cases the non-dimensional salient width lay in the range $X/S = (0.05 \div 0.30)$, which are reduced values compared to their corresponding ones that would be expected for an array of emergent breakwaters with similar ratios B/S. It is noted that $X/S \sim 1$ corresponds to a tombolo. A similar non-monotonic behavior of the salient width was also observed numerically by Koutsouvela (2010). One partial explanation is that as the structure's length increases beyond a limit, the interaction of the two vortices generated in its lee starts to become negligible, resulting to a neutral zone behind the center of the structure were no significant circulation takes place. However, the phenomenon is more complex since the varying length of the permeable breakwaters alters the relative significance of diffraction, refraction, breaking, overtopping and flow through the pores. Thus, it is much more difficult for a monotonic behavior to be established compared to impermeable, emergent breakwaters. The shapes of salients observed are not all similar (see also Black and Andrews, 2001) and in most cases, also erosion took place near them. It can be observed both behind the gaps, e.g. $B/S \approx 0.90$, as well as behind the structures, e.g. $B/S \approx 0.60$. Thus, a specific pattern is difficult to be recognized. In all the cases, the maximum erosion of the shoreline (onshore movement) is less than 30-50% of the maximum width of the nearby salient. However, the erosion areas are generally wider than the accretive ones, especially for small ratios B/S.

7.2.2 Effect of submerged breakwaters' distance from shoreline

The second geometric design parameter that was studied was the distance from the initial shoreline to the submerged breakwaters, S. In particular, 5 different values of the ratio B/S were considered. The breakwaters' length $B = 3.0$ m was retained constant and S was modified in each run giving ratios $B/S = 0.60, 0.87, 1.20, 1.80, 2.00$, respectively. The ratio G/B was kept constant equal to 1/3 and the wave conditions were those of the laboratory test No. 4, i.e. T = 2.0 s, H_o = 0.08 m and the simulation period 4.3 hrs. The final shoreline for the 5 test cases is depicted in Figs 7.18 to 7.22.

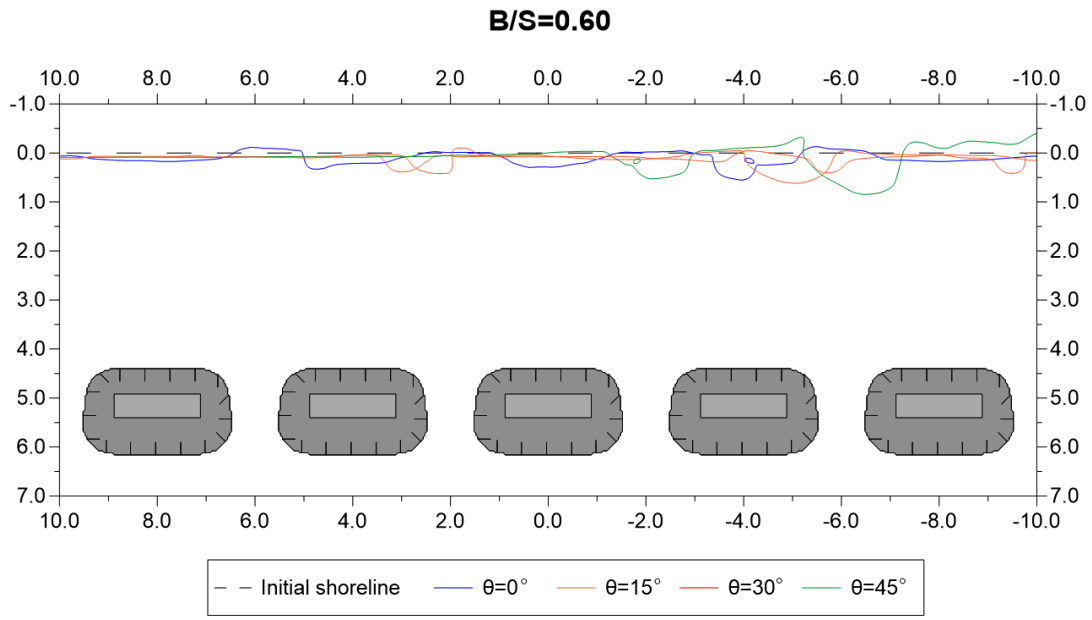

Fig. 7.18. Final computed shoreline for various angles of wave incidence, $S = 5.0$ m and ratio $B/S = 0.60$.

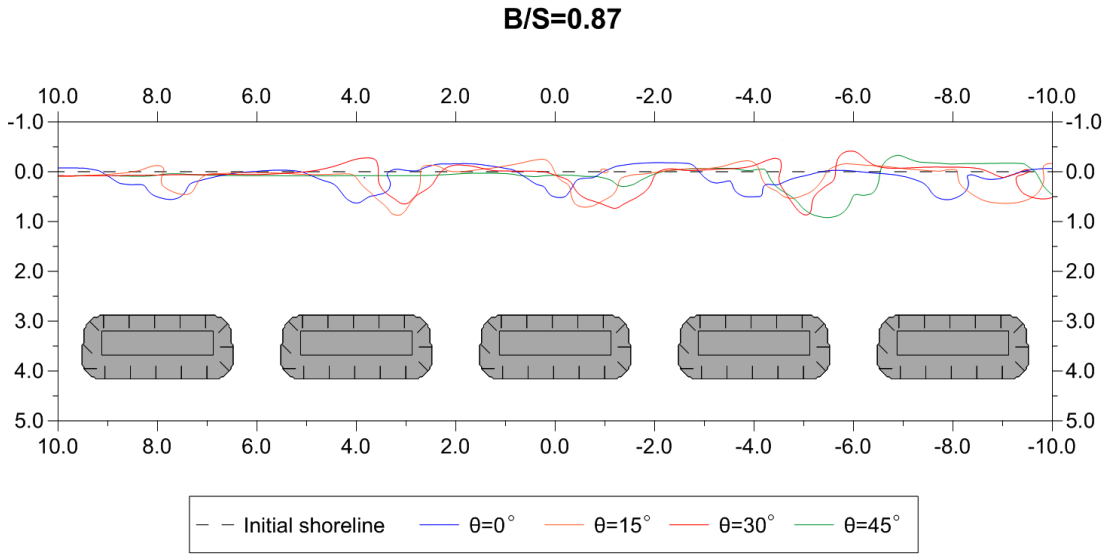

Fig. 7.19. Final computed shoreline for various angles of wave incidence, $S = 3.45$ m and ratio $B/S = 0.87$.

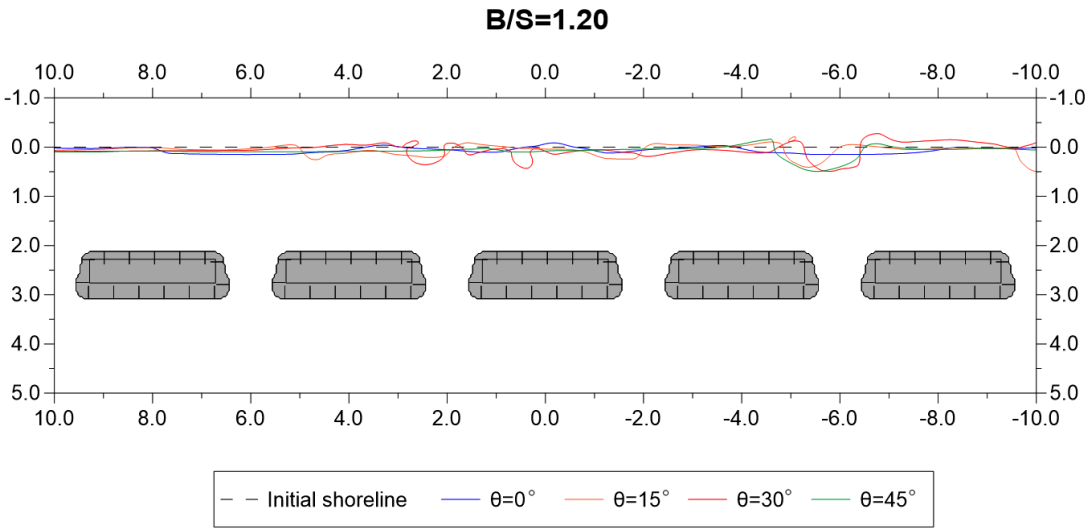

Fig. 7.20. Final computed shoreline for various angles of wave incidence, $S = 2.5$ m and ratio $B/S = 1.20$.

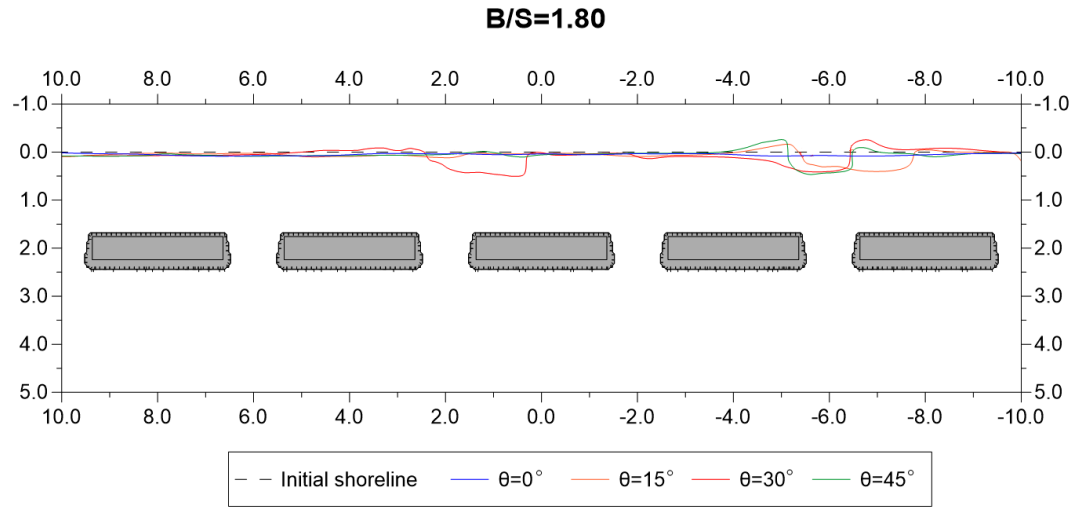

Fig. 7.21. Final computed shoreline for various angles of wave incidence, $S = 1.67$ m and ratio $B/S = 1.80$.

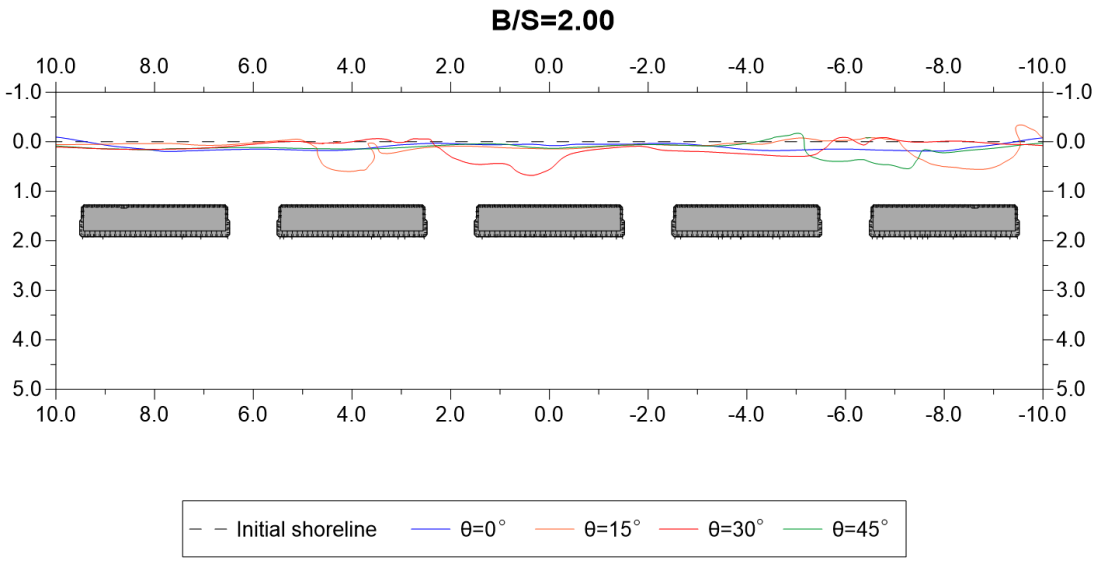

Fig. 7.22. Final computed shoreline for various angles of wave incidence, $S = 1.50$ m and ratio $B/S = 2.00$.

The above results are summarized in Fig. 7.23, which represents the variation of the non-dimensional salient width, X/S, with the ratio B/S.

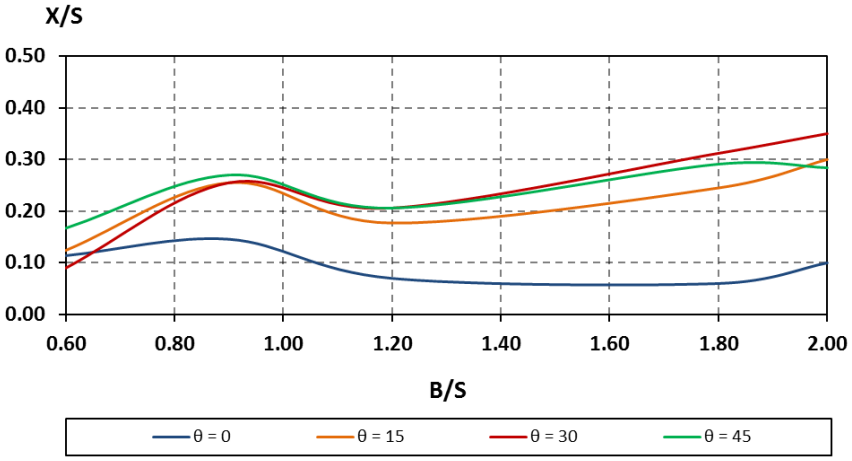

Fig. 7.23. Variation of computed non-dimensional salient width X/S with ratio B/S by modifying S.

Figure 7.23 shows that as the submerged breakwaters are placed closer to the shoreline, the non-dimensional salient width, X/S, increases. However, this is true only up to a specific limit, i.e. approximately $B/S \approx 0.90$. Beyond this limit, a further onshore movement of the structures results to a reduction of the non-dimensional salient width. As the breakwaters are moved onshore and closer or inside the surf zone, the two eddies behind each of them are suppressed and merge with the formed rip currents across the gaps. This procedure may even result to weak erosion behind some of the breakwaters (see Fig. 7.20). For shore-normal wave incidence the ratio X/S remains practically independent from B/S for a further increase of the

latter. In particular, the circulation very close to the shoreline is very weak leading to an insignificant evolution of the shoreline. However, when oblique incidence is at play, the non-dimensional salient width X/S increases again with B/S for values of the latter greater than about $B/S \approx 1.20$. This distinction was also commented by Ranasinghe and Turner (2006) (see also Fig. 7.4). It should be mentioned that in all the cases the free board was 0.05 m, regardless of the position of the breakwaters. Similarly to subsection 7.2.1, it is observed that the non-dimensional salient widths are again low, within the range $X/S = (0.05 \div 0.35)$, compared the expected corresponding ones behind a similar array of emergent breakwaters.

7.2.3 Effect of the gap length

The impact of the length of the gap, G, between two adjacent submerged breakwaters was also studied in the present thesis. In this subsection, the breakwaters' length and distance from the initial shoreline were those of the laboratory test case 4, i.e. $B = 3.0$ m and $S = 3.45$ m, respectively, giving a ratio $B/S = 0.87$. Five different values of the ratio G/B were considered, $G/B = 0.20$, 0.30, 0.40, 0.50 and 0.60. The generated waves had period T = 2.0 s and wave height H_o = 0.08 m. Hence, at the region of the structure the wavelength was approximately $L = 3.0$ m. Thus, the gap length lay in the range $(0.2 \div 0.6)L$, while for a system of emergent breakwaters the formation of a tombolo is only expected if $G \geq L$, according to Eq. (7.2). However, for an expected salient, such a requirement does not exist. The final shoreline for the 5 test cases is depicted in Figs 7.24 to 7.28.

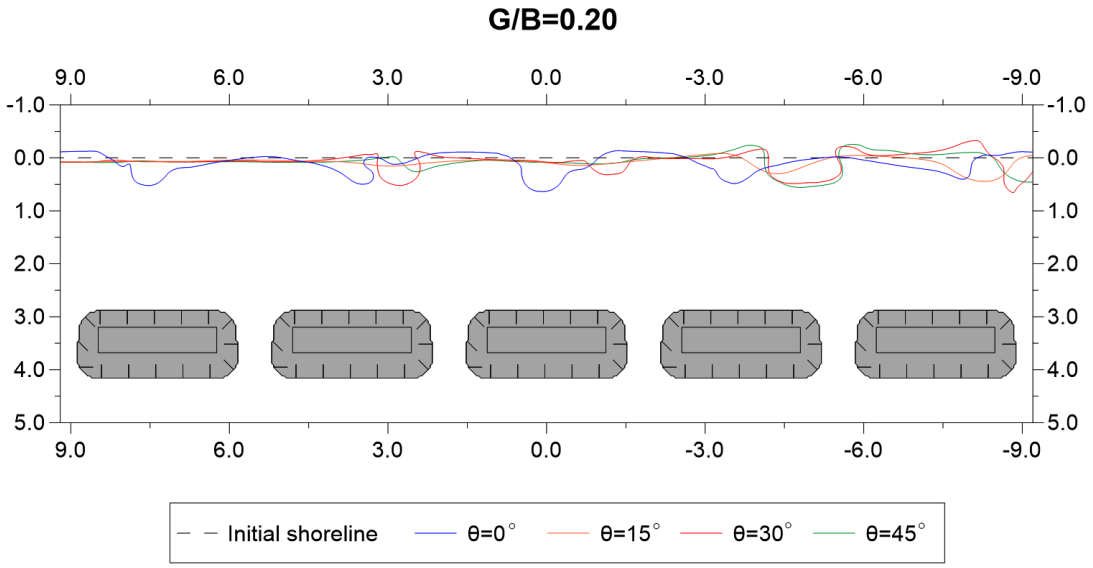

Fig. 7.24. Final computed shoreline for various angles of wave incidence, $B = 3.0$ m, $S = 3.45$ m and ratio $G/B = 0.20$.

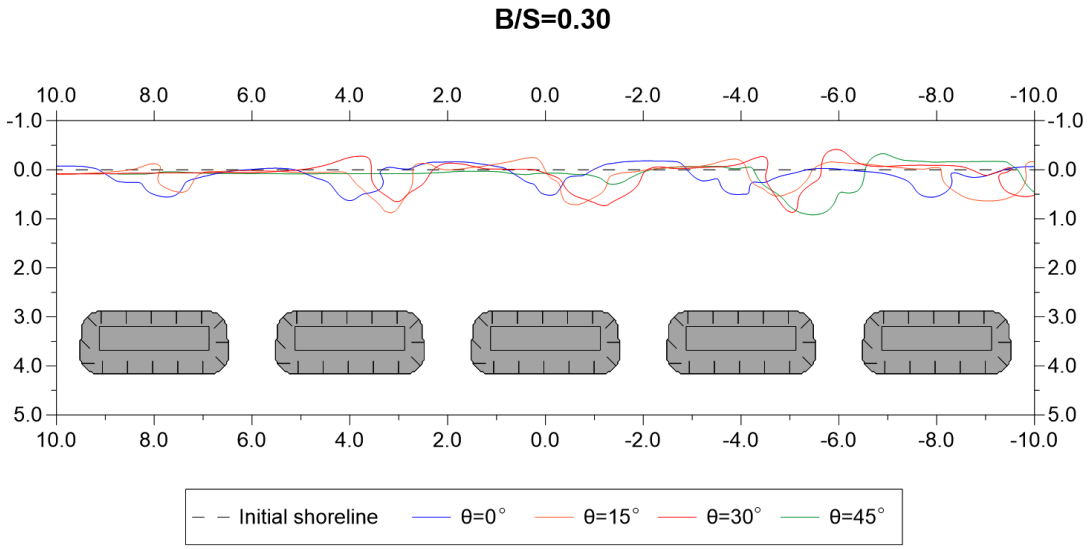

Fig. 7.25. Final computed shoreline for various angles of wave incidence, $B = 3.0$ m, $S = 3.45$ m and ratio $G/B = 0.30$.

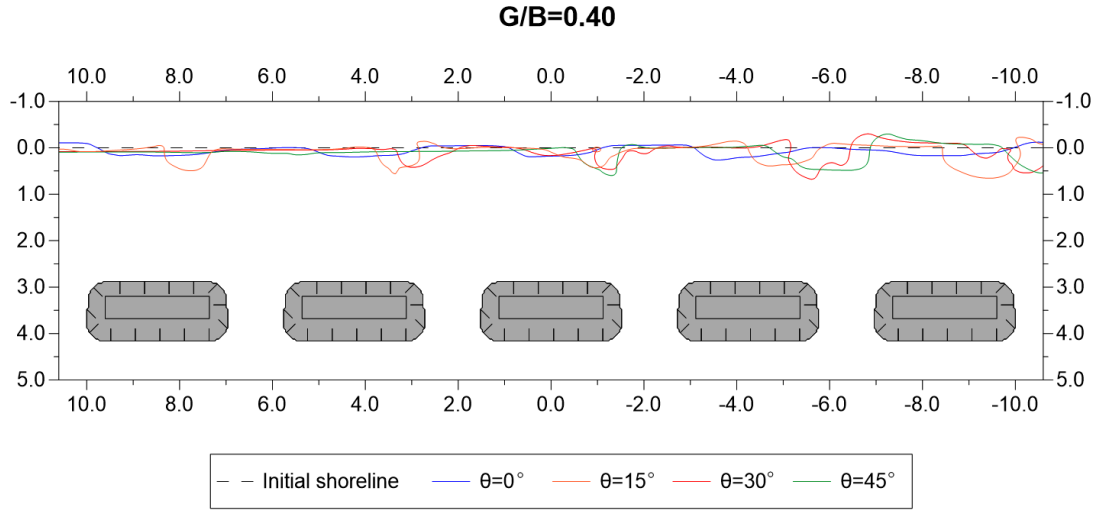

Fig. 7.26. Final computed shoreline for various angles of wave incidence, $B = 3.0$ m, $S = 3.45$ m and ratio $G/B = 0.40$.

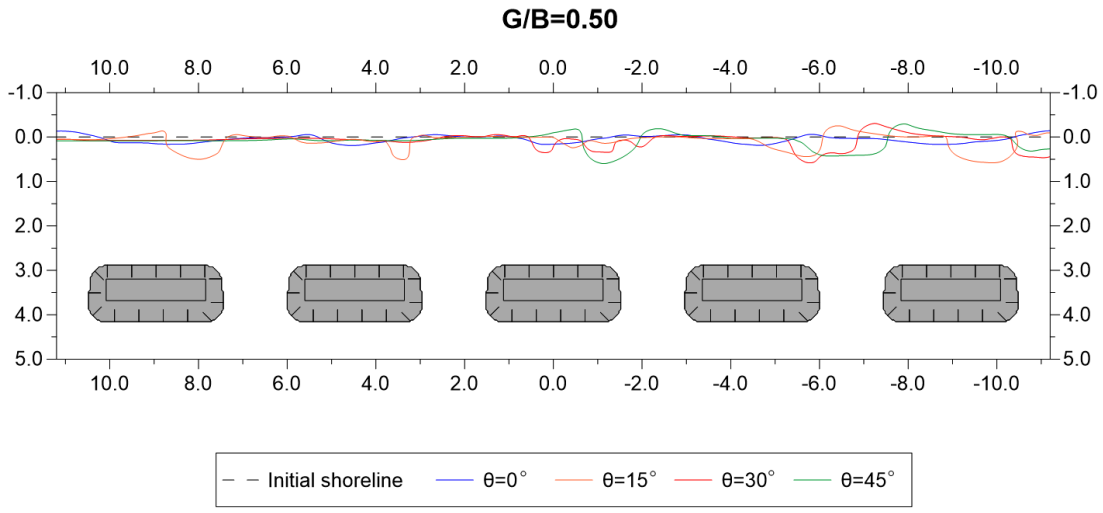

Fig. 7.27. Final computed shoreline for various angles of wave incidence, $B = 3.0$ m, $S = 3.45$ m and ratio $G/B = 0.50$.

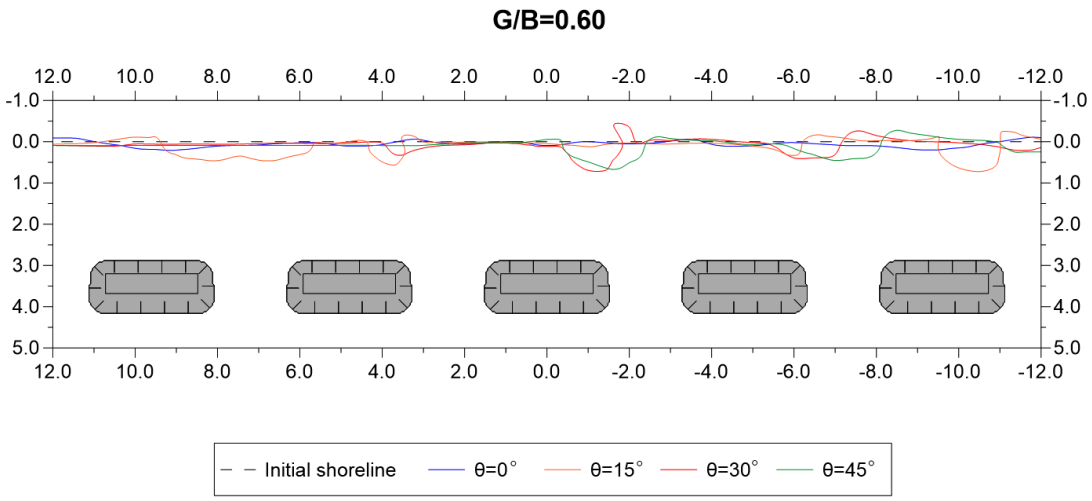

Fig. 7.28. Final computed shoreline for various angles of wave incidence, $B = 3.0$ m, $S = 3.45$ m and ratio $G/B = 0.60$.

The above results are summarized in Fig. 7.29, which represents the variation of the non-dimensional salient width, X/S, with the ratio B/S.

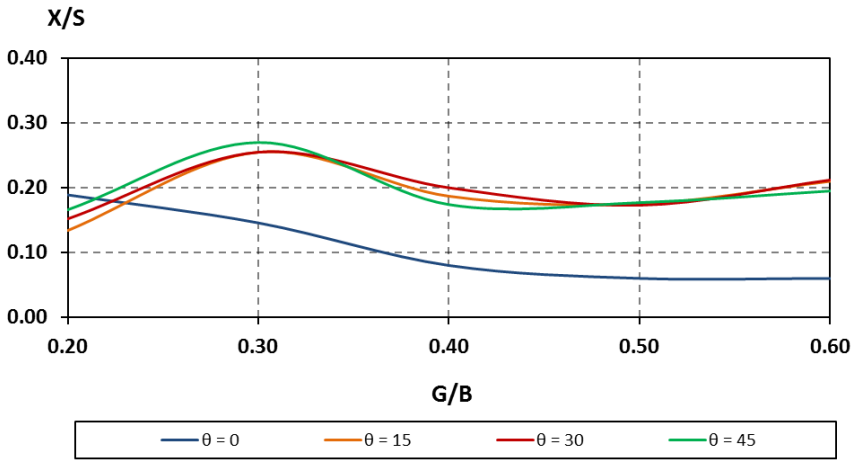

Fig. 7.29. Variation of computed non-dimensional salient width X/S with ratio G/B by modifying G.

Figure 7.29 shows that for shore-normal wave incidence, increase of the gap length results to reduction of the salient width. This is true for gap lengths less than, say, $G/B \approx 0.45$. Beyond this limit the ratio X/S appears to converge to a low value ~ 0.06. In addition, from Figs 7.24 to 7.28, it is concluded that as the gap length reduces, the erosion behind them increases. This fact was also commented by Zyserman *et al*. (2005) and Koutsouvela (2010) and it can be attributed to the increase of the rip current velocities. On the other hand, the behavior of the shoreline for oblique wave incidence reveals an increase of the salient width up to about $G/B \approx 0.30$, followed by a decrease up to $G/B \approx 0.40 \div 0.45$, and then a further, weaker, increase. It also appears that the maximum created salient behind the array of the breakwaters has a more or less similar width, regardless of the wave angle.

7.2.4 Effect of the porosity of submerged breakwaters

Another parameter that was studied and it is associated with the efficiency of an array of submerged breakwaters is their porosity. The permeability of the structure, along with the overtopping and the diffraction, are related to the wave transmission coefficient, which is associated with morphological response and the shoreline evolution in the lee of the low-crested breakwaters (Hanson and Kraus, 1991; Pilarczyk, 2003; Cáceres *et al*., 2005). In the present subsection, six different values of the porosity were considered, $\lambda = 0.0$, 0.30, 0.35, 0.40, 0.45 and 0.50, respectively. The case $\lambda = 0.0$ refers to impermeable submerged breakwaters. The layout considered referred to $B = 3.0$ m, $S = 3.45$ m and $G = 1.0$ m, leading to ratios $B/S = 0.87$ and $G/B = 1/3$. The generated waves had a period of T = 2.0 s and a wave height of H_o = 0.08 m. The final shoreline for the 6 test cases is depicted in Figs 7.30 to 7.35.

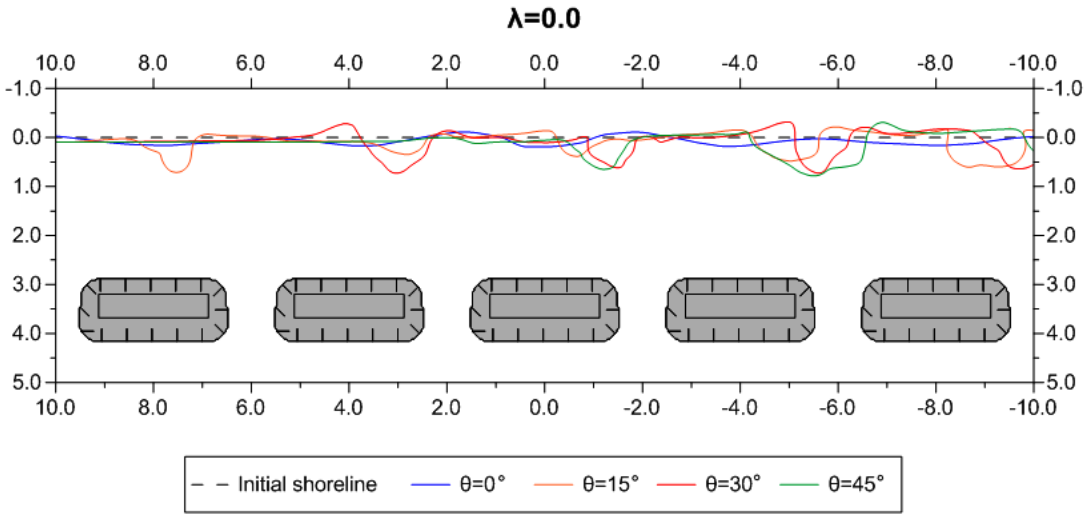

Fig. 7.30. Final computed shoreline for various angles of wave incidence, $B = 3.0$ m, $S = 3.45$ m, $G = 1.0$ m, and $\lambda = 0.0$.

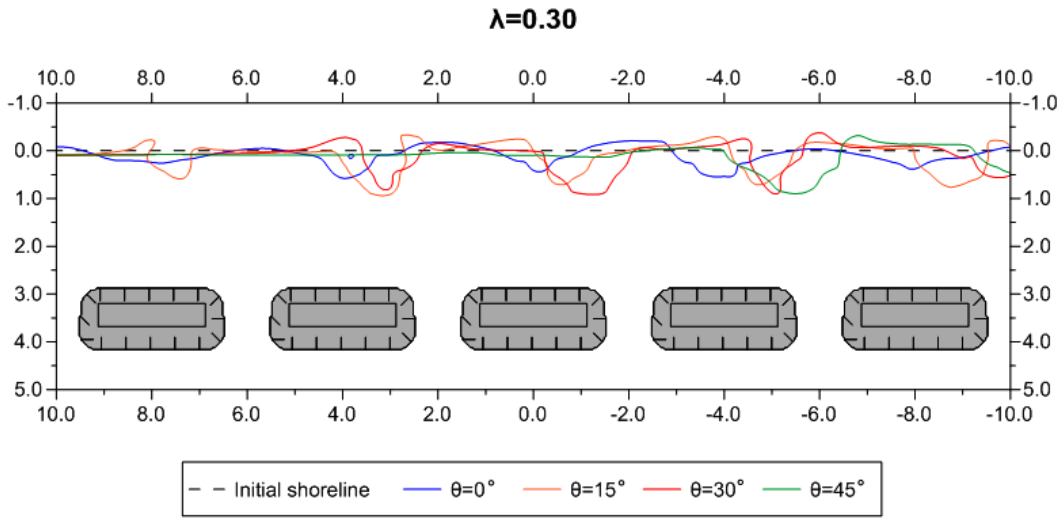

Fig. 7.31. Final computed shoreline for various angles of wave incidence, $B = 3.0$ m, $S = 3.45$ m, $G = 1.0$ m, and $\lambda = 0.30$.

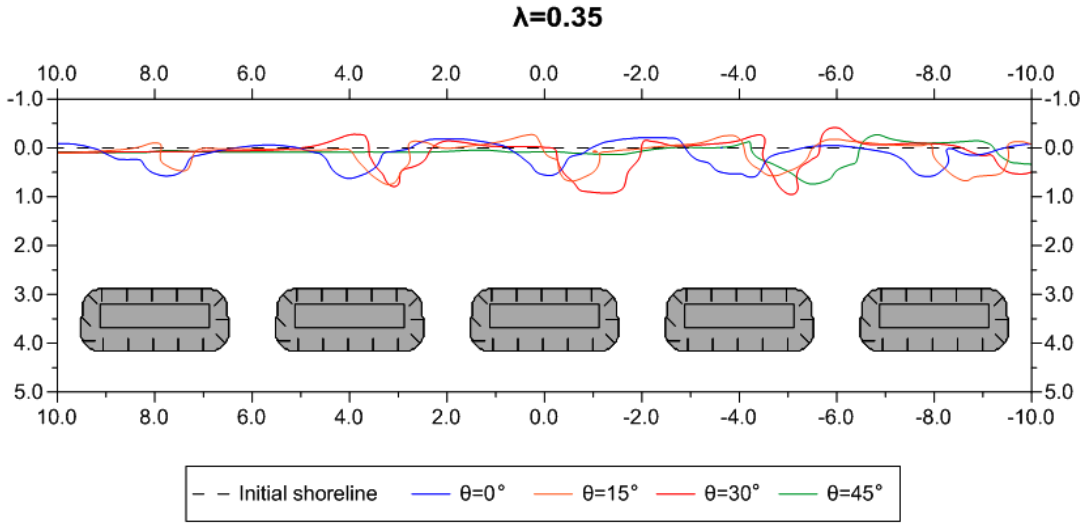

Fig. 7.32. Final computed shoreline for various angles of wave incidence, $B = 3.0$ m, $S = 3.45$ m, $G = 1.0$ m, and $\lambda = 0.35$.

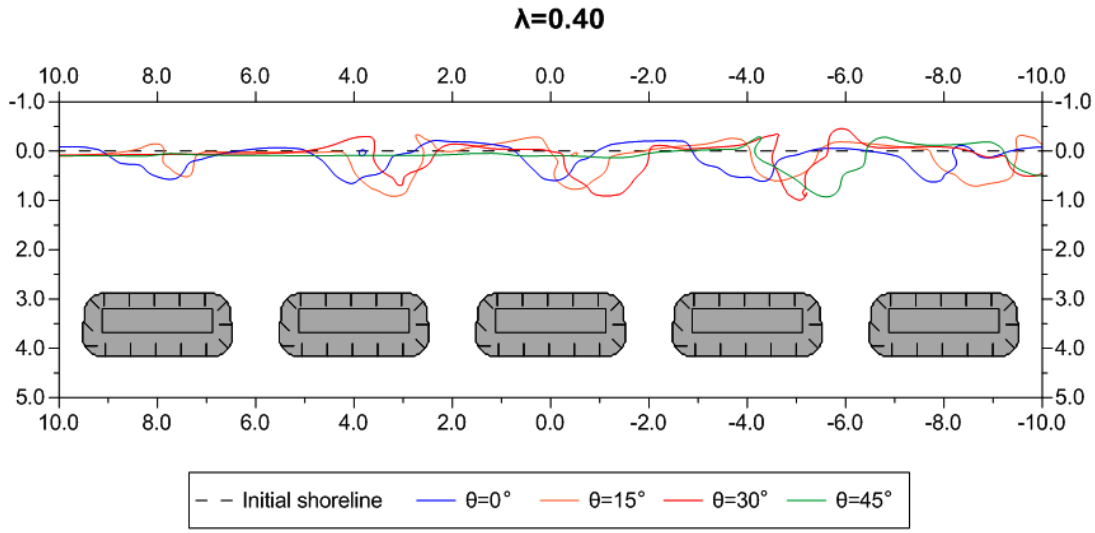

Fig. 7.33. Final computed shoreline for various angles of wave incidence, $B = 3.0$ m, $S = 3.45$ m, $G = 1.0$ m, and $\lambda = 0.40$.

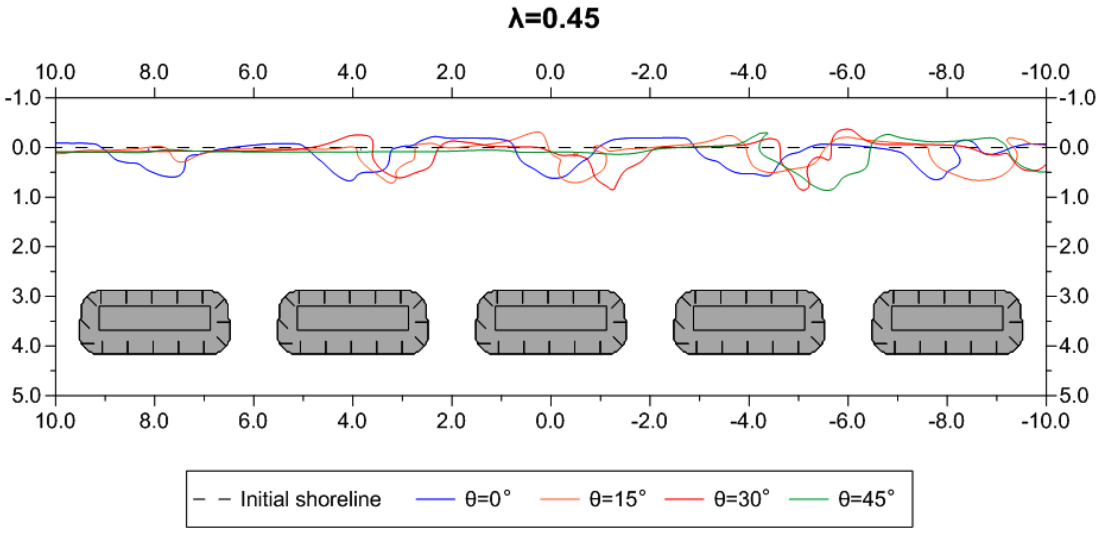

Fig. 7.34. Final computed shoreline for various angles of wave incidence, $B = 3.0$ m, $S = 3.45$ m, $G = 1.0$ m, and $\lambda = 0.45$.

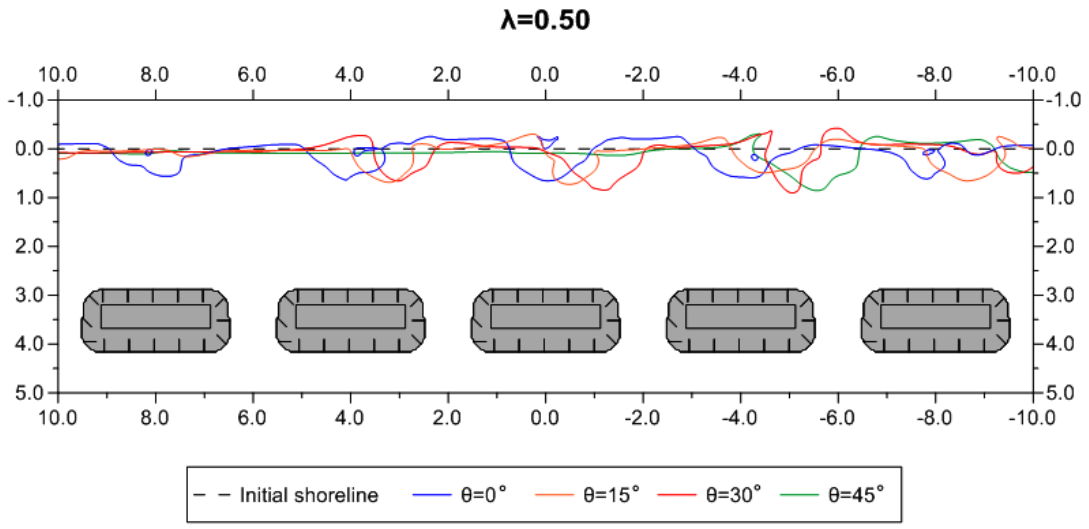

Fig. 7.35. Final computed shoreline for various angles of wave incidence, $B = 3.0$ m, $S = 3.45$ m, $G = 1.0$ m, and $\lambda = 0.50$.

The variation of the non-dimensional salient width, X/S, with the porosity of the submerged breakwaters, λ, is depicted in Fig. 7.36 for $B/S = 0.87$ and $G/B = 1/3$.

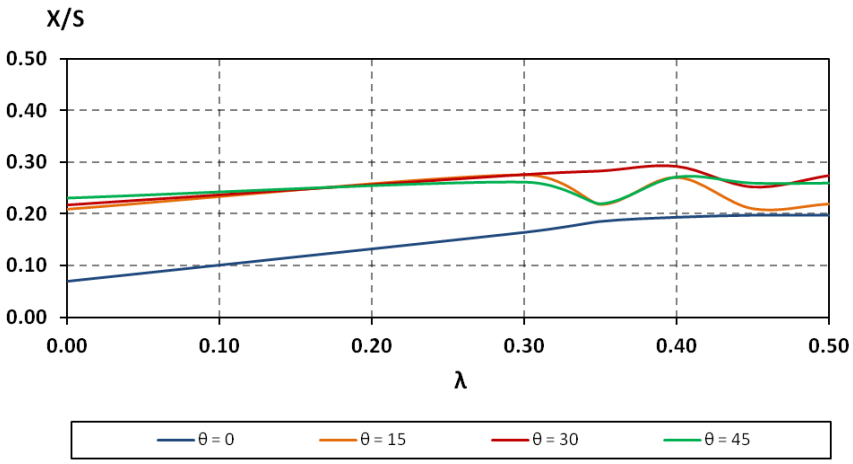

Fig. 7.36. Variation of computed non-dimensional salient width X/S with the porosity λ of the submerged breakwaters.

Figure 7.36 shows that increase of the porosity of the submerged breakwaters also results to an increase of the salient width. This is true up to $\lambda \approx (0.35 \div 0.40)$, for all the wave directions considered. For shore-normal wave incidence, the ratio X/S appears to converge to a value of about 0.20 for porosities greater than 0.40. A similar behavior is also observed for oblique wave incidence, but for some oscillations around this point. In overall, λ = 0.40 seems to be the optimal value for the design of submerged breakwaters, with respect to beach accretion. In addition, Figs 7.30 to 7.35 show that increase of porosity also results to enhanced erosion behind the gaps between the breakwaters. This conclusion is further supported by Fig. 7.37 which shows the wave-induced currents field above and around the system of breakwaters for λ = 0.0 and λ = 0.50. In the former case, the breakwaters are impermeable and the entire wave energy 'passes' over the structures, resulting to a pronounced onshore current along the axis of symmetry and two pronounced vortices behind the heads. On the other hand, in the case of λ = 0.50, the velocities over the structures are much lower and the two eddies weaker, since a portion of the energy goes through the pores. Nevertheless, the formed rip currents close to the shoreline are more intense, leading to increased erosion behind the gaps. However, these velocities are weakened over a narrow zone, and thus the rip currents close to the gaps are more significant in the case of impermeable breakwaters.

(a)

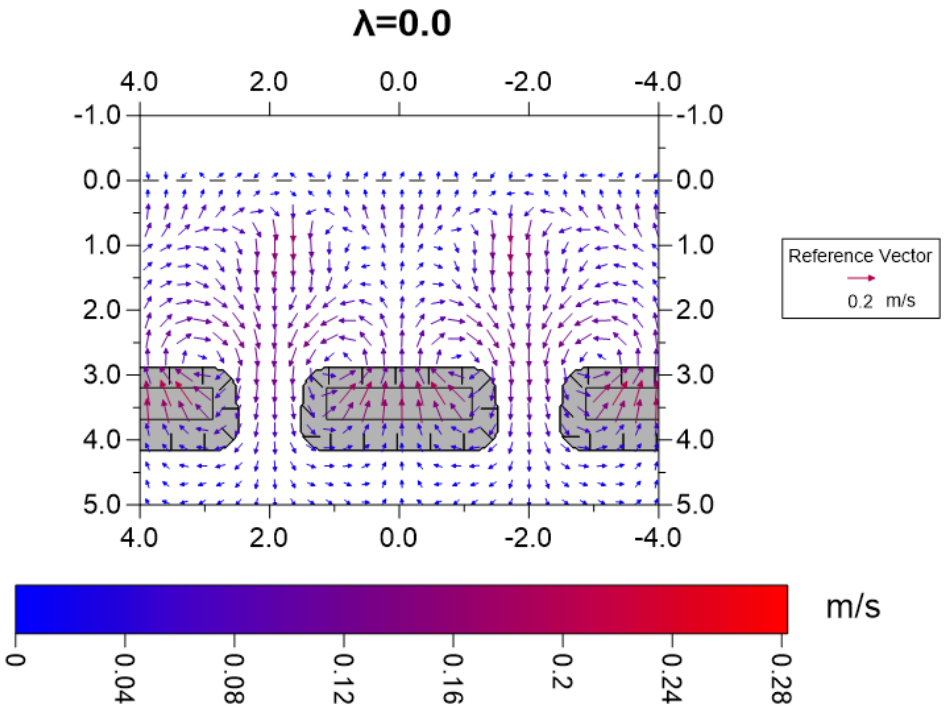

(b)

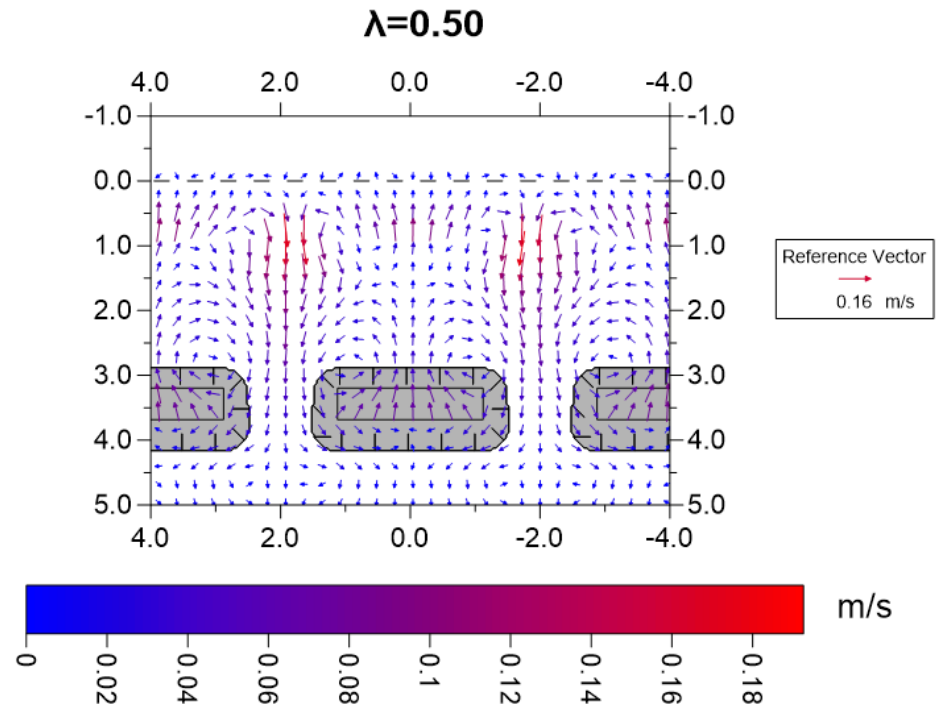

Fig. 7.37. Wave-induced current field for shore-normal wave incidence and (a) λ = 0 and (b) λ = 0.50.

7.2.5 Effect of wave conditions

Apart from the geometrical design parameters studied in the previous subsections, the wave characteristics are also crucial for the mode of the shoreline response. In order to study their effect, a fifth set of numerical experiments was performed. The layout referred to an array of 5 identical permeable submerged breakwaters with $B = 3.0$ m, $S = 3.45$ m and $G = 1.0$ m, leading to ratios $B/S = 0.87$ and $G/B = 1/3$. The effect of the wave period was studied through a set of five regular test cases whose characteristics are summarized in table 7.2. The second and third columns refer to the wave height at depth $d = 0.45$ m and the wave period, respectively. The fourth column refers to the wavelength at the same depth, while L_{SB} is the wavelength at $d = 0.25$ m, where the breakwaters were placed. The last two columns include the wave slope in deep water and the Ursell number at $d = 0.45$ m, respectively. The final shoreline for the 5 test cases is depicted in Figs 7.38 to 7.42.

Table 7.2. Wave characteristics of the various numerical experiments performed.

Test No.	H_o (m)	T (s)	$L_{d=0.45}$ (m)	L_{SB} (m)	H_{deep}/L_{deep} (%)	Ur
S5.1	0.08	1.00	1.492	1.304	13.09	1.96
S5.2	0.08	1.25	2.122	1.747	5.87	3.95
S5.3	0.08	1.50	2.728	2.173	3.41	6.53
S5.4	0.08	2.00	3.884	3.000	1.56	13.24
S5.5	0.08	2.50	4.998	3.810	0.88	21.93

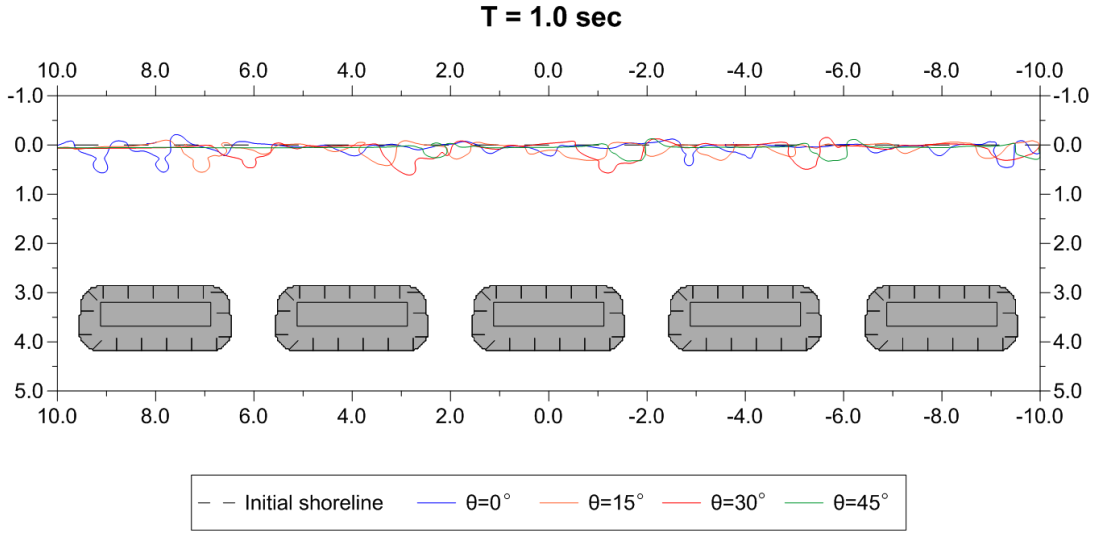

Fig. 7.38. Final computed shoreline for various angles of wave incidence, $B = 3.0$ m, $S = 3.45$ m, $G = 1.0$ m, and wave period $T = 1.0$ s.

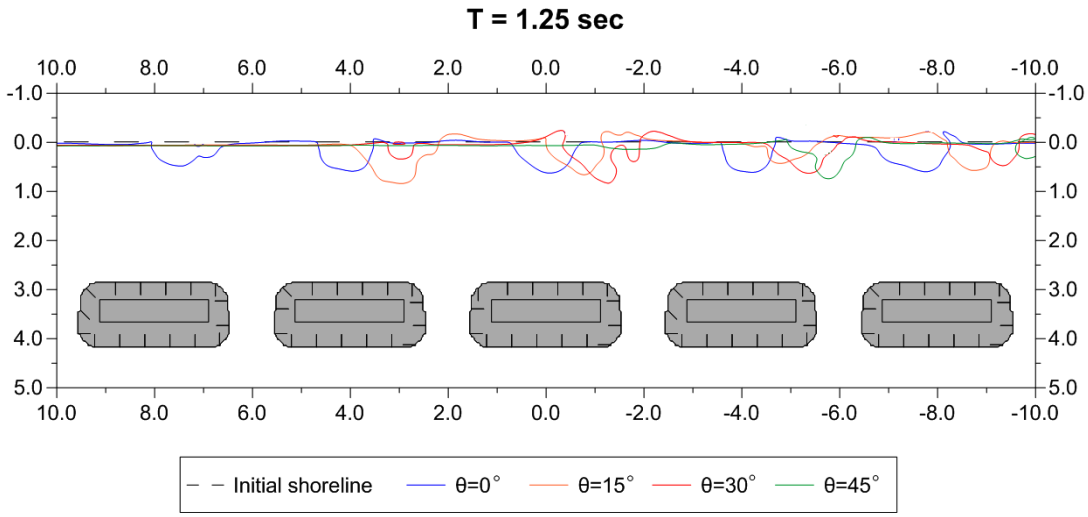

Fig. 7.39. Final computed shoreline for various angles of wave incidence, $B = 3.0$ m, $S = 3.45$ m, $G = 1.0$ m, and wave period $T = 1.25$ s.

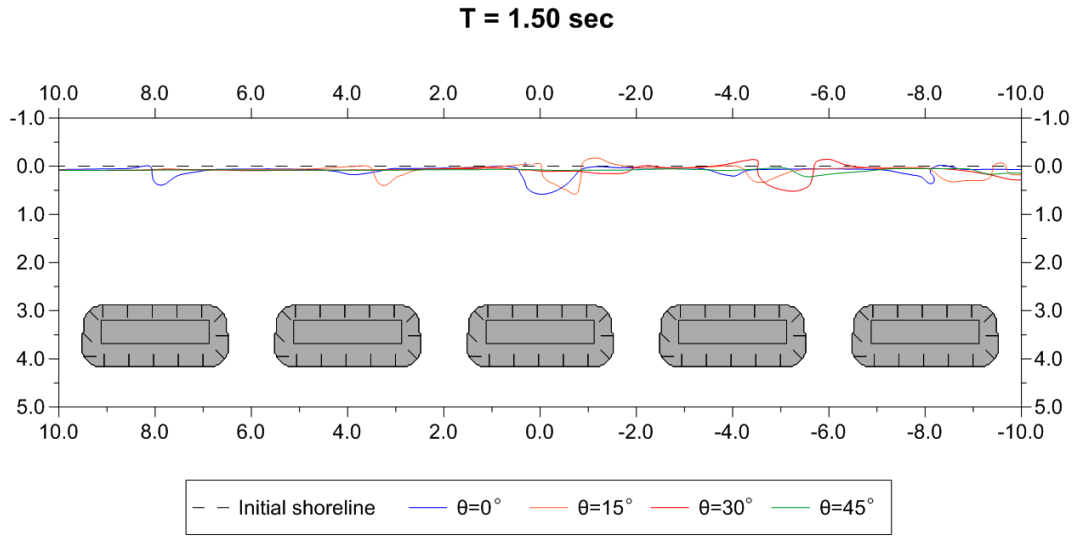

Fig. 7.40. Final computed shoreline for various angles of wave incidence, $B = 3.0$ m, $S = 3.45$ m, $G = 1.0$ m, and wave period $T = 1.50$ s.

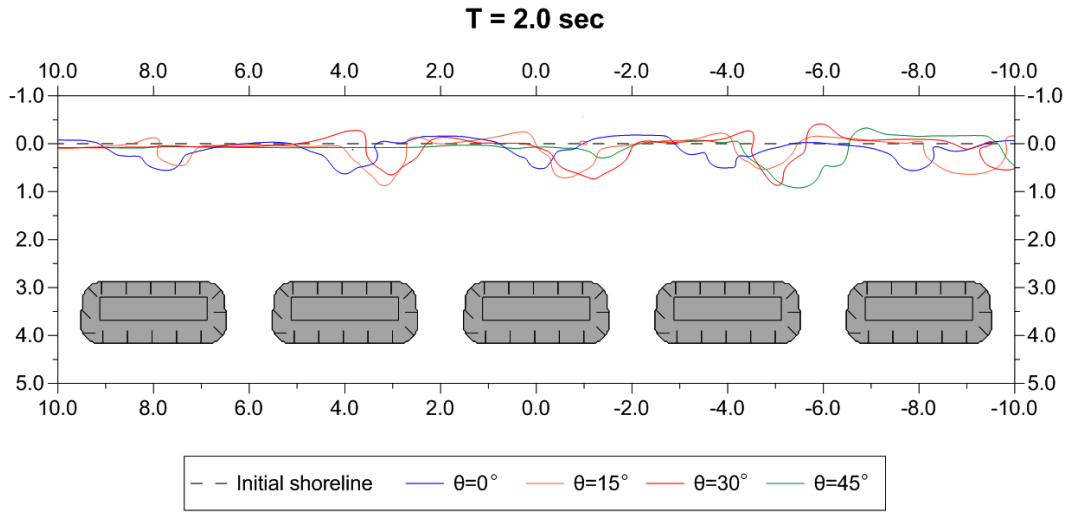

Fig. 7.41. Final computed shoreline for various angles of wave incidence, $B = 3.0$ m, $S = 3.45$ m, $G = 1.0$ m, and wave period $T = 2.0$ s.

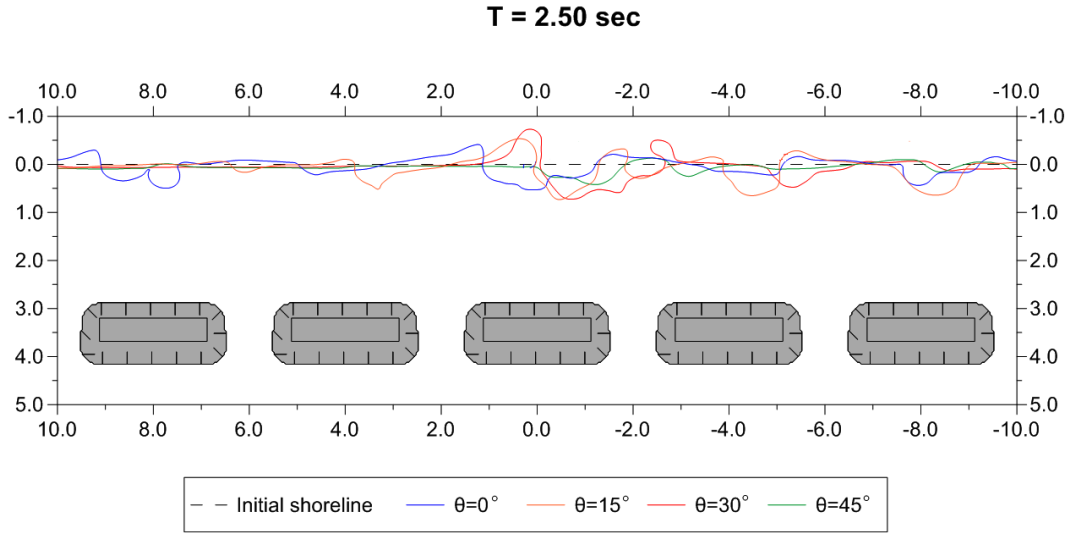

Fig. 7.42. Final computed shoreline for various angles of wave incidence, $B = 3.0$ m, $S = 3.45$ m, $G = 1.0$ m, and wave period $T = 2.50$ s.

The variation of the non-dimensional salient width, X/L, with B/L and G/L is depicted in Figs 7.43 and 7.44, respectively. The employed wavelength, L, refers to the water depth at the breakwaters ($d = 0.25$ m).

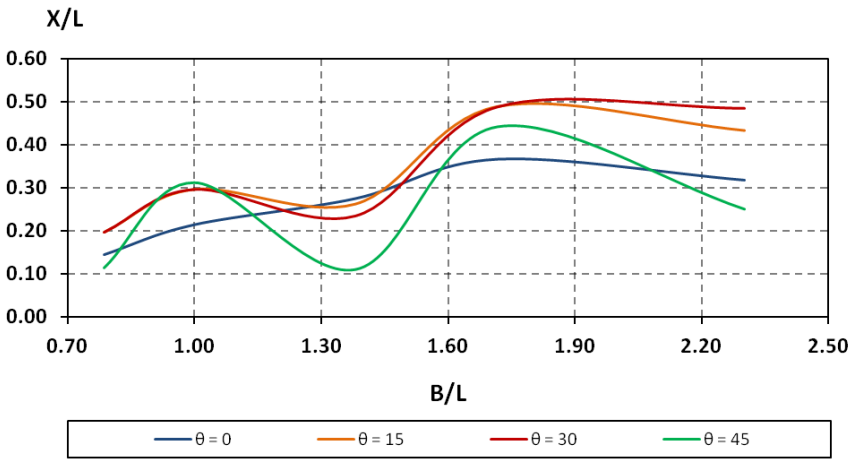

Fig. 7.43. Variation of computed non-dimensional salient width X/L with the ratio B/L for varying wavelength.

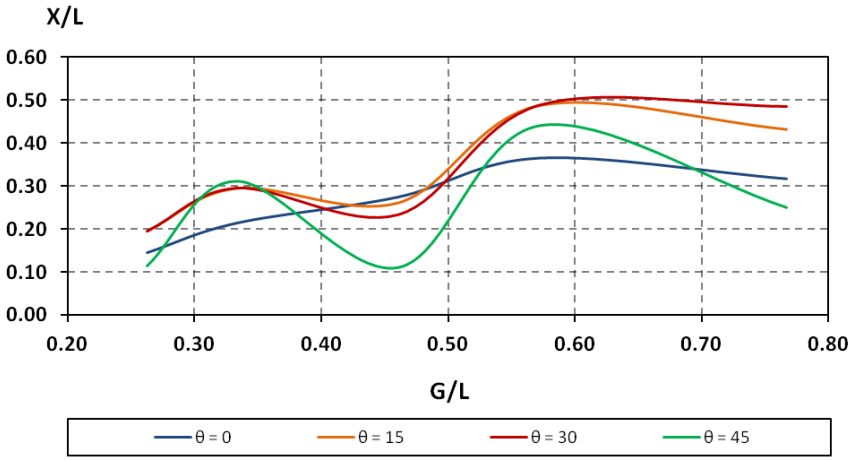

Fig. 7.44. Variation of computed non-dimensional salient width X/L with the ratio G/L for varying wavelength.

The above figures show that for shore-normal wave incidence the non-dimensional salient width increases with the non-dimensional structures' length up to approximately $B/L = 1.70$. Beyond that limit a weak reduction takes place. A similar variation of X/L is observed with respect to G/L and the corresponding maximum occurs at $G/L = 0.57$. On the other hand, for oblique wave incidence, a decrease of X/L is observed for B/L between 1.0 and 1.4 and then an increase up to again $B/L = 1.70$. Beyond that limit a weak decrease takes place, which is more intense for $\theta = 45°$.

The variation of the non-dimensional salient width X/S with the wave slope in deep water and the Ursell number is depicted in Fig. 7.45. The latter refers to water depth $d = 0.45$ m which is located at the toe of the sloping beach. It can be said that, in general, longer waves

tend to favor enhanced accretion. Furthermore, the salient width increases for Ursell numbers less than 4.0 and then presents insignificant variations.

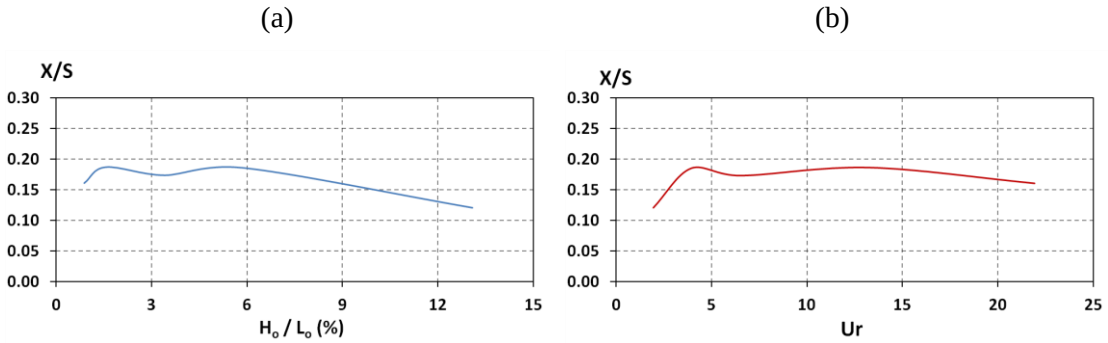

Fig. 7.45. Variation of computed non-dimensional salient width X/S with (a) the wave slope in deep water and (b) the Ursell number at the toe of the sloping beach where $d = 0.45$ m.

7.3 Discussion on shoreline response

In chapter 6, the model was validated against laboratory experiments performed in the context of this Ph.D. thesis. The experiment included one single permeable submerged breakwater. However, the lateral fully reflective boundaries acted as axes of symmetry in the case of shore-normal wave incidence. Thus, practically, the layout represented an array of submerged breakwaters. Nevertheless, the restricted number of tests could not offer a detailed investigation of the shoreline response to such a system of breakwaters. Numerical models have the advantage of simulating a larger number of test cases compared to physical models in the same time. Hence, in the present chapter five different sets of numerical experiments were performed in order to investigate the effect of some significant design parameters on the shoreline response. The simulations included an array of five inline, permeable submerged breakwaters and the geometrical and hydrodynamic characteristics of each run are summarized in table 7.3. Each test was performed for $\theta = 0°$ (normal incidence), 15°, 30° and 45°.

Table 7.3. Characteristics of the various test cases.

Sets	Test No.	H_o (m)	T (s)	B (m)	S (m)	G (m)	λ	B/S	G/B
1st set (modifying B)	S1.1	0.08	2.0	1.04	3.45	0.35	0.52	0.30	0.33
	S1.2	0.08	2.0	2.07	3.45	0.69	0.52	0.60	0.33
	S1.3	0.08	2.0	3.11	3.45	1.04	0.52	0.90	0.33
	S1.4	0.08	2.0	4.14	3.45	1.38	0.52	1.20	0.33
	S1.5	0.08	2.0	5.18	3.45	1.73	0.52	1.50	0.33
	S1.6	0.08	2.0	6.21	3.45	2.07	0.52	1.80	0.33
	S1.7	0.08	2.0	7.25	3.45	2.42	0.52	2.10	0.33

	S1.8	0.08	2.0	8.28	3.45	2.76	0.52	2.40	0.33
	S1.9	0.08	2.0	9.32	3.45	3.11	0.52	2.70	0.33
	S1.10	0.08	2.0	10.35	3.45	3.45	0.52	3.00	0.33

Sets	**Test No.**	H_o **(m)**	T **(s)**	B **(m)**	S **(m)**	G **(m)**	λ	B/S	G/B
2nd set (modifying S)	S2.1	0.08	2.0	3.0	5.00	1.0	0.52	0.60	0.33
	S2.2	0.08	2.0	3.0	3.45	1.0	0.52	0.87	0.33
	S2.3	0.08	2.0	3.0	2.50	1.0	0.52	1.20	0.33
	S2.4	0.08	2.0	3.0	1.67	1.0	0.52	1.80	0.33
	S2.5	0.08	2.0	3.0	1.50	1.0	0.52	2.00	0.33
3rd set (modifying G)	S3.1	0.08	2.0	3.0	3.45	0.6	0.52	0.87	0.20
	S3.2	0.08	2.0	3.0	3.45	0.9	0.52	0.87	0.30
	S3.3	0.08	2.0	3.0	3.45	1.2	0.52	0.87	0.40
	S3.4	0.08	2.0	3.0	3.45	1.5	0.52	0.87	0.50
	S3.5	0.08	2.0	3.0	3.45	1.8	0.52	0.87	0.60
4th set (modifying λ)	S4.1	0.08	2.0	3.0	3.45	1.0	0.00	0.87	0.33
	S4.2	0.08	2.0	3.0	3.45	1.0	0.30	0.87	0.33
	S4.3	0.08	2.0	3.0	3.45	1.0	0.35	0.87	0.33
	S4.4	0.08	2.0	3.0	3.45	1.0	0.40	0.87	0.33
	S4.5	0.08	2.0	3.0	3.45	1.0	0.45	0.87	0.33
	S4.6	0.08	2.0	3.0	3.45	1.0	0.50	0.87	0.33
5th set (modifying T)	S5.1	0.08	1.00	3.0	3.45	1.0	0.52	0.87	0.33
	S5.2	0.08	1.25	3.0	3.45	1.0	0.52	0.87	0.33
	S5.3	0.08	1.50	3.0	3.45	1.0	0.52	0.87	0.33
	S5.4	0.08	2.00	3.0	3.45	1.0	0.52	0.87	0.33
	S5.5	0.08	2.50	3.0	3.45	1.0	0.52	0.87	0.33

It should be stressed that in all the numerical simulations performed sponge layers were considered at both lateral boundaries of the domain. The width of both the absorbing boundaries was 5.28 m and they were placed to absorb the outgoing wave energy, both due to oblique incidence of the generated waves and to wave diffraction. In all figures in the previous subsection, the right and left lateral boundaries represented the inner boundaries of the sponge layers, and thus only the clear computational domain was presented. However, despite the application of the absorbing boundaries, some side reflection always existed, causing an artificial numerical diffraction. This fact slightly infected the computational domain and hence the narrow areas near the lateral boundaries should be considered as buffer zones to establish the desired conditions.

In the analysis presented in subsection 7.2 the initial bathymetry was that of test case No. 4 of the laboratory experiments, mirrored symmetrically along the centerline of each gap

between adjacent breakwaters. Thus, the initial shoreline was straight and the maximum salient width, X, was explored as a function of various design parameters. This maximum apex was not always formed behind the same one of the 5 breakwaters. In addition to the created salients, the shoreline erosion, in general induced behind the gaps, is also a significant issue when designing submerged breakwaters as a coastal defense system. This aspect has drawn less attention to engineers compared to salients and tombolos. In Fig. 7.46 the variation of the non-dimensional maximum erosion width, X_g/S, is depicted as a function of the non-dimensional gap length, G/B (see Fig. 7.2). The variation of X_g/X as a function of G/B is shown in Fig. 7.47. It appears that the maximum erosion of the shoreline lies within the range of 20-60 % of its maximum accretion. However, in many cases, the length of the erosion zones is larger than the peaky salients. Furthermore, for shore-normal wave incidence, after some weak increase, a decrease of the non-dimensional shoreline retreat X_g/S is observed with G/B. A similar behavior is observed for oblique wave incidence with $\theta =$ (30°-45°). However, for $\theta \sim$ 15°, an oscillating response is obtained.

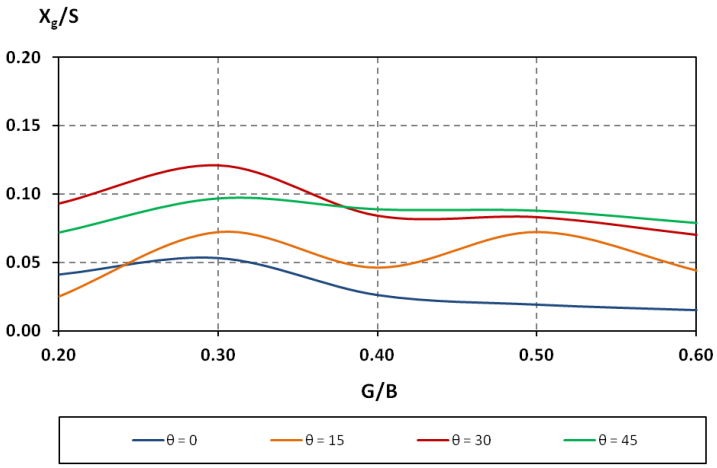

Fig. 7.46. Variation of computed non-dimensional erosion width X_g/S with the ratio G/B (for varying gap length).

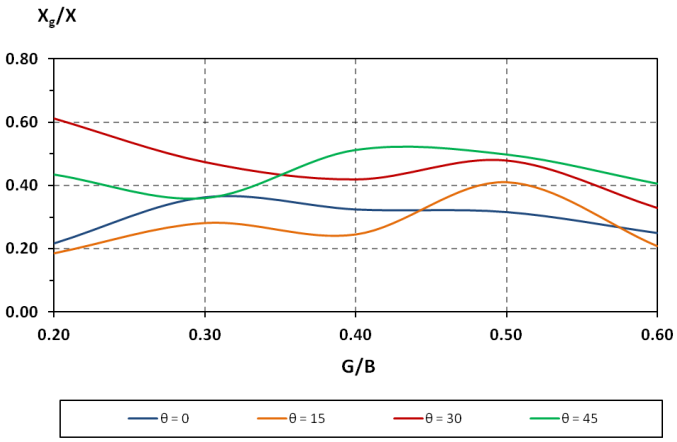

Fig. 7.47. Variation of computed non-dimensional erosion width X_g/X with the ratio G/B (for varying gap length).

The shoreline erosion was also related to the wave conditions in the context of the set of numerical experiments described in subsection 7.2.5. The geometrical characteristics of the layout in these runs are summarized in table 7.4. The variation of X_g/L with G/L is presented in Fig. 7.48 with L the wavelength at $d = 0.25$ m, where the breakwaters were placed. It appears that an optimal design of an array of submerged breakwaters implies that the gap between two adjacent breakwaters is 40-50% of the wavelength. However, this only refers to the induced erosion, while the desired accretion should be also taken into account. In addition, as already mentioned, only layouts with $G \leq 0.8L$ have been considered, while larger gap lengths up to even $(1.0 \div 2.0)L$ should be studied. This is left as a future research.

Table 7.4. Characteristics of the layout in the numerical experiments for studying the shoreline erosion.

Parameter	Value
Breakwaters length - B	3.0 m
Distance from initial shoreline - S	3.45 m
Gaps length - G	1.0 m
Porosity of breakwaters - λ	0.52
Ratio B/S	0.87
Ratio G/B	0.33

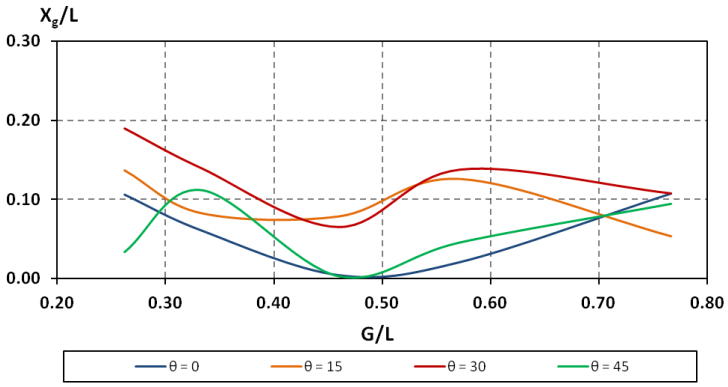

Fig. 7.48. Variation of computed non-dimensional erosion width X_g/L with the ratio G/L (for varying wavelength).

Black and Andrews (2001) studied a large number of data sets referring to the shoreline response to natural reefs and islands. They applied a calibration analysis and fitted a sigmoid curve to the data. This curve gave the non-dimensional cross-shore position of the shoreline, y/X, as a function of the non-dimensional longshore coordinate, x/X ($x = 0$ at the position of the salient apex, $y > 0$ in the offshore direction and X the salient width as above). This curve

is given in Fig. 7.49. The corresponding non-dimensional model results are also shown for three selected cases, S1.1, S1.3 and S1.9. The comparison shows that the Black and Andrews's (2001) formula does not describe accurately the shoreline response behind the system of submerged breakwaters. However, it should be stressed that the specific formula has been proposed based on measurements for natural reefs and islands and not submerged coastal structures. In any case, it is difficult to derive a single mathematical formula for describing the shoreline response under the combined action of such complex physical processes, as the morphological evolution behind arrays of permeable submerged breakwaters, in particular when no provision is made for the initial conditions with regard to sediment transport rates in the studied area.

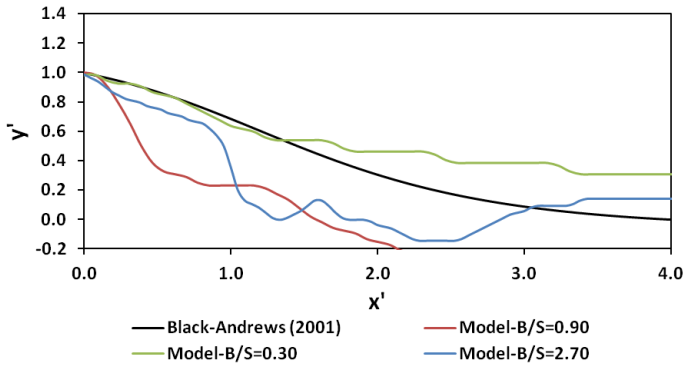

Fig. 7.49. Non-dimensional final shoreline as predicted by Black and Andrews (2001) and computed by the model for various test cases.

In chapter 3, a discussion on the computational time of the model was made. It only referred to the Boussinesq-type wave module and not to the compound model including the flow through the porous media, the sediment transport and the geomorphological modules. Herein, a similar investigation was made for the final version of the compound model. Test S1.5 was chosen as a case study and it was simulated in three different PCs. The characteristics of three processors are shown in table 3.1 from where the 2, 8 and 12-cored processors were employed. In all the computations parallel computing was used. The computational domain included 771x1105 grid points. The variation of the computational time with the number of time steps for the various processors is depicted in Fig. 7.50.

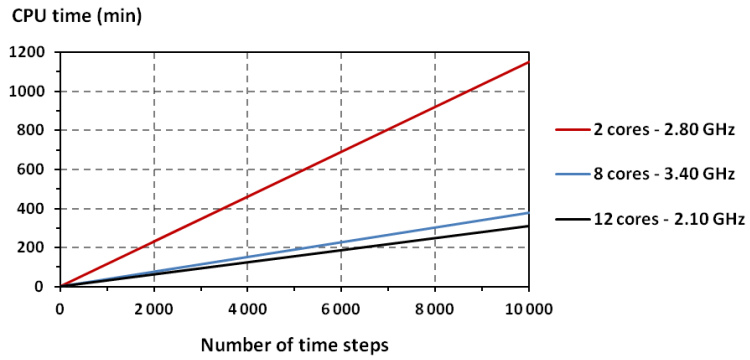

Fig. 7.50. Computational time for three different processors for 771x1105 grid points.

It can be observed that the increase of the number of cores leads to a significant decrease of the required computational time. This is mainly true for low number of cores, but as this number increases the gain in CPU time is reduced significantly. As a practical conclusion, it can be said that simulation of 5 hrs of morphological evolution in a domain of a coastal zone with dimensions 1 km x 1 km would require about 1.5-2 days of computational time on an 8-cored PC similar to the one employed herein.

In this chapter a numerical investigation of the shoreline response behind arrays of permeable submerged breakwaters was performed. The results are far from offering a detailed and well-established set of functional design rules for these coastal structures. However, some practical conclusions referring to basic design parameters have been derived for their effect on shoreline evolution. Nevertheless, a more extensive investigation, both experimental and numerical, is definitely required in order to get a deeper insight into the behavior of such coastal structures and their efficient multi-parametrical design.

References

Ahrens, J. P., and Cox, J. (1990). "Design and performance of reef breakwaters." *J. Coast. Res.*, 6 (1), 61-75.

Beji, S., and Nadaoka, K. (1996). "A formal derivation and numerical modelling of the improved Boussinesq equations for varying depth." *Ocean Eng.*, 23(8), 691-704.

Black, K., and Andrews, C. (2001). "Sandy shoreline response to offshore obstacles: Part 1. Salient and tombolo geometry and shape." *J. Coast. Res.*, Special Issue 29 Natural and Artificial Reefs for Surfing and Coastal Protection, pp. 82– 93.

Burcharth, H. F., Hawkins, S. J., Zanuttigh, B., and Lamberti, A. (2007). *Environmental design guidelines for low crested coastal structures*. Amsterdam: Elsevier, 376 pp.

Cáceres, I., Sánchez-Arcilla, A., Alsina, J.-M., González-Marco, D., and Sierra, J. P. (2005). "Coastal dynamics around a submerged barrier." Proc. Coastal Dyn. '05, A. Sanchez-Arcilla, ed., ASCE, Barcelona, Spain, pp. 1-14.

Chasten, M. A., Rosati, J. D., McCormick, J. W., and Randall, R. E. (1993). "Engineering design guidance for detached breakwaters as shoreline stabilization structure." *Tech. Rep.*, CERC-93-19, U.S. Army Engineer Waterways Experiment Station, Vicksburg, MS, U.S.A.

Dally, W. R., and Pope, J. (1986). "Detached breakwaters for shore protection." *Tech. Rep.*, CERC-86-1, U.S. Army Engineer Waterways Experiment Station, Vicksburg, MS, U.S.A.

Dean, R. (1991). "Equilibrium beach profiles: principles and applications." *J. Coast. Res.*, 7 (1), 53–84.

Gourlay, M. R. (1981). "Beach processes in the vicinity of offshore breakwaters." *Proc. 5th Australian Conf. on Coastal and Ocean Eng.*, Perth, Australia, 129-134.

Hanson, K., and Kraus, C. K. (1991). "Numerical simulation of shoreline change at Lorain, Ohio." *J. Waterw. Port Coast. Ocean Eng.*, 117 (1), 1-18.

Hsu, J. R. C., and Silvester, R. (1990). "Accretion behind single offshore breakwater." *J. Waterw. Port Coast. Ocean Eng.*, 116 (3), 362-381.

Inman, D. L., and Frautschy, J. D. (1965). "Littoral processes and the development of shorelines." *Proc., Coast. Eng.*, Santa Barbara, CA, U.S.A., pp. 511-536.

Karambas, Th., Krestenitis, I., and Koutitas, Ch. (2016). *Coastal Engineering – Shore Protection Structures*. Hellenic Academic Libraries, 156 pp. (in greek).

Koutsouvela, D. (2010). "Soft shore protection methods against coastal erosion: submerged breakwaters." Ph.D. thesis, University of the Aegean, Greece (in greek).

Koutsouvela, D., Karambas, Th. V., Avgeris, I., and Karathanassi, E. (2007). "Functional design of submerged breakwaters for coastal protection using two wave/morphological models." *Proc. Coastal Structures '07*, Venice, Italy, pp. 1205-1216.

Mohr, M. C. (1994). "Presque Isle shoreline erosion control project." *Shore and Beach*, 62 (2), 23-28.

Nir, Y. (1982). "Offshore artificial structures and their influence on the Israel and Sinai Mediterranean beaches." *Proc. 18th Int. Conf. on Coastal Engineering*, B. L. Edge, ed., Cape Town, South Africa, pp. 1837-1856.

Noble, R. M. (1978). "Coastal structures' effects on shorelines." *Proc. 16th Int. Conf. on Coastal Engineering*, ASCE, Hamburg, Germany, pp. 2069-2085.

Pilarczyk, K. W. (2003). "Design of low-crested (submerged) structures – an overview –." *6th International Conference on Coastal and Port Engineering in Developing Countries*, Colombo, Sri Lanka.

Pope, J., and Dean, J. L. (1986). "Development of design criteria for segmented breakwaters." *Proc. 20th Int. Conf. on Coastal Engineering*, B. L. Edge, ed., Taipei, Taiwan, pp. 2144-2158.

Ranasinghe, R., Hacking, N., and Evans, P. (2001). "Multi-functional artificial surf breaks: a review." *Rep.*, No. CNR 2001.015, NSW Dept. of Land and Water Conservation, Parramatta, Australia.

Ranasinghe, R., Larson, M., and Savioli, J. (2010). "Shoreline response to a single shore-parallel submerged breakwater." *Coast. Eng.*, 57 (11-12), 1006–1017.

Ranasinghe, R., and Turner, I. L. (2006). "Shoreline response to submerged structures: A review." *Coast. Eng.*, 53 (1), 65-79.

Ranasinghe, R., Turner, I. L., and Symonds, G. (2006). "Shoreline response to multi-functional artificial surfing reefs: A numerical and physical modelling study." *Coast. Eng.*, 53 (7), 589–611.

Seiji, M., Uda, T., and Tanaka, S. (1987). "Statistical study on the effect and stability of detached breakwaters." *Coastal Eng. Japan*, 30 (9), 131-141.

Suh, K., and Dalrymple, R. A. (1987). "Offshore breakwaters in laboratory and field." *J. Waterw. Port Coast. Ocean Eng.*, 113 (2), 105-121.

U.S. Army Corps of Engineers (1984). *Shore Protection Manual* (SPM), vol. I, 650 pp.

U.S. Army Corps of Engineers (2006). "Shore protection projects." *Coastal Engineering Manual* (CEM), part V, chapter 3, pp. V-3-I –V-3-110.

Zyserman, A. J., Johnson, K. H., Zanuttigh, B., and Martinelli, L. (2005). "Analysis of far field erosion induced by low crested rubble-mound structures." *Coast. Eng.*, 52 (10-11), 977–994.

Chapter 8

Conclusions and future research

8.1 Concluding remarks

The core aim of the present dissertation was to develop a numerical model that describes the morphodynamics in a sandy beach protected by an array of submerged breakwaters. In this context, laboratory experiments including a permeable submerged breakwater were also performed at the scale of a physical model. The model validation with these measurements revealed that the main scope of the thesis was achieved at a satisfactory level. In order to fulfill this overarching objective, additional intermediate objectives were also set, as described in chapter 1. Thus, the conclusions reached on way to all these objectives are presented in the following.

Coastal erosion is a global problem caused by both natural processes and human activities. However, it is also true that, in most cases, it is greatly intensified and accelerated by the latter. Thus, humanity and, in particular, coastal engineers are called to find global, as well as site-specific solutions in order to protect the vulnerable coastal zones. Coastal defense is a dynamic issue raising extensive discussions throughout the international literature. In recent years, the scientific and engineering interest has turned to the so-called "mild" protection concept, which also include the use of submerged breakwaters. Hence, the present Ph.D. thesis can be considered as part of this research field. From the literature review that was performed in the context of the thesis, as well as from some examples of submerged breakwaters that have been already constructed and monitored, a number o general conclusions can be stated:

- Submerged breakwaters are generally less effective, in technical engineering terms, than the emergent ones.
- They enable increased water renewal compared to conventional breakwaters.

- They are environmentally friendlier due to their reduced impact on the biotic and a-biotic factors of the coastal area.
- They are superior by means of aesthetics.
- They are usually of lower cost.

The efficiency of the different submerged breakwaters that have been constructed worldwide varies greatly. There have been reported cases that erosion was observed in their lee. It is true that, until nowadays, their design has been rather empirical, based on experience with conventional breakwaters (Pilarczyk, 2003). However, the significant variation of the effectiveness of the aforementioned coastal defense projects proves that the physical processes associated with submerged and emergent breakwaters can be quite different. Until now, no general, consistent and well-established set of design rules has been proposed for submerged breakwaters, with regard to the induced bed morphology evolution in their lee. Perhaps, due to the increased complexity of such a system and the multiple interacting factors at the same time, it is not even possible to derive mathematical formulations that are of broad validity. However, our understanding of the mechanisms causing erosion or accretion in the lee of a system of permeable submerged breakwaters is not yet cleared up to a level that would allow a reliable answer to the aforementioned question (Ranasinghe and Turner, 2006).

Fig. 8.1. Array of submerged breakwaters in Katerini beach, Greece (from Google, 2014).

The Greek coasts, having a total shoreline length of more than 15000 km, face significant erosion problems and the discussion about milder interventions, in terms of coastal defense projects, is on-going (Avgeris *et al*., 2004; Kontaxi and Memos, 2005; Makris *et al*., 2007; Koutsouvela, 2010; Karambas *et al*., 2012; Metallinos and Memos, 2012; Memos, 2013;

Ziros *et al*., 2014; Koftis *et al*., 2015). In this context, the first system of submerged breakwaters in Greece was constructed in Katerini beach, as shown in Fig. 8.1. Soon after the construction, accretion was observed in the leeward side of the works, followed though by intense shoreline erosion behind the gaps (Kombiadou *et al*., 2012). This behavior is another proof of the complexity of the morphological processes associated to such works and the multiple factors that have to be taken into account in their design. It is also concluded that long-term monitoring and field measurements are a necessity for supporting such mild protection projects.

With regard to the main objective of the present Ph.D. thesis the following conclusions can be drawn:

- An integrated 2DH numerical model was developed for predicting the evolution of bed morphology in the lee of a system of permeable submerged breakwaters. The model embeds enhanced nonlinearity compared to its weakly nonlinear counterparts and the sediment transport formulae that are employed are more advanced compared to other compound models relying on Boussinesq-type equations. The validation with the laboratory measurements performed in the context of the thesis showed satisfactory accuracy. The tests referred to various wave conditions, including both regular and irregular waves. Thus, it can be claimed that the presented model forms a robust tool for studying the complex hydrodynamic and morphodynamic processes related to arrays of submerged breakwaters.

- The presented tool is a compound numerical model incorporating four individual parts, namely the wave, the hydrodynamic, the sediment transport and the geomorphological modules. On the way to develop the final compound model, each of these parts was extensively validated. Thus, the model is generally capable of describing the hydrodynamic and morphological processes in coastal zones, regardless of the presence of submerged breakwaters.

- The application of the morphological acceleration factor technique, in combination with the increased power of modern computers allows practical applications of compound geomorphological models based on phase-resolving wave models. Thus, the present model can be practically applied for simulations referring to short-term morphological evolution, to the order of hours or a few days. Nevertheless, care must be taken not to exaggerate with the value of the morphological factor in order to be able to describe realistically the interaction of the wave, hydrodynamic and morphology modules.

- 3D laboratory experiments including a sandy bed in the lee of a permeable submerged breakwater were also conducted in the context of the dissertation. The morphological evolution in the entire coastal area and the shoreline response were not far from the ones theoretically expected. However, these theoretical predictions did not rely on widely accepted criteria since the latter have not been adequately verified. In all the eight scenarios considered the ratio of the structure length to its distance from the initial shoreline was about 0.87 and in all cases a salient was formed behind the breakwater. This is in accordance with Black and Andrew's (2001) general observation that the formation of a salient requires a ratio $B/S < 2.0$. In addition, the beach response index defined by Ahrens and Cox (1990) had a value of $I_s \approx 3.9$ which theoretically correspond to subdued salients (see subsection 7.1). This result was also verified by the present measurements. Black and Andrew's (2001) analytical expression would predict a salient with a non-dimensional width of approximately $X/S \approx 0.48$, while the maximum value observed in these experiments was 0.15. However, it should be mentioned that the analytical expression was derived based on measurements referring to natural reefs and not man-made rubble mound submerged breakwaters. In addition, Ranasinghe *et al*. (2001) doubted about the validity of Black and Andrew's (2001) methodology. Briefly, it can be concluded that the morphological behavior of submerged breakwaters, including the shoreline response, can be also studied in a movable-bed physical model, if care is taken for respecting the spatial and time scale laws. In particular, the morphological time scale is one of the most difficult parameters to be determined and the availability of field observations on this issue is of great importance.

- Both the laboratory experiments and their simulation by the model showed the formation of a salient in the lee of the permeable submerged breakwater. The length and width of the salient varied with the wave characteristics. Shorter waves with larger wave height resulted to more peaky salients than longer ones. In addition, regular waves led to wider salients (in the cross-shore direction) compared to the corresponding irregular test cases with the same significant wave height and peak period. In the present work, neither the laboratory nor the numerical experiments ever led to the formation of a tombolo. Pilarczyk (2003) mentioned that a tombolo may be formed behind a submerged breakwater if this is placed very close to the shoreline. However, reservations are expressed about this issue since the mass flux and the rip currents are generated too close to the shoreline transporting the sand towards the gaps (see subsection 5.2.2).

- From the numerical experiments performed it is concluded that the shoreline response to an array of submerged breakwaters depends on some core geometrical parameters of the

layout, namely the length of the structures, B, their distance from the initial shoreline, S, the gap length, G, and the porosity of the breakwaters, λ. In addition, the shoreline evolution also depends on the wave characteristics, i.e. wave height, period, angle of incidence. It can be also said that a critical design parameter is the wave transmission coefficient. However, in contrary to emergent breakwaters, these dependencies are not generally monotonic. For example, placing the breakwaters more and more close to the shoreline does not necessarily lead to an increase of the resulting salient. If the works are placed too close to the shoreline, it is possible that erosion occurs instead of accretion. Similar considerations are at play for the increase of the structure length. Therefore, it can be argued that the morphological processes governing the shoreline response to submerged and emergent structures are different because the hydrodynamic behavior of these two types of breakwaters is not the same. Due to the increased complexity of the associated processes, it is difficult to derive general design rules or simple criteria for submerged breakwaters similar to those for emergent ones (see subsection 7.1). A numerical investigation on this issue was performed in the present thesis and some diagrams were produced quantifying the shoreline evolution as a function of various design parameters. Some of the results also referred to the erosion induced behind the gaps between adjacent breakwaters. However, these results should be treated as a first indication of the effect of the various parameters and further verification with measurements, especially in the field, should follow.

On the way to fulfill the principle objectives of the specific research, some intermediate aims were set and achieved. During this procedure additional conclusions were drawn from the individual parts of the thesis. The first step was to decide the Boussinesq wave module that would form the basis of the compound model. In this context:

- ✓ The 1DH Boussinesq-type model by Karambas and Koutitas (2002) was enhanced with respect to nonlinearity. In particular, enhanced equations were derived by retaining additional terms of $O(\varepsilon^2\sigma^2)$ to the already existing of $O(1, \varepsilon, \sigma^2, \varepsilon\sigma^2)$ in the original model. Following a similar derivation a 2DH version of the equations was derived. From both mathematical analysis and numerical applications it was proven that the new model offers an improvement over its previous counterpart with respect to nonlinear dispersion under highly nonlinear conditions, e.g. close to the surf zone. The linear dispersion and shoaling characteristics of the model are very accurate up the limit of deep water, i.e. $kd = 3$, while the second-order transfer functions are predicted with a maximum error of 10% up to $kd \approx 1.16$. Briefly, it can be concluded that the derived basic Boussinesq solver forms an upgraded version of its predecessor (Karambas and Koutitas, 2002). In

addition, it was considered that the adoption of an even more highly nonlinear model, e.g. Madsen and Schäffer (1998), would go beyond the objective of the present thesis with its very complex numerical implementation.

- ✓ The basic Boussinesq-type solver was also extended to account for wave propagation over permeable beds. This implied the inclusion of an additional Darcy-Forchheimer equation for describing the flow through the porous medium. A similar extension was presented by Avgeris *et al*. (2004) based on Karambas and Koutitas (2002) Boussinesq model. However, in the present work additional terms of $O(\sigma^2)$ were retained in the aforementioned equation compared to the ones of $O(1, \varepsilon)$ that existed in the latter model. From the theoretical analysis performed, it was found that these extra terms are significant in intermediate water. In particular, the NSWE for porous media can estimate the spatial damping rate up to $kd \approx 0.5$ within a 10% error. In contrary, if terms of $O(\sigma^2)$ are also included, the aforementioned limit increases to $kd \approx 1.0$. Thus, this contribution is significant when simulating wave propagation over permeable submerged breakwaters located in intermediate waters. This theoretical result was further supported by the validation tests referring to short wave propagation (see subsection 6.3).

The next step was to incorporate a number of additional features to the basic Boussinesq solver in order to account for integrated nearshore dynamics. Some important points should be highlighted from this task:

- ➢ The wave module was extended to the surf zone by applying the eddy viscosity concept (Kennedy *et al*., 2000; Chen *et al*., 2000). This formulation was easily incorporated to the basic solver and offered good numerical stability properties. The breaking module was tested for both spilling and plunging breakers and gave results of reasonable accuracy. However, in some cases, an over-estimation of the wave height in the inner surf zone was observed.

- ➢ Extension to the swash zone was achieved by applying a modified slot technique (Madsen *et al*., 1997; Kennedy *et al*., 2000). The applied modification ensured the water mass conservation when water is above the top of the slot. Nevertheless, some small mass loss still exists when water level is below the top of the slot. In addition, bed friction and subgrid turbulent mixing were also incorporated to the model.

- ➢ Due to its nonlinear character, the Boussinesq-type model can offer an inherent estimation of the wave-induced current field, while the wave-current interaction is well-reproduced. This is a significant result since the traditional decoupled process of running

consecutively the wave and the hydrodynamic models, apart from being time-consuming, it also ignores the aforementioned interaction.

- The hydrodynamic module includes the effect of the undertow. However, it only offers estimation of its depth-averaged and near-bed values, rather than its detailed three-dimensional variation. The latter requires an extra sophisticated module for computing the turbulent mechanisms in the wave-current bottom boundary layer.

- The numerical model relies on a generalized multi-step predictor-corrector scheme. It embeds improved numerical stability properties as compared to the Adams-Bashforth-Moulton predictor-corrector scheme applied in some predecessors of the present model (Karambas and Koutitas, 2002; Karambas and Karathanassi, 2004; Memos *et al*., 2005).

- The model showed good response to an extensive validation including a number of physical wave processes such as shoaling, depth and current refraction, diffraction, breaking, run-up, overtopping, nonlinear energy transfer and interactions with the wave-induced current field. Thus, it can be argued that it forms a quite robust tool for studying the most important wave-induced nearshore phenomena.

- The computational time required for the wave model to run is not prohibitive. Indicatively, it can be said that simulation of 20 min of wave propagation in a domain of a coastal zone with dimensions 1 km x 1 km would require about 1 day of computational time.

As soon as the wave and hydrodynamic modules were developed and validated, a reliable basis was obtained for building the sediment transport and morphology modules. This process also offered some important conclusions:

- The sediment transport module uses as input the results from the Boussinesq-type wave model which is phase-resolving. Thus, significant aspects such as the wave skewness and asymmetry, wave irregularity, bound and free long waves, wave groups and nonlinear interactions are directly taken into account from the intra-wave sediment transport formulation. These features are usually excluded when combining sediment transport with phase-averaged wave models.

- The adopted sediment transport formula for the bed load incorporates quite significant phase-lag effects (Camenen and Larson, 2006, 2007). The exclusion of these unsteady effects may lead to inaccuracies in the magnitude and direction of the computed sediment transport rates. This theoretical result was also supported by a sensitivity analysis performed for the sediment transport module.

- The sediment transport module successfully describes the inception of sediment's movement. This is also due to the accurate associated criterion used which allows the estimation of the sediment transport rates even close to the threshold of movement (Camenen and Larson, 2006).

- A critical parameter for the accurate estimation of the sediment transport load was found to be the near-bottom reference concentration which affects the calculation of the suspended load. This parameter has a high degree of uncertainty, depending also on the actual reference level used each time. The model proved to be sensitive to the value of this concentration. A too high value may enhance unrealistically the domination of the suspension as the main transport mechanism. On the other hand, too low a value may lead to the under-estimation of this mechanism.

- The compound model was validated with a number of 1DH and 2DH tests involving sediment transport and bed morphology evolution. In general, it responded with reasonable accuracy with respect to the main morphological features, i.e. formation of a breaking bar, trough down-wave of the latter, swash berm, foreshore erosion, creation of a salient or tombolo. Thus, the presented model forms a reliable tool for studying the complex processes of coastal morphology evolution.

- As already mentioned, the morphological accelerator factor technique proved to be an effective method for studying 2DH short-term changes of bed morphology. Indicatively, it can be said that simulation of 1hour of real time morphological evolution in a domain of a coastal zone with dimensions 1 km x 1 km would require about 3 hours of computational time.

The compound model was also extended to account for porous beds. The last step of the dissertation included a number of numerical experiments referring to the shoreline response to an array of permeable submerged breakwaters. In particular, the effect of various important design parameters on the shoreline evolution was investigated. As mentioned above, a number of diagrams were produced to express some features of the shoreline as a function of the aforementioned parameters. Therefore, some additional conclusions can be reached:

- The salient width, X, was found to be a function of the breakwater length, B. However, in contrary to emergent breakwaters, this function is not monotonically increasing. In particular, assuming a constant distance from the breakwaters to the initial shoreline, S, the non-dimensional width X/S increased with the ratio B/S up to approximately the value 0.90 of the latter. Beyond this limit, a weak decrease was observed, up to approximately $B/S \approx 2.0$. Further increase of B/S results to a further increase of X/S,

but again the oscillating behavior seemed to continue beyond $B/S \approx 3.0$. A similar behavior was observed, more or less, for all the wave angles considered. An explanation of this behavior is presented in subsection 7.2.1.

- The salient width was also found to be a function of the distance from the breakwaters to the initial shoreline. In particular, assuming a constant breakwaters' length, the non-dimensional width X/S increased with the ratio B/S up to approximately $B/S \approx 0.90$. Beyond this limit, a further onshore movement of the structures resulted to a reduction of the non-dimensional salient width. This behaviour may be attributed to the suppression of the two vortices behind the structures and their merging with the formed rip currents, a mechanism which counteracts the creation of a salient. This procedure may even result to weak erosion behind the breakwaters. For shore-normal wave incidence the ratio X/S remained practically independent of B/S for a further increase of the latter. However, under oblique wave incidence, the former ratio increased for values of the latter greater than $B/S \approx 1.20$. Comparison between Figs 7.17 and 7.23 reveals that X/S is also a function of the individual values of B and S and not only of their ratio.

- Assuming constant values for B and S and shore-normal wave incidence, the non-dimensional salient width, X/S, was found to be a decreasing function of the non-dimensional gap length, G/B, up to a value approximately 0.45 of the latter. Beyond this limit, the ratio X/S seemed independent of G/B. On the other hand, under oblique wave incidence, an increase of the salient width was observed up to $G/B \approx 0.30$, followed by a decrease up to $G/B \approx 0.40 \div 0.45$, and then a further, weaker, increase.

- Increase of the porosity of the breakwaters, λ, up to a value of about 0.40, resulted to an increase of the salient width. Beyond this value, the ratio X/S appeared to be independent of the porosity for shore-normal waves. On the other hand, for oblique incidence, an oscillating behavior was observed around this value. In overall, λ = 0.40 seemed to be the optimal value for the design of submerged breakwaters, with respect to beach accretion. In addition, the increase of porosity resulted to enhanced erosion behind the gaps between the breakwaters.

- The effect of the wave characteristics was also investigated. In overall, the non-dimensional salient width X/L was found to be an increasing function of the non-dimensional length, B/L, where L is the wavelength at the position of the works, up to approximately a value of 1.70 of the latter. This behavior was monotonic for normal incidence, but not for oblique one. Beyond this limit, the ratio X/L appeared to be practically invariant for normal, or almost normal, wave incidence, but decreasing for

increased wave angles. Furthermore, it was concluded that lower deep water wave steepness favors the shoreline accretion. The same is true for the wave nonlinearity.

- In general, the observed values of the non-dimensional salient width X/S were lower compared to the expected ones for a corresponding layout including emergent breakwaters. Indeed, some of the considered geometric layouts would be expected to even result to the formation of tombolos ($X/S = 1.0$), if emergent breakwaters replaced the submerged ones. In addition, the shoreline erosion behind the gaps was investigated. It appeared that an optimal design of an array of submerged breakwaters implies that the gap between two adjacent breakwaters is 40-50% of the wavelength, L. However, this only refers to the induced erosion at the shore facing the gaps, while the desired accretion behind the breakwaters should be also taken into account (see 3rd bullet). In addition, as already mentioned, only layouts with $G \leq 0.8L$ have been considered.

The present subsection summarizes the main conclusions reached during this research. Some additional conclusions, of lower importance, can be found in the last subsections of each chapter which include the associated discussions.

8.2 Future research

This dissertation ends with some suggestions for future research related to the topic discussed herein. At first, the performance of additional 3D laboratory experiments involving submerged breakwaters on movable beds would be of great value. Efforts have focused on developing numerical tools for studying the behavior of such a coastal defense system with respect to the morphodynamics. However, there is a significant lack of measurements referring to the bed morphology evolution. In the context of the present thesis, some original experiments have been performed, but much more are needed. Similar experiments would both help in deriving some direct conclusions from the observations, and also obtaining datasets for more reliable validation of numerical models. However, the experiments should be performed in large wave tanks in order to restrict the associated scale effects. In addition, modelling of oblique wave incidence is also important. In this case, large wave tank dimensions are required so that there is enough space for the wave-induced longshore current to be established. Moreover, a recirculation system for the latter is essential for establishing a steady state (Visser, 1991).

The performance of field measurements is of even greater importance. There is not a great number of coastal defense projects worldwide which include submerged breakwaters. Thus, there are restricted options for performing in situ measurements referring to bed morphology.

However, monitoring of the performance of some of them has been reported (Funakoshi *et al*., 1994; Dean *et al*., 1997; Jackson *et al*., 2002), also in Greece (Kombiadou *et al*., 2012). Similar measurements referring to the bed elevation in the lee of submerged breakwaters or the shoreline evolution can offer valuable information for a direct evaluation of the efficiency of the design and also the validation of numerical models with data in natural scale.

In addition to the requirement for extra measurements, the research effort could also focus on a number of issues related to improving the presented numerical model. At first, the basic Boussinesq equations can be extended to include additional terms of $O(\sigma^4, \varepsilon\sigma^4)$, similarly to other higher-order models (Madsen and Schäffer, 1998; Gobbi *et al*., 2000). This extension is expected to significantly improve the internal kinematics of the model (Gobbi *et al*., 2000), as well as its nonlinear properties. However, this modification will alter the basic solver of the wave module since a pentadiagonal algebraic system will have to be solved. A generalized Thomas algorithm (Fletcher, 1991) can be employed for accomplishing the solution. Furthermore, including higher order nonlinear terms will add to the mathematical complexity of the equations and, most probably, it will also intensify the problems related to the nonlinear numerical stability. An additional issue that needs some investigation refers to the nonlinear shoaling properties of the equations. A Fourier analysis, similar to the one performed herein for linear shoaling, can be applied to examine this issue, which can be of importance in the near breaking zone.

Another issue that future research could focus on is the vertical vorticity transport. As already mentioned in chapter 3, the order of the embedded vertical vorticity is not exactly consistent with the order of the wave motion as described by the Boussinesq equations. This inconsistency could be treated by retaining higher-order terms in the series expansion of the water particle velocity during the derivation procedure (Chen, 2006). The additional terms that will be introduced following this method are usually small in the surf zone, because the values of σ^2 are typically small there. However, they could be significant for the accurate computation of the breaking-induced nearshore circulation, as vertical vorticity generated by wave breaking can be transported outside the surf zone to deeper water.

The source function technique for the generation of the waves is another issue that is open for improvements. It has been formally derived for the linearized model version. However, due to the nonlinearity of the wave equations, spurious free higher-order waves will be unintentionally introduced. Thus, higher-order corrections should be used based on the theoretical transfer functions associated to Boussinesq equations (see also Madsen and Sørensen, 1993).

With regard to the undertow velocity, the present model accounts for its depth-averaged and near bottom values. However, future efforts could focus on incorporating in the model a

detailed computation of the variation of the undertow velocity over depth. This would further improve the sediment transport estimations. This feature could be added by computing the vertical variation of shear stress and the near bed streaming (Deigaard *et al*., 1988; Rakha *et al*., 1997; Rakha, 1998). The latter, requires an additional module for describing the mechanisms in the turbulent wave-current bottom boundary layer (Brøker and Fredsøe, 1984; Fredsøe, 1984; Fredsøe *et al*., 1985).

Research may also be orientated to numerical issues. For example a staggered Arakawa C-grid would offer better stability and higher accuracy. In addition, a flux-formulation instead of depth-averaged velocities would be more convenient for solving the Boussinesq equations in their conservative form (Abbott *et al*., 1978; Madsen *et al*., 1997). Furthermore, in order to resolve the highly nonlinear phenomena in the surf zone a much finer grid is required compared to deep water. This onshore refinement of the grid makes the finite difference formulations less attractive, in terms of computational time. Thus, it would be of interest to also examine finite element or finite volume formulations using unstructured meshes or curvilinear coordinate systems (Shi *et al*., 2001; Sørensen *et al*., 2004; Roeber and Cheung, 2012; Kirby *et al*., 2013). These unstructured meshes can offer higher degree of flexibility when handling computational domains with complex boundaries. Finally, a comparison between different modelling techniques for the simulation of wave runup and run-down could optimize the associated choice (Brocchini *et al*., 2002; Militello *et al*., 2004).

Another point of interest for future investigation refers to the vertical eddy diffusivity of sediments, ε_v. In the present thesis, a constant value over depth was considered for this coefficient, although the energy dissipation due to wave breaking and wave-current bottom friction were taken into account. Thus, it would be interesting to apply a more sophisticated approach that relates the eddy diffusivity to the turbulent kinetic energy by implementing a (k - ε) model (Deigaard *et al*., 1986; Rakha *et al*., 1997; Rakha, 1998).

The developed model refers only to non-cohesive material. However, it could be extended to also account for cohesive sediments. In order to achieve this, the sediment transport module should be considered as consisting of a "water-column" and an "in-the-bed" module. The former is related to the solution of an AD-equation which takes into account the organic matter. In the latter, the bed is considered to be consisting of multiple layers of different levels of density and consolidation (Mehta *et al*., 1989). The two modules are connected through empirical source/sink terms depending on whether the local hydrodynamic conditions cause the bed to become eroded or allow deposition to occur.

With regard to the model's extension to porous beds, some additional issues require further investigation. At first, it would be useful to apply a linear shoaling and a nonlinear analysis of the extended equations for permeable bottoms. This procedure will be similar to the Fourier

analysis performed in chapter 2 for impermeable beds. In addition, in order to further enhance the dispersive and nonlinear characteristics of the wave module, terms of $O(\varepsilon\sigma^2)$ or higher can be retained in Darcy-Forchheimer equation. Also, by extending to porous beds the above discussion for the conservation of the vertical vorticity, additional terms should be also included in this latter equation, following Chen (2006).

It would be also of interest to investigate the effect of additional design parameters, i.e. free board, crest width, slopes, etc., on the shoreline response to submerged breakwaters. This can be studied by conducting more numerical experiments. In addition, as already mentioned, only gaps with length $G \leq 0.8L$ were considered in the present dissertation. However, for a system of emergent breakwaters, a tombolo may be expected only if $G \geq L$ (Dally and Pope, 1986). Hence, larger gaps with lengths up to $(1.0 \div 2.0)L$ should be also studied.

Finally, future research should focus on exploiting the powerful recently developed GPU (Graphics Processing Unit) technology. This process requires modifications of the algorithm and the source code of the presented model. However, it is well worth the effort, since the GPU technique may reduce impressively the CPU time when introduced to Boussinesq modelling. Indicatively, speed-up factors even higher than 100 have been reported for similar 2DH models in the international literature as compared to 4-6 for a 12-cored computer using the conventional technology.

References

Abbott, M. B., Petersen, H. M., and Skovgaard, O. (1978). "On the numerical modelling of short waves in shallow water." *J. Hydraul. Res*., 16 (3), 173-203.

Ahrens, J. P., and Cox, J. (1990). "Design and performance of reef breakwaters." *J. Coast. Res.*, 6 (1), 61-75.

Avgeris, I., Karambas, Th. V., and Prinos, P. (2004). "Boussinesq modeling of wave interaction with porous submerged breakwaters." *Proc. 29th Int. Conf. on Coastal Eng.*, J. M. Smith, ed., Lisbon, Portugal, 604-616.

Black, K., and Andrews, C. (2001). "Sandy shoreline response to offshore obstacles: Part 1. Salient and tombolo geometry and shape." *J. Coast. Res.*, Special Issue 29 Natural and Artificial Reefs for Surfing and Coastal Protection, pp. 82– 93.

Brocchini, M., Svendsen, I. A., Prasad, R. S., and Belloti, G. (2002). "A comparison of two different types of shoreline boundary conditions." *Comput. Methods Appl. Mech. Engrg*., 191 (39-40), 4475-4496).

Brøker, I., and Fredsøe, J. (1984). "Resulting sediment transport due to non-linear effects in waves." *Progr. Rep.*, 61, ISVA (Inst. Hydrodyn. Hydraul. Eng.), Technical University, Lyngby, Denmark, pp. 55-66.

Camenen, B., and Larson, M. (2006). "Phase-lag effects in sheet flow transport." *Coast. Eng.*, 53 (5-6), 531–542.

Camenen, B., and Larson, M. (2007). "A unified sediment transport formulation for coastal inlet application." *Tech. rep. ERDC/CHL CR-07-1*, U.S. Army Engineer Research and Development Center, Vicksburg, MS, U.S.A., 231 pp.

Chen, Q. (2006). "Fully nonlinear Boussinesq-type equations for waves and currents over porous beds." *J. Eng. Mech.*, 132 (2), 220-230.

Chen, Q., Kirby, J. T., Dalrymple, R. A., Kennedy, A. B., and Chawla, A. (2000). "Boussinesq modeling of wave transformation, breaking and runup. II: 2D." *J. Waterw. Port Coast. Ocean Eng*., 126 (1), 48-56.

Dally, W. R., and Pope, J. (1986). "Detached breakwaters for shore protection." *Tech. Rep.*, CERC-86-1, U.S. Army Engineer Waterways Experiment Station, Vicksburg, MS, U.S.A.

Dean, R. G., Chen, R., and Browder, A. E. (1997). "Full scale monitoring study of a submerged breakwater." *Coast. Eng.*, 29 (3-4), pp. 291– 315.

Deigaard, R., Fredsøe, J., and Brøker Hedegaard, I. (1986). "Suspended sediment in the surf zone." *J. Waterw. Port Coast. Ocean Eng.*, 112 (1), 115-128.

Deigaard, R., Fredsøe, J., Brøker Hedegaard, I., Zyserman, J., and Andersen, O. H. (1988). "Littoral drift model for natural environments." *Proc. 21st Int. Conf. on Coastal Engineering*, ASCE, Malaga, Spain, pp. 1603-1617.

Fletcher, C. A. J. (1991). *Computational techniques for fluid dynamics. Volume 1: Fundamental and general techniques.* 2nd edition, Springer Series in Computational Physics, Springer, xiv+401 pp.

Fredsøe, J. (1984). "Turbulent boundary layer in wave-current motion." *J. Hydraul. Eng.*, 110 (8), 1103-1120.

Fredsøe, J., Andersen, O. H., and Silberg, S. (1985). "Distribution of suspended sediment in large waves." *J. Waterw. Port Coast. Ocean Eng.*, 111 (6), 1041-1059.

Funakoshi, H., Shiozawa, T., Tadokoro, T., and Tsuda, S. (1994). "Drifting characteristics of littoral sand around submerged breakwater." *Proc. Int. Conf. on Hydro-technical Eng. for Port and Harbor Construction*, Yokosuka, Japan, pp. 1157–1178.

Gobbi, M. F., Kirby, J. T., and Wei, G. (2000). "A fully nonlinear Boussinesq model for surface waves. Part 2. Extension to $O(kh)^4$." *J. Fluid Mech.*, 405, 181-210.

Karambas, Th. V., and Karathanassi, E. K. (2004). "Longshore sediment transport by nonlinear waves and currents." *J. Waterw. Port Coast. Ocean Eng.*, 130(6), 277-286.

Karambas, Th., Koftis, Ch., Koutandos, E., and Prinos, P. (2012). "Innovative submerged structures/vegetation effects on coastal erosion: numerical modeling of hydro-morphological processes." *Proc. 22nd Int. Offshore and Polar Eng. Conf.*, Rhodes, Greece, June 17-22, PP. 1328-1334.

Karambas, Th. V., and Koutitas, C. (2002). "Surf and swash zone morphology evolution induced by nonlinear waves." *J. Waterway, Port, Coastal, Ocean Eng.*, 10.1061/(ASCE)0733-950X(2002)128:3(102), 102-113.

Kennedy, A. B., Chen, Q., Kirby, J. T., and Dalrymple, R. A. (2000). "Boussinesq modeling of wave transformation, breaking and runup. I: 1D." *J. Waterw. Port Coast. Ocean Eng*., 126 (1), 39-47.

Kirby, J. T., Shi, F., Tehranirad, B., Harris, J. C., and Grilli, S. T. (2013). "Dispersive tsunami waves in the ocean: Model equations and sensitivity to dispersion and Coriolis effects." *Ocean Model*., 62, 39-55.

Koftis, Th., Prinos, P., Galiatsatou, P., and Karambas, Th. (2015). "An integrated methodological approach for the upgrading of coastal structures due to climate change effects." *E-proceedings of the 36th IAHR World Congress*, The Hague, the Netherlands, 28 June - 3 July, 2015.

Kombiadou K., Krestenitis Y. N., Baltikas V., and Kalantzi G. (2012). "Coastal Erosion Problems in Katerini: Methods and Measures." *Protection and Restoration of the Environment XI*, Thessaloniki, Greece, July 3-6, pp. 758-767.

Kontaxi, Ch., and Memos, C. (2005). "Submerged breakwaters as artificial habitats." *Proc. XXXI IAHR Cong.*, Seoul, South Korea, pp. 3967-3975.

Koutsouvela, D. (2010). "Soft shore protection methods against coastal erosion: submerged breakwaters." Ph.D. thesis, University of the Aegean, Greece (in greek).

Madsen, P. A., and Schäffer, H. A. (1998). "Higher-order Boussinesq-type equations for surface gravity waves: derivation and analysis." *Phil. Trans. R. Soc. Lond. A*, 356(1749), 3123-3184.

Madsen, P. A., and Sørensen, O. R. (1993). "Bound waves and triad interactions in shallow water." *Ocean Eng*., 20(4), 359-388.

Madsen, P. A., Sørensen, O. R., and Schäffer, H. A. (1997). "Surf zone dynamics simulated by a Boussinesq type model. Part I. Model description and cross-shore motion of regular waves." *Coast. Eng*., 32 (4), 255-287.

Makris, Ch., Avgeris, I., and Memos, C. "Hydraulic Behaviour of Submerged Breakwaters: a Case Study." *Proc. 4th PDCE Conference*, Black Sea Coastal Association (BSCA), Varna, Bulgaria.

Mehta, A. J., Hayter, E. J., Parker, W. R., Krone, R. B., and Teeter, A. M. (1989). "Cohesive Sediment Transport. I: Process Description." *J. Hydraul. Eng.*, 115 (8), 1076-1093.

Memos, C. (2013). "Submerged Coastal Structures: Overview of Some Recent Results." *35th IAHR World Congress*, 8-13 September, Chengdu, China (Invited Lecture).

Memos, C. D., Karambas, Th. V., and Avgeris, I. (2005). "Irregular wave transformation in the nearshore zone: experimental investigations and comparison with a higher order Boussinesq model." *Ocean Eng*., 32 (11-12), 1465-1485.

Metallinos, A. S., and Memos, C. D. (2012). "Wave-induced kinematics inside submerged porous structures." *J. Hydraul. Res*., 50 (4), 388-394.

Militello, A., Reed, C. W., Zundel, A. K., and Kraus., N. C. (2004). "Two-Dimensional Depth-Averaged circulation model M2D: version 2.0, Report 1, technical documentation and user's guide." US Army Corps of Engineers, ERDC/CHL TR-04-2.

Pilarczyk, K. W. (2003). "Design of low-crested (submerged) structures – an overview –." *6th International Conference on Coastal and Port Engineering in Developing Countries*, Colombo, Sri Lanka.

Rakha, K. A. (1998). "A Quasi-3D phase-resolving hydrodynamic and sediment transport model." *Coast. Eng*., 34 (3-4), 277–311.

Rakha, K. A., Deigaard, R., and Brøker, I. (1997). "A phase-resolving cross-shore transport model for beach evolution." *Coast. Eng.*, 31 (1-4), 231-261.

Ranasinghe, R., Hacking, N., and Evans, P. (2001). "Multi-functional artificial surf breaks: a review." *Rep*., No. CNR 2001.015, NSW Dept. of Land and Water Conservation, Parramatta, Australia.

Ranasinghe, R., and Turner, I. L. (2006). "Shoreline response to submerged structures: A review." *Coast. Eng.*, 53 (1), 65-79.

Roeber, V., and Cheung, K. F. (2012). "Boussinesq-type model for energetic breaking waves in fringing reef environments." *Coast. Eng*., 70, 1-20.

Shi, F., Dalrymple, R. A., Kirby, J. T., Chen, Q., and Kennedy, A. B. (2001). "A fully nonlinear Boussinesq model in generalized curvilinear coordinates." *Coast. Eng.*, 42(4), 337–358.

Sørensen, O. R., Schäffer, H. A., and Sørensen, L. S. (2004). "Boussinesq-type modelling using an unstructured finite element technique." *Coast. Eng*., 50 (4), 181-198.

Visser, P. J. (1991). "Laboratory measurements of uniform longshore currents." *Coast. Eng.*, 15 (5-6), 563-593.

Ziros, A., Mandelou, M., and Memos, C. (2014). "Velocity measurements over a submerged natural breakwater at Sounion area." *Proc. 6th National Conference of Management and Improvement of Coastal Zone*, Athens, Greece, 24-27 November, pp. 33-42 (in greek).